Springer Proceedings in Physics 297

Olena Fesenko
Leonid Yatsenko *Editors*

Nanoelectronics, Nanooptics, Nanochemistry and Nanobiotechnology, and Their Applications

Selected Proceedings of the 10th International Conference on Nanotechnologies and Nanomaterials (NANO2022), 25–27 August 2022, Ukraine

Springer

Springer Proceedings in Physics

Volume 297

Indexed by Scopus

The series Springer Proceedings in Physics, founded in 1984, is devoted to timely reports of state-of-the-art developments in physics and related sciences. Typically based on material presented at conferences, workshops and similar scientific meetings, volumes published in this series will constitute a comprehensive up to date source of reference on a field or subfield of relevance in contemporary physics. Proposals must include the following:

- Name, place and date of the scientific meeting
- A link to the committees (local organization, international advisors etc.)
- Scientific description of the meeting
- List of invited/plenary speakers
- An estimate of the planned proceedings book parameters (number of pages/ articles, requested number of bulk copies, submission deadline).

Please contact:

For Americas and Europe: Dr. Zachary Evenson; zachary.evenson@springer.com
For Asia, Australia and New Zealand: Dr. Loyola DSilva; loyola.dsilva@springer.com

Olena Fesenko · Leonid Yatsenko
Editors

Nanoelectronics, Nanooptics, Nanochemistry and Nanobiotechnology, and Their Applications

Selected Proceedings of the 10th International Conference on Nanotechnologies and Nanomaterials (NANO2022), 25–27 August 2022, Ukraine

Springer

Editors
Olena Fesenko
Institute of Physics
National Academy of Sciences of Ukraine
Kyiv, Ukraine

Leonid Yatsenko
Institute of Physics
National Academy of Sciences of Ukraine
Kyiv, Ukraine

ISSN 0930-8989 ISSN 1867-4941 (electronic)
Springer Proceedings in Physics
ISBN 978-3-031-42707-7 ISBN 978-3-031-42708-4 (eBook)
https://doi.org/10.1007/978-3-031-42708-4

This Springer imprint is published by the registered company Springer Nature Switzerland AG
The registered company address is: Gewerbestrasse 11, 6330 Cham, Switzerland

Paper in this product is recyclable.

Contents

Contributors

Taniya Rose Abraham School of Energy Materials, Mahatma Gandhi University, Kottayam, Kerala, India

O. M. Alekseev Taras Shevchenko National University of Kyiv, Kyiv, Ukraine

M. A. Alieksandrov Taras Shevchenko National University of Kyiv, Kyiv, Ukraine

V. L. Andriichuk Institute of Physics, NAS of Ukraine, Kyiv, Ukraine

D. A. Andrusenko Taras Shevchenko National University of Kyiv, Kyiv, Ukraine

V. A. Barbash National Technical University of Ukraine "Igor Sikorsky Kyiv Polytechnic Institute", Kyiv, Ukraine

Aleksandra Bazan-Wozniak Faculty of Chemistry, Adam Mickiewicz University in Poznań, Poznań, Poland

M. V. Borysenko Chuiko Institute of Surface Chemistry, National Academy of Sciences of Ukraine, Kyiv, Ukraine

A. V. Brytan Physics Faculty, Taras Shevchenko National University of Kyiv, Kyiv, Ukraine

T. O. Busko Taras Shevchenko National University of Kyiv, Kyiv, Ukraine

O. O. Chumak Institute of Physics, NAS of Ukraine, Kyiv, Ukraine

O. O. Dan'kiv Department of Physics and Information Systems, Drohobych Ivan Franko State Padagogical University, Drohobych, Ukraine

Zbigniew Dendzik Faculty of Science and Technology, University of Silesia in Katowice, Chorzów, Poland

L. A. Derzhypolska Institute of Physics, NAS of Ukraine, Kyiv, Ukraine

A. G. Derzhypolsky Institute of Physics, NAS of Ukraine, Kyiv, Ukraine

R. V. Dinzhos V.O. Sukhomlynskyi Mykolaiv National University, Mykolayiv, Ukraine

V. E. Diyuk Taras Shevchenko National University of Kyiv, Kyiv, Ukraine

O. P. Dmytrenko Taras Shevchenko National University of Kyiv, Kyiv, Ukraine

Tetiana Dontsova Igor Sikorsky Kyiv Polytechnic Institute, Kyiv, Ukraine

I. Doycho Odesa I.I. Mechnikov National University, Odesa, Ukraine

Z. A. Duriagina Department of Materials Science and Engineering, Lviv Polytechnic National University, Lviv, Ukraine;
Department of Materials Engineering, The John Paul II Catholic University of Lublin, Lublin, Poland

A. G. Dyachenko Chuiko Institute of Surface Chemistry, National Academy of Sciences of Ukraine, Kyiv, Ukraine;
Institute of Physical Chemistry, Polish Academy of Sciences, Warsaw, Poland

L. Filevska Odesa I.I. Mechnikov National University, Odesa, Ukraine;
Department of Experimental Physics, Wrocław University of Science and Technology, Wrocław, Poland

S. V. Gaidai Taras Shevchenko National University of Kyiv, Kyiv, Ukraine

I. Ye. Galstian G. V. Kurdyumov Institute for Metal Physics of the N.A.S. of Ukraine, Kyiv, Ukraine;
Institute for Solid State Research, Leibniz IFW Dresde, Dresden, Germany

A. M. Gaponov Taras Shevchenko National University of Kyiv, Kyiv, Ukraine

Olena Gnatko Dnipro, Ukraine

A. M. Goltsev Institute for Problems of Cryobiology and Cryomedicine, NAS of Ukraine, Kharkiv, Ukraine

O. V. Goncharuk National Technical University of Ukraine, Igor Sikorsky Kyiv Polytechnic Institute, Kyiv, Ukraine

Krzysztof Gorny Faculty of Science and Technology, University of Silesia in Katowice, Chorzów, Poland

V. Grinevych Department of Experimental Physics, Wrocław University of Science and Technology, Wrocław, Poland

S. V. Gryn Taras Shevchenko National University of Kyiv, Kyiv, Ukraine

Anna Gusak Igor Sikorsky Kyiv Polytechnic Institute, Kyiv, Ukraine

O. V. Ischenko Taras Shevchenko National University of Kyiv, Kyiv, Ukraine

O. D. Kachkovsky Institute of Bioorganic Chemistry and Petrochemistry, National Academy of Sciences, Kyiv, Ukraine

D. S. Kamenskyh V.P. Kukhar Institute of Bioorganic Chemistry and Petrochemistry of National Academy of Sciences of Ukraine, Kyiv, Ukraine

V. M. Khodakovskiy Institute of Physics, NAS of Ukraine, Kyiv, Ukraine

Iryna Kosogina Kyiv, Ukraine

Mykhaylo Kotyk National Technical University of Ukraine "Igor Sikorsky Kyiv Polytechnic Institute", Kyiv, Ukraine

V. I. Kovalchuk Taras Shevchenko National University of Kyiv, Kyiv, Ukraine

Ihor Kovalenko Dnipro, Ukraine

T. M. Kovbasiuk Department of Materials Science and Engineering, Lviv Polytechnic National University, Lviv, Ukraine

I. G. Kovzun F.D.Ovcharenko Institute of Biocolloidal Chemistry of NAS of Ukraine, Kyiv, Ukraine

D. P. Koziarskyi Department of Electronics and Power Engineering, Yuriy Fedkovych Chernivtsi National University, Chernivtsi, Ukraine

I. P. Koziarskyi Department of Electronics and Power Engineering, Yuriy Fedkovych Chernivtsi National University, Chernivtsi, Ukraine

Grigorii Krymets Igor Sikorsky Kyiv Polytechnic Institute, Kyiv, Ukraine

M. P. Kulish Taras Shevchenko National University of Kyiv, Kyiv, Ukraine

V. V. Kulyk Department of Materials Science and Engineering, Lviv Polytechnic National University, Lviv, Ukraine

M. O. Kumeda Sumy State University, Sumy, Ukraine

O. V. Kuzyk Department of Physics and Information Systems, Drohobych Ivan Franko State Padagogical University, Drohobych, Ukraine

M. M. Lazarenko Taras Shevchenko National University of Kyiv, Kyiv, Ukraine

E. G. Len G. V. Kurdyumov Institute for Metal Physics of the N.A.S. of Ukraine, Kyiv, Ukraine;
Kyiv Academic University, N.A.S. and M.E.S. of Ukraine, Kyiv, Ukraine

Ya. Lepikh Odesa I.I. Mechnikov National University, Odesa, Ukraine

Frolova Liliya Ukrainian State University of Chemical Technology, Dnipro, Ukraine

V. V. Lisnyak Taras Shevchenko National University of Kyiv, Kyiv, Ukraine

Marta Litynska Igor Sikorsky Kyiv Polytechnic Institute, Kyiv, Ukraine

E. A. Lysenkov Petro Mohyla Black Sea National University, Mykolayiv, Ukraine

P. Ya. Lyutyy Department of Materials Science and Engineering, Lviv Polytechnic National University, Lviv, Ukraine

E. V. Maistruk Department of Electronics and Power Engineering, Yuriy Fedkovych Chernivtsi National University, Chernivtsi, Ukraine

Skiba Margarita Dnipro, Ukraine

I. V. Matsniev Institute of Physics, NAS of Ukraine, Kyiv, Ukraine

O. V. Melnychuk V.P. Kukhar Institute of Bioorganic Chemistry and Petrochemistry of National Academy of Sciences of Ukraine, Kyiv, Ukraine;
National Technical University of Ukraine "Igor Sikorskyi Kyiv Polytechnic Institute", Kyiv, Ukraine

O. V. Mischanchuk Chuiko Institute of Surface Chemistry, National Academy of Sciences of Ukraine, Kyiv, Ukraine

A. I. Misiura Taras Shevchenko National University of Kyiv, Kyiv, Ukraine

A. I. Momot Taras Shevchenko National University of Kyiv, Kyiv, Ukraine

H. Yu. Mykhailova G. V. Kurdyumov Institute for Metal Physics of the N.A.S. of Ukraine, Kyiv, Ukraine

V. D. Myshak Institute of Macromolecular Chemistry of the National Academy of Sciences of Ukraine, Kyiv, Ukraine

S. G. Nedilko Taras Shevchenko National University of Kyiv, Kyiv, Ukraine

A. M. Negriyko Institute of Physics, NAS of Ukraine, Kyiv, Ukraine

V. B. Neimash Institute of Physics, National Academy of Sciences, Kyiv, Ukraine

Olga Niemiec Institute of Physical Chemistry, Polish Academy of Sciences, Warsaw, Poland

O. M. Nikipelova Engineering and Technology Institute "Biotechnika" of NAAS of Ukraine, Khlibodarske, Odes'ka Oblast, Ukraine;
Odessa State Environmental University, Odessa, Ukraine

T. Yu. Nikolaienko Taras Shevchenko National University of Kyiv, Kyiv, Ukraine

B. O. Nizhnik V.P. Kukhar Institute of Bioorganic Chemistry and Petrochemistry of National Academy of Sciences of Ukraine, Kyiv, Ukraine;
National Technical University of Ukraine "Igor Sikorskyi Kyiv Polytechnic Institute", Kyiv, Ukraine

S. Nowak Department of Biotechnology, Institute of Biology and Biotechnology, College of Natural Sciences, University of Rzeszow, Rzeszow, Poland

Sergeyeva Olga Ukrainian State University of Chemical Technology, Dnipro, Ukraine

A. P. Onanko Taras Shevchenko National University of Kyiv, Kyiv, Ukraine

A. V. Panko F.D.Ovcharenko Institute of Biocolloidal Chemistry of NAS of Ukraine, Kyiv, Ukraine

L. K. Patrylak V.P. Kukhar Institute of Bioorganic Chemistry and Petrochemistry of National Academy of Sciences of Ukraine, Kyiv, Ukraine;
National Technical University of Ukraine "Igor Sikorskyi Kyiv Polytechnic Institute", Kyiv, Ukraine

O. L. Pavlenko Taras Shevchenko National University of Kyiv, Kyiv, Ukraine

O. O. Perederiy Institute of Physics, NAS of Ukraine, Kyiv, Ukraine

O. P. Pertko V.P. Kukhar Institute of Bioorganic Chemistry and Petrochemistry of National Academy of Sciences of Ukraine, Kyiv, Ukraine

T. M. Pinchuk-Rugal Taras Shevchenko National University of Kyiv, Kyiv, Ukraine

Serhii I. Pokutnii Chuiko Institute of Surface Chemistry of National Academy of Sciences of Ukraine, Kyiv, Ukraine;
Institute of Physics of National Academy of Sciences of Ukraine, Kyiv, Ukraine

Ruslan Politanskyi Yuriy Fedkovych Chernivtsi National University, Chernivtsi, Ukraine

V. M. Popruzhko Taras Shevchenko National University of Kyiv, Kyiv, Ukraine

V. A. Povazhnyi V.P. Kukhar Institute of Bioorganic Chemistry and Petrochemistry of National Academy of Sciences of Ukraine, Kyiv, Ukraine

V. A. Prokopenko F.D.Ovcharenko Institute of Biocolloidal Chemistry of NAS of Ukraine, Kyiv, Ukraine;
National Technical University of Ukraine «KPI», Kyiv, Ukraine

O. V. Pryhunova Taras Shevchenko National University of Kyiv, Kyiv, Ukraine

Przemyslaw Raczynski Faculty of Science and Technology, University of Silesia in Katowice, Chorzów, Poland

M. Romerowicz-Misielak Department of Biotechnology, Institute of Biology and Biotechnology, College of Natural Sciences, University of Rzeszow, Rzeszow, Poland

E. G. Rudnikov Taras Shevchenko National University of Kyiv, Kyiv, Ukraine

Yurii Rudyak I. Horbachevsky Ternopil National Medical University, Ternopil, Ukraine

E. Rysiakiewicz-Pasek Department of Experimental Physics, Wrocław University of Science and Technology, Wrocław, Poland

V. P. Scherbatskyi Taras Shevchenko National University of Kyiv, Kyiv, Ukraine

M. Ya. Shevchenko G. V. Kurdyumov Institute for Metal Physics of the N.A.S. of Ukraine, Kyiv, Ukraine

Margarita Skiba Ukrainian State University of Chemical Technology, Dnipro, Ukraine

A. O. Sobchuk Taras Shevchenko National University of Kyiv, Kyiv, Ukraine

L. V. Stepanyuk Institute for Problems of Cryobiology and Cryomedicine, NAS of Ukraine, Kharkiv, Ukraine

A. I. Stolyarchuk Department of Physics and Information Systems, Drohobych Ivan Franko State Padagogical University, Drohobych, Ukraine

I. D. Stolyarchuk Department of Physics and Information Systems, Drohobych Ivan Franko State Padagogical University, Drohobych, Ukraine

L. B. Sukhodub Sumy State University, Sumy, Ukraine

L. F. Sukhodub Sumy State University, Sumy, Ukraine

Sabu Thomas Mahatma Gandhi University, Priyadarshini Hills, Kottayam, Kerala, India

S. Yu. Tkachev Taras Shevchenko National University of Kyiv, Kyiv, Ukraine

E. A. Tsapko G. V. Kurdyumov Institute for Metal Physics of the N.A.S. of Ukraine, Kyiv, Ukraine

O. A. Tsyganovich F.D.Ovcharenko Institute of Biocolloidal Chemistry of NAS of Ukraine, Kyiv, Ukraine;
National Technical University of Ukraine «KPI», Kyiv, Ukraine

Georgii Vasyliev National Technical University of Ukraine “Igor Sikorsky Kyiv Polytechnic Institute”, Kyiv, Ukraine

B. D. Vasyliv Department of Hydrogen Technologies and Alternative Energy Materials, Karpenko Physico-Mechanical Institute of the NAS of Ukraine, Lviv, Ukraine

S. V. Vasylyuk Physics Faculty, Taras Shevchenko National University of Kyiv, Kyiv, Ukraine;
IT Department, National University of Life and Environmental Sciences of Ukraine, Kyiv, Ukraine

V. I. Vavrukh Department of Materials Science and Engineering, Lviv Polytechnic National University, Lviv, Ukraine

V. V. Vira Department of Strength of Materials and Structural Mechanics, Lviv Polytechnic National University, Lviv, Ukraine

Maria Vistak Danylo Halytsky Lviv National Medical University, Lviv, Ukraine

N. O. Volkova Institute for Problems of Cryobiology and Cryomedicine, NAS of Ukraine, Kharkiv, Ukraine

Victoria Vorobyova National Technical University of Ukraine "Igor Sikorsky Kyiv Polytechnic Institute", Kyiv, Ukraine

Viktorya Vorobyova Kyiv, Ukraine

R. Wojnarowska-Nowak Center for Microelectronics and Nanotechnology, Institute of Materials Engineering, University of Rzeszow, Rzeszow, Poland

K. S. Yablochkova Taras Shevchenko National University of Kyiv, Kyiv, Ukraine

A. V. Yakovenko V.P. Kukhar Institute of Bioorganic Chemistry and Petrochemistry of National Academy of Sciences of Ukraine, Kyiv, Ukraine

M. M. Yakymchuk G. V. Kurdyumov Institute for Metal Physics of the N.A.S. of Ukraine, Kyiv, Ukraine

O. S. Yakymenko National Technical University of Ukraine "Igor Sikorsky Kyiv Polytechnic Institute", Kyiv, Ukraine

O. V. Yashchenko National Technical University of Ukraine "Igor Sikorsky Kyiv Polytechnic Institute", Kyiv, Ukraine

A. V. Yatsymyrskyi Taras Shevchenko National University of Kyiv, Kyiv, Ukraine

M. S. Yukhta Institute for Problems of Cryobiology and Cryomedicine, NAS of Ukraine, Kharkiv, Ukraine

D. V. Zaitsev Shupyk National Healthcare University of Ukraine, Kyiv, Ukraine

Nanochemistry and Nanobiotechnology

Extraction of Organosolv Pulp and Nanocellulose from Harvested Corn Residues

V. A. Barbash, O. V. Yashchenko, O. S. Yakymenko, and V. D. Myshak

Abstract The study describes the production of pulp and nanocellulose from harvested corn residues (HCR). Organosolvent corn pulp (OCP) was obtained by an environmentally friendly method of delignification of HCR by extraction with a NaOH solution and cooking using a mixture of acetic acid and hydrogen peroxide. It has been established that pre-washing the HCR with hot or cold water reduces the content of K, Fe, P and Mg but does not remove Ca and Si, which a priori indicates the need to carry out the decalcification process of plant material. The SEM data confirmed that under the action of a cooking solution of peracetic acid, there is a partial destruction of HCR fibers with a decrease in their length. FTIR and XRD methods confirmed that during the thermochemical treatment of HCR, the content of residual lignin and amorphous part decreases and the crystallinity of cellulose samples increases. A stable transparent nanocellulose gel was extracted from OCP by acid hydrolysis followed by ultrasonic treatment. Nanosizes of nanocellulose were confirmed by AFM method. Thermographic analysis data also confirm the formation of a dense homogeneous structure between nanocellulose particles in the process of thermochemical treatment and ultrasonic homogenization. Corn nanocellulose had nanocrystalline particles with a cross-sectional size in the range of 3–18 nm, a density of up to 1.2 g/cm^3, a tensile strength of up to 22 MPa, a transparency of up to 57% and crystalline index of 74.9%. Corn nanocellulose with such physical and mechanical

V. A. Barbash (✉) · O. V. Yashchenko · O. S. Yakymenko
National Technical University of Ukraine "Igor Sikorsky Kyiv Polytechnic Institute", Kyiv, Ukraine
e-mail: v.barbash@kpi.ua

O. V. Yashchenko
e-mail: voliav@ukr.net

O. S. Yakymenko
e-mail: olgayakymenko@i.ua

V. D. Myshak
Institute of Macromolecular Chemistry of the National Academy of Sciences of Ukraine, Kyiv, Ukraine
e-mail: myshak_vd@ukr.net

O. Fesenko and L. Yatsenko (eds.), *Nanoelectronics, Nanooptics, Nanochemistry and Nanobiotechnology, and Their Applications*, Springer Proceedings in Physics 297,
https://doi.org/10.1007/978-3-031-42708-4_1

parameters can be used as a strengthening additive in the production of cardboard, paper and cement products, as a basis for obtaining smart electronics devices.

1 Introduction

With the development of modern life, one cannot ignore the impact of the materials surrounding a person on the environment. Therefore, in recent years, new sources of raw materials and the development of new materials to replace polymers from fossil sources—oil, gas and coal—have been intensively researched. These types of raw materials include cellulose-containing materials, in particular agricultural waste. Cellulose, as the most abundant natural biomass material on earth, has low cost and wide renewability and has degradability and biocompatibility [1]. Cellulose macromolecules have the characteristics of high hydrophilicity and density of hydroxyl groups, which contributes to the modification of functional groups with the formation of new products with unique properties [2, 3]. Nanocellulose (NC) is one of the most promising substances obtained from cellulose-containing raw materials. Nanocellulose is a biodegradable material with high mechanical strength, transparency and chemical resistance, lightweight and low coefficient of thermal expansion. Nanocellulose is widely used in industry to increase the mechanical strength and improve the barrier properties of paper and cardboard, polymer and cement composites, electric batteries and biomedical applications [4–6].

For the extraction of nanocellulose, mechanical, chemical and biotechnological methods are used the technological parameters which depend on the type of the original cellulose-containing material and the requirements for the properties of nanocellulose. Mechanical methods are characterized by significant energy consumption [7, 8], the costs which can be reduced by carrying out preliminary enzymatic or chemical treatment cellulose [9]. At the same time, enzymatic treatment of cellulosic material is usually a time-consuming and expensive process [10]. Therefore, a typical method of extracting nanocellulose from cellulose-containing materials is the use of acid hydrolysis. Mineral acids such as sulfuric, hydrochloric, nitric, hydrobromic and phosphoric acids, or their mixtures are used in the hydrolysis process [11].

To obtain nanocellulose, bleached wood pulp and microcrystalline cellulose from cotton are more often used as starting materials, which have a negligible residual content of lignin, hemicelluloses and extractives. In the global pulp industry, the dominant production technologies are sulfate and sulfite methods, which pollute the air and water bodies with harmful toxic sulfur compounds [12]. The use of several classes of organic compounds, alcohols and carboxylic acids, ethers and esters, ketones and amines, makes it possible to replace sulfur-containing cooking liquors and reduce harmful emissions into the atmosphere. For example, acetic acid, due to its relatively low cost, can be considered a potential agent for achieving extensive delignification [13]. The use of hydrogen peroxide in cooking with acetic acid improves the delignification of plant materials and increases the whiteness of the pulp. A mixture of acetic acid and hydrogen peroxide forms peracetic acid, which, as

a strong oxidizing agent, is characterized by excellent delignification and bleaching properties [14]. This mixture selectively dissolves lignin and minimally damages cellulose [15]. The peracetic acid cooking process is applicable to both wood and non-wood plant materials and is carried out at a low temperature, which contributes to low energy consumption [16]. Countries with limited forest resources are encouraged to use non-wood plant raw materials, which will help conserve timber stocks and improve the environment. According to the annual volume of fibrous mass, corn stalks (750 million tons) take the first place in the world among cereal crops [17]. It is used as a valuable raw material for the production of bioethanol and solid biofuel, animal feed and raw material for the production of paper and cardboard-paper products [18]. After harvesting corn for grain, a large amount of harvested corn residues (HCR) remains, which is considered as a source of fibers for the production of cellulose and nanocellulose. Therefore, the purpose of this work is to obtain cellulose from harvested corn residues by an ecologically safe method and to extract nanocellulose from it by an acid method with determination of its characteristics.

2 Experimental Details

2.1 Materials and Chemicals

To obtain pulp for extraction nanocellulose, we used harvested corn residues (HCR) from the Sumy region of Ukraine after the 2021 harvest. Harvested corn residues were crushed on a disintegrator and sieved on sieves with holes of 0.25 and 0.5 mm to separate the fibrous part of the HCR from leaves, dust and small parts of raw materials. The HCR fraction remaining on a sieve with holes of 0.5 mm was used to obtain cellulose. The raw materials of these three fractions are stored in a desiccator to maintain constant humidity.

According to TAPPI standards [19], the chemical composition of the HCR was determined, in comparison with the chemical composition of the most common representatives of plant raw materials. The analysis of the chemical composition of HCR and the process of cellulose hydrolysis was carried out using chemically pure substances. Chemicals: sodium hydroxide, glacial acetic acid, hydrogen peroxide, sulfuric acid ethanol were chemically pure, obtained from Khimreaktiv LLC (Ukraine) and used without additional purification. Distilled water was used throughout the experiments.

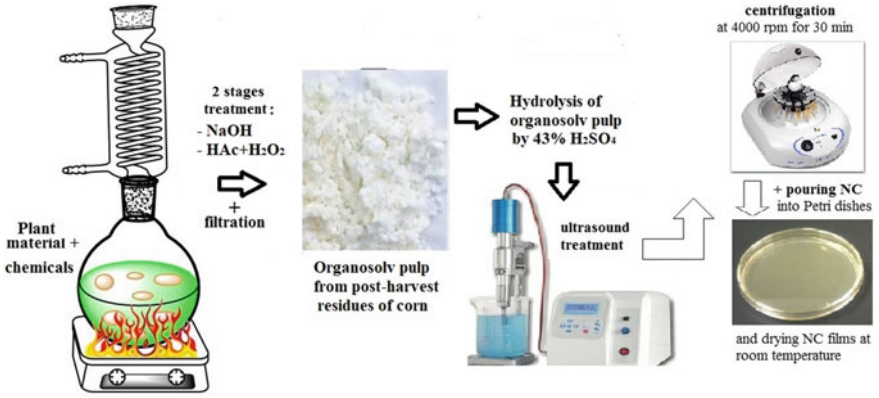

Fig. 1 General scheme for extraction OCC and NC from HCR

2.2 Obtaining the Organosolv Corn Cellulose

The production of pulp from harvested corn residues was carried out according to the method described in previous publications [20, 21]. The general scheme for obtaining organosolv corn cellulose (OCC) and nanocellulose from HCR is shown in Fig. 1.

Briefly, the chopped harvested corn residues were placed in a conical flask, where NaOH solution was added at a consumption of 5% of the raw material to remove most of the hemicelluloses and minerals and partially remove lignin from the plant material. The mixture was boiled under reflux on a hot plate with a water bath for 180 min. At the second stage, to remove residual lignin and extractives, organosolv cooking was carried out using a solution of glacial acetic acid and 35% hydrogen peroxide in a volume ratio of 70:30% at a temperature of 97 ± 2 °C for 30–180 min. After the end of the cooking time, the pulp was washed several times with distilled water to ensure complete removal of residual lignin and non-cellulosic components. The obtained organosolv corn cellulose was stored wet in an airtight bag to produce nanocellulose.

2.3 Extraction of the Corn Nanocellulose

Nanocellulose was obtained by hydrolysis of the OCC by using procedures described in [22, 23]. Hydrolysis of the never dried OCC was carried out by solution of sulfuric acid with a concentration of 43%, at the liquid-to-solid ratio 10:1 and at temperature 60 °C for the duration of 60 min for obtaining of nanocellulose. The calculated amount of sulfate acid with the corresponding concentration was slowly added into the flask with the OCC suspension. Upon expiration of the reaction time, the hydrolysis was stopped by tenfold dilution with distilled water and subsequent cooling of

the suspension to room temperature. The hydrolyzed nanocellulose was rinsed with distilled water three times through centrifugation at 4000 rev/min and subsequent dialysis until reaching a neutral pH. Ultrasound treatment of corn nanocellulose with concentration 0.6% was performed using ultrasound disintegrator UZDN-A (SELMI, Ukraine) with 22 kHz for 60 min. The nanocellulose suspension was placed in an ice bath to prevent overheating during treatment. A stable transparent nanocellulose gel was extracted from OCC by acid hydrolysis followed by ultrasonic treatment. The NC suspension was poured into Petri dishes and dried at room temperature to obtain the films that were analyzed.

2.4 Methods

The method of ***scanning electron microscopy (SEM***) is used for morphological studies of HCR, obtained OCC and NC films. The research was carried out on a PEM-106I microscope (SELMI, Ukraine) at an accelerating voltage of 20 kV. The samples were sputter-coated with a layer of gold using the sputtering technique.

Fourier transform infrared spectroscopy (FTIR) spectra of the HCR, OCC and NC films were recorded on Tensor 37 Fourier transform infrared spectrometer with 4 cm^{-1} resolution in the 400–4000 cm^{-1} frequency range (BRUKER, Germany).

The ***X-ray diffraction (XRD)*** was measured for HCR, OCC and NC with an Ultima IV diffractometer (Rigaku, Japan) using Cu Kα radiation at 40 kV and 30 mA. Scattered radiation was detected in the range of $2\theta = 5$–$40°$ at a scan rate of 5°/min.

The ***crystallinity index (CrI)*** of the HCR and their derivatives was calculated from the heights of the peak of the crystalline phase 200 (I_{200}) and the minimum intensity between the peaks 200 and 110, which corresponds to the amorphous phase (I_{am},) using Segal's method [24]:

$$\text{CrI} = [(I_{200} - I_{\text{am}})/I_{200}] \times 100\%,$$

where I_{200} is the intensity of the (200) reflection for the crystalline phase at $2\theta = 22.5°$, and I_{am} is the intensity of the amorphous phase at $2\theta = 18.5°$.

Atomic force microscopy (AFM) was used to determine the topography and morphology of corn NC samples. Measurements were accomplished with Si cantilever, operating in a tapping mode on the device Solver Pro M (NT-MDT). The scanning speed and area were 0.6 line/s and 2×2 μm^2, respectively. The transparency of NC films was determined by electronic absorption spectra, which were recorded at a wavelength of 600 nm on a double-beam spectrophotometer 4802 (UNICO, USA) with a resolution of 1 nm.

Thermogravimetric (TG) and derivative thermogravimetric (DTG) analyses of samples of OCC and NC films were carried out simultaneously by using a Q50 thermal analyzer (TA Instrument, USA) with a resolution of 0.02 μg as a function of temperature. The weight of samples was within 10 mg; the standard substance for calibrating the temperature scale is nickel, crucible material—platinum. Runs

were carried out at heating rates 20 °C min^{-1} from ambient temperature to 700 °C under high-purity nitrogen at a flow rate of 40 ml min^{-1}. Deviations of weight were registered and processed according to a program involving the use of computer technology.

The ***density*** of corn nanocellulose films was determined according to ISO 534:1988. The tensile strength of the nanocellulose films was measured at a controlled temperature (23 ± 1 °C) and humidity (50 ± 2%) according to ISO 527-1. ***Tension tests*** were performed at a crosshead speed of 0.5 mm/min on the TIRAtest-2151 (Germany) instrument equipment with a 2-N load stress. For testing, test strips with 10 ± 2 mm width and 25 ± 5 mm long were used. The tensile strength of the NC films was calculated on five test pieces, expressing the results as an average and standard deviation.

3 Results and Discussion

3.1 Cooking Corn Pulp

The chemical composition of the main components of HCR in comparison with representatives of coniferous and deciduous wood is given in Table 1. As can be seen from the above data, with approximately the same content of the main component of plant raw materials—cellulose, HCR contains less lignin and resin, fats, waxes (RFW) and more minerals and substances extracted with hot water and 1% alkali solution.

The chemical composition of mineral substances in the initial HCR and HCR after sieving and washing with cold and hot water is given in Table 2.

The data in Table 2 indicate that sieving is an effective way of cleaning the HCR from the remains of sand, dust and the main components that give a high content of the mineral component—Ca and Si. At the same time, washing with water reduces the content of such components as K, Fe, P and Mg but does not remove Ca and Si components from HCR. Such a chemical composition of HCR a priori indicates the need to pay attention to both the process of delignification and decriminalization of this plant material.

Table 1 Chemical composition of the main components of HCR

Plant raw material	Extraction in		RFW* %	Cellulose, %	Lignin, %	Ash, %
	H_2O %	NaOH %				
Chopped HCR	14.9	40.0	1.7	44.5	19.3	2.4
Spruce [12]	7.3	18.3	2.9	46.1	28.5	0.2
Poplar [12]	2.8	22.2	2.7	51.0	21.9	0.9

Table 2 Chemical composition of mineral substances from the fractions of the CPR

Chemical elements	Initial HCR	HCR after sieving	HCR after washing with cold water	HCR after washing with hot water
12Mg	8.042 ± 0.538	9.270 ± 0.520	6.893 ± 0.467	5.793 ± 0.437
14Si	8.038 ± 0.117	6.989 ± 0.108	13.208 ± 0.134	14.584 ± 0.141
15P	5.354 ± 0.147	5.454 ± 0.142	4.555 ± 0.145	4.126 ± 0.146
16S	3.776 ± 0.083	3.882 ± 0.084	3.614 ± 0.082	3.422 ± 0.081
19K	13.571 ± 0.091	12.630 ± 0.084	4.758 ± 0.034	4.088 ± 0.031
20Ca	57.951 ± 0.363	57.863 ± 0.354	64.598 ± 0.357	64.485 ± 0.356
22Ti	0.302 ± 0.019	0.206 ± 0.014	0.266 ± 0.020	0.513 ± 0.024
25Mn	0.256 ± 0.008	0.207 ± 0.006	0.335 ± 0.010	0.300 ± 0.010
26Fe	2.232 ± 0.022	3.055 ± 0.025	1.491 ± 0.018	2.370 ± 0.023
29Cu	0.083 ± 0.002	0.203 ± 0.003	0.053 ± 0.002	0.042 ± 0.002
30Zn	0.277 ± 0.004	0.137 ± 0.002	0.184 ± 0.003	0.194 ± 0.003
37Rb	0.025 ± 0.001	0.020 ± 0.001	0.007 ± 0.001	0.007 ± 0.001
38Sr	0.043 ± 0.001	0.036 ± 0.001	0.030 ± 0.001	0.029 ± 0.001
39Y	0.002 ± 0.001	0.001 ± 0.001	0.003 ± 0.001	0.002 ± 0.001
40Zr	0.016 ± 0.001	0.007 ± 0.001	0.005 ± 0.001	0.010 ± 0.001

Therefore, after processing plant raw materials at the first stage with a 5% alkali solution, a corn pulp was obtained with a yield of 58.9%, with a residual content of lignin of 2.97% and mineral substances of 2.6%. The alkaline treatment naturally extracts readily soluble polysaccharides (hemicelluloses) and extractives (resins, fats, waxes, minerals) from plant raw materials and insignificantly lignin, the content which remains at the level of the initial hemp fibers. The dependence of the yield of corn pulp on the duration of peracetic cooking is shown in Fig. 2.

Carrying out subsequent peracetic cooking leads to significant removal of lignin and residual minerals. The organosolv corn pulp obtained as a result of peracetic cooking had a residual lignin content of 0.08% and an ash content of 0.34%. Such values of the quality indicators of corn pulp are close to the values of organosolv pulps obtained earlier from other representatives of non-wood plant materials—wheat straw, flax, kenaf, miscanthus, reed and hemp [20–23]. The resulting OCC is suitable for chemical processing, in particular for the production of corn nanocellulose.

3.2 Morphology of the OCC and Corn NC

Using scanning electron microscopy, morphological changes in the structure of plant material during its thermochemical processing were observed (Fig. 3).

As can be seen from Fig. 3a, the raw material has densely arranged fibers, which as a result of alkaline extraction are divided into individual fibers and smaller than in

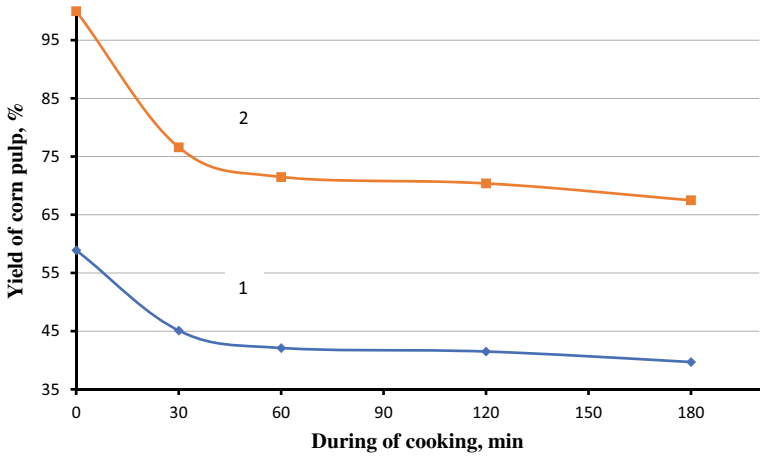

Fig. 2 Dependence of the yield of corn pulp on the duration of cooking: 1—relative to the raw material; 2—relative to the II stage of processing

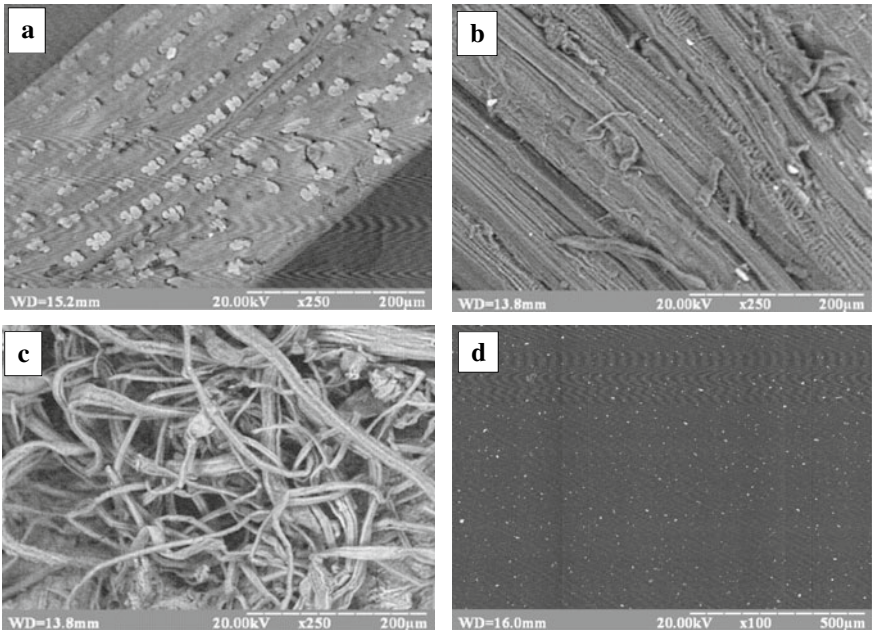

Fig. 3 SEM images: **a** HCR; **b** pulp after alkaline extraction; **c** OCC; **d** nanocellulose

the raw material content of hemicelluloses and minerals. There is a partial removal of lignin, which bound the fibers in the raw material (Fig. 3b). Figure 3c shows parts of PRC fibers with small residues of lignin and extractives. Due to the action of the cooking solution of peracetic acid, there is a partial destruction of the fibers with a decrease from length to 60–350 μm (Fig. 3c). Due to the action of sulfuric acid in the process of hydrolysis of OCC, there is a destruction of 1–4 glycosidic bonds between glucopyranose units of cellulose macromolecules, dissolution of the amorphous part of cellulose and reducing the size of fibers to nanoparticles (Fig. 3d).

3.3 Chemical Purity of Corn Materials

The change in the chemical composition of corn fiber during its thermochemical processing was confirmed by infrared spectroscopy data. Figure 4 shows the Fourier IR spectra of HCR, corn pulps after alkaline extraction and peracetic acid cooking and NC. All spectra have the same typical peaks that characterize stretching vibrations of hydroxyl groups included in intramolecular and intermolecular hydrogen bonds (3000–3750 cm^{-1}), valence asymmetric (2920 cm^{-1}) and symmetric (2853 cm^{-1}) vibrations of the methyl and methylene groups, deformation vibrations of the bonds $–CH_2$ and –O–H in CH_2OH groups. The band in the spectrum near 1736 cm^{-1} is assigned mainly to the C=O stretching vibration of the carbonyl and acetyl groups in hemicelluloses and in lignin and the ester groups of cellulose in nanocellulose [25].

Alkaline extraction removes carbonyl groups from hemicellulose (spectrum 2), but subsequent organosolv cooking increases the amount of carbonyl groups due to oxidation of cellulose with hydrogen peroxide (spectrum 3). The absence of bands at 1512 and 1244 cm^{-1} in the spectra 2–4 in Fig. 3 testifies to the removal of lignin

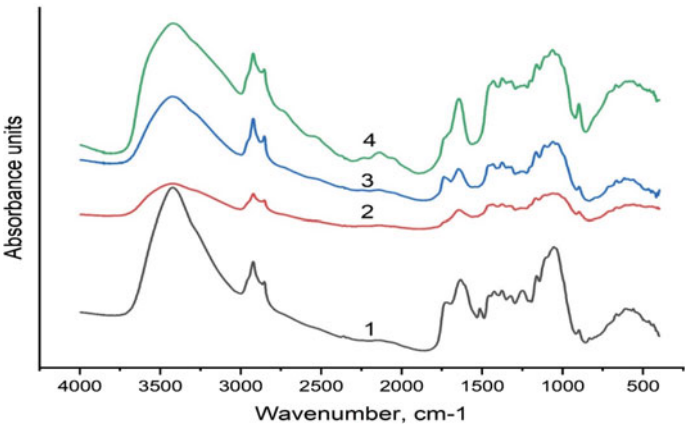

Fig. 4 FTIR spectra of samples: **1** HCR; **2** corn pulp after alkaline extraction; **3** OCC; and **4** corn NC

from the corn pulp. Spectral bands in the region of 1645 cm^{-1} are associated with the presence of adsorbed water and characterize the degree of sample moisture [26].

3.4 Pulp Crystallinity

The X-ray diffractograms of initial HCR, OCC and corn NC are depicted in Fig. 5. Analysis of the X-ray diffractograms shows that the peak with greater intensity at 22.2°–22.9° 2θ reflection belongs to the (200) crystallographic plane of cellulose *I*. The peak with maximum reflection in the range of 14.4°–14.9° corresponds to the crystallographic plane (1–10), the peak in the range of 15.5–16.2° 2θ reflection assigned to the crystallographic plane (110) and the peak around 34.6° belongs to the crystallographic plane (004) cellulose *I* [27].

The presence of these peaks in all samples indicates that crystalline structure of corn cellulose had not changed during the thermochemical treatments of sulfuric acid and belongs to the typical structure of cellulose *I*. Based on the analysis of diffraction patterns and changes in the ratio of the amorphous and crystalline parts of the samples under study, their crystallinity index (CrI) was calculated (Table 3).

As can be seen from obtained data, crystallinity index of corn pulps increases in the following order: initial harvested corn residues—corn pulp after alkaline extraction—organosolv corn cellulose—nanocellulose. This is due to the fact that during thermochemical treatments, CrI increases due to the removal of non-cellulose components from the plant raw material and the removal of amorphous regions of cellulose under

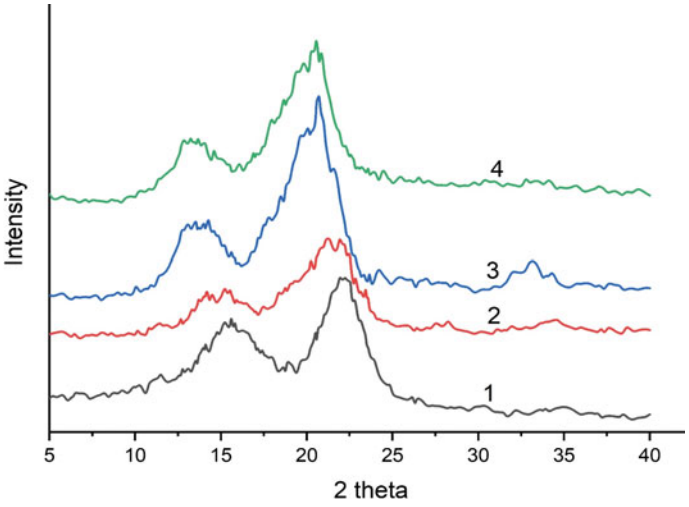

Fig. 5 X-ray diffraction patterns of: **1** HCR; **2** corn pulp after alkaline extraction; **3** OCC; and **4** corn NC

Table 3 Crystallinity index of corn materials

No. sample	Corn materials	Crystallinity index, %
1	Harvested corn residues	60.7
2	Corn pulp after alkaline extraction	68.3
3	Organosolv corn cellulose	72.4
4	Corn nanocellulose	74.9

the action of sulfuric acid. An increase in the CrI values of nanocellulose in comparison with the CrI of the initial cellulose was also found for other representatives of plant raw materials [20–22, 28].

3.5 Properties of Corn Nanocellulose

Nanocellulose obtained as a result of treatment of corn organosolv pulp with 43% sulfuric acid solution at a temperature of 60 °C for 60 min and ultrasonic treatment for 60 min had the following physical and mechanical parameters: density 1.2 g/cm^3, tensile strength 22 MPa, transparency 57% at the wavelength of 600 nm. Topographic characteristics of corn NC were determinate by AFM (Fig. 6).

As can be seen from Fig. 6, corn nanocellulose particles form a multilayer structure between nanoparticles due to the action of hydrogen bonding and van der Waals forces [29]. Analysis of AFM images (Fig. 6) showed that suspensions of corn NC extracted by sulfuric acid method consist of nanocrystal particles in the form of needles with a transverse size in the range of 3–18 nm (Fig. 6b), and a length of several micrometers. Such values of the transverse dimensions of corn NC are confirmed by the data for nanocellulose extracted by acid hydrolysis of organosolv pulps from other representatives of non-wood plant raw materials: wheat straw (10–45 nm), flax (15–65 nm), kenaf (10–28 nm), miscanthus (10–20 nm) [23].

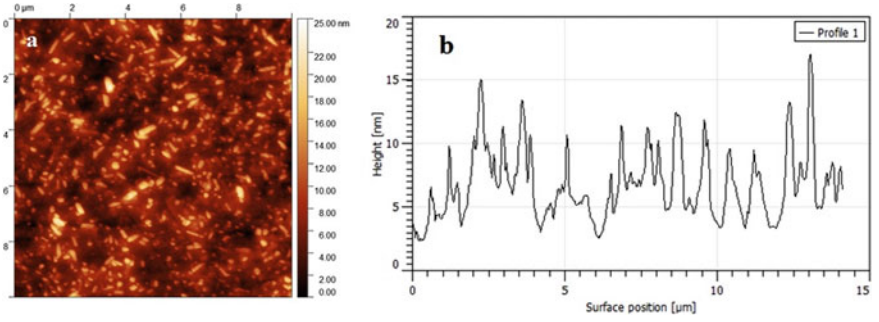

Fig. 6 AFM images of a nanocellulose films in height (**a**) and surface position (**b**) of corn NC particles extracted by acid hydrolysis methods

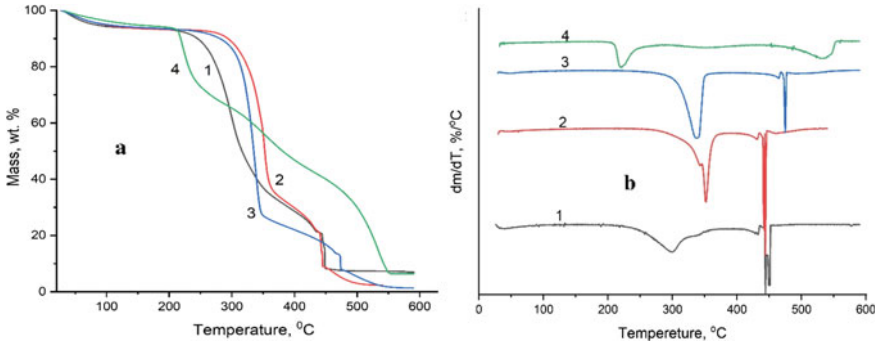

Fig. 7 TG (**a**) and DTG (**b**) curves of thermal analysis: **1** HCR; **2** corn pulp after alkaline extraction; **3** OCC; and **4** corn NC

3.6 Thermal Analysis

The effect of temperature on the stability of HCR, OCC and corn NC was investigated by thermogravimetric (TG) and derivative thermogravimetric (DTG) analyses (Fig. 7).

TG curves show changes in the weight of the samples during heating, and its derivative (DTG) shows the temperature peaks at which significant weight loss occurs. It can be seen from the thermogravimetric curves (Fig. 7a) that the initial temperature of mass loss for all samples is about 100 °C, which is associated with the evaporation of free moisture from them. For HCR raw materials, thermal destruction begins at a temperature of 250 °C, which is associated with the release of intermolecular water. The main stage of the thermal destruction process of HCR takes place in the temperature range of 270–330 °C, after which about 30% of the mass of HCR remains. The second peak of HCR destruction is observed at a temperature of 440–450 °C, after which only 10% of the mass remains. The mass loss of samples (2) and (3) occurs under approximately the same conditions. For sample (2), a characteristic sharp onset of mass loss is observed in the temperature range of 310–360 °C, and for sample (3), in the range of 307–350 °C. In these temperature intervals, the release of bound water occurs, and a sharp loss of mass of samples (2) and (3) occurs at temperatures of 450 °C and 475 °C, respectively.

The temperature destruction of the nanocellulose film (curve 4) has a slightly different character. In the temperature range of 200–250 °C, a loss of up to 30% of the NC mass is observed, which is confirmed by a smooth small peak on the differential curve (Fig. 7b). A sharp loss of mass in the temperature range of 250–500 °C is not characteristic of nanocellulose films. At a temperature of 500 °C, up to 30% of the mass of corn NC is preserved, while for samples (**1**), (**2**) and (**3**) at this temperature, 7%, 3% and 5% of the mass remain, respectively. That is, thermographic analysis data confirm the formation of a dense homogeneous structure between nanocellulose particles in the process of thermochemical treatment and ultrasonic homogenization.

The beginning of the destruction of corn nanocellulose films at a relatively lower temperature than the raw plant material and OCC is explained by the presence of ester sulfate groups on the surface of cellulose and a larger number of free ends of NC chains, which decompose at a lower temperature [27]. The presence of ester sulfate groups reduces the thermal stability of corn nanoparticles, since less energy is required to remove sulfuric acid residues from the hydroxyl group at the 6th carbon atom in the pyranose ring of cellulose than to destroy the glucopyranose ring of OCC. According to temperature resistance and mass retention at a temperature of 500 °C, the studied corn samples are arranged in the following sequence: pulp after alkaline extraction—organosolv cellulose—harvested corn residues—corn nanocellulose.

4 Conclusion

1. Harvested corn residues (HCR) were used as a source of pulp for the extraction of nanocellulose. The pulp from HCR is obtained by an environmentally friendly organosolv method using a solution of peracetic acid. It has been established that pre-washing HCR with hot or cold water reduces the content of such components as K, Fe, P and Mg but does not remove Ca and Si components. Such a chemical composition of HCR a priori indicates the need for effective processes of decalcification and delignification of this plant material.
2. The SEM data confirmed that under the action of a cooking solution of peracetic acid, there is a partial destruction of HCR fibers with a decrease in their length. It was found that due to the action of sulfuric acid in the process of hydrolysis of pulp, the destruction of 1-4 glycosidic bonds between glucopyranose links of cellulose macromolecules, the dissolution of the amorphous part of cellulose and the reduction of fiber sizes to nanoparticles occur.
3. It was established that in the process of thermochemical treatment of corn samples, the amount of residual lignin content and the amorphous part decreases and the crystallinity index of cellulose samples increases, which is confirmed by the data of FTIR and XRD. Thermographic analysis data also confirm the formation of a dense homogeneous structure between nanocellulose particles in the process of thermochemical treatment and ultrasonic homogenization. Corn nanocellulose films had transverse size in the range of 3–18 nm, a density of up to 1.2 g/cm^3, a tensile strength of up to 22 MPa, a transparency of up to 57% and crystalline index of 74.9% that are close to this values of nanocelluloses obtained earlier from other representatives of non-wood plant materials. Corn nanocellulose with such physical and mechanical parameters can be used as a strengthening additive in the production of cardboard, paper and cement products, as a basis for obtaining smart electronics devices. Studies have shown that chemical methods can be effective for extracting nanocellulose from corn post-harvest residues.

References

1. Y. Sun, Y. Chu, W. Wu, H. Xiao, Nanocellulose-based lightweight porous materials: a review. Carbohydr. Polym. **255**, 117489 (2021). https://doi.org/10.1016/j.carbpol.2020.117489
2. D. Liu, Y. Gao, Y. Song, H. Zhu, L. Zhang, Y. Xie, H. Shi, Z. Shi, Q. Yang, C. Xiong, Highly sensitive multifunctional electronic skin based on nanocellulose/mxene composite films with good electromagnetic shielding biocompatible antibacterial properties. Biomacromolecules **23**(1), 182–195 (2022). https://doi.org/10.1021/acs.biomac.1c01203
3. K.J. Nagarajan, N.R. Ramanujam, M.R. Sanjay, S. Siengchin, B. Surya Rajan, K. Sathick Basha, P. Madhu, G.R. Raghav, A comprehensive review on cellulose nanocrystals and cellulose nanofibers: pretreatment, preparation, and characterization. Polym. Compos. **42**(4), 1588–1630 (2021). https://doi.org/10.1002/pc.25929
4. A. Isogai, Emerging nanocellulose technologies: recent developments. Adv. Mater. **33**(28), 2000630 (2020).https://doi.org/10.1002/adma.202000630
5. R. Reshmy, E. Philip, S. Paul et al., Nanocellulose-based products for sustainable applications: recent trends and possibilities. Rev. Environ. Sci. Biotechnol. (2020). https://doi.org/10.1007/s11157-020-09551-z
6. H. Du, W. Liu, M. Zhang, C. Si, X. Zhang, B. Li, Cellulose nanocrystals and cellulose nanofibrils based hydrogels for biomedical applications. Carbohydr. Polym. **209**, 130–144 (2019). https://doi.org/10.1016/j.carbpol.2019.01.020
7. Y. Yang, Z. Chen, J. Zhang, G. Wang, R. Zhang, D. Suo, Preparation and applications of the cellulose nanocrystals. Int. J. Polym. Sci. (2019). https://doi.org/10.1155/2019/1767028
8. V. Kumar, P. Pathak, N.K. Bhardwaj, Waste paper: an underutilized but promising source for nanocellulose mining. Waste Manage. **102**, 281–303 (2020). https://doi.org/10.1016/j.wasman.2019.10.041
9. P. Phanthong, P. Reubroycharoen, X. Hao, G. Xu, G. Abudula, G. Guan, Nanocellulose: extraction and application. Carbon Resour. Convers. **1**, 32–44 (2018)
10. A. Sharma, M. Thakur, M. Bhattacharya, T. Mandal, S. Goswamia, Commercial application of cellulose nano-composites—a review. Biotechnol. Rep. (2019). https://doi.org/10.1016/j.btre.2019.e00316
11. J.-W. Rhim, J.P. Reddy, X. Luo, Isolation of cellulose nanocrystals from onion skin and their utilization for the preparation of agar-based bio-nanocomposites films. Cellulose (2014). https://doi.org/10.1007/s10570-014-0517-7
12. G.A. Smook, *Handbook for Pulp and Paper Technologists*, 3rd edn. (Angus Wilde Publications, Inc, 2003), p. 425
13. R. Kumar, F. Huc, C.A. Hubbell, A.J. Ragauskas, C.E. Wyman, Comparison of laboratory delignification methods, their selectivity, and impacts on hysiochemical characteristics of cellulosic biomass. Biores. Technol. **130**, 372–381 (2013). https://doi.org/10.1016/j.biortech.2012.12.028
14. J.H. Choi, S.Y. Park, J.H. Kim, S.M. Cho, S.K. Jang, C. Hong, I.G. Choi, Selective deconstruction of hemicellulose and lignin with producing derivatives by sequential pretreatment process for biorefning concept. Bioresour. Technol. **291**, 121913 (2019). https://doi.org/10.1016/j.biortech.2019.121913
15. M.H. Karbalaei Esmaeil, M. Talaeipour, B. Bazyar, S.A. Mirshokraei, H. Khademi Eslam, Two-step delignification of peracetic acid and alkali from sugar cane bagasse. BioResources **14**(4), 9994–10003 (2019)
16. I. Deykun, V. Halysh, V. Barbash, Rapeseed straw as an alternative for pulping and papermaking. Cellulose Chem. Technol. **52**(9–10), 833–839 (2018)
17. Y. Fahmy, T.Y. Fahmy, F. Mobarak, M. El-Sakhawy, M. Fadl, Agricultural residues (wastes) for manufacture of paper, board, and miscellaneous products: background overview and future prospects. Int. J. Chem. Tech. Res. **2**(10), 424–448 (2017)
18. C.W. Smith, J. Betrán, E.C.A. Runge, *Corn: Origin, History, Technology, and Production.* (Wiley, March 8, 2004). ISBN 978-0-471-41184-0

19. *TAPPI Test Methods* (Tappi Press, Atlanta, 2004)
20. V. Barbash, O. Yashchenko, Preparation, properties and use of nanocellulose from non-wood plant materials, in *Novel Nanomaterials*, ed. by K. Krishnamoorthy (IntechOpen, London), pp. 1–23. https://doi.org/10.5772/intechopen.94272
21. V.A. Barbash, O.V. Yashchenko, O.S. Yakymenko, R.M. Zakharko, Extraction of organosolv pulp and production nanocellulose from hemp fibers. KPI Sci. News (3), 83–90 (2021). https://doi.org/10.20535/kpisn.2021.3.25145
22. V.A. Barbash, O.V. Yashchenko, O.A. Vasylieva, Preparation and application of nanocellulose from *Miscanthus* × *giganteus* to improve the quality of paper for bags. SN Appl. Sci. **2**, 727 (2020). https://doi.org/10.1007/s42452-020-2529-2
23. V.A. Barbash, O.V. Yashchenko, O.S. Yakymenko, R.M. Zakharko, V.D. Myshak, Preparation of hemp nanocellulose and its application for production of paper for automatic food packaging. Cellulose (2022). https://doi.org/10.1007/s10570-022-04773-6
24. L.C. Segal, J.J. Creely, A.E.J. Martin, C.M. Conrad, An empirical method for estimating the degree of crystallinity of native cellulose using the x-ray diffractometer. Text. Res. J. **29**(10), 786–794 (1959). https://doi.org/10.1177/004051755902901003
25. H.A. Silvério, W.P.F. Neto, N.O. Dantas, D. Pasquini, Extraction and characterization of cellulose nanocrystals from corncob for application as reinforcing agent in nanocomposites. Ind. Crops Prod. **44**, 427–436 (2013). https://doi.org/10.1016/j.indcrop.2012.10.014
26. N.A. Rosli, W.H.W. Ishak, I. Ahmad, Eco-friendly high-density polyethylene/amorphous cellulose composites: environmental and functional value. J. Cleaner Prod **290**, 125886–131259 (2021)
27. A. Kumar, Y.S. Negi, V. Choudhary, N.K. Bhardwaj, Characterization of cellulose nanocrystals produced by acid hydrolysis from sugarcane bagasse as agro-waste. JPCM **2**(1), 1–8 (2014)
28. M. Nuruddin, M. Hosur, E. Triggs, S. Jeelani, Comparative study of properties of cellulose nanofibers from wheat straw obtained by chemical and chemi-mechanical treatments, in *Proceedings of the ASME 2014 International Mechanical Engineering Congress & Exposition, November 14–20, Montreal, Canada, V014T11A042* (ASME, 2014). https://doi.org/10.1115/IMECE2014-36174
29. M. Poletto, H.L. Ornaghi Júnior, A.J. Zattera, Native cellulose: structure, characterization and thermal properties. Materials **7**, 6105–6119 (2014). https://doi.org/10.3390/ma7096105

Study of Biocarbons Derived from the Residues After Supercritical Extraction of Raw Plants from Adsorption of Gaseous NO_2—Mini Review

Aleksandra Bazan-Wozniak

Abstract Development of civilization and industry inevitably brings increasing levels of pollution to the natural environment. This forces the activity aimed on the one hand at limiting the amount of pollutants introduced into water and air and on the other hand at effective removal of polluting substances already present in the natural environment. One of the methods for the removal of pollutants is adsorption, and one of the best adsorbents is activated carbon. Activated carbons are microcrystalline materials which show a well-developed surface area and porous structure, so they can be used for removal of pollutants from liquid and gas phase. Thanks to their unique sorption properties, activated carbons have been used in many areas of industry. Wider and wider range of their application cause increasing demands for these materials and stimulate the search for new precursors. Thanks to their unique sorption properties, activated carbons have been used in many areas. Widening panoply of their applications caused increasing demands for these materials and stimulated the search for their new precursors. One of them is plants, which are materials left after supercritical extraction. The present paper provides an overview of reports on adsorption of pollutants from gas phase (NO_2) for biomaterials obtained from the residues after supercritical extraction of raw plants.

Highlights

An alternative method for biowaste utilization has been proposed.

The activated biocarbons have been used for NO_2 adsorption.

The capacity of biocarbons to adsorb nitrogen dioxide was primarily dependent on the conditions of the adsorption process.

A. Bazan-Wozniak (✉)
Faculty of Chemistry, Adam Mickiewicz University in Poznań, Uniwersytetu Poznańskiego 8, 61-614 Poznań, Poland
e-mail: aleksandra.bazan@amu.edu.pl

O. Fesenko and L. Yatsenko (eds.), *Nanoelectronics, Nanooptics, Nanochemistry and Nanobiotechnology, and Their Applications*, Springer Proceedings in Physics 297,
https://doi.org/10.1007/978-3-031-42708-4_2

1 Introduction

Today, we live in a time of dynamic civilization and technological development, which have enabled people to make their professional and private lives easier. Unfortunately, this progress brings positive and negative consequences. One of the negative effects of human activity is the increase in air, water and soil pollution [1–3]. According to the World Health Organization, 80% of the world's population live in areas where air pollution concentrations exceed acceptable standards. This is influenced by both natural and anthropogenic factors [4].

Pollutants in the atmosphere have a significant impact on human health, the condition of ecosystems or climate change [5, 6]. In addition, atmospheric pollutants are difficult to abate because they cannot be confined to a certain area, as they have the potential to spread widely. Toxic gases emitted into the earth's atmosphere mainly include nitrogen, sulfur and carbon oxides, volatile organic compounds and hydrogen sulfide. These compounds contribute to the destruction of the ozone layer and are responsible for the formation of smog and the greenhouse effect [7–10].

Porous carbon materials, e.g., activated carbons, activated fibers, carbon blacks and mesoporous carbons, are very popular among a wide group of materials used in adsorption of gas pollutants [11, 12]. Carbon adsorbents should be characterized by high sorption capacity, short duration of sorption processes, no toxic by-products and relatively low production cost. These requirements make that activated carbons are one of the most popular carbon materials used in adsorption process [13, 14].

The growing demand for activated carbons and increasing requirements in the field of environmental protection have resulted in a search for new activated carbons precursors [15–18] and methods of their production [19–21]. An interesting group of precursors may be the residues after supercritical extraction of raw plants. In the literature, you can find a huge number of reports on the use of the supercritical extraction process to obtain natural substances contained in herbal plants. This process allows the extraction of natural dyes, flavors and fatty acids, which are the valuable raw materials for the food, cosmetic and pharmaceutical industries [22–24]. The raw materials subjected to the supercritical extraction process are mainly hop cones, rape seeds and sunflower seeds, as well as herbs such as nettle, marigold and camomile. The use of these materials for the production of carbon adsorbents can be an excellent alternative for their disposal, because today the main method of dealing with post-extraction wastes is their incineration. Obtaining cheap adsorbents from this type of precursors will allow to obtain activated carbons with interesting physicochemical properties and good sorption properties against gaseous pollutants [24–28].

This paper is a review of the reports on the possibility of removal of gaseous NO_2 with the use of activated carbons obtained from residues after supercritical extraction of camomile, marigold and hops.

2 Biocarbons Obtained from the Residues After Supercritical Extraction of Camomile Flowers

Adsorbents were obtained by physical activation of the residues after supercritical extraction of camomile flowers. Physicochemical and sorption properties toward NO_2 of the biocarbons were determined [29]. The starting raw material in the form of powder was subjected to carbonization process at two temperature variants, at 500 or 700 °C (C5 and C7). The process was performed in a tube furnace in nitrogen atmosphere. The biochars were then subjected to physical activation (A) with CO_2 in the same tube furnace. Two activation temperatures were applied, of 700 or 800 °C (A7 and A8), and the samples were thermostated for 60 min. As a result of the physical activation of starting material, four biocarbons were obtained for which physicochemical characterization was carried out. All the adsorbents obtained were characterized by: low-temperature nitrogen adsorption, pH of water extracts of the adsorbents and the contents of acidic and basic oxygen functional groups on the surface of activated carbons by the Boehm method [30].

According to the results presented in Table 1, physical activation of the residues after supercritical extraction of camomile flowers leads to the production of mesoporous carbon adsorbents with a surface area in the range 9–104 m^2/g. It has been shown that raising the activation temperature by 100°C leads to an enhancement of the textural parameters of the biocarbons and an increase in the proportion of micropores in the sample structures. However, the surface area of the samples obtained by physical activation of the residues after supercritical extraction of camomile flowers is much lower than that of commercial products [31, 32].

Chemical character of the obtained biocarbons was determined by Boehm titration. Moreover, the acid–base properties of the samples were confirmed by measurement of pH of the water extracts of these biocarbons (Table 1). The results of determination of the content of oxygen functional groups clearly indicated that the carbonization and activation processes with CO_2 lead to the production of biocarbon adsorbents with only basic functional groups on their surface [33, 34]. The largest amount of this type of group was produced for sample obtained by carbonization at 700 °C,

Table 1 Textural parameters and acid–base properties of the biocarbons obtained from the residues after supercritical extraction of camomile flowers [29]

Sample	Textural parameters			Surface oxygen functional groups (mmol/g)		pH
	Surface area (m^2/g)	Total pore volume (cm^3/g)	Average pore diameter (nm)	Acidic	Basic	
C5A7	9	0.04	19.39	0.00	2.34	10.4
C7A7	18	0.03	6.39	0.00	2.89	10.7
C5A8	64	0.06	3.71	0.00	2.81	10.5
C7A8	104	0.09	3.41	0.00	3.52	11.0

followed by activation at 800 °C. Results of the Boehm titration for samples C5A7, C7A7, C5A8 and C7A8 are confirmed by the pH values of the samples water extracts that fall in the range 10.4–11.0.

The obtained biocarbons were tested as adsorbents of the gas pollutant, NO_2. Four variants of adsorption were used during the research [35]. The process of adsorption was carried out in dry (D) or wet (W, 70% humidity) conditions. Moreover, in order to check the effect of moisture content on the sorption abilities of the samples studied, they were subjected to prehumidization (M) with humid air (70% humidity) for 30 min. After this time, the adsorption tests were made in dry (MD) and wet (MW) conditions [36]. The effectiveness of NO_2 removal was observed to depend on the carbonization/activation temperature and conditions of adsorption. The sorption capacity of sample varied from 2.0 to 59.1 mg/g. The most effective adsorbent was sample C7A8 obtained by carbonization at 700 °C and activation at 800 °C, which was able to absorb between 19.1 and 57.1 mg NO_2/g_{ads}, depending on the adsorption variant. Sorption capacities of the biocarbon samples obtained were significantly dependent on the adsorption conditions. As indicated by the data from Fig. 1, prehumidization of the carbon adsorbent bed for 30 min prior to adsorption, conducted in dry (MD) and wet (MW) conditions, has a beneficial effect on the adsorption capacity. Only for samples C5A7 and C7A7, the relation is different.

Another observation following from the data collected in Fig. 1 is that the effectiveness of NO_2 removal by the biocarbons studied increases with increasing temperature of carbonization. The effect of the activation temperature was slightly more varied. In the case of samples C5A7 and C5A8, it was observed that the increase in activation temperature was accompanied by a slight decrease in the NO_2 removal efficiency when the adsorption test was carried out under MD and MW conditions. An inverse

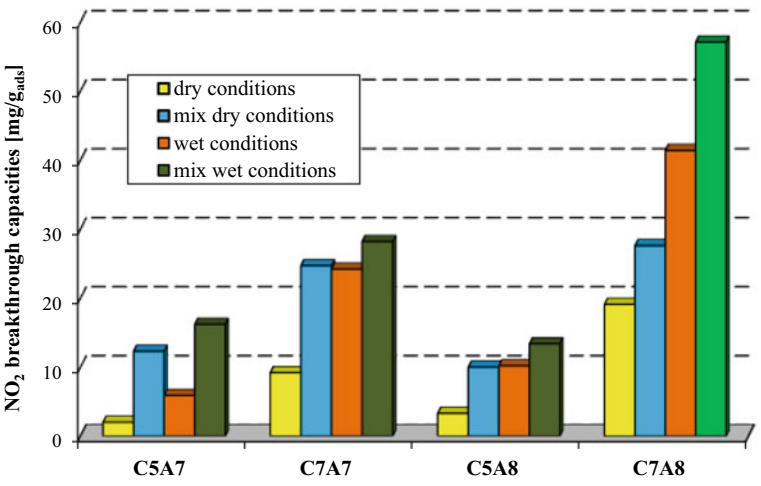

Fig. 1 NO_2 breakthrough capacities of the samples obtained from the residues after supercritical extraction of camomile flowers [29]

relationship was observed for analogous samples obtained from the residues after supercritical extraction of camomile flowers subjected to carbonization at 700 °C.

The work showed that the residues after supercritical extraction of camomile flowers can be cheap and easily available precursor for obtaining biocarbons with good sorption capacity toward nitric(IV) oxide. The obtained results indicate a significant influence of the conditions of the adsorption process on the obtained sorption capacities. It has been shown that, despite the low specific surface area, the samples show high sorption capacity toward NO_2, especially when the adsorption process was carried out in mix-dry and mix-wet conditions. The biomaterials obtained by physical activation with CO_2 show not well-developed porous structure and surface area, so further studies should be aimed at optimization of textural parameters.

3 Biocarbons Obtained from the Residues After Supercritical Extraction of Marigold Flowers

Next precursor was the residues after supercritical extraction of marigold flowers [37]. The starting material (M) was subjected to carbonization process that was carried out in a quartz tubular reactor heated by horizontal furnace, under a stream of nitrogen. The samples were heated from room temperature to the final carbonization temperature of 500 (M5) and 700 °C (M7) and kept at the maximum temperature for 60 min and then cooled down in inert atmosphere. Carbonization products were next subjected to physical activation (A). This process was carried out at temperature of 700 (A7) or 800 °C (A8) under a stream of carbon dioxide for 60 min.

The elemental analysis (Table 2) showed that the obtained carbon materials are characterized by higher content of elemental carbon and mineral substances than the initial material. Biocarbons showed higher content of N^{daf} relative to the precursor, which may follow from the presence of heterocyclic nitrogen groups resistant to the effect of high temperatures. The content of sulfur in the carbon adsorbents obtained is similar, irrespective of the activation temperature. The changes in content of oxygen and hydrogen were more complex. Unfortunately, as was the case with camomile, the physical activation of the residues after supercritical extraction of marigold flowers also does not permit effective development of surface area. The surface area of the samples varies from 2 to 206 m^2/g. The most developed surface area and porous structure showed sample M5A8, obtained by activation of biochar M5 at 800 °C. The textural parameters of the activated carbons discussed in [29, 37] indicate that the physical activation of the residues after supercritical extraction of raw plants should be carried out at a temperature not lower than 800 °C. Nevertheless, the results presented in Fig. 2 prove that the textural parameters of activated carbons depend on type of precursor and activation conditions. Each of starting materials requires an individual approach in determining the most optimal production procedure. According to the results collected in Table 2, the precursor used in the studies shows acidic character of surface. Interestingly, the processes of both carbonization

Table 2 Elemental analysis, textural parameters and acid–base properties of the biocarbons obtained from the residues after supercritical extraction of marigold flowers [37]

Sample	Ash	C^{daf}	H^{daf}	N^{daf}	S^{daf}	O^{daf*}	Surface area (m^2/g)	Surface oxygen functional groups (mmol/g)	
								Acidic	Basic
M	9.0	49.0	11.3	3.3	0.1	36.3	–	5.25	1.29
M5A7	33.9	79.8	0.4	4.8	0.4	14.6	2	0.00	5.51
M7A7	38.0	82.8	0.6	4.7	0.5	11.4	4	0.00	5.75
M5A8	49.2	59.1	2.5	5.2	0.3	32.9	206	0.00	7.74
M7A8	53.9	81.0	2.3	6.9	0.6	9.2	125	0.00	8.37

^{daf}dry ash-free basis, *by difference

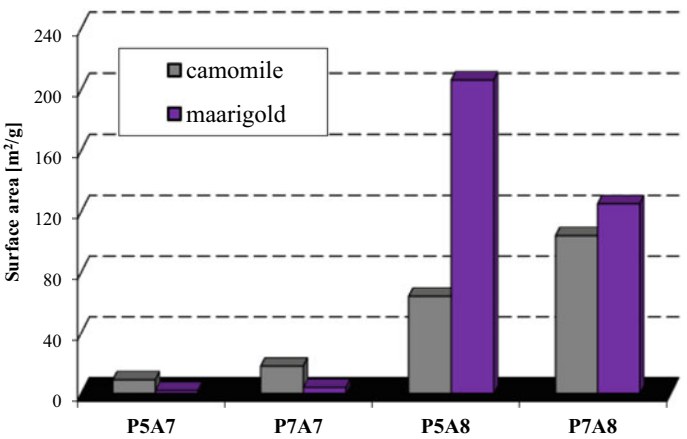

Fig. 2 Specific surface area of biocarbons obtained by physical activation of the residues after supercritical extraction of camomile and marigold flowers (P5/P7—carbonization temperature 500/700 °C; A7/A8—physical activation temperature700/800 °C) [29, 37]

and activation, irrespective of their temperatures, result in removal of acidic groups and a considerable increase in the basic groups. The number of basic oxygen groups on the surface depends to a significant degree on the temperature of carbonization and activation. With increasing temperature of carbonization and activation, the number of basic groups increases. The strongly basic character of the surfaces of activated carbons obtained is probably a consequence of the fact that the activator applied (CO_2) and the high temperature of activation are favorable for generation of basic groups [38].

The study has shown that the effectiveness of gas pollutants (NO_2) removal depends first of all on the conditions of adsorption. The samples were tested in two variants: in dry conditions (D) and after pre-humidification of activated carbon's bed by the air of 70% humidity for 30 min-mix-dry conditions (MD). The most effective

adsorbent in dry conditions was sample M7A8 whose sorption capacity of 29.2 mg/g was about twice higher than that of the other samples. Also in mix-dry conditions, this sample showed very good sorption capacity. The most effective adsorbent in mix-dry conditions was, however, sample M5A7, whose sorption capacity reached over 102.1 mg NO_2/g_{ads}, which was over 6 times greater than in the dry conditions (16.3 mg/g). For the other carbon samples studied, preliminary wetting with humid air resulted in only twice increased sorption capacity.

In turn, in the work [39], the residues after supercritical extraction of marigold flowers were carbonized at 600 °C in a nitrogen atmosphere for 60 min. The biochar (M6) was next subjected to physical activation at temperature of 700 (A7) and 800 °C (A8) under a stream of carbon(IV) oxide for 60 min. The processes of carbonization and activation were carried out in a quartz tubular reactor heated by horizontal furnace. Biocarbons obtained were characterized by elemental analysis, low-temperature nitrogen sorption and content of surface oxygen functional groups. Biocarbons were tested for the removal of NO_2 from the gaseous phase in dry, mix-dry, wet and mix-wet conditions (Table 3). All biocarbons are characterized by a higher content of elemental carbon than the starting material [29]. The highest content of elemental carbon was found in sample M6A8 obtained by activation of biochar M6 at 800 °C. Each of the activation products showed a very high mineral admixture content, as the contribution of ash varies from 27.2 to 32.7 wt%. The physical activation of the residues after supercritical extraction of marigold flowers does not permit effective development of their surface area. The BET surface area of the bicarbons varies from only 44 to 57 m^2/g. The data characterizing the acid–base nature indicated that the surfaces of the studied materials show basic character as there are no functional groups of acidic nature. As indicated by the data presented in Table 3, the efficiency of nitrogen dioxide removal depends first of all on the conditions under which the adsorption test was carried out. The highest sorption capacities were measured in wet as well as mix-wet conditions. High sorption capacities in these conditions are related to water film formation on the carbonaceous adsorbent's surface, which favors the capture and bonding of NO_2 molecules or even nitric acid formation [40].

The studies summarized in the articles [29, 37, 39] confirmed that it is necessary to optimize the process of producing biocarbons from the residues after supercritical extraction of raw plants.

4 Biocarbons Obtained from the Residues After Supercritical Extraction of Hops

In the next stage of the research, residues left after supercritical extraction of hops were used as a precursor for the production of biocarbons [41]. The production of hop has been continuously developing along with beer industry [42]. Although it is mostly used for beer production, the properties of hop have made it an attractive

Table 3 Textural parameters, acid–base properties and NO_2 breakthrough capacities of the biocarbons obtained from the residues after supercritical extraction of marigold flowers

Sample	Ash	C^{daf}	H^{daf}	N^{daf}	S^{daf}	O^{daf*}	Surface area (m^2/g)	Surface oxygen functional groups (mmol/g)		NO_2 breakthrough capacities (mg/g)			
								Acidic	Basic	Dry	Mix-dry	Wet	Mix-wet
M6A7	27.2	74.9	2.9	4.4	0.5	17.3	44	0.00	5.69	12.5	20.0	31.6	101.1
M6A8	32.7	75.1	3.4	5.6	0.5	15.4	57	0.00	8.32	50.8	51.6	71.6	102.6

^{daf}dry ash-free basis, *by difference

raw product for medicine, pharmacy or in cosmetic and food industry [43–45]. On industrial scale, extract from hop is obtained by supercritical CO_2 extraction [46]. This type of plants extraction leaves much waste that has to be utilized, and one of the methods proposed for their utilization is production of carbon adsorbents.

The precursor (H) was at first subjected to carbonization process in a traditional resistance pipe furnace at 500 for 1 h. Carbonization product was next subjected to physical activation (A) with carbon(IV) oxide at 800 °C for 1 h. The final product of activation was divided into two parts. One of them was washed distilled water ($H5A_{H2O}$), while the second part of the biocarbon ($H5A_{HCl}$) was subjected to demineralization with HCl and H_2O.

According to the data in [41], the ash content in the activated biocarbons varies from 5.3 to 32.2 wt% (Table 4). Due to the ash components, may block some pores in the activated carbon structure, thus reducing their surface area. That is why we introduced the process of washing of the carbon material with a 5% HCl solution and/or distilled water. Sample $H5A_{H2O}$ has a half-reduced content of ash than sample H5A. On the other hand, sample $H5A_{HCl}$, washed with HCl solution and distilled water, has over sixfold lower content of ash than biocarbon H5A and threefold lower content of ash than sample $H5A_{H2O}$. Biocarbon $H5A_{HCl}$ shows the most developed surface area and porous structure and is the only sample whose S_{BET} exceeds 1000 m^2/g. The surface area of the biocarbons obtained depends significantly on the variant of sample washing after activation. Washing with HCl causes unblocking of pores in the biocarbon structure and improves its textural properties [47]. It is evident from the data presented in Table 4 that the surfaces of samples H5A and $H5A_{H2O}$ show basic character. On the other hand, the washing at first with HCl solution and then with distilled water favors generation of acidic functional groups. This change in acid-base characteristics is due to the fact that HCl removes a considerable amount of mineral substance, which is usually basic in nature.

According to the data from Table 4, the effectiveness of removal of NO_2 depends considerably on the conditions of adsorption. For all biocarbons, the sorption capacities toward NO_2 were higher when adsorption took place in the presence of steam. The highest sorption capacity toward NO_2 showed sample H5A which has a relatively high content of mineral substance whose presence may be conducive to adsorption of gas pollutants such as nitrogen(IV) oxide [48]. The other two samples showed

Table 4 Ash content, textural parameters, acid–base properties and NO_2 breakthrough capacities of the biocarbons obtained from the residues after supercritical extraction of hops [41]

Sample	Ash (wt%)	Surface area (m^2/g)	Surface oxygen functional groups (mmol/g)		NO_2 breakthrough capacities (mg/g)	
			Acidic	Basic	Dry	Wet
H5A	32.2	413	0.00	4.87	42.0	72.1
$H5A_{H2O}$	16.0	664	0.00	4.39	36.7	58.0
$H5A_{HCl}$	5.3	1039	1.44	0.55	10.0	24.4

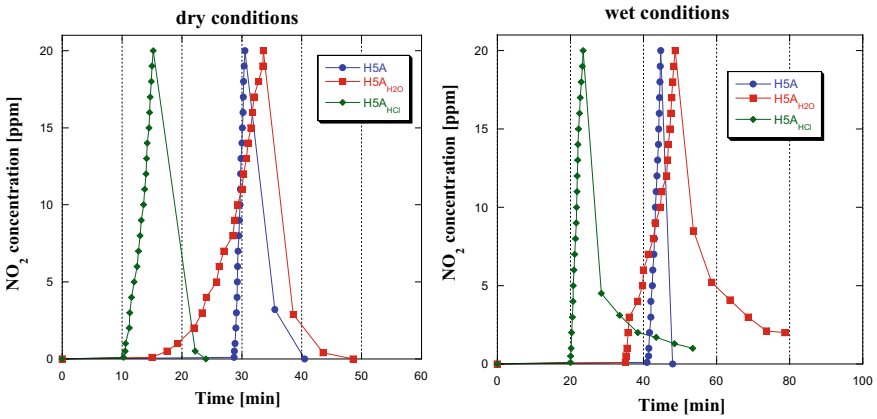

Fig. 3 NO_2 breakthrough curves for biocarbons studied in dry and wet conditions

much lower sorption capacities toward NO_2. It should be mentioned that the highest effectiveness of NO_2 removal by sample H5A is beneficial from the ecological and economic points of view as washing is related to additional cost and use of large volumes of water.

The curves in Fig. 3 illustrating changes in NO_2 upon adsorption in dry and wet conditions suggest that the process of NO_2 removal for the samples takes place according to the similar mechanism. For all samples, the concentration of NO_2 was equal to zero for a certain period of time, and only after the breakthrough, a gradual increase in NO_2 concentration was observed. A similar course of the curves was observed in the case of samples obtained by physical activation of the residues after supercritical extraction of camomile and marigold flowers [29, 37]. The results in work [41] confirmed the beneficial influence of the mineral substance content in the adsorbents on their sorption capacity toward nitrogen(IV) oxide.

In the next stage of the research, an attempt was made to obtain carbon adsorbents with a strongly developed surface area and microporous structure, as well as high sorption capacity toward NO_2. The method allowing production of such adsorbents is chemical activation by a series of activating agents such as: NaOH, KOH, K_2CO_3, H_3PO_4 and $ZnCl_2$ as it gives biocarbons of highly developed surface area and pore size distribution needed [49–51].

The residues left after supercritical extraction of hops (H) were divided into two parts [52]. One of them was impregnated with Na_2CO_3 solution (weight ratio Na_2CO_3:precursor 2:1—sample $H_{2:1}$ or 3:1—sample $H_{3:1}$) and subjected to chemical activation at 700 °C and kept for 45 min. The second part was first subjected to pyrolysis (HP) at 500 °C for 1 h. Pyrolysis product was next subjected to chemical activation with Na_2CO_3. Chemical activation by Na_2CO_3 was performed at 750 °C with an alkali/biochar weight ratio of 2:1—sample $HP_{2:1}$ or 3:1—sample $HP_{2:1}$ in nitrogen for 45 min. Chemical activation and carbonization were carried out in a quartz tubular reactor heated by horizontal laboratory furnace. After the activation

process, the final products were subjected to two-step washing procedure, first with a hot 5% solution of HCl and later with demineralized water until free of chloride ions.

According to the results presented in Table 5 and Fig. 4, the chemical activation of the residue after supercritical extraction of hop allows for a much more effective development of the surface area and the porous structure compared by physical activation of residues after supercritical extraction of raw plants. The surface area of the products varies in the range 897–1095 m^2/g. The textural parameters of the biocarbons depend on the weight ratio of the activating agent to the precursor or biochar. It should be noted that the surface areas of all activated biocarbons obtained in work [52] were larger than those of many commercial products available on the market [31]. Although obtained by different procedures, all the biocarbons obtained have similar acid–base properties. The highest total content of surface oxygen groups was found on sample $H_{3:1}$, obtained by chemical activation of precursor by Na_2CO_3, at the alkali:biochar ratio of 3:1. The lowest total content of functional groups was on the surface of sample $H_{2:1}$, on which only acidic functional groups were found. For the other activated biocarbon samples also, the acidic surface functional groups were dominant over the basic ones. Analysis of the effect of the variant of activation showed that the activation of the precursor favors the generation of a greater number of groups of acidic character and a smaller number of those of basic character in comparison to their number on the samples obtained by chemical activation of the biochar.

Each sample of activated biocarbon obtained was tested as adsorbent of NO_2 in dry and wet conditions. The results of the adsorption tests showed that biocarbons obtained are characterized by very good sorption capacity toward nitric(VI) oxide. Sorption capacity of the biocarbons in dry conditions is from 65.8 to 77.2 mg NO_2/g_{ads} and in wet conditions from 67.3 to 155.3 mg NO_2/g_{ads}. Comparison of the textural parameters with sorption capacities toward NO_2 reveals the effect of the degree of surface area development on the biocarbons adsorption capacity of this toxic gas. The higher capacities (especially in wet conditions) observed for samples $H_{3:1}$ and $HP_{3:1}$ are most probably related to better developed porous structure of these

Table 5 Textural parameters, acid–base properties and NO_2 breakthrough capacities of the biocarbons obtained from the residues after supercritical extraction of hops [52]

Sample	Textural parameters		Surface oxygen functional groups (mmol/g)		NO_2 breakthrough capacities (mg/g)	
	Surface area (m^2/g)	Average pore diameter (nm)	Acidic	Basic	Dry	Wet
$H_{2:1}$	897	2.65	1.86	0.00	75.1	79.7
$H_{3:1}$	1095	6.06	3.17	0.12	77.2	155.3
$HP_{2:1}$	1048	2.53	1.75	0.15	65.8	67.3
$HP_{3:1}$	1062	2.65	1.90	0.18	69.2	86.8

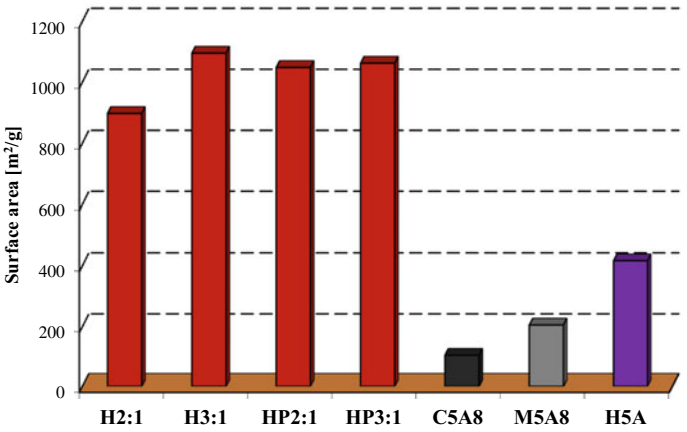

Fig. 4 Specific surface area of biocarbons obtained by chemical activation of the residues after supercritical extraction of hops [52] and physical activation of the residues after supercritical extraction of camomile [29] and marigold flowers [37]

samples. However, the sorption capacity depends also on the type of porous structure and mean pore size. According to literature, the adsorbents with mesopores of the sizes from the range of 5–10 nm are more effective in removal of gas pollutants [53].

The curves showing changes in the NO_2 concentration during the processes of adsorption in dry and wet conditions (Fig. 5) are similar for all biocarbon samples studied, so it can be assumed that the sorption on these samples takes place according to similar mechanism. However, the character of the desorption section of the isotherms (Fig. 5) revealed significant differences between the samples. After cutting off the inflow of NO_2 to the adsorbent bed, for samples $H_{3:1}$ (dry conditions) and $HP_{3:1}$ (dry and wet conditions), the concentration of NO_2 was maintained at a high level even after 30 min of washing with a flux of pure air, which proved weak bonding of nitrogen(IV) oxide in the porous structure of the adsorbent. It is worth pointing out that in the case of samples obtained by physical activation of the residues after supercritical extraction of camomile/marigold flowers and hops, an inverse relationship was observed [29, 37]. A rapid decrease in NO_2 concentration after cutting off its flow to the adsorbent bed suggests that the majority of adsorbed NO_2 has been permanently bound in the porous structure of the activated carbons, so it underwent chemisorption.

Based on the literature data [40, 54], it can be expected that adsorption of NO_2 in dry conditions takes place according to the following mechanism:

$$
\begin{aligned}
&-C^* + NO_2 \rightarrow C(O) + NO \\
&-C(O) + NO_2 \rightarrow -C(ONO_2) \\
&-C{-}C(ONO_2) \rightarrow CO_2 + NO + -C^* \\
&-C{-}C(ONO_2) \rightarrow CO + NO_2 + -C^*,
\end{aligned}
$$

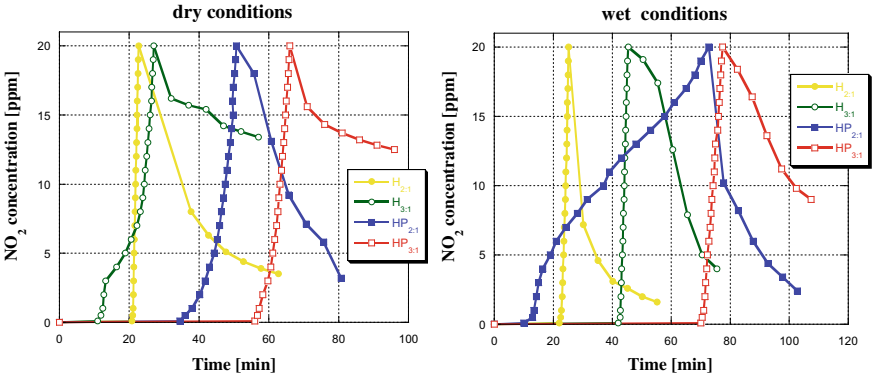

Fig. 5 NO_2 breakthrough curves for biocarbons studied in dry and wet conditions [52]

where –C* represents a carbon active site and –C(O) carbon oxygen complexes. Generally speaking, oxidation process of the carbons surface occurs, according to reactions:

$$C + 2NO_2 \rightarrow CO_2 + 2NO$$
$$C + NO_2 \rightarrow CO + NO.$$

During adsorption in wet conditions, the reaction of nitrogen dioxide with water can lead to formation of nitric acid or a mixture of nitric and nitrous acids:

$$3NO_2 + H_2O \rightarrow 2HNO_3 + NO$$
$$2NO_2 + H_2O \rightarrow HNO_3 + HNO_2,$$

which increases the sorption capacity toward NO_2 for the biocarbon samples studied.

5 Conclusion

This paper presents the results of research on the preparation of biocarbons from the residues after supercritical extraction of hops, camomile and marigold flowers. Biocarbons were synthesized based on two methods: physical and chemical activation. Carbon adsorbents were subjected to physicochemical characteristics and evaluation of sorption capacity toward NO_2.

1. It was found that the textural parameters of biocarbons depend on the method of activation and the starting material used for the research. The most favorable textural parameters were demonstrated by the samples obtained by activation of residues after supercritical extraction of hops, in particular the adsorbents obtained by chemical activation of this precursor.

2. The textural parameters of adsorbents obtained by physical activation depend on the carbonization and activation temperature. In addition, the surface area of the biocarbons obtained from the residues after supercritical extraction of hops depends significantly on the variant of sample washing after activation. Washing with HCl causes unblocking of pores in the biocarbon structure and improves its textural properties
3. Physical activation of the residues after supercritical extraction of hops, camomile and marigold flowers leads to the obtaining of activated carbons with a clearly basic surface character. On the other hand, adsorbents obtained by chemical activation have clear advantage of acidic surface character.
4. The study has also shown that the effectiveness of NO_2 removal depends first of all on the conditions of adsorption. The presence of water vapor and the previous wetting of the biocarbon bed had a beneficial effect on the sorption capacity obtained.
5. Poorly developed specific surface and a mineral substance in the structure of biocarbons obtained by physical activation of the residues after supercritical extraction of raw plants does not compromise their usefulness in the removal of gaseous pollutants.

References

1. G.Z. Guo, Y. Yu, K.C.S. Kwok, Y. Zhang, Air pollutant dispersion around high-rise buildings due to roof emissions. Build. Environ. **219**, 109215 (2022). https://doi.org/10.1016/j.buildenv.2022.109215
2. N. Elfikrie, Y.B. Ho, H. Juahir, E.S.S. Tan, Occurrence of pesticides in surface water, pesticides removal efficiency in drinking water treatment plant and potential health risk to consumers in Tengi River Basin. Malaysia. Sci. Total Environ. **712**, 136540 (2020). https://doi.org/10.1016/j.scitotenv.2020.136540
3. B. Mohammed, T. Mohammed, E. M'hammed, A. Tarik, Physiological and physico-chemical study of the effect of chromium VI on the nutritional quality of maize (*Zea mays*. L). Procedia Comput. Sci. **191**, 464–468 (2021). https://doi.org/10.1016/j.procs.2021.07.058
4. http://www.who.int/en/
5. S. Jones, N. Richardson, M. Bennett, S.R. Hoon, The application of magnetic measurements for the characterization of atmospheric particulate pollution within the airport environment. Sci. Total Environ. **502**, 385–390 (2015). https://doi.org/10.1016/j.scitotenv.2014.09.010
6. D. Landau, L. Novack, M. Yitshak-Sade, B. Sarov, I. Kloog, R. Hershkovitz, I. Grotto, I. Karakis, Nitrogen Dioxide pollution and hazardous household environment: what impacts more congenital malformations. Chemosphere **139**, 340–348 (2015). https://doi.org/10.1016/j.chemosphere.2015.06.091
7. Y. Dai, X. Cai, J. Zhong, A. Mazzeo, A.R. MacKenzie, Chemistry, transport, emission, and shading effects on NO_2 and O_x distributions within urban canyons. Environ. Pollut. **315**, 120347 (2022). https://doi.org/10.1016/j.envpol.2022.120347
8. Y. Zhao, S. Su, Y. Xing, L. Yu, S. Cui, D. Jiang, Z. Xiao, The green bonus: carbon reduction effect of sulfur dioxide emissions trading pilot scheme. Front. Environ. Sci. (2022). https://doi.org/10.3389/fenvs.2022.917887

9. X. Zhang, B. Gao, A.E. Creamer, C. Cao, Y. Li, Adsorption of VOCs onto engineered carbon materials: a review. J Hazard. Mater. **338**, 102–123 (2017). https://doi.org/10.1016/j.jhazmat.2017.05.013
10. M. Ligaray, C.M. Futalan, M.D. de Luna, M.-W. Wan, Removal of chemical oxygen demand from thin-film transistor liquid-crystal display wastewater using chitosan-coated bentonite: isotherm, kinetics and optimization studies. J. Cleaner Prod. **174**, 145–154 (2018). https://doi.org/10.1016/j.jclepro.2017.12.052
11. M. Marciniak, J. Goscianska, M. Norman, T. Jesionowski, A. Bazan-Wozniak, R. Pietrzak, Equilibrium, kinetic, and thermodynamic studies on adsorption of rhodamine B from aqueous solutions using oxidized mesoporous carbons. Materials **15**, 5573 (2022). https://doi.org/10.3390/ma15165573
12. Y. Li, Q. Dua, T. Liua, X. Peng, J. Wang, J. Sun, Y. Wang, S. Wu, Z. Wang, Y. Xia, L. Xia, Comparative study of methylene blue dye adsorption onto activated carbon, graphene oxide, and carbon nanotubes. Chem. Eng. Res. Des. **91**, 361–368 (2013). https://doi.org/10.1016/j.cherd.2012.07.007
13. A. Bazan-Wozniak, J. Cielecka-Piontek, A. Nosal-Wiercińska, R. Pietrzak, Adsorption of organic compounds on adsorbents obtained with the use of microwave heating. Materials **15**, 5664 (2022). https://doi.org/10.3390/ma15165664
14. E.L. da Silva, M. Torres, P. Portugau, A. Cuña, High surface activated carbon obtained from Uruguayan rice husk wastes for supercapacitor electrode applications: correlation between physicochemical and electrochemical properties. J. Energy Storage **44**, 103949 (2021). https://doi.org/10.1016/j.est.2021.103494
15. I. Enniyaa, L. Rghioui, A. Jourania, Adsorption of hexavalent chromium in aqueous solution on activated carbon prepared from apple peels. Sustain. Chem. Pharm. **7**, 9–16 (2018). https://doi.org/10.1016/j.scp.2017.11.003
16. J. Saleem, U.B. Shahid, M. Hijab, H. Mackey, G. McKay, Production and applications of activated carbons as adsorbents from olive stones. Biomass. Convers. Biorefin. **9**(4), 775–802 (2019). https://doi.org/10.1007/s13399-019-00473-7
17. J. McGinley, M.G. Healy, P.C. Ryan, P.-E. Mellander, L. Morrison, J.H. O'Driscoll, A. Siggins, Batch adsorption of herbicides from aqueous solution onto diverse reusable materials and granulated activated carbon. J. Environ. Manage. **323**, 116102 (2022). https://doi.org/10.1016/j.jenvman.2022.116102
18. G. Tang, L. Zhang, X. Zhu, X. Zhu, The preparation of activated carbon from walnut shell bio-oil distillation residues. New Carbon Mater. **34**, 434–440 (2019). https://doi.org/10.1016/j.carbon.2019.10.091
19. O. Baytar, Ö. Şahin, C. Saka, Sequential application of microwave and conventional heating methods for preparation of activated carbon from biomass and its methylene blue adsorption. Appl. Therm. Eng. **138**, 542–551 (2018). https://doi.org/10.1016/j.applthermaleng.2018.04.039
20. W. Ao, J. Fu, X. Mao, Q. Kang, C. Ran, Y. Liu, J. Dai, Microwave assisted preparation of activated carbon from biomass. Renew. Sustain. Energy Rev. **92**, 958–979 (2018). https://doi.org/10.1016/j.rser.2018.04.051
21. M.J. Puchana-Rosero, M.A. Adebayo, E.C. Lima, F.M. Machado, P.S. Thue, J.C.P. Vaghetti, M. Gutterres, Microwave-assisted activated carbon obtained from the sludge of tannery-treatment effluent plant for removal of leather dyes. Colloids Surf. A Physicochem. Eng. Asp. **504**, 105–115 (2016). https://doi.org/10.1016/j.colsurfa.2016.05.0
22. E. Uquichea, N. Cirano, S. Millao, Supercritical fluid extraction of essential oil from Leptocarpha rivularis using CO_2. Ind. Crop. Prod. **77**, 307–314 (2015). https://doi.org/10.1016/j.indcrop.2015.09.001
23. A. Rai, B. Mohanty, R. Bhargava, Supercritical extraction of sunflower oil: a central composite design for extraction variables. Food Chem. **192**, 647–659 (2016). https://doi.org/10.1016/j.foodchem.2015.07.070
24. S. Millao, E. Uquiche, Extraction of oil and carotenoids from pelletized microalgae using supercritical carbon dioxide. J. Supercrit. Fluid. **116**, 223–231 (2016). https://doi.org/10.1016/j.supflu.2016.05.049

25. M.M.R. de Melo, A.J.D. Silvestre, C.M. Silva, Supercritical fluid extraction of vegetable matrices: applications, trends and future perspectives of a convincing green technology. J. Supercrit. Fluid. **92**, 115–176 (2014). https://doi.org/10.1016/j.supflu.2014.04.007
26. S. Zhao, D. Zhang, Supercritical fluid extraction and characterisation of Moringaoleifera leaves oil. Sep. Purif. Technol. **118**, 497–502 (2013). https://doi.org/10.1016/j.seppur.2013.07.046
27. L. López-Hortas, P. Rodríguez, B. Díaz-Reinoso, M.C. Gaspar, H.C. de Sousa, M.E.A. Braga, H. Domínguez, Supercritical fluid extraction as a suitable technology to recover bioactive compounds from flowers. J Supercrit Fluids. **188**, 105652 (2022). https://doi.org/10.1016/j.supflu.2022.105652
28. H.H. Rassem, A.H. Nour, R.M. Yunus, Y.H. Zaki, H.S.M. Abdlrhman, Yield optimization and supercritical CO_2 extraction of essential oil from jasmine flower. Indones. J. Chem. **19**, 479–485 (2019). https://doi.org/10.22146/ijc.39710
29. A. Bazan, P. Nowicki, R. Pietrzak, Removal of NO_2 by adsorbents made of a residue from supercritical extraction of chamomile. Przem. Chem. **95**(4), 856–860 (2016). https://doi.org/10.15199/62.2016.4.29
30. H.P. Boehm, Some aspects of the surface chemistry of carbon blacks and other carbons. Carbon **32**, 759–769 (1994). https://doi.org/10.1016/0008-6223(94)90031-0
31. N.M.A. Al-Lagtah, A.H. Al-Muhtaseb, M.N.M. Ahmad, Y. Salameh, Chemical and physical characteristics of optimal synthesised activated carbons from grass-derived sulfonated lignin versus commercial activated carbons. Micropor. Mesopor. Mat. **225**, 504–514 (2016). https://doi.org/10.1016/j.micromeso.2016.01.043
32. Z. Ioannou, C. Karasavvidis, A. Dimirkou, V. Antoniadis, Adsorption of methylene blue and methyl red dyes from aqueous solutions onto modified zeolites. Water Sci. Technol. **67**(5), 1129–1136 (2013). https://doi.org/10.2166/wst.2013.672
33. P. Nowicki, The effect of mineral matter on the physicochemical and sorption properties of brown coal-based activated carbons. Adsorption **22**(4–6), 561–569 (2016). https://doi.org/10.1007/s10450-015-9729-x
34. J. Kazmierczak-Razna, P. Nowicki, R. Pietrzak, Characterization and application of bio-activated carbons prepared by direct activation of hay with the use of microwave radiation. Powder Technol. **319**, 302–312 (2017). https://doi.org/10.1016/j.powtec.2017.06.062
35. P. Nowicki, J. Kazmierczak, R. Pietrzak, Comparison of physicochemical and sorption properties of activated carbons prepared by physical and chemical activation of cherry stones. Powder Technol. **269**, 312–319 (2015). https://doi.org/10.1016/j.powtec.2014.09.023
36. R. Pietrzak, T.J. Bandosz, Activated carbons modified with sewage sludge derived phase and their application in the process of NO_2 removal. Carbon **45**(13), 2537–2546 (2007). https://doi.org/10.1016/j.carbon.2007.08.030
37. A. Bazan, P. Nowicki, R. Pietrzak, Removal of NO_2 by carbonaceous adsorbents obtained from residue after supercritical extraction of marigold. Adsorption **22**, 465–471 (2016). https://doi.org/10.1007/s10450-015-9709-1
38. P. Nowicki, R. Pietrzak, H. Wachowska, Comparison of physicochemical properties of nitrogen-enriched activated carbons prepared by physical and chemical activation of brown coal. Energy Fuels **22**, 4133–4138 (2008). https://doi.org/10.1021/ef800251w
39. A. Bazan-Wozniak, P. Nowicki, R. Wolski, R. Pietrzak, Activated bio-carbons prepared from the residue of supercritical extraction of raw plants and their application for removal of nitrogen dioxide and hydrogen sulfide from the gas phase. Materials **14**, 3192 (2021). https://doi.org/10.3390/ma14123192
40. A.M. Ebrahim, T.J. Bandosz, Effect of amine modification on the properties of zirconium–carboxylic acid based materials and their applications as NO_2 adsorbents at ambient conditions. Microporous Mesoporous Mater. **188**, 149–162 (2014). https://doi.org/10.1016/j.micromeso.2014.01.009
41. A. Bazan-Wozniak, P. Nowicki, R. Pietrzak, The effect of demineralization on the physicochemical and sorption properties of activated bio-carbons. Adsorption **25**(3), 337–343 (2019). https://doi.org/10.1007/s10450-019-00009-5

42. S.F. Turner, C.A. Benedict, H. Darby, L.A. Hoagland, P. Simonson, J.R. Sirrine, K.M. Murphy, Challenges and opportunities for organic hop production in the United States. Agron. J. **103**(6), 1645–1654 (2011). https://doi.org/10.2134/agronj2011.0131
43. J.S. Bland, D. Minich, R. Lerman, G. Darland, J. Lamb, M. Tripp, N. Grayson, Isohumulones from hops (*Humulus lupulus*) and their potential role in medical nutrition therapy. PharmaNutrition **3**, 46–52 (2015). https://doi.org/10.1016/j.phanu.2015.03.001
44. A. Formato, M. Gallo, D. Ianniello, D. Montesano, D. Naviglio, Supercritical fluid extraction of α and β-acids from hops compared to cyclically pressurized solid–liquid extraction. J. Supercrit. Fluid **84**, 113–120 (2013). https://doi.org/10.1016/j.supflu.2013.09.021
45. V. Sanz, M.D. Torres, V.J. López, H. Domínguez, What is new on the hop extraction? Trend Food Sci. Tech. **93**, 12–22 (2019). https://doi.org/10.1016/j.tifs.2019.08.018
46. A. Capuzzo, M.E. Maffei, A. Occhipinti, Supercritical fluid extraction of plant flavors and fragrances. Molecules **18**, 7194–7238 (2013). https://doi.org/10.3390/molecules18067194
47. A. Bazan-Wozniak, J. Cielecka-Piontek, A. Nosal-Wiercińska, R. Pietrzak, Activation of waste materials with carbon(IV) oxide as an effective method of obtaining biochars of attractive sorption properties towards liquid and gas pollutants. Materials **15**, 8000 (2022). https://doi.org/10.3390/ma15228000
48. A. Bazan-Wozniak, P. Nowicki, R. Pietrzak, The influence of activation procedure on the physicochemical and sorption properties of activated carbons prepared from pistachio nutshells for removal of NO_2/H_2S gases and dyes. J. Clean. Prod. **152**, 211–222 (2017). https://doi.org/10.1016/j.jclepro.2017.03.114
49. M. Kılıç, E. Apaydın-Varol, A.E. Pütün, Preparation and surface characterization of activated carbons from Euphorbia rigida by chemical activation with $ZnCl_2$, K_2CO_3, NaOH and H_3PO_4. Appl. Surf. Sci. **261**, 247–254 (2012). https://doi.org/10.1016/j.apsusc.2012.07.155
50. A. Elmouwahidi, E. Bailón-García, A.F. Pérez-Cadenas, F.J. Maldonado-Hódar, F. Carrasco-Marín, Activated carbons from KOH and H_3PO_4-activation of olive residues and its application as supercapacitor electrodes. Electrochim. Acta **229**, 219–228 (2017). https://doi.org/10.1016/j.electacta.2017.01.152
51. K.Y. Foo, B.H. Hameed, Preparation and characterization of activated carbon from pistachio nut shells via microwave-induced chemical activation. Biomass Bioenerg. **35**, 3257–3261 (2011). https://doi.org/10.1016/j.biombioe.2011.04.023
52. A. Bazan-Wozniak, P. Nowicki, R. Pietrzak, Production of new activated bio-carbons by chemical activation of residue left after supercritical extraction of hops. Environ. Res. **161**, 453–463 (2018). https://doi.org/10.1016/j.envres.2017.11.041
53. M. Florent, M. Tocci, T.J. Bandosz, NO_2 adsorption at ambient temperature on urea-modified ordered mesoporous carbon. Carbon **63**, 283–293 (2013). https://doi.org/10.1016/j.carbon.2013.06.081
54. P. Nowicki, R. Pietrzak, Effect of ammoxidation of activated carbons obtained from subbituminous coal on their NO_2 sorption capacity under dry conditions. Chem. Eng. J. **166**(3), 1039–1043 (2011). https://doi.org/10.1016/j.cej.2010.11.101

Impact of the Alkali Metals Ions on the Dielectric Relaxation and Phase Transitions in Water Solutions of the Hydroxypropylcellulose

M. M. Lazarenko, O. M. Alekseev, S. G. Nedilko, A. O. Sobchuk, V. I. Kovalchuk, S. V. Gryn, V. P. Scherbatskyi, S. Yu. Tkachev, D. A. Andrusenko, E. G. Rudnikov, A. V. Brytan, K. S. Yablochkova, E. A. Lysenkov, R. V. Dinzhos, Sabu Thomas, and Taniya Rose Abraham

Abstract The properties of water solutions of hydroxypropylcellulose (HPC) of different concentrations with added salts of the first group alkali metals (chlorides of Li, Na, K, Rb, and Cs) with the physiological saline concentration of 154 mmol L^{-1} were studied using electroconductivity, turbidimetry, densitometry, viscometry, dynamic light scattering, dielectric, and luminescence spectroscopy methods. All HPC-water-salt systems were shown to exhibit lower critical solution temperature (LCST) at temperatures between 40 and 50 °C. Adding ions to the

M. M. Lazarenko (✉) · O. M. Alekseev · S. G. Nedilko · A. O. Sobchuk · V. I. Kovalchuk · S. V. Gryn · V. P. Scherbatskyi · S. Yu. Tkachev · D. A. Andrusenko · E. G. Rudnikov · A. V. Brytan · K. S. Yablochkova
Taras Shevchenko National University of Kyiv, Kyiv, Ukraine
e-mail: lazmaxs@knu.ua

O. M. Alekseev
e-mail: alan@univ.kiev.ua

D. A. Andrusenko
e-mail: and_@univ.kiev.ua

A. V. Brytan
e-mail: a_britan@ukr.net

E. A. Lysenkov
Petro Mohyla Black Sea National University, Mykolayiv, Ukraine
e-mail: ealysenkov@ukr.net

R. V. Dinzhos
V.O. Sukhomlynskyi Mykolaiv National University, Mykolayiv, Ukraine

T. R. Abraham
School of Energy Materials, Mahatma Gandhi University, Kottayam, Kerala 686 560, India

S. Thomas
Mahatma Gandhi University, Priyadarshini Hills, Kottayam, Kerala 686 560, India
e-mail: sabuthomas@mgu.ac.in

O. Fesenko and L. Yatsenko (eds.), *Nanoelectronics, Nanooptics, Nanochemistry and Nanobiotechnology, and Their Applications*, Springer Proceedings in Physics 297,
https://doi.org/10.1007/978-3-031-42708-4_3

HPC-water solutions leads to the decrease in LCST and the appearance of agglomeration of nanoparticles at temperatures above LCST. At low temperatures, when the solutions are solid, the presence of ions in the solution shifts the dielectric relaxation to lower temperatures. This shift negatively correlates with the mass of ions in the solution. The ions are shown to affect several physical properties in both solid and liquid states similarly. Such similarity is attributed to the ability of ions to affect the structure of the hydrate shell and the close surroundings of HPC, as well as to the change of this structure with increasing temperature. The observed effects appear to be macroscopic attributes (markers) of the change in the structure and its kinetic properties due to impurities or thermal motion.

1 Introduction

The impact of ions on the structural transition with a lower critical solution temperature (LCST) in water solutions of a number of polymers has been extensively researched [1–4]. This transition is attributed not only to the formation of hydrogen bonds between the polymer network and water molecules but also to the presence of hydrophobic interaction between the water molecules and radicals in polymer molecules. The change in the structure of the polymer bond network in water imposed by the presence of impurities of various factors (electrolytes, for instance) can affect the temperature of the phase transition. A direct interaction between the ions and polymer molecules in water [1] is also possible, if the parts of the system form nanoclusters. To determine which mechanisms are at play, a comprehensive study of the physical properties of the water-polymer-electrolyte systems in a wide range of temperatures is significant. The subject of our study is the water solution of an non-ionic hydroxypropylcellulose (HPC) polymer by adding different groups of first group alkali metals. An HPC is known to undergo a phase transition with LCST, allowing to determine the impact of the ionic doping of the system both in liquid, and in solid state, as such ions play a role in the crystallization process [5]. The solid phase in water solution of electrolytes is known to be accompanied by the formation of ice nanocrystals without ionic impurities enveloped by the boundary layers of salt solution with a higher than initial concentration of ions [5]. In addition to that process, crystalline hydrates are also formed. The latter fact is a significant factor in the complex process of water purification in the water cycle of nature.

In our previous work, we have approached the issue of the sol–gel transition in water solution of cellulose derivatives both experimentally [6, 7] and by theoretical modeling [8].

The HPC is one of the thermosensitive materials important for biomedical application due to its thermally reversible sol–gel transition. It has various biomedical applications, e.g., in controlled drug delivery systems (both bulk hydrogels and nanoparticles), in sensors and actuators, “smart” cells, etc. [9]. It has been noted that HPC gels consist of natural cellulose ether macromolecules which have been

approved by the United States Food and Drug Administration (FDA). Thus, they have significant comparative advantage over often cancerogenic synthetic gels.

The presence of salts in HPC-water solution affects the temperature and other characteristics of sol–gel transition and can thus be used for engineering of smart system properties [10]. In the view of the biomedical application of these materials, understanding the mechanisms of ions-solution interaction is of importance [11, 12], in particular how the alkali-halide salts impact the structural transitions.

The role of salt ions play in the transition characteristics depends on the type of the added ions and on their ability to modify the structure of water in the vicinity of the polymer molecules in solution. This question has attracted an extensive interest of researchers [1–4, 13–15]. However, the research on the impact of the alkali-halide salt on the behavior of water solutions of HPC is somewhat limited (see, among others [16–19]).

For instance, the water solution of NaCl was used, foremost, as the environment for the surfactant-free hydroxypropyl cellulose (HPC) microgels synthesis, and the impact on the concentration of NaCl on HPC solutions was studied only as an outcome of such synthesis. The effect of anions in the composition of the fluoride, chloride, bromide, and iodide salts of sodium on the HPC solution was the main goal of the study described in [17]. A very practical question of determining the phase transition temperature of water-HPC system in the presence of NaCl was reported earlier [18, 19]. As per [19], it described the impact of NaCl on the properties of aqueous HPC foams, not on the properties aqueous HPC solutions.

This brief analysis demonstrates that the temperature behavior of the HPC in the alkali-halide water solutions was not studied systematically. Particularly, there are no data about change of the transition characteristics in the row of ions of the same charge, but possessing different ionic radii. At the same time, these particular data are very important for understanding the physical mechanisms of sol–gel transitions in similar system, as well as for the practical use of these materials in biomedical applications.

Thus, the objective of this work is to determine how the ions of alkali metals of the homologous series $Li^+ \rightarrow Na^+ \rightarrow K^+ \rightarrow Rb^+ \rightarrow Cs^+$ and the Cl^- anion alter the physical properties of the HPC in water solution and the phase transitions in this system. The systems were all studied in the wide range of temperatures, which included both liquid–solid phase transition and the LCST transition. All these systems can form nano-sized structural inhomogeneities near the phase transition temperatures, whose properties can be affected by both polymer and ionic impurities. A set of experimental methods—viscometry, turbidimetry, electroconductivity, dielectric spectroscopy and the dynamic scattering of light—were used to determine the relation between the content and the physical properties of these systems. A valuable addition to the barrage of the above-listed methods traditionally used to study the sol-gel transition is the luminescent analysis. This method, as other optical methods (dynamic scattering of light, light transmittance, etc.), is contactless and known for its high sensitivity. Luminescence analysis has been used in previous research [20–24].

2 Experimental Section

2.1 Materials

We used 0.2, 1, and 2% (by mass) water solutions of hydroxypropyl cellulose (Alfa Aesar, M.W. 100,000, molecular weight 10^5, degree of substitution 75.7 [25], further referred to as HPC-water solutions). The 1st group alkali metals' ions (Li, Na, K, Rb, and Cs chlorides) were added to modify the system (these solutions are further referred to as HPC-water-salt solutions). The molar concentration of salt in all samples was identical and equal to that of a physiological saline (154 mmol L^{-1}).

2.2 Methods

The data for the specific electric conductivity of the samples were obtained with the help of a three-electrode capillary cell and an AC bridge P5083, which was used to measure the resistance between electrodes. The specific conductivity was then calculated using resistances measured at frequency 50 kHz at temperatures between 10 and 75 °C [26]. Density of samples was measured using density meter DMA 4500 M from Anton Paar at temperatures between 10 and 75 °C.

Dynamic viscosity of samples was measured using viscosity meter Lovis 2000 M/ME at temperatures between 10 and 75 °C using a capillary of 1.59 mm diameter.

The temperature-dependent dynamic light scattering (DLS) size distributions were measured by Zetasizer Nano ZS (Malvern) instrument at 173° backscatter geometry for water-HPC solution and water-HPC solutions with 154 mmol L^{-1} of NaCl. The temperature was increased from 25 to 60 °C at given intervals; equilibration time was 120 s.

Luminescent characteristics were measured using DFS-12 spectral monochromator equipped with two grates (1200 grooves/mm; linear dispersion 1 mm/nm) and FEU-79 photomultiplier. A diode-pumping lasers with excitation wavelengths of $\lambda_{ex} = 405$ nm were used as a light source of photoluminescence excitation. All the PL spectra were corrected for the spectral response of the registering system. 2) The photoluminescence intensity was determined as an integral (an area under the spectral curve in relative units) in the spectral range of 425–775 nm. All samples were placed in the quarts cuvette of 10 mm thickness.

Transmission spectra of the solutions were measured using the same spectral monochromator. The KGM halogen lamp was used as source of wide-band emission and cuvette filled with water was used as reference sample.

The dielectric properties were studied in 1–50 kHz frequency range and – 190–100 °C temperature range using an automated installation based on a P5083 AC bridge and a four-electrode thermostatic cell, with an option of a sample thickness control. The samples were placed into enclosed polyethylene capsules, allowing us

to perform measurements in a temperature interval which includes phase transition regions [27, 28].

Turbidity of the samples was measured using methods and a setup described in [29].

3 Results and Discussion

3.1 Electroconductivity

The thermal behavior of electric conductivity σ was recorded for the 2% water solution of HPC with 1st group alkali metal ion impurities (chlorides of Li, Na, K, Rb, and Cs) and presented in Fig. 1. The electrical conductivity of the pure water-HPC system is of three orders of magnitude smaller than that of the water-HPC-salt system, clearly suggesting the presence of ions in the latter.

No interesting behavior of $\sigma(T)$ is observed near phase transition of LCST temperature, indicating the absence of the spatial inhomogeneity of the ion distribution in the polymer molecules clusters that appear during the phase transition with LCST.

3.2 Turbidimetry

The variations of transparency of the 2% water solution of HPC with 1st group alkali metal ion impurities (chlorides of Li, Na, K, Rb, and Cs) with temperature are shown in Fig. 2. All curves in Fig. 2 are normalized to the transparency of the HPC-water sample at 25 °C.

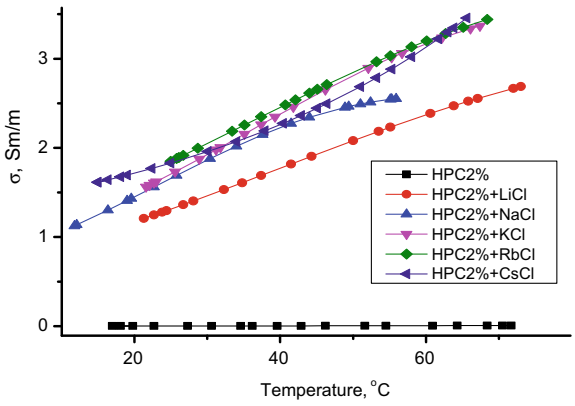

Fig. 1 Thermal dependence of electrical conductivity of the 2% water solution of HPC with 1st group alkali metal ion impurities (chlorides of Li, Na, K, Rb, and Cs)

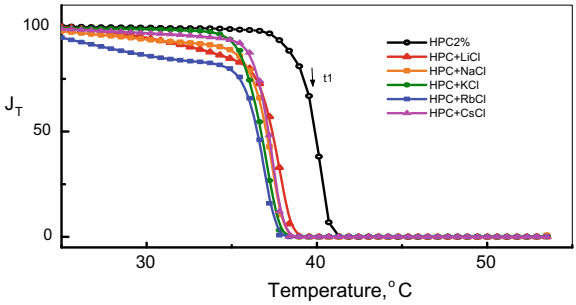

Fig. 2 Thermal dependency of the transparency J_T of 2% water solution of HPC with 1st group alkali metal ion impurities. The rate of heating is 1.1 °C min^{-1}

In order to interpret the results of turbidity experiment, the following formalism is applied [30], which we have previously used to describe the kinetics of the first-order phase transitions in the variable temperature field. Below is the short description of this approach.

Let phases A and B be in equilibrium at temperature $T = T_0$ and let a phase transition $A \rightarrow B$ takes place at $T > T_0$. Assuming the temperature of the system increases linearly with time [31], the following expression can be derived.

$$\ln \theta_A(T) = -\xi (T - T_0)^{3(1+\alpha)} \exp\left\{-\frac{M}{(T - T_0)^2}\right\}, \tag{1}$$

where θ_A is the relative volume of phase A; ξ, T_0, α, and M are experimentally determined parameters. In [30], the ratio of the surface tension coefficients on the sol- and gel phases interface in the samples used in the experiment was shown to be expressed as

$$\sigma'/\sigma_1 = (M'/M_1)^{1/3}, \tag{2}$$

where dash corresponds to the properties of solutions with ions.

Table 1 summarizes the values of parameters in expression (1) obtained by minimizing the RMS deviation and assuming $\xi = 0.1 \cdot 10^{-13} K^{-3(1+\alpha)}$, $T_0 = 296\,\mathrm{K}$ (optimal values for all measurements).

The presence of ions in the solution seems to decrease the coefficient of the interphase surface tension. Such observation can be explained in the following way. Cellulose derivatives are relatively rigid-chained polymers [6], whose macromolecules in different solvents form conformations determined by both the type of solvent, concentration of polymers, and other parameters. For instance, the authors of [32] have demonstrated that in 1–5% water solution of HPC (by mass) its polymeric chain has a random coil conformation.

An equilibrium state of a polymer random coil at $T = T_0$ is characterized by a RMS radius and mean square radius of gyration which, in turn, is determined by the balance of the electrostatic repulsion of monomers (leading to the expansion of the coil) and the restoring elastic forces [31]. The transition from the equilibrium

Table 1 Parameters in expression (1) and the of inter-phase surface tension coefficients σ in the presence of ionic impurities in polymer solution

n	Ions	α	$M \times 10^3$, K^2	σ_n/σ_1
1	–	4.033	3.659	1
2	Li^+	3.933	2.051	0.825
3	Na^+	4.191	2.299	0.856
4	K^+	3.925	1.698	0.774
5	Rb^+	3.969	1.829	0.794
6	Cs^+	4.565	2.987	0.935

state into gel is accompanied by the increase in temperature and the expansion of the polymer coil [33]. The presence of ions in the solution further increases the expansion of the coil due to shielding of the interaction between the links of the polymer chain (Fig. 1) and the decrease in work necessary to form a unit surface area of sol–gel interface. We believe this mechanism can qualitatively explain the decrease in the coefficient of the interphase surface tension in presence of 1st group alkali metals ions in the solution.

3.3 Dynamic Light Scattering

The dynamic light scattering at different temperatures was determined for the 0.2% water solution of HPC with 1st group alkali metal ion impurities (chlorides of Li, Na, K, Rb, and Cs) and presented in Figs. 3 and 4. The 0.2% solution of HPC at 25 °C contains nanoparticles of sizes of order 30–300 nm. As the temperature increases and approaches the phase transition, smaller nanoparticles disappear (Fig. 3). The size of larger nanoparticles first, as the temperature approaches the phase transition temperature, decreases to 200 nm and then increases to 550 nm at 50 °C (Fig. 4). At 60 °C the size of particle decreases to 500 nm.

HPC solution with ions also contains nanoparticles of two sizes at 25 °C: small nanoparticles of 30 nm diameter and larger nanoparticles of 500 nm diameter. The former disappear as the temperature increases. Around phase transition temperature, the diameter of larger nanoparticles first decreases to 400 nm and then increases dramatically to 3500–4000 nm at 50 °C and then somewhat decreases to 1500–200 nm at 60 °C (Fig. 4).

3.4 Luminescence Properties

Cellulose and its derivatives in solid state are known to exhibit luminescent properties at several photoexcitation wavelengths [23]. In light of this, we have measured the

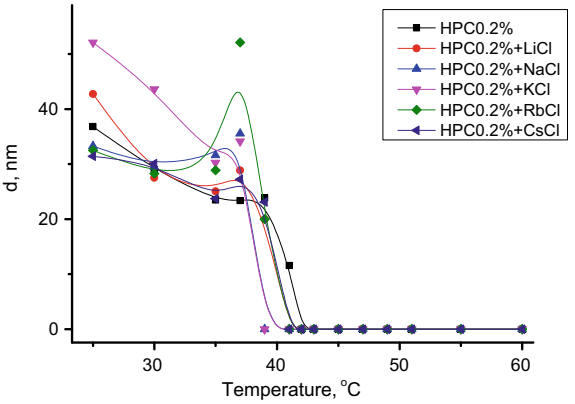

Fig. 3 Variation of the size of small nanoparticles with temperature in 0.2% water solution of HPC with 1st group alkali metal ion impurities (chlorides of Li, Na, K, Rb, and Cs)

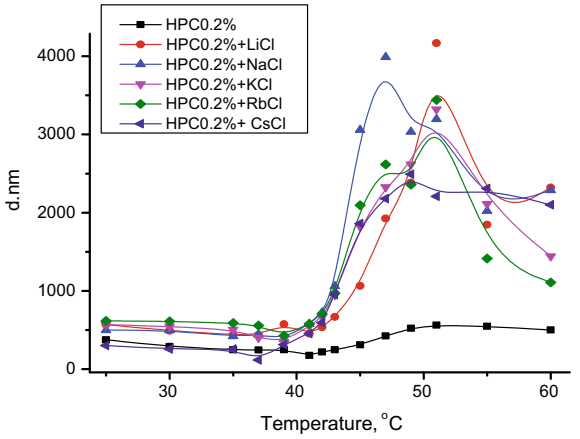

Fig. 4 Variation of the size of larger nanoparticles with temperature in 0.2% water solution of HPC with 1st group alkali metal ion impurities (chlorides of Li, Na, K, Rb, and Cs)

spectrum of the initial solid powder of the hydroxypropylcellulose. As expected, the emission spectrum of HPC is wide, being a superposition of several components centered at approximately 495, 540, 575, and 640 nm. (see arrows in Fig. 5) The efficiency of luminescence of the spectral components depends on the excitation wavelength λ_{ex} as demonstrated in Fig. 5.

As the excitation wavelength increases from 405 to 532, the more efficient excitation of the longer wavelength components in the HPC spectrum becomes, shifting the PL spectrum maxima from 540 to 580 nm.

The spectrum we have obtained and its behavior are similar to those reported earlier for cellulose-based composites [23, 34–36].

Based on this similarity, we may conclude that the emission spectrum observed is due to the luminescence process in the HPC itself. Photoluminescence of cellulose is usually attributed to a number of sources such as, for instance, molecular fluorophores belonging to cellulose matrices. Unfortunately, the question of PL origin and the role particular parts of cellulose and its derivatives play in it is still under-researched.

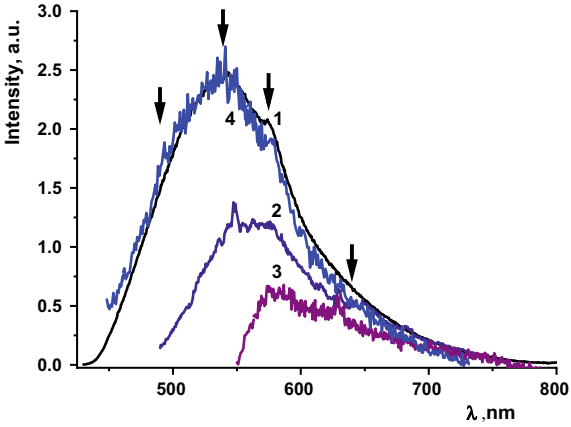

Fig. 5 PL spectra of the HPC powder (1–3) and HPC powder obtained from HPC-CsCl gel (4) with different excitation wavelengths: $\lambda_{ex} = 405$ nm (1, 4), $\lambda_{ex} = 473$ nm (2), and $\lambda_{ex} = 532$ nm (3)

As the excitation wavelength of 405 nm corresponds to the HPC absorption edge, both absorption and luminescence due to this excitation must be caused, foremost, by certain surface molecular groups or defects.

Due to external factors, the number and the efficiency of different PL sources can change, leading to the change in their emission spectrum—exactly what is observed for the emission spectrum of the water solution of HPC with electrolytes at increasing temperatures.

Figure 6 shows PL spectra of the water solution of HPC in the temperature range from 17 to 60 °C. A total of 24 spectra were recorded and labeled p1 through p24 in order of increasing temperatures. Some of these spectra are shown in Figs. 6 and 7.

The presence of water shifts the PL spectra toward longer wavelengths ($\lambda >$ 500 nm) even at the initial temperatures of 18–20 °C. The 495 nm component, clearly

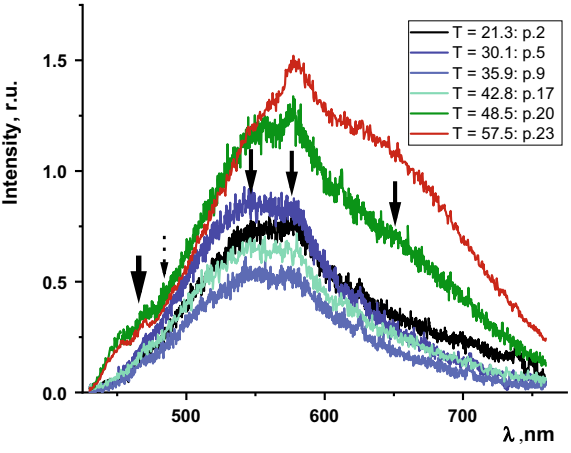

Fig. 6 PL spectra of HPC solutions (1–3) at different temperatures excited by $\lambda_{ex} = 405$ nm

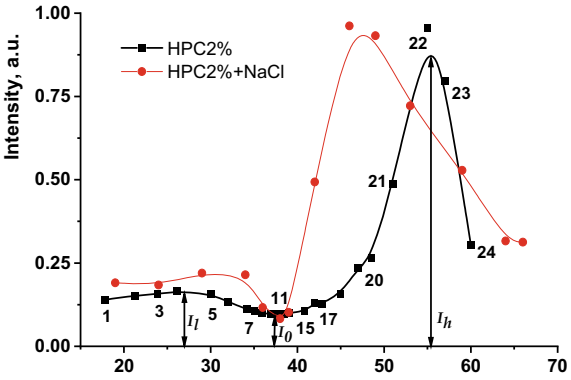

Fig. 7 Temperature dependences of the PL intensity of the HPC (black curve) and HPC-NaCl (red curve) systems

visible in the HPC powder spectra, practically disappears (its position in Fig. 6 is indicated by an arrow).

A certain turbidity is first detected visually at temperatures above 38.5 °C, which is exactly the temperature at which the intensity of the long wavelength light (600–750 nm) begins to increase.

A further analysis of the thermal behavior of PL should take form of the comparison of the spectral changes with the changes in the integral intensity of the emission (Fig. 7).

The thermal dependency of PL intensity of the HPC solution has two distinct regions: the low-temperature (17–38 °C) and high-temperature (38–60 °C) regions. Within each region, the intensity of the emission first increases and then decreases. However, the nature of these changes is different.

Evidently, the starting point of the behavior and the corresponding spectra in Fig. 6 correspond to the individual, detached HPC molecules (should they exist in the water solution) and HPC molecular chains. The intensity of this emission compared to the intensity of PL in powder is low, due to the decay of the vibronic excitation of HPC molecules into high-frequency vibrations of water molecules from their closest surrounding (hydrate shell).

As the temperature increases, HPC chains associate. Consequently, the deactivating PL impact of water on the part of the HPC molecules (chains) located in the inner parts of associate decreases, and the intensity of PH increases with increasing temperatures (up to 27 °C). Further on, as the temperature increases to 38–40 °C, the above-described effect is damped by the competing action of the molecules of hydrate shell, as the probability of non-radiative transitions increases exponentially with temperature.

In the low-temperature region, the HPC solution is transparent in visible light area; thus, associates present there are, mostly, nano-sized (up to 200 nm). Along with this, the redistribution of the radiation toward a short wavelength, observed in this range of temperatures (Fig. 6, p. 2 through p. 17), is the evidence that the number of associates of larger sizes increases. These optical observations agree with

the dynamic light scattering data, as the majority of particles in the temperature range from 20 to 40 °C are small (30–40 nm).

As the threshold of the structural transition (38–40 °C) is attained, the intensity of the PL begins to increase again, first slowly and then, above 50 °C, at a higher rate. We may assume that the first, slow phase of intensity growth is due to the particles of the small size, whereas the next abrupt increase in the intensity is due to the amalgamation of both small and large particles in macro-sized associates/coils of sizes 2 μm and larger. These coils, as mentioned earlier, display the high efficiency of PL. Consequently, a long wavelength component impact in the PL spectra increases (Fig. 6, curves p.20 through p. 23). The further decrease in the PL intensity, as will be explained later, is not caused by the change in temperature but rather is the consequence of the self-association of the macro-sized groups and their deposition at the bottom of the cuvette. As a result, the amount of luminescent material along the excitation laser track decreases. A similar conclusion about the self-association mechanism at temperatures above the phase transition is drawn in [36], where the thermal behavior of the HPC-water solution was studied using Rayleigh light scattering methods.

When MCl salts are added to the solution, the thermal behavior of the HPC solution's PL spectrum essentially remains the same. However, as shown in Fig. 8, the presence of NaCl in the solution leads to a more distinct separation of the regions of the small- and large-size associate formation and the sol–gel transition stage.

Moreover, the low-temperature region for HPC-NaCl systems appears to have two subregions (Fig. 7, red curve): a plateau from 17 to about 25 °C and a subregion with a maximum at about 32 °C. The latter, we believe, is due to the more active formation of the larger particles when NaCl salt is present in the solution. Evidently, these changes in the PL behavior should be attributed to the destruction of the hydrate shell of water/HPC chains by Na^+ ions and the subsequent formation of the hydrate-solvation shell. The latter's effect on the luminescent properties in the luminescent centers is not identical to the effect of a hydrate shell.

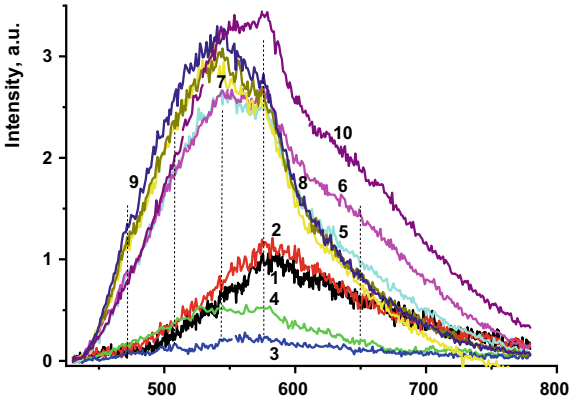

Fig. 8 PL spectra of the HPC-NaCl solutions at different temperatures: T = 19 (1), 34 (2), 38 (3), 39 (4), 42 (5), 46 (6), 53 (7), 59 (8), 64 (9), and 64 °C (10)

Table 2 Temperatures T_1, T_0, and T_h (°C), values of R_{lum} for water solution of HPC та water-HPC-MCl systems (M = Li, Na, K, Rb, and Cs)

Solution	T_1	T_0	T_h	R_{lum}
HPC	27.1	37.3	55.1	12.8
HPC-LiCl	25.9	38.2	52.3	3.91
HPC-NaCl	31.7	38.1	46.2	6.32
HPC-KCl	24.8	35.8	43.5	4.03
HPC-RbCl	27.0	41.3	43.4	2.26
HPC-CsCl	30.2	41.2	46.0	4.14

The thermal behavior of the spectra and luminescence intensity of HPC-water-MCl (M = Li, K, Rb, and Cs) systems was similar to that of HPC-NaCl. The position of extremums (T_1, T_0, and T_h in Fig. 7) and the PL intensities at these temperatures (I_1, I_0, and I_h in Fig. 7) evidently have different values for systems with different salts and are listed in Table 2.

Since the mechanisms affecting the PL spectrum in low- and high-temperature regimes are different, it is convenient to use a quantity R_{lum}, which takes into account the luminescent characteristics of the solutions in these two temperature ranges:

$$R_{\text{lum}} = \frac{I_h - I_l}{I_l - I_0}, \tag{3}$$

where I_1, I_0, and I_h are PL intensities at temperatures T_1, T_0, and T_h, as outlined above. The values of temperatures T_1, T_0, and T_h, as well as the values of R_{lum} are all listed in Table 2

The examination of Table 2 shows that the values of T_1 and T_0 do not exhibit any trends or regularities for the homologous series salts present in the solutions. This can be expected, as in low-temperature region at least two processes are at play and it is currently impossible to untangle the impact of each. The value of T_0 then plays a merely technical role: to determine the value of I_0.

In contrast, both the values of T_{h} and R_{lum} consistently decrease for solutions with cations $Li^+ \rightarrow Na^+ \rightarrow K^+ \rightarrow Rb^+$. Clearly, this trend is due to the ionic mechanism of alkali metals ion's impact on the structure of water in the nearest surrounding of the HPC molecules/chains.

3.5 Viscometry

The variations of density and dynamic viscosity with temperature were recorded for the 0.2, 1, and 2% HPC solutions (Fig. 9a).

Thermal dependency of the dynamic viscosity of all samples exhibits a two-phase transition around 40–50 °C, which will be discussed later in this work.

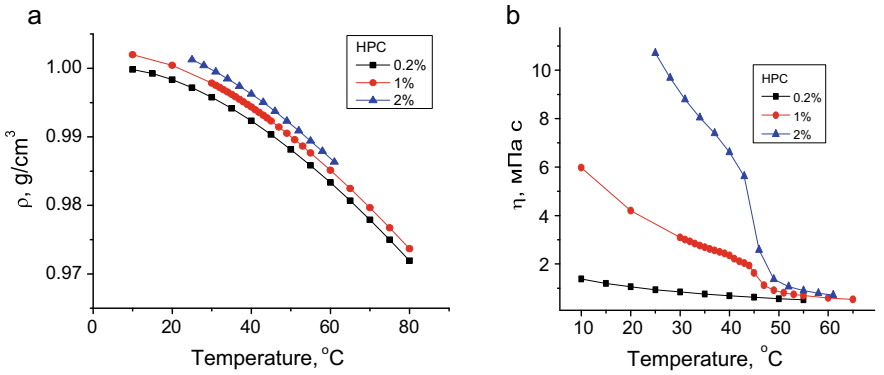

Fig. 9 Thermal dependencies of the density (**a**) and dynamic viscosity (**b**) of 0.2, 1, and 2% water solution of HPC

As the concentration of HPC in water increases, so does its density (Fig. 9a) and its dynamic viscosity (Fig. 9b). The dependence of dynamic viscosity on temperature can be used to approximate experimental data using the model of motion of the viscous fluid molecules:

$$\eta = \eta_0 \exp\left(\frac{E}{k(T + T_0)}\right), \tag{4}$$

where η_0—constant, k—Boltzmann's constant, E—potential barrier height, T_0—temperature correction.

As result of the dynamic viscosity of HPC solutions temperature dependences approximation by formula (1), we obtained the values of $E = 3.5$, 4.2, and 4.8 kJ/mol for HPC concentrations of 0.2, 1, and 2%, respectively. That is, as the concentration of HPC increases, the value of the potential barrier that the flowing particles must overcome also increases.

The variations of density with temperature were recorded also for the 0.2, 1, and 2% HPC solutions with the 1st group alkali metal ions (chlorides of Li, Na, K, Rb, and Cs) of molar concentration 154 mmol L^{-1} (Fig. 10). The density of the water-HPC-ions system appears to increase with the increasing mass of the ions.

Finally, the variations dynamic viscosity with temperature were recorded for the 0.2, 1, and 2% HPC solutions with the 1st group alkali metal ions (chlorides of Li, Na, K, Rb, and Cs) of molar concentration 154 mmol L^{-1} (Fig. 11).

The thermal dependencies of the dynamic viscosity of the 1 and 2% HPC-water-ions systems (Figs. 11 and 12) indicate that the double transition seems to shift toward lower temperatures. To determine the precise temperatures of the transition, the first derivatives of the dynamic viscosity variation with temperature were plotted for all 1% HPC-water-ions systems (Fig. 13).

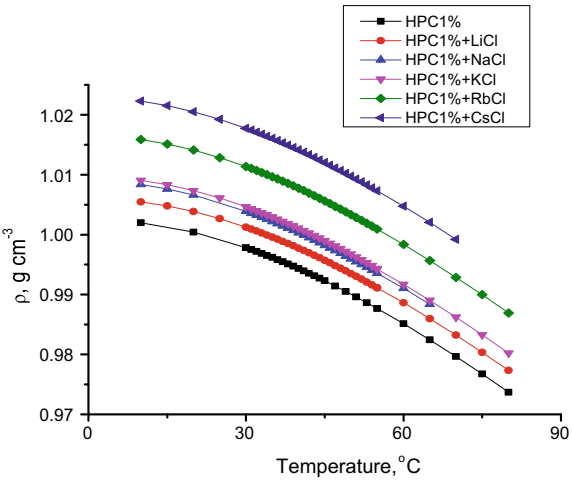

Fig. 10 Thermal dependencies of the density of the 1% HPC-water solution with 1st group alkali metal ions (chlorides of Li, Na, K, Rb, and Cs)

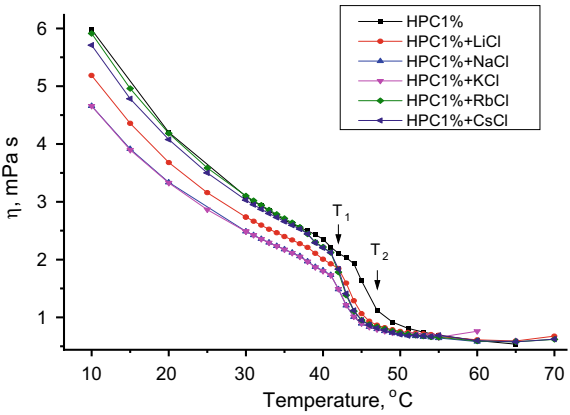

Fig. 11 Thermal dependencies of the dynamic viscosity of the 1% HPC-water solution with 1st group alkali metal ions (chlorides of Li, Na, K, Rb, and Cs)

Thermal dependencies of the rate of change of the dynamic viscosity of the 1% HPC-water solution with 1st group alkali metal ions exhibit two minima, corresponding to two transitions. The temperatures of these transitions were determined for all samples to elucidate a possible trend. Figure 14 clearly suggests that when ions are added to the system, both transitions occur at lower temperatures.

Expression (1) was then applied to model the thermal dependencies of dynamic viscosity for the 0.2% HPC solution with ions of alkali metals. Using this expression, the values of potential barriers were determined for each system. This data is summarized in Fig. 15, showing the variation of the energy of the potential barrier with the mass of the ions in the solution; the height of the barrier appears to correlate positively with the mass of the ion.

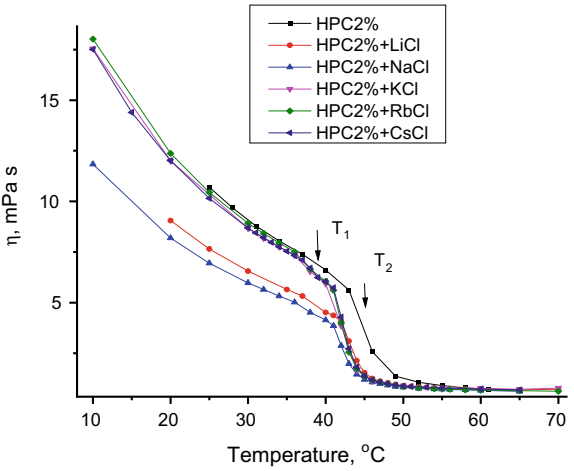

Fig. 12 Thermal dependencies of the dynamic viscosity of the 2% HPC-water solution with 1st group alkali metal ions (chlorides of Li, Na, K, Rb, and Cs)

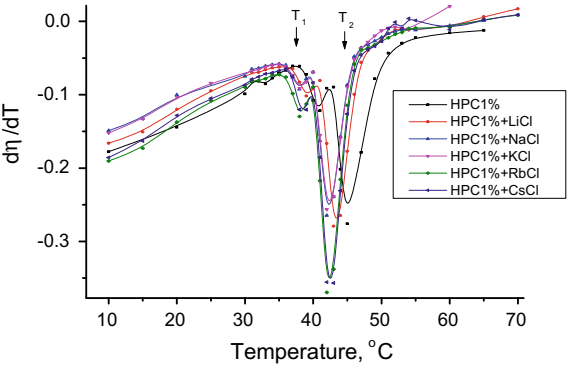

Fig. 13 Thermal dependencies of the rate of change of the dynamic viscosity of the 1% HPC-water solution with 1st group alkali metal ions (chlorides of Li, Na, K, Rb, and Cs)

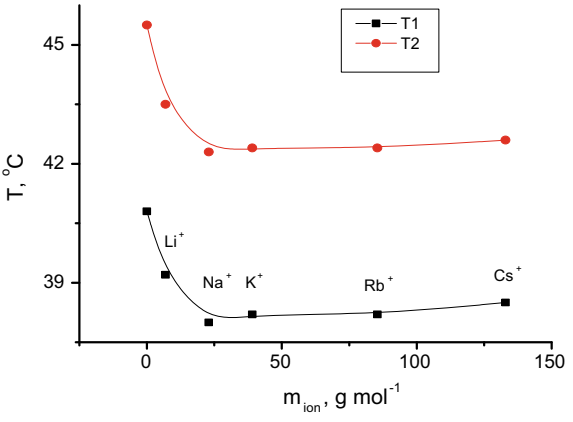

Fig. 14 Transition temperatures for the 1% water solution of HPC with alkali metal ions of different mass

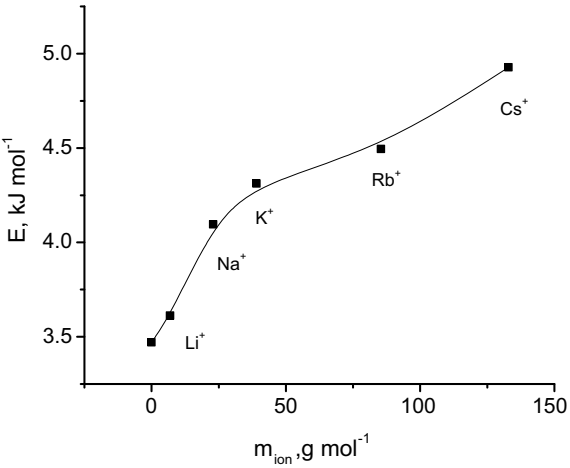

Fig. 15 Potential barrier determining dynamic viscosity of the solution and the mass of ions added to the solution

3.6 Dielectric Properties

Temperature dependencies of the real ε' and imaginary ε'' components of the complex dielectric permittivity ε^* were recorded in the temperature range from –100 to 50 °C at frequencies $f = 5$, 10, 20, and 50 kHz for both pure H_2O («Ultra-pure water» from Anton Paar) and 0.2, 1, and 2% water solutions of HPC (Fig. 16).

At lower temperatures, an inflection is observed on the solid H_2O (ice) temperature dependence of the real component of the complex dielectric permittivity $\varepsilon'(T)$ (Fig. 16a). This inflection appears to shift to higher temperatures with increasing frequencies. In contrast, the thermal dependency of the water's complex component of the dielectric permittivity $\varepsilon''(T)$ has a peak (Fig. 16b). As the frequency increases, this peak also shifts toward higher temperatures. These two observations indicate the presence of a relaxation process in H_2O in this region [37]. A further abrupt increase in the dielectric permittivity at about 0 °C is due to the melting of ice.

A similar behavior of the real and imaginary components of the complex dielectric permittivity is observed for the 0.2, 1, and 2% water solutions of HPC: the real component's dependence exhibits and inflection (Fig. 16c, e, g), whose position shifts toward higher temperatures with increasing frequency, whereas the imaginary component's dependence has a peak (Fig. 16d, f, h). This peak too shifts to higher temperatures with increasing temperatures, indicating that a relaxation process occurs for this temperature region in the water solution of HPC as well. The temperature of this relaxation process also appears to shift to higher temperatures with an increasing concentration of HPC in the solution.

The addition of the 154 mmol L^{-1} of alkali metal salts to the 0.2, 1, and 2% water solution of HPC produced qualitatively similar results (Figs. 17, 18, 19, 20 and 21). The variation of the real component of the complex dielectric permittivity with temperature exhibits an inflection for all samples, and the position of this inflection consistently shifts toward higher temperatures with increasing frequency. The

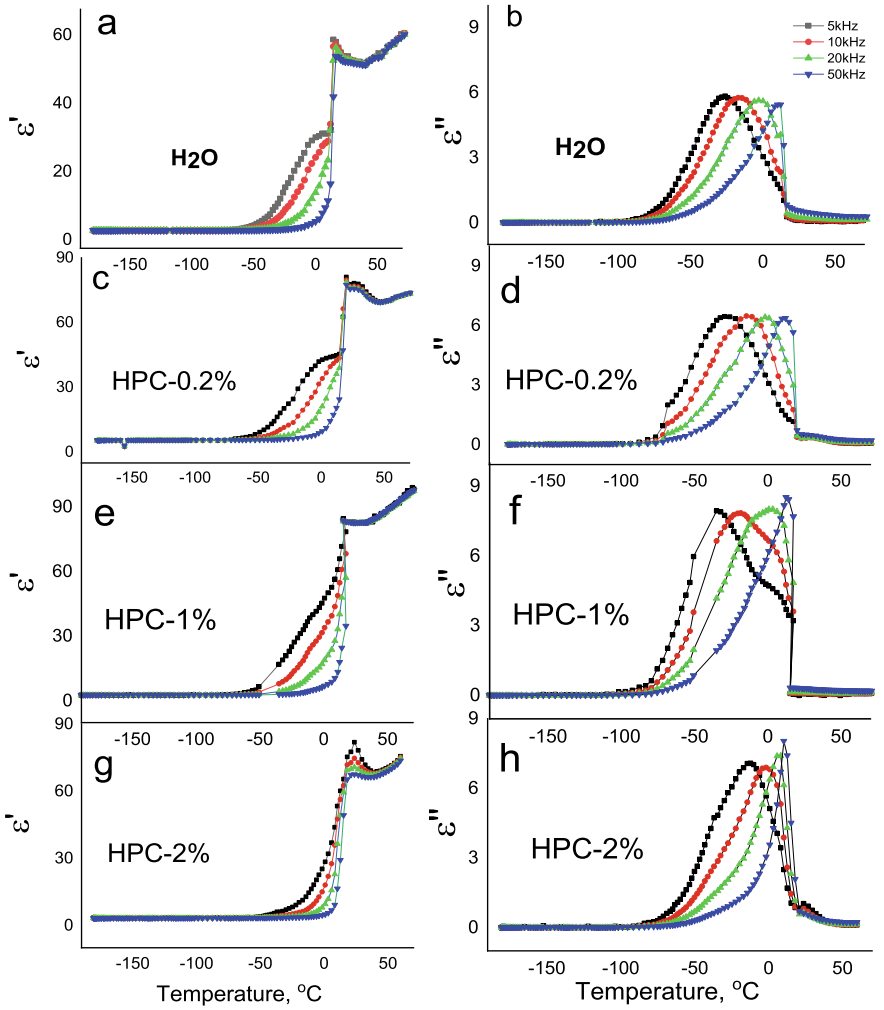

Fig. 16 Thermal dependencies of the real $\varepsilon'(T)$ and imaginary $\varepsilon''(T)$ parts of the complex dielectric permittivity for pure H_2O (**a**, **b**) and 0.2% (**c**, **d**), 1% (**e**, **f**), and 2% (**g**, **h**) water solutions of HPC at different frequencies

variation of the imaginary component of the complex dielectric permittivity variation with temperature has a peak (Figs. 17, 18, 19, 20 and 21), which shifts toward higher temperatures at increasing frequencies. Therefore, for all solutions studied, a relaxation process is observed. An abrupt increase in the dielectric permittivity at temperature above the temperature range of the relaxation process is due to the samples.

Relaxation process in H_2O-salt systems is attributed to hydrated ions [38]. Different ions form different hydrated shells formed around them [39], leading to a

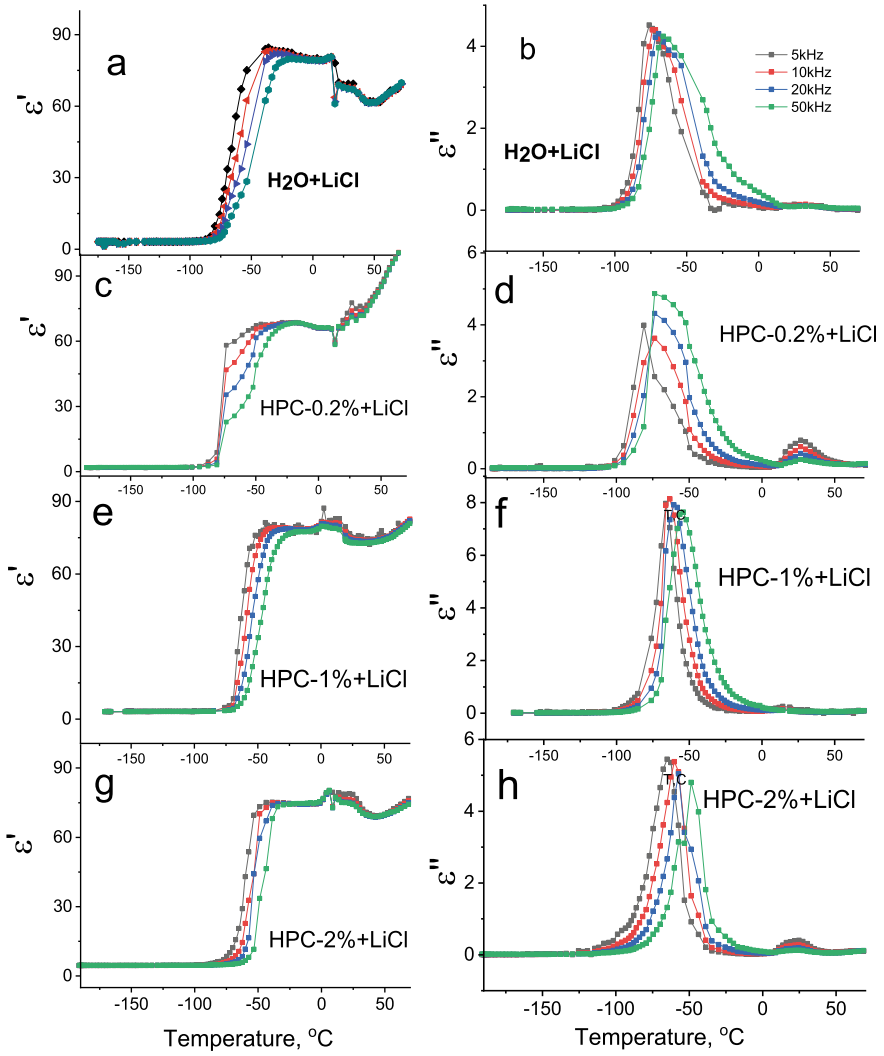

Fig. 17 Thermal dependencies of the real $\varepsilon'(T)$ and imaginary $\varepsilon''(T)$ parts of the complex dielectric permittivity for H_2O + LiCl (**a**) and 0.2% (**c**, **d**), 1% (**e**, **f**), and 2% (**g**, **h**) H_2O + HPC + LiCl at different frequencies

variety of changes in the physical properties of the H_2O-salt systems, such as, for instance, as the decrease in the melting temperature. When such systems are cooled at normal pressure, first nanocrystals of pure ice I_1h form [40]. These nanocrystals are surrounded by liquid shells of the water-salt solution, whose concentration increases to eutectic values as the crystals continue to grow, eventually forming crystals of water with salt [41].

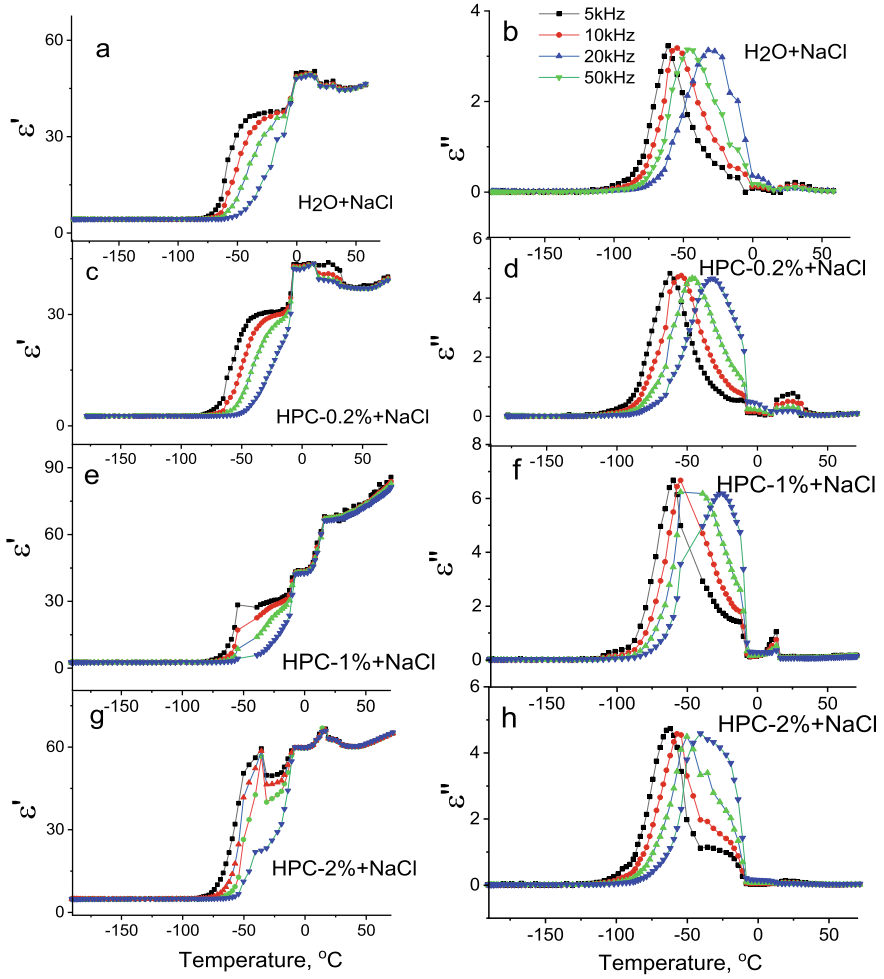

Fig. 18 Thermal dependencies of the real $\varepsilon'(T)$ and imaginary $\varepsilon''(T)$ parts of the complex dielectric permittivity for H_2O + NaCl (**a**) and 0.2% (**c**, **d**), 1% (**e**, **f**), and 2% (**g**, **h**) H_2O + HPC + NaCl at different frequencies

In a nutshell, the following processes may affect the dielectric properties of polycrystalline water-salt solutions at low temperatures:

1. Relaxation process in the crystals of pure ice, which are due to the motion of Bjerrum's orientational defects (types *L* and *D*) and ion pair defects with H_3O^+ and OH^- [42];
2. Relaxation of hydration shells of ions in the region where water-salt crystals melt [38].
3. Melting of pure ice which leads to an increase in the concentration of liquids water, and a dielectric permittivity much higher than that of ice.

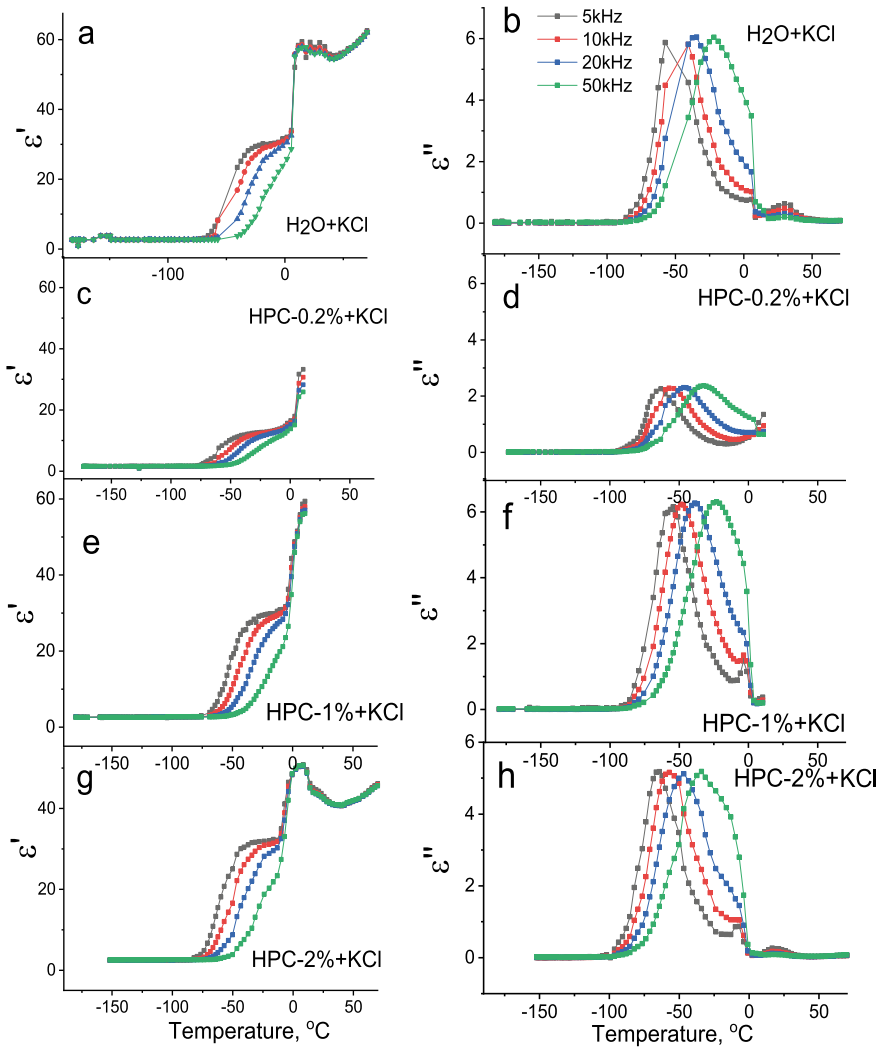

Fig. 19 Thermal dependencies of the real $\varepsilon'(T)$ and imaginary $\varepsilon''(T)$ parts of the complex dielectric permittivity for H_2O + KCl (**a**) and 0.2% (**c**, **d**), 1% (**e**, **f**), and 2% (**g**, **h**) H_2O + HPC + KCl at different frequencies

To determine the quantitative input of each of these processes in the thermal behavior of the complex dielectric permittivity additional, intense research is necessary, which is beyond the scope of the present work since our present work focuses on the major essential experimental features of the impact of ions on the low-temperature relaxation processes in HPC-water solution.

To demonstrate the impact of different ions on the solution's relaxation temperature, Fig. 22 was plotted: It shows how the temperature corresponding to the

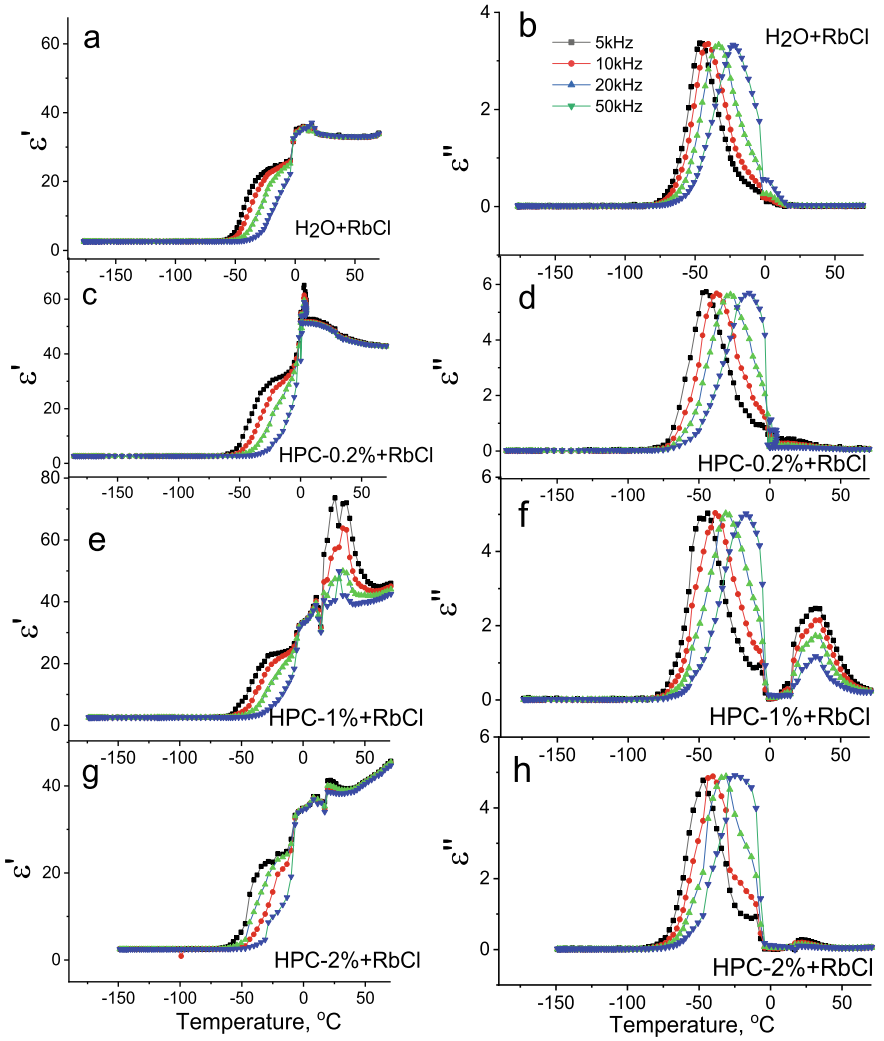

Fig. 20 Thermal dependencies of the real $\varepsilon'(T)$ and imaginary $\varepsilon''(T)$ parts of the complex dielectric permittivity for H_2O + RbCl (**a**) and 0.2% (**c**, **d**), 1% (**e**, **f**), and 2% (**g**, **h**) H_2O + HPC + RbCl at different frequencies

maximum of the relaxation process varies with the masses of the ions in each of the three solutions.

The presence of the ions in the solution shifts the maximum of the dielectric relaxation at a given frequency to lower temperatures (Fig. 22). The value appears to be inversely proportional to the mass of ions in the solution: the smaller is the mass of the ion of the salt added to the HPC-water solution, the greater is the shift of the dielectric relaxation toward lower temperatures.

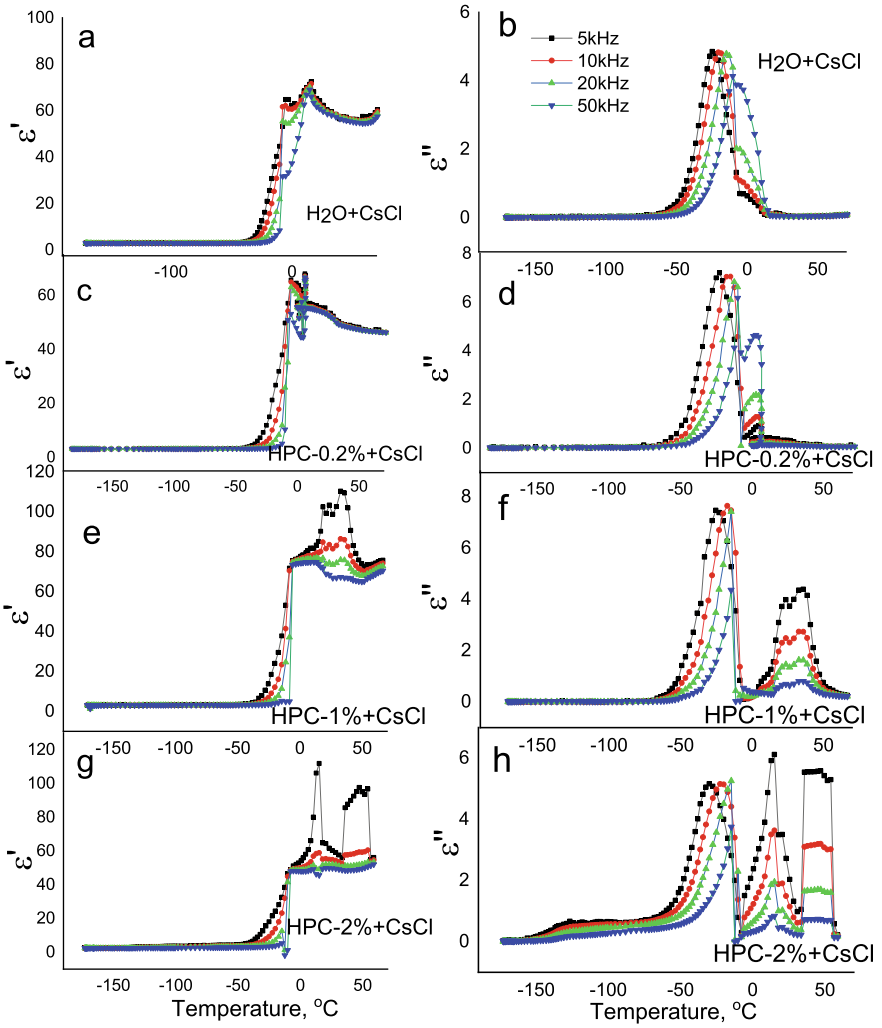

Fig. 21 Thermal dependencies of the real $\varepsilon'(T)$ and imaginary $\varepsilon''(T)$ parts of the complex dielectric permittivity for $H_2O + CsCl$ (**a**) and 0.2% (**c**, **d**), 1% (**e**, **f**), and 2% (**g**, **h**) $H_2O + HPC + CsCl$ at different frequencies

The energy properties of the dielectric relaxation can be estimated using the following model. If the activation entropy is taken into account, the relaxation time can be expressed as

$$\tau = \tau_0 \exp(U - T\Delta S)/kT, \tag{5}$$

where $\tau_0 = 10^{-12}$ s, U is the activation energy, T is the absolute temperature of the solution, ΔS is the activation entropy, and k is Boltzmann constant [43].

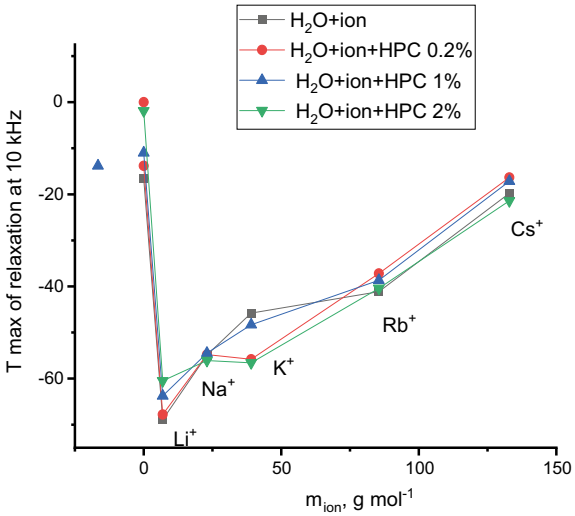

Fig. 22 Temperature of the dielectric relaxation maximum and the mass of the ions in the 0.2, 1, and 2% water solution of HPC

The maximum of the relaxation process is attained when $\omega\tau = 1$, where $\omega = 2\pi f$ is the angular frequency of the external field oscillation, leading to the following:

$$\ln f = -\ln 2\pi\tau_0 + \Delta S/k - U/kT. \tag{6}$$

Arrhenius equations $\ln f(1/T)$ were plotted to fit the experimental data for the water-salt (chlorides of Li, Na, K, Rb, and Cs) systems (Figs. 23, 24, 25 and 26).

In all Figs. 23, 24, 25, 26 and 27, the dielectric relaxation appears to shift toward lower temperatures when 1st group alkali metals' ions are added to the water solution of HPC with the value of shift inversely proportional to the mass of ions.

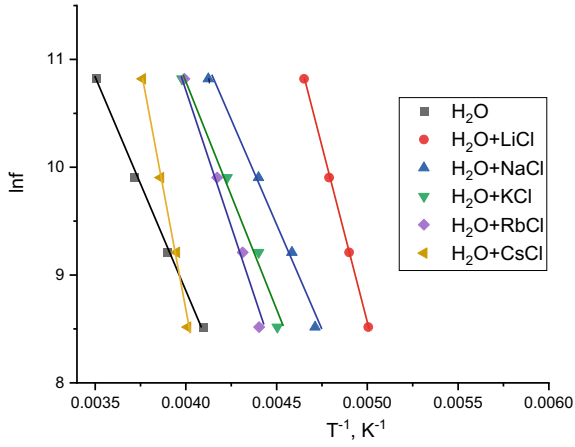

Fig. 23 Arrhenius equation $\ln f(1/T)$ for the solid water solutions of the chlorides of 1st group alkali metals (Li, Na, K, Rb, and Cs)

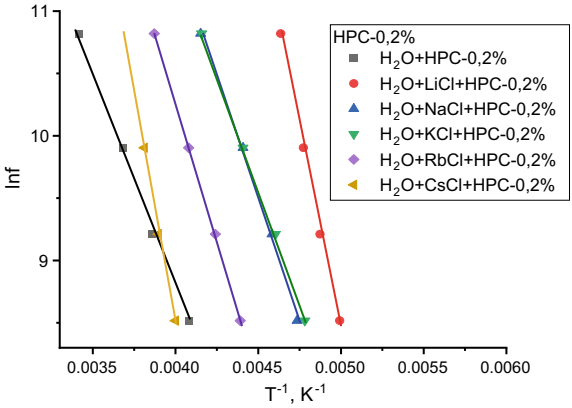

Fig. 24 Arrhenius equation $\ln f(1/T)$ for the solid 0.2% water solution of HPC with ions of the 1st group alkali metals (chlorides of Li, Na, K, Rb, and Cs)

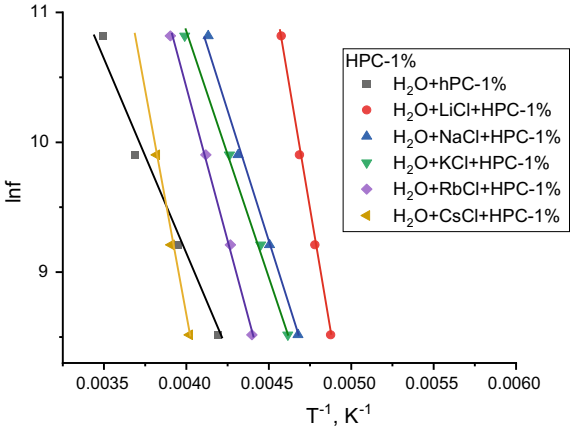

Fig. 25 Arrhenius equation $\ln f(1/T)$ for the solid 1% water solution of HPC with ions of the 1st group alkali metals (chlorides of Li, Na, K, Rb, and Cs)

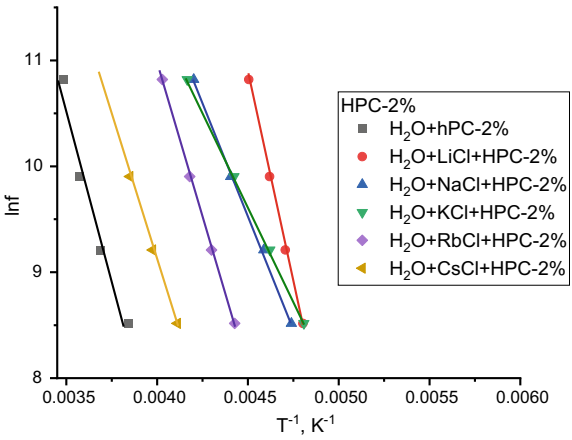

Fig. 26 Arrhenius equation $\ln f(1/T)$ for the solid 2% water solution of HPC with ions of the 1st group alkali metals (chlorides of Li, Na, K, Rb, and Cs)

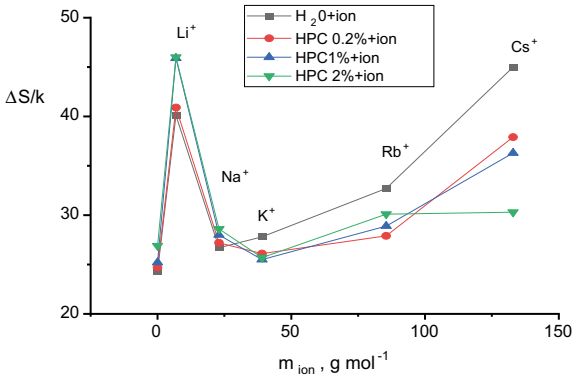

Fig. 27 Activation entropy and the mass of ions in the HPC-water-salt (chlorides of Li, Na, K, Rb, and Cs) solutions

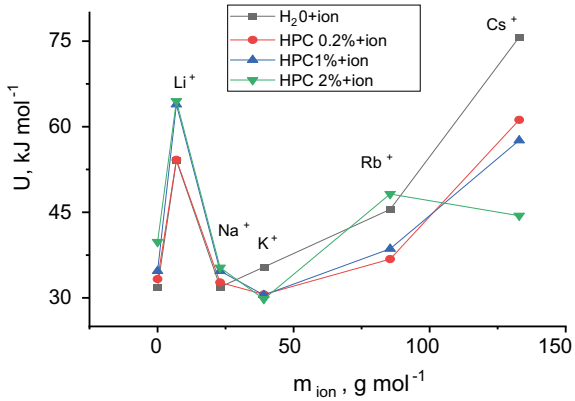

Fig. 28 Activation energy and the mass of ions in the HPC-water-salt (chlorides of Li, Na, K, Rb, and Cs) solutions

Arrhenius equation ln $f(1/T)$ and expression (6) can be used to determine the values of the activation entropy ï $\Delta S/k$ and activation energy U. The obtained values of these parameters are plotted for all studied systems in Figs. 27 and 28, respectively.

As Figs. 27 and 28 demonstrate that the greater the mass of ions in the HPC-water solution, the greater the activation entropy and activation energy with the exception of Li^+ ion.

In order to compare the obtained values for relaxation times τ at different temperatures T with available data [42], we have plotted the τ versus T^{-1} graphs for the following systems: water and water-salt (chlorides of Li, Na, K, Rb, and Cs) solutions (Fig. 29), 0.2, 1, and 2% HPC-water solutions (Fig. 30), and 0.2, 1, and 2% HPC-water solutions with ions of 1st group alkali metals' salts (chlorides of Li, Na, K, Rb, and Cs) added (Figs. 31, 32, and 33).

Figure 30 demonstrates that adding HPC to water shifts relaxation processes to lower temperatures. The obtained values correspond to the data from [42]. Adding ions to the solution reverses this effect. The relaxation process shifts to higher temperatures, with the greatest shift observed for the ions of the least mass.

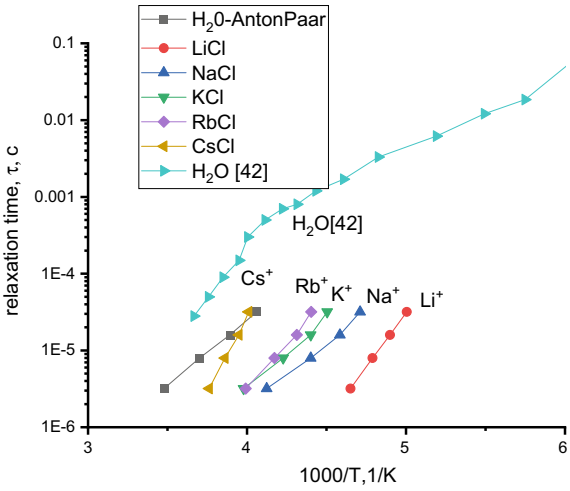

Fig. 29 Time of relaxation versus inverse temperature for pure H_2O and water solutions of the 1st group alkali metals' salts (chlorides of Li, Na, K, Rb, and Cs) $c = 154$ mmol L^{-1}

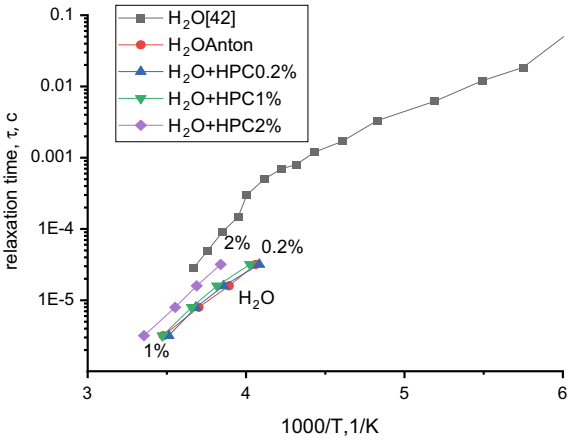

Fig. 30 Time of relaxation versus inverse temperature for pure H_2O and 0.2, 1, and 2% water solutions of HPC

4 Remarks

Some authors [44] suggest that the thermal behavior of the physical properties, especially in the phase transition and relaxation processes regions, is determined by the structure and kinetic properties of the hydrogen network in water, which are affected by external factors and impurities (including ions and molecules of polymers).

We have plotted the variation of the size of nanoparticles in the 0.2% of the HPC-water-salt solutions at 50 °C with the masses of ions in the solution (Fig. 34a). Next to it, we have plotted the shift in temperature corresponding to the peak of the PL spectrum for the HPC-water-salt solution relative to the peak of the PL spectrum for

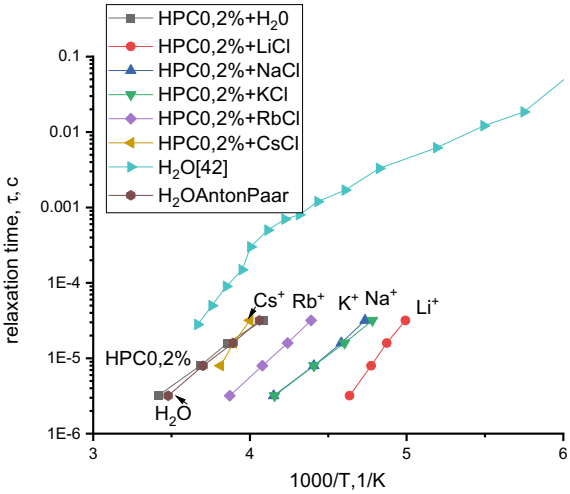

Fig. 31 Time of relaxation versus inverse temperature for pure H_2O and 0.2% water solutions of HPC with ions of salts of the 1st group alkali metals (chlorides of Li, Na, K, Rb, and Cs) $c =$ 154 mmol L^{-1}

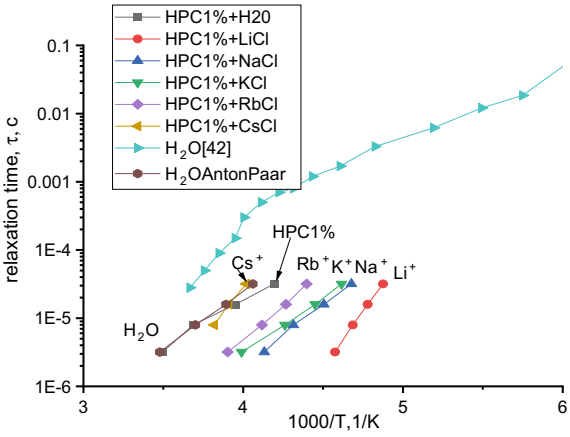

Fig. 32 Time of relaxation versus inverse temperature for pure H_2O and 1% water solutions of HPC with ions of salts of the 1st group alkali metals (chlorides of Li, Na, K, Rb, and Cs) $c =$ 154 mmol L^{-1}

the HPC-water solution in the temperature region 38–60 °C with the masses of ions in the solution (Fig. 34b).

The variation of the shift in the LCST for the 2% HPC-water-salt solution relative to the LCST for the HPC-water solution with the mass of ions in the solution obtained in turbidity measurements is plotted in Fig. 35a, and viscosity measurements data are plotted in Fig. 35b. Next to them is the variation of the shift in the maximum of the dielectric relaxation obtained for the imaginary component of the dielectric permittivity at 10 kHz for the 2% HPC-water-salt solution relative to the 2% HPC-water solution with the mass of ions (c).

Both figures indicate that as ions are added to the solutions, all measured quantities increase relative to their values for the HPC-water solutions. The greatest deviation

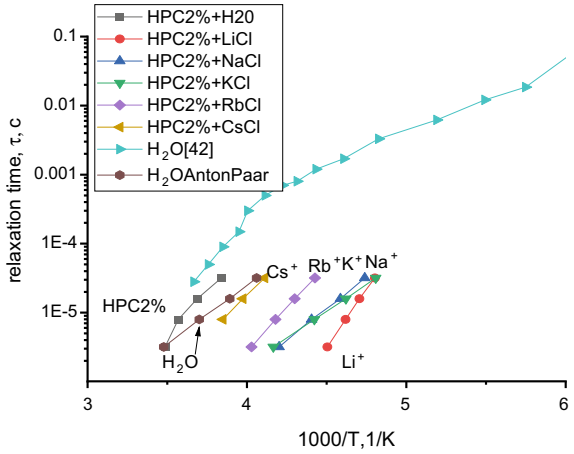

Fig. 33 Time of relaxation versus inverse temperature for pure H_2O and 2% water solutions of HPC with ions of salts of the 1st group alkali metals (chlorides of Li, Na, K, Rb, and Cs) $c = 154$ mmol L^{-1}

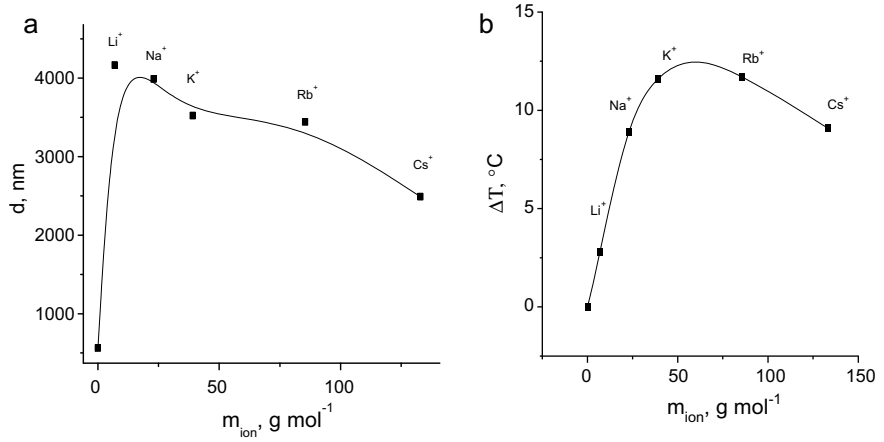

Fig. 34 Size of nanoparticles of the 0.2% HPC-water-salt solution with salts of 1st group alkali metals (chlorides of Li, Na, K, Rb, and Cs) at 50 °C (**a**). The shift in temperature corresponding to the peak of the PL spectrum for the HPC-water-salt solution relative to the peak of the PL spectrum for the HPC-water solution in the temperature region 38–60 °C (**b**)

in the properties is observed for HPC-water-LiCl solution, especially for the size of nanoparticles (Fig. 29a) and the dielectric relaxation maximum (Fig. 35c).

As the mass of ion increases, the deviation in the values of the measured quantities decreases and the HPC-water-salt solution behaves more like the HPC-water solution.

As the curves in Figs. 34 and 35 have similar shapes, one may conclude that the impact of the presence of alkali metals' ions on these effects is qualitatively similar.

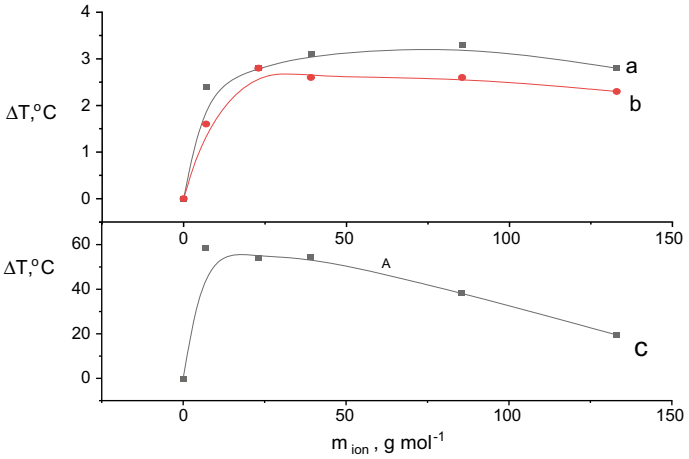

Fig. 35 Shift in the LCST for the 2% HPC-water-salt solution relative to the LCST for the HPC-water solution obtained in turbidity measurements (a) and viscosity measurements (b). Shift in the maximum of the dielectric relaxation obtained for the imaginary component of the dielectric permittivity at 10 kHz for the 2% HPC-water-salt solution relative to the 2% HPC-water solution (c)

We believe that this similarity is due to the structure of the hydrate shells and the close surrounding of both ions and HPC, as well as the change of this structure with temperature.

5 Conclusions

We have studied properties of water solutions of salts of the first group alkali metals (chlorides of Li, Na, K, Rb, and Cs) with the physiological saline concentration of 154 mmol L^{-1} as well as the properties of the 0.2, 1 and 2% water solutions of HPC with added salts of the first group alkali metals (chlorides of Li, Na, K, Rb, and Cs) with the physiological saline concentration. The methods applied included electroconductivity, turbidimetry, densitometry, viscometry, dynamic light scattering, dielectric, and luminescence spectroscopy methods. By applying a plethora of experimental approaches to the HPC-water-salt and water-salt systems in the wide range of temperatures (from − 190 to + 50 °C), both in solid and in liquid states, we attempted to find the similarities between the ways different ions affect the physical properties of such systems.

We have demonstrated that HPC in solid powder state, in water solutions and in HPC-water-salt systems, exhibits photoluminescent properties, whose characteristics are similar to PL of other cellulose-containing materials. Since the sources of the observed PL are the various molecular groups of HPC, its emission spectrum is multicomponent. As the water affects the PL of HPC differently in solid and liquid

phases, the PL spectra of HPC-water systems in solid and liquid states are different. Luminescence characteristics of the HPC (spectral profiles and intensity) appear to be sensitive to the changes in the structure of the water in the HPC-water-salt solutions, that allowed us to monitor the thermal behavior of sol–gel phase transition in the studied systems.

In particular, luminescent analysis has revealed the presence of the temperature of self-association of large HPC particles (size > 2 μm) which decreases from ~ 55 to 43 °C along the homological group $Li^+ \rightarrow Na^+ \rightarrow K^+ \rightarrow Rb^+$. The presence of ions in the HPC solution decreases the LCST and leads to the appearance of large nanoparticles at temperatures above LCST.

At low temperatures, when the solutions are in solid state, the presence of ions in the solution shifts the dielectric relaxation toward lower temperatures and to the increase in the activation energy. The value of this shift correlates negatively with the mass of ions.

The analysis of the results points at the qualitative similarities in the way ions affect several physical properties of the solutions in both solid and liquid states. We believe, such similarity can be attributed to the ability of ions to affect the structure of the hydrate shell and the close surroundings of HPC, as well as to the change of this structure with increasing temperature. The observed effects thus appear to be macroscopic attributes (markers) of the change in the structure and its kinetic properties due to impurities or thermal motion.

References

1. Y. Zhang, S. Furyk, D.E. Bergbreiter, P.S. Cremer, Specific ion effects on the water solubility of macromolecules: PNIPAM and the Hofmeister series. J. Am. Chem. Soc. **127**, 14505 (2005)
2. I. Ohmine, T.J. Tanaka, Salt effects on the phase transition of ionic gels. Chem. Phys. **77**, 5725
3. T. Park, A.S. Hoffman, Sodium chloride-induced phase transition in nonionic poly(N-isopropylacrylamide) gel. Macromolecules **26**(19), 5045
4. X. Zhang, Z. Hu, Y. Li, The phase transition and shear modulus of ionic N-isopropylacrylamide gels in concentrated salt solutions. J. Appl. Polym. Sci. **63**, 1851 (1997)
5. C.P. Lamas, C. Vega, E.G. Noya, Freezing point depression of salt aqueous solutions using the Madrid-2019 model. J. Chem. Phys. **156**(13), 134503 (2022)
6. O.M. Alekseev, Y.F. Zabashta, V.I. Kovalchuk, M.M. Lazarenko, L.A. Bulavin, The structure of polymer clusters in aqueous solutions of hydroxypropyl Cellulose. Ukr. J. Phys. **64**(3), 238 (2019)
7. O.M. Alekseev, Y.F. Zabashta, V.I. Kovalchuk, M.M. Lazarenko, E.G. Rudnikov, L.A. Bulavin, Structural transition in dilute solutions of rod-like macromolecules. Ukr. J. Phys. **65**(1), 50 (2020)
8. V.K. Kovalchuk, Phase separation dynamics in aqueous solutions of thermoresponsive polymers. Cond. Matt. Phys. **24**, 43601 (2021)
9. S. Mohapatra, S. Ranjan, N. Dasgupta, R. Kumar, S. Thomas, *Characterization and Biology of Nanomaterials for Drug Delivery: Nanoscience and Nanotechnology in Drug Delivery* (Elsevier, 2018), 682p

10. M. Lazarenko, S. Nedilko, S. Gryn, V. Scherbatskyi, V. Kovalchuk, M. Lazarenko, A. Sobchuk, D. Andrusenko, O. Alekseev, Influence of Na+ and Cl− ions on the properties of hydroxypropylcellulose solutions, in *IEEE 41st International Conference on Electronics and Nanotechnology (ELNANO)* (2022), pp. 418–421
11. K. Holmberg, B. Jönsson, B. Kronberg, B. Lindman, *Surfactants and Polymers in Aqueous Solution*, 2nd edn. (Wiley, West Sussex, UK, 2002), 562p
12. J. Gao, G. Haidar, X. Lu, Z. Hu, Self-association of hydroxypropylcellulose in water. Macromolecules **34**(7), 2242 (2001)
13. N. Sardar, M. Kamil, M. Sajid Ali, Solution behavior of nonionic polymer hydroxypropylmethyl cellulose: effect of salts on the energetics at the cloud point. J. Chem. Eng. Data **56**, 984 (2011)
14. G. Cavallaro, G. Lazzara, S. Milioto, Aqueous phase/nanoparticles interface: hydroxypropyl cellulose adsorption and desorption triggered by temperature and inorganic salts. Soft Matter **8**(13), 3627 (2012)
15. M. Ali, D. Kumar, H.A. Al-Lohedan, Salt effect on the cloud point phenomenon of amphiphilic drug-hydroxypropylmethyl cellulose system. J. Chem. **2014**, 293972 (2014)
16. X. Xia, S. Tang, X. Lu, Z. Hu, Formation and volume phase transition of hydroxypropyl cellulose microgels in salt solution. Macromolecules **36**(10), 3695 (2003)
17. P. Khuman, W.B.K. Singh, S.D. Devi, H. Naorem, Viscosity-temperature behavior of hydroxypropyl cellulose solution in presence of an electrolyte or a surfactant: a convenient method to determine the cloud point of polymer solutions. J. Macromol. Sci. A **51**(11), 924 (2014)
18. Y.-S. Yang, Y. Zhou, F.B.Y. Chiang, Y. Long, Temperature-responsive hydroxypropylcellulose based thermochromic material and its smart window application. RSC Adv. **6**(66), 61449 (2016)
19. E. Weißenborn, B. Braunschweig, Hydroxypropyl cellulose as a green polymer for thermoresponsive aqueous foams. Soft Matter **15**(13), 2876 (2019)
20. S. Claesson, H. Odani, Fluorescence depolarization in sheared solutions of dye-tagget polymers. Discuss. Faraday Soc. **49**, 268 (1970)
21. F.M. Winnik, M.A. Winnik, S. Tazuke, C.K. Ober, Synthesis and characterization of pyrene-labeled hydroxypropyl cellulose and its fluorescence in solution. Macromolecules **20**(1), 38–44 (1987)
22. H. Itagaki, I. Takahashi, M. Natsume, T. Kondo, Gelation of cellulose whose hydroxyl groups are specifically substituted by the fluorescent groups. Polym. Bull. **32**(1), 77 (1994)
23. M. Nedielko, S. Hamamda, O. Alekseev, V. Chornii, M. Dashevskii, M. Lazarenko, K. Kovalov, S.G. Nedilko, S. Tkachov, S. Revo, V. Scherbatskyi, Mechanical, dielectric, and spectroscopic characteristics of "micro/nanocellulose+ oxide" composites. Nanoscale Res. Lett. **12**, 1–11 (2017)
24. S. Thomas, R. Thomas, A.K. Zachariah, R.K. Mishra, *Spectroscopic Methods for Nanomaterials Characterization*, vol. 2 (Elsevier, 2017), 444p
25. Hydroxypropyl Cellulose. https://www.alfa.com/en/catalog/043400/
26. M.M. Lazarenko, S.G.Nedilko, S.A. Alekseev, S.Y. Tkachov, D.O. Shevtsov, V.P. Scherbatskyi, V.A. Barbash, K.S. Yablochkova, M.V. Ushcats, V.I. Kovalchuk, D.A. Andrusenko, D. Izvorska, R.V. Dinzhos, O.M. Alekseev, Electric and spectral properties of solid water-nanocellulose systems in a wide range of temperatures, in *International Conference on Nanotechnology and Nanomaterials*, (Springer, 2020), pp. 51–73
27. A.N. Alekseev, M.M. Lazarenko, M.V. Lazarenko, K.N. Kovalev, S.Y. Tkachev, Characterization of dielectric properties in liquid–solid phase transition. Inorg. Mater. **53**(15), 1473 (2017)
28. M.M. Lazarenko, K.I. Hnatiuk, S.A. Alekseev, K.S. Yablochkova, R.V. Dinzhos, F. Ublekov, M.V. Lazarenko, D.A. Andrusenko, A.N. Alekseev, Low-temperature dielectric relaxation in the system silica gel–undecylenic acid, in *IEEE 10th International Conference Nanomaterials: Applications & Properties (NAP)* (IEEE, 2020), pp. 01NIC02-1
29. V.I. Kovalchuk, O.M. Alekseev, M.M. Lazarenko, Turbidimetric monitoring of phase separation in aqueous solutions of thermoresponsive polymers. J. Nano-Electron. Phys. **14**(1), 01004 (2022)

30. Y. Zabashta, V. Kovalchuk, O. Svechnikova, L. Bulavin, Determination of the surface tension coefficient of polymer gel. Ukr. J. Phys. **67**(5), 365 (2022)
31. Y.F. Zabashta, V.I. Kovalchuk, L.A. Bulavin, Kinetics of the first-order phase transition in a varying temperature field. Ukr. J. Phys. **66**, 978 (2021)
32. S.A. Vshivkov, *Phase Transitions and Structure of Polymer Systems in External Fields* (Cambridge Scholars Publishing, 2019), 381p
33. P.J. Flory, *Principles of Polymer Chemistry* (Cornell University Press), 672p
34. M.Z. Gavrilov, I.N. Ermolenko, A study of cellulose luminescence. J. Appl. Spectr. **5**, 542 (1966)
35. V. Pikulev, S. Loginova, V. Gurtov, Luminescence properties of silicon-cellulose nanocomposites. Nanoscale Res. Lett. **7**, 426 (2012)
36. P. Grönroos, M. Bessonoff, K. Salminen, J. Paltakari, S. Kulmala, Phosphorescence and fluorescence of fibrillar cellulose films. Nordic Pulp. Paper Res. J. **33**, 246 (2018)
37. C. Hölzl, H. Forbert, D. Marx, Dielectric relaxation of water: assessing the impact of localized modes, translational diffusion, and collective dynamics. Phys. Chem. Chem. Phys. **23**(37), 20875 (2021)
38. X. Song, L. Zhong, J. Gao, Direct evidence of ice crystallization inhibition by dielectric relaxation of hydrated ions. Materials **14**(22), 6975 (2021)
39. P. Lo Nostro, B.W. Ninham, Hofmeister phenomena: an update on ion specificity in biology. Chem. Rev. **112**(4), 2286 (2012)
40. K. Sasaki, R. Kita, N. Shinyashiki, S. Yagihara, Dielectric relaxation time of ice-Ih with different preparation. J. Phys. Chem. B **120**(16), 3950 (2016)
41. D. Wei, G.N. Patey, Dielectric relaxation of electrolyte solutions. J. Chem. Phys. **94**(10), 6795 (1991)
42. I. Popov, A. Puzenko, A. Khamzin, Y. Feldman, The dynamic crossover in dielectric relaxation behavior of ice I_h. Phys. Chem. Chem. Phys. **17**(2), 1489 (2015)
43. K.M. Kovalov, O.M. Alekseev, M.M. Lazarenko, Y.F. Zabashta, Y.E. Grabovskii, S.Y. Tkachov, Influence of water on the structure and dielectric properties of the microcrystalline and nanocellulose. Nanoscale Res. Lett. **12**(1), 468 (2017)
44. A. Lyashchenko, A. Lileev, Dielectric relaxation of water in hydration shells of ions. J. Chem. Eng. Data **55**(5), 2008 (2010)

The Influence of the Processes of Microbiogenic Deposition of Carbonates on the Surface of Iron-Aluminosilicate Marine Suspensions and the Transformation of the Resulting Bottom Sediments

A. V. Panko, I. G. Kovzun, V. A. Prokopenko, O. M. Nikipelova, and O. A. Tsyganovich

Abstract Mechanisms of microbiogenic deposition of nanoparticles and microparticles in fresh, salty, and marine suspensions of iron-aluminosilicates (clays) in the presence of carbonate admixtures, oxides of iron and manganese, and trace elements, as well as mechanisms of nanochemical biocolloidal transformation and separation of mineral components of suspensions and their enrichment were considered. It is shown that the study of these mechanisms is important for understanding the fundamental laws of complex physical, chemical, geomechanical, and biocolloidal transformation processes of the components of iron-aluminosilicate systems and materials, widely distributed in the Earth's crust and on its surface. From a practical point of view, it is important for the development of new highly efficient technologies for obtaining such materials, taking into account achievements of green chemistry. The importance of established regularities in the development of ideas about the biocolloidal formation of various ore deposits, primarily iron and iron-manganese nodules, is also shown taking into account the important role of periphyton in such processes in the presence of microorganisms and bacteria. General ideas concerning the basis for the creation of highly effective materials and eco-biotechnologies in the conditions of synergic

A. V. Panko (✉) · I. G. Kovzun · V. A. Prokopenko · O. A. Tsyganovich
F.D.Ovcharenko Institute of Biocolloidal Chemistry of NAS of Ukraine, Ak.Vernadskogo Blvd. 42, Kyiv 03142, Ukraine
e-mail: gr.k.ibcc@ukr.net

V. A. Prokopenko · O. A. Tsyganovich
National Technical University of Ukraine «KPI», Peremohy Ave. 37, Building 4, Kyiv 03056, Ukraine

O. M. Nikipelova
Engineering and Technology Institute "Biotechnika" of NAAS of Ukraine, Maiakska Str. 26, Khlibodarske, Odes'ka Oblast 67667, Ukraine

Odessa State Environmental University, Lvivska Str. 15, Odessa 65016, Ukraine

O. Fesenko and L. Yatsenko (eds.), *Nanoelectronics, Nanooptics, Nanochemistry and Nanobiotechnology, and Their Applications*, Springer Proceedings in Physics 297,
https://doi.org/10.1007/978-3-031-42708-4_4

action of periphyton complexes of microorganisms and bacteria under the influence of the laws of physicochemical geomechanics have been developed. Recommendations are provided for optimizing the methods of obtaining clay iron-aluminosilicate materials with improved properties under the influence of complex natural groups of bacteria and periphyton microorganisms, which allows, in some cases, to increase the efficiency of their use in technological processes by 6–12 times. Ways of applying the obtained results in various fields of human activity are outlined.

1 Introduction

It is known that the processes of precipitation of minerals from salty (i.e., marine), as well as fresh-water suspensions—mainly iron-aluminosilicate ones (IASS), are always accompanied, depending on the period of deposition, by the formation of bottom sediments [1–5]. Classical ideas about such processes are based on the fact that there is a huge number of groups of bacteria and microorganisms on the dispersed solid particles of suspensions, which in general belong to the periphyton [4], which includes bacteria and microorganisms—fungi, algae, protozoa, worms, mollusks, etc. that live on the border of solid and liquid phases [1, 3]. Thus, for example, it was established that in one cm^3 of suspension, only the number of heterotrophic bacteria reaches 16×10^6, and diatoms and other algae—3×10^6 cells with more than tens of thousands of their species [4]. The modern work [3] also shows that in fresh and salty sediments, there are thousands of species and tens of groups of specialized bacteria and microorganisms that take part in the formation of biogenic siderite, pyrite, magnetite, etc., and iron-manganese nodules.

A large number of different species and groups of bacteria, diatoms, animalcular microorganisms, and various iron-aluminosilicate fine particles in fresh, salty, and marine suspensions make them the site of many active biological, nanochemical, colloid-chemical, and mechanochemical interactions at the interface between water and mineral carbonates, and iron-aluminosilicates [3]. From the point of view of modern nanoscience, such interactions are characterized as nanobiocolloidal and are accompanied by the transformation of suspension components under the action of biochemogenic, biocolloidal, and physical–mechanical nanotransformations and inorganic reactions [3, 4, 6–11].

On the surface of solid particles of marine suspensions, a large number of various species and groups of bacteria and diatoms make them not only a place of complex biocolloidal transformations but of other processes too. Thus, causing changes in the environment, periphyton microorganisms of marine suspensions not only take part in the deposition of carbonates on microparticles of suspensions but also in releasing microelements from their inorganic mineral structures [11]. The latter processes are also accompanied by a chemical nanobiocolloidal transformation of minerals and their separation according to the laws of physicochemical geomechanics [3]. This is partly proved by the formation of iron ore deposits contaminated with

iron-aluminosilicates aided by bacteria about two billion years ago [12], in recent millennia [11, 13, 14], and in present conditions [15–22].

Thus, a more detailed study of the effect of microbiogenic (biocolloidal) precipitation of carbonates on the surface of particles of iron-aluminosilicate marine suspensions on the nanochemical transformation of formed bottom sediments and their redistribution on the bottom of reservoirs according to the laws of physicochemical geomechanics and nanochemistry should be considered very relevant, and therefore, it is assigned in the basis of this study.

2 Materials and Methods

2.1 Materials

Study of the biocolloidal nanostructural geo- and mechanochemical dispersion processes and transformation of polymineral microdispersed iron-aluminosilicate systems (IASSs), and materials (IASMs) of natural and technogenic origin (iron ores, soils, pelitic sediments, natural and thermotreated clays, sands, etc.) have shown that as a result of changes in influencing factors in microdisperse (IASSs) and nanodisperse (NIASSs) systems, various very complex interactions can occur between their components [1, 3, 6, 8–16]. Such interactions include low- and high-temperature reduction or oxidation, dispersion or contact interparticle compaction, Ostwald ripening, change in the surface nanostructural phase composition, chemical leaching, adsorption, adhesion, cohesion, ion exchange, etc. Such interactions give new properties and change the chemical and mineralogical characteristics of dispersed IASSs and NIASSs. Similar changes occur in the Earth's crust, as well as on its surface, most often, as a result of the natural and technogenic processing of mineral rocks and their weathering. However, until now, the processes that occur in the studied systems were judged by their final parameters, but that does not explain the initial causes and mechanisms of the observed transformations. There is still no single, scientifically based approach to the explanation of the phenomena of polymineral IASSs transformation in conditions of their geomechanochemical and biocolloidal nanochemical dispersion. There are also no principal models of colloid-chemical interactions in similar systems that would provide an opportunity to justify the processes of controlling the behavior and characteristics of IASSs and NIASSs. Based on this, the selection of research objects was based on their general features, which are typical for most carbonate-iron-aluminosilicate systems and materials. Such materials should primarily include soils, clays, sedimentary iron ores of biocolloidal origin, pelitic sediments, and peloids. As iron-aluminosilicate materials, it was studied: various soils and clays; polymineral iron-aluminosilicate compositions formed from iron ores; pelagic shallow and deep-water sediments and peloids of the Black and Azov seas, Dashukovski bentonite and montmorillonite [1, 3, 6, 8–17].

Based on the given data (Figs. 1, 2 and 3 and Table 1), it was studied and analyzed the behavior of suspensions of the Azov and Black Seas and the transformation of iron ore (Fig. 3) of biocolloidal origin formed 15,000 years ago in the Azov–Black Sea region [17].

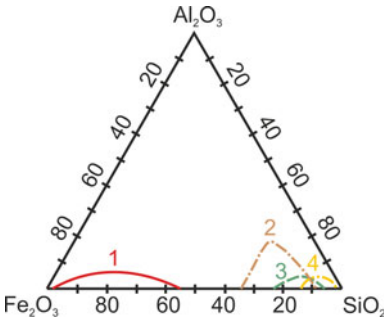

Fig. 1 Areas of the existence of various iron-aluminosilicate materials. 1—iron concentrates and ores; 2—clays, 3—peloids, oozes; 4—quartz and feldspar sands, (2–4)—soils

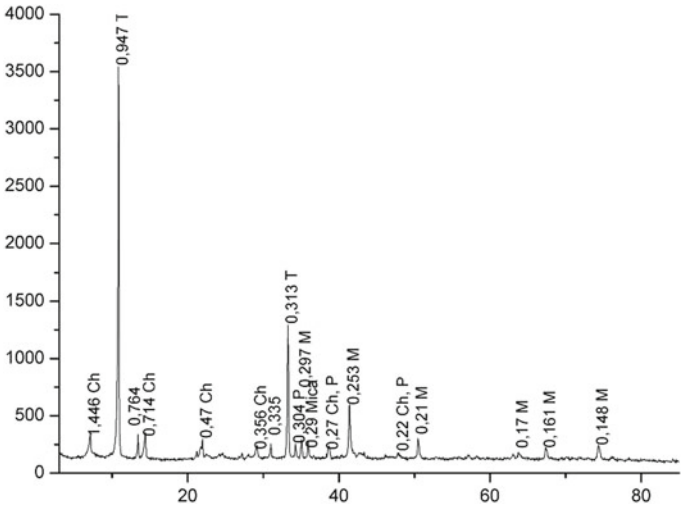

Fig. 2 XRD pattern of natural jaspilite microcrystalline ore. (Ch—chlorite, T—talc, P—pyrite, M—magnetite, Mica—mica)

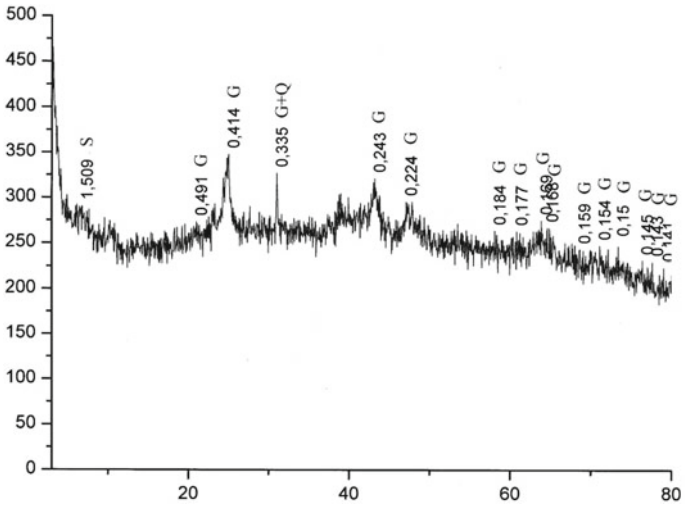

Fig. 3 XRD pattern of sedimentary nanostructured iron ore of biocolloidal origin (G—goethite, Q—quartz, S—saponite)

Table 1 Chemical composition of iron-aluminosilicate materials

Content of oxides, wt%	Polymineral iron-aluminosilicate compositions			Saponite-goethite clay	Black sea mud	River sand	Dashukovsky montmorillonite
SiO_2	18.34	18.31	19.46	46.73	54.57	98.83	49.52
Al_2O_3	2.09	1.76	1.93	5.12	11.35	0.06	21.06
Fe_2O_3	3.18	8.34	2.79	2.76	5.54	1.05	2.72
FeO	56.15	49.23	51.16	23.21	–	–	–
CaO	2.17	1.65	1.98	3.87	8.87	0.01	5.7
MgO	0.73	0.61	0.56	11.43	1.80	–	1.61
MnO	2.48	3.24	7.87	0.35	0.04	–	–
Na_2O	0.45	0.31	0.24	0.82	1.19	–	0.37
K_2O	0.33	0.25	0.26	0.36	1.86	–	0.28
LOI	14.21	16.26	13.67	8.57	13.03	–	17.98

LOI loss of ignition

2.2 Research Methods

Chemical, rheological, XRD, DTA, SEM, and adsorption methods of analysis, magnetic and gravitational separation, as well as medical and biological methods, were used in the research of IASSMs.

Chemical and X-ray fluorescence analyses used in the study of samples were carried out according to known methods of qualitative and quantitative methods of analysis of iron-aluminosilicate rocks.

XRD analysis of the samples was carried out on a Dron-UM-1 diffractometer with CoKα radiation and a nickel filter at room temperature. The diffractometer was connected to a computer for the automatic recording of diffractograms. The survey was carried out under the following conditions: surveying speed—1 degree/min. Registration of X-ray radiation was carried out on a BDS-6 scintillation counter. The determination of minerals was carried out according to the tables. Samples for research were prepared according to standard methods. The decoding of radiographs was carried out according to the data of the ASTM card file.

Electron microscopy (SEM) of the studied samples. SEM images were obtained with the help of an electronic microscope Selmi PEMU in the light field mode. The studied samples were prepared by the method of suspensions. TESLA BN, JEOL NeoScope JCM-5000, and JEOL JSM6490 LV scanning microscopes with INSA ENERGY-450 energy dispersive device (Oxford, Great Britain) were also used.

The rheological characteristics of the studied systems and materials were determined using a rotary viscometer with coaxial cylinders Rheotest-2 connected to a PC. The structural and mechanical properties of dispersions were studied on a Weiler-Rebinder device with automatic recording of strain–time curves. When performing rheological studies, the size distribution of particles was also determined.

Particle size distribution was determined using laser correlation spectrometry (MALVERN 3000 device).

3 Results and Discussion

Analogies in carbonate deposition in periphyton and on marine iron-aluminosilicate suspension, established by the analysis of literature data, simulation, and experimental studies, indicate that communities of various microorganisms are developing on solid particles of suspensions [1, 3, 13, 14]. This allows us to assume that along with the mechanism of microbiogenic (biocolloidal) precipitation of carbonates, the recently established features of the mechanism of nanobiocolloidal rearrangement of carbonates on the surface of dispersed iron-aluminosilicates [7–11] are applied to marine suspensions, depending on the mixing speed of the suspension. They are characterized by an increase in the number of carbonate nanoformations with an increase in the rate of turbulent mixing of the coastal suspension, for example, during storms and hurricanes, and in the conditions of laminar mixing of the suspension in metabolic processes—periphyton microorganisms deposit carbonate microparticles. For example, among microorganisms that deposit carbonates on the IASSs are diatoms, the number of species exceeds 12,000. Using the carbon dioxide of hydrocarbonates during intensive photosynthesis, they shift the carbonate balance in seawater in the direction of carbonate deposition [3, 4]:

$$Ca(HCO_3)_2 \rightarrow CO_2 + CaCO_3 \downarrow + H_2O \quad (1)$$

Precipitation of carbonates also occurs in the presence of heterotrophic bacteria:

$$(NH_4)_2CO_3 + CaSO_4 \rightarrow CaCO_3 \downarrow + (NH_4)_2SO_4 \quad (2)$$

$$Ca(HCO_3)_2 + 2NH_3 \rightarrow CaCO_3 \downarrow + (NH_4)_2CO_3 \quad (3)$$

$$2NH_3 + H_2O \rightarrow NH_4OH \quad (4)$$

$$Ca(HCO_3)_2 + NH_4OH \rightarrow CaCO_3 \downarrow + (NH_4)_2CO_3 + H_2O \quad (5)$$

or during denitrification:

$$Ca(NO_3)_2 + 3H_2 + C \rightarrow CaCO_3 \downarrow + H_2O + N_2 \quad (6)$$

or in the following way:

$$CaSO_4 + 2C \rightarrow CO_2 + CaS \text{ or } CaSO_4 + 4H_2 \rightarrow CaS + H_2O \quad (7)$$

and further:

$$CaS + CO_2 + H_2O \rightarrow CaCO_3 \downarrow + H_2S \quad (8)$$

$$\begin{aligned} &2CH_3CH - OH - COONa + MgSO_4 \\ &\rightarrow MgCO_3 \downarrow + 2CH_3COONa + CO_2 + H_2S + H_2O \end{aligned} \quad (9)$$

$$\begin{aligned} &2CH_3CHOHCOONa + CaSO_4 \\ &\rightarrow CaCO_3 \downarrow + 2CH_3COONa + CO_2 + H_2O + H_2 \end{aligned} \quad (10)$$

$$\begin{aligned} &2KOOCCH_2CHOHCOOK + MgSO_4 \\ &\rightarrow MgCO_3 \downarrow + 4K_2CO_3 + 3CO_2 + H_2O + 3H_2S \end{aligned} \quad (11)$$

or when bacteria oxidize calci salts of organic acids:

$$Ca(HCOO)_2 + H_2O \xrightarrow[\text{(periphyton)}]{\text{bacteria}} CaCO_3 + CO_2 + H_2 \quad (12)$$

$$2Ca(HCOO)_2 \xrightarrow{\text{bacteria}} 2CaCO_3 + CO_2 + CH_4 \quad (13)$$

$$Ca(CH_3COO)_2 + H_2O \rightarrow CaCO_3 + CO_2 + 2CH_4 \quad (14)$$

$$Ca(CH_3CH_2CH_2COO)_2 + 3H_2O \rightarrow CaCO_3 + 2CO_2 + 5CH_4 \quad (15)$$

$$Ca(CH_3CH_2COO)_2 + 5H_2O \rightarrow CaCO_3 + 3CO_2 + 8CH_4 \quad (16)$$

$$Ca(CH_3CH_2COO)_2 + 7H_2O \rightarrow CaCO_3 + 4CO_2 + 11CH_4 \quad (17)$$

$$Ca(CH_3(CH_2)_8COO)_2 + 9H_2O \rightarrow CaCO_3 + 5CO_2 + 14CH_4 \quad (18)$$

$$Ca(CH_3COO)_2 + O_2 \rightarrow CaCO_3 + 3CO_2 + 3H_2O \quad (19)$$

The noted reactions (2)–(19) are presented in normal physiological processes of the metabolism of microorganisms: sulfate reduction, denitrification, use of salts of organic acids, or mineralization of the dead microorganism material. All conditions for reactions (2)–(19) exist in the slime of microorganisms on the surface of iron-aluminosilicate suspensions and in periphyton. In the marine environment, accordingly, there are conditions for additional allocation of microelements and nanochemical and mineralogical restructuring of iron-aluminosilicates in suspensions. In other words, in a such marine environment, there are all necessary substances and possibilities for bioflotation and enrichment of the forming ore deposits of jaspilites, iron-manganese nodules, iron ores of biocolloidal origin, peloids, sands, etc. [1, 3–14]. This is also confirmed by the fact that in 13 reactions out of 19 [reactions (6), (8)–(19)], carbonates are formed by microorganisms regardless of the content of hydrocarbonates, carbonate ions, and carbon dioxide in the surrounding water. Carbonate particles are also formed by reactions (1)–(5), (7). Their passage requires hydrocarbons, which are always present in seawater, or carbon dioxide, which is continuously produced by bacteria.

It is known that the amount of suspended ooze (suspension) in the World Ocean is approximately 13.7×10^9 tons [18–20]. The annual flow of rivers from land into the World Ocean according to the data of measurements in the Azov, Black, Mediterranean, and Red Seas, as well as in Antarctica, Indian, Pacific, and Atlantic Oceans gives an average value of carbonate content of about 7% in the suspension falling on the seabed. These carbonates are of microbiogenic (biocolloidal) origin [4].

As for iron-aluminosilicate sediments, their behavior within the framework of the developing scientific direction in recent years not only contributed to clarifying the mechanisms of ore-genesis in solid, sedimentary, and porous rocks and dispersed materials. It led to the development of new approaches to the relevant effective technologies of dispersion transformations, processing, and their use in large-scale production processes and also helped to develop ideas about the structural mechanisms of critical phenomena (creep, earthquakes, etc.) [1, 3].

The research of biocolloidal, microbiological, and biochemical processes based on the use of the phenomenon of selective heterocoagulation of mineral substances with microorganisms, highlighted in works [3, 8], as well as in the processes of recrystallization of oceanic nodules [1, 3, 6, 21] had the maximum development in this direction. Further development of these areas made it possible to assess the interrelationship of microbiological, physicomechanical, and nanochemical features of self-dispersion processes for both dense and crushed or porous rocks [3]. But these results were obtained without assessing the impact of periphyton microorganisms on them.

Figure 4 shows the data confirming the total influence of microorganisms from various ecotrophic groups, including periphyton, on the properties of pelitic-turbiditic sediments of the Black Sea. These data indicate, on the one hand, the ability of marine sediments to restore their biomedical activity while an increasing number of colony-forming units (CFU). On the other hand, with an increase in the sediment exposure time, the values of the effective viscosity and the corresponding shear stress increase too. This increase correlates with the increase in the amount of divalent iron (II) in the sediment, formed as a result of the vital activity of iron-reducing bacteria, and also correlates with the increase in the number of nanoparticles and the decrease in the number of microparticles (Table 2). Such data indicate that the vital activity of microorganisms in the composition of biocolloidal periphyton aggregates leads to the activation of the synergetic effect on the dispersion of the mineral part of sediments [2, 3, 5]. This allows the well-known scheme [3] to be presented for the biocolloidal process in the presence of periphyton in the following form:

$$\begin{aligned} &Fe_2O_{3(micro)} \xrightarrow[\text{periphyton}]{\text{bacteria and}} Fe(OH)_2 + Fe(OH)_3 \xrightarrow{CO_2} GR \cdot CO^{2-}_{3(nano)} \\ &\rightarrow FeO_{(nano)} + Fe_2O_{3(nano)} + Fe_3O_{4(nano)} \end{aligned} \tag{20}$$

GR Green Rust.

Reactions of the transformation of iron-aluminosilicates are transformed in the following way:

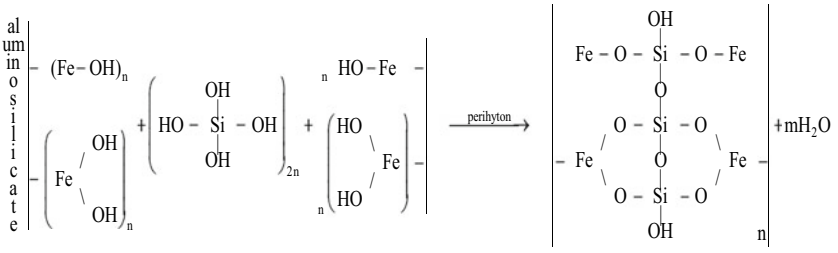

(21)

n phase contact nanostructures.

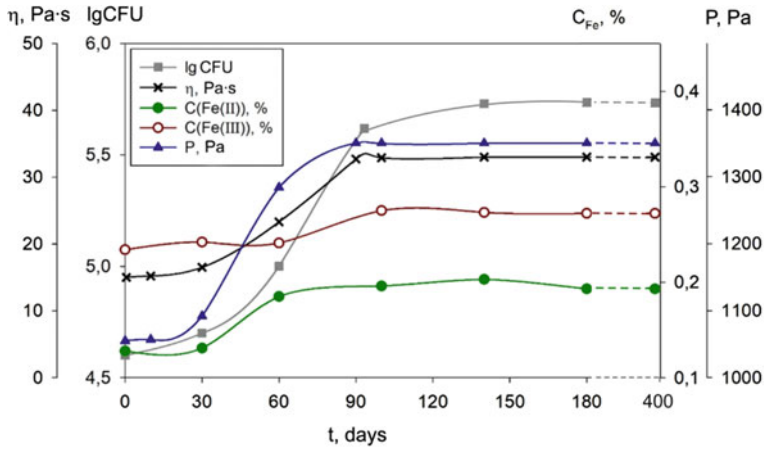

Fig. 4 Dependences of viscosity (η), shear stress (P), concentration (C, %) of Fe^{2+} (C(FeII)) and Fe^{3+}(C(FeIII)), and the number of colony-forming units (lgCFU) in the Black Sea nanostructured pelitic-turbiditic sediments taken from a depth of 2000 m, from the time of their exposure at a humidity of 46% in the presence of a natural complex of bacteria and microorganisms, including periphyton

Table 2 Physicochemical indicators of marine pelagic precipitations for water 46%

Index	Exposure, days				
	0	10	30	60	100
pH of liquid phase	7.0	7.1	7.3	7.4	7.4
Shear stress, Pa	1060	1070	1080	1290	1340
Viscosity, Pa·s	15	16	23	33	33
Concentration of particles < 250 μm, %	0.8	0.8	0.7	0.6	0.5
Concentration of nanoparticles, %	0.1	0.1	0.3	0.4	0.4
lgCFU	4.6	4.6	4.7	5.1	5.7

Such nanostructures, formed according to schemes (20) and (21), will most strongly bind aggregates of IASSMs, aluminosilicate, and silicate minerals in aqueous dispersions in the presence of complexes of various microorganisms, which is confirmed by the increasing values of viscosity and shear stress (Fig. 4; Table 2).

Therefore, along with physicochemical and nanochemical processes in dispersed iron-aluminosilicate sediments in the structure of pelites and peloids under the action of surface-active substances—metabolites of microorganisms and periphytons, biocolloidal interactions are activated. It affects the formation of nanodisperse-structured organic-clay-carbonate products that enrich bottom pelagic sediments and peloids with organic substances, clays, iron oxides, and carbonates, changing the chemical and mineralogical composition of the sediments.

4 Analysis of Nanostructural Phenomena in IASSs and NIASSs Associated with Rheological Processes in the Presence of Periphyton

It is known that clay minerals, especially montmorillonite, which is part of bentonite and polymineral clays, have the greatest influence on the rheological properties of nanostructured IASSs and NIASSs. They partially self-disperse in aqueous suspensions up to nanoparticles. The behavior of the latter does not correlate with the water content of the dispersions but has a significant dependence on the nanostructuring processes associated with the nanochemical properties and chemical structure of montmorillonite nanoparticles, as well as the properties of the biological products of bacteria and periphyton organisms. Thus, suspensions of calcium bentonite at a water content of 50% are characterized by the so-called hyperanomalous change in viscosity, but at a water content of 75%, the effect of hyperanomaly viscosity is no longer present. At the same time, after the nanochemical treatment of clay in the presence of periphyton organisms with the formation of sodium bentonite, the effect of hyperanomaly viscosity takes place again even when the humidity of the suspension reaches 90%. Its appearance is explained by an increase in the number of small nanoparticles of Na-montmorillonite and calcite in the composition of bentonite (Bt) due to the microbiogenic nanochemical process [3, 4, 14]:

$$Bt^{2-} + Ca^{2+} + Na_2CO_3 \xrightarrow[\text{peiphyton}]{\text{bacteria}} 2(Bt^{-} \cdot Na^{+})_n + (CaCO_3)_n \tag{22}$$

$$\begin{aligned} &Na_2CO_3 + 2H_2O \rightleftarrows 2NaOH + H_2CO_3; \\ &Bt^{2-} \cdot Ca^{2+} + 2NaOH \rightleftarrows 2(Bt^{-} \cdot Na^{+}) + Ca(OH)_2; \\ &Ca(OH)_2 + H_2CO_3 \rightarrow (CaCO_3)_n + H_2O \end{aligned} \tag{23}$$

n nanophase contact groups.

According to these schemes, calcite nanoparticles are deposited on the surface of sodium bentonite nanoparticles, which are covered with a slime layer under the action of bacteria and periphyton organisms—protozoa, fungi, microalgae, mollusks, etc. [2, 4, 14]. Slimes, which are composed of extracellular polysaccharides and polyuronides [14], isolate the formed nanophase contact groups from an external aggressive environment, such as CO_2, and give such groups stability. The main role of periphyton in such processes is traced.

But calcite is almost always present in natural bentonites and polymineral clays. Therefore, another process of formation of $CaCO_3$ nanoparticles is possible in parallel with Na-montmorillonite nanoparticles with the participation of CO_2 from the air [3, 4, 6]:

increase of laminar flow (Ostwald ripening) – formation of microparticles

$$CaCO_{3(micro)} + CO_2 + H_2O \rightleftarrows Ca(HCO_3)_2 \rightleftarrows CaCO_{3(nano)} + H_2O \quad (24)$$

Increase of turbulent flow (nanochemical recondensation) – formation of nanoparticles

The direct reaction (24) of nanochemical recondensation occurs at high-rate turbulent mixing of clay suspensions (high shear rates in rheoviscosimeter), and the reverse at low mixing rates (laminar flow) [3]. However, the reverse reaction practically does not occur in the presence of slime produced microbiogenically thanks to periphyton.

Thus, the processes of nanostructuring of clay iron-aluminosilicate suspensions in the presence of periphyton, nanochemical processes of their transformation, including biocolloidal microbiogenic processes, as well as chemical and mineralogical restructuring of nanoparticles, have a significant impact on the rheological behavior of suspensions associated with the precipitation of solid components from them in bottom polymineral sediments and their separation by natural bioflotation into different compositions, for example, presented in Fig. 1.

Thus, the features of the formation of iron-aluminosilicates present in river and sea suspensions in the presence of bacteria, microorganisms, and periphyton [2–4, 21, 22], which, in addition to bacteria, includes protozoa, fungi, worms, crustaceans, mollusks, etc., which live on solid phases within a certain biotope. It was shown that redox processes in suspensions are accompanied by transitions of Fe(II) into $Fe(OH)_3$, FeOOH (goethite) and $FeCO_3$ (siderite), and Mn(II) into MnO_2 or Mn_3O_4. When such suspensions enter marine estuaries, from the point of view of modern nanoscience, they become the site of many active biological, nanochemical, and biocolloidal interactions at the interface between aqueous solution and solid carbonates, and iron-aluminosilicates. Such interactions are also accompanied by layer-by-layer separation of suspensions into three layers, which arise and form under the influence of periphyton and bacteria for up to 15 thousand years with the formation of ore deposits—iron ore, iron-manganese nodules, etc. of biocolloidal origin and have an amorphous structure (Figs. 3 and 4). At the same time, the lower enriched layer is composed of iron hydroxides doped with manganese and trace elements with admixtures of carbonates, sands, silts, soils, etc. (Fig. 1); the upper layer, accordingly, is enriched with iron hydroxides and depleted with admixtures of carbonates, manganese compounds, trace elements, sand, etc., which is partially confirmed also by known results [2–4, 15–22].

Based on the above considerations, the graphical data for load–unload curves of elastic–plastic materials, to which the authors of the work [3] include bentonite and other formations (Fig. 1), polymineral clay suspensions with bacteria and microorganisms in the conditions of hyperanomaly or ultraanomaly of viscosity effect presence [3] were obtained. Thus, the rheological indices can be shown in the coordinates of viscosity (η)–shear stress (P) in the form given in Fig. 5.

As can be seen from the given curves, the hyperanomaly of viscosity is more often characterized by curves 1 and 3, and the previously unknown effect of ultraanomaly of viscosity is more often by curve 2, and sometimes by curve 1. Both effects have been experimentally confirmed by numerous rheograms for different

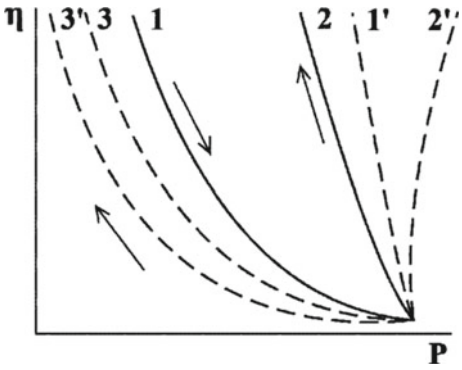

Fig. 5 Load–unload curves (1, 1′ and 2, 2′ respectively) in the conditions of plastic flow of elastic–plastic biocolloidal iron oxide silicate material; 3, 3′—load–unload curves under the conditions of the start of the hyperanomaly or ultraanomaly viscosity effect [3]

types of clays, pelitic sediments, and peloids given in [3], but the influence of periphyton on them. A preliminary conclusion should be drawn from these data that the effect of hyperanomaly viscosity more often is characteristic for less concentrated suspensions and with a lower content of iron compounds in them, and the effect of ultraanomaly viscosity is characteristic for more concentrated suspensions or at lower shear rates if the other previously mentioned factors remain stable [3]. At the same time, the water content of dispersions (W) changes as follows: $W_{1\text{-}3} < W_{1\text{-}2} < W_{1'\text{-}2'}$. These data and numerous data obtained for many sediments, soils, and sands indicate a significant role of rheological effects in the occurrence of critical processes in marine suspensions and oozes activated by bacteria that are the part of periphyton organisms (Fig. 4). But these results need an even deeper further comparative analysis and systematization.

The established regularities of nanostructural biocolloidal phenomena in dense and disperse materials of the Earth's crust also made it possible to develop and implement a number of methods of directional control of the structure of IASSs and NIASSs, based on the achievements of physicochemical geomechanics, biocolloidal chemistry and on the regularities of nanochemical contact interphase interactions [1, 3–5]. The conducted theoretical generalizations and experimental data made it possible to consider the kinetics and mechanisms of the transformation of dispersed IASSs as a result of their self-dispersion with the participation of nanochemical and microbiological processes in the presence of periphyton with the formation of new disperse structures with thermodynamically stable mineral phases; to develop the ideas of the mechanisms of elastic–plastic creep under similar conditions of IASSs suspensions; to outline further ways of development of the specified fundamental problems with the application of the obtained laws in geological sciences, colloid and biocolloidal chemistry with the aim of creating modern technological processes for application in eco-biotechnologies of environmental protection, ore mining, metallurgy, oil and gas production, ceramic, construction, and other industries, in agriculture, and in medicine for the development of new methods of rehabilitation and spa treatment of patients, prophylaxis of hemophilia, creation of wound-healing, burn-treatment, and medical-cosmetic products, etc. (Fig. 6).

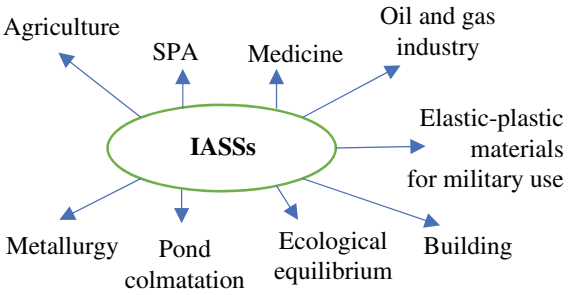

Fig. 6 Fields of application of iron-aluminosilicate materials activated by bacteria and periphyton organisms

The data shown in Fig. 6 are explained on a standalone example for a storage pond of salty mine waters, which are formed during the extraction of deep iron-aluminosilicate ore deposits in the Kryvyi Rih Basin (Fig. 7).

The data in Fig. 7a show that the bottom sediment was washed out through the karst pores of the rocks underlying the bottom of the pond during the 25 years of operation of the pond. After filling the bottom of the pond in 2012 with a suspension of coastal polymineral clay with alkaline admixtures, the subsidence of the bottom of the pond decreased six times, and the calculated stability of the dam increased up to six years (Fig. 7b). After adding biocolloidal nanostructural clay colmatants with bacteria and periphyton to the sediment, the durability of the dam increased up to 10–12 years or more (Fig. 7c).

5 Conclusions

Thus, the obtained results indicate that in the processes of precipitation in fresh, salty, and marine suspensions based on iron-aluminosilicates, along with processes with carbonates, the important ones are those that take place with the participation of microbiogenic reduction of Fe^{3+}—the fourth most common element of the Earth's crust. Under reductive conditions, the process of microbial biocolloidal iron reduction is accompanied by the formation of new minerals [3, 6, 17, 21] such as siderite, pyrite, magnetite, and iron-manganese nodules. Those are formed in lakes and estuaries due to the vital activity of organisms such as Metallogenium personatum, Caulococeus manganifer, etc. In anaerobic conditions of iron reduction, in the microbial combination, the activity of organisms with a respiratory type of metabolism, which performs the decomposition of cellulose, hydrocarbons, ammonification, nitrification, and oxidation of iron is inhibited. On the contrary, anaerobic fermenters, iron reducers, sulfate reducers, and actinomycetes increase their activity along with the activity of periphyton.

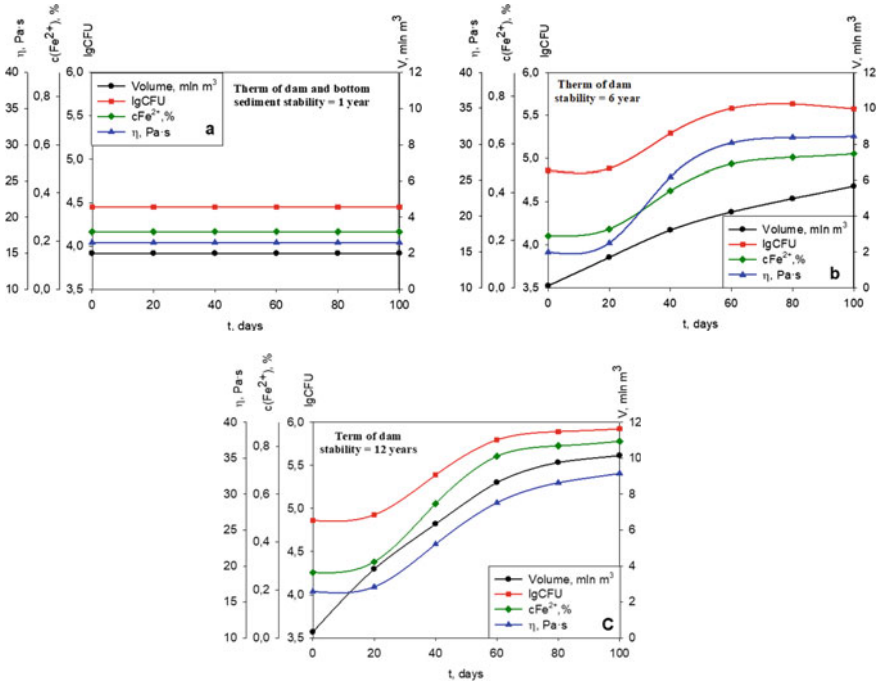

Fig. 7 Dependence of the ooze properties of the storage pond of mine iron ore waters from the conditions in it: **a** before the implementation of the technology (term of stability of the bottom and dam was 1–2 years); **b** after treatment with alkaline nanostructured inorganic clay colmatants (the term of stability of the bottom and dam was increased to six years); **c** after the implementation of biocolloidal nanostructural clay colmatants with bacteria and periphytons (the term of stability of the bottom and dam is increased to 10–12 years)

Generalized ideas have been developed for the creation of new highly effective materials and eco-biotechnologies concerning the conditions of synergetic action of complexes of periphyton organisms according to the laws of physicochemical geomechanics. Additionally, the understanding of processes with polymineral carbonate-iron-aluminosilicate particles leading to the formation of new mineral structures and their enrichment, has been expanded. Recommendations are provided for optimizing the methods of obtaining new materials and controlling eco-bio-geo-technological processes in the presence of complex natural communities of microorganisms and periphyton.

References

1. A.V. Panko, I.G. Kovzun, V.A. Prokopenko, O.M. Nikipelova, Nano-, micro- and macrotransformations of marine sediments under the influence of biocolloidal processes and aspects of nanotechnologies of their enrichment and application, in *Nanooptics and Photonics, Nanochemistry and Nanobiotechnology, and Their Applications. NANO 2020. Springer Proceedings in Physics*, vol 264, eds. by O. Fesenko, L. Yatsenko. (Springer, Cham, 2021). https://doi.org/10.1007/978-3-030-74800-5_13
2. A.A. Protasov, *Fresh Water Periphyton (Presnovodnyj perifiton)* (Naukova dumka, Kyiv, 1994)
3. I.G. Kovzun, V.A. Prokopenko, A.V. Panko, O.A. Tsyganovich, V.O. Oliinyk, O.M. Nikipelova, Z.R. Ulberg, *Nanochemical, Nanostructural and Biocolloidal Aspects of Transformations in Dispersions of Iron-Aluminosilicate Minerals* (PH "Akademperiodyka", Kyiv, 2020). https://doi.org/10.15407/akademperiodyka.416.188
4. Yu.A. Gorbenko, On microbiogenic precipitation of carbonates on the surface of marine suspension in the Black Sea and the World Ocean. Sediment. Mineral. (3), 90–94 (1976) (O mikrobiogennom osazhdenii karbonatov na poverhnosti morskoj vzvesi v CHernom more i ,Mirovom okeane. Mineralogiya osadochnyh obrazovanij, vyp.3)
5. Y.I. Voitenko, Synergetics of geological mediums and its impact on the effectiveness of the exploitation and exploration for mineral deposits. Mineral Resour. Ukraine (3), 15–21 (2019). https://doi.org/10.31996/mru.2019.3.15-21
6. V.A. Emel'janov, *Basics of Marine Geoekology (Osnovy morskoj geoekologii) (in Russian)* (Naukova dumka, Kyiv, 2003)
7. A.V. Panko, I.G. Kovzun, V.A. Prokopenko, O.M. Nikipelova, O.A. Tsyganovich, V.O. Oliinyk, Catastrophic phenomena on marine slopes and in artificial dams in a presence of nanostructured iron-aluminosilicates, in *Nanomaterials and Nanocomposites, Nanostructure Surfaces, and Their Applications. Springer Proceedings in Physics*, vol 246, eds. by O. Fesenko, L. Yatsenko (Springer, Cham, 2020). https://doi.org/10.1007/978-3-030-51905-6_28
8. A.V. Panko, I.G. Kovzun, Z.R. Ulberg, V.A. Oleinik, E.M. Nikipelova, K.D. Babov, Colloid-chemical modification of peloids with nano- and microparticles of natural minerals and their practical use, in *Nanophysics, Nanophotonics, Surface Studies, and Applications*, vol. 183, eds. by O. Fesenko, L. Yatsenko (Springer, Cham, 2016), pp 163–177. https://doi.org/10.1007/978-3-319-30737-4_14
9. A.V. Panko, I.G. Kovzun, O.M. Nikipelova et al., Nanostructural effects in iron oxide silicate materials of the Earth's crust, in: *Nanophotonics, Surface Studies and Applications. Springer Proceedings in Physics*, vol. 221, eds. by O. Fesenko, L. Yatsenko Nanophysics (Springer, Cham, 2019), pp. 367–386. https://doi.org/10.1007/978-3-030-17759-1_25
10. A.V. Panko, I.G. Kovzun, O.M. Nikipelova et al., Nanostructural and nanochemical processes in peloid sediments aided with biogeocenosis, in *Nanophysics, Nanophotonics, Surface Studies and Applications. NANO 2017. Springer Proceedings in Physics*, vol. 214, eds. by O. Fesenko, L. Yatsenko (Springer, Cham, 2018), pp. 215–230. https://doi.org/10.1007/978-3-319-92567-7_13
11. A.V. Panko, I.G. Kovzun, V.A. Prokopenko, O.A. Tsyganovich, V.O. Oliinyk, O.M. Nikipelova, Nano- and microdisperse structures in processes of metamorphism, reduction sintering, and component separation of iron-oxide-silicate materials, in *Nanophysics, Nanomaterials, Interface Studies, and Applications. NANO 2016. Springer Proceedings in Physics*, vol. 195, eds. by O. Fesenko, L. Yatsenko (Springer, Cham, 2017), pp. 743–755. https://doi.org/10.1007/978-3-319-56422-7_57
12. A.Yu. Rozanov, G.A. Zavarzin, Bacterial paleontology. Herald Russ. Acad. Sci. **67**(6), 241–245 (1997)
13. B.V. Burkinskii, K.D. Babov, O.M. Nikipelova et al., Kuyalnytsky estuary: realities and prospects of recreational use (Kuyal′nyts′kyy lyman: realiyi ta perspektyvy rekreatsiynoho vykorystannya) (in Ukrainian). Helgenetika, Odessa (2019)
14. B.A. Nasibullin, S.G. Gushcha, O.M. Nikipelova, S.I. Nikolenko, L.V. Tikhokhid, O.Y. Oleshko, O.I. Bakholdina, Pathophysiological mechanisms of biological activity of colored

clays (Patofiziolohichni mekhanizmy biolohichnoi aktyvnosti kolorovykh hlyn) (in Ukrainian). Zoloti storinky, Kharkiv (2017). ISBN 978-966-400-418-0
15. C.S.F. Gomes, M. Rautureau, J.H.C. Gomes, E.A.F. Silva, Interactions of clay and clay minerals with the human health, in *Minerals latu sensu and Human Health*, eds. by C. Gomes, M. Rautureau (Springer, Cham, 2021). https://doi.org/10.1007/978-3-030-65706-2_7
16. C.F. Gomes, J.H. Gomes, E.F. da Silva, Bacteriostatic and bactericidal clays: an overview. Environ. Geochem. Health **42**, 3507–3527 (2020). https://doi.org/10.1007/s10653-020-00628-w
17. N.P. Sherbak, V.I. Pavlishin, A.L. Litvin et al., *Mineralyi Ukrainyi: Kratkiy spravochnik (Minerals of Ukraine: A Quick Reference)* (Naukova dumka, Kyiv, 1990)
18. I. Verhoogen, F.I. Turner, L.E. Weiss, C. Wahrhaftig, W.S. Fyfe, *The Earth. An Introduction to Physical Geology* (Holt.Rinehart and Winston Inc, New York-Montreal-London-Sydney, 1970)
19. R.A. Horne, *Marine Chemistry* (Wiley Interscience, New York, 1969), p. 401
20. P.K. Weyl, *An Introduction to the Marine Environment* (Wiley, New York, 1970)
21. N.M. Strakhov, *Selected Works. Problems of Sedimentary Ore Formation (Izbrannye trudy. Problemy osadochnogo rudoobrazovaniya)* (Nauka, Moscow, 1986), pp. 218–219, 288–290
22. D.R. Loveley, E.J.P. Phillips, Organic matter mineralization with reduction of ferric iron in anaerobic sediments. Appl. Environ. Microbiol. **51**, 683–689 (1986)

Natural Zeolites Modified with Silver Nanoparticles as Promising Sorbents with Antibacterial Properties

L. K. Patrylak, A. V. Yakovenko, B. O. Nizhnik, O. P. Pertko, V. A. Povazhnyi, D. S. Kamenskyh, and O. V. Melnychuk

Abstract To improve the porous properties of natural Ukrainian clinoptilolite, it was treated with ethylenediamine tetraacetic acid. Ag-containing zeolite and gamma-alumina samples were obtained by their impregnation with silver nitrate and the thermal decomposition of the latter. Synthesized samples were investigated by using SEM, TEM, low temperature nitrogen adsorption/desorption, FTIR spectroscopy, and DTA/TG. Nanosized silver particles of 5–10 nm were detected on the zeolite sample only. Total viable count determination was used to investigate the antibacterial properties of the samples. Water samples from three Kyiv's lakes (Sonyachne, Svyatoshynske, and Radunka) were used in the study. In comparison with Ag–Al_2O_3, Ag-containing zeolite sample demonstrates better performance in antibacterial activity. The latter can be caused by the nanodimensionality of Ag species on the zeolite surface as well as by the stronger interaction of silver with zeolite cations.

1 Introduction

Today, more than eighty types of natural zeolites are known [1, 2]. The latter, in contrast to synthetic zeolites, usually contain a number of impurities from other rocks. Clinoptilolite, as a zeolite of the heulandite group, finds considerable application [1–4] in various fields. It is one of the most stable and common natural zeolites in the world. Big deposits of clinoptilolite are available in the Transcarpathian region of Ukraine. Despite its significant deposits, the use of the latter as a basis for catalysts and sorbents is currently insignificant. The shortcomings of the porous structure of

L. K. Patrylak (✉) · A. V. Yakovenko · B. O. Nizhnik · O. P. Pertko · V. A. Povazhnyi · D. S. Kamenskyh · O. V. Melnychuk
V.P. Kukhar Institute of Bioorganic Chemistry and Petrochemistry of National Academy of Sciences of Ukraine, Kyiv, Ukraine
e-mail: lkpg@ukr.net

L. K. Patrylak · B. O. Nizhnik · O. V. Melnychuk
National Technical University of Ukraine "Igor Sikorskyi Kyiv Polytechnic Institute", Kyiv, Ukraine

O. Fesenko and L. Yatsenko (eds.), *Nanoelectronics, Nanooptics, Nanochemistry and Nanobiotechnology, and Their Applications*, Springer Proceedings in Physics 297,
https://doi.org/10.1007/978-3-031-42708-4_5

the clinoptilolite, on the other hand, limit the widespread usage of Ukrainian natural zeolites.

In the past, silver in all of its forms has been utilized either alone or in conjunction with other technologies as an antibacterial agent [5, 6]. Utilizing this metal as silver nitrate or silver sulfadiazine has been studied for use in food packaging to prevent contamination, in home appliances such as refrigerators and washing machines, and in several industrial applications [6–10]. With the development of new knowledge in nanotechnology and related sciences [11], it becomes possible to explore the antibacterial potential of Ag nanoparticles deposited on carriers, too.

Silver nanoparticles have been imposed as an excellent antimicrobial agent being able to combat bacteria in vitro and in vivo causing infections [5].

Ag nanoparticles have especially been employed as antibacterials, antifungals, and antioxidants in agriculture and medicine. Ag demonstrates antibacterial activity against gram-positive and gram-negative bacteria. However, the exact mechanism of such behavior is still under discussion. The existing experimental evidence supports different mechanisms that consider the physicochemical properties of Ag nanoparticles, such as size and surface, which allow them to interact with or even pass through cell walls or membranes and directly affect intracellular components. The growth and multiplication of many bacteria, including *Bacillus cereus, Staphylococcus aureus, Citrobacter koseri, Salmonella typhii, Pseudomonas aeruginosa, Escherichia coli, Klebsiella pneumonia, Vibrio parahaemolyticus,* and *Candida albicans*, are shown to be stopped by Ag nanoparticles by binding Ag/Ag^+ with the biomolecules [13]. Silver nanoparticles may produce free radicals and reactive oxygen species, which can cause apoptosis and cell death by blocking cell replication.

In the paper [14], investigations were made into the antibacterial properties of the Ag-coated Ti powder. A potential antibacterial effect has been noted. It was also demonstrated that *E. coli* bacteria cannot survive in close proximity to these Ti–Ag surfaces, and the observed antibacterial capabilities may not be connected to the alloy's release of a water-soluble component. Therefore, Ti–Ag alloys are a promising material for antibacterial implants due to their local antibacterial properties, which may also make them biocompatible.

Inorganic $AgNO_3$-containing sorbents are widely used for the localization of radioactive iodine volatile compounds [15].

The silver-containing sorbents, based on mineral carriers like alumina and silica systems with a meso- and macro-porous structure, are chemically composed to be both hydrophilic and hydrophobic. When compared to analogues, these sorbents are quite inexpensive. Such sorbents can be used in gaseous and liquid media, for example, for thiophenic compounds and mercury adsorption [16, 17]. It should be taken on board that the use of sorbents, catalysts, or composite materials with developed surface area and porosity is a necessary condition for the effective course of a range of heterogeneous processes [18–20].

Therefore, the aim of this study was to obtain promising nanoscale silver-containing antibacterial sorbents using a complex modification of natural Ukrainian zeolites.

2 Experimental

2.1 Synthesis of the Samples

The raw starting material was clinoptilolite zeolite rock from the Sokyrnytsja village deposit in the Transcarpathian region (Ukraine). Clinoptilolite was initially crushed and fractionated. Medium-sized grains (0.5–1.0 mm) were used for further processing. The modification process involved dispersing the zeolite sample in water, adding crystals of ethylenediamine tetraacetic acid (EDTA), and boiling the resulting mixture for three hours. The sample was then washed, its chemical composition was determined, and it underwent further processing four times. The total treatment time was 12 h.

One weight percent of silver was added to the sample by impregnating it with silver nitrate according to its moisture content. Then, the sample was calcined at 480–500 °C for 2 h. A gamma-Al_2O_3 sample with silver was prepared for comparison according to the same modification procedure. Initial gamma-alumina (DSTU 8136-85) was produced by JS "Katalizator" (Kamjanske, Ukraine).

Total viable count (TVC) determination was used to investigate the antibacterial properties of the samples. The TVC was studied using the method of deep sowing of water in nutrient agar according to the methodological instructions "Sanitary and Microbiological Control of Drinking Water" approved by Order of the Ministry of Health of Ukraine No. 60 of the 02/03/2005. All colonies, including microorganisms that grew at 36 °C for 24 h and could be seen at a 2–5 times magnification, were considered. According to the procedure described by the authors' group, sterilization of nutritional agar was carried out in a microwave oven for 2 min (30 s + 30 s + 1 min) at a radiation strength of 750 W [21].

2.2 Methods

SEM and TEM. Scanning electron microscopy (Zeiss EVO MA 10, Carl Zeiss Microscopy GmbH, Germany) and transmission electron microscopy (JEM 2100F, JEOL, Japan) were used for investigation of samples.

N_2 adsorption. Low temperature nitrogen adsorption/desorption isotherms for samples were measured on a Quantachrome Autosorb NOVA 1200e® automatic analyzer (USA) after thermal dehydration in the muffle furnace at 380 °C for 2 h and additional in situ evacuation at 250 °C for 1 h. Utilizing the NOVAWin software, the parameters of the porous structure were computed.

X-ray fluorescence (XRF) analysis. The determination of the silver content in the obtained samples as well as the silica-to-alumina ratio was realized using XRF analysis (Oxford Instruments X-Supreme 8000 analyzer, Great Britain).

FTIR spectroscopy. A Shimadzu IR Affinity-1S FTIR spectrometer (Japan) was used to record the FTIR spectra of zeolites in the 400–1500 cm^{-1} region of the framework vibration. The spectral resolution was 2 cm^{-1}.

DTA/TG. Using a Linseis STA 1400 system type derivatograph (Germany), the zeolite samples were subjected to simultaneous thermogravimetric (TG) and differential thermal analysis (DTA) in the temperature range of 20–1000 °C. As a reference material, 1200 °C-calcined alumina was used. Every determination was made in a typical atmospheric setting. Each experiment used a sample amount of about 25 mg.

3 Results and Discussion

3.1 Samples Characterization

The first stage of zeolite sample modification involved the EDTA-induced four-fold dealumination/decationation of its pores. Both processes occur simultaneously. After this gentle process, the SiO_2/Al_2O_3 ratio changed from 7.3 to 8.7 according to XRF data, the specific surface area (S_{BET}) increased from 11 to 92 m^2/g, and the micropore volume (Vt_{micro}) raised from 0.002 to 0.036 cm^3/g (Fig. 1; Table 1). Furthermore, the latter happened mostly as a result of better access to the sample microporous structure. S_{BET}, micropore surface (St_{micro}), and volume (Vt_{micro}) all marginally decreased after Ag impregnation, while overall pore volume (V_{sum}) remained constant. Adsorption properties of the clinoptilolite samples are quite different to those for mordenite–clinoptilolite rocks of Transcarpathia [22, 23] and similar to mineral acid-treated sample of clinoptilolite [24, 25]. In general, natural zeolites are characterized by significantly lower surface areas compared to synthetic zeolites, for which the surface areas according to BET are up to several hundred square meters per 1 g [26, 27].

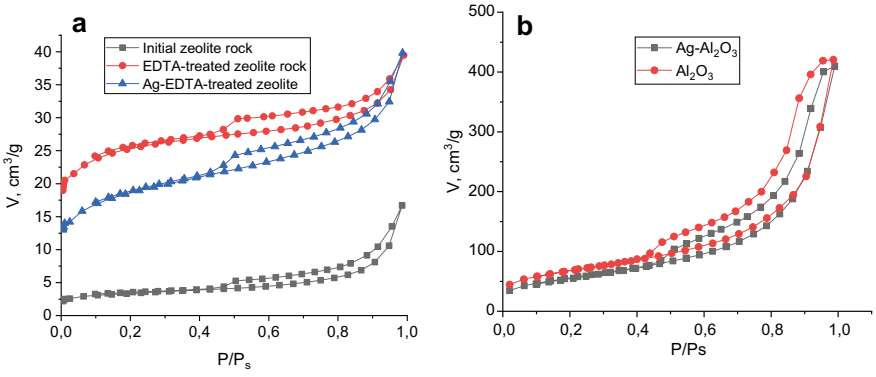

Fig. 1 Low temperature nitrogen adsorption/desorption isotherms for synthesized zeolite (**a**) and alumina (**b**) samples

Table 1 Adsorption properties of the samples

Sample	S_{BET}, m^2/g	St_{micro}, m^2/g	Vt_{micro}, cm^3/g	V_{sum}, cm^3/g
Initial zeolite	11	5.5	0.002	0.031
EDTA-treated zeolite	92	79	0.037	0.0621
Ag-EDTA-zeolite	69	55	0.026	0.061
Al_2O_3	221	7	0.01	0.651
Ag–Al_2O_3	201	6	0.002	0.634

SEM images of the initial zeolite rock and dealuminated zeolite samples (Fig. 2a, b) show typical crystals for natural zeolites [28–31], but images of the initial sample show some impurities on the zeolite crystals, which were removed after EDTA treatment. Some external surface additions we can see after Ag impregnation on zeolite (Fig. 2d, e). It is interesting that in the case of the zeolite sample, we have some cloud-like Ag species and some nanoparticles, whose dimensions are difficult to determine from SEM images. On the alumina sample, only cloud-like species are formed in spite of the same procedure for their preparation (Fig. 2f).

Figure 3 displays TEM images of initial clinoptilolite rock (a), EDTA-treated sample with Ag nanospecies (b, c), and an alumina sample after silver impregnation of Ag–Al_2O_3 (d). Clinoptilolite is the main phase in the initial rock, but it also contains mordenite and magnetite as impurities. Despite XRF analysis confirming the presence of 1 wt% of silver on the alumina sample, silver nanoparticles are not visible in TEM images (d). On clinoptilolite, however, we can see many nanoparticles measuring 5–10 nm. It is known that silver nitrate decomposition is negligible below the melting point, but becomes appreciable around 250 °C and fully decomposes at 440 °C with Ag(0) formation. Silver oxide cannot be formed because it decomposes at a lower temperature than silver nitrate, so the decomposition of silver nitrate yields elemental silver instead. Why we do not see Ag species in the case of Ag–Al_2O_3? With the purpose of understanding these peculiarities, an Ag–Al_2O_3 sample was additionally washed, and the water after treatment was analyzed for Ag-ion presence. The reaction was negative. Therefore, silver nitrate is absent on the sample. Silver nitrate, on the other hand, can react with amphoteric alumina to form AgOH. The latter hydrolyzes to Ag_2O oxide after being washed with hot water. The Ag–Al_2O_3 sample became gray after that. Thus, under the same conditions of impregnation and thermal decomposition of silver nitrate on aluminum oxide, the formation of visible silver nanoparticles is not observed. Obviously, silver forms a powdery or porous layer on the alumina, which can be seen on SEM images as clouds.

Figure 4 shows the FTIR spectra of initial and EDTA-treated zeolite rock in the region of lattice vibrations. The spectrum of the sample did not undergo significant changes after processing, which indicates the absence of sample amorphization and the preservation of its crystalline structure. However, there is a shift of absorption bands of antisymmetrical valence vibrations of the (Si,Al)–O bond at 1015 cm^{-1} for the initial sample into the high-frequency region to 1035 cm^{-1}, which is associated with an increase in the proportion of silicon, that is, the silica-to-alumina ratio. This

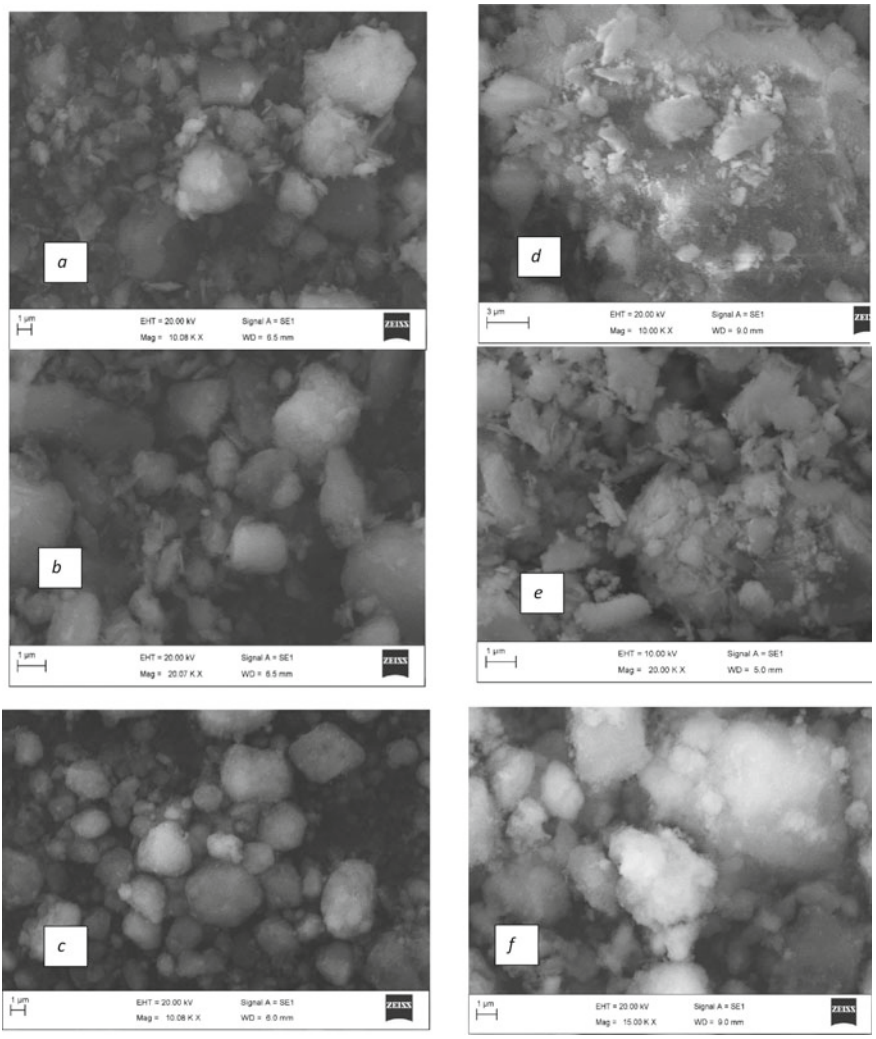

Fig. 2 SEM images of synthesized samples: **a** initial zeolite; **b** EDTA-treated zeolite; **c** Al_2O_3; **d**, **e** Ag-EDTA-zeolite; **f** Ag–Al_2O_3

is consistent with the postulate of Woiciehovska et al. [32]: The higher the Si/Al ratio, the band-specific ring oscillations shift toward higher frequencies.

The original form of the clinoptilolite rock and the EDTA-teared sample were investigated using the DTA/TG method. Figure 5 shows the corresponding curves. It is known that the loss of water from zeolite samples often takes place between 100 and 400 °C, and it may be seen in the DTA profiles as an extended endothermic effect [29, 33].

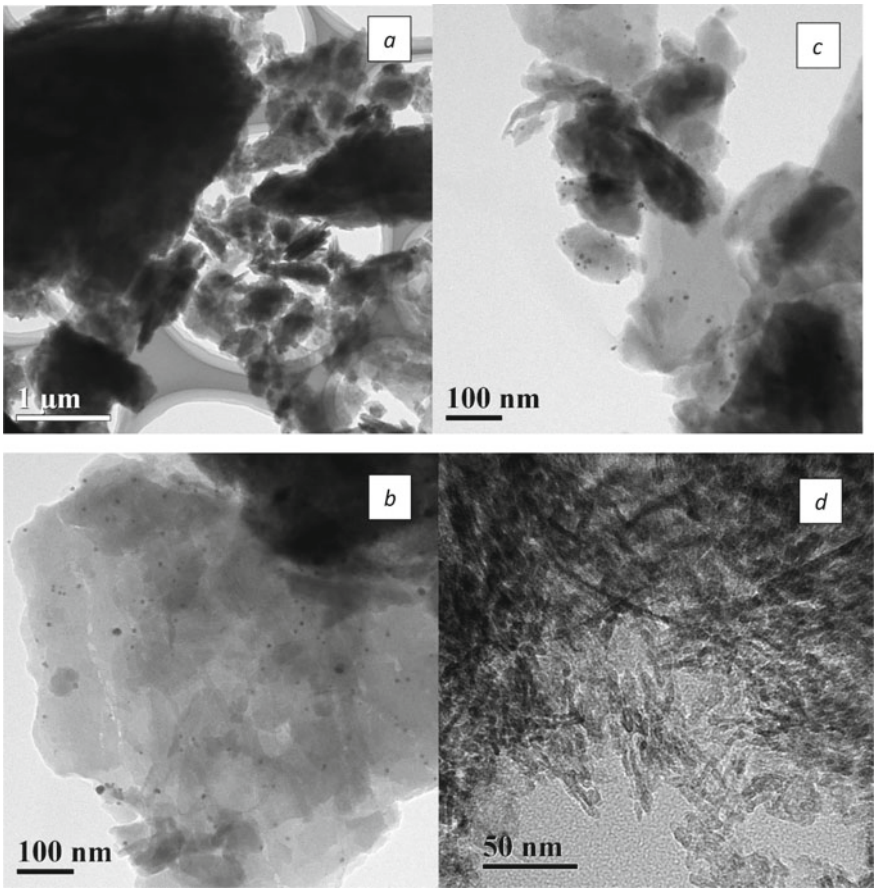

Fig. 3 TEM images: **a** initial zeolite; **b**, **c** Ag-EDTA-zeolite; **d** Ag–Al_2O_3

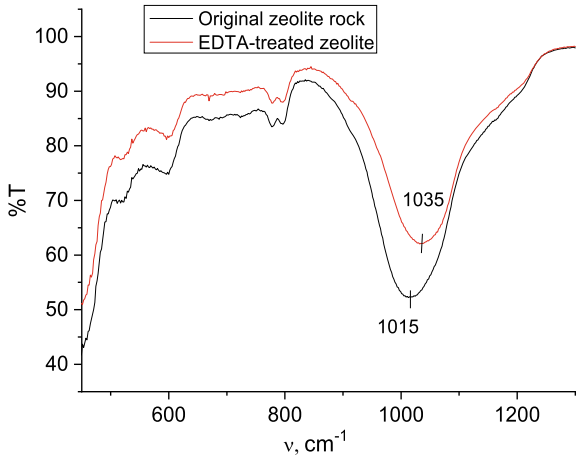

Fig. 4 FTIR spectra of initial and EDTA-treated zeolite

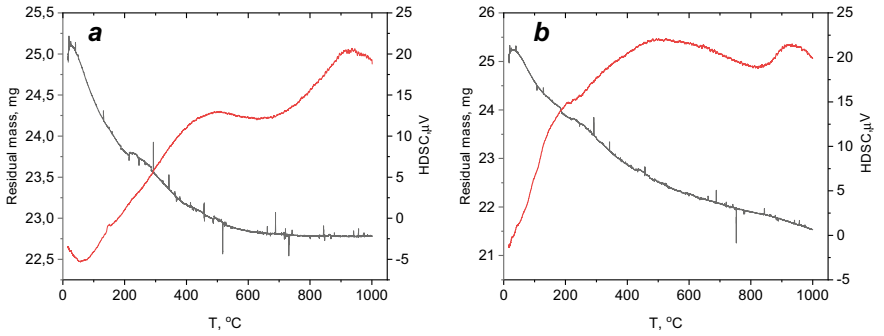

Fig. 5 DTA and TG results for original clinoptilolite zeolite rock (**a**) and EDTA-treated zeolite (**b**)

The original rock is characterized by an endotherm near 100 °C related to the dehydration process. The dehydration rate is substantially higher in the original sample than in the treated sample. For the first sample, dehydration is stopped at 500 °C, whereas for EDTA-treated zeolite, the dehydration process smoothly follows by the dehydroxylation of acid sites, which is triggered after acid treatment. In the case of original rock, there are no acid sites, and only dehydration takes place. Clinoptilolite zeolite is one of the most thermally stable natural minerals that does not show major structural changes until 800–900 °C, but a phase transition process, indicated by an exothermic effect on the DTA curve, is observed at temperature close to 900 °C.

3.2 Antibacterial Properties

To determine the starting point of bacterial contamination, the water of three of Kyiv's lakes (Sonyachne, Svyatoshynske, and Radunka) was previously examined. Water samples were tested in June 2022. The initial characteristics of the water samples were as follows: Lake Radunka—70–200 colony-forming units per cm^3 (CFUs/cm^3); Lake Sviatoshynske—150–250 CFUs/cm^3; Lake Soniachne—1350–3100 CFUs/cm^3. According to TVC values, Lake Radunka water meets standards for both drinking water (up to 100 CFUs/cm^3 of water) and open water bodies (up to 1000 CFUs/cm^3 of water). The warnings for Lake Svyatoshynske water are a little more ominous. Thus, Lake Sonyachne water ended up being the worst. Therefore, this water sample was selected for further study.

In Table 2, we have the results of deep sowing of water into peptone-yeast agar in the presence of 0.1 or 0.2 g of zeolite and alumina samples with silver. Using Ag-zeolite increases the purification of water samples by 60–200 times. As a result, according to this indicator, the water sample now fully meets the regulations for

Table 2 Results of the deep sowing of water into nutrient agar in the presence of zeolite and alumina oxide samples

Sample	The number of microorganisms, CFUs/cm^3	
	0.1 g	0.2 g
Ag-EDTA-zeolite	51	16
Ag–Al_2O_3	225	90
Initial water	3010	

surface water and, moreover, even the regulations for drinking water. Then, Ag-alumina requires only 13 and 30 times as much water for purification. Such peculiarities can be caused by different states of applied silver particles, which are both nanoscale and cloud-like in the case of zeolite and only cloud-like in the case of alumina. But we cannot deny the role of Ag species' interactions with zeolite matrix, too. It is known, that the Si–O–Si groups are one of the clinoptilolite functional groups with which heavy metals interact [34]. This interaction can be like the interaction of Brönsted and Lewis acid sites in zeolites and Brönsted/Lewis acid sites with metal species that promote high zeolite acidity and activity [19, 36]. Ag nanoparticles that localize near zeolites exchange cations can be stabilized by cations, which additionally improve their antibacterial properties.

The effect of different sizes of silver nanoparticles on the zeolite matrix on antimicrobial properties and possible silver aggregation requires further investigation.

These conclusions are consistent with the findings of a group of authors [36–38] who discovered that the Ag-clinoptilolite composite has a strong antimicrobial effect against gram-negative bacteria and yeasts, as well as a significant effect on the vital activity of *S. aureus*. It was determined also that the native form of clinoptilolite has a better antibacterial effect against *E. coli* than its H-form. However, antagonistic activity against *S. aureus* was worse than against *E. coli* in both forms. When different forms of clinoptilolite are combined with Ag(I), their antibacterial activity is increased [37, 38].

4 Conclusions

The chemical modification of the Transcarpathian clinoptilolite rock with EDTA resulted in the soft dealumination of the rock, the removal of impurities, and a significant improvement of its porous properties according to the results of low temperature nitrogen adsorption. Ag nanoparticles of 5–10 nm on the zeolite surface can be obtained by impregnation with silver nitrate, followed by the thermal decomposition of the latter, in contrast to a gamma-alumina sample. A considerable drop in the values of total viable count of lake water suggests the potential of Ag-zeolite application in the purification of not only surface water, but drinking water too. In comparison with Ag–Al_2O_3, which also demonstrates some antibacterial properties,

Ag-containing zeolite samples demonstrate better performance in antibacterial properties. The latter can be caused by the nanodimensionality of Ag species as well as the stronger interaction of silver with zeolite cations.

Acknowledgements The authors acknowledge the assistance and support of I. M. Frantsevych Institute for Problems of Materials Science of National Academy of Sciences in conducting the electron transmission microscopy experiments.

References

1. K. Stocker, M. Ellersdorfer, M. Lehner, J.G. Raith, Characterization and utilization of natural zeolites in technical applications. Berg Huettenmaenn. Monatsh. **162**, 142–147 (2017). https://doi.org/10.1007/s00501-017-0596-5
2. M. Krol, Natural versus synthetic zeolites. Crystals **10**, 622–630 (2020). https://doi.org/10.3390/cryst100706223
3. Z.O. Znak, S.A. Kornii, A.S. Mashtaler, O.I. Zin, Production of nanoporous zeolites modified by silver ions with antibacterial properties. Mater. Sci. **56**, 536–543 (2021). https://doi.org/10.1007/s11003-021-00461-1
4. Z.Y. Ji, J.S. Yuan, X.G. Li, Removal of ammonium from wastewater using calcium form clinoptilolite. J. Hazardous Mater. **141**, 483–488 (2007). https://doi.org/10.1016/j.jhazmat.2006.07.010
5. T. Bruna, F. Maldonado-Bravo, P. Jara, N. Caro, Silver nanoparticles and their antibacterial applications. Int. J. Mol. Sci. **22**, 7202 (2021). https://doi.org/10.3390/ijms22137202
6. L.P. Silva, A.P. Silveira, C.C. Bonatto, I.G. Reis, P.V. Milreu, Silver nanoparticles as antimicrobial agents: past, present, and future, in *Nanostructures for Antimicrobial Therapy: Nanostructures in Therapeutic Medicine Series* (Elsevier, Amsterdam, 2017), pp. 577–596. ISBN 9780323461511
7. J.W. Tong, Case reports on the use of antimicrobial (silver impregnated) soft silicone foam dressing on infected diabetic foot ulcers. Int. Wound J. **6**, 275–284 (2009)
8. C.N. Miller, N. Newall, S.E. Kapp, G. Lewin, L. Karimi, K. Carville, T. Gliddon, N.M. Santamaria, A randomized-controlled trial comparing cadexomer iodine and nanocrystalline silver on the healing of leg ulcers. Wound Repair Regen. **18**, 359–367 (2010)
9. J.J. Castellano, S.M. Shafii, F. Ko, G. Donate, T.E. Wright, R.J. Mannari, W.G. Payne, D.J. Smith, M.C. Robson, Comparative evaluation of silver-containing antimicrobial dressings and drugs. Int. Wound J. **4**, 114–122 (2007)
10. Y.T. Kim, K. Kim, J.H. Han, R.M. Kimmel, Antimicrobial active packaging for food. Smart Packag. Technol. Fast Mov. Consum. Goods **76**, 99–110 (2008)
11. Y. Kampmann, E. De Clerck, S. Kohn, D.K. Patchala, R. Langerock, J. Kreyenschmidt, Study on the antimicrobial effect of silver-containing inner liners in refrigerators. J. Appl. Microbiol. **104**, 1808–1814 (2008)
12. A. Kedziora, M. Speruda, E. Krzyzewska, J. Rybka, A. Łukowiak, G. Bugla-Płoskonska, Similarities and differences between silver ions and silver in nanoforms as antibacterial agents. Int. J. Mol. Sci. **19**, 444 (2018)
13. K.S. Siddiqi, A. Husen, R.A.K. Rao, A review on biosynthesis of silver nanoparticles and their biocidal properties. J. Nanobiotechnol. **16**, 14 (2018). https://doi.org/10.1186/s12951-018-0334-5
14. L. Somlyai-Sipos, P. Baumli, A. Sycheva, G. Kaptay, E. Szőri-Dorogházi, F. Kristály, T. Mikó, D. Janovszky, Development of Ag nanoparticles on the surface of Ti powders by chemical reduction method and investigation of their antibacterial properties. Appl. Surf. Sci. **533**, 147494 (2020). https://doi.org/10.1016/j.apsusc.2020.147494

15. B.J. Riley, S. Chong, R.W. Asmussen, A. Bourchy, M.H. Engelhard, Polyacrylonitrile composites of Ag–Al–Si–O aerogels and xerogels as iodine and iodide sorbents. ACS Appl. Polym. Mater. **3**(7), 3344–3353 (2021). https://doi.org/10.1021/acsapm.1c00237
16. M. Wdowin, M.M. Wiatros-Motyka, R. Panek, L.A. Stevens, W. Franus, C.E. Snape, Experimental study of mercury removal from exhaust gases. Fuel **128**, 451–457 (2014). https://doi.org/10.1016/j.fuel.2014.03.041
17. Y. Liu, J. Liao, L. Chang, W. Bao, Ag modification of SBA-15 and MCM-41 mesoporous materials as sorbents of thiophene. Fuel **311**, 122537 (2022). https://doi.org/10.1016/j.fuel.2021.122537
18. F. Rouqerol, J. Rouqerol, K. Sing, *Adsorption by Powders and Porous Solids: Principles, Methodology and Applications* (Academic Press, San Diego, 1999)
19. J. Weitkamp, M. Hunger, in *Introduction to Zeolite Molecular Sieves*. ed. by J. Cejka, H. van Bekkum, A. Corma, F. Schueth (Elsevier, New York, 2007), pp.787–836
20. I. Ivanenko, A. Voronova, I. Astrelin, Y. Romanenko, Structural and catalytic properties of Ni–Co spinel and its composites. Bull. Mater. Sci. **42**, 172 (2019).https://doi.org/10.1007/s12034-019-1854-9
21. S.M. Hontarenko, A.M. Herasymenko, Method of agar sterilization for biotechnological investigations. Bioenergetyc **1**, 36–38 (2019) (in Ukrainian). https://doi.org/10.47414/be.1.2019.229288
22. F.M. Bobonich, V.N. Solomakha, V.V. Bobik, Features of the distribution of aluminum in mordeniteclinoptilolite catalysts for the hydroisomerization of n-hexane. Theoret. Exp. Chem. **38**(5), 330–334 (2002)
23. L.K. Patrylak, O.P. Pertko, A.V. Yakovenko, Yu.G. Voloshyna, V.A. Povazhnyi, M.M. Kurmach, Isomerization of linear hexane over acid-modified nanosized nickel-containing natural Ukrainian zeolites. Appl. Nanosci. **12**, 411–425 (2022). https://doi.org/10.1007/s13204-021-01682-1
24. O. Korkuna, R. Leboda, J. Skubiszewska-Zieba, T. Vrublevska, V.M. Gunko, J. Ryczkowski, Structural and physicochemical properties of natural zeolites: clinoptilolite and mordenite. Micropor. Mesopor. Mater. **87**, 243–254 (2006). https://doi.org/10.1016/j.micromeso.2005.08.002
25. L. Patrylak, S. Konovalov, A. Yakovenko, O. Pertko, V. Povazhnyi, M. Kurmach, Y. Voloshyna, M. Filonenko, S. Zubenko, Fructose transformation into 5-hydroxymethylfurfural over natural transcarpathian zeolites. Chem. Chem. Technol. **16**(4), 521–531 (2022)
26. L.K. Patrylak, M.M. Krylova, O.P. Pertko, Y.G. Voloshyna, Linear hexane isomerization over Ni-containing pentasils. J. Por. Mater. **26**(3), 861–868 (2019). https://doi.org/10.1007/s10934-018-0685-1
27. L. Patrylak, M. Krylova, O. Pertko, Y. Voloshyna, A. Yakovenko, n-Hexane isomerization over nickel-containing mordenite zeolite. Chem. Chem. Technol. **14**(2), 234–238 (2020). https://doi.org/10.23939/chcht14.02.234
28. Z. Znak, O. Zin, A. Mashtaler, S. Korniy, Y. Sukhatskiy, R. Gogate Parag, R. Mnykh, P. Thanekar, Improved modification of clinoptilolite with silver using ultrasonic radiation. Ultrason. Sonochem. **73**, 105496 (2021). https://doi.org/10.1016/j.ultsonch.2021.105496
29. N. Mansouri, N. Rikhtegar, H.A. Panahi, B.K. Shahraki, Porosity, characterization and structural properties of natural zeolite-clinoptilolite-as a sorbent. Environ. Protect. Eng. **39**, 139 (2013). https://doi.org/10.5277/EPE130111
30. M. Minceva, R. Fajgar, L. Markovska, V. Meshko, Comparative study of Zn^{2+}, Cd^{2+}, and Pb^{2+} removal from water solution using natural clinoptilolitic zeolite and commercial granulated activated carbon. Equilibrium of adsorption. Separation Sci. Technol. **43**, 2117–2143 (2008). https://doi.org/10.1080/01496390801941174
31. J.L. Sihombing, S. Gea, A.N. Pulungan, Y.A. Hutapea, The characterization of Sarulla natural zeolite crystal and its morphological structure, in *AIP Conference Proceedings, The 3rd International Seminar on Chemistry: Green Chemistry and its Role for Sustainability* vol. 2049, no. 1 (2018), p. 020062. https://doi.org/10.1063/1.5082467

32. K.M. Wojciechowska, M. Król, T. Bajda, W. Mozgawa, Sorption of heavy metal cations on mesoporous ZSM-5 and mordenite zeolites. Materials **12**, 3271 (2019). https://doi.org/10.3390/ma12193271
33. M. Afzal, G. Yasmeen, M. Saleem, P.K. Butt, A.K. Khattak, J. Afzal, TG and DTA study of the thermal dehydration of metal-exchanged zeolite-4A samples. J. Therm. Anal. Calorim. **62**, 721–727 (2000). https://doi.org/10.1023/A:1026725509732
34. M.E. Argun, Use of clinoptilolite for the removal of nickel ions from water: kinetics and thermodynamics. J. Hazard. Mater. **150**, 587–595 (2008). https://doi.org/10.1016/j.jhazmat.2007.05.008
35. L.K. Patrylak, I.A. Manza, V.I. Vypirailenko, A.S. Korovitsyna, R.V. Likhnevskii, Study of the mechanism of hexane isomerization under micropulse conditions. Theoret. Exp. Chem. **39**, 263–267 (2003). https://doi.org/10.1023/A:1025729530977
36. V.O. Vasylechko, V.O. Fedorenko, O.M. Gromyko, G.V. Gryshchouk, Y.M. Kalychak, O.A. Zaporozhets, M.T. Lototska, Solid phase extractive preconcentration of silver from aqueous samples and antimicrobial properties of the clinoptilolite-Ag composite. Adsorpt. Sci. Technol. **35**, 602–611 (2017). https://doi.org/10.1177/0263617417703509
37. V.O. Vasylechko, V.O. Fedorenko, O.M. Gromyko, G.V. Gryshchouk, Y.M. Kalychak, S. Tistechol, I. Us, A. Tusyp, A novel solid-phase extraction method for preconcentration of silver and antimicrobial properties of the Na-clinoptilolite-Ag-composite. Mater Today: Proceed. **35**, 548–551 (2021). https://doi.org/10.1016/j.matpr.2019.10.049
38. V.O. Vasylechko, V.O. Fedorenko, O.M. Gromyko, G.V. Gryshchouk, Y.M. Kalychak, S. Tistechol, I. Us, A. Tusyp, Sorption preconcentration of silver for atomic absorption analysis and antibacterial propeerties of the acid-modified clinoptilolite-Ag composite. Methods Objects Chem. Anal. **15**, 73–82 (2020). https://doi.org/10.17721/moca.2020.73-82

Mechanisms of Structural Functionalization of the A-Form of Polyamide-6 with Methylene Blue

V. M. Popruzhko, T. M. Pinchuk-Rugal, O. P. Dmytrenko, A. I. Momot, O. L. Pavlenko, A. I. Misiura, M. A. Alieksandrov, M. P. Kulish, T. O. Busko, and A. P. Onanko

Abstract The study of the crystal structure, electrical conductivity, dynamic mechanical properties, and fluorescence of polyamide-6 (PA-6) systems structurally functionalized with the dye methylene blue (MB) was carried out. Quantum-chemical modeling of PA-6 structure, electronic structure, and vibrational spectra was performed. It is shown that the structural functionalization of PA-6 with the MB dye leads to the rearrangement of the electronic and vibrational structure, the degree of crystallinity, and the mechanical properties, which contributes to the increase of electrical conductivity in the percolation region caused by the strengthening of tunnel transitions.

1 Introduction

Polyamide belongs to a special class of polymers, the monomer link of which includes an amide group –NHCO–. The presence of such groups gives rise to the formation of hydrogen bonds between the nearest macrochains. Such connections contribute to the establishment of various forms of crystalline phases in polyamides. Thus, in PA-6 it is possible to have two types of crystalline forms α- and γ, which are characterized by different crystal structures, stable in low- and high-temperature regions, separated by the Brill transition [1, 2]. Such polymers are characterized by a high degree of crystallinity, which leads to high mechanical properties, including significant strength, chemical, thermal, and ionizing radiation resistance.

The presence of amide groups causes the appearance of amide vibrational modes, the characteristic bands of which in the Raman or neutron scattering spectra undergo rearrangement with increasing temperature and absorption doses due to different crystal states [3–7]. In addition to the specified properties, electro- and photo-physical

V. M. Popruzhko (✉) · T. M. Pinchuk-Rugal · O. P. Dmytrenko · A. I. Momot · O. L. Pavlenko · A. I. Misiura · M. A. Alieksandrov · M. P. Kulish · T. O. Busko · A. P. Onanko
Taras Shevchenko National University of Kyiv, Kyiv, Ukraine
e-mail: vladyslav.popruzhko@gmail.com

O. Fesenko and L. Yatsenko (eds.), *Nanoelectronics, Nanooptics, Nanochemistry and Nanobiotechnology, and Their Applications*, Springer Proceedings in Physics 297,
https://doi.org/10.1007/978-3-031-42708-4_6

characteristics of α- and γ-crystalline forms of PA-6 occupy an important place. Research using terahertz spectroscopy of the absorption of PA-6 at different temperatures in a wide frequency range indicates a change in the behavior of the absorption bands characteristic of different vibrational modes when approaching the Brill transition temperature ($T_{Br} \approx 160$ °C) and the forcing temperature ($T_g \approx 50$ °C). Such a rearrangement of absorption spectra indicates the transformation of crystalline phases and the influence on the molecular vibrations of the surrounding amorphous phase, as a consequence of the non-equilibrium nature of crystalline polymers and the heterogeneity of their structure [8]. The UV absorption spectra for polyamides, including those more complex in structure compared to the structure of PA-6, are very similar to the electronic absorption spectra of organic proteins. They are mainly in the wavelength range of 280–340 nm and are explained by the presence, including peptide bonds and their separate form of hydrogen bonds. For individual polyamides, absorption bands can also be located at longer wavelengths, which are associated with π-π* or n-π* transitions of functional groups C–C, C=O, N–N [9]. No less important for polyamide-6 is the nature of fluorescence in the α- and γ-phases. It is assumed that the recombination mechanism of luminescence is implemented in these polymers. The presence of a peptide bond in PA-6 contributes to the modification of its properties due to the creation of nanocomposites based on it with various nanoparticles, primarily carbon nanotubes [10–16]. In the event of preliminary functionalization of nanotubes and their grafting onto PA-6 macromolecules, it results in a more effective creation of a conductive cluster and consequently elevates percolation electrical conductivity [17, 18].

At the same time, when studying electrical conductivity at the point of contact of filler particles is important. Contact resistance includes not only the Ohm component, but also the fulfillment of the conditions for the tunneling of charge carriers. Improvement of these conditions can be realized by modifying the conductive properties of the polymer matrix, for example, due to the creation of polyene structures in the matrix [19–21]. It can be expected that the structural functionalization of polymers with molecular systems in which delocalized π-electrons are present will also contribute to the improvement of the tunneling conductivity.

The aim of the work is to establish the mechanisms of tunnel conduction in the PA-6 system functionalized with methylene blue.

2 Methodology of the Experiment

To prepare a PA-MB nanocomposite, PA-6 powder (Ukraine) with $\rho = 1.14$ g/cm^3 and methylene blue $C_{16}H_{18}ClN_3S$ powder (Ukraine) with a density of $\rho = 1.0$ g/cm^3 were used. The composites were obtained by hot pressing. The PA powder was mixed thoroughly with the addition of the appropriate amount of the dye. The temperature was 220 °C. PA-MB composites in the form of the disks had a diameter of 30 mm. The concentrations of the dye in the polymer matrix were 0; 0.001; 0.002; 0.007; 0.01;0.015, 0,017 vol. fract.

Crystalline structure of PA-MB nanocomposites has been determined by means of X-ray diffractometer (DRON-3 M) with the usage of monochromatic CuKα ($\lambda =$ 0.154178 nm) irradiation.

Raman spectra and luminescence of MB, PA-6, PA-MB were measured at the room temperature by means of a triple spectrometer (Horbia Jobin Yvon T64000, Japan), provided with a cooled CCD detector. To excite Raman scattering spectra, Ar–Kr ionic laser was used with the wavelength $\lambda = 488$ nm. Excitation of the photoluminescence spectra was performed with He–Cd laser, wavelength $\lambda =$ 325 nm.

For the investigation of the mechanical properties of nanocomposites PA-MB, an ultrasonic KERN-4 computerized velocity meter was used. The dynamic elastic Young's modulus was determined by the formula: $E_{-} = \rho V^2_{\mathrm{l}}$, where ρ is the sample density, V_{l} is the velocity of quasi-longitudinal ultrasonic elastic waves. The dynamic shear modulus was obtained by the formula:

$G_{-} = \rho V^2_{\mathrm{tr}}$, where V_{tr} is the velocity of quasi-transverse ultrasonic elastic waves.

3 Results and Discussion

3.1 Quantum-Chemical Modeling of Electronic and Vibrational Properties of System Molecules PA-6–MB

To determine the electronic structure of PA-6, the monomer and dimer links of the macromolecule, which includes the –NHCO– peptide bond, were chosen. Figure 1 shows the optimized geometry of the specified PA-6 links and the distribution of charges on atoms.

It can be seen that there is a significant redistribution of charges on atoms with the largest values of positive charge ($q = +0.610$e), that is, on the carbon atom included in the peptide bond. On the neighboring N and O atoms, the charges are negative and smaller compared to the C atom (4). The dipole moment for the monomer link is D = 3.383 Debye.

Figure 2 shows the distribution of electronic levels, the shape of molecular orbitals, and their localization in the region of the energy gap for the PA-6 monomer unit. A similar picture applies to the dimer link (Fig. 3).

It can be seen that for the given molecular orbitals HOMO–1, HOMO, LUMO, LUMO+1, their shapes differ significantly. The specified distribution of energy levels and molecular orbitals determines the position and strength of the transition oscillator for the considered energy states, which are shown in Table 1 and Fig. 2.

Figure 4 shows the optimized geometry of the complex PA-MB.

The dipole moment of this complex has increased compared to pure PA and is equal to $D = 4.6$ Debye. Figure 5 shows the distribution of electronic levels, the

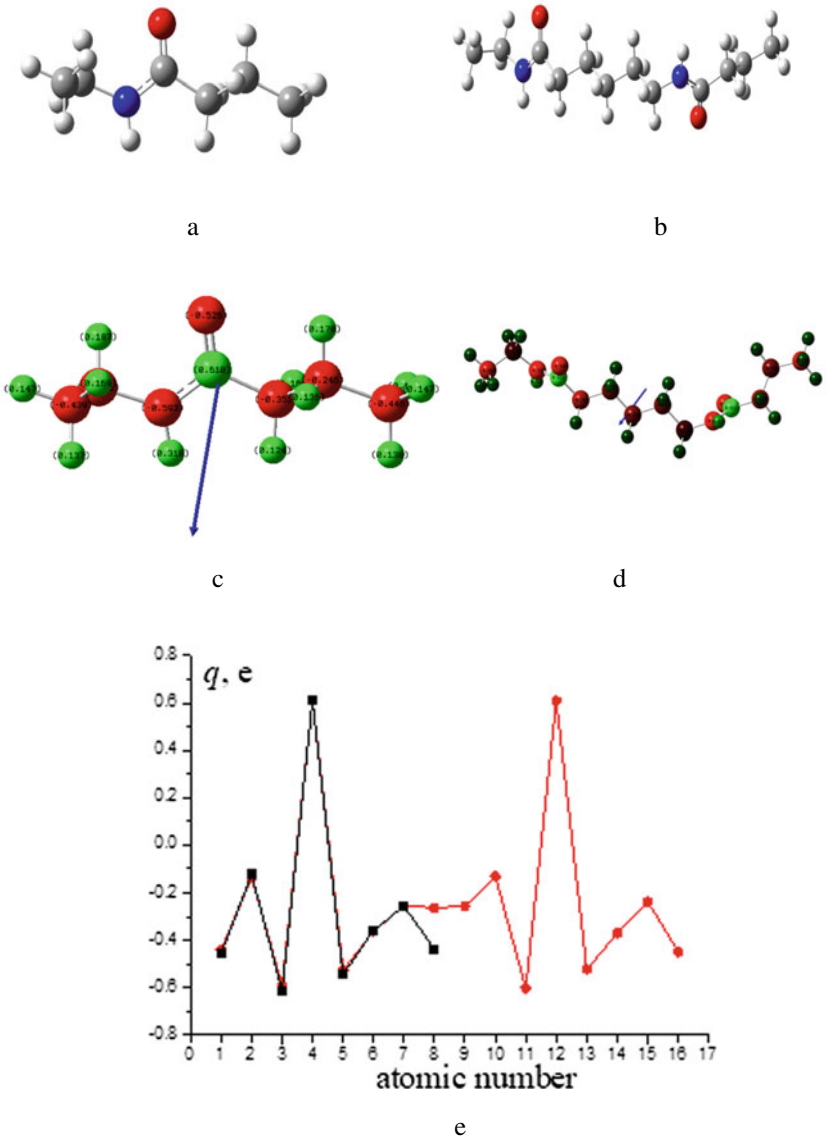

Fig. 1 Optimized geometry of the monomeric (**a**) and dimeric (**b**) links of the PA-6 polymer and charge distribution on the atoms of the monomeric (**c**) and dimeric (**d**, **e**) links. (The magnitude and direction of the dipole moment is shown by the arrow, the distribution of charges q of the monomeric and dimer links on e) is shown by multi-colored curves 1 and 2, the green color of the circles corresponds to the positive charge, and the red one to the negative charge

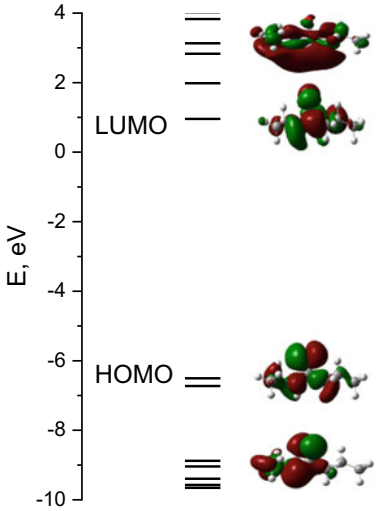

Fig. 2 Distribution of electronic levels, the shape of molecular orbitals, and their localization in the region of the energy gap for the monomer link of PA-6

Table 1 Wavelengths of optical absorption band maxima and oscillator strengths for individual energy transitions in the PA-6 monomer chain

Wavelength, nm	Oscillator power	
172	0.1209	HOMO–1 → LUMO
164	0.0580	HOMO–1 → LUMO + 1
163	0.0502	HOMO → LUMO + 1

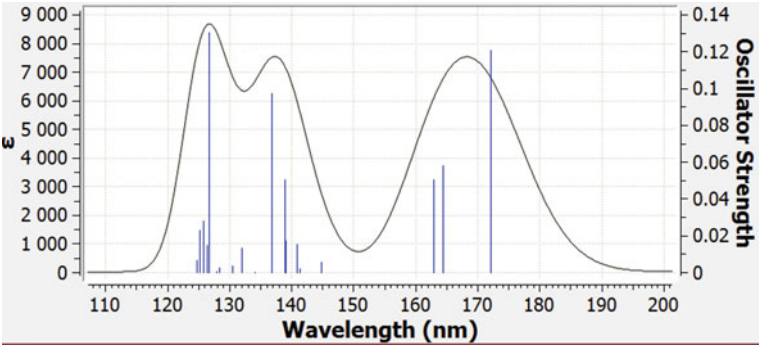

Fig. 3 Optical absorption spectra by the monomer unit of PA-6

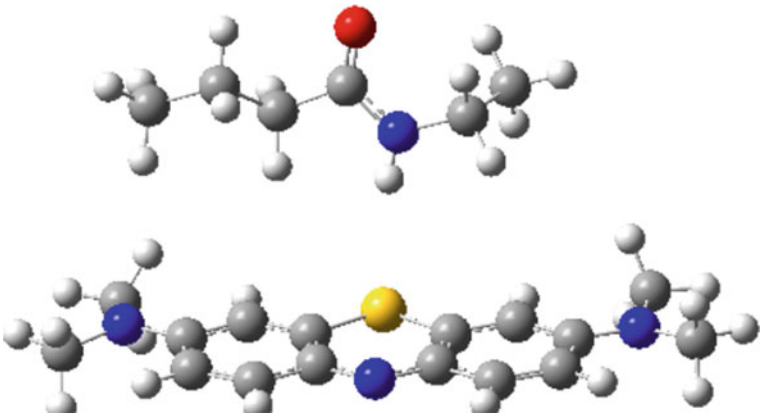

Fig. 4 Optimized geometry of the complex PA-MB

shape of molecular orbitals, and their localization in the region of the energy gap for the polyamide-6, MB, and PA-MB.

The electronic levels of the polymer are at − 6.5 eV for the HOMO and 1 eV for the LUMO, which determine the first electronic transition, which is in the high-energy range and is responsible for the absorption of the polymer in the ultraviolet range. Molecular orbitals belong to the σ type and are strongly bonded, and when forming a complex with a dye, they do not form orbitals localized on both components of

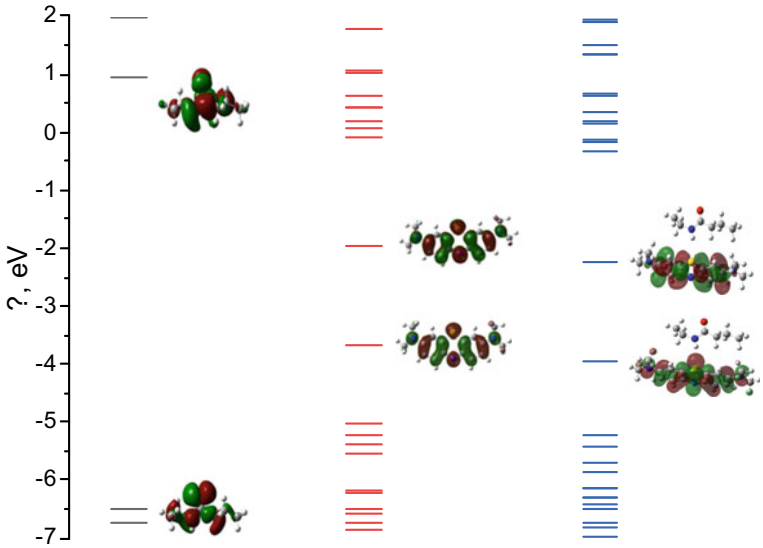

Fig. 5 Distribution of electronic levels, the shape of molecular orbitals and their localization in the region of the energy gap for the polyamide-6, MB, and PA-MB

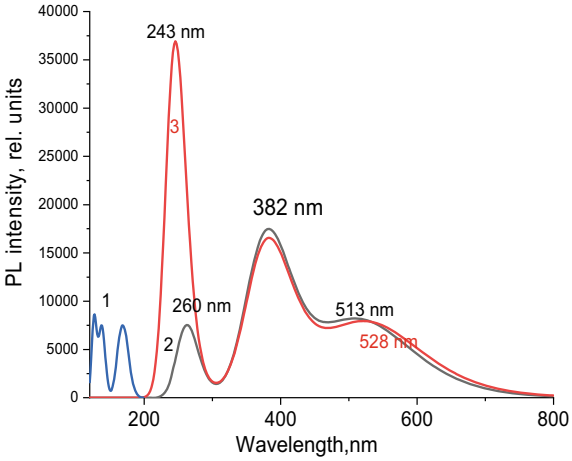

Fig. 6 Optical absorption spectra by the monomer unit of PA-6 (1), MB (2), and PA-MB (3)

the complex. The HOMO and LUMO of the complex are delocalized on the π-conjugated chromophore of the dye, as in the dye itself, and slightly shifted due to the presence of the polymer link.

Figure 6 shows optical absorption spectra by the monomer unit of PA-6 (1), MB (2), PA-MB (3).

The optical absorption spectrum of the polyamide molecule in complex with the dye did not undergo noticeable changes. At the same time, a restructuring of the optical absorption spectrum of MB is observed. There is a shift to the ultraviolet region of the band from 260 to 243. The intensity of this band has increased compared to other bands of the dye. The optical absorption band for MB in the complex shifted from the position of the maximum to the long-wavelength region from 513 to 528 nm. Thus, in the complex, the main changes in optical absorption occur for MB, which can lead to a more significant delocalization of the available π electrons.

Computer modeling of Raman spectra for polymers using the Gaussian software package is generally incorrect, as it requires to be limited to individual molecules. It is convenient to choose monomer links with such molecules for the polymer. As the number of such monomer units in the molecule increases, their conformation changes, which affect the behavior of Raman spectra. Taking into account not only the presence of the zigzag-trans configuration of the molecular structure, but also the rearrangement of the linear conformation to the conformation in the form of a bend of the molecular chain shows for several links of polyamide-6 (PA-6) a better agreement between the calculated and experimentally obtained frequencies of vibrational modes. This result appears despite the fact that the equilibrium value of conformations in the form of a bent molecule is very small. It can be assumed that in reality the number of such molecules due to the existence of periodic boundary conditions in a solid polymer is actually significant. However, an increase in the length of the polymer chains does not lead to the appearance of new, clearly expressed

vibrational modes, but only a broadening of the bands obtained at shorter lengths of the polymer chain.

Figure 7 shows optimized geometry of the molecule $(C_6H_{11}NO)_1$ corresponding to one PA-6 monomer chain.

In Fig. 8, the structure of the mentioned monomeric link near the peptide bond is shown.

It can be seen that the zigzag-trans configuration is preserved in all considered molecules, the conformation gradually changes from a linear to a bent chain.

In Fig. 9, the calculated Raman spectrum of $(C_6H_{11}NO)_1$ molecules is presented.

The intensive bands appear in the frequency range of 1250–1700 cm^{-1} and near 3000 and 3500 cm^{-1}. For each of the conformations of the molecules, the band frequencies correspond to certain values, that is, the vibrational modes are shifted. Frequencies shifts for valence vibrations of methylene groups CH_2 near 3000 cm^{-1} and amino group NH near 3500 cm^{-1} are especially noticeable.

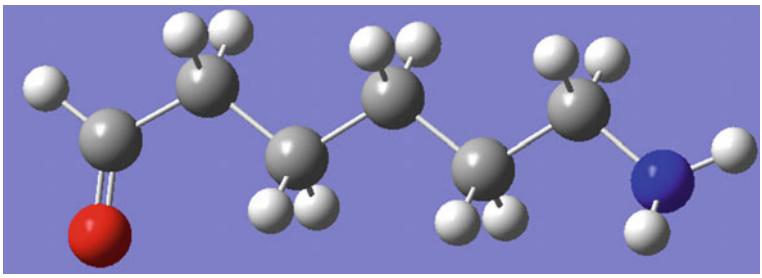

Fig. 7 Optimized geometry of the molecule $(C_6H_{11}NO)_1$ corresponding to one PA-6 monomer chain

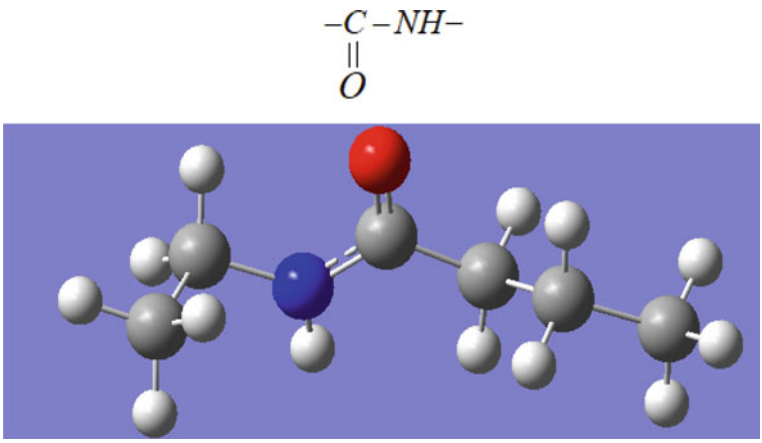

Fig. 8 Optimized geometry of the $(C_6\,H_{11}\,NO)_1$ molecule, which corresponds to the length of one PA-6 monomer link near the peptide bond

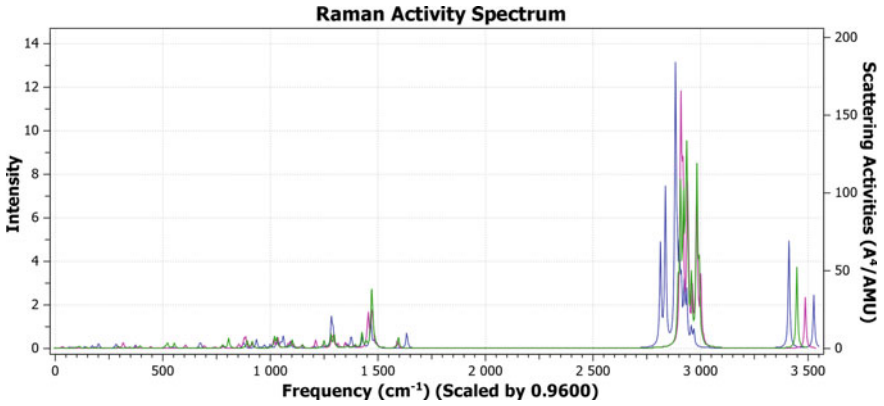

Fig. 9 Calculated Raman spectra of molecules $(C_6H_{11}NO)_1$, respectively, whose optimized geometry corresponds to a linear conformation

3.2 Optical Properties of MB

MB belongs to heterocyclic aromatic compounds containing a thiazine ring. The structure of this dye facilitates its use in microbiological medicine, including for the purpose of diagnosing diseases. Along with its effective use as a therapeutic agent, MB leads to a number of adverse consequences. Equally important is the use of this dye to solve photophysical and optoelectric problems, as well as when doping polymers to ensure polariton (bipolariton) conductivity [22].

Figure 10 shows the spectrum of the optical density for a solution in water of MB with a concentration of $c = 1.6 \times 10^{-4}$ mol/l.

It can be noted that the spectrum of the optical density of MB is quite complex and includes a set of bands with maxima at different wavelengths. The highest value of the optical density corresponds to the long-wave band with a maximum near 608 nm. This band is wide enough and can be decomposed into three components, the maxima of which are located at 623, 587, and 568 nm. The last bands belong to the component whose maxima are located at 623, 587, and 568 nm. The last bands belong to the monomer, dimer, and trimer phases. A complex fluorescence spectrum (FL) also occurs for the solution in water and films, Fig. 11.

As for the optical density spectrum, a set of bands is observed in the PL spectrum. Thus, in addition to the shortest broad band for the solution in water and films, a number of narrow bands appear. At the same time, the intensity of narrow bands for solutions exceeds the radiation intensity of the short-wave band, but for films, on the contrary, their intensity is less noticeable against the background of the main short-wave band, i.e., the PL in the long-wave range undergoes quenching. It should be noted that for films there is also a shift to the long-wave region of the wavelength of the optical density maximum.

Figure 12 shows the Raman spectrum for MB powder.

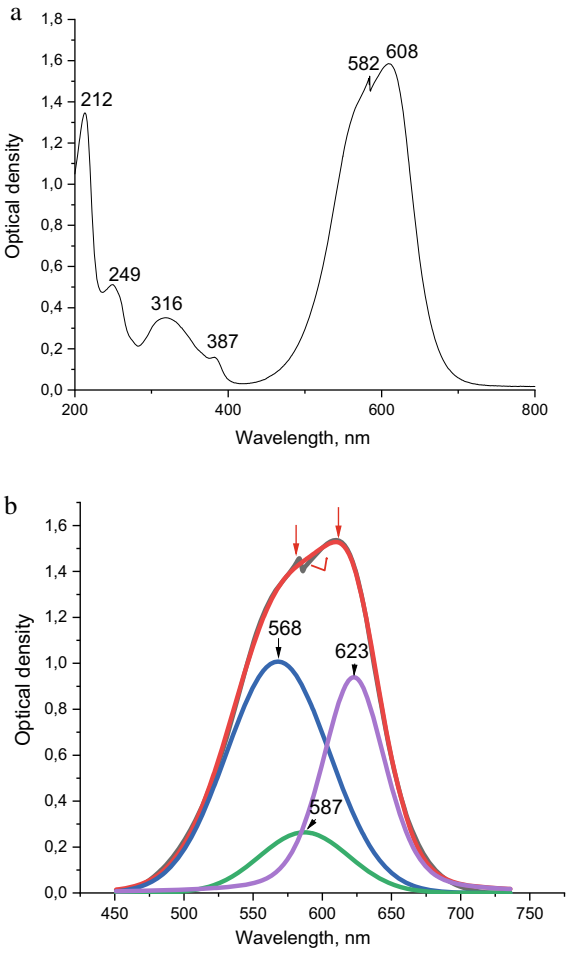

Fig. 10 Spectra of the optical density of a solution of methylene blue in water with a concentration of $c = 1.6 \times 10^{-4}$ mol/l in the wavelength ranges of 200–800 nm (**a**) and 450–750 nm (**b**). The additional bands show the breakdown of the spectrum into three components; the numbers indicate the positions of the band maxima

The spectrum of Raman scattering of the MB is in good agreement with the analytical spectra [36] and is characterized by the invisibility of a set of bands corresponding to the set of vibrational modes characteristic of the MB. Such modes include deformation vibrations of the C–N–C group (480 cm^{-1}), bending vibrations ω out of the plane of the C–H groups (659 cm^{-1}), bending vibrations ω in the plane of the C–H groups (1168 cm^{-1}), symmetric stretching vibrations νs of the C–N groups (1394 cm^{-1}), asymmetric stretching vibrations νas of C–N groups (1453 cm^{-1}), symmetric stretching vibrations of the ring of C–C groups ν (1616 cm^{-1}).

Such spectra are important not only for the detection of MB, but also for establishing its binding mechanisms in molecular systems.

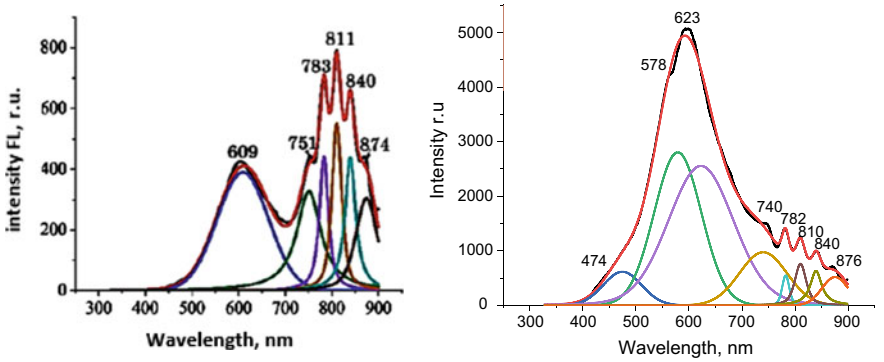

Fig. 11 Fluorescence spectrum of a methylene blue solution in water with a concentration of $c = 1.6 \times 10^{-4}$ mol/l (**a**) and a thin film (**b**). The substrate of the film is glass, film thickness **d** = 200 nm, $\lambda_{ex} = 325$ nm, additional lines are components of the decomposition

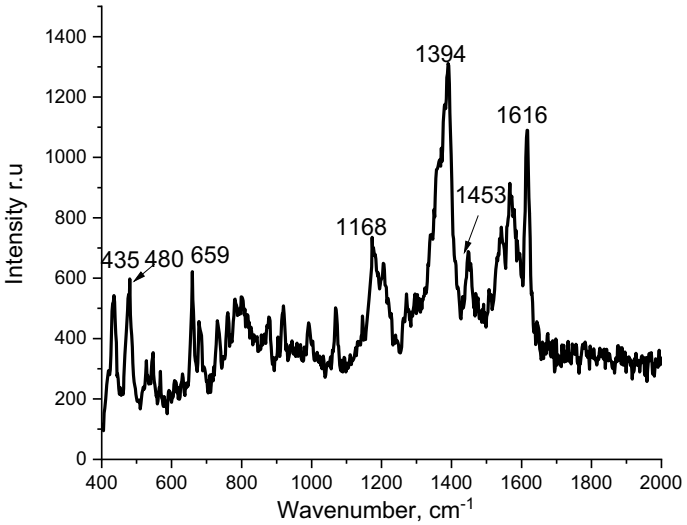

Fig. 12 Raman spectrum for methylene blue powder ($\lambda_{ex} = 532$ nm)

3.3 Physical Properties of PA-6

Depending on the thermal conditions of production of PA-6 samples, different forms of the crystal structure are formed, which significantly affect the properties of this polymer. The presence of these forms is manifested in the X-ray diffraction patterns characteristic of the corresponding syngonias. In the range of diffraction angles 2θ up to 40°, the α-form of the crystal structure manifests itself in the form of two more

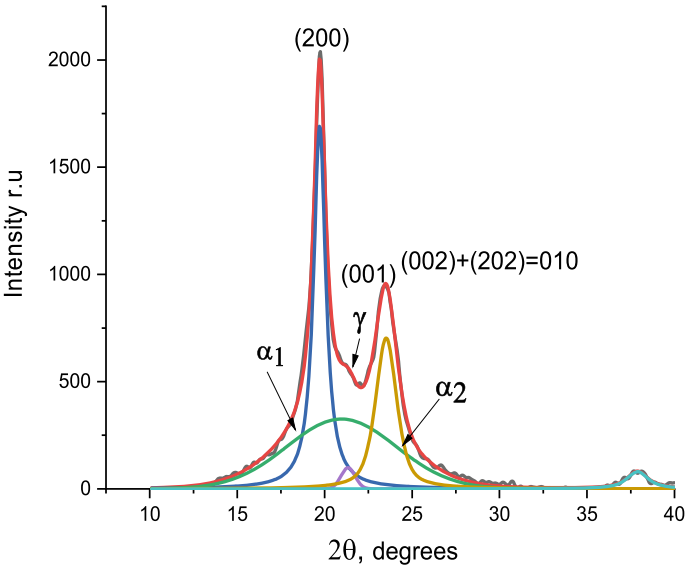

Fig. 13 X-ray diffraction image of a bulk sample of polyamide-6 ($\lambda_{cu} = 0.54$ nm, $T = 293$°K)

intense peaks (200) and (002) + (202) = 010 and one peak (001) of the γ-form of the monoclinic syngonia crystal form.

Figure 13 shows the diffraction pattern of X-rays for a bulk sample of polyamide-6 that underwent the previously indicated thermomechanical treatment.

It can be seen that α-phase with peak positions (200) near $2\theta 1 = 20°$ and peak (010) near $2\theta 2 = 23.5°$ is mainly formed in the sample. At the same time, a (001) peak is observed near $2\theta 3 = 21°$, which corresponds to the γ-crystal structure. The lattice parameters of the α-crystal structure corresponding to monoclinic syngonia are $a = 8.32$A, $b = 9.60$A, $c = 17.2$A, $\beta = 65°$. The specified parameters agree well with the known values of these characteristics of the α-phase crystal lattice [1, 2]. It is known that the structure of the α-phase can be represented in the form of sheets lying in the plane of vectors $\vec{b} \times \vec{c}$. These sheets are formed between chains due to hydrogen bonds generated by peptide groups. The distance between adjacent sheets is smaller than between adjacent chains, which leads to the asymmetry of the lattice structure ($a \neq b$). The structure of γ-crystals consists of twisted chains, which are also connected to each other by hydrogen bonds. At the same time, the parameters of the hook $\vec{a}_i \vec{b}$ are close to each other. It is worth noting that the characteristic features of α- and γ-phases are not only X-ray diffraction images, but also absorption spectra in the terahertz range. Thus, the α-phase is characterized by two bands near 3.2 and 8.7 THz with high absorption and a number of less intense bands. In the case of the γ-phase, two broad absorption bands appear near 3.2 and 9.3 THz [8].

From the diffraction pattern, in addition to the lines belonging to the α- and γ-phases, the presence of a halo caused by the presence of an amorphous phase can be seen. The calculated degree of crystallinity is æ = 55.3%. It can be expected

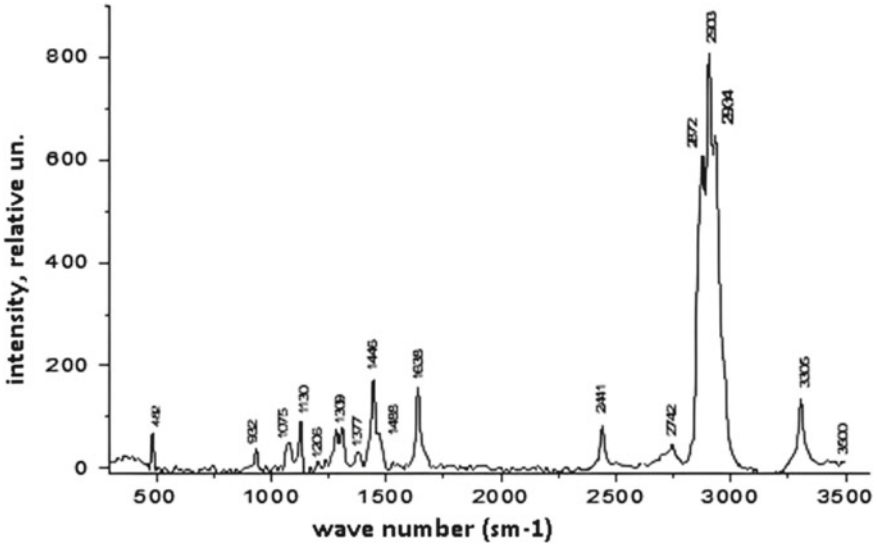

Fig. 14 Raman scattering spectrum for a bulk PA-6 sample ($\lambda_{ex} = 514$ nm, $T = 293$°K)

that in case of PA-6 polymer doping, the degree of crystallinity of its α-phase will vary depending on the content of the modifier. In the case of the formation of bonds between polymer chains and the modifier material, it is possible to rearrange not only the electronic structure of PA-6, but also its vibrational spectra caused by Raman scattering.

Figure 14 shows the Raman spectrum for a bulk sample of PA-6.

The Raman spectrum of PA-6 includes a set of bands of different intensities corresponding to vibrational modes of different types. This spectrum is in good agreement with the Raman light scattering spectra given earlier [8]. Thus, in the interval from 580 to 630 cm^{-1} there is a broad low-intensity band corresponding to the vibrational modes of amide VI (g N–H), amide IV (d C=O). A band appears near 932 cm^{-1} due to C–CO stretching. In the spectrum, there are more intense bands near 1075 cm^{-1}, 1130 cm^{-1}, which are characteristic of vibrational C–C stretching modes. Less intense bands in the interval between the 1130 and 1309 cm^{-1} bands are associated with fan (N–H), amide III, torsional (CH_2) vibrational modes. A weakly intense band near 1377 cm^{-1} and a strongly intense band near 1446 cm^{-1} are observed, which are associated with fan-like and bending vibrations of the CH_2 methylene group. The band near 1638 cm^{-1} corresponds to the vibrational mode of amide I (n C=O). The set of bands near 2872, 2903, 2934 cm^{-1} are associated with symmetric and antisymmetric stretching in CH_2 methylene groups. The band near 3305 cm^{-1} is also intense for PA-6, which is caused by valence vibrations of the functional group of the polyamide N–H bond. The features of the structure of PA-6, which are manifested in the vibrational spectra, are also consistent with the Raman calculations when taking into account only a few monomer units in the PA-6

model. Thus, despite the differences in the frequency values of the Raman spectrum calculated for the molecule of the monomer unit $(C_6H_{11}NO)_1$ and the experimental results of Raman spectroscopy, for both cases three regions of the spectrum are clearly observed. It can be seen that the calculation reveals a band characteristic of valence vibrations of N–H. The shift of this band toward higher frequencies, in comparison with the experimental wave number ($\nu = 3305$ cm^{-1}), depends on the placement of the peptide bond. In the second region near 3000 cm^{-1}, a set of bands corresponding to valence vibrations of the CH_2 methylene group appears. The position of these bands also depends on the choice of placement of the peptide bond. The calculated spectra also include bands for vibrational modes of amides. At the same time, the displacement of these bands in comparison with their positions for the experimental spectra is insignificant. The placement of the bands for other vibrational modes, for example, for the bending vibrations of the methylene group CH_2 (1446 cm^{-1}), agrees satisfactorily. There are no bands near 2441 and 2742 cm^{-1} in the theoretical spectrum, as they do not belong to functional vibrational modes. Thus, the model representation of PA-6 by choosing only the monomeric link is quite satisfactory for the interpretation of the vibrational modes characteristic of the polymer. The calculated spectra become even more pronounced and more accurate in comparison with the experimental Raman when several monomer units are selected for modeling, taking into account their confirmation changes.

The uniqueness of the structure of the crystalline phases and the presence of peptide bonds in the PA-6 macromolecule are accompanied by important photophysical properties. It turned out that upon excitation of PA-6 samples with α- and γ-forms of the crystal structure by laser radiation with a wavelength of $\lambda = 267$ nm, photoluminescence (PL) spectra appear. The shapes of the spectra and the positions of the maxima of the PL bands for each of the crystal forms are significantly different. Thus, for the PA-6 sample with the α-form, a main band with a maximum near 340 nm and an extended long-wave tail appear. In the case of the sample with the γ-form of the crystalline phase, a broad PL band appears with a maximum in the visible region of 500 nm.

Another feature of PL was the presence of afterglow. For the α-form, the indicated fluorescence with a time delay is observed at room temperature and is absent for the sample with the γ-form of the crystal structure. Moreover, as the excitation wavelength increases from $\lambda_{ex} = 300$ nm to $\lambda_{ex} = 312$ nm, the PL band shifts from a position near 340 nm to a maximum near 390 nm. In the case of the sample with the γ-form of the crystalline phase, as λ increases, there is a sequential shift of the maximum of the PL band.

Afterglow is also characterized by temperature dependence. The analysis of the results of the PL and afterglow spectra indicates that the afterglow occurs as a result of the recombination of photo-induced charges with an almost continuous distribution of energy accumulated on the traps after excitation. Excitation relaxation occurs as a result of recombination of trapped electrons with holes. Under conditions of low mobility of electrons and holes localized on the traps due to their capture, fluorescence occurs with a time delay and PL bands shift when the excitation wavelength λ_{ex} changes. In PA-6 with different forms of the crystalline phase, the energy distribution

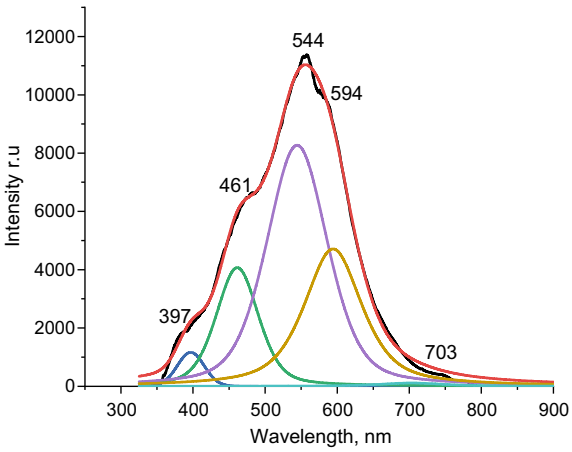

Fig. 15 Fluorescence spectrum for a bulk sample of PA-6 with the α- form of the crystalline phase (λ_{ex} = 325 nm, T = 293ºK; separate strips-components of the schedule)

of the traps is different, which leads to different manifestations of the PL and afterluminescence spectra [23, 24].

In Fig. 15, the PL spectrum for the α-form of PA-6 is shown.

The PL band for PA-6 with the α-form of the crystal structure is quite complex. For its spectrum, several components with maxima near 397, 461, 554, and 594 nm can be distinguished. If we follow the recombination model of photoinduced charges, it can be assumed that for this sample there is a certain set of traps in which electrons and holes captured by them are localized. In these traps, at room temperature, there is an accumulation of charges located at certain energy levels. Recombination between electrons and holes localized on the traps is accompanied by emission, which leads to a complex PL spectrum. The concentration of traps corresponding to certain energy states differs significantly. It can be noted that the highest intensity of recombination of charge carriers corresponds to a wavelength of 554 nm. At the same time, traps of various nature also take an active part in recombination processes. It can be assumed that the nature of shallower and deeper traps is connected with defects in the crystal lattice, including complexes of point defects, which are largely determined by the conditions of preparation of PA-6 samples.

3.4 Physical Properties of the PA-MB

When considering the physical properties of polymer composites using polyamides, the type of polyamide and filler are important. The creation of nanocomposites with improved conductive properties is mainly considered. Among polyamides, aromatic polyamides are of interest. Thus, when investigating the electrical conductivity of a polymer nanocomposite containing graphene fillers based on fluorine-substituted aromatic polyamide (polyamide-24). In this polymer, there is a conjugated system consisting of two benzene rings in a chain, which are connected to each other by a

peptide bond –CO–NN–. In a separate case, it can be assumed that the π-electrons of the carbonyl group of the C=O peptide bond and the lone pair of electrons of the amide group HH of the same bond can together with the π-electrons of the benzene rings form a common conjugated system. In the general case, this does not happen, because the flexibility of these polyamides is caused by rotations around N–Ph and C–Ph bonds, despite the absence of rotation around C–N bonds. For this reason, polyamides consisting of benzene rings separated by peptide bonds remain dielectrics, since a homogeneous collective π-electron system is not formed. At the same time, the possibility of interaction of the π-system of polyamide fragments, including the CO–NN peptide group and conjugated dopant fragments, is not excluded. It is known that π-electron systems are able to approach at a distance of 0.34 nm. Thus, when choosing a dopant for the polyamide-24 graphene polymer matrix, the occurrence of a stack interaction is noted, which is accompanied by a shift in the energy levels of the model structures of the polymer and graphene. At the same time, higher molecular orbitals HOMO–3 and LUMO+2 take part in the delocalization of π-electrons, unlike the boundary molecular orbitals HOMO and LUMO. The width of the energy gap in the polyamide-24–graphene system drops to 4.4 eV compared to the value of 6 eV for the polymer, which is explained by the appearance of the aforementioned stacking interaction. Thus, with the doping of the polymer with graphene, the energy barrier decreases. The appearance of π-electron bridges created by graphene between monomer units of polyamide, which occurs as a result of the appearance of stack interaction between π-systems of polymer fragments and graphene, leads to an increase in the electrical conductivity of the polymer [25].

The structure of PA-6 lacks phenolic rings corresponding to π-conjugated systems. At the same time, the presence of polyamide groups under the condition of structural functionalization of PA-6 with the dopant methylene blue, the structure of which includes several benzene rings, can also contribute to the appearance of stack interaction between individual fragments of the polymer matrix and the dopant. This interaction can be facilitated by the existing hydrogen bond, as well as cross-linking between fragments of chains that include CH_2 methylene groups. The presence of these interactions can enhance the tunneling interchain and intrachain transfer of charges and, as a result, increase the electrical conductivity of the doped MB polymer matrix.

In Fig. 16, the dependence of electrical conductivity of PA-6 on the content of MB is shown.

It can be seen that the electrical conductivity of pure PA-6 with the α-form of the crystal structure is $\sigma \approx$ 10–12.7 S/cm. With the doping of the MB polymer at low dopant concentrations, an increase in the value of σ to a value of ≈10–11.9 S/cm is observed, i.e., the increase in electrical conductivity reaches about one order of magnitude. At higher concentrations, the influence of the dopant is almost absent. It can be assumed that the yield of the concentration dependence on saturation is due to the aggregation of dopant molecules. At lower MB concentrations, there is an increase in tunnel transitions in the polymer matrix, due to the occurrence of, among other things, stacking interaction, which induces the creation of new conduction channels due to the dopant.

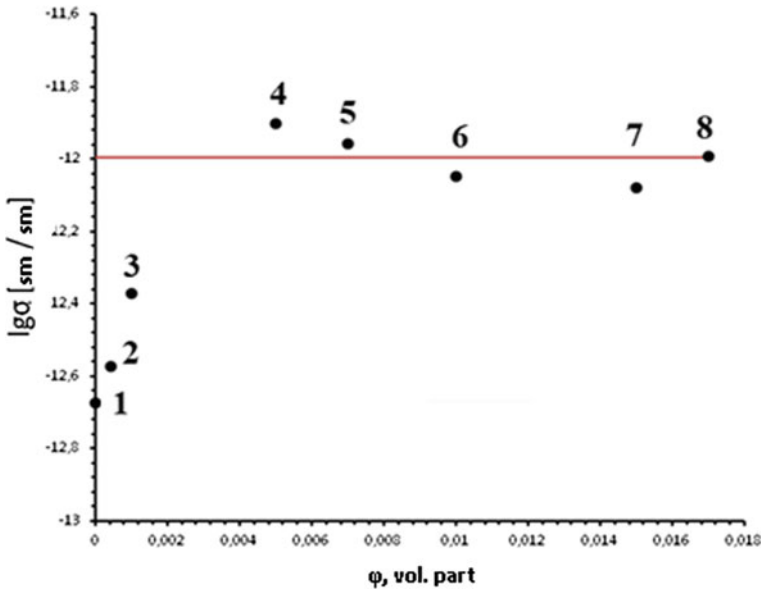

Fig. 16 Dependence of electrical conductivity (in a logarithmic scale) of bulk PA-6 with the α-form of the crystalline phase on the concentration of MB 0 (1), 0.001 (2), 0.002 (3), 0.005 (4), 0.007 (5), 0.01 (6), 0.015 (7), 0.017 vol. part (8) ($T = 293$°K)

It can be expected that the appearance of a stacking interaction caused by π-electrons will lead to the rearrangement of the electronic structure and, as a consequence, to the transformation of PL spectra. The PL bands obtained for bulk polymer PA-6 with different MB content are shown in Fig. 17.

When the MB dopant concentration is increased, the PL spectra are rearranged in a complex way, which indicates the energy rearrangement of the traps, which are transformed due to the influence of the MB on the internal and interchain interactions of PA-6 macromolecules. A noticeable rearrangement of the PL spectrum occurs already at a low concentration of MB (0.001 vol. part). If for pure PA-6 the components of the PL bands were concentrated in the short-wavelength region, then in the doped polymer the maximum of the main band changes from 544 nm for pure PA-6 to 446 nm for the doped polymer. Inflections near 530 and 595 nm are concentrated on the long-wave tail of the band.

The addition of 0.002 and 0.005 vol. parts of MB with changes in the relative intensity of the components has little effect on the spectral behavior of the PL band. The position of the maximum of the main PL band varies from 446 nm (0.001 vol. part) to 455 nm (0.002 vol. part) and 451 nm (0.005 vol. part. MB). At higher MS concentrations, the PL spectra undergo further transformation, which indicates the rearrangement of the electronic structure of PA-6, which affects the behavior of electrical conductivity. At the same time, not only the change in the electronic structure due to the interaction of PA-6 and MB is responsible for the behavior of

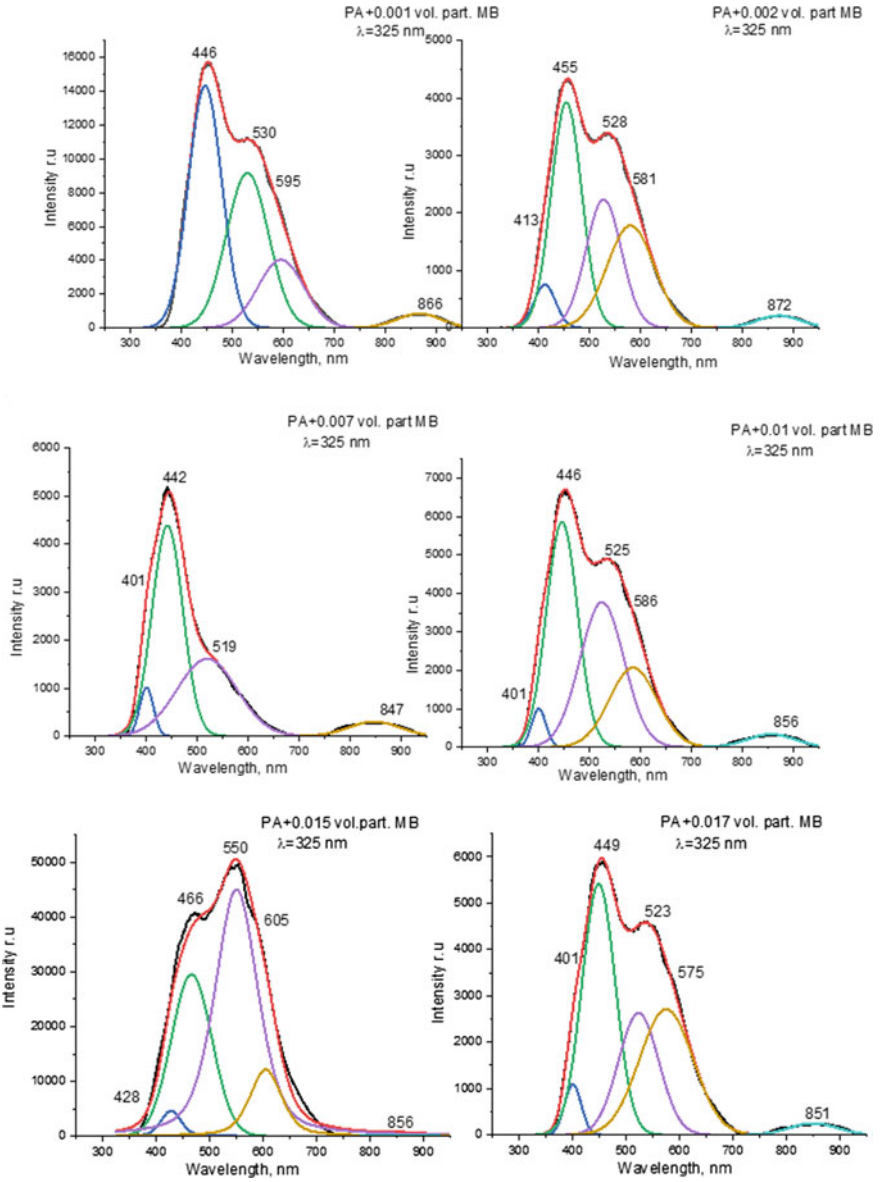

Fig. 17 PL spectra for bulk PA-6 with an α-crystalline structure functionalized by MS with concentrations of 0.001 (**a**), 0.002 (**b**), 0.005 (**c**), 0.007 (**d**), 0.01 (**e**), 0.015 (**f**), 0.017 vol. part. (h) (λ_{ex} = 325 nm, $T = 293$°K)

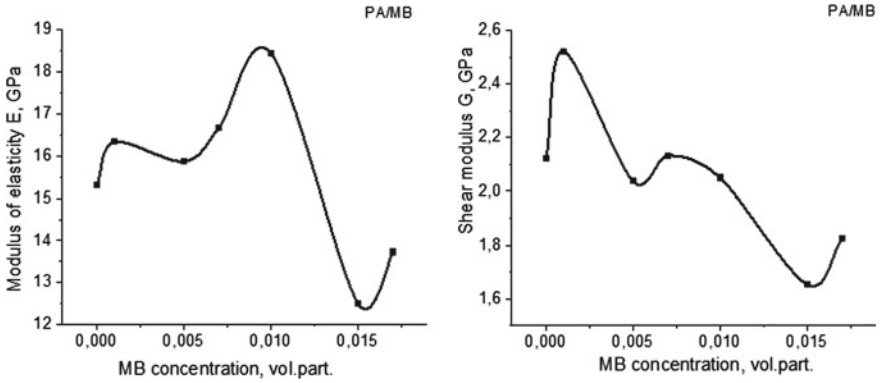

Fig. 18 Dependence of the dynamic moduli of elasticity E (**a**) and shear G (**b**) of polyamide-6 with the α-form of the crystalline phase, which is structurally functionalized with the dopant methylene blue with a concentration of 0, 0.001, 0.002, 0.005, 0.007, 0.01, 0.015, 0.017 vol. part (load frequency ν 1 MHz and at $T = 293$°K)

electrical conductivity. It can be assumed that the doping of PA-6 with methylene blue can affect the crystal structure of the polymer and the electronic structure, the defect structure and, as a result, the formation of traps and their energy distribution, as well as the mechanical properties.

Figure 18 shows the behavior of the dynamic modulus of elasticity (E) and shear (G) of polyamide-6 with an increase in the concentration of MB in the polymer matrix at a loading frequency of ~ 1 MHz.

A complex behavior of the dynamic modulus of elasticity (E) and shear (G) is observed when the content of the methylene blue dopant in the polyamide-6 polymer matrix with an α-crystalline phase increases. At the same time, for both modules, two concentration intervals can be noted in which the behavior of the mechanical properties changes. Thus, the modulus of elasticity increases to a concentration of $\phi = 0.010$ vol. MB, and with further increase in the dopant content, its value decreases. Similarly, the shear modulus increases up to a concentration of $\phi = 0.002$ vol., and with a further increase in the MB concentration, its value also begins to decrease. It can be assumed that the indicated moduli changes occur as a result of the influence of the dopant on the crystalline structure of PA-6. With increasing MB content, at low concentrations, the dopant plays the role of crystal phase nucleation centers, which leads to improved mechanical characteristics. With a further increase in the MB content, it plays a degrading role, possibly due to the disruption of hydrogen bonds and the formation of a defective structure with an increase in the number of traps for charge carriers. At high MB concentrations, the moduli of doped PA-6 have lower values than for the pure polymer.

Thus, MB dopant molecules have a complex effect on the electronic and crystalline structure of PA-6, which, on the one hand, improves electrical conductivity due to the occurrence of stacking interaction, which contributes to the tunneling of charge

carriers in the matrix, and on the other hand, can worsen the degree of crystallinity with the generation of structure defects, which act as charge traps.

4 Conclusion

Quantum-chemical modeling of the structure, distribution of charges, distribution of electronic levels, shape of molecular orbitals, their localization, and electronic transitions indicates the complex nature of the electronic structure, shape and localization of molecular orbitals, which leads to an optical absorption spectrum with several bands located in the UV region for the monomer unit of polyamide-6.

The vibrational spectrum of Raman scattering for one or more monomer units has almost the same appearance and is only shifted in frequency. It reflects the presence of all vibrational modes characteristic of the experimental spectrum of Raman scattering of light.

When PA-6 is doped with methylene blue, the electronic structure and vibrational spectra of the PA-6–MB system undergo changes, primarily due to a decrease in the energy gap.

The obtained X-ray pattern for the PA-6 bulk sample indicates that it mainly consists of the α-crystalline phase of monocrystalline syngonia with a degree of crystallinity of æ = 55.3%

Excitation at $\lambda_{ex} = 325$ nm of a bulk sample of polyamide-6 leads to a PL band with a maximum near 544 nm and inflections, the occurrence of which can be explained by the recombination of electrons localized in traps and holes arising in the α-phase due to structural defects and, possibly, the presence of, complexes of point charges. When PA-6 is doped with methylene blue with different concentrations, the spectra of the PL band are rearranged as a result of the stacking interaction between individual fragments of the structure of PA-6 and MB. Such an interaction affects the processes of recombination of charge carriers captured by traps.

As a result of the structural functionalization of PA-6 with a dopant, there is an increase with a transition to saturation of electrical conductivity with an increase in the MC content. Such an increase in electrical conductivity is associated with the appearance of bridges for the intra-interchain transfer of π-electrons when a stacking interaction occurs between fragments of the π-systems of PA-6 and MB.

The change in electrical conductivity also depends on the degree of the crystal structure and its defectiveness, which, on the one hand, affects the change in the electronic structure during the structural functionalization of PA-6 with a dopant, and on the other hand, leads to a complex dependence of the dynamic modulus of elasticity and shear on the content of the methylene blue dopant in the polymer matrix.

References

1. S. Ellahi, R.E. Hester, K.P.J. Williams, Waveguide resonance Raman spectroscopy of degraded PVC. Spectrochim. Acta Part A Mol. Biomol. Spectrosc. **51**(4), 549–553 (1995)
2. D.R. Holmes, C.W. Bunn, D.J. Smith, The crystal structure of polycaproamide: Nylon. J. Polym. Sci. **17**(84), 159–177 (1955)
3. P. Papanek, J.E. Fischer, N.S. Murthy, Low-frequency amide modes in different hydrogen-bonded forms of nylon-6 studied by inelastic neutron scattering and density-functional calculations. Macromolecules **35**, 4175–4182 (2022)
4. C. Menchaca, L. Rejón, A. Alvarez-Castillo, M. Apátiga, V.M. Castaño, Structural analysis of crystalline nylon 6,12 exposed to gamma radiation. Inter. J. Polymer. Mater. **48**, 135–143 (2000)
5. C. Menchaca, A. Alvarez-Castillo, H. López-Valdivia, H. Carrasco, H. Lara, P. Bosch, V.M. Castaño, Radiation-induced morphological changes in polyamide fibers. Inter. J. Polymer. Mater. **51**(9), 769–781 (2002)
6. C. Menchaca, A.Alvarez-Castillo, G. Martinez-Barrera, H. Lopez-Valdivia, H. Carrasco, V.M. Castano, Mechanisms for the modification of nylon 6,12 by gamma irradiation. Int. J. Mater Product Technol. **19**(6), 521–529 (2003)
7. C. Menchacaa, B. Manouna, G. Martínez-Barrerac , V.M. Castañod , H. López-Valdiviae, In situ high-temperature Raman study of crystalline nylon 6,12 fibers gamma-irradiated in argon atmosphere. J. Phys. Chem. Solids. **67**, 2111–2118 (2006)
8. H. Suzuki, S. Ishii, C. Otani, H. Hoshina, Low-frequency vibrations of polyamide-6 as a function of temperature and thermal history investigated by terahertz absorption spectroscopy. Eur. Polym. J. **67**, 284–291 (2015)
9. P.J. Hendra, W.F. Maddams, I.A.M. Royaud, H.A. Willis, V. Zichy, The application of Fourier transform Raman spectroscopy to the identification and characterization of polyamides—I. Single number nylons. **47,** 747–756 (1990)
10. O. Meinckea, D. Kaempfera, H. Weickmanna, C. Friedricha, M. Vathauerb, H. Warth, Mechanical properties and electrical conductivity of carbon-nanotube filled polyamide-6 and its blends with acrylonitrile/butadiene/styrene. Polymer **45**, 739–748 (2004)
11. P.V. Kodgire, A.R. Bhattacharyya, S. Bose, N. Gupta, A.R. Kulkarni, A. Misra, Control of multiwall carbon nanotubes dispersion in polyamide6 matrix: an assessment through electrical conductivity. Chem. Phys. Lett. **432**, 480–485 (2006)
12. B. Krause, P. Pötschke, L. Häußler, Influence of small scale melt mixing conditions on electrical resistivity of carbon nanotube-polyamide composites. Compos. Sci. Technol. **69**, 1505–1515 (2009)
13. H. Deng, T. Skipa, R. Zhang, D. Lellinger, E. Bilotti, I. Alig, T. Peijs, Effect of melting and crystallization on the conductive network in conductive polymer composites. Polymer **50**, 3747–3754 (2009)
14. P. Liu, Modifications of carbon nanotubes with polymers. Eur. Polym. J. **41**, 2693–2703 (2005)
15. S. Lučić Blagojević, N. Šorgo, Z. Buhin Šturlić, Influence of carbon nanotubes on polyamide properties. Chem. Biochem. Eng. Q. **33**(3), 337–346 (2019)
16. A. Šehić, J. Vasiljević, A. Demšar, M. Leskovšek, V. Bukošek, J. Medved, M. Čolović, I. Jerman, B. Simonci, Polyamide 6 composite fibers with incorporated mixtures of melamine cyanurate, carbon nanotubes, and carbon black. J. Appl. Polym. Sci. **136**(5), 47007 (2018)
17. S. Huang, T. Liu, W.-D. Zhang, W.C. Tjiu, C. Hec, X. Lud, Grafting polyamide 6 onto multi-walled carbon nanotubes using microwave irradiation. Polym. Int. **59**, 1346–1349 (2010)
18. G. Gorrasi, S. Bredeau, C. Di Candia, G. Patimo, S. De Pasquale, P. Dubois, Electroconductive polyamide 6/MWNT nanocomposites: effect of nanotube surface-coating by in situ catalyzed polymerization. Macromol. Mater. Eng. **296**, 408–413 (2011)
19. T.M. Pinchuk-Rugal, O.P. Dmytrenko, M.P. Kulish, O.S. Nychyporenko, Yu.Ye. Grabovskyy, V.V. Strelchuk, A.S. Nikolenko, M.I. Shut, V.V. Shlapatska, Structure and electronic properties of nanocomposites of polyvinylchloride with carbon nanotubes under an irradiation. Nanosyst. Nanomater. Mamotechnol. **13**(2), 325–336 (2015)

20. T.M. Pinchuk-Rugal, O.P. Dmytrenko, M.P. Kulish, Yu. I. Prylutskyy, O.S. Nychyporenko, M.I. Shut, V.M. Tkach, V.V. Shlapatska, The electron radiation effect on polyvinylchloride (PVC) nanocomposites with multiwalled carbon nanotubes, in *Proceedings in Physics*, vol. 195 (Springer, 2017), pp. 757–770
21. T.M. Pinchuk-Rugal, O.P. Dmytrenko, M.P. Kulish, M.A. Alieksandrov, O.L. Pavlenko, A.P. Onanko, Yu.E. Grabovskiy, V.V. Strelchuk, O.F. Kolomys, Mechanisms of stack interaction in polymer composites of polyvinylchloride with methylene blue, in *Proceedings in Physics*, vol. 247 (Springer, 2021), pp. 245–254
22. H.M. Zidan, N.A. El-Ghamaz, A.M. Abdelghany, A. Lotfy, Structural and electrical properties of PVA/PVP blend doped with methylene blue dye. Int. J. Electrochem. Sci. **11**, 9041–9056 (2016)
23. M.V. Vasnetsov, V.V. Ponevchinsky, A.A. Mitryaev, D.O. Plutenko, Observation of room-temperature afterglow in polyamide-6 under UV excitation. SPQEO **22**, 333–337 (2019)
24. M.V. Vasnetsov, V.V. Ponevchinsky, D.O. Plutenko, G.V. Klishevich, A.A. Mitryaev, O.I. Gudymenko, V.P. Kladko, Luminescence peculiarities of polyamide-6 α and γ forms. Appl. Phys. B **127**, 53 (2021)
25. A.D. Kachkovsky, E.L. Pavlenko, E.V. Sheludko, N.P. Kulish, O.P. Dmitrenko, V.A. Sendyuk, P.S. Smertenko, V.V. Kremenitsky, O.P. Tarasyuk, S.P. Rogalsky, Composite 'graphene nanoplatelets-fluorine-containing polyamide': synthesis, properties and quantum-chemical simulation of electroconductivity. Funct. Mater. **26**, 100–106 (2019)

Self-sealing Properties of Phospholipid Membranes After Interactions with Various Nanostructures—MD Study

Przemyslaw Raczynski, Krzysztof Gorny, and Zbigniew Dendzik

Abstract Over the last decades, significant amount of research has been devoted to the search of better nanostructures for targeted delivery of the cargo to the interior of the cell. One of the considered methods is to deliver substances via phospholipid bilayer, the natural barrier protecting the interior of the cell from the outside environment. However, the real danger of this solution is possibility of the damage to the bilayer on the scale that will lead to the death of the cell. Taking into account this extremely undesirable scenario, in this work we analyze the self-sealing abilities of the phospholipid bilayer after indentation with various nanostructures, such as nanotubes, graphene sheets, and nanospears. Using Molecular Dynamics simulations, we have modeled the withdrawal part of the indentation process when the nanostructure is removed from the bilayer. The membrane damage remaining after indentation and the time required for the lipids can level it are analyzed and discussed. Phospholipid bilayer exhibits unexpectedly high abilities to self-seal. The results presented here may be helpful to assess the optimal type, size, and rate of the indenter to avoid the permanent damage of the phospholipid membrane.

1 Introduction

Phospholipid bilayer is a thin polar membrane forming a continuous barrier surrounding cells. Membrane proteins are embedded in the bilayer. This provides efficient cell protection and communication with outside environment. The bilayers are usually composed of two layers of amphiphilic phospholipids that have a hydrophilic phosphate head and hydrophobic tail consisting of two fatty acid chains. Cholesterol molecules located between phospholipids control the fluidity of the membrane [1, 2].

Nowadays, much attention is paid on the targeted cargo delivery, the method to deliver drugs, to the interior of the cell encapsulated inside some nanocarriers [3–5]. The broadest examined candidates are nanotubes because of their potential to reduce

P. Raczynski (✉) · K. Gorny · Z. Dendzik
Faculty of Science and Technology, University of Silesia in Katowice, 41-500 Chorzów, Poland
e-mail: przemyslaw.raczynski@us.edu.pl

O. Fesenko and L. Yatsenko (eds.), *Nanoelectronics, Nanooptics, Nanochemistry and Nanobiotechnology, and Their Applications*, Springer Proceedings in Physics 297,
https://doi.org/10.1007/978-3-031-42708-4_7

the side effects of some drugs, for example, highly toxic anticancer medicines [6–9]. Some drugs were successfully inserted into carbon nanotubes in the water environment [10]. Not only homogeneous, but also heterogeneous nanotubes are examined as due to their partially ionic character they provide higher reactivity which might be helpful to facilitate aimed sidewall functionalization [11, 12]. Besides nanotubes, graphene sheets are also examined. Graphene has been used in mechanical resonators [13] or as a functional material in water purification [14]. Graphene chemical properties are quite promising [15, 16]. Also nanospears are taken into account as they are recognized as nanostructures that could mechanically disrupt the cell membranes without causing irreversible membrane damage to cells [17].

In this paper, we examine self-sealing ability of the phospholipid bilayer during withdrawal process by analyzing average force, deflection experienced by membrane, changes in the density profile, and assessing the number of molecules permanently removed from the membrane. In extreme harmful cases also the membrane structural configuration was analyzed after piercing process (without withdrawal). Apart from various nanostructures, we have also assess the impact of nanostructures movement rate on the damage caused during withdrawal as well as their size.

Our studies were performed by means of computer simulations. It is increasingly popular and wide used approach and was successfully applied to investigate a wide range of biologically important phenomena [18–21]. Taking into consideration the complexity of the systems studied and required computational power, only the classical Molecular Dynamics (MD) technique can be applied.

Below, we describe the research methodology and extraordinarily high degree to which the phospholipid bilayer can fix the significant damages to its structure.

2 Materials and Methods

Steered Molecular Dynamics [22, 23] simulations were performed using the NAMD application with the all atom–atom CHARMM force field [24–26]. The applied structure of the phospholipid bilayer consists of 232 1,2-dimyristoyl-sn-glycero-3-phosphocholines (DMPC) and 48 cholesterols [1]. Models for phospholipid and cholesterol molecules, as well as atomic charges for membrane lipids were taken from [27]. All simulations were performed at the physiological temperature $T = 310$ K and in aqueous environment. TIP3P [28] model of water, implemented in NAMD, was used. All simulations were repeated five times, and all results presented here are of the averages of independent simulation runs. Thanks to repetition of the simulated systems, sufficient sampling of the configuration space was achieved. Time step was equal to 0.5 fs.

Periodic boundary conditions were applied for all studied systems. The size of the PBC box was equal, approximately, to 100×85 Å along x and y axis, respectively. Size of the box along z axis differs because it depends on the length of the indenter.

Initial configurations of all systems studied were obtained from a series of NPT simulations. During this stage the pressure (set to 1 atm) was controlled using

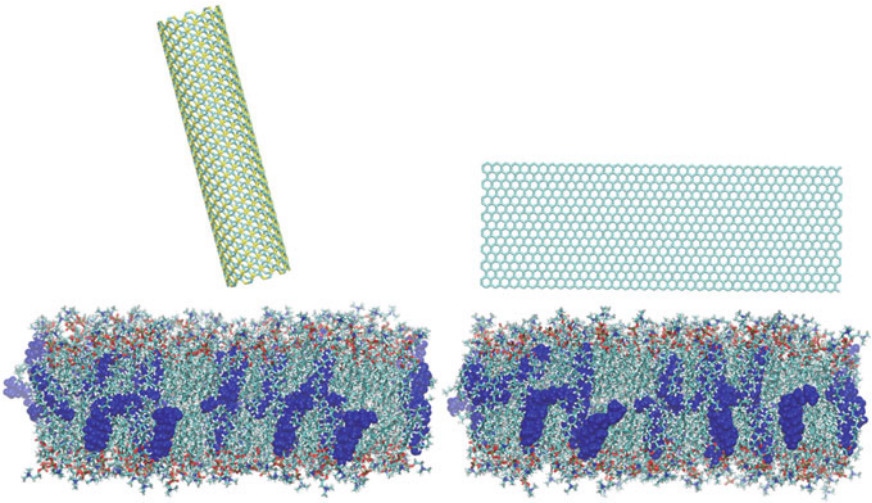

Fig. 1 Initial configurations of the systems with SiCNT (left) and graphene sheet (right)

Langevin barostat implemented in NAMD. This part of simulation was set to 1 ns for each system studied. Next, the systems were equilibrated in NVT ensemble for the same time. During minimization stage the nanostructures were kept about 8 Å above the bilayer. Two examples of configuration after equilibration and for the systems with SiCNT (silicon–carbide nanotube) and graphene are shown in Fig. 1.

After equilibration process, the main simulations were started, and the nanostructures were move with the rate ranging from 0.5 up to 2.5 m/s perpendicularly to the membrane, toward it, until the bilayer was fully pierced. After piercing stage, the nanostructures were pulled out of the membrane, and the damage as well as time required for self-improvement of the membrane was assessed.

The nanostructures used in our simulations are.

- (15 15) carbon nanotube (CNT), not titled away from z axis
- (10, 10) silicon–carbide nanotube (SiCNT), titled away from the z axis by an angle equal to 15^{o}
- 96 Å width and 32 Å high graphene plane (width of graphene and PBC box are similar), not titled, in plane perpendicular to the membrane
- silicon nanospear with the largest diameter equal to 21.7 Å.

The results presented in the next section for CNT, SiCNT, and nanospear are for the narrow section of the membrane. The reason is to capture the key changes in the membrane structure in calculations. The fragment used in calculation of bending of the membrane and its density profile is illustrated in Fig. 2.

Moreover, in case of density profile plots, the 60-point seventh degree polynomial fit is shown to better visualize the changes in the phospholipid bilayer density.

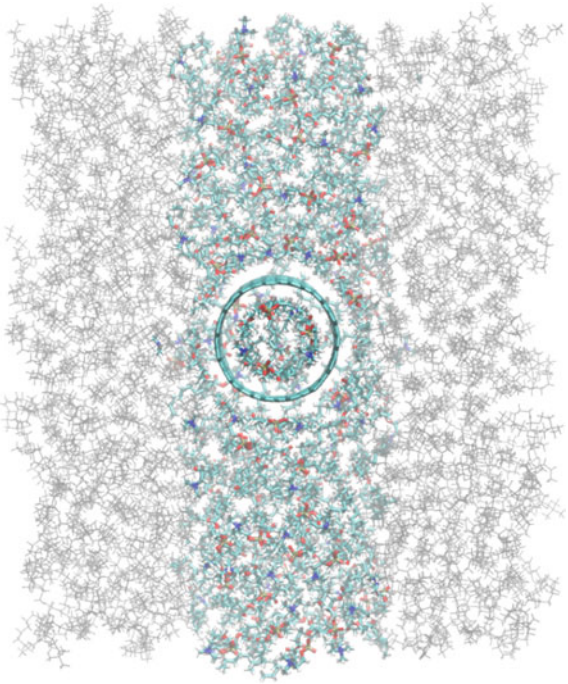

Fig. 2 Illustration of the molecules which were taken to density profile and average dislocation calculations (colored). Gray molecules were not included during calculations of these quantities

3 Results and Discussion

Figure 3 shows average density profile for membrane lipids (phospholipid and cholesterol molecules) for two pulling out rates, 0.5 and 2.5 m/s. All density profiles discussed in this work were calculated for one of the axis (x or y) that lies in the plane of the membrane. The curves presented in Fig. 3 are for the system with CNT. Four positions of nanostructure tip were taken into account—when the nanostructure tip is between phospholipids carbon chains of the upper layer (black line), when it is between phospholipids glycerol backbones (red line), when it leaves the membrane (blue line), and when it is about 13 Å above the membrane (dark cyan line). The same coloring convention is used in subsequent figures (Figs. 4 and 5). In calculations of the density profiles of the membrane, for the systems with CNT and SiCNT, molecules located inside nanotubes were excluded to avoid the distortion of the results caused by lipids which are no longer part of the membrane.

For both rates studied, the plots of the density profile are similar. When the nanotube is deeply immersed in the membrane, the value of the density profile plot is the highest on the sides (about − 40 and 40 Å) and the smallest in the middle. When the nanotube is pulled out of the membrane these changes diminish. This suggests that membrane lipids systematically occupy the free volume which is created by the removed nanotube. This process is quite efficient, the difference in plots when the nanotube edge is in the membrane (black and red curves) and when it is between

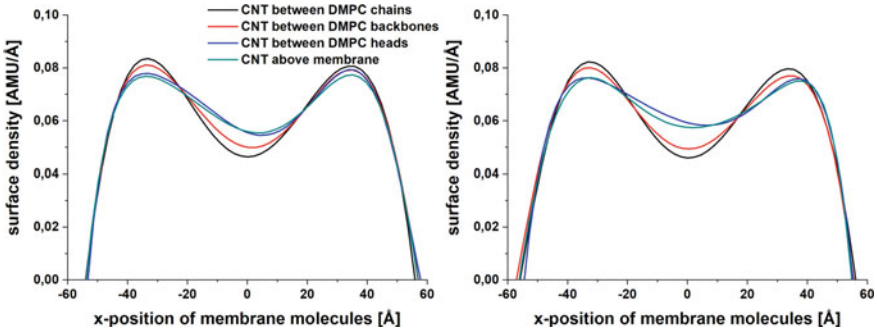

Fig. 3 Average density profile for phospholipid and cholesterol molecules, for systems with CNT and for fast (left) and low (right) withdrawal rates

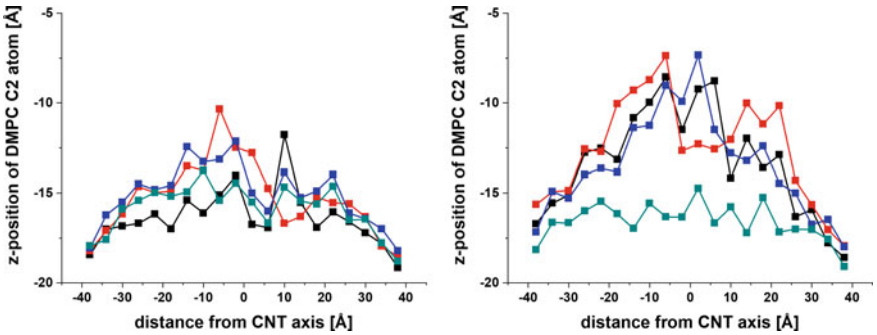

Fig. 4 Average dislocation of DMPC C2 atoms, for systems with CNT and for fast (left) and small (right) withdrawal rates

loose phospholipid heads or outside of the membrane (blue and dark cyan curves) can be clearly observed. For the system with inserted nanotube (black curve) and with lower withdrawal rate, the average difference between maximal and minimal values of density profile is 0.036 AMU/Å, whereas for the position of the CNT about 13 Å above the membrane (dark cyan) it is two times smaller (0.019 AMU/ Å). This clearly shows that the system tries to mitigate the changes caused by removing the nanotube, lipids are more evenly distributed and the volume freed by the pulled out nanotube is occupied by phospholipids or cholesterols. The time required for this process is only 7.7 ns (time CNT needs to travel with the small rate from the position represented by black line to the position represented by dark cyan line). This confirms that the self-sealing process is fast and efficient. One can notice the differences in the minimal values of density profile (dark cyan curves) for high (0.055 AMU/Å) and low (0.057 AMU/Å) withdrawal rates. These differences can suggest that in case of higher rate the self-sealing process of the membrane is slower; however, it is only the result of different rate at which the volume is released by the nanotube. The higher rate means that the CNT edge quicker reaches the position 13 Å above

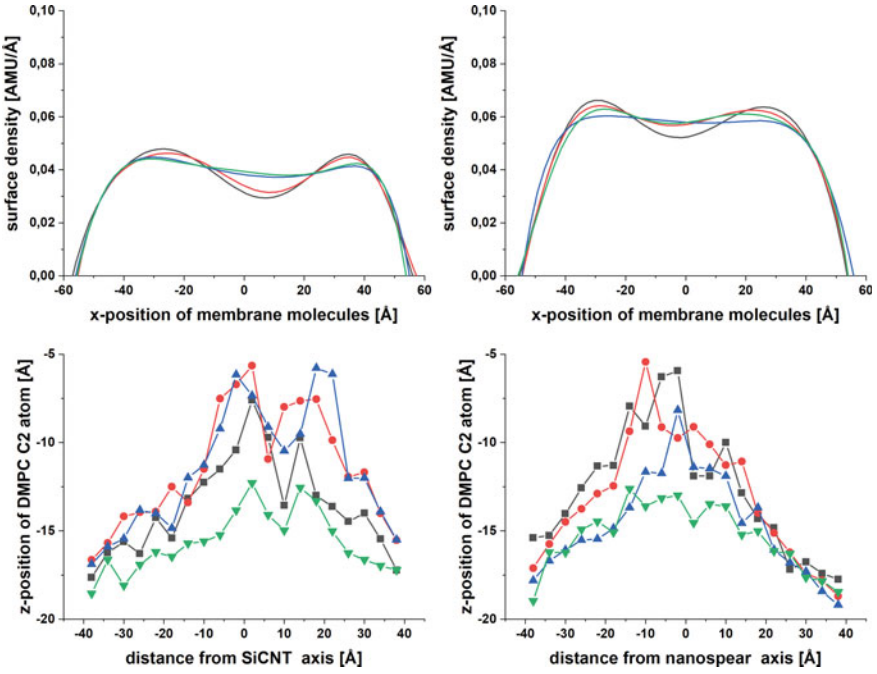

Fig. 5 Average surface density profile (top layer) and average dislocations of DMPC C2 atoms (bottom layer) for SiCNT (left) and nanospear (right)

the membrane, represented by dark cyan curve, but the difference between minimal values of the density profile for high and small rate is only 0.002 AMU/Å.

During withdrawal process, CNT pulls up the membrane. The largest dislocation is experienced by the lipids closest to the nanotube. It can be seen from Fig. 4, where average dislocation of C2 phospholipid atoms from the upper layer of the membrane, for high (left) and small (right) rate, is shown.

Lipids in the systems where nanotube is moved with small rate are dislocated to the higher degree as they are able to accommodate changes caused by the movement of the nanotube. However, for both withdrawal speeds, when the nanotube leaves the membrane, dislocation caused by CNT is compensated quickly—dark cyan curves is quite flat, indicating, that membrane is able to relax to the configuration before the indentation. For the low speed studied it takes about 2.7 ns (time CNT needs to travel from the z-position of about 0 Å—blue curve, when the CNT tip leaves phospholipid heads—and $z = 13$ Å, when the nanotube tip is not in contact with the membrane—dark cyan curve). The membrane for the fast withdrawal rate is less balanced finally, because the time needed to travel the distance about 13 Å is shorted in case of higher speed.

The top plots in Fig. 5 show the changes in density profile for the silicon–carbide and nanospear (left and right panels, respectively). Only the low indentation rate is included in Fig. 5 as from the above discussion of the results it can be concluded that

there are not significant changes between the slow and fast withdrawal rate and the changes caused by faster moving nanostructure are less pronounced.

The SiCNT withdrawal process is similar to the CNT case. The membrane quickly reverses the changes caused by SiCNT, and after it leaves the membrane, the phospholipids efficiently fill the gap left by nanotube. A bit different character of density profile plots occurs in case of nanospear (Fig. 5 top, right panel) as there is no sudden change as in case of nanotube, where the diameter is constant all along the nanostructure length. In case of the nanoneedle diameter slowly and steadily decreases to zero. As a result the volume freed by the nanostructure withdrawal is decreasing during the process, allowing the phospholipids to rearrange faster than in case of the nanotube, this is reflected by the very similar plots of red, blue, and dark cyan curves.

As in case on CNT, also SiCNT and nanospear pull the membrane lipids up, however to the larger scale, what can be seen in maximal values of DMPC C2 atoms dislocation. In this context, the carbon nanotube with the relatively large diameter of about 20 Å diameter is less invasive than silicon–carbide nanotube with the diameter 16.6 Å and the nanospear with the largest diameter 21.7 Å.

Table 1 shows the number of molecules which were permanently removed from the membrane during first indentation and next, withdrawal processes.

The silicon–carbide nanotubes seems to be the most destructive nanostructure in this case. However, more interesting is number of molecules located on the outer surface of nanostructures because, taking into account idea of the use nanostructures for the drug delivery, the interior of them will be filled. Taking into consideration the number of molecules located on nanostructure outer surfaces and removed from the membrane, the conclusion is, that the damages caused by each nanostructure used are negligible. The model of the membrane consists of 280 molecules. The highest number of molecules removed from the membrane during single simulation run was 2, that means less 0.7% of the total number of molecules forming the membrane. The nanoindentation of the phospholipid bilayer with various nanotubes or their derivatives has also been studied [7, 29–34], although the main focus of the mentioned research concentrated on mechanical properties of the bilayers and force and work required for membrane piercing and not the withdrawal process.

Table 1 Average number of lipids removed from membrane during indentation and withdrawal processes. In the last column, first number represents number of molecules that were able to enter to the nanostructure inner cavity, and second number represents the number of molecules on the nanostructure outer surface

Nanostructure	Rate	Number of removed inside/outside
CNT	High	1/0
CNT	Low	5/0
SiCNT	High	5.2/0
SiCNT	Low	7.2/0.4
Nanospear	High	0/0
Nanospear	Low	0/0.4

The self-sealing abilities of phospholipid bilayer discussed above are promising but what in case of large scale damages? Fig. 1 (right panel) shows that the graphene sheet has the same width as a membrane (after taking into account size of PBC box). This means that during indentation process whole membrane was cut by graphene. Moreover, virtual springs used in SMD method were added to the furthest from membrane graphene atoms (top row in Fig. 1 right). This procedure made piercing the membrane very difficult and many attempts failed because graphene has rotated before it reached the membrane, and instead of pushing graphene, it was pulled. However, some simulation runs were successful, and the membrane was damaged significantly as shown in Fig. 6, where the next stages of example of ruined bilayer simulation run are shown. Details concerning the force and work required to insert the graphene sheets of different size are presented in our previous work [35]. In this work, we will concentrate only on the process of membrane recuperation and on the situation in which the graphene surface rotated inside the membrane, causing further damage to its structure.

The initial system is shown in Fig. 1, right panel. From the next instantaneous configurations presented in Fig. 6 one can see that graphene sheet had started to pierce membrane, next it rotated inside bilayer and only then left the membrane. Described above cutting process created water channel along the cut. In the places where the water channel was relatively narrow, and lipids were able to interact with each other despite the water presence, the self-sealing process started. Figure 7, left panel, shows the changes in the density profile initially, after 10, 20, and 30 ns of simulation.

It is clear that distribution of lipids becomes more uniform with time. Moreover, by visual observations we have noticed, that after 30 ns of simulation runs (in one case of only five nanoseconds) water was completely removed from the membrane, and in three cases only minor water channels were observed inside the membrane. In the case of one system, water channel was still large, suggesting that the membrane was not able to quickly reverse the damage caused by cutting with graphene layer. The configuration of the membrane for the same system as shown in Fig. 6, after self-sealing process, is shown in Fig. 7, right panel. From this figure one can see, that

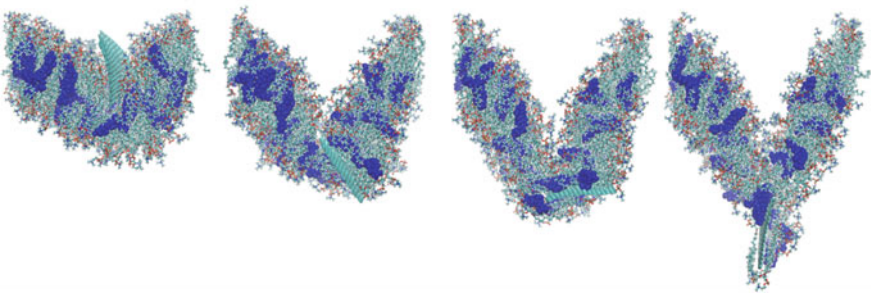

Fig. 6 Next stages of indentation of the bilayer by 92 × 32 Å graphene plane. The rate of indenter is equal to 2 m/s. Water molecules are not shown for clarity of the picture

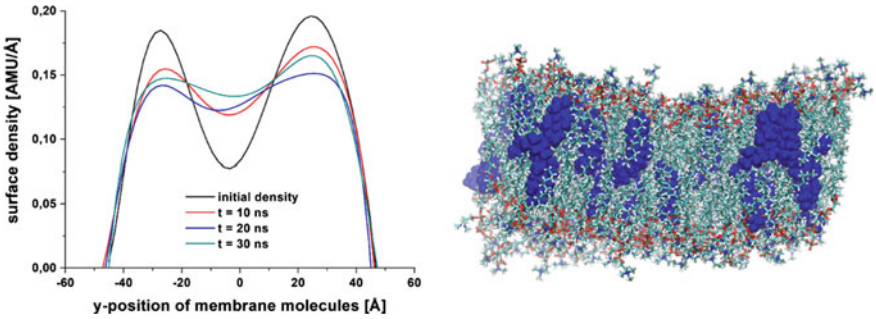

Fig. 7 Average surface density profile during membrane self-sealing process after huge damage—right. The example of final configuration of the membrane after self-sealing process preceded by huge damage of the membrane—left

membrane is still deflected but in the scale incomparably smaller than that is shown in the last panel of Fig. 6. During indentation process analyzed bilayer (shown in Figs. 6 and 7, right panel) lost 8.6% of lipids, (they were permanently removed by the graphene). Despite this and the size of water channel which was assessed to be, on average, 76 × 14 Å, membrane was able to regain continuity what was confirmed by density profile and visual inspection of simulation configurations.

4 Conclusions

Membrane ability to self-seal is remarkably high. It was confirmed by two aspects of our simulations. When the CNT, SiCNT, or nanospear was removed from the membrane, it was distorted in small scale, and self-sealing process takes from a few to several nanoseconds. During this time the distribution of lipids becomes regular and the membrane compensate pulling up effect regardless of the withdrawal rate. However, it seems that the higher speed of indenter during withdrawal is more advantageous because membrane around nanostructure experiences smaller dislocation, and smaller number of molecules were permanently removed from the membrane.

Membrane is also able to patch definitely larger damages. This process takes significantly longer time but thanks to long hydrophobic tails phospholipids are able to exclude the water molecules from the interior of the membrane.

Our simulations examine the interactions between phospholipid bilayer and various nanostructures at the atomic scale level. It can be helpful in further research on the use of the nanostructures as containers to deliver cargo to the interior of the cell.

References

1. B. Alberts, *Molecular Biology of the Cell* (Garland Science, New York, 2008)
2. N. Sperelakis, *Cell Physiology Sourcebook Essentials of Membrane Biophysics* (Elsevier/AP, Amsterdam, Boston, 2012)
3. D. Losic, S. Simovic, Self-ordered nanopore and nanotube platforms for drug delivery applications. Expert Opin. Drug. Deliv. **6**, 1363–1381 (2009). https://doi.org/10.1517/17425240903300857
4. A.A. Bhirde, V. Patel, J. Gavard, G. Zhang, A.A. Sousa, A. Masedunskas, R.D. Leapman, R. Weigert, J.S. Gutkind, J.F. Rusling, Targeted killing of cancer cells in vivo and in vitro with EGF-directed carbon nanotube-based drug delivery. ACS Nano **3**, 307–316 (2009). https://doi.org/10.1021/nn800551s
5. E. Heister, V. Neves, C. Lamprecht, S.R.P. Silva, H.M. Coley, J. McFadden, Drug loading, dispersion stability, and therapeutic efficacy in targeted drug delivery with carbon nanotubes. Carbon **50**, 622–632 (2012). https://doi.org/10.1016/j.carbon.2011.08.074
6. S.K. Vashist, D. Zheng, G. Pastorin, K. Al-Rubeaan, J.H.T. Luong, F.-S. Sheu, Delivery of drugs and biomolecules using carbon nanotubes. Carbon **49**, 4077–4097 (2011). https://doi.org/10.1016/j.carbon.2011.05.049
7. P. Raczynski, K. Gorny, V. Raczynska, M. Pabiszczak, Z. Dendzik, Z. Gburski, On the impact of nanotube diameter on biomembrane indentation—computer simulations study. Biochim. Biophys. Acta-Biomembr. **1860**, 310–318 (2018). https://doi.org/10.1016/j.bbamem.2017.10.030
8. T.A. Hilder, J.M. Hill, Modelling the encapsulation of the anticancer drug cisplatin into carbon nanotubes. Nanotechnology **18**, 275704 (2007). https://doi.org/10.1088/0957-4484/18/27/275704
9. T.A. Hilder, J.M. Hill, Probability of encapsulation of paclitaxel and doxorubicin into carbon nanotubes. Micro Nano Lett. **3**, 41–49 (2008). https://doi.org/10.1049/mnl:20080008
10. Y.-C. Liu, Q. Wang, Dynamic behaviors on zadaxin getting into carbon nanotubes. J. Chem. Phys. **126**, 124901 (2007). https://doi.org/10.1063/1.2714517
11. A. Mavrandonakis, G.E. Froudakis, M. Schnell, M. Mühlhäuser, From pure carbon to silicon−carbon nanotubes: an Ab-initio study. Nano Lett. **3**, 1481–1484 (2003). https://doi.org/10.1021/nl0343250
12. M. Menon, E. Richter, A. Mavrandonakis, G. Froudakis, A.N. Andriotis, Structure and stability of SiC nanotubes. Phys. Rev. B **69**, 115322 (2004). https://doi.org/10.1103/PhysRevB.69.115322
13. A. Sharma, U. Varshney, Y. Lu, Electronic applications of graphene mechanical resonators. IET Circ. Devices Syst. **9**, 413–419 (2015). https://doi.org/10.1049/iet-cds.2015.0134
14. L. Meng, Y. Sun, H. Gong, P. Wang, W. Qiao, L. Gan, L. Xu, Research progress of the application of graphene-based materials in the treatment of water pollutants. Carbon **153**, 804–804 (2019). https://doi.org/10.1016/j.carbon.2019.06.092
15. V.B. Mohan, K. Lau, D. Hui, D. Bhattacharyya, Graphene-based materials and their composites: a review on production, applications and product limitations. Compos. Pt B-Eng. **142**, 200–220 (2018). https://doi.org/10.1016/j.compositesb.2018.01.013
16. A.D. Moghadam, E. Omrani, P.L. Menezes, P.K. Rohatgi, Mechanical and tribological properties of self-lubricating metal matrix nanocomposites reinforced by carbon nanotubes (CNTs) and graphene—a review. Compos. Pt B-Eng. **77**, 402–420 (2015). https://doi.org/10.1016/j.compositesb.2015.03.014
17. E.Y.W. Chong, C.Y.P. Ng, V.W.Y. Choi, L. Yan, Y. Yang, W.J. Zhang, K.W.K. Yeung, X.F. Chen, K.N. Yu, A diamond nanocone array for improved osteoblastic differentiation. J. Mater. Chem. B **1**, 3390–3396 (2013).https://doi.org/10.1039/C3TB20114G
18. J. Gujt, E. Cazares Vargas, L. Pusztai, O. Pizio, On the composition dependence of thermodynamic, dynamic and dielectric properties of water-dimethyl sulfoxide model mixtures. NPT molecular dynamics simulation results. J. Mol. Liq. **228**, 71–80 (2017). https://doi.org/10.1016/j.molliq.2016.09.024

19. J.C. Chandler, N.S. Gandhi, R.L. Mancera, G. Smith, A. Elizur, T. Ventura, Understanding insulin endocrinology in decapod crustacea: molecular modelling characterization of an insulin-binding protein and insulin-like peptides in the eastern spiny lobster, *Sagmariasus verreauxi*. Int. J. Mol. Sci. **18**, 1832 (2017). https://doi.org/10.3390/ijms18091832
20. S.S. Stachura, C.J. Malajczuk, R.L. Mancera, Molecular dynamics simulations of a DMSO/water mixture using the AMBER force field. J. Mol. Model **24**, 174 (2018). https://doi.org/10.1007/s00894-018-3720-x
21. S. Promsri, G.M. Ullmann, S. Hannongbua, Molecular dynamics simulation of HIV-1 fusion domain-membrane complexes: insight into the N-terminal gp41 fusion mechanism. Biophys. Chem. **170**, 9–16 (2012). https://doi.org/10.1016/j.bpc.2012.07.002
22. J.C. Phillips, R. Braun, W. Wang, J. Gumbart, E. Tajkhorshid, E. Villa, C. Chipot, R.D. Skeel, L. Kalé, K. Schulten, Scalable molecular dynamics with NAMD. J. Comput. Chem. **26**, 1781–1802 (2005). https://doi.org/10.1002/jcc.20289
23. L. Kale, R. Skeel, M. Bhandarkar, R. Brunner, A. Gursoy, N. Krawetz, J. Phillips, A. Shinozaki, K. Varadarajan, K. Schulten, NAMD2: greater scalability for parallel molecular dynamics. J. Comput. Phys. **151**, 283–312 (1999). https://doi.org/10.1006/jcph.1999.6201
24. B.D. MacKerell, D. Bellott, J.D. Evanseck, M.J. Field, S. Fischer, J. Gao, H. Guo, S. Ha, D. Joseph-McCarthy, L. Kuchnir, K. Kuczera, F.T.K. Lau, C. Mattos, S. Michnick, T. Ngo, D.T. Nguyen, B. Prodhom, W.E. Reiher, B. Roux, M. Schlenkrich, J.C. Smith, R. Stote, J. Straub, M. Watanabe, J. Wiórkiewicz-Kuczera, D. Yin, M. Karplus, All-atom empirical potential for molecular modeling and dynamics studies of proteins†. J. Phys. Chem. B **102**, 3586–3616 (1998). https://doi.org/10.1021/jp973084f
25. J.B. Klauda, R.M. Venable, J.A. Freites, J.W. O'Connor, D.J. Tobias, C. Mondragon-Ramirez, I. Vorobyov, MacKerell ADJr, Pastor RW, Update of the CHARMM all-atom additive force field for lipids: validation on six lipid types. J. Phys. Chem. B **114**, 7830–7843 (2010). https://doi.org/10.1021/jp101759q
26. B.R. Brooks, C.L. Brooks, A.D. Mackerell, L. Nilsson, R.J. Petrella, B. Roux, Y. Won, G. Archontis, C. Bartels, S. Boresch, A. Caflisch, L. Caves, Q. Cui, A.R. Dinner, M. Feig, S. Fischer, J. Gao, M. Hodoscek, W. Im, K. Kuczera, T. Lazaridis, J. Ma, V. Ovchinnikov, E. Paci, R.W. Pastor, C.B. Post, J.Z. Pu, M. Schaefer, B. Tidor, R.M. Venable, H.L. Woodcock, X. Wu, W. Yang, D.M. York, M. Karplus, CHARMM: the biomolecular simulation program. J. Comput. Chem. **30**, 1545–1614 (2009). https://doi.org/10.1002/jcc.21287
27. J. Henin, C. Chipot, Hydrogen-bonding patterns of cholesterol in lipid membranes. Chem. Phys. Lett. **425**, 329–335 (2006). https://doi.org/10.1016/j.cplett.2006.04.115
28. W.L. Jorgensen, J. Chandrasekhar, J.D. Madura, R.W. Impey, M.L. Klein, Comparison of simple potential functions for simulating liquid water. J. Chem. Phys. **79**, 926 (1983). https://doi.org/10.1063/1.445869
29. E.J. Wallace, M.S.P. Sansom, Blocking of carbon nanotube based nanoinjectors by lipids: a simulation study. Nano Lett. **8**, 2751–2756 (2008). https://doi.org/10.1021/nl801217f
30. P. Raczynski, V. Raczynska, K. Gorny, Z. Gburski, Properties of ultrathin cholesterol and phospholipid layers surrounding silicon-carbide nanotube: MD simulations. Arch Biochem. Biophys. **580**, 22–30 (2015). https://doi.org/10.1016/j.abb.2015.06.008
31. S. Pogodin, V.A. Baulin, Can a carbon nanotube pierce through a phospholipid bilayer? ACS Nano **4**, 5293–5300 (2010). https://doi.org/10.1021/nn1016549
32. P. Raczynski, K. Gorny, Z. Dendzik, J. Samios, Z. Gburski, Modeling the impact of silicon-carbide nanotube on the phospholipid bilayer membrane: study of nanoindentation and removal processes via molecular dynamics simulation. J. Phys. Chem. C **123**, 18726–18733 (2019). https://doi.org/10.1021/acs.jpcc.9b05100
33. V.K. Gangupomu, F.M. Capaldi, Interactions of carbon nanotube with lipid bilayer membranes. J. Nanomater. **2011**, e830436 (2011). https://doi.org/10.1155/2011/830436

34. P. Raczynski, K. Gorny, P. Beldowski, S. Yuvan, B. Marciniak, Z. Dendzik, Steered molecular dynamics of lipid membrane indentation by carbon and silicon-carbide nanotubes-the impact of indenting angle uncertainty. Sensors **21**, 7011 (2021). https://doi.org/10.3390/s21217011
35. P. Raczynski, K. Gorny, P. Beldowski, S. Yuvan, Z. Dendzik, Application of graphene as a nanoindenter interacting with phospholipid membranes-computer simulation study. J. Phys. Chem. B **124**, 6592–6602 (2020). https://doi.org/10.1021/acs.jpcb.0c02319

Green and Rapid Fabrication of Plasmonic Nanomaterials: Colorimetric Properties for Pesticide Residue Detection

Skiba Margarita, Ihor Kovalenko, Olena Gnatko, Iryna Kosogina, and Viktorya Vorobyova

Abstract The investigation of modern methods of nanomaterial synthesis and their properties remains an urgent task In this study, the ecological benefits of plasma-chemical technologies for the synthesis of plasmonic metal nanomaterials (gold and silver) were determined. The results of experimental and theoretical research on the synthesis of gold and silver nanoparticles with anodic plasma suction are presented. The colorimetric properties of plasmonic metal nanoparticles for pesticide residue detection have been demonstrated.

1 Introduction

Obtaining and researching nanomaterials of various structural organization and functional properties, along with improvement and creation of new synthesis methods, is an urgent task of fundamental and applied sciences and is one of the priority areas of development of science and technology in most countries of the world. Marketing research and annual reports of the world's largest companies on the acquisition, research, and implementation of nanomaterials and nanotechnologies (Future

S. Margarita (✉) · I. Kovalenko · O. Gnatko
Dnipro, Ukraine
e-mail: margaritaskiba88@gmail.com

I. Kovalenko
e-mail: il-kovalenko@ukr.net

O. Gnatko
e-mail: olena.gnatko@gmai.com

I. Kosogina · V. Vorobyova
Kyiv, Ukraine
e-mail: kosoginairyna@gmail.com

V. Vorobyova
e-mail: vorobyovavika1988@gmail.com

O. Fesenko and L. Yatsenko (eds.), *Nanoelectronics, Nanooptics, Nanochemistry and Nanobiotechnology, and Their Applications*, Springer Proceedings in Physics 297,
https://doi.org/10.1007/978-3-031-42708-4_8

Markets Inc., «The Global Nanotechnology and Nanomaterials Market Opportunity Report 2020–2027») [1–4] testify to the undeniable leadership of the development of the nanoindustry itself and its implementation of nanotechnologies in various spheres of people's lives and activities.

Currently, the general market for nanotechnology is conventionally segmented according to the following categories: types of nanomaterials, types of technologies, methods of application. Depending on the type, nanomaterials and nanocomposites have the largest share of the market and are stable world leaders due to the growth of demand from end-user segments, according to analysts.

Therefore, the size of the world market for nanomaterials in 2020 was estimated at $8.0 billion. U.S.A. And according to marketing forecasts, it is only expected to grow from 2021 to 2028 at a compound annual growth rate of 14.1%. Analysts testify that the main current drivers of the world market for nanomaterials are the following factors: increasing the introduction of existing materials into the market, lowering the prices of nanomaterials, improving the properties of materials, expanding scientific research activities related to new materials, increasing public and private spending on nanotechnology research, increasing support from state institutions, rapid development of new materials and applications [1–3, 5], effective functioning of partnerships and strategic alliances of domestic and foreign companies and organizations, increasing the number and cooperation between industry participants, including the growth of international research and production cooperation in nanotechnology. According to the same data, the most researched and commercially attractive directions are related to the creation (design), research of functional characteristics (properties) of nanosystems of different structure and composition and the practice of their functional use in various fields.

In publications [1–5], a thorough analysis was conducted, and a detailed report was provided on the state of obtaining a wide variety of nanomaterials. The level of their commercialization was determined based on a thorough analysis of indicators like the level of readiness of traditional and modern technologies, annual production volume, efficiency, and projected annual market growth rates during twenty-five "life cycles" of technology and nanomaterials (Fig. 1). According to various estimates, nanomaterials, specifically plasmonic nanometals nanosilver (Ag NPs) and nanogold (Au NPs), now belong to materials with a high level of commercialization and demand, taking into consideration the current state of technology and prospects for practical use.

While nanosilver belongs to the category "fully tested and/or in operation according to various technologies" in various industries (Fig. 1), and nanogold belongs to materials that have the results of field tests, a basic prototype and/or a final prototype and fully commercialized mainly in medicine and as sensors. In the latest reports of the international program Project on Emerging Nanotechnologies (PEN, (http://www.nanotechproject.org) and numerous marketing research reports, there are already more than 1814 consumer products from 622 companies in more than 32 countries of the world, which are engaged in the production and commercial sale of silver and gold NP products, both as an independent material and as part of various other products for various industries. Currently, there is a trend of steady

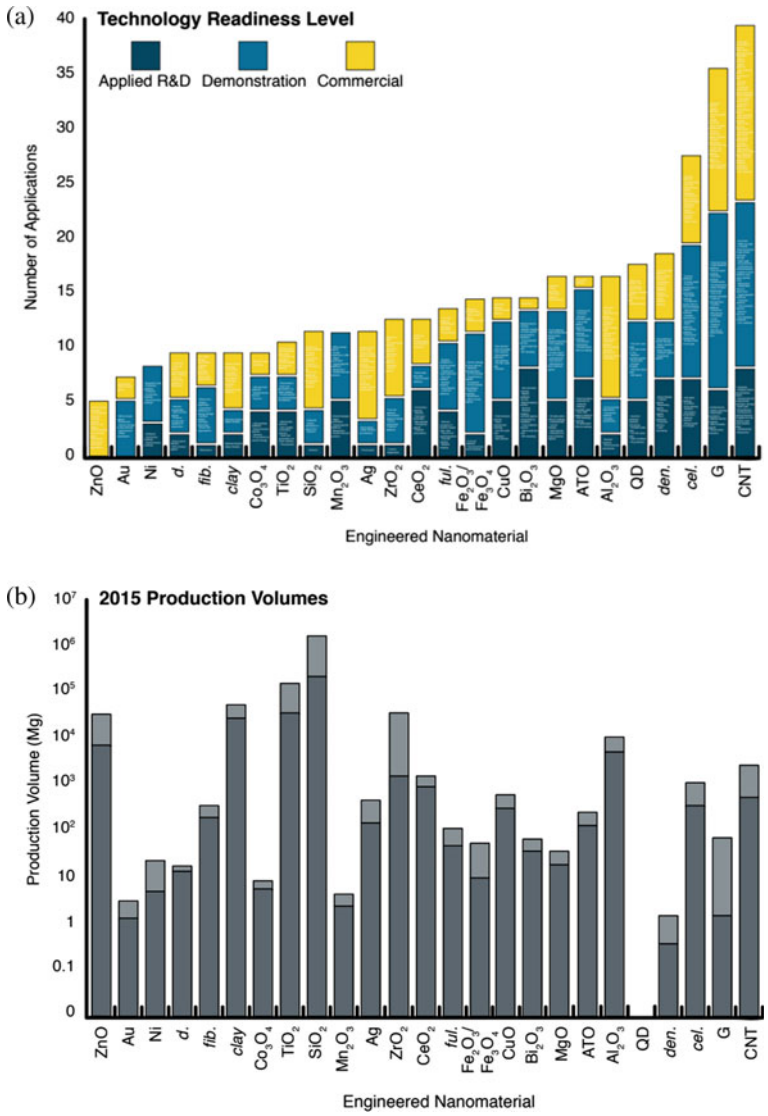

Fig. 1 State of obtaining and commercializing nanomaterials within different levels of technological readiness and industrial volumes of production [1, 2]

growth in the global market of Ag NPs, and the growth rate is increasing annually: for nanosilver it is within 360–450 t/year, for gold this indicator is 50–100 t/year [1–4, 6, 7]. It is also predicted that the global consumption of Ag NPs and gold NPs will only grow due to a number of factors (with a special emphasis on the epidemiological situation and the threat of other mutations and the increase in industrial demand according to forecasts [1–7] by 2027 will amount to more than ~ 800 t/year

[4, 5]. Due a number of factors and the increase in industrial demand according to forecasts [2–7] by 2027 will amount to more than ~ 800 t/year [4, 5].

Plasmonic nanometals are characterized by a unique combination of a number of properties and, as a result, polyfunctionality. As a result, these materials are especially promising for usage in a variety of science and technological disciplines. The Scopus and Web of Science Core Collection databases' analyses of publications on research and fields of practical use of various nanomaterials using the keywords "material + nano + environmental safety" and "material + nano + environment" (Fig. 2) reveal a lengthy list of applications for plasmonic nanomaterials, including those in medicine, environmental protection technologies, health and safety, the cosmetics industry, and others [4, 5].

The main characteristics that determine the main properties of nanosystems are the morphometric indicators of nanoparticles (NPs) (size, shape, and polydispersity) and stability during storage. These characteristics, in turn, are determined by methods of nanoparticle synthesis. These parameters depend on a significant number of synthesis factors. Even slight changes in experimental conditions can significantly affect the polydispersity of particles and size effects and change the properties of the entire system, which makes it difficult, and sometimes impossible, to obtain NPs with specified (controlled) properties. Therefore, solving the issue of developing methods for the controlled synthesis of NPs with given parameters is extremely important.

2 Environmental Assessments of Various Approaches to the Synthesis of Nanomaterial

For specific NP morphologies or surface chemistries to be included into a given industry's products, various synthesis techniques can be required. To date, various methods of obtaining nanomaterials are known. Technologies for obtaining NPs are currently conventionally divided into three groups. The first includes technologies where NPs are formed as a result of combining atoms and molecules ("Button-Up"). The second is a result of dispersing materials ("Top-Down") and the third group combines methods related to groups 1 and 2. Numerous review articles deal examination and the discussion of their benefits and drawbacks. Studies that evaluate how different synthesis techniques affect the environment are more uncommon.

In the work of the authors [1, 7], on the example of the production of 1 kg of Ag NPs, an assessment of the global impact on the environment (according to various parameters) of six different synthesis methods (two chemical and four physical) as well as thirteen different modifications of them was carried out in combination with annual estimates of Ag NP production, with the provision of optimistic and skeptical assessments. It was considered from the category of chemical methods of synthesis (synthesis using microwave irradiation (MW), chemical reduction (CR) using citrate, borohydrate, ethylene glycol/PVP polymer, soluble

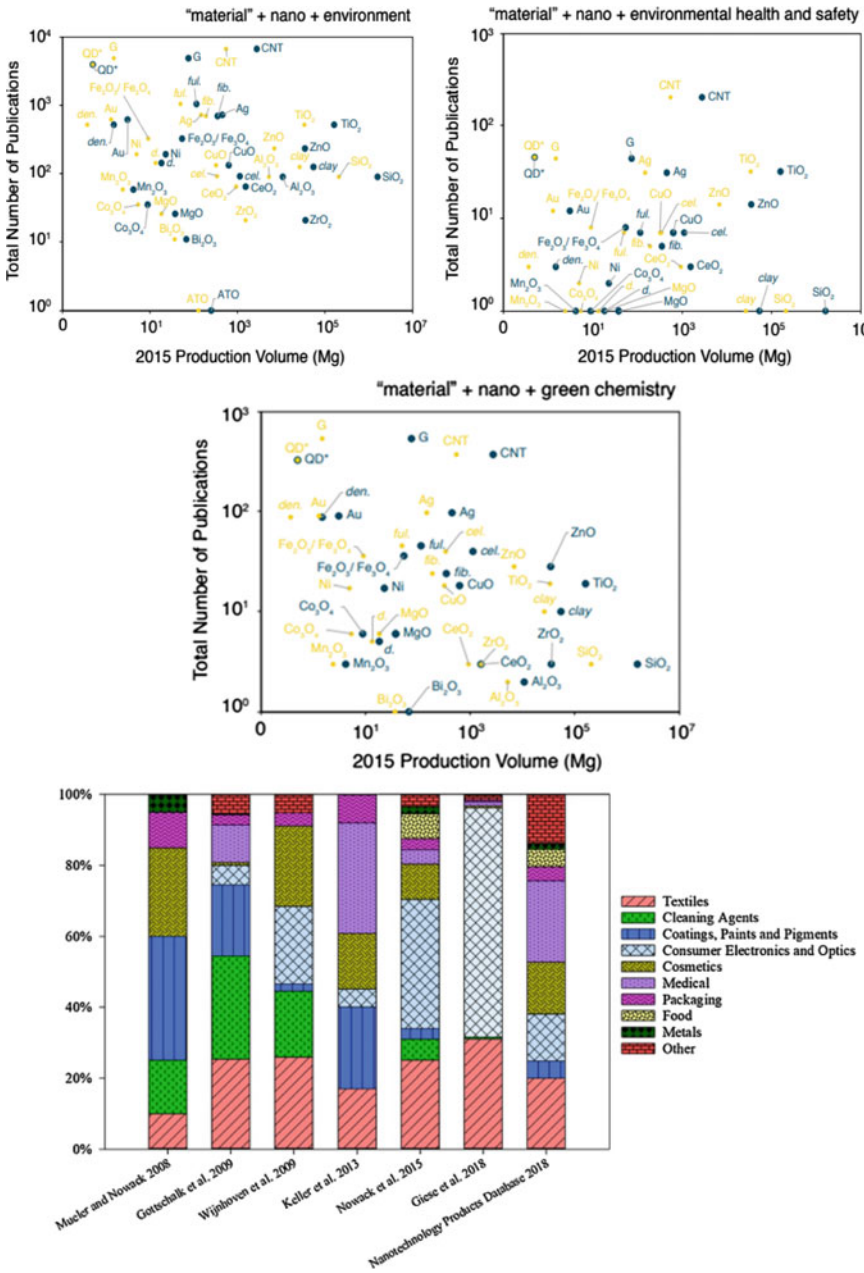

Fig. 2 Search results for publications in the Scopus and Web of Science Core Collection databases using the terms "material + nano + environmental health and safety," "material + nano + environment," and "material + nano + green chemistry" [1] and market demand for commercialized nanomaterials by areas of application [2–5]

starch), and from the category of physical methods (Flame Spray Pyrolysis (FSP-MS), plasma discharges (Arc Plasma) of 4 types, reactive magnetron sputtering (RMS-Ar-N), spark reduction (Spark-TUD). The authors selected categories of environmental impact along with their units and abbreviations: ozone depletion (ODP in kg CFC11-eq.), global warming (GWP in kg CO_2-eq.), smog (SP in kg O_3-eq.), acidification (AP in kg SO_2-eq.), eutrophication (EP in kg N-eq.), carcinogenics (HHCP in CTUh), non-carcinogenics (HHNCP in CTUh), respiratory effects (RP in kg PM2.5-eq.), ecotoxicity (ETP in CTUe), and fossil fuel depletion (FFP in MJ surplus energy) potentials. Figure 3 shows data on the impact on the environment of various synthesis methods for the production of 1 kg of Ag NPs according to the indicators listed above.

The authors' general conclusions indicate that the impact of synthesis methods on the environment decreases in the following order: magnetron sputtering, microwave irradiation, plasma discharges, chemical reduction, spark reduction, and pyrolysis (Fig. 3). When compared to CR, microwave synthesis did not exhibit larger consequences in any of the probable environmental impact categories, with the exception of ODP and AP. The higher impacts in these two categories are primarily caused by the use of microwaves, which consumes electricity. Chemical reduction techniques increase the environmental effects of manufacturing throughout the life cycle since they require a number of chemicals as reducing and stabilizing agents. Due to having the lowest affects across all impact categories, CR-SB is proven to be the least environmentally damaging CR approach. Additionally, CR-starch has the greatest effects on AP, EP, HHNCP, and ETP. Due to the usage of trichloromethane in insecticides and fertilizers to produce starch in potatoes, this approach contributes the most to these categories. Since the synthesis is carried out at high temperatures for heating, which results in higher emissions, CR-TSC has the greatest influence on GWP and ODP. Due to the utilization of raw materials derived from fossil fuels, CR-EG performs with the highest impact in terms of FFP, SP, HHCP, RP, and CED. Due to the low inputs of chemicals and electricity required for synthesis, RMS-Ar-N has the lowest environmental impact when considering all impact categories when using physical chemistry methods. Despite having comparable material and energy inputs, AP and Spark systems have different life cycle implications because of different energy delivery strategies. In comparison with the spark technique, AP generally performs worse for the environment. With the exception of ODP, the Spark approach does not exhibit the highest impact, which may be attributable to its comparatively low material demand. ODP has a greater impact since a lot of electricity is required to feed the spark system with energy that has different frequencies.

As evidenced by the above data, plasma-chemical methods of synthesis, in various variations, occupy an intermediate place on the list of chemical and physical methods. Also an important conclusion of the authors is the statement that scaling up can reduce emissions to the environment by up to 90% worldwide and up to 83% for the industrial sector, indicating that the global impact of NPs on the environment can vary significantly depending on the method of synthesis, scale, and desired application of the product.

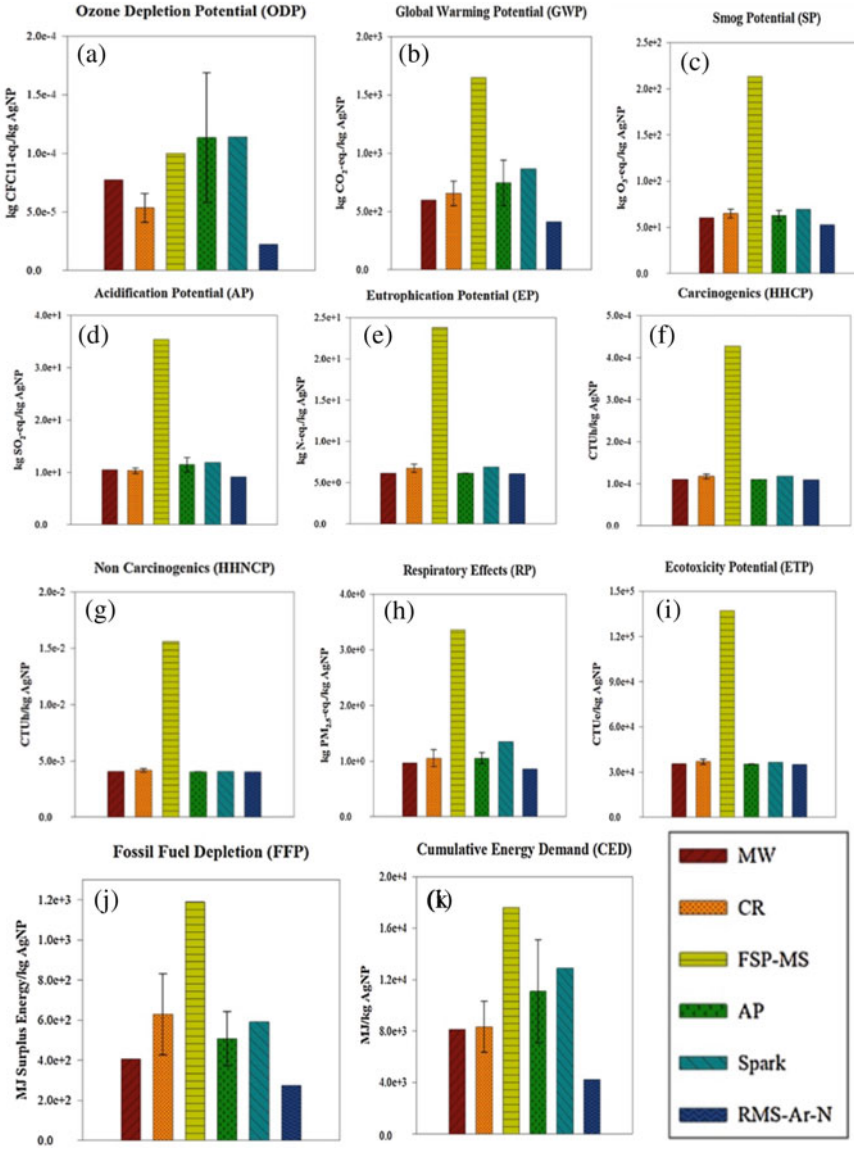

Fig. 3 Environmental impacts of multiple synthesis routes for 1 kg AgNPs, using multiple impact categories as **a** ODP, **b** GWP, **c** SP, **d** AP, **e** EP, **f** HHCP, **g** HHNCP, **h** RP, **i** ETP, **j** FFP and **k** CED [1]

3 Plasma-Liquid Systems for Nanomaterials Synthesis (Silver NPs)

The global trend in the development of nanomaterials technology is short-term plasma-liquid synthesis (PLS), which enables targeted production of nanomaterials and composites for various functional purposes [8–10]. To date, there have been a significant number of publications on reaction products that are formed in solutions depending on the types of plasma (anode plasma and cathode plasma) (Fig. 4).

- Secondary electrons can dissolve into liquid in both the liquid-cathode and liquid-anode cases, forming hydrated electrons (e_{aq}), which are very strong reducing species in the NP synthesis process [10]. Furthermore, other plasma species such as atomic hydrogen, H_2, H_2O_2 (with varying reducing abilities depending on pH) and hydride (H) (a very strong reducing species) can reduce metal ions in both cases. However, in the liquid-anode case, the yield of these reducing species is much lower than in the liquid-cathode case. Some oxidizing species, such as atomic oxygen, ozone, and $OH^{\cdot}$ radicals, can be generated during PLIs.
- It was discovered that the type of metal ions has a significant impact on the synthesis process as well as the quality of the resulting NPs. Under similar plasma conditions, for example, Au NPs were found at both the plasma cathode and the anode, whereas Ag NPs were found only at the plasma cathode [10].

Despite a sufficient number of fundamental studies of gas superfluid discharge with electrolyte electrodes, the formation of nanomaterials (mono- and bimetallic metals and composites) using PLS has not been studied enough. The question of choosing the conditions of plasma-chemical controlled synthesis for obtaining plasmonic nanometals and composites with polyfunctional properties to solve the actual

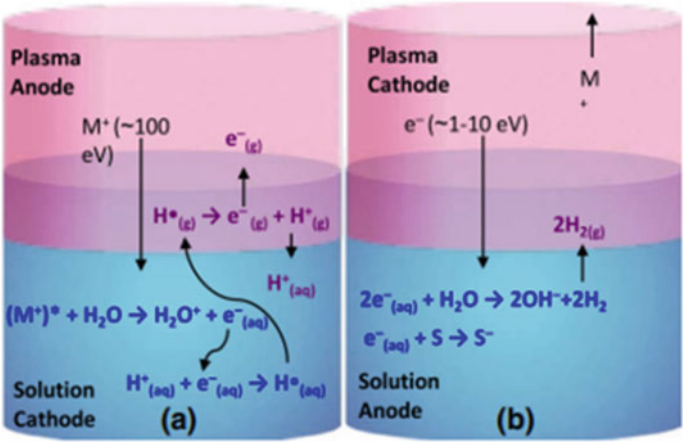

Fig. 4 Schematic of proposed charge transfer processes in **a** liquid cathode (plasma anode) and **b** liquid anode (plasma cathode) configurations [8–10]

problems of using such materials in various industries and spheres of human activity remains an undefined applied problem.

Thus, there is a need to carry out complex studies to study the patterns of obtaining nanosystems of mono- and bimetallic plasmonic metals (Ag and Au) and composites based on them; the determination of technological features of synthesis under the conditions of plasma-liquid discharge; and the establishment of functional properties of nanosystems of various applications.

The main regularities of the formation of plasmonic metal nanosystems-monometallic nanoparticles (Ag, Au) in an aqueous medium by an anode-type superfluid plasma discharge from metal precursors have been established.

The transformations in two types of systems were investigated in order to establish the regularities of the plasma-chemical formation of monometallic silver nanosystems in an aqueous medium by a anode-type liquid plasma type discharge using a complex analysis: the first «aqueous solution of precursor (Ag^+) + stabilizer (STAB)» and the second «aqueous solution of precursor (Ag^+)/absence of (STAB)».

Based on a series of studies (Fig. 5), it was determined that the degree of nanoparticle formation for both nanosystems, as a function of changes in the intensity of SPR absorption and the equilibrium concentration of Ag^+, has an extreme character with the passage of the critical time (τ_{kr}) of NP formation and various types of changes after that: for the systems «(Ag^+) + (CTAB)»—a stable state or a shift of the peak to the short-wavelength zone (at constant absorption intensity values), caused by a change in the properties and processes of NP formation—a reduction in the size of the form/NPs, stabilization; for the "Ag^+/(absence of STAB)" systems, there is no shift/or shift of the peak into the long-wavelength zone with an obligatory extreme decrease in absorption intensity, which is due to the aggregation of nanoparticles and defects on the surface, etc.

It was established that the formation of NPs by reducing metal cations (Me^+) from the systems «(Ag^+) + stabilizer (STAB)/absence of STAB» by a complex of oxidizing compounds (hydrated electrons e_{aq}, $H^·$, $OH^·$ radicals, etc.) is common to the studied systems. The formation of which is initiated by a superfluid plasma discharge, and the stabilizing reagents in the plasma-chemically processed system during the synthesis of nanoparticles do not make a significant contribution to the reduction of Ag^+. The Ag^+ reduction rate constants in the plasma-chemical reactor are 0.4–0.6 min^{-1} ($R = 0.98$).

The electrolyte-cathode discharge model of in publication [8–11] explains the impact of positive ions (10–100 eV) on the surface of a liquid. The chemical processes come in two steps, producing H_3O^+ (H^+), OH, H radicals, and solvated electrons. It is unclear how positive ions move through liquids. However, authors [11, 12] conducted an experimental investigation of the solvation of H^+ ions by water molecules in the gas phase. The authors proposed the structure H^+-$(H_2O)_n$ ($n = 2$ to 4) for the solvation production. The authors' publication [11] demonstrates a solvation structure in which the H_3O^+ is surrounded by three nearby water molecules in bulk liquid water that is comparable to this structure. It makes sense to assume that H^+ from plasma forms ion-water clusters above the plasma-liquid boundary after being solvated by water

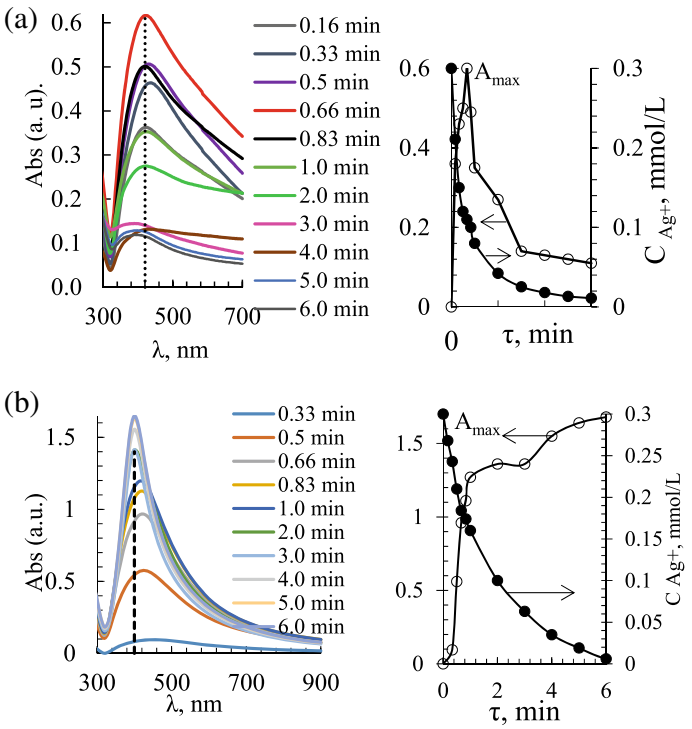

Fig. 5 UV–vis absorption spectra with a corresponding dependences decrease of the equilibrium concentration of argentum ions and changes of maximum SPR for the colloidal Ag NPs synthesized by plasma-liquid anode discharge: «(Ag^+) + stabilizer (STAB-Cit)» (**a**) and «(Ag^+) + absence of STAB» (**b**)

vapor molecules and subsequently diffuses in the liquids. The transfer of H^+ from plasma to liquids is also taken into consideration by authors.

The author [8–11] verified that the liquids are exposed to both free electrons and positive ions from the AC glow discharge. As a result, the liquid is filled with reactive species including OH radicals and solvated electrons (e_{aq}).

E_{aq} reacts with numerous metal ions to lower the oxidation state and has a typical redox potential of − 2.9 V. Nearly, all metal ions can be oxidized by OH radicals with a conventional redox potential of 2.7 V to a higher oxidized value (Fig. 6).

The final products of these reactions are likely to be metal ions with lower oxidized values or neutral atoms. Figure 5 depicts the process by which some metal ions interact with these species to alter their amount of redox potential. It demonstrates that the reduction reaction's rate constant is lower than its oxidation process counterpart.

Based on the results of TEM/SEM microscopy, it was established that the use of different ratios of the stabilizer and the initial concentration of the precursor in the range of 0.3–3.0 mmol/L allows controlling the dimensional characteristics of

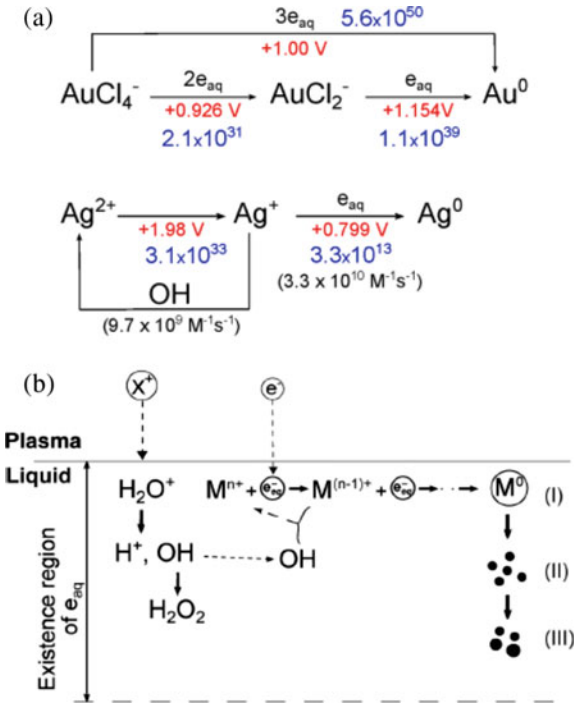

Fig. 6 Schematic representation of the pathway reaction between Ag and Au ions with e_{aq} and OH radicals. Red and blue numbers are indexed for the redox potential (E_0) and the equilibrium constant (K_{eq}) calculated, respectively [11, 12] (**a**) and schematic representation of the nano-synthesis process by AC glow discharge (**b**) [11, 12]

nanoparticles in the range of $d = 12$–32 nm during synthesis, resulting in the formation of stable nanosystems with characteristic zeta potential values ($\zeta = -21.7$ to -44.0 mB), Fig. 7. Systems without a stabilizer allow for the formation of nanosystems with dimensional characteristics (30–65 nm); however, they are unstable ($\zeta = -14.1$ mB).

4 Plasma-Liquid Systems for Nanomaterials Synthesis (Gold NPs)

On the basis of the analysis of kinetic transformations under the action of a plasma discharge, it was established that, similar to silver nanosystems, nanogold is characterized by a typical staged process with pronounced differences in the characteristics of nanosystems when processing two different systems in the presence and absence of stabilizers "(Au^{3+}) + (CTAB)/absence of CTAB."

The analysis of a set of experimental studies of the main stages of the formation of nanosystems as a result of transformations in the systems "aqueous solution of precursor (Au^{3+}) + stabilizer (STAB)/absence of STAB" under the action of a plasma discharged made it possible to conclude that the patterns of the formation of

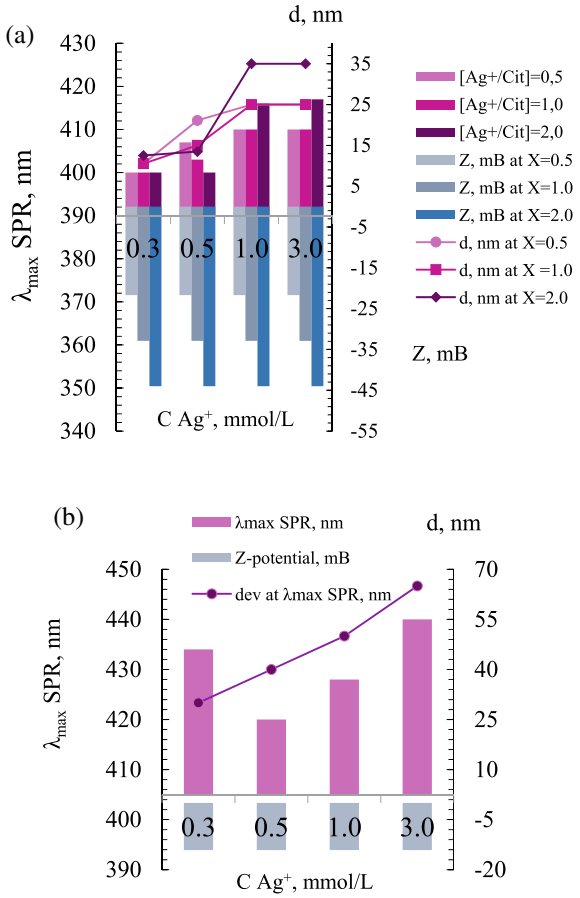

Fig. 7 Effect of initial concentration and stabilizer (ratio) on the dimensional characteristics and zeta potential of silver nanosystems obtained by plasma treatment: «(Ag^+) + stabilizer (STAB-Cit)» (**a**) and «(Ag^+) + absence of STAB» (**b**)

gold nanosystems under the action of a plasma discharge are also similar to those established for silver nanosystems (Fig. 8).

It was established that an increase in the initial concentration of the precursor increases the core size of the nanoparticles in the obtained nanosystems, with a corresponding shift of the plasmon resonance to the long-wavelength zone. Plasma-chemically obtained systems are more stable without the use of stabilizer reagents; however, for long-term storage, the use of stabilizer reagents is necessary. It was demonstrated that varying the ratio of precursor to stabilizer (X = 1–10) allows varying the size of nanoparticles (35–80 nm) (Fig. 9).

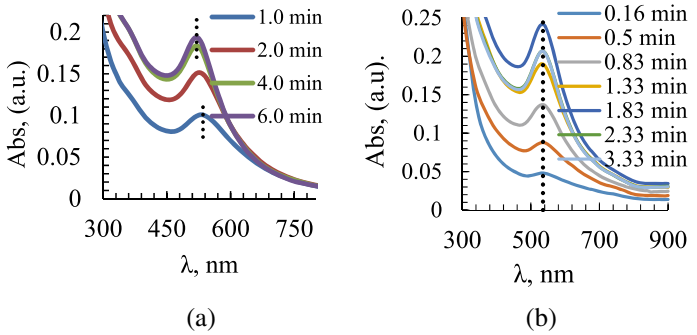

Fig. 8 UV–vis absorption spectra and changes of maximum SPR for the colloidal Au NPs synthesized by plasma-liquid cathode discharge: «(Au^{3+}) + stabilizer (STAB-Cit)» (**a**) and «(Au^{3+}) + absence of STAB» (**b**)

Fig. 9 Effect of initial concentration (**a**) and stabilizer (ratio (Au^{3+}) + stabilizer) on the dimensional characteristics and zeta potential of gold nanoparticles obtained by plasma treatment: «(Au^{3+}) + stabilizer (STAB-Cit)» (**a**) and «(Au^{3+}) + absence of STAB» (**b**)

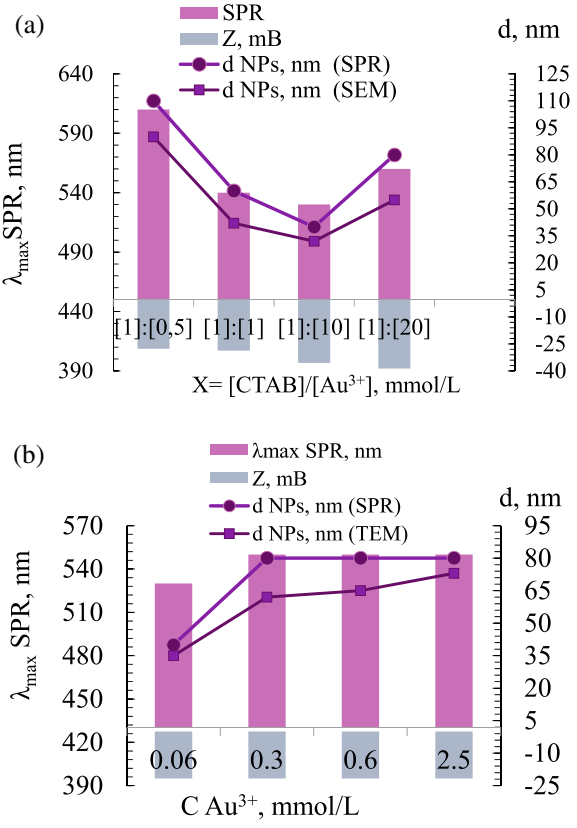

5 Plasmonic Nanoparticles as a Colorimetric Sensor for Rapid Pesticide Residue Detection

Terbuthylazine (TBA) is a popular pre- and post-bud herbicide that is mostly used to get rid of annual and broad-leaved weeds [4, 5]. TBA, however, is the main cause of food poisoning and environmental damage. They have some detrimental consequences on people's health and safety, and the issue keeps becoming worse [13, 14]. The TBA was one of 74 pesticides that the European Union (EU) designated as having chronic toxicity for humans in 2015. The governments of the EU have separately set the maximum residue limits (MRL) of TBA in water or food at 0.05 mg/kg (i.e., 0.22 M for TBA). The UV–vis absorption spectra after being incubated with TBA at various doses (0.1–5.0 M) were fixed. The SPR band was observed with a red shift when TBA concentration added and increased at increase amount TBA 0.1–5.0 M. The absorption peak at 520 nm progressively decreased, while the absorption peak at 650 nm steadily increased, indicating that more Au NPs accumulated. The fluctuation of Au NPs' absorption peak intensity was used in the quantitative detection of TBA. It was established that impurities from the series (Cl^-, NO_3^-, CO_3^{2-}) do not affect the UV absorption spectrum, during the research, they preserved the red color of nanoparticles and were similar to the control sample, while the sample with TBA is characterized by a blue color. These results demonstrate that these potential environmental contaminants do not affect the detection of TBA by Au NPs.

A plot of A_{650}/A_{520} as a function of TBA concentration with a range of 0.1–5.0 mM is shown in Fig. 10. A plot of A_{650}/A_{530} as a function of TBA concentration with a range of 0.1–5.0 M is also shown in Fig. 10. A_{650} and A_{520}, respectively, are the UV–vis absorbance of each sensor at 650 and 520 nm with TBA added. TBA concentrations between 0.1 and 0.8 M were found to have a linear association ($R^2 = 0.98$) with the ratio of A_{650}/A_{530}. This finding shows that TBA in the concentration range of 0.1–0.9 M may be quantitatively analyzed using an Au NP-based colorimetric sensor. The findings indicate that this probe can detect TBA with a theoretical detection limit of 0.015 M. This theoretical detection limit is not only significantly lower than the MRL of TBA (0.22 M).

6 Conclusions

In recent decades, there has been a lot of interest in the synthesis, properties, and applications of plasmonic NPs. Summarized data on the "environmental friendliness" of the main methods of synthesis of nanometals (using nanosilver as an example) are presented. This work presents the effectiveness of using nanoparticles of plasmonic metals (gold and silver) using the superfluid plasma discharge technology of the anode type. It has been demonstrated that the use of stabilizer reagents allows controlling the dimensional parameters of metal nanoparticles. The effectiveness of

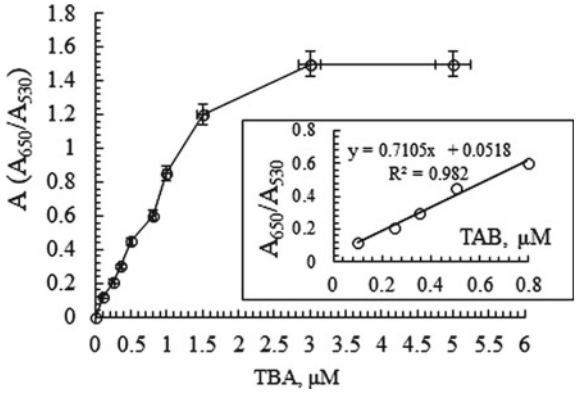

Fig. 10 Plot of A_{650}/A_{520} as a function of the TBA concentrations

using gold nanoparticles as a colorimetric sensor for the determination of pesticide residues has been demonstrated.

References

1. S. Temizel-Sekeryan, L.H. Andrea, Global environmental impacts of silver nanoparticle production methods supported by life cycle assessment. Resour. Conserv. Recycl. **156**, 104647 (2020). https://doi.org/10.1016/j.resconrec.2019.104676
2. N.Z. Janković, D.L. Plata, Engineered nanomaterials in the context of global element cycles. Environ. Sci. Nano **6**, 2697–2711 (2019). https://doi.org/10.1039/C9EN00322C
3. V. Harish, D. Tewari, M. Gaur, A.B. Yadav, S. Swaroop, M. Bechelany, A. Barhoum, Reviewon nanoparticles and nanostructured materials: bioimaging, biosensing, drug delivery, tissue engineering, antimicrobial, and agro-food applications. Nanomaterials **12**(3), 457 (2022). https://doi.org/10.3390/nano12030457
4. L. Pourzahedi, M.E. Vance, M.J. Eckelman, Life cycle assessment and release studies for 15 nanosilver-enabled consumer products: investigating hotspots and patterns of contribution. Environ. Sci. Technol. **51**(12), 7148–7158 (2017). https://doi.org/10.1021/acs.est.6b05923
5. V. Castellani, E. Sanyé-Mengual, S. Sala, Environmental impacts of household goods in Europe: a process-based life cycle assessment model to assess consumption footprint. Int. J. Life Cycle Assess. **26**(10), 2040–2055 (2021). https://doi.org/10.1007/s11367-021-01987-x
6. A.L. Hicks, S. Temizel-Sekeryan, Understanding the potential environmental benefits of nanosilver enabled consumer products. NanoImpact **16**, 100183 (2019). https://doi.org/10.1016/j.impact.2019.100183
7. M. Slotte, R. Zevenhoven, Energy requirements and life cycle assessment of production and product integration of silver, copper and zinc nanoparticles. J. Clean. Prod. **148**, 948–957 (2017). https://doi.org/10.1016/j.jclepro.2017.01.083
8. F. Rezaei, P. Vanraes, A. Nikiforov, R. Morent, N. De Geyter, Applications of plasma-liquid systems: a review. Materials **2**(17), 2751 (2019). https://doi.org/10.3390/ma12172751
9. P. Rumbach, D.B. Go, Perspectives on plasmas in contact with liquids for chemical processing and materials synthesis. Top Catal. **60**, 799–811 (2017). https://doi.org/10.1007/s11244-017-0745-9
10. H.E. Delgado, D.T. Elg, D.M. Bartels, P. Rumbach, D.B. Go, Chemical analysis of secondary electron emission from a water cathode at the interface with a nonthermal plasma. Langmuir **36**(5), 1156–1164 (2020). https://doi.org/10.1021/acs.langmuir.9b03654

11. V.-P. Thai, H. Furuno, N. Saito, K. Takahashi, T. Sasaki, T. Kikuchi, The essential role of redox potential/equilibrium constant in the ability of non-equilibrium plasma for nano-synthesis in liquids. J. Appl. Phys. **128**(4), 043305 (2020). https://doi.org/10.1063/5.0012983
12. C. Richmonds, R.M. Sankaran, Plasma-solution electrochemistry: rapid synthesis of colloidal metal NPs by microplasma reduction of aqueous cations. Appl. Phys. Lett. **93**, 131501 (2008). https://doi.org/10.1063/1.2988283
13. J. Sun, L. Yuexiang, L. He, J. Pang, F. Yang, Y. Liu, Colorimetric sensor array based on gold nanoparticles: design principles and recent advances. TrAC, Trends Anal. Chem. **122**, 115754 (2020)
14. Y. Qian Qian, L. Feng Fan, L.Y. Ma, H. Yang, N.H. Song, Residues of reduced herbicides terbuthylazine, ametryn, and atrazine and toxicology to maize and the environment through salicylic acid ACS. Omega **6**(41), 27396–27404 (2021). https://doi.org/10.1021/acsomega.1c04315

Effect of Metal Ions on the Porosity and Antimicrobial Properties of ZnO-Alginate-Chitosan Composites

L. B. Sukhodub, M. O. Kumeda, and L. F. Sukhodub

Abstract ZnO-Alg/CS composites doped with Ca^{2+}, Zn^{2+}, Cu^{2+}, and Ag^{+} ions were synthesized for potential application in the treatment of damaged areas of the skin. Polyelectrolyte binding of oppositely charged polymer chains of Alginate (Alg) and Chitosan (CS), as well as additional "cross-linking" with metal ions, ensure the composite's stability in a physiological environment and provide antimicrobial properties. Loading of composites with metal ions provides enhanced antimicrobial properties and increases the degree of porosity, which positively affects the ability of materials to absorb liquid and exudate and accelerate wound healing. It has been experimentally proven that the Gram-negative *E. coli ATCC 25922* is more sensitive to the action of composites than the Gram-positive *S. Aureus ATCC 25923*. At the same time, Cu-doped samples exert an antimicrobial effect on both bacteria. The effect of Ca^{2+} ions in the composition of the composite material is noteworthy. Calcium by itself is not an antibacterial agent, but in a complex with CS, it shows antimicrobial activity. The integrated indicator of antimicrobial activity for samples containing Ca^{2+}, Zn^{2+}, Cu^{2+}, and Ag^{+} ions is close to or slightly higher than for commercial pharmaceutical agents Chlorhexidine and Metrogyl Denta.

1 Introduction

Porous biomaterials based on polymers are widely used in the treatment of purulent wounds and infected ulcers. Such materials include a highly absorbent material capable of removing and storing a large amount of exudate, have high flexibility, adhere well to the wound surface, and minimize pain [7]. Rapid wound closure is the first goal of treatment for acute or chronic wounds that are difficult to heal due to infections that can delay the healing process. Wound infection is caused by local microflora or the environment growing directly in the wound area. Therefore, antibacterial agents play an important role in preventing wound infection. Historically, the

L. B. Sukhodub (✉) · M. O. Kumeda · L. F. Sukhodub
Sumy State University, Sumy, Ukraine
e-mail: l.sukhodub@gmail.com

O. Fesenko and L. Yatsenko (eds.), *Nanoelectronics, Nanooptics, Nanochemistry and Nanobiotechnology, and Their Applications*, Springer Proceedings in Physics 297,
https://doi.org/10.1007/978-3-031-42708-4_9

resistance of microorganisms to antimicrobial drugs is the reason for their excessive and long-term use. As microbes are exposed to therapeutic agents, they develop resistance to antimicrobial agents through their rapid reproduction and genetic diversity. Thus, there is a need to develop safe, non-toxic compositions that prevent microbial proliferation [8].

Among biopolymers, natural CS and Alg have great scientific appeal in the fields of medicine, biotechnology, pharmacy, and cosmetics due to their biocompatibility with native tissues of the macroorganism, biodegradation, and antimicrobial activity. CS derivatives are characterized by wound-healing properties, as they exhibit greater antimicrobial activity compared to pure CS [4]. Chitosan is a polysaccharide component of crustacean shells, one of the few natural cationites. In the structure, CS has three types of reactive functional groups that ensure its chemical interactions, namely amino groups in the C-2 position, as well as primary and secondary hydroxyl groups in the C-6 and C-3 positions, respectively. This gives chitosan such properties as biocompatibility with native tissues of the macroorganism, biodegradation, and antimicrobial activity [3]. Glucosamine links in the chitosan structure are places of attachment to its molecular chain. Thus, amino groups in the protonated form allow attachment through electrostatic interaction. The nucleophilic properties of amines allow attachment by covalent bonds because amines have an active ionic pair of electrons on the electronegative nitrogen atom. Metal ions bind to chitosan through complexation mechanisms. The above properties of chitosan are widely used in practice in combination with growth factors and antibacterial agents [15].

Another polysaccharide of natural origin is alginate, which is a component of brown seaweed and is often used in tissue engineering due to its high biocompatibility and ability to easily and quickly form a gel in very mild conditions [5]. Modification of biomedical materials with metal ions and bioactive substances to provide additional properties is one of the modern approaches in medical materials science. A key property of functional polymers is their ability to form complexes with various metal ions in solutions. The addition of divalent cations such as calcium, zinc, and copper in an aqueous solution forms crosslinks between Alg and CS molecules, which leads to the formation of hydrogels—a three-dimensional network that stabilizes polymers [2].

ZnO nanoparticles are used as fillers for the polymer matrix due to their excellent antibacterial activity. Moreover, they do not show any negative effect on normal cells when used in appropriate concentrations [13]. The skin is the largest organ of the body. One of the serious problems in wound healing is the infection of the damaged part of the skin with microorganisms, such as bacteria. Infection delays skin recovery and can lead to further problems [4].

Therefore, wound dressings with antimicrobial activity are useful in minimizing microbial wound infections. In addition, porosity is a necessary and important characteristic of the absorbing biomaterial, which ensures interaction with exudate and its adsorption, and also ensures the necessary degree of water vapor penetration (water vapor transition). At the same time, the degree of porosity should provide the necessary mechanical stability to maintain the structural integrity of the biomaterial. Thus,

the goal of this project is to create a composite material doped with metal ions and to study the effect of metal ions on the degree of porosity and antimicrobial properties.

2 Experiment Details

2.1 Materials

The following materials and chemicals were used in the course of work: alginate (Alg, E401) with a molecular weight of 15 kDa, chitosan (CS, Mm 300 kDa, Acros organics, USA), zinc oxide ZnO (own synthesized), zinc nitrate $Zn(NO_3)_2$, polyethylene glycol (PEG-400), TWEEN-80, (China production).

2.2 Composite Preparation

The basis was a 3% solution of sodium alginate. Fine powders ($\leq$ 63 μm) of ZnO were mixed with 3% Alg aqueous solution in the ratio Alg: (ZnO) = 2:1 in terms of dry substances. The 0.5% of TWIN-80 та 5% polyethylene glycol was added to the above mixture, followed by sonification. The resulting colloidal suspension was poured into the mold 5 mm thick and lyophilized (− 55 °C) for 24 h. After lyophilization, the composite was first immersed for 4 h in a 1% solution of CS for polyelectrolyte interaction of CS and Alg functional groups. Additional ionic cross-linking of CS macromolecules was carried out in 0.25 M solutions of $CaCl_2$, $ZnSO_4$, $CuSO_4$, and $AgNO_3$ for 40 min. The samples were then immersed in ethyl alcohol (50% solution), washed thoroughly with deionized water, and dried at 37 °C under pressure.

According to our protocol, ZnO was synthesized in the presence of Alg [9]. Briefly, 4 ml of a 3 wt% solution of sodium alginate was added to 200 ml of a 0.2 M zinc nitrate hexahydrate solution. The formation of the ZnO compound started after the addition of 15 ml of a 25 wt% ammonia solution. Then, the entire volume of the solution was additionally heated to a temperature of 80 °C with magnetic stirring to complete the formation of ZnO. After cooling, the sample was repeatedly rinsed with distilled water until neutral, and ZnO fraction was separated by centrifugation. The product dried at 37 °C was crushed to a powder with a dispersion of < 63 μm.

The obtained ZnO-Alg/CS composite subsequently served as a control (Control). Since the contents of Alg, CS, and ZnO are constant in all samples, these components are not reflected in the sample's name. According to the type of metal ion present, the composites were named Ca, Zn, Cu, and Ag.

2.3 Research Methods

The surface morphology investigation was carried out using an SEM FEI Inspect S 50. *Porosity* (P) determination of the experimental composites was carried out using the earlier described method [14].

The elemental composition of synthesized samples was studied by an X-ray fluorescence (XRF) analysis using an ElvaX Light SDD spectrometer (www.elvatech.com). It is capable of identifying elements from Na ($Z = 11$) to U ($Z = 92$). A rhodium anode tube is used to obtain X-ray radiation. The voltage of the X-ray tube was 12 kV. The current was selected automatically to provide a sufficient load of simultaneously registered characteristic photons of ~ 50,000 counts. The registration time was the 30 s.

The antimicrobial activity of Me-ions doped biopolymer composites was studied against Gram-negative *Escherichia coli ATCC 25922,* and Gram-positive *Staphylococcus aureus ATCC 25923* bacteria test cultures. The Agar diffusion methods carried out for the antimicrobial assessment. For this, the sterile Müller-Hinton nutrient medium was poured into sterile Petri dishes with a 4 mm thick layer. The plates were left at room temperature to solidify. Then, a suspension of the test microorganisms (inoculum) was prepared. A pure daily culture grown on a solid nutrient medium was used for that purpose. Identical, clearly isolated colonies were selected. The loopful of cells from a single colony was transferred to a test tube with a sterile saline solution. The inoculum turbidity was adjusted to a McFarland standard of 0.5, corresponding to 1.5×10^8 CFU (colony forming units) in 1 ml. The 2 ml inoculum pipetted on the surface of the nutrient medium in a Petri dish was evenly spread over the agar surface by shaking, and then the excess liquid was removed. The opened cups were left at room temperature for 10 min for drying. The 6 mm disks were cut from experimental samples preliminarily moistened in sterile water and placed on the surface of the nutrient. After the sample's application, the Petri dishes were incubated at 37 °C for 24 h in a thermostat, and then the growth inhibition zone (ZOI) of the target microorganism was measured.

Integral index of antibacterial activity (A) is expected according to the methodology [12] by the following formula:

$$A = \sqrt{(a_1 \cdot D_1/25)^2 + \cdots + (a_n \cdot D_n/25)^2},$$

where

a_n—the proportion of patients with selected pathogenic microorganisms in a particular disease (range 0–1); D_n—the average value of the diameter of zones of inhibition growth of the studied test strains of microorganisms; A—integral index of the antimicrobial drug activity; 25—constant. Ranges of the efficiency indicator: 1.0–1.5—the drug shows a weak antimicrobial activity; 1.5–2.5—drug shows a mean antimicrobial activity; more than 2.5 shows strong antimicrobial activity.

Statistical data was processed using the program Excel (VS Office 2003) with geometric mean and the possibility of discrepancies (p) indicators.

3 Results and Discussion

The ZnO polymer scaffold is a macroporous three-dimensional network formed by the polyelectrolyte interaction between macromolecules of natural polymers Alg and CS, in the pores of which are immobilized particles of zinc oxide (ZnO). Polyelectrolyte binding of polymers ensures the stability of the composites in a physiological environment. To provide antimicrobial properties and increase mechanical stability, the synthesized materials were additionally cross-linked with metal ions from 0.25 M solutions of $CaCl_2$, $ZnSO_4$, $CuSO_4$, and $AgNO_3$. Previous in vitro studies regarding samples' structural integrity in the buffer solution SBF (simulated body fluid) proved that the composite is a three-layer structure, which has two surface layers doped with metal ions Ca^{2+}, Zn^{2+}, Cu^{2+}, Ag^{+} and an inner porous layer, represented by a grid of lyophilized Alg fibrils with immobilized ZnO particles. The surface layers were resistant to degradation, dispersion, and swelling, while the inner layer swelled much faster and acquired the consistency of a gel after 3 days of being in the SBF. CS macromolecules were first of all bound to Alg macromolecules located on the surface, forming a compacted film. In turn, metal ions bound to CS macromolecules form bridges between Alg and CS and also adhere to the surface of inorganic ZnO microparticles. Figure 1 schematically shows the composite components' interaction and the material's structure.

Figure 2 shows the XRF spectra of experimental samples, which confirm the content of metal ions in the composite structure.

As already mentioned, the degree of porosity is of great importance for biomaterials that can potentially be used as wound dressings. Studies have proven the influence of metal ions (Ca, Zn, Cu, Ag) on the porosity of the composite material (Fig. 3).

Doping composites with metal ions increases the degree of porosity compared to the control sample. The change in porosity is influenced by the state of the dispersed system caused by the action of adsorbed metal ions, namely the balance of the energies of electrostatic attraction and repulsion between charged particles. The predominance of the repulsive energy of similarly charged adsorbed ions leads to the formation of a positive "wedging" pressure, which causes the repulsion of surfaces and, in turn, affects porosity.

In electrolyte solutions, Cu^{2+}, Zn^{2+}, Ca^{2+}, and Ag^{+} ions are adsorbed on the particles of the dispersed phase of the samples, giving them a positive charge. As a result, repulsive forces arise, which, according to the theory of DLFO (Deryagin–Landau–Fairway–Overbeek), are electrostatic in nature. A positive wedging pressure is formed, which leads to an increase in the distance between macromolecules. This is the reason for the increase in the porosity of samples containing metal ions.

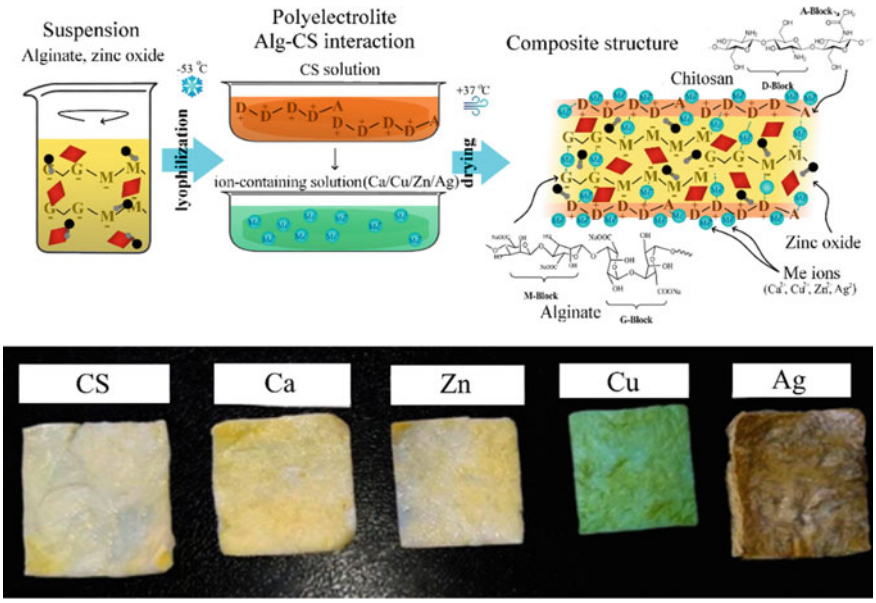

Fig. 1 Schematic representation of the interaction of components, the structure of the composite, and the appearance of the composite material doped with metal ions

The morphology of the cross-sections of the experimental samples is shown in Fig. 4. The images confirm the porous structure of the samples with a highly developed surface, which facilitates the absorption and retention of fluid and exudate when used as wound dressings.

Macromolecules of CS form with metal ions chelate complexes, which are able to exert an enhanced antimicrobial effect [11]. In vitro studies proved that the outer layers of the formed scaffold doped with metal ions showed increased mechanical stability in SBF.

Figure 5 shows the antimicrobial effect of metal ions containing composites in the form of zones of growth inhibition (ZOI) of Gram-positive *S. Aureus ATCC 25923* and Gram-negative *E. coli ATCC 25922* microorganisms. Quantitative values of ZOI are given in Table 1.

As the experiment shows, *E. coli ATCC 25922* is more sensitive to the action of composite materials. At the same time, Cu-doped samples have a good antimicrobial effect against both Gram-negative *E. coli ATCC 25922* and Gram-positive *S. Aureus ATCC 25923* bacteria. The action of calcium ions in the composite material is remarkable. Calcium by itself is not an antibacterial agent, but when combined with chitosan, it has an antimicrobial effect. The antimicrobial activity of samples containing Ag^+ ions is surprisingly low. This happens as a result of the interaction of silver ions with the components of the reaction mixture with the formation of poorly soluble compounds and, as a result, weak diffusion of Ag^+ ions. So, for example, the

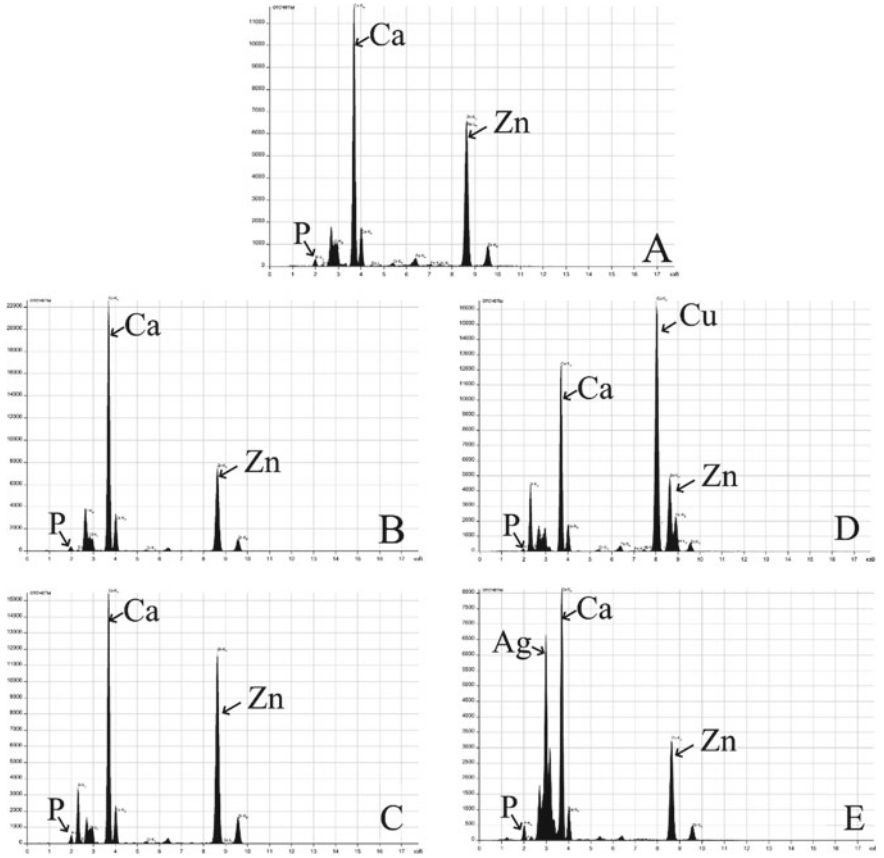

Fig. 2 XRF spectra of synthesized samples: Control ZnO-Alg/CS (**a**); Ca, Zn, Cu, Ag containing composites—**b**–**e**, respectively

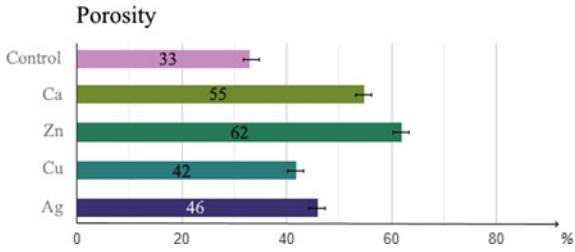

Fig. 3 Degree of porosity (%) of the experimental samples in dependence on the metal ion present

formation of poorly soluble silver carbonate in the solution is likely: $2Ag^{+} + CO_3^{2-} \rightarrow Ag_2CO_3\downarrow$.

For the comparative characterization of the experimental samples' antimicrobial ability against the investigated test strains, the calculation of the integral indicator (*A*)

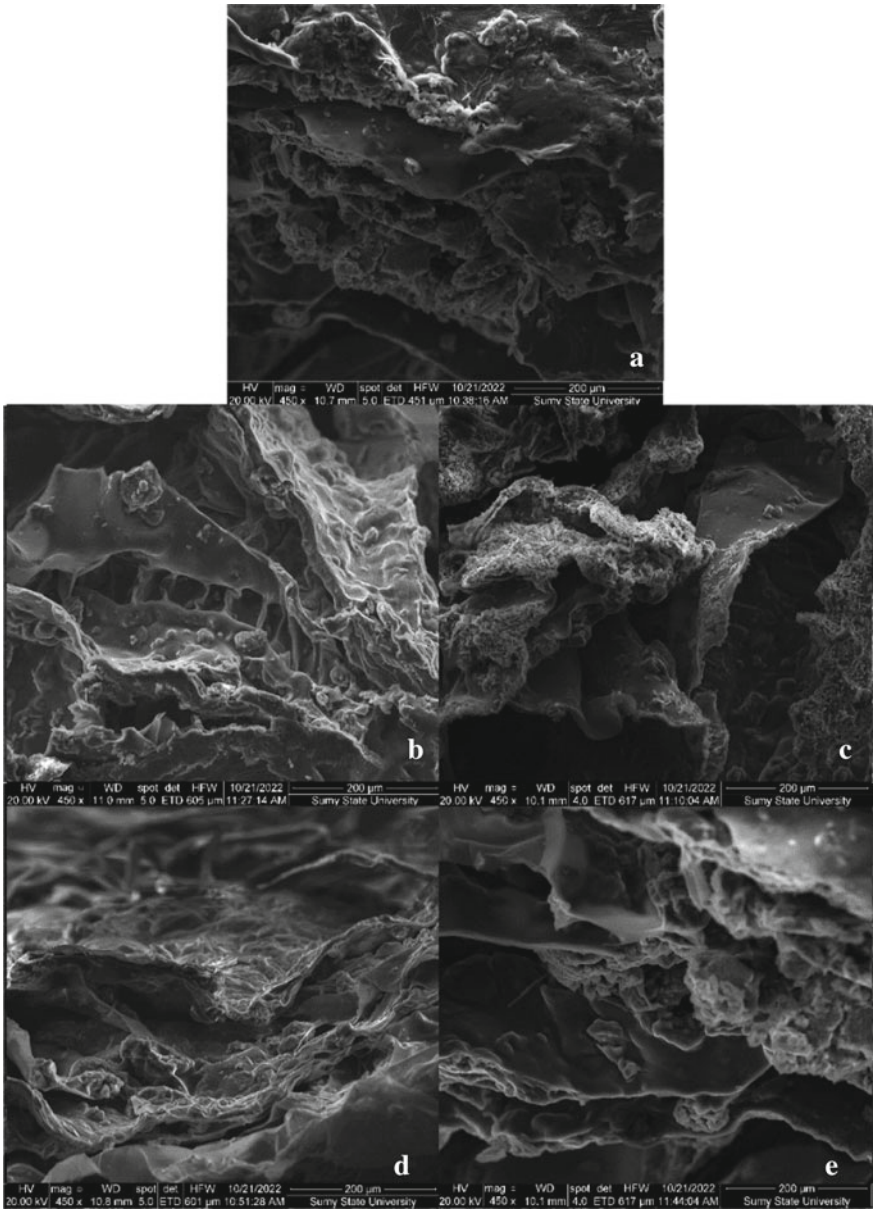

Fig. 4 SEM images of synthesized samples: Control (**a**), Ca, Zn, Cu, Ag containing composites—**b**–**e**, respectively

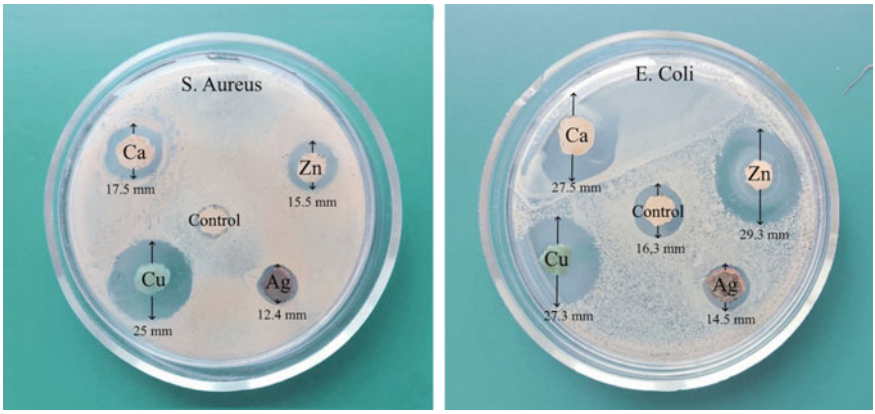

Fig. 5 Antimicrobial action of synthesized composites containing metal ions against *E. coli ATCC 25922* and *S. Aureus ATCC 25923* microorganisms

Table 1 Zones of growth inhibition of microorganisms under the influence of experimental samples

Sample	ZOI, mm		Integral indicator of antimicrobial activity (*A*)	
	E. coli ATCC 25922	*S. Aureus ATCC 25923*	Regarding chlorhexidine	Regarding metrogyl denta
Control	16.3 ± 0.15	1 ± 0.05	0.79	1.00
Ca	27.5 ± 0.2	17.5 ± 0.13	1.51	1.97
Zn	29.3 ± 0.14	15.5 ± 0.11	1.55	2.01
Cu	27.3 ± 0.16	25 ± 0.15	1.67	2.21
Ag	14.5 ± 0.1	12.4 ± 0.1	0.87	1.14

Integral index *A* of the sample's antimicrobial activity. $p \leq 0.05$

of antimicrobial activity was carried out in relation to the commercial Chlorhexidine and Metrogyl Denta, which are used as antimicrobials in dentistry. The applied vector theory made it possible to represent *A* as a vector in *n*-dimensional space with coordinates in the form of a growth inhibition zone for each test microorganism. The results showed that the value of *A* for samples containing Ca^{2+}, Zn^{2+}, Cu^{2+}, and Ag^{+} ions is close to or higher than for the above pharmaceuticals. The smallest A value is for the Control. According to methodological recommendations, the samples are classified as having medium antimicrobial activity, except for Control and Ag, whose antimicrobial activity is weak.

Scientific sources provide two main mechanisms of antimicrobial action: (a) the toxic effect of metal ions on the cell membrane of bacteria; (b) the toxicity of ROS (reactive oxygen particles), formed with the participation of ZnO, on the components of the bacterial cell. Antibacterial activity is the result of the formation of

such ROS as hydrogen peroxide (H_2O_2), peroxide anion (O^{2-}), and hydroxyl radicals (OH^-). These particles damage cellular components such as DNA, lipids, and proteins [1]. Positively charged metal ions can also directly interact with negatively charged components of the bacterial wall [10]. Composites containing ZnO disrupt the integrity of the cell membrane, which leads to damage to membrane proteins and the lipid layer [6]. In addition, it is shown that chelate complexes of chitosan with metal ions exhibit greater antimicrobial activity compared to pure chitosan [11]. Positively charged sites of CS, joining the negatively charged surface of a microbial cell, disrupt its metabolism.

4 Conclusions

ZnO-Alg/CS composites doped with Ca^{2+}, Zn^{2+}, Cu^{2+}, and Ag^+ ions were created for potential application in the treatment of damaged areas of the skin. Polyelectrolyte binding of oppositely charged polymer chains Alg and CS and additional cross-linking with metal ions ensure the stability of composites in a physiological environment and provide antimicrobial properties. Doping composites with metal ions increase the degree of porosity compared to the control sample, which positively affects the ability of the material to absorb liquid and exudate. The advantage of the repulsive energy of the same charged metal ions adsorbed on inorganic particles leads to the formation of a positive "wedging" pressure, which causes the repulsion of the surfaces and, in turn, affects the porosity.

It was experimentally proven that the Gram-negative microorganism *E. coli ATCC 25922* is more sensitive to the action of composites than the Gram-positive *S. Aureus ATCC 25923*. At the same time, Cu-doped samples exert an antimicrobial effect on both bacteria. The effect of Ca^{2+} ions in the composite is remarkable. Calcium is not an antibacterial agent, but it has antimicrobial activity in a complex with CS. The integrated indicator of antimicrobial activity for samples containing Ca^{2+}, Zn^{2+}, Cu^{2+}, and Ag^+ ions is close to or slightly higher than for commercial pharmaceutical agents Chlorhexidine and Metrogyl Denta.

Acknowledgements The National Research Foundation of Ukraine financially supported the research within the framework of the program Science for Security and Sustainable Development of Ukraine 0122U001154 and the Ministry of Science of Ukraine in the frame of a research topic 0122U000775.

References

1. L.C. Ann, S. Mahmud, S.K.M. Bakhori et al., Antibacterial responses of zinc oxide structures against *Staphylococcus aureus*, pseudomonas aeruginosa and streptococcus pyogenes. Ceram Int. **40**, 2993 (2014). https://doi.org/10.1016/j.ceramint.2013.10.008
2. S. Blatt, B. Al-Nawas, A systematic review of latest evidence for antibiotic prophylaxis and therapy in oral and maxillofacial surgery. Infection **47**, 519–555 (2019). https://doi.org/10.1007/s15010-019-01303-8
3. E.M. Costa, S. Silva, F.K. Tavaria, M.M. Pintado, Study of the effects of chitosan upon *Streptococcus mutans* adherence and biofilm formation. Anaerobe **20**, 27–31 (2013). https://doi.org/10.1016/j.anaerobe.2013.02.002
4. S. Koosehgol, M. Ebrahimian-Hosseinabadi, M. Alizadeh, A. Zamanian, Preparation and characterization of in situ chitosan/polyethylene glycol fumarate/thymol hydrogel as an effective wound dressing. Mater Sci. Eng. C **79**, 66–75 (2017). https://doi.org/10.1016/j.msec.2017.05.001
5. T. Kumar Giri, D. Thakur, Ajazuddin, et al., Alginate based hydrogel as a potential biopolymeric carrier for drug delivery and cell delivery systems: present status and applications. Curr. Drug Deliv. **9**, 539–555 (2012).https://doi.org/10.2174/156720112803529800
6. N. Padmavathy, R. Vijayaraghavan, Interaction of ZnO Nanoparticles with microbes—a physio and biochemical assay. J. Biomed. Nanotechnol. **7**, 813–822 (2011). https://doi.org/10.1166/jbn.2011.1343
7. W. Paul, C.P. Sharma, *Advances in Wound Healing Materials: Science and Skin Engineering* (Smit.RT Ltd., Shropshire, UK, 2015)
8. L. Pinheiro, C.I. Brito, V.C. Pereira et al., Susceptibility profile of *Staphylococcus epidermidis* and *Staphylococcus haemolyticus* isolated from blood cultures to vancomycin and novel antimicrobial drugs over a period of 12 years. Microb. Drug Resist. **22**, 283–293 (2016). https://doi.org/10.1089/mdr.2015.0064
9. A. Pogrebnjak, L. Sukhodub, L. Sukhodub et al., Composite material with nanoscale architecture based on bioapatite, sodium alginate and ZnO microparticles. Ceram Int (2019). https://doi.org/10.1016/j.ceramint.2019.01.043
10. R. Sinha, R. Karan, A. Sinha, S.K. Khare, Interaction and nanotoxic effect of ZnO and Ag nanoparticles on mesophilic and halophilic bacterial cells. Bioresour. Technol. **102**, 1516 (2011). https://doi.org/10.1016/j.biortech.2010.07.117
11. L. Sukhodub, Metal ions doped chitosan nanoparticles. J. Nano-Electron Phys. **6** (2014)
12. L.B. Sukhodub, G.E. Khrystian, L.F. Sukhodub et al., Composite materials based on zinc sulfide and zinc oxide: structural and biocidal properties. Ann. Mechnikov Inst. **4**, 34–39 (2016)
13. L.B. Sukhodub, M. Kumeda, V. Bielai, L.F. Sukhodub, Hydroxyapatite-biopolymers-ZnO composite with sustained ceftriaxone release as a drainage system for treatment of purulent cavities. Carbohydr. Polym. **266**, 118137 (2021). https://doi.org/10.1016/j.carbpol.2021.118137
14. L.F. Sukhodub, L.B. Sukhodub, O. Litsis, Y. Prylutskyy, Synthesis and characterization of hydroxyapatite-alginate nanostructured composites for the controlled drug release. Mater Chem. Phys. **217**, 228–234 (2018). https://doi.org/10.1016/j.matchemphys.2018.06.071
15. B. Sultankulov, D. Berillo, K. Sultankulova et al., Progress in the development of chitosan-based biomaterials for tissue engineering and regenerative medicine. Biomolecules **9**, 470 (2019). https://doi.org/10.3390/biom9090470

Synthesis of Silver Nanoparticles Using Ionic Liquid Solvent-Based Grape Pomace Extracts

Victoria Vorobyova, Margarita Skiba, Mykhaylo Kotyk, and Georgii Vasyliev

Abstract Aqueous and ionic liquid-based extracts of grape pomace were utilized for silver nanoparticles (AgNPs) synthesis. The ionic liquid-based extracts contained higher levels of phenolic acids and flavanols that are natural capping agents and showed higher synthesis efficiency. Three extracts of grape pomace (GPE) could produce silver nanoparticles. Specifically, syntheses silver nanoparticles by water and ionic liquid solvent GPE showed various sizes, 19–33 nm and 8–15 nm, respectively and various colloidal stability. The used DESs-based extracts lead to synthesis of silver nanoparticles with improved dispersion and colloidal stability. The effective colloid stability of AgNPs is believed to be the result of the DESs stability, used in the synthesis of colloidal system. All synthesized AgNPs by both water and DESs extracts showed activity against *Escherichia coli*, but the AgNPs prepared with DES have the highest antibacterial activity against microorganisms.

1 Introduction

The search for new methods of synthesis of nanomaterials belongs to the key priorities of the development of innovative, energy- and resource-saving "green" methods of modern chemical technology for the production of nanostructured oxide materials and attracts considerable attention of researchers, as indicated by the number of

V. Vorobyova (✉) · M. Kotyk · G. Vasyliev
National Technical University of Ukraine "Igor Sikorsky Kyiv Polytechnic Institute", Prosp. Peremohy 37, Kyiv 03056, Ukraine
e-mail: vorobyovavika1988@gmail.com

M. Kotyk
e-mail: m.kotyk@kpi.ua

G. Vasyliev
e-mail: g.vasyliev@kpi.ua

M. Skiba
Ukrainian State University of Chemical Technology, Gagarin Ave. 8, Dnipro 49005, Ukraine

O. Fesenko and L. Yatsenko (eds.), *Nanoelectronics, Nanooptics, Nanochemistry and Nanobiotechnology, and Their Applications*, Springer Proceedings in Physics 297,
https://doi.org/10.1007/978-3-031-42708-4_10

publications in leading world publications [1–3]. The work of domestic and foreign scientists in this field relates to increasing the effectiveness of traditional, mostly well-known, chemical methods. The use of solvothermal synthesis methods allows varying the structural and sorption characteristics, and the CVD method allows obtaining powders of different morphologies. However, the above-mentioned methods require further study in order to establish the possibility of obtaining a wider list of nanosized materials with a simultaneous study of the influence of the method and the conditions of the synthesis on the properties and morphology of the obtained materials and their multifunctional properties.

Today, green/phytochemical synthesis methods, which involve the use of plant extracts, have significant popularity [4–9]. An alternative develops the green method synthesized metal nanoparticles from corresponding metal ions using the reducing and capping agents of phytochemical from agro waste extracts. Among foreign scientists, "green" nanotechnologies, which use environmentally safe chemical, technological, and production processes, have acquired rapid development. At the same time, the "green" method is understood as the use of extracts of plant raw materials and their processing waste [4], as well as the use of physical methods of exposure: ultrasonic treatment [5] or microwave irradiation [6]. The advantages of these methods are the possibility of obtaining a wide range of nanomaterial with high reactivity and pronounced polyfunctional properties. In their work, foreign scientists use extracts of plant raw materials for the synthesis of nanosized particles of metals (Ag, Fe) [10–12] and oxide compounds of various component composition TiO_2, SnO_2, CuO, Ag–SnO_2 [13–23] and materials based on them for use as sorption-photocatalytic, sensory, antioxidant, anti-corrosion materials. The extracts play the role of both a reducing agent and a capping agent. Often, extracts are prepared with known solvents, such as water, ethanol, and mixtures thereof. The search for biodegradable and effective, "green" solvents for the extraction of natural organic compounds from plant raw materials is one of the main trends in the development of modern chemical technology and engineering. However, there are absolutely no studies on the use of plant extracts based on deep eutectic solvents for the phytochemical/biomimetic synthesis of nanomaterials [24–28]. For the extraction of natural secondary metabolites of plant raw materials, the overwhelming majority use toxic and aggressive organic solvents or the most common are "traditional" solvents. Deep eutectic solvent (DES) are a recently discovered category of potentially more stable alternative solvents. For the reasons set out above, the so-called low-temperature eutectic solvents, namely deep eutectic solvent are attractive, generally recognized in the world as absolutely safe, which fully comply with the principles of green chemistry and are considered 4th generation solvents for the chemical technology of the twenty-first century. These modern solvents have some advantages such as non-flammability, low toxicity, and biocompatibility. These solvents have special qualities which are not feasible with normal solvents, like lower melting mixtures, lower-transition temperature mixtures, or deep eutectic ionic liquids. Their properties can be adjusted by modifying the hydrogen bond acceptor/donor structures or by changing the molar ratio of their components. Due to its properties, the III type of DES is of the greatest interest. Therefore, there is a prospect of research and application of

this type of solvents for extraction of plant raw materials and synthesis of nanomaterials. Using these solvents, it is possible to increase the yield of phenolic compounds by increasing the operating temperature without damaging the active substances, due to the increase in the solubility and diffusion coefficients of polyphenolic compounds in the solvents. Their polarity can be changed by modifying their composition, so they can be used to solubilize a wide range of biologically active compounds. The studies consider DES based on choline chloride because of its historical primacy and practical qualities (low cost, zero toxicity, extensive previous industrial experience with this material). However, it has a certain drawback: extracts obtained on its basis are limited in practical use due to the presence of chloride in its composition. To expand the scope of application, it is necessary to use a less toxic acceptor for the formation of hydrogen bonds. The literature reports that betaine and proline can be an alternative to choline chloride. It is a cheap natural resource, biodegradable, non-toxic and can be obtained from sugar beets. At the same time, DESs based on betaine and proline have a wide prospect of application. There are publications in the literature that describe the use of aqueous-ethanol extracts of grape pomace for the synthesis of silver nanoparticles [27–29]. A fundamental flaw in water-based extracts is the absence of the necessary viscosity to ensure the structural stability of the medium, which requires using a lot of compounds to stabilization AgNPs. Thus, given the lack of research on "green"/phytochemical synthesis based on plant extracts obtained with the latest solvents, the authors suggest conducting research in this direction.

In this work, it is proposed to compare the physicochemical properties of silver nanoparticles obtained by synthesis using a traditional aqueous (water) extract of grape pomace (W-EGP) and based on a betaine/pyrrolidine-2-carboxylic acid-based natural deep eutectic solvent (DES-EGP).

2 Comparative Characterization of Grape Pomace Extract Obtained with Water and Deep Eutectic Solvents for Nanomaterials Synthesis

2.1 DES Preparation

DES was prepared according to the procedure described in previous works [29]. Betaine and Pyrrolidine-2-carboxylic acid (Sigma Aldrich, 98.9% purity) and 2-Hydroxypropanoic acid (*D,L*-lactic acid, Sigma Aldrich, 91.4% purity) to prepare the DES were used. (Table 1). For this, lactic acid and betaine were mixed in sealed glass flasks with a capacity of 100 ml, taken in molar ratios, respectively. The mixture was continuously stirred at a temperature of 60 °C at a speed of 400 rpm in a magnetic stirrer until the mixture formed a clear solution.

Table 1 Composition of the studied DESs and their abbreviations for AgNPs synthesis

DES-nominal composition	HBA	HBD	Molar ratio
DES-1	2-hydroxypropanoic acid	Pyrrolidine-2-carboxylic acid	2:1
DES-2	2-hydroxypropanoic acid	Betaine	2:1
Conventional solvent	H_2O		

2.2 Extraction Procedure

Aqueous and DES extractions of the grape pomace were done following the method described in previous work [29]. Prepared DESs were utilized to extract phytochemicals from grape pomace with 1:10 solid to liquid ratio, 45 min at room temperature. The suspension was then filtrated through a filter paper to obtain the extract. The macerated extracts using Whatman filter paper were filtered. The resulting extracts were named as follows: W-GPE and DES-1, DES-2.

2.3 Extract Composition

The analysis of the extracts was carried out using the methods of high-performance liquid chromatography with a diode array detector (HPLC–DAD) and high-performance liquid chromatography-mass spectrometry (HPLC–MS). The identification was confirmed by comparing the retention time, UV and mass spectra of the detected compound with the spectra of a pure standard. LC-DAD analysis was performed on an Agilent Technologies 1260 Infinity HPLC equipped with a Thermo Scientific Hypersil Gold C18 column (150 × 4.6 mm, 5 μm) and a diode array detector. The mobile phases were (A) 2.5% v/v acetic acid in water and (B) 2.5% v/v acetic acid in methanol, flow rate 1 mL/min, temperature column temperature was 25 °C, and the injection volume—10 μl. Before introducing the samples, a 5-min equilibration with 5% B was carried out. Elution was carried out according to a linear gradient with the following conditions: 0 min, 5% B; 20 min, 20% B; 15 min, 40% B; 18 min, 30% B; 28 min, 20% B; 35 min, 0% B. The run time was 35 min, and data were recorded at 325 and 354 nm for the identification of phenolic acids, flavonols, and flavonoids.

The identification was confirmed by a liquid chromatography-mass spectrometric system. LC–DAD–MS analysis was performed on a Thermo Fisher Scientific UltiMate 3000 RSLC equipped with a Thermo Scientific Hypersil Gold aQ C18 column (150 × 4.6 mm, 5 μm particle size), a diode array detector coupled to a Thermo Scientific TSQ triple quadrupole mass—Fortis spectrometer with ESI source. The mobile phases were (A) 0.1% v/v formic acid in water and (B) methanol, the flow rate was 0.6 mL/min, the column temperature was 25 °C, and the injection volume

was 5 mcl. Equilibration with 10% B was carried out for 3 min before the introduction of samples. Elution was carried out according to a linear gradient with the following conditions: 0 min, 10% B; 30 min, 50% B; 45 min, 100% B; 50 min, 100% B; 60 min, 10% B. Run time was 60 min, and data were recorded at 256, 282, 325, and 354 nm to identify phenolic acids, flavonols, and flavonoids. The electrospray ionization (ESI) source was operated in negative ion mode at 4.5 kV and scanned from m/z 170 to 700.

Figure 1 shows percentage (%) of the polyphenolic compounds extracted from the grape pomace extracts obtained by DESs and water (Fig. 1). The use of water made it possible to extract flavonols and hydroxycinnamic acids; therefore, it was used as a standard to evaluate the diversity of the studied extracted compounds from grape pomace. According to the present study, the main component of water grape pomace extract is hydroxycinnamic acids.

Soluble conjugated flavonoids or phenols were the main phenolic components that could be isolated from grape pomace. It was found that the phenolic acids are represented by compounds: gallic acid, protocatechuic acid, *p*-hydroxybenzoic acid, coutaric acid, caffeic acid, epicatechin, syringic acid, *p*-coumaric acid. In particular, hydroxycinnamic acids are eluted in the first 10 min of working time, while flavonoids are eluted later. In addition, hydroxycinnamic acids showed higher intensity peaks at 325 nm, while flavonoids are more easily seen at 354 nm. Preliminary identification of anthocyanins and hydroxycinnamic acids was carried out using UV spectra of

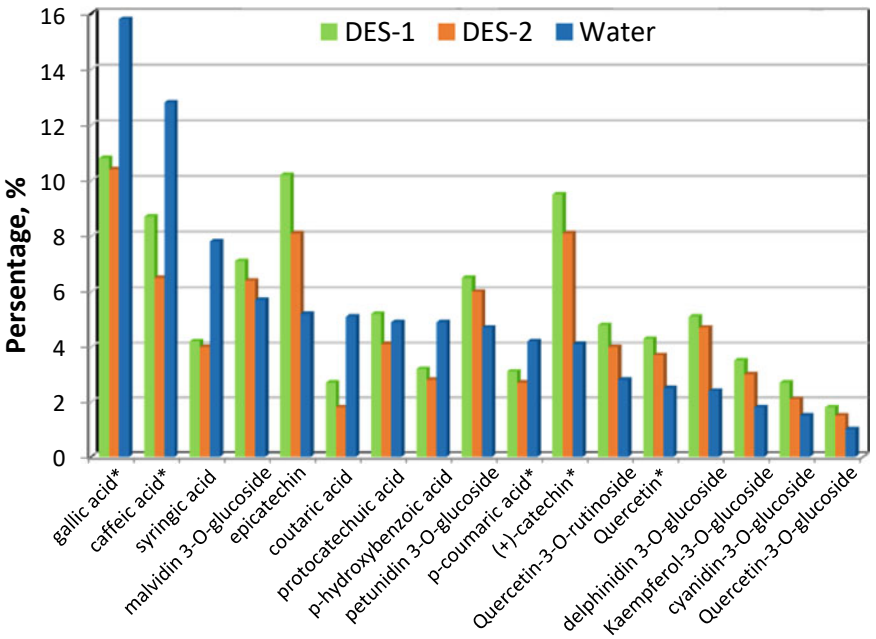

Fig. 1 Percentage (%) the polyphenolic compounds extracted from the grape pomace extracts

each peak obtained on DAD-LC chromatograms and compared with UV spectra of standard compounds. The main component of DESs grape pomace extract is anthocyanins. It was established that the higher the content of flavonoids and anthocyanin is observed in DES solvents. Grape pomace extract mainly consists of phenolic compounds, predominantly 3,4,5-trihydroxybenzoic acid (gallic acid 10.8%) and 3-(3,4-Dihydroxyphenyl)-2-propenoic acid (caffeic acid (8.7%). When using water as a solvent, a low content of flavonoids in the extract was recorded. Because extraction with this solvent at a pH close to neutral favors the extraction of more polar biologically active compounds, such as hydroxycinnamic acids. For example, caffeic and syringic acids are more soluble in water than flavonoids. These compounds are known today for their reducing ability. The dominant anthocyanins were identified are petunidin 3-O-glucoside and delphinidin 3-O-glucoside. Comparative characteristics of the component composition of the extracts indicate that the aqueous extract contains phenolic acids to a greater extent. While the extracts obtained by DES contain anthocyanins and flavonoids to a greater extent. The analysis of the component composition the aqueous grape pomaces extract indicate that it contains a more lower content of anthocyanins and higher content of phenolic acids therefore is a probably can provide higher reducing capacity. While the extract obtained with DES, having a similar composition, but higher content of anthocyanins, flavonoids and higher viscosity and may be more effective for stabilizes colloidal stability.

2.4 Reducing Power of the Extracts

Due to high polarity of the DES are often used as solvent for extraction polyphenolic compounds. DES and water extracts were characterized for their total phenolic content (TPC), total flavonoids content (TFC), and reducing activity. In general, the higher the total phenolic contents in the extract, the greater the reducing forces. The highest content of TFC was found in the extracts obtained by DES, namely in the extracts obtained by DES-1. The extract obtained by DES contained a large amount of flavonoids compared with water extract. This could be associated with interactions that are present due to hydrogen bonds, formed among molecules of DES and flavonoids of extract. The polarity and viscosity of DES are the main properties that affect the extraction of flavonoids. The data obtained are consistent with the results of chromato-mass spectral analysis, according to which the extracts obtained by DES have a high content of anthocyanins and catechins, which belong to flavonoids. Comparing extracts of both type solvents, it was observed that DES was able to present good extraction of flavonoid content.

Figure 2 presents a bar graph representing reducing power of water grape pomace extract and DES-based extracts. The reducing ability of the aqueous extract is slightly higher than that of the extracts obtained by DES. However, the values of reducing capacity of DESs are of the same order, so it can be proposed that the reducing ability of the studied extracts is sufficient for the reduction of silver ions.

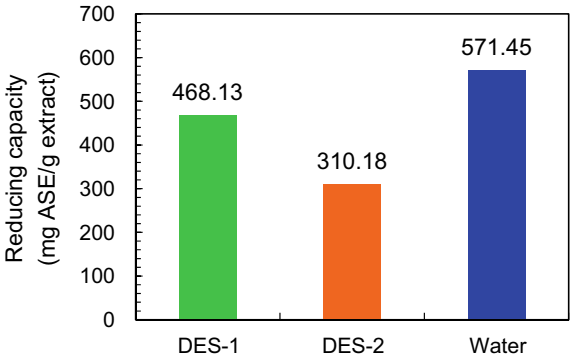

Fig. 2 Reducing power of the grape pomace extracts evaluated by phosphomolybdenum method

Chemical evaluation of reducing ability was compared to the electrochemical one. From electrochemical point of view, a reduction ability agrees well with the ability to donate an electron and can be estimated by the value of oxidation potential and anodic current.

The potential scan range was –1.0–1.2 V/SSCE with a scan rate of 50 mV/s. The scan started from the OCP in cathodic direction and reversed once the potential reached 1.2 V/SSCE. Totally, five cycles were measured in each solution to ensure data convergence. The electrochemical measurements for water solution were not performed, due to low width of electrochemical stability window on platinum electrodes. The Versa STAT 3 Potentiostat Galvanostat (AMETEK Scientific Instruments, USA) was used to conduct polarization measurements.

The cyclic voltammograms are shown in Fig. 3. Curves for both extracts shows to reduction peaks in the similar potential range: − 0.17 and + 0.24 V/SSCE for DES-1 and − 0.10 and + 0.39 V/SSCE for DES-2. However, the anodic current is nearly one order of magnitude higher for DES-1 (1.1 mA) comparing to DES-2 (0.17 A) meaning DES-1 would act better as a reducing agent in the synthesis of NPs. The electrochemical approach agrees well with the phosphomolybdenum method, where DES-2 also showed lower reducing capacity.

2.5 Synthesis Procedure of Silver Nanoparticles (AgNPs)

In this study, grape pomace DESs extract (DES-1 and DES-2-GPE, and water extract (W-GPE) was used to synthesize AgNPs. Green synthesis of AgNPs was synthesized from 0.01 M $AgNO_3$ using the reducing and capping agents of water and ionic liquid-based grape pomace extracts. The equivalent volumes of the extract solution and 0.01 M $AgNO_3$ were heated separately in the glass beakers in the water bath to the temperature of 80 °C. The success of biosynthesized of Ag NPs was confirmed by spectroscopic study.

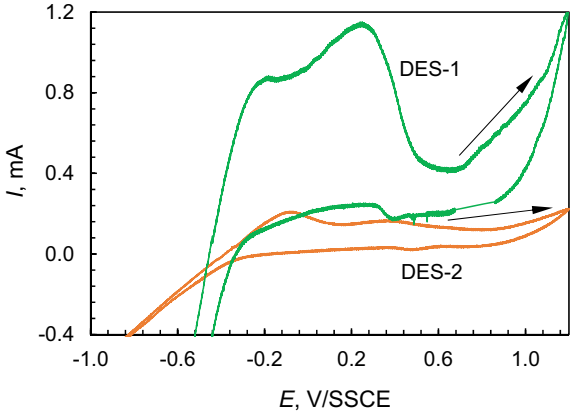

Fig. 3 Cyclic voltammograms for ionic liquid-based grape pomace extract, showing the different reducing ability depending on the nature of the DES. Arrows indicate the scan start direction

2.6 UV–vis Characterization of AgNPs

The UV–visible spectrum of AgNPs exhibits the maximum absorption at 436 nm after 48 min, 48 h, 96 h, and 1 month after the synthesis of nanoparticles (Fig. 4).

For the reaction mixtures in which $AgNO_3$ was mixed with only DESs was no recorded by UV–vis spectra surface plasmon resonance which indicates the no color change and formation of Ag NPs. Comparison of the UV spectra (Fig. 4) indicates that the aqueous extract has a higher reduction power than the DES extracts. Thus, UV spectra of colloidal systems W-GTE obtained using an aqueous extract (after 45 min reaction) of grapes contained more intensive peak (3.23 a.u.) confirming the formation of nanoparticles in the range 400–450 nm. Probably, after 45 min, the maximum amount of silver nitrate was reduced in the reaction mixture with water extract. Plasmon resonance centered at 430 nm which indicates that the particle size in reaction mixture is higher, and the product of synthesized AgNPs is more polydisperse. The UV–visible spectrum of AgNPs synthesized by W-GPE exhibits the maximum absorption also at 436 nm and the position of the peak remains unchanged despite of the 48–96 h of the storages time. The dispersed solutions of reaction mixtures synthesized by the extracts based on DESs have higher values of the absorption spectra after 96–120 h. The data obtained confirm that the reducing ability of the extract based on proline-lactic acid (DES-1) is higher than that of betaine-lactic acid (DES-2), as evidenced by the higher values of the absorption spectra (2.8 a.u. and 1.5 a.u., respectively) (Fig. 5). When colloid systems by uses of DES-based extracts were formed, the signal peak of absorption spectra was vitiated from 2.11 to 2.03 during the time, which was mainly due to the formation of an intermolecular hydrogen bond between organic compounds and DES. After 96 h the UV-peak in the visible spectrum for the system of nanoparticle that was synthesis by using water grape pomace extract was decreased.

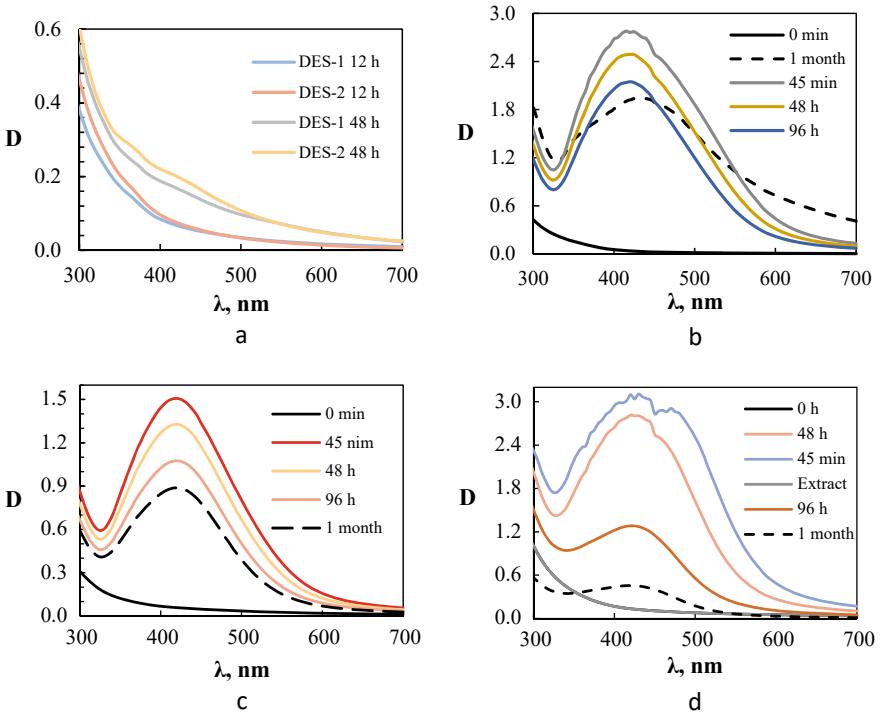

Fig. 4 UV–visible spectra of $AgNO_3$ with pure DESs (**a**) in water and "green" synthesized silver nanoparticles with grape pomace extract obtained by DES-1 (**b**), DES-2 (**c**), W-GPE (**d**)

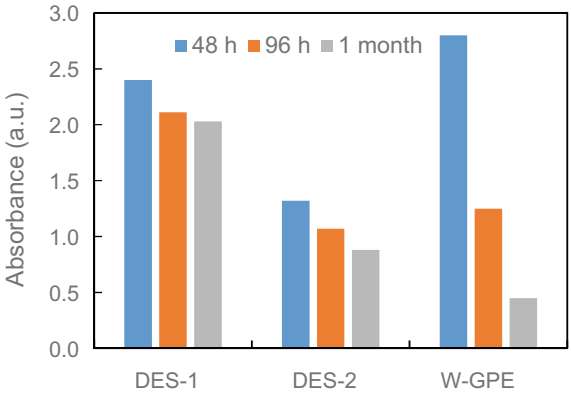

Fig. 5 Characterization results (absorbance of UV–visible spectra) of AgNPs depending on the type of the solvent that be used for extracted of grape pomace and storage time

Analysis of the data obtained indicates that both studied synthesized systems are stable even after a long period of time, namely 1 month. Generally speaking, the reducing of silver is mainly influenced by reducing capacity of the compounds of the extract but on the stability of system influence intermolecular interactions between the capping compounds of the extracts and DES. The UV–Vis spectra show that only DESs (Fig. 4a) used by the synthesis of AgNPs were not as efficient as DES-based extract grape pomace (Fig. 4b, c). Specifically, solution DES with silver barely displayed an SPR band after 45 min. These results indicate that a higher concentration of phenolic compounds in the aqueous extract of grape pomace results in a higher reducing capacity of the extract. Thus, it can be concluded that the higher reducing potential of the water grape pomace extract leads to the more efficient synthesis of silver nanoparticles. However, when using an aqueous extract, the presence of capping components is not completely sufficient, which leads to the formation of particles of a larger size and polydispersity. While when uses DESs extract, an additional contribution to colloidal stability is probably provided by an ionic liquid. Due to its high viscosity, DES acts as a structuring component on the stabilization process of AgNP. All synthesis colloidal systems appeared to contain AgNPs on the UV–Vis spectra. However, the intensity the absorbance of UV-peak in visible spectra for the DES-1-GPE was higher than for the DES-2 extract. Thus, the lower synthesis efficiency of AgNP by uses DESs extracts was apparently associated with lower phenolic aced and flavanols levels. It should be noted that DES-based systems are more stable. After 1 month the intensity the absorbance of the UV-peak in visible spectra for the extract DES-1 and DES-2 were higher than for the W-GPE. Through UV-analysis it was found that DESs in extracts exerted constructive effects on AgNP synthesis, although the DESs themselves cannot reduce silver ions. This suggests that these DES may be intermolecular capping compounds during the formation of AgNP.

2.7 Morphology of Silver Nanoparticles

Surface morphology of the prepared AgNPs was evaluated using scanning electron microscopy. The SEM images clearly showed a uniform spherical shape with smooth surface of the synthesized AgNPs by DES and water-based grape pomace extract. These results indicate that AgNPs mainly in the spherical shape of nanoparticles (8–15 nm) (Fig. 6). The SEM images of AgNPs synthesized by water-based grape pomace extract showed the existence of small spherical nanoparticles with a size ranged from 19 to 33 nm. Although all systems were either spherical or nearly spherical, the DES-based AgNPs displayed different sizes than the water-based AgNPs. An addition, compared with the water extract, the morphology of the AgNPs synthesized by DES-based extracts of did not change significantly depending on the type of ionic liquid, which further showed that DES has capping action. Therefore, it is supposed that DES may play role by functioning on the surface of the AgNPs to enhance their dispersion. The two systems of AgNPs (DES-1 and DES-2) displayed

different stability and the same morphology. It should be noted that the type of extract also exhibited varying degrees of effects on the stability of colloidal system. However, AgNPs synthesized by the DES extract had better dispersion than from the water extract, what does a narrow and clear peak indicate on UV–vis spectra. Between the two extracts the water-based one a more showy effect on the synthesis, but DESs-based extracts additional on capping process. The positive capping effect of the DES facilitates the stability to the surfaces of the Ag^{o}, which can enhance their property in the application.

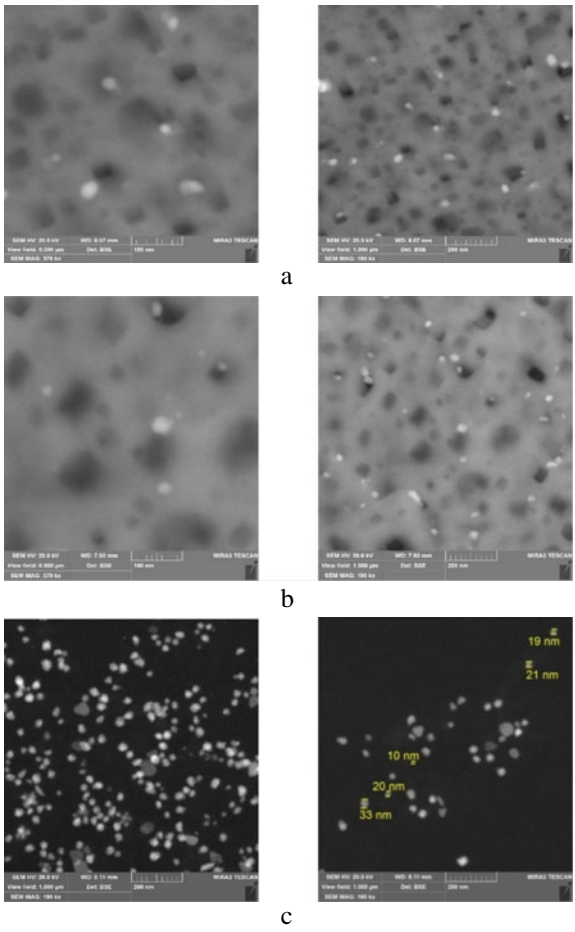

Fig. 6 SEM analysis of "green" synthesized AgNPs with grape pomace extract obtained by DES-1 (**a**), DES-2 (**b**), W-GPE (**c**)

Table 2 Total phenolic and flavonoid contents in grape pomace extracts

Extract	The total phenolic content (TPC)	The total flavonoid content (TFC)
DES-1	92.15 ± 1.75	51.36 ± 1.22
DES-2	80.75 ± 1.75	47.41 ± 1.22
Water	82.10 ± 1.75	19.11 ± 1.21

Table 3 Inhibition zone by AgNPs as standard antibiotics for Gram-negative bacteria

A type of bacteria	Exposure time (h)	AgNPs	ZI (mm)
E. coli ATCC 25922	24	DES-1	7.1 ± 0.1
		DES-2	4.5 ± 0.1
		W-GPE	2.3 ± 0.1
	48	DES-1	10.2 ± 0.1
		DES-2	8.0 ± 0.1
		W-GPE	7.2 ± 0.1

2.8 Antibacterial Properties

The formation of AgNP based on DES-based extract makes a high degree of versatility, suitable for a variety of applications. The obtained silver nanoparticles show disinfectant (antimicrobial) properties (Table 2) against pathogenic bacteria *Escherichia coli* ATCC 25922 [30]. Table 3 presents the results of antibacterial activity for the AgNPs. The entire colloids systems variable ZI was fixed. The result showed that the W-GPE exhibited negligible inhibition zone against strain of bacteria. A maximum of 10.2 mm diameter ZI was recorded for DES-1, followed by 8 mm against DES-2 and $\leq$ 7.0 mm against W-GPE.

3 Conclusions

In this study, green synthesis of Ag NPs was successfully synthesized using the reducing and capping agents of aqueous and ionic liquid-based extracts of grape pomace. During extraction with DES, it was possible to obtain a complex mixture of hydroxycinnamic acids and flavonoids, while the traditional solvent used mainly hydroxycinnamic acids. The AgNPs was characterized by UV and SEM analysis result which confirmed the spherical form of nanosilver. The ionic liquid-based GPE shows profitably effects on the synthesis efficiency and nanoparticle properties of AgNPs as compared with water-based. The results showed that DESs provide high extraction yields for grape pomace green reducing compounds which could potentially improve effectiveness process of synthesis. It was revealed that the positive effects of DESs extracts originated from their combined actions as extraction solvents

and stable colloids media. AgNPs exhibited antimicrobial activity against for Gram-negative (*E. coli*) bacteria. This work broadens the understanding influence of DES relatively of the improving the stability colloid systems for their next industrial application.

Acknowledgements The authors thank students of National Technical University of Ukraine «Igor Sikorsky Kyiv Polytechnic Institute» for actively participating in the discussion on the study topic.

Funding Statement This work was supported by the Ministry of Education and Science of Ukraine [registration no. 0121U100409, 2021].

References

1. M. Rafique, I. Sadaf, M.S. Rafique et al., A review on green synthesis of silver nanoparticles and their applications. Artif. Cells Nanomed. Biotechnol. **45**(7), 1272–1291 (2017). https://doi.org/10.1080/21691401.2016.1241792
2. P. Phanjom, G. Ahmed, Effect of different physicochemical conditions on the synthesis of silver nanoparticles using fungal cell filtrate of *Aspergillus oryzae* (MTCC No. 1846) and their antibacterial effect. Adv. Nat. Sci. Nanosci. Nanotechnol. **8** (2017). https://doi.org/10.1088/2043-6254/aa92bc
3. S. Iravani, H. Korbekandi, S.V. Mirmohammadi et al., Synthesis of silver nanoparticles: chemical, physical and biological methods. Res. Pharm. Sci. **9**, 385–406 (2014)
4. V.K. Sharma, C.M. Sayes, B. Guo et al., Interactions between silver nanoparticles and other metal nanoparticles under environmentally relevant conditions: a review. Sci. Total Environ. **653**, 1042–1051 (2019). https://doi.org/10.1016/j.scitotenv.2018.10.411
5. A.A. Ramanathan, M.W. Aqra, An overview of the green road to the synthesis of nanoparticles. J. Mater. Sci. Res. Rev. **2**(3), 1–11 (2019). https://doi.org/10.9734/JMSRR/2019/46014
6. G. Vasyliev, V. Vorobyova, M. Skiba, L. Khrokalo, Green synthesis of silver nanoparticles using waste products (apricot and black currant pomace) aqueous extracts and their characterization. Adv. Mater. Sci. Eng. **2020**, 4505787 (2020). https://doi.org/10.1155/2020/4505787
7. G. Vasyliev, V. Vorobyova, Valorization of food waste to produce eco-friendly means of corrosion protection and green synthesis of nanoparticles. Adv. Mater. Sci. Eng. **2020**, 6615118 (2020)
8. K. Mcnamara, S.A.M. Tofail, K. Mcnamara et al., Advances in physics: X nanoparticles in biomedical applications. Adv. Phys. X **2**, 1–35 (2017). https://doi.org/10.1080/23746149.2016.1254570
9. O.A. Pivovarov, M.I. Skiba, A.K Makarova et al., One-pot synthesis of silver nanoparticles using nonequilibrium low temperature plasma in the presence of polyvinyl alcohol. Voprosy khimii i khimicheskoi tekhnologii. **3**, 113–120 (2018)
10. M.I. Skiba, A.A. Pivovarov, A.K. Makarova, et al., Plasma-chemical synthesis of silver nanoparticles in the presence of citrate. Chem. J. Moldova. **13**(1), 7–14 (2018). https://doi.org/10.19261/cjm.2018.475
11. K.M.M. Abou El-Nour, A. Eftaiha, A. Al-Warthan et al., Synthesis and applications of silver nanoparticles. Arab. J. Chem. **3**, 135–140 (2010). https://doi.org/10.1016/j.arabjc.2010.04.008
12. S. Ahmed, M. Ahmad, B.L. Swami, S. Ikram, A review on plants extract mediated synthesis of silver nanoparticles for antimicrobial applications: a green expertise. Int. J. Adv. Eng. Technol. **7**, 17–28 (2016). https://doi.org/10.1016/j.jare.2015.02.007
13. V. Vorobyova, G. Vasyliev, M. Skiba, Eco-friendly "green" synthesis of silver nanoparticles with the black currant pomace extract and its antibacterial, electrochemical, and antioxidant activity. Appl. Nanosci. **10**, 4523–4534 (2020). https://doi.org/10.1007/s13204-020-01369-z

14. N. Tarannum, Y.K. Gautam, Facile green synthesis and applications of silver nanoparticles: a state-of-the-art review. RSC Adv. **9**(60), 34926–34948 (2019). https://doi.org/10.1039/C9RA04164H
15. J. Singh, T. Dutta, K.H. Kim et al., Green synthesis of metals and their oxide nanoparticles: applications for environmental remediation. J. Environ. Nanotechnol. **16**(1), 84 (2018). https://doi.org/10.1186/s12951-018-0408-4
16. S. Ghotekar, T. Pagar, S. Pansambal, et al., A review on green synthesis of sulfur nanoparticles via plant extract, characterization and its applications. Adv. J. Chem. Sect. B. **2**(3), 128–143 (2020). https://doi.org/10.33945/SAMI/AJCB.2020.3.5
17. S. Li, B. Zhou, B. Ren et al., Preparation of MgO nanomaterials by microemulsion-based oil/water interface precipitation. Mater. Lett. **171**, 204–207 (2016). https://doi.org/10.1016/j.matlet.2016.02.048
18. V. Pillai, P. Kumar, M.J. Hou, P. Ayyub et al., Preparation of nanoparticles of silver halides, superconductors and magnetic materials using water-in-oil microemulsions as nano-reactors. Adv. Coll. Interface Sci. **55**, 241–269 (1995). https://doi.org/10.1016/0001-8686(94)00227-4
19. R.D. Rivera-Rangel, M.P. González-Muñoz, M. Avila-Rodriguez et al., Green synthesis of silver nanoparticles in oil-in-water microemulsion and nano-emulsion using geranium leaf aqueous extract as a reducing agent. Colloids Surf., A **536**, 60–67 (2018)
20. A. Abo-Hamad, M. Hayyan, Abdul Hakim, M. AlSaadi et al., Potential applications of deep eutectic solvents in nanotechnology. Chem. Eng. J. **273**, 551–567 (2015).https://doi.org/10.1016/j.cej.2015.03.091
21. J.-S. Lee, Deep eutectic solvents as versatile media for the synthesis of noble metal nanomaterials. Nanotechnol. Rev. **6**(3) (2017). https://doi.org/10.1515/ntrev-2016-0106
22. A. Safavi, M. Shekarnoush, M. Ajamian, High-yield synthesis, characterization, self-assembly of extremely thin gold nanosheets in sugar based deep eutectic solvents and their high electrocatalytic activity. J. Mol. Liq. **279**, 208–223 (2019). https://doi.org/10.1016/j.molliq.2019.01.111
23. A. Söldner, J. Zach, M. Iwanow et al., Preparation of magnesium, cobalt and nickel ferrite nanoparticles from metal oxides using deep eutectic solvents. Chem. Eur. J. **22**(37), 13108–13113 (2016). https://doi.org/10.1002/chem.201602821
24. D.O. Oseguera-Galindo, R. Machorro-Mejia, N. Bogdanchikova et al., Silver nanoparticles synthesized by laser ablation confined in urea choline chloride deep-eutectic solvent. Colloid Interface Sci. Commun. **12**, 1–4 (2016). https://doi.org/10.1016/j.colcom.2016.03.004
25. W. Da Silva, C.M.A. Brett, Novel biosensor for acetylcholine based on acetylcholinesterase/poly(neutral red)—deep eutectic solvent/Fe_2O_3 nanoparticle modified electrode. J. Electroanal. Chem. **872**, 114050 (2020). https://doi.org/10.1016/j.jelechem.2020.114050
26. F. Aghazadeh, M. Aghazadeh, Effects of deep eutectic solvents in prearation of nanoparticles TiO_2. Int. J. Bio-Inorg. Hybr. Nanomater. **6**(4), 215–220 (2017). http://ijbihn.iauvaramin.ac.ir/article_660057_33411bbb370d1c83fba283a2ab449298.pdf
27. G.D. Saratale, R.G. Saratale, K. Dong-Su et al., Exploiting fruit waste grape pomace for silver nanoparticles synthesis, assessing their antioxidant, antidiabetic potential and antibacterial activity against human pathogens. Novel Approach Nanomater. **10**(8), 1457–1472 (2020). https://doi.org/10.3390/nano10081457
28. M. Skiba, V. Vorobyova, Green synthesis of silver nanoparticles using grape pomace extract prepared by plasma-chemical assisted extraction method. Mol. Cryst. Liq. Cryst. **674**(1), 142–151 (2018). https://doi.org/10.1080/15421406.2019.1578520
29. G. Vasyliev, K. Lyudmyla, K. Hladun et al., Valorization of tomato pomace: extraction of value-added components by deep eutectic solvents and their application in the formulation of cosmetic emulsions. Biomass Convers. Biorefinery. **12**, 95–111 (2022). https://doi.org/10.1007/s13399-022-02337-z
30. N. El-Desouky, K. Shoueir, I. El-Mehasseb et al., Synthesis of silver nanoparticles using bio valorization coffee waste extract: photocatalytic flow-rate performance, antibacterial activity, and electrochemical investigation. Biomass Conv. Bioref. (2022). https://doi.org/10.1007/s13399-021-02256-5

Effect of Silver Nanoparticles on Cryopreserved Mesenchymal Stem Cells from Cartilage Tissue

N. O. Volkova, L. V. Stepanyuk, M. S. Yukhta, and A. M. Goltsev

Abstract The finding of the presence/absence of silver nanoparticles (AgNPs) cytotoxic action is important direction of nanobiotechnological researches. The influence of AgNPs on viability, DNA fragmentation, processes apoptosis/necrosis, morphological characteristics, and proliferative potential of cryopreserved mesenchymal stem cells (CrMSCs) from cartilage tissue was investigated. The AgNPs with an average size of 15 nm were used in the study. CrMSCs from cartilage tissue were incubated with AgNPs at final concentrations of 0 (control), 4, 6, 10, 20 μg/mL for 1 h. The use of 4 and 6 μg/mL AgNPs did not influence on studied parameters in CrMSCs from cartilage tissue. AgNPs at concentrations of 10 and 20 μg/mL decreased the clonogenic potential (1.3- and 1.4-fold, respectively), proliferative activity (1.2- and 1.6-fold, respectively), and synthesis collagen type II (1.6- and 1.9-fold, respectively) if compared with the control. Morphological characteristics were also changed compared to control samples on the 10th day of culturing of cartilage CrMSCs after preliminary incubation with AgNPs at concentrations of 10 and 20 μg/mL. Thus, it was found that AgNPs in concentrations of 4 and 6 μg/mL are safe for CrMSCs from cartilage tissue, while increasing up to 10 μg/mL has a toxic effect that manifested by the change of morphological and functional characteristics. The presented results are belonged to the field of applied nanobiotechnology that spreads to the regenerative medicine, especially in the area of cartilage restoration.

1 Introduction

In the field of medicine, silver has been used for a long time. Due to the unique physical and chemical properties and generally accepted method of synthesis, silver nanoparticles (AgNPs) are very attractive for use in biomedical products. A number of works have shown that nanoparticles of noble metals (gold, silver, platinum) can

N. O. Volkova (✉) · L. V. Stepanyuk · M. S. Yukhta · A. M. Goltsev
Institute for Problems of Cryobiology and Cryomedicine, NAS of Ukraine, Pereyaslavska Str. 23, Kharkiv 61016, Ukraine
e-mail: volkovana781@gmail.com

O. Fesenko and L. Yatsenko (eds.), *Nanoelectronics, Nanooptics, Nanochemistry and Nanobiotechnology, and Their Applications*, Springer Proceedings in Physics 297,
https://doi.org/10.1007/978-3-031-42708-4_11

be used as reducers of oxidative stress in tissues [1, 2]. Therefore, the use of metal nanoparticles as components of cell therapy is a promising direction in the creation of the novel nanomedical technologies. And many among them have been developed just on the basis of AgNPs [1–3]. Due to its antimicrobial activity, silver nanoparticles are already used in medicine for a long time, for example, for coating catheters or implant materials; however, there are some reports of adverse reactions after using wound patches that contained AgNPs [4, 5]. In the authors' research, it was shown that nanoparticles of metals, such as gold and silver, when interacting with cells, are able to influence their enzymatic activity, exhibit antioxidant and antimicrobial properties [6, 7]. Although the use of nanoparticles as a component of combination therapy can significantly improve treatment outcomes and the potential is significant, there are still many challenges that need to be addressed before they can be adopted for clinical use.

Except medical purpose, nanosized silver particles with a diameter of 1–100 nm have been widely used commercially. But it should be noted that nanoparticles from different manufacturers have different physical and chemical characteristics, which can cause different reactions in biological systems, namely, cause cytotoxicity, provoke carcinogenesis, and change differentiating properties. Larger AgNPs are reported to have higher reactivity due to their larger surface area [8]. The cytotoxicity of AgNPs depends on such factors as size, concentration, surface functionalization, dispersion [9]. Thus, in the studies of the authors, it was shown that the size of AgNPs is an important factor in their cytotoxicity and genotoxicity, and the toxic effect was realized through the activation of the processes of apoptosis and necrosis [10].

Silver nanoparticles can enter the human body in various ways (for example, inhalation, injection, ingestion, or physical contact with intact skin and mucous or wounds). Obviously, caution is necessary in the use of products containing AgNPs, because some data from in vivo experiments indicate that even low concentrations of nanoparticles can be toxic in some cases [9]. In addition, AgNPs have the ability to pass through biological membranes, penetrate even very small capillaries throughout the body, thereby accumulating in cells [10]. Thus, subcutaneous injections of a solution of gold nanoparticles into rats lead to their distribution in various organs, including kidneys, liver, spleen, brain, and lungs. In addition, repeated intravenous administration of AgNPs to rats led to their accumulation in liver, lungs, and spleen [11].

Cytotoxicity of AgNPs for cartilage stem cells has been examined in a few in vivo and in vitro studies so far although cell type and their source are also of great importance in this matter. Earlier several research groups have shown that cells derived from cartilage tissue also meet the criteria for MSCs. They have high proliferative and clonogenic potential, multipotent properties, and an immunophenotype inherent to MSCs. These cells in the literature [12] can be mentioned as "cartilage-derived stromal cells", "dedifferentiated chondrocytes", or "articular-derived dedifferentiated chondrocytes". It should be noted that the regulators of prochondrogenic cells and direct chondrogenic differentiation are a number of intracellular signaling molecules and growth factors [13].

It is also known that the physical and chemical properties of nanosized materials can change depending on the administrated dose. Nevertheless, there is a serious lack of information on the biological activity of nanosized silver in mammalian tissue cells. Mammalian organism consists of a large number of stem and specialized cell types, for example, bone marrow MSCs, skin epidermal cells, neuronal cells or cells of the immune system [14]. However, not all cells in the body are capable of proliferation and differentiation. In general, only stem cells and progenitor cells have the ability to differentiate into specialized cell types [15]. During differentiation, some genes are activated and others on the contrary are deactivated that leads to the appearance of specialized structures and the production of specific proteins typical for each type of cells. Thus, the influence of nanoparticles on stem cells can lead to unexpected consequences in the functioning of organs and tissues until all the cells that arose during the division of primary stem cells cease to exist. So, MSCs of cartilage tissues of rats were chosen as a model object for studying the effect of AgNPs on stem cells as a potential cell source for arthritis therapy.

The aim of the work is to study the effect of silver nanoparticles on the morphological and functional characteristics of cryopreserved mesenchymal stem cells from cartilage tissue under culturing.

2 Materials and Methods

Outbreed white sexually immature male rats were used in the study. All the manipulations were carried out in accordance to the Euroconvention for the protection of vertebrate animals used for experimental and other scientific purposes (Strasbourg, 18.03.1986). The study protocols were approved by the Bioethics Committee of Institute for Problems of Cryobiology and Cryomedicine of the NAS of Ukraine (Permit No 2016-05).

Primary suspension of cells from biopsies of cartilage tissues of rats ($n = 15$) was obtained by enzymatic digestion [16]. To do this, tissue samples were washed with Hanks' solution (PAA, Austria) with gentamicin (150 μg/mL) (Farmak, Ukraine) and incubated in a type II collagenase solution (1.5 mg/mL) (PanEco, Russia) at 4 °C for 18 h. Then, cells were isolated from biopsies by resuspension followed by centrifugation at 1500 rpm for 3 min. Supernatant was removed, culture medium was added to the precipitate, and the cell suspension was placed on culture plastic. The seeding density of the cells was 1×10^4 per 1 cm^2 of culture flasks. The culture medium in all cases contained: IMDM medium (PAA, Austria), 10% fetal bovine serum (HyClone, USA), kanamycin (150 μg/mL) (Farmak, Ukraine), and amphotericin B (5 μg/mL) (PAA, Austria). The culture medium was changed every 3 days. The standard culturing conditions at 37 °C in an atmosphere of 5% CO_2 in an incubator (Sanyo, Japan) were used. Upon reaching a monolayer, cell cultures were subcultured using a 0.25% solution of trypsin (PAA, Austria) and Versene (PanEco, Russia) in a ratio of 1:1.

Cryopreservation of MSC cultures was carried out under the protection of 10% dimethyl sulfoxide (Sigma-Aldrich, USA) with an addition of 20% fetal bovine serum. The cryoprotectant solution was prepared *ex tempore* on the culture medium. The resulting suspension was placed in Nunc CryoTubes (Sigma-Aldrich, USA) in an amount of 1 mL. The cooling rate was 1 °C/min to –80 °C followed by immersion in liquid nitrogen [17]. Warming was carried out in a water bath at 40 °C until the liquid-phase appearance. Removal of the cryoprotectant was performed by adding of Hank's solution (PAA, Austria) 1:9 followed by centrifugation at 1500 rpm for 5 min.

A colloidal solution of AgNPs (Sigma-Aldrich, USA) with an average size of 15 nm was used in the work. The range of studied concentrations was 4, 6, 10, 20 μg/mL. AgNPs were introduced into cells by the method of passive diffusion (incubation at 37 °C for 1 h). The samples of CrMSCs incubated under the same conditions without AgNPs were taken as a control. A scheme of the experiment is shown in Fig. 1.

The CrMSCs after incubation with AgNPs were cultured using the same conditions as for primary cultures. The percentage of viable cells in the samples immediately after 1-h incubation was determined using an express trypan blue exclusion test [18].

The processes of apoptosis and necrosis in CrMSCs and DNA fragmentation upon interaction with AgNPs were studied using flow cytofluorometry. Necrosis–apoptosis processes were after 1-h incubation studied using Annexin-V-FITC (Annexin

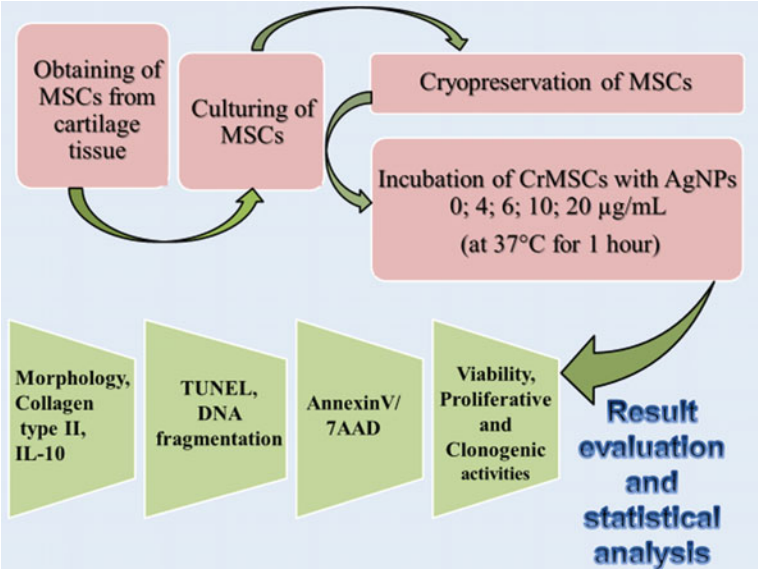

Fig. 1 Experimental scheme

V) (BD, USA) and 7-Amino-Actinomycin D (7AAD) (BD, USA) dyes. DNA fragmentation was evaluated at the same term by TUNEL method on preparations of CrMSCs using a set of reagents from the company "BioVision" (USA) according to the manufacturer's instructions. FACS Calibur (Becton Dickinson, USA) was used for these two tests. Data were analyzed using WinMDI v.2.8.

Clonogenic efficiency was determined by counting the colonies contained at least 30 cells that defined as colony-forming unit (CFU). Cells were seeded in 6-well plates at low-density limiting dilution (final concentration was 15 cells/cm^2) and cultured in IMDM with 20% fetal bovine serum for 10 days. Then cells were fixed with 4% paraformaldehyde solution and stained with azure and eosin by Romanovsky and Himza for 10 min at room temperature. A number and size of colonies and number of cells in them were determined.

At culturing periods 1, 3, 7, 10 days, the proliferative activity was determined using the MTT test, which is based on the ability of dehydrogenases of living cells to reduce 3-(4,5-dimethylthiazolyl-2)-2,5-diphenyltetrazolium bromide (MTT, Sigma, USA) into purple formazan crystals, insoluble in water [19]. The optical density of formazan in DMSO was measured on a biochemical analyzer (ERBA CHEM 7) at a wavelength of 540 nm. A medium without cells was used as a comparison solution.

The detection of interleukin-10 (IL-10) in the culture medium of CrMSCs from cartilage tissue was carried out on the 10th day of culturing by the ELISA method using a Sigma-Aldrich kit (USA) according to the manufacturer's instructions [20].

For morphological study, the cells were fixed on the 10th day in a 4% solution of paraformaldehyde followed by azure-II and eosin staining by Romanovsky-Giemsa. ZEISS Primo Star light microscope (Carl Zeiss Microscopy GmbH, Germany) was used for the analysis of preparations. Staining for collagen type II was performed using monoclonal antibodies to COL-II (Sigma-Aldrich, USA) in dilution 1:200 and CF™ 488A (Sigma-Aldrich, USA) according to the manufacturer's instructions. The cell nuclei were additionally stained with DAPI (Sigma-Aldrich USA) at a concentration of 1 μg/mL for 30 min. Fluorescent microscopy of MSCs was performed using confocal scanning microscope LSM 510 Meta (Carl Zeiss, Germany). On the obtained images, the relative number of cells stained to collagen type II was determined.

Kruskal–Wallis test and Student–Newman–Keuls multiple comparison tests were applied to compare the difference between the groups using Statistica 8 (StatSoft, USA) software.

3 Results and Discussion

In our previous studies, it was established that the addition of AgNPs (40 nm) to the incubation medium of CrMSCs from the bone marrow in concentrations of 6 and 10 μg/mL led to a decrease in the integrity of membranes, mitochondrial activity and an increase in the percentage of cells in a state of apoptosis [21]. In order to obtain a comparative picture of the effect of AgNPs on changes in the state of MSCs from

cartilage tissues, this study was carried out. As is known that at a temperature of 37 °C endocytosis—a process of capturing substances by a cell through retracting a section of the plasma membrane, followed by the formation of vesicles with extracellular content inside the cell—is occurred in cells [22].

The first stage of the work was the study of the influence of incorporated in such way AgNPs on the integrity of the membranes of CrMSCs from cartilage tissue. The obtained results are presented in Fig. 2a.

In the untreated CrMSCs from cartilage tissue (control group), 78.2% of the cells had an intact membrane. The impact of AgNPs in the concentrations of 4 and 6 μg/mL did not lead to changes in the studied indicator. The number of cells with an intact membrane after incubation with AgNPs at the concentrations of 10 and 20 μg/mL was reduced by 12.5% and 18.3%, respectively, relative to the control samples. Our results showed that cell viability is inversely proportional to the concentration of AgNPs.

The next stage of the work was to conduct a research on tracking DNA fragmentation in CrMSCs from cartilage tissue under the conditions of interaction with AgNPs. The obtained results are presented in Fig. 2b. The analysis of the results of the immunocytochemical reaction for the detection of DNA fragmentation showed that the severity of the DNA fragmentation process in all the studied groups was not high.

It was shown that the use of AgNPs at concentrations of 4 and 6 μg/ml did not lead to significant changes in the index of DNA fragmentation in CrMSC samples. After using of AgNPs at the concentrations of 10 and 20 μg/mL, a 1.4- and 2.0-fold increase in the number of cells with signs of DNA fragmentation was respectively observed in CrMSCs from cartilage tissues compared to the control.

The TUNEL immunocytochemical method detects DNA fragmentation that occurs in cells both in the state of apoptosis and in the state of necrosis [23]. In order to distinguish the types of cell death and to estimate the percentage of viable

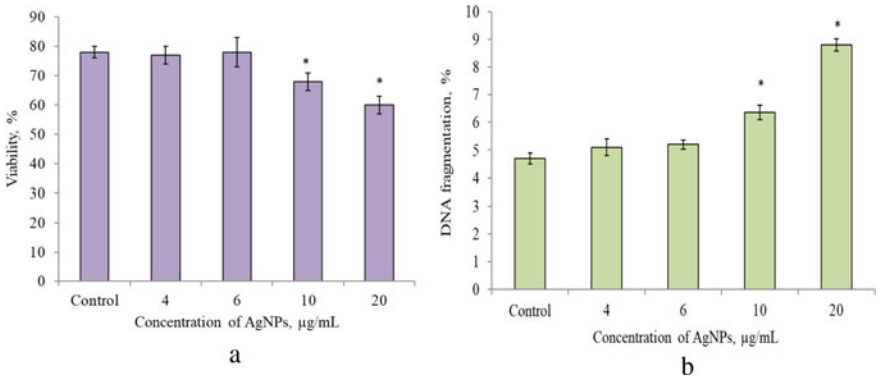

Fig. 2 Effect of incubation of cartilage-derived MSCs in the media with AgNPs on the number of: viable cells (**a**) and cells with DNA fragmentation (**b**). *Note**—the difference is statistically significant compared to the control ($p < 0.05$, $n = 5$)

cells in the experimental groups, we considered it necessary to involve the method of flow cytofluorometry with simultaneous Annexin V and 7AAD staining that allows detection of both necrotic cells and cells that have entered the path of apoptosis. At the early stage of apoptosis, the integrity of the cell membrane is preserved, but its phospholipid components are rearranged and phosphatidylserine appears on the cell surface. Annexin V is a protein that has a high affinity to phosphatidylserine and binds to cells that express it only on the outer surface of the membrane.

To resolve the issue of activation of apoptosis/necrosis processes in CrMSCs of cartilage tissues, as a reaction to interaction with AgNPs already in the early stages, the suspension of CrMSCs was incubated with AgNPs for 1 h. The obtained results are presented in Table 1.

The use of AgNPs in concentrations of 4 and 6 μg/mL did not lead to the activation of apoptosis and necrosis processes in CrMSCs of cartilage tissue. In the samples with the addition of higher concentrations of AgNPs (10 and 20 μg/mL), there was an significant increase in the number of cells in the state of early apoptosis (Annexin $V^+/7AAD^-$) by 1.8- and 2.4-fold and necrosis (Annexin $V^+/7AAD^+$ + Annexin $V^-/7AAD^+$) by 1.2- and 1.4-fold, respectively, relative to the control.

The results of studying of AgNP effect on clonogenic potential of cartilage-derived CrMSCs are shown in Fig. 3a.

The MSCs' colony formation rate after cryopreservation and subsequent incubation with 4 and 6 μg/mL AgNPs did not differ from the control. The addition of AgNPs at concentrations of 10 and 20 μg/mL before culturing of CrMSCs of cartilage tissue caused a significant decrease in the colony formation index in comparison with control, namely by 1.27- (10 μg/mL) and 1.43- (20 μg/mL) fold. After incubation of MSCs with AgNPs, large (> 300 cells), average (50–300 cells), and small (30–100 cells) colonies were formed. It is known that differences in colony morphology indicate their different qualities of CFU-f within one population of stromal cells. For the analysis, the wells that contain all types of cell colonies with more than 30 cells were selected. After isolation of individual colonies of MSCs cultured with the addition of AgNPs at a concentration of 4 and 6 μg/mL and further passaging, the formation of new colonies was observed. Descendants of colonies of MSCs cultured with the addition of low concentrations of AgNPs were actively proliferated and

Table 1 Cytofluorometric analysis of CrMSCs of cartilage tissue after incubation with AgNPs

Samples/region	Annexin $V^-/7AAD^-$	Annexin $V^+/7AAD^-$	Annexin $V^+/7AAD^+$ + Annexin $V^-/7AAD^+$
Control	74.19 ± 1.27	3.44 ± 1.55	22.37 ± 1.42
AgNPs 4 μg/mL	74.08 ± 0.42	3.91 ± 0.71	22.01 ± 1.21
AgNPs 6 μg/mL	73.28 ± 1.25	3.94 ± 1.05	22.78 ± 1.16
AgNPs 10 μg/mL	65.82 ± 1.18*	6.35 ± 0.52*	27.83 ± 0.92*
AgNPs 20 μg/mL	60.83 ± 0.72*	8.33 ± 0.79*	30.84 ± 0.62*

Annexin V and 7AAD staining, % of cells ($M \pm \sigma$, $p < 0.05$)
*Note**—the difference is statistically significant compared to the control ($p < 0.05$; $n = 5$)

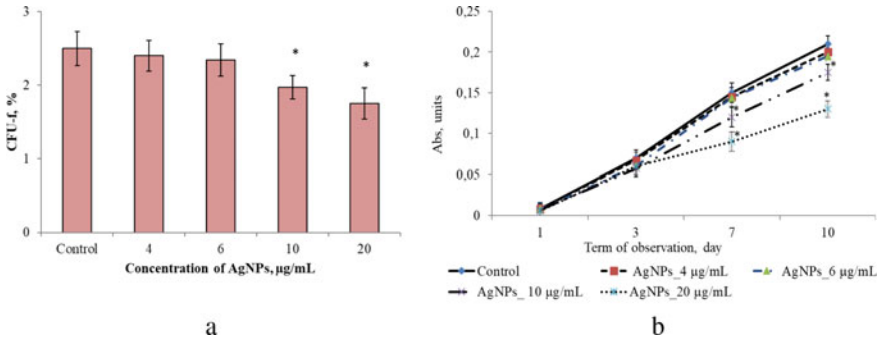

Fig. 3 Effect of AgNPs on the clonogenic (**a**) and proliferative (**b**) potentials in cartilage-derived CrMSCs. *Note**—the difference is statistically significant compared to the control ($p < 0.05$, $n = 5$)

formed a monolayer. In this application, AgNPs at concentrations of 10 and 20 μg/mL decreased the colony formation activity in the further subculture.

The proliferative activity of CrMSCs of cartilage tissue after interaction with AgNPs was measured using MTT test (Fig. 3b). The growth dynamics of CrMSCs in the presence of nanoparticles in all studied concentrations was similar to the corresponding indicators in the control. The growth rate of MSCs after cryopreservation and subsequent incubation with AgNPs (4 and 6 μg/mL) did not significantly differ from the control at all observation periods.

Addition of AgNPs in concentrations of 10 and 20 μg/mL in the culture of CrMSCs of cartilage tissue caused a significant decrease in proliferative activity compared to control starting from the 7th day of culturing, namely by 1.3- (10 μg/mL) and 1.7- (20 μg/mL) fold, and persisting on the 10th day by 1.2- and 1.6-fold, respectively.

As it is known, cytokines are a group of polypeptide mediators involved in the formation and regulation of the body's protective reactions [24]. The biological effects of cytokines are mediated through specific cellular receptor complexes that bind cytokines with very high affinity, and individual cytokines may use common receptor subunits. Depending on the nature of the effect on the inflammatory process, cytokines are divided into pro-inflammatory, involved in the initiation and progressing of inflammation, and anti-inflammatory with reverse action [25]. The key pro-inflammatory cytokine is IL-1, and the main anti-inflammatory one is IL-10.

The obtained results of the influence of AgNPs on the synthesis of IL-10 by CrMSCs from cartilage tissue are shown in Fig. 4.

The analysis of experimental data showed that AgNPs at the concentrations of 4 and 6 μg/ml did not affect the synthesis of IL-10 in the samples of CrMSCs from cartilage tissues. When using AgNPs at the concentrations of 10 and 20 μg/mL, a significant decrease in IL-10 content in cartilage-derived CrMSCs was observed by 1.3- and 1.5-fold, respectively, compared to the control. A relationship between a decrease in the level of IL-10 and an increase in the concentration of nanoparticles

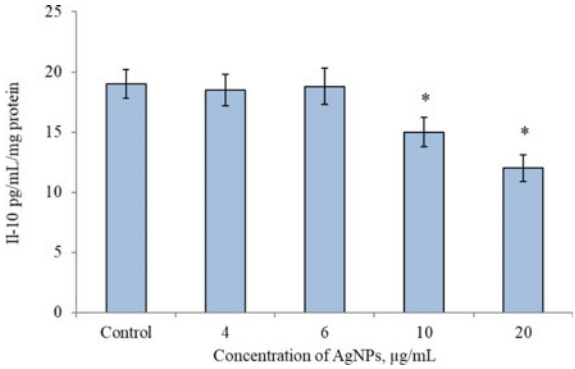

Fig. 4 Effect AgNPs on synthesis of IL-10 in cartilage-derived CrMSCs. *Note**—the difference is statistically significant compared to the control ($p < 0.05$, $n = 5$)

was found, which confirms their cytotoxic effect and leads to a decrease in the anti-inflammatory potential of CrMSCs.

The results of the study morphological characteristics of CrMSCs, as well as their ability to synthesize type II collagen, are presented in Fig. 5.

MSCs from the cartilage tissue of the control group were represented by spindle-shaped and polygonal cellular elements, 93.6 ± 6.7% of which were stained positively to type II collagen. Incubation with AgNPs in concentrations of 4 and 6 μg/mL did not lead to the changes in morphological characteristics and relative number of cells that synthesized type II collagen (89.5 ± 3.8% and 87.2 ± 5.3%, respectively) compared to control samples. The use of AgNPs in concentrations of 10 and 20 μg/mL led to the detachment of CrMSCs from the cultural surface and to decreasing in the relative number of cells positively stained to type II collagen (it was equal to 57.6 ± 2.1% and 49.3 ± 2.5%, respectively). It should be noted that the cells from these groups mainly have degenerative changes in their cytoskeleton.

So, the results of the study of the effect of AgNPs on synthetic processes in CrMSCs showed that the use of concentrations of 10 and 20 μg/mL led to a decrease in the relative number of cells positively stained to type II collagen. As it is known that the decrease in the synthetic activity of MSCs is one of the main indicators of attenuation of their functioning [26, 27].

Today, research into the properties of nanomaterials and nanoparticles, which is rapidly developing, poses the task of studying their impact on living systems, both at the level of the whole organism and on individual cells and intracellular structures. Detection of cellular effects is particularly important due to the nanosize of active agents that directly affect intracellular environmental. A comparative analysis of the obtained results showed that AgNPs at the concentrations of 4 and 6 μg/mL do not affect viability, proliferative activity, and apoptosis/necrosis processes in CrMSCs from cartilage tissue. A study of the effect of AgNPs in the concentrations of 10 and 20 μg/mL on CrMSCs of cartilage tissues showed a decrease in proliferative activity, as well as an increase in the percentage of cells with signs of DNA fragmentation and cells in a state of apoptosis. When using AgNPs at a concentration of 20 μg/mL,

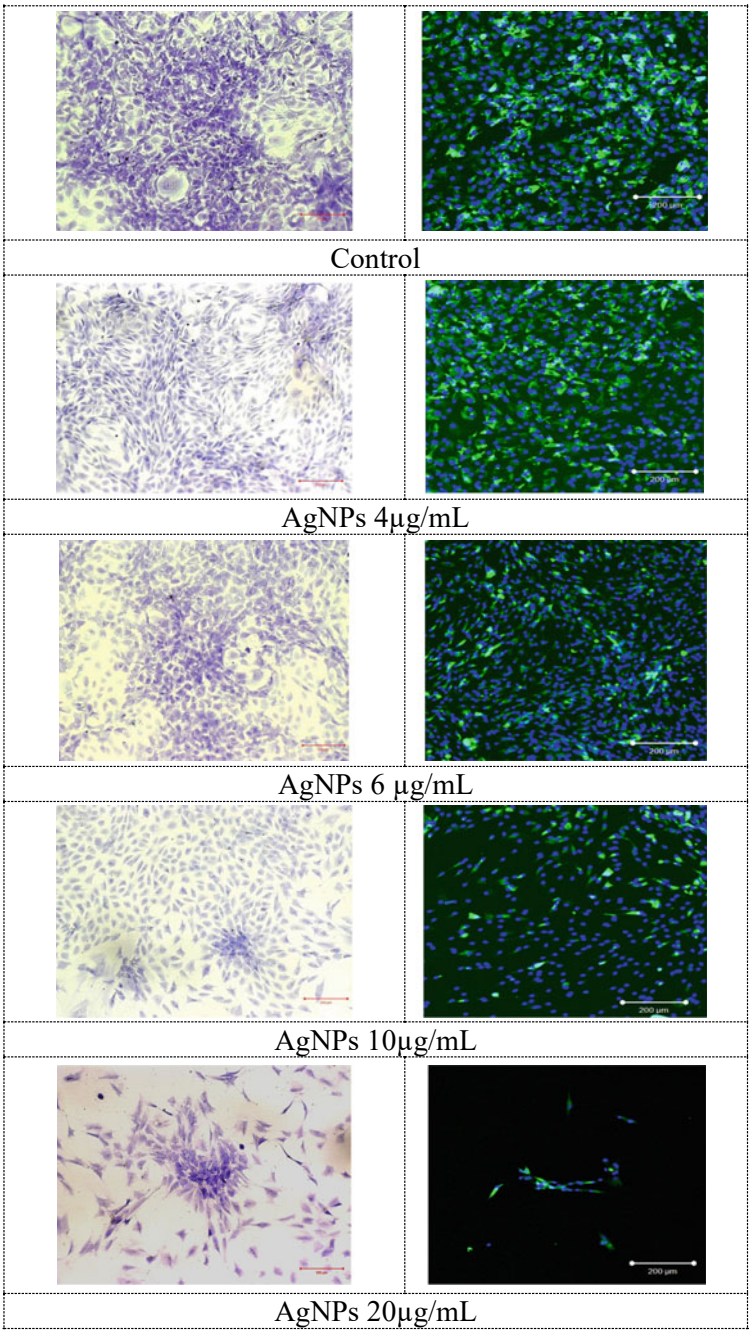

Fig. 5 Effect of AgNPs on morphological characteristics and type II collagen synthesis in CrMSCs from cartilage tissue, the 10th day of culturing. The first column—light microscopy (staining with azure-eosin); the second column—fluorescence microscopy (green color indicates collagen type II, blue color shows cell nuclei)

more pronounced lesions were determined in cells compared to a concentration of 10 μg/mL.

Due to the limited number of studies, the exact effect of AgNPs on the proliferation and differentiation ability of MSCs is not conclusive. Implants usually remain in the body for a long time; therefore, long-term or continuous studies may help to understand the exact effects of AgNPs on MSCs. In addition, the size, shape, and concentration of nanoparticles must be established in addition to the duration of action to achieve consistent results. The source or tissue from which MSCs are isolated may also influence their tolerance to AgNPs. Therefore, toxicological studies of AgNPs need to continue to understand the effects of nano- and ionic silver, especially on stem cells.

The obtained in this work results refer to the field of applied biotechnology, which extends to clinical medicine, and for the first, to the creation of directed delivery of drugs to target cells or organs.

4 Conclusion

In the present study, we analyzed the effects of 15 nm AgNPs in different concentrations on morphological and functional state of cartilage-derived CrMSCs. It was shown that the use of AgNPs in the concentrations of 4 and 6 μg/mL did not lead to the significant changes in viability, state of apoptotic and necrotic processes, morphological characteristics, synthesis of type II collagen, proliferative and clonogenic potentials of the cells. The AgNPs' application in the concentrations of 10 and 20 μg/mL resulted in a decrease of proliferative activity, synthesis of IL-10 and type II collagen, percentage of Annexin $V^-/7AAD^-$ cells and in an increase of the number of apoptotic cells compared with the control samples of CrMSCs. In sum, the presented results are related to the field of applied nanobiotechnology and spread to regenerative medicine, especially to the development of techniques for the use of CrMSCs in combination with AgNPs in clinical practice for treatment of damages of the tissues of musculoskeletal system, in particular rheumatoid arthritis.

Acknowledgements This work was supported by the program of the National Academy of Science of Ukraine «Genomic, molecular and cellular bases of development of innovative biotechnologies», contract number 2.2.6.132/21.

References

1. E. Boisselier, D. Astruc, Gold nanoparticles in nanomedicine: preparations, imaging, diagnostics, therapies and toxicity. Chem. Soc. Rev. **38**(6), 1759–1782 (2009). https://doi.org/10.1039/b806051g
2. D. Di Bella, J.P.S. Ferreira, R.N.O. Silva et al., Gold nanoparticles reduce inflammation in cerebral microvessels of mice with sepsis. J. Nanobiotechnol. **19**(1), 52 (2021). https://doi.org/10.1186/s12951-021-00796-6

3. H.H. Lara, E.N. Garza-Treviño, L. Ixtepan-Turrent et al., Silver nanoparticles are broad-spectrum bactericidal and virucidal compounds. J. Nanobiotechnol. **9**, 30 (2011). https://doi.org/10.1186/1477-3155-9-30
4. C. You, C. Han, X. Wang et al., The progress of silver nanoparticles in the antibacterial mechanism, clinical application and cytotoxicity. Mol. Biol. Rep. **39**(9), 9193–9201 (2012). https://doi.org/10.1007/s11033-012-1792-8
5. T. Faunce, A. Watal, Nanosilver and global public health: international regulatory issues. Nanomedicine (Lond) **39**(4), 617–6322012 (2010)
6. S.W.P. Wijnhoven, W.J.G.M. Peijnenburg, C.A. Herberts et al., Nano-silver—a review of available data and knowledge gaps in human and environmental risk assessment. Nanotoxicology **3**(2), 109–138 (2009). https://doi.org/10.1080/17435390902725914
7. R. Lima, A.B. Seabra, N. Durán, Silver nanoparticles: a brief review of cytotoxicity and genotoxicity of chemically and biogenically synthesized nanoparticles. J. Appl. Toxicol. JAT **32**(11), 867–879 (2012). https://doi.org/10.1002/jat.2780
8. M.V. Park, A.M. Neigh, J.P. Vermeulen et al., The effect of particle size on the cytotoxicity, inflammation, developmental toxicity and genotoxicity of silver nanoparticles. Biomaterials **32**(36), 9810–9817 (2011). https://doi.org/10.1016/j.biomaterials.2011.08.085
9. P.V. AshaRani, G. Low Kah Mun, M.P. Hande et al., Cytotoxicity and genotoxicity of silver nanoparticles in human cells. ACS Nano **3**(2), 279–290 (2009). https://doi.org/10.1021/nn800596w
10. P.V. Asharani, M.P. Hande, S. Valiyaveettil, Anti-proliferative activity of silver nanoparticles. BMC Cell Biol. **10**, 65 (2009). https://doi.org/10.1186/1471-2121-10-65
11. Y. Xue, S. Zhang, Y. Huang et al., Acute toxic effects and gender-related biokinetics of silver nanoparticles following an intravenous injection in mice. J. Appl. Toxicol. JAT **32**(11), 890–899 (2012). https://doi.org/10.1002/jat.2742
12. L. Peng, Z. Jia, X. Yin et al., Comparative analysis of mesenchymal stem cells from bone marrow, cartilage, and adipose tissue. Stem Cells Develop. **17**(4), 761–773 (2008). https://doi.org/10.1089/scd.2007.0217
13. R. Levato, W.R. Webb, I.A. Otto, The bio in the ink: cartilage regeneration with bioprintable hydrogels and articular cartilage-derived progenitor cells. Acta Biomater. **61**, 41–53 (2017). https://doi.org/10.1016/j.actbio.2017.08.005
14. F.P. Barry, J.M. Murphy, Mesenchymal stem cells: clinical applications and biological characterization. Int. J. Biochem. Cell Biol. **36**(4), 568–584 (2004). https://doi.org/10.1016/j.biocel.2003.11.001
15. G. Almeida-Porada, A.J. Atala, C.D. Porada, Therapeutic mesenchymal stromal cells for immunotherapy and for gene and drug delivery. Mol. Ther. Methods Clin. Develop. **16**, 204–224 (2020). https://doi.org/10.1016/j.omtm.2020.01.005
16. N. Volkova, M. Yukhta, A. Goltsev, Influence of growth factors on cryopreserved mesenchymal stromal cells. Fiziologichnyi Zhurnal **65**(2), 12–21 (2019) (in Ukrainian). https://doi.org/10.15407/fz65.02.012
17. N.A. Volkova, A.N. Goltsev, Cryopreservation effect on proliferation and differentiation potential of cultured chorion cells. Cryo. Lett. **36**(1), 25–29 (2015)
18. M. Norkus, L. Kilmartin, D. Fay et al., The effect of temperature elevation on cryopreserved mesenchymal stem cells. Cryo. Lett. **34**(4), 349–359 (2013)
19. T. Mosmann, Rapid colorimetric assay for cellular growth and survival: application to proliferation and cytotoxicity assays. J. Immunol. Methods **65**(1–2), 55–63 (1983). https://doi.org/10.1016/0022-1759(83)90303-4
20. O.R. Mahon, D.C. Browe, T. Gonzalez-Fernandez et al., Nano-particle mediated M2 macrophage polarization enhances bone formation and MSC osteogenesis in an IL-10 dependent manner. Biomaterials **239**, 119833 (2020). https://doi.org/10.1016/j.biomaterials.2020.119833
21. N.A. Volkova, M.S. Yukhta, E.V. Pavlovich, et al., Change in functional state of bone marrow-derived mesenchymal stem cells after incubation with silver nanoparticles, in *Nanophotonics, Nanooptics, Nanobiotechnology, and Their Applications, NANO 2018*, ed. by O. Fesenko, L.

Yatsenko, Springer Proceedings in Physics, vol. 222 (Springer, Cham). https://doi.org/10.1007/978-3-030-17755-3_19
22. I. Khan, K. Saeed, I. Khan, Nanoparticles: properties, applications and toxicities. Arab. J. Chem. **12**(7), 908–931 (2019). https://doi.org/10.1016/j.arabjc.2017.05.011
23. S. Hackenberg, A. Scherzed, M. Kessler, Silver nanoparticles: evaluation of DNA damage, toxicity and functional impairment in human mesenchymal stem cells. Toxicol. Lett. **201**(1), 27–33 (2011). https://doi.org/10.1016/j.toxlet.2010.12.001
24. S. Kany, J.T. Vollrath, B. Relja, Cytokines in inflammatory disease. Int. J. Mol. Sci. **20**(23), 6008 (2019). https://doi.org/10.3390/ijms20236008
25. J.A. Smith, Regulation of cytokine production by the unfolded protein response; implications for infection and autoimmunity. Front. Immunol. **9**, 422 (2018). https://doi.org/10.3389/fimmu.2018.00422
26. N. Volkova, O. Pavlovich, O. Fesenko et al., Studies of the influence of gold nanoparticles on characteristics of mesenchymal stem cells. J. Nanomater. **2017**, 6934757 (2017). https://doi.org/10.1155/2017/6934757
27. A. Damle, R. Sundaresan, J.M. Rajwade et al., A concise review on implications of silver nanoparticles in bone tissue engineering. Biomater. Adv. **141**, 213099 (2022). https://doi.org/10.1016/j.bioadv.2022.213099

Investigation of the Process of Synthesis of Oxygen-Containing Cobalt Compounds

Sergeyeva Olga and Frolova Liliya

Abstract The study was conducted using laboratory equipment and software modules of the HSC Chemistry 5.11 package. To find the preliminary conditions for the formation of phase boundaries, diagrams in the coordinates of the E-pH potential of the aqueous medium (Pourbaix diagram) were used. It was found that depending on the initial state of $Co(OH)_2$ in the solution, the mass fraction of oxygen in the sediment may change. At the same time, an increase in the concentration of hydrogen peroxide leads to a decrease in the share of hydroxide compounds in precipitations. X-ray analysis revealed the presence of CoO, CoOOH, Co_3O_4, β-$Co(OH)_2$, Co content in dry sediments. It is calculated that the particle sizes lie in the range of 10–110 nm. Photomicrographs confirm the agreement of these calculations with experimental data. The quality of sediment is affected by the following factors: current density and anion concentration, process temperature. An increase in temperature increases the diffusion coefficient, but requires a higher current density to produce a powder. It was found that the reduction of the liquid layer contributes to the increase in the yield of oxide compounds.

1 Introduction

Currently, cobalt oxide compounds are used in such products as: batteries for mobile phones, computers, hybrid cars, and other "gadgets"; superalloys for turbine blades, mainly in jet engines; pigments and dyes; wear-resistant and heat-resistant alloys; catalysts, including for gas liquefaction; magnets [1–3]. It is also possible to use cobalt particles in the creation of new catalysts for various industrial processes, as a filler for varnishes and paints, in the production of galvanic cells and other areas of technology [4–7]. At the same time, the characteristics and options for their practical application largely depend on the method of production, which usually determines their structure, dimensions, physical and chemical properties, etc. [8]. In this regard,

S. Olga · F. Liliya (✉)
Ukrainian State University of Chemical Technology, Dnipro 49005, Ukraine
e-mail: 19kozak83@gmail.com

O. Fesenko and L. Yatsenko (eds.), *Nanoelectronics, Nanooptics, Nanochemistry and Nanobiotechnology, and Their Applications*, Springer Proceedings in Physics 297,
https://doi.org/10.1007/978-3-031-42708-4_12

research devoted to the search for ways to improve technological processes that allow obtaining particles with given properties is relevant.

Cobalt, nickel, ferrum, and chromium hydroxides are very convenient precursors for further synthesis of semiconductors, dielectrics, ferroelectrics, and ferroelectrics. A special role in this group of oxides is occupied by cobalt hydroxide, which, as part of ferrimagnets, gives them specific properties, as a result of which magnetic nanomaterials find various applications [9–13]. Therefore, the study of the physicochemical bases of the production of cobalt hydroxides remains an urgent task at present.

The development of methods aimed at obtaining these materials is of great importance in obtaining materials with a certain composition, morphology, and structure. One such method that allows you to adjust the composition of hydroxide and oxide materials is the precipitation method. Previously, the systems γ-FeOOH–H_2O–NaOH, $FeSO_4$–NaOH–H_2O, $FeSO_4$–H_2O–H^+/OH^-–O_2, $FeSO_4$–$CoSO_4$–$Al_2(SO_4)_3$–NaOH were studied in detail in [14–17].

Among the methods of obtaining micro- and nanoparticles, large groups of chemical [18], electrochemical [19], electropulse [20], and plasma-chemical [11] synthesis methods can be distinguished.

The purpose of this study was to analyze the technology synthesis of cobalt compounds using contact non-equilibrium low-temperature plasma and identification of directions for its further improvement.

2 Experimental

The object of this study is the process of obtaining oxide and metal particles from aqueous solutions using contact non-equilibrium plasma of reduced pressure. Thermodynamic analysis was carried out using laboratory equipment and software modules of the HSC Chemistry 5.11 package (Outotec, Finland).

All the precipitates were washed to a negative reaction to the sulfate ion. After precipitation, the suspension was left for 48 h in a mother liquor. After standing, the precipitate was separated by magnetic separation. The washed and filtered precipitates were dried at 100 °C.

Structural studies were carried out by powder X-ray diffraction (DRON-2.0, Cu-Kα-radiation) at $T = 298$ K.

A REM-106I raster electron microscope was used to obtain images of sediments, and images were obtained in secondary electron mode. The final pressure in the microscope column (in the area of the gun) is no more than 6.7×10^{-4} Pa. The current of the gun is 115 mA.

3 Results and Discussion

A plasma-chemical reactor, in which the main transformations take place in liquid media, is a device in which a whole complex of processes is combined. The main ones can be considered electrochemical, plasma-chemical, chemical, processes of cavitation of gas bubbles formed as a result of water decomposition, diffusion, heat exchange, etc.

The general scheme of processes taking place in a plasma-chemical reactor is given in [14].

Note that the main processes leading to the appearance of new components in the solution occur at the phase interface and at the cathode. However, when using solutions, the course of chemical processes in the entire volume of liquid is also possible.

It should be emphasized that the most easily controlled methods are based on the use of electrochemical processes of various orientations.

In technologies based on the application of non-equilibrium contact plasma, the latter is used to process solutions in order to obtain new compounds under conditions that promote the active interaction of atoms and ions with the formation of nanoparticles. However, it is necessary to determine the optimal parameters of the process.

To find the preliminary conditions for the formation of phase boundaries, we used diagrams in the coordinates of the potential E-pH of the aqueous medium (Pourbaix diagrams) [21]. These diagrams clearly reflect the thermodynamically stable forms of existence of elements (ions, molecules, atomic crystals, and metals) in solutions at different values of the hydrogen indicator pH and redox potential E.

The choice of sulfuric acid solution is due to its cheapness, simplicity, and stability of composition. The HSC Chemistry application program package [22] was used for calculations, which includes built-in reference databases on thermodynamic, physical and chemical properties of inorganic and organic substances, and calculation modules, including a module for calculating E-pH diagrams. The calculation result for the Co–H_2O system is shown in Fig. 1. (Similar values were obtained for cobalt concentrations of 0.01, 0.1, and 1 mol/l).

The calculations considered the effect of pressure, concentrations, and temperatures.

Note that the initial concentration of Co^{2+} affects the qualitative composition of the solution. When the content of cobalt (II) increases, the area of existence of $Co(OH)_2(s)$ decreases due to the appearance of hydroxocomplexes.

Analyzing Figs. 1 and 2, we can say that the conditions that contribute to the formation and stable existence of oxide forms of cobalt correspond to the lower limit—the range from pH = 2, $E = \geq 1.2$ V, to pH = 4.3, $E = \geq 0.4$ V; from the value of pH = 4.3, the value of E changes in such a way that the limit runs parallel to the limits of water stability. The upper border is set back from the upper border by almost 1 V and runs parallel to it. Therefore, according to the calculations, it is advisable to carry out the process in conditions corresponding to the upper limit of

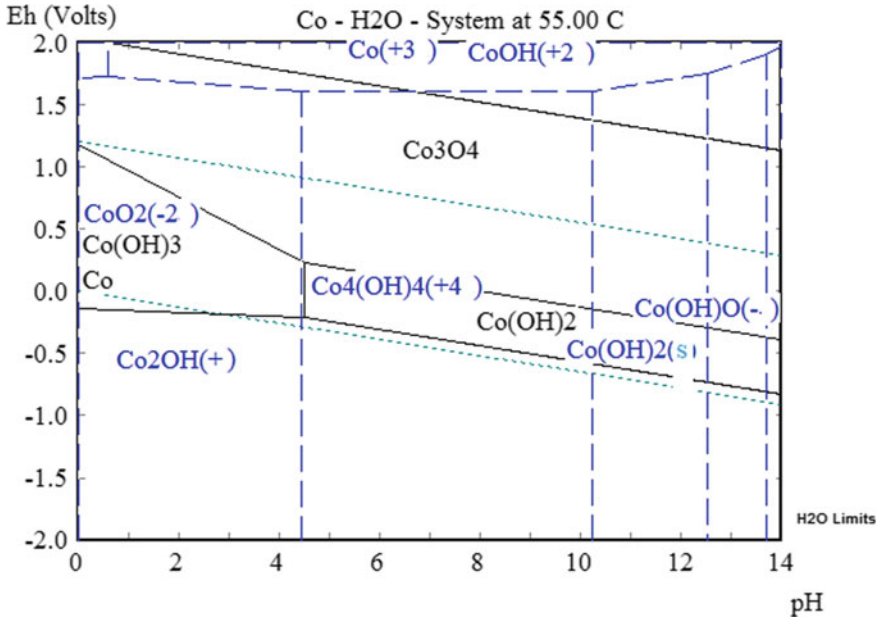

Fig. 1 Pourbaix diagram for the Co–H_2O system $C = 1$ mol/l, $P = 0.2$ atm

water stability, which coincides with the conditions of the near-surface limit of the liquid in the reactor.

When the solution was processed, it was clearly visible how the color changes, starting with the surface zone of the liquid in the reactor.

Chromatographic and derivatographic (Fig. 2) show the results of these methods and X-ray (Fig. 3) research methods were used to study the obtained sediment.

As can be seen from Fig. 2, depending on the initial form of $Co(OH)_2$ in water, the share of oxygen in the sediment may change. At the same time, the addition of hydrogen peroxide led to a decrease in the share of hydroxide compounds in sediments.

X-ray analysis revealed the presence of CoO, CoOOH, Co_3O_4, β-$Co(OH)_2$, Co among the dry deposits. The nature of the diffractograms of cobalt compounds indicates the presence of oxide and hydroxide compounds, and the latter in the β-form.

The analysis of diffractograms made it possible to obtain data on the dimensional characteristics of dry sediment particles, which are listed in Table 1. As can be seen from Table 1, the particle sizes are in the range of 10–110 nm.

Photomicrographs (Fig. 4) confirm the correspondence of the experimental data with the calculated ones.

If cations fall into the field of solubility of cations or into the field of stability of Co_3O_4, the process of changing the color of the liquid in the near-surface zone of the liquid was observed almost from the first seconds of treatment with a contact

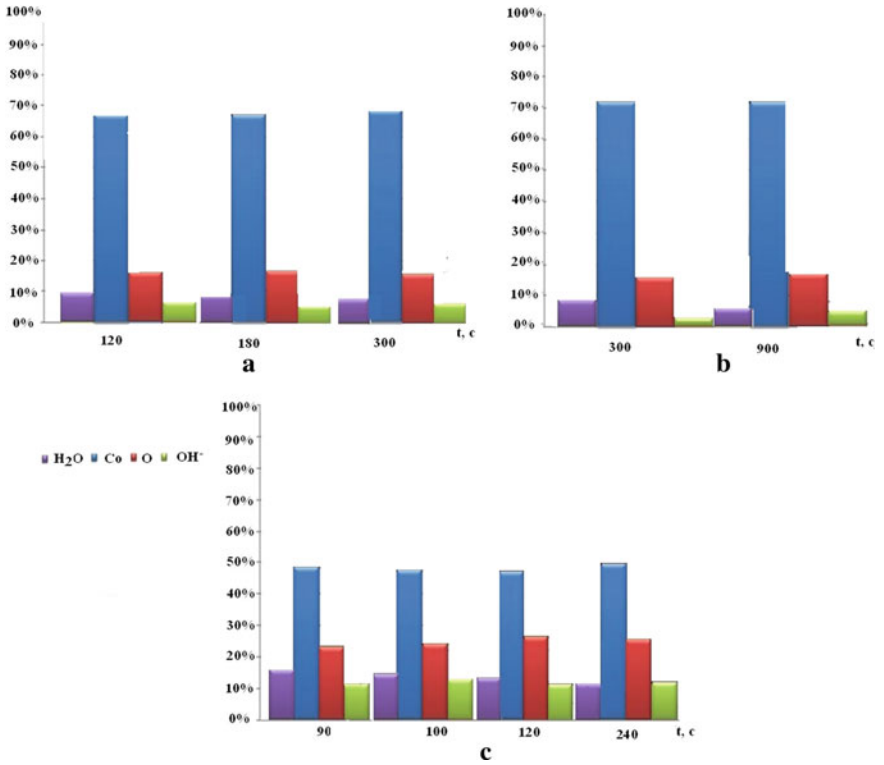

Fig. 2 Elemental composition of cobalt-containing sediment, % after processing. The initial composition of the treated medium: **a** $Co(OH)_2$ solution (pink); **b** $Co(OH)_2$ (blue) + H_2O_2 solution (3%); **c** $Co(OH)_2$ (blue)

non-equilibrium plasma of reduced pressure. This testifies to the correspondence of the experimental calculations, which is also confirmed.

Changing the process parameters affects the quality characteristics of the process. The main parameters that can be changed are pressure, concentrations, temperature, and the layer of the liquid being processed.

At the same time, an increase in the current in the reactor leads to an increase in the speed of the transformation process due to the intensification of processes at the plasma–liquid interface, which contributes to the production of a larger number of oxygen-containing compounds.

It should be noted that the reduction of the liquid layer helps to increase the yield of oxide compounds. Also, when the thickness of the treated liquid layer decreases, the size of the sediment particles decreases, and obviously, this happens due to an increase in the number of nuclei and a decrease in concentration.

In addition, the crystalline structure of the particles is not formed immediately, but after a certain time. It was established that the structure of the primary parts is mostly amorphous. Then, the crystallization process takes place in the volume of

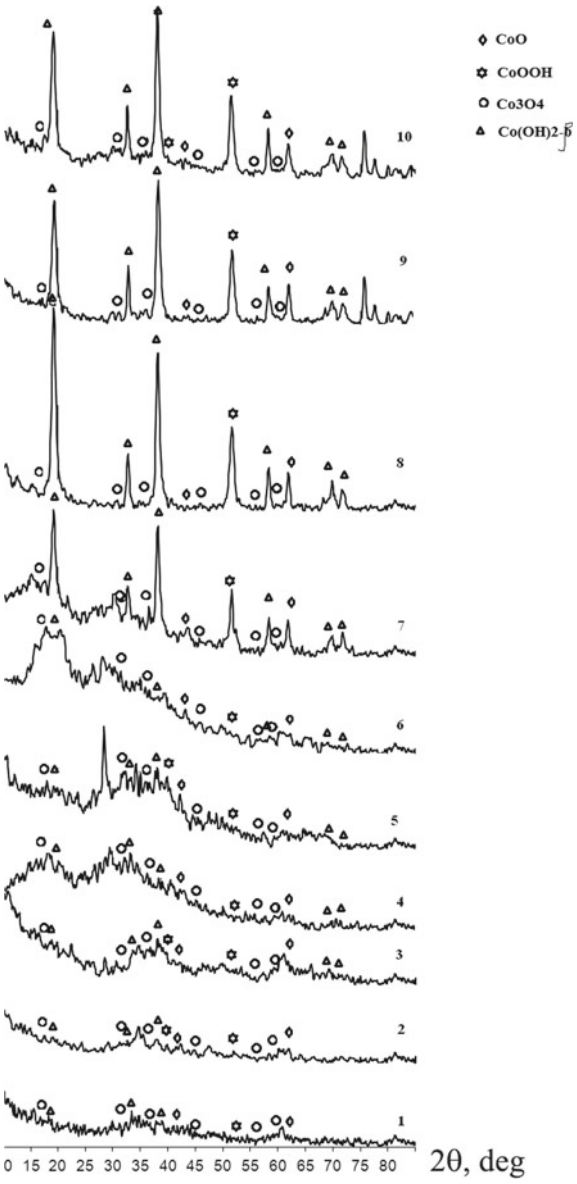

Fig. 3 X-ray pattern of cobalt compounds

the particles, and spherical large particles with a radius of about 10–6 m disintegrate into many small particles, but already of a crystalline structure. Thus, the size of the obtained crystalline particles is determined not only by the conditions of nucleation and growth of amorphous particles, but also by the conditions of their crystallization.

The quality of sediment is affected by the following factors: current density, anion concentration, process temperature. An increase in temperature increases the

Table 1 Characteristics of powders dried at room temperature

№	Size range (nm)				Time of contact with plasma (s)	Notes*
	0–29	30–59	60–99	≥ 100		
	Number of particles (%)					
1	54.95	39.55	5.5	–	300	WR
2	56.89	37.72	5.38	–	300	BRWB
3	55.67	37.11	6.19	1.03	180	FS
4	45.56	46.66	7.78	–	180	OS
5	61.80	35.96	2.24	–	120	WR
6	48.72	41.03	8.54	1.7	120	BRWB
7	22.08	54.55	23.38	–	90	FS
8	60.82	35.06	4.12	–	300	OS
9	57.89	37.89	4.12	–	180	AP
10	52.71	42.04	4.25	1	900	FS

** WR* Without rinsing with water before drying
BRWB By rinsing with water before drying
FS Fresh solution
OS Old solution
AP Addition of H_2O_2, 3%—15 ml/l

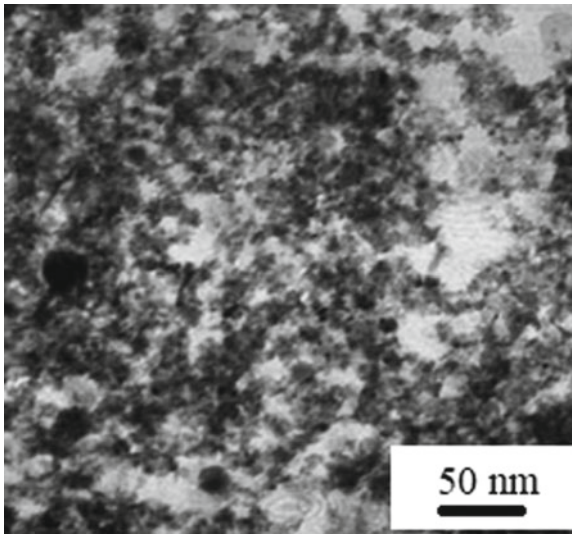

Fig. 4 Sediment particles after plasma-chemical treatment

diffusion coefficient, but requires a higher current density to produce a powder. However, we take into account that when the pressure in the reactor is 0.2 bar, the temperature of the solution does not exceed 55 °C.

In addition to the processes occurring during plasma-chemical treatment, the quality of sediments is affected by drying conditions. They depend on the surface area of the wet sediment, process temperature, humidity of the sediment, etc.

Thus, it can be considered that the difficulties in this technology are:

1. correct selection of parameters, both medium and plasma discharge, which is the main processing tool;
2. the need to select parameters of the drying process that allow obtaining products of the required quality.

As a result, we note that the most significant factors affecting the limits of stability of compounds and elements in solutions are their concentration, pH, and the thickness of the layer of the treated liquid and the parameters of the plasma discharge, which is due to the fact that the physicochemical mechanisms of the reactions are quite complex and synergistic effects are observed during their course, the dependencies of which are not completely clear.

The technological scheme is presented in Fig. 5. Soluble salt ($CoSO_4 \cdot 7\ H_2O$) is mixed with water in container 10. Alkali is added. In the centrifuge 11, the obtained $Co(OH)_2$ is separated, and then, it is diluted with water in the tank 12. Then, the resulting suspension is transferred to the plasma-chemical reactor 13 for processing, from where it enters the filter/dryer 16 and further to packaging 17.

In addition, there is a possibility of reusing the liquid that remains after filtering the sediment.

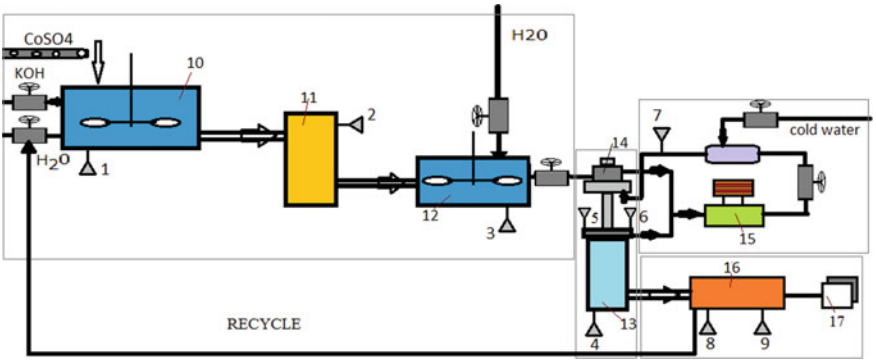

Fig. 5 Schematic diagram of the process of obtaining oxygen-containing compounds of cobalt using a plasma-chemical reactor. 1—sensor, 2—tachometer, 3—SO^{2-}_4 content analysis, 4—sensor, 5—temperature sensor, 6—strain gauge, 7—pressure sensor, 8—temperature sensor, 9—psychrometer, 10—mixing tank, 11—centrifuge, 12—tank for washing, 13—plasma-chemical reactor with built-in condition assessment sensors, 14—compressor, 15—heat exchanger, 16—filter/dryer, 17—packaging

4 Conclusion

The results of the analysis allow us to conclude that when using technologies of plasma-chemical processing of liquid media to obtain ultra- and nanosized compounds, there is a need to choose parameters that are optimal for this process.

This allows us to draw a conclusion about the possibility of improving the technological scheme due to:

1. control of the input pH of the solution, which ensures optimal yield of compounds;
2. use of the spent solution in a container with the original solution for its acidification;
3. refinement of the reactor unit in order to process the solution in a film or close to it mode, which should lead to an increase in the yield of oxides and a decrease in particle size;
4. selection of the correct set of sediment drying parameters.

References

1. S. Iravani, R.S. Varma, Sustainable synthesis of cobalt and cobalt oxide nanoparticles and their catalytic and biomedical applications. Green Chem. **22**(9), 2643–2661 (2020)
2. R. Kumar, et al., Microwave-assisted thin reduced graphene oxide-cobalt oxide nanoparticles as hybrids for electrode materials in supercapacitor. J. Energy Storage. **40**, 102724 (2021)
3. T. Rasheed, et al., Biogenic synthesis and characterization of cobalt oxide nanoparticles for catalytic reduction of direct yellow-142 and methyl orange dyes. Biocatalysis Agric. Biotechnol. **19**, 101154 (2019)
4. M. Jahani, et al., Effects of foliar application of cobalt oxide nanoparticles on growth, photosynthetic pigments, oxidative indicators, non-enzymatic antioxidants and compatible osmolytes in canola (*Brassica napus* L.). Acta Biologica Cracoviensia. Series Botanica. **61**(1) (2019)
5. A. Venkatesan, et al., Synthesis, characterization and magnetic properties of Mg^{2+} doped green pigment Cobalt aluminate nanoparticles. J. Mate. Sci. Mater. Electron. **33**(27), 21246–21257 (2022)
6. M. Yoneda, et al., Solid-state synthesis and characterization of cobalt blue core-shell pigment particles. J. Am. Ceramic Soc. **102**(6), 3468–3476 (2019)
7. L. Frolova, A. Pivovarov, T. Butyrina, Synthesis of pigments in Fe_2O_3-Al_2O_3-CoO by co-precipitation method. Pigment Resin Technol. (2017)
8. N. Ullah, et al., Mechanistic approaches and current trends in the green synthesis of cobalt oxide nanoparticles and their applications. Asian J. Green Chem. **4**(3), 340–354 (2020)
9. L. Frolova, A. Derimova, T. Butyrina, Structural and magnetic properties of cobalt ferrite nanopowders synthesis using contact non-equilibrium plasma. Acta Physica Polonica A. **133**(4), 1021–1023 (2018)
10. L. Frolova, O. Khmelenko, Investigation of the magnetic properties of ferrites in the CoO-NiO-ZnO using simplex-lattice design. J. Nanomater. (2018)
11. L. Frolova, Photocatalytic activity of spinel ferrites $Co_xFe_{3-x}O_4$ ($0.25< x< 1$) obtained by treatment contact low-temperature non-equilibrium plasma. Appl. Nanosci. **10**(12), 4585–4590 (2020)
12. G. Yang, et al., Strong adsorption of tetracycline hydrochloride on magnetic carbon-coated cobalt oxide nanoparticles. Chemosphere. **239**, 124831 (2020)

13. A.A. Azab, S.A. Esmail, M.K. Abdelamksoud, Studying the effect of cobalt doping on optical and magnetic properties of zinc oxide nanoparticles. Silicon **11**(1), 165–174 (2019)
14. L.A. Frolova, The mechanism of nickel ferrite formation by glow discharge effect. Appl. Nanosci. **9**(5), 845–852 (2019)
15. F. R. Costa, U. Wagenknecht, G. Heinrich, LDPE/Mg–Al layered double hydroxide nanocomposite: thermal and flammability properties. Polym. Degrad. Stab. **92**(10), 1813–1823 (2007)
16. L. Frolova, V. Shuvalov, The technology of obtaining complex anticorrosive pigments from zinc-containing waste water. Chem. Chem. Technol. **7**(2), 1–5 (2013)
17. L. Frolova, et al., Investigation of phase formation in the system $Fe^{2+}/Co^{2+}/O_2/H_2O$. Восточно-Европейский журнал передовых технологий. **6**(6), 64–68 (2016)
18. K. Sinkó, G. Szabó, M. Zrínyi, Liquid-phase synthesis of cobalt oxide nanoparticles. J. Nanosci. Nanotechnol. **11**(5), 4127–4135 (2011)
19. D. Samchenko, et al., Sustainable approach for galvanic waste processing by energy-saving ferritization with AC-magnetic field activation. Cogent Eng. **9**(1), 2143072 (2022)
20. H. Yu, et al., Electrochemical preparation of N-doped cobalt oxide nanoparticles with high electrocatalytic activity for the oxygen-reduction reaction. Chem. Eur. J. **20**(12), 3457–3462 (2014)
21. R.M. Garrels, in *Solutions, Minerals & Equilibria*, ed. by R.M. Garrels, C. L. Christ (Jones & Bartlett Publishers, 1990), 464 p
22. Outotec HSC Chemistry [Electronic resource]. Outotec. Available at: \www/URL: http://www.outotec.com/hsc

Nanostructured Adsorbents for Arsenic Compounds' Removal

Marta Litynska, Tetiana Dontsova, Grigorii Krymets, and Anna Gusak

Abstract The paper analyzed the usage and efficiency of different types (zero-valent iron, oxides, hydroxides, oxyhydroxides, composites, etc.) of nanostructured adsorbents for arsenic compounds' removal. Increasing of arsenic content in natural waters due to changes of groundwater level and mining activities is the significant problem of drinking water treatment. Arsenic is one of the most dangerous elements in world. According to European Commission, the maximum allowable level of arsenic in drinking water is 10 μg/l. High arsenic concentration in natural water is typical for India, China, Bangladesh, Taiwan, Vietnam, Hungary, the USA, Mexico, Chile, Argentina, Ghana, Iran, etc. Chronic arsenic exposure provokes a lot of different health problems, including cancer of skin and internal organs, endocrine disorders, hyperkeratosis, melanosis, etc. It was noted that inorganic sorption materials, especially iron-based adsorbents, are effective in removal arsenic compounds from polluted water and in immobilization from contaminated soils and sediments. In the paper, various compositions and applications of nanostructured adsorbents are observed.

M. Litynska (✉) · T. Dontsova · G. Krymets · A. Gusak
Igor Sikorsky Kyiv Polytechnic Institute, Kyiv, Ukraine
e-mail: m.litynska-2017@kpi.ua

T. Dontsova
e-mail: dontsova@ua.fm

G. Krymets
e-mail: krimets@xtf.kpi.ua

A. Gusak
e-mail: maril91@ukr.net

O. Fesenko and L. Yatsenko (eds.), *Nanoelectronics, Nanooptics, Nanochemistry and Nanobiotechnology, and Their Applications*, Springer Proceedings in Physics 297,
https://doi.org/10.1007/978-3-031-42708-4_13

1 General

1.1 Introduction

Arsenic compounds are often considered pollutants in environmental science due to significant toxicity and inability for natural degradation [1]. There are a lot of contamination sources and pathways, including such natural and anthropogenic processes as leaching from arsenic minerals, volcanic activity, mining, coal burning, infiltration from industrial wastes, etc. [2–4]. Mining activity and sedimentary formations are two of the main arsenic sources in Europe, Asia, the USA, and Africa (Fig. 1).

Arsenic compounds pollute air, soils, and water and eventually cause significant environmental problems and health risks. Arsenic pollution of soils often leads to obtaining of contaminated food products, including rice and other agricultural crops. Arsenic concentrations in rice grain are very significant in a lot of cases: 0.4 mg/kg in Kazakhstan, 0.53 mg/kg in Bolivia, 0.58 mg/kg in Bangladesh, and 0.87 mg/kg in Iran [5].

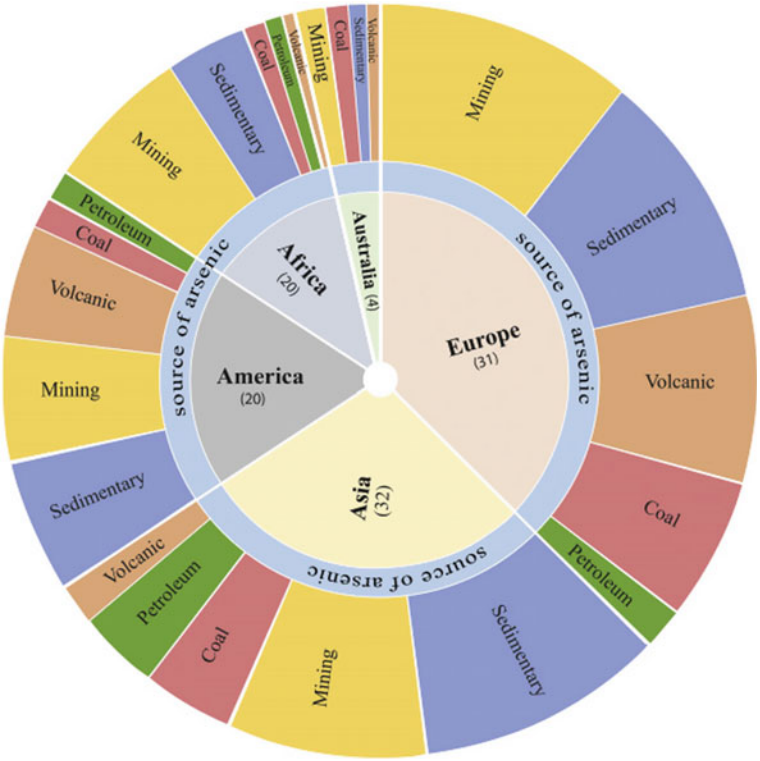

Fig. 1 Characterization of main arsenic sources [2]

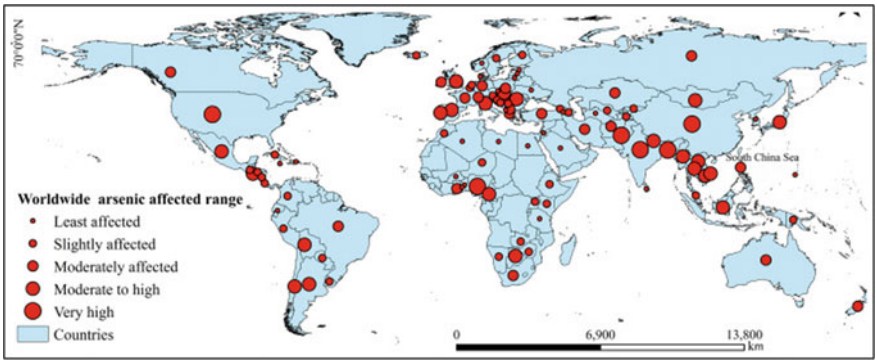

Fig. 2 Arsenic affected countries [2]

Leaching from minerals and infiltration from industrial wastes, especially after mining, are among the main ways of natural water pollution and aquatic organism's contamination. Seafood often contains significant arsenic (about 10–100 mg/kg dry weight) [6]. Such processes as changes of groundwater level and acidic rains intensify arsenic leaching. Increasing of arsenic content in natural waters due to these processes is the significant problem of drinking water treatment. Arsenic is one of the most dangerous elements in world. According to European Commission and recommendations of World Health Organization, the maximum allowable level of arsenic in drinking water is 10 μg/l. High arsenic concentration in natural water is typical for India, China, Bangladesh, Taiwan, Vietnam, Hungary, the USA, Mexico, Chile, Argentina, France, Portugal, Ghana, Iran, etc. [3, 7]. Millions people are affected by arsenic exposure: 2.4 millions in Cambodia (1610 μg As/l), 13 millions in Pakistan (2620 μg As/l), 19.6 millions in China (2000 μg As/l), 50 millions in India (3880 μg As/l), 85 millions in Bangladesh (4730 μg As/l) etc. (Fig. 2).

Chronic arsenic exposure provokes a lot of different health problems, including cancer of skin and internal organs, endocrine disorders, hyperkeratosis, melanosis, genotoxic and cytotoxic effects, etc. [8–10]. Oral arsenic exposure is significantly dangerous than dermal and causes more negative health effects [11]. In addition to the path of entry, people age is also very important. In consonance with work [11], in Jinghui irrigation district (China), where the main source of arsenic is industrial wastewater, the carcinogenic risk for adults is higher than for children, but the non-carcinogenic risk for children is higher. Thereby, prevention of oral arsenic exposure is very necessary. That is why it is very important to treat polluted water and remediate soils.

Nowadays, there are a lot of treatment methods, especially dosing of different chemicals, creation of biological systems, etc., but usage of sorption materials, especially nanostructured, is one of the most popular approaches both in water treatment and soil remediation due to small particle size, high surface area, and significant adsorption efficiency [1, 12, 13].

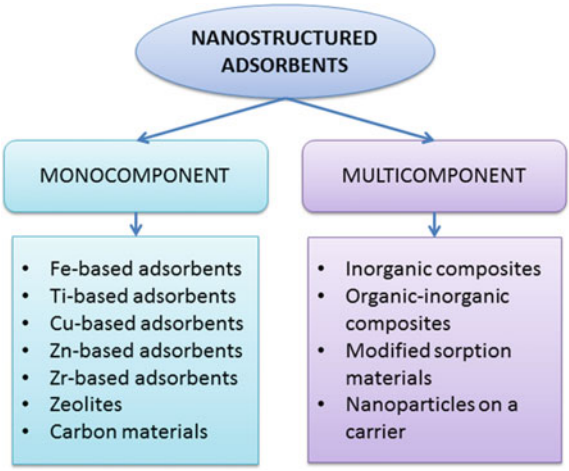

Fig. 3 Types of adsorbents for arsenic removal

1.2 Types of Adsorbents for Arsenic Removal

Presently nanosized structures have a significant impact on technological advancements in different fields, especially environmental applications [14]. There are a lot of diverse types of nanostructured adsorbents for arsenic removal, including various oxides, hydroxides, composites, and nanoparticles on a carrier (Fig. 3).

Nanostructured adsorbents often are one-component: iron oxides, iron hydroxides, iron oxyhydroxides, zero-valent iron, titanium oxides, calcium titanate, copper oxides, zinc oxides, zirconium oxides, aluminum oxides, carbon nanotubes, zeolites, etc. [15–21]. But multicomponent adsorbents often are more effective than one-component due to combining benefits of different materials. There are a lot of both environmental and economic effective adsorbents for arsenic removal, but main part of them contains iron or its compounds due to low-cost and significant efficiency in arsenic immobilization [12, 19].

2 Usage and Perspectives of Nanostructured Adsorbents for Arsenic Compounds' Removal

2.1 Application and Perspectives of Iron-Based Nanostructured Adsorbents for Arsenic Compounds' Removal

Iron-based adsorbents can be one-component and multicomponent, which contain metal nanoparticles, oxides, oxyhydroxides, ferrites, etc.

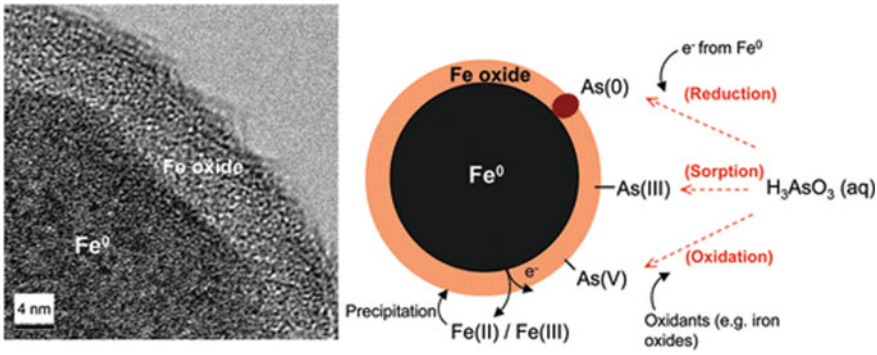

Fig. 4 Structure of ZVI nanoparticles and mechanisms of arsenic pollutants removal [23]

Zero-valent iron nanoparticles (nZVIs) and their composites have extremely wide usage for ecological purposes, including removal from water organic and inorganic arsenic compounds, soil and sediments remediation and treatment of arsenic-contaminated water in wells [17]. There are two methods to obtain treated water from polluted wells: the first one is an injection of nZVIs to form a reactive barrier, the second one is an injection of mobile nZVIs to form an nZVI plume [17].

These nanoparticles have typical core–shell structure formed in an aqueous medium due to interactions with water and dissolved oxygen [18, 22]. Zero-valent iron is the core and reducing agent in redox reactions with arsenic compounds. Iron oxides/hydroxides are the main components of shell [22]. Figure 4 demonstrates shell–core structure of nanoparticle and mechanisms of arsenic compounds' immobilization.

According to review data which are represented in [18], sizes of nZVIs increase from 5 to 10.7 nm due to corrosion processes, what is more the thickness of the oxide/oxyhydroxide layer is about 3.6 nm. Thus, nZVIs can effective immobilize both As(III) and As(V) compounds due to its specific core–shell structure [18]. For example, nZVIs can remove 102 mg As(III)/g or 118 mg As(V)/g [17].

But multicomponent sorption materials based on nZVIs often are more effective, than single nZVIs. It can be modifications, including sulfide-modified nZVIs or different combinations with other oxides, zeolites, grapheme, etc. [24–29]. Sepiolite-supported nanoscale zero-valent iron can remove 165.86 mg As(III)/g from water solution [27]. According to the work [28], adsorption capacity of zeolite-supported sulfide nanoscale zero-valent iron is 204.36 mg As(V)/g. Cu^0 nano-shell-decorated nZVIs are significantly more effective than conventional nZVIs, and its adsorption capacity is 453 mg As(III)/g [29].

Magnetite nanoparticles also are effective in arsenic compounds' immobilization, but their adsorption properties are lower than nZVIs and effective pH range is smaller [30].

Nanostructured iron oxyhydroxide is other effective adsorbent for arsenic compounds' removal. It demonstrates adsorption capacity of As(III) and As(V) about

70 mg/g [3, 19]. But iron oxyhydroxide does not have magnetic properties which makes the separation of nanoparticles more difficult than in case nZVIs or magnetite.

Manganese ferrite nanoparticles are significantly less effective in arsenic compounds' removal than nZVIs, iron oxides or oxyhydroxides. Its adsorption capacity of As(III) and As(V) is about 35 mg/g at pH 8 [31]. This is too small to compete with other iron-based sorption materials.

2.2 *Usage and Perspectives of Titanium-Based Nanostructured Adsorbents for Arsenic Compounds' Removal*

Titanium (IV) oxide is the most popular titanium-based nanostructured adsorbent. This material is both effective in removal of inorganic and organic arsenic compounds due to its adsorption and photocatalytic properties. According to review data which are represented in [32], hydrous TiO_2 with particle size 3–8 nm has surface area of 312 m^2/g and adsorption capacity of 83–96 mg As(III)/g; titania nanotubes with same surface area can adsorb 60 mg As(III)/g or 208 mg As(V)/g.

Iron (III) titanium (IV) mixed binary oxide has similar efficiency as hydrous TiO_2 (85 mg As(III)/g) [32]. This material is cheaper than pure titanium (IV) oxide, but less efficient in photocatalytic treatment. Well-dispersed TiO_2 nanoparticles anchored on Fe_3O_4 magnetic nanosheets have significantly smaller adsorption capacity (about 31 mg As(III)/g and 36 mg As(V)/g) although both components may be involved in photocatalytic reactions [33].

Calcium titanate nanoparticles prepared by the sol–gel method are even less efficient adsorbent. It demonstrates maximum adsorption capacity of As(III) about 11 mg/g [20].

Thereby, titanium (IV) oxide nanoparticles are not suitable for use to remove inorganic arsenic compounds from polluted water or to remediate contaminated soils and sediments due to high cost of these adsorbents, which becomes impossible to reuse after such processes.

2.3 *Usage and Perspectives of Copper-Based Nanostructured Adsorbents for Arsenic Compounds' Removal*

Copper oxide nanoparticles can remove arsenic under a wide range of water content without adjusting the pH and removal such competing anions as phosphate or silicate [34]. But copper nanoparticles and copper oxide nanoparticles do not use as one-component adsorbent for water treatment due to their irreversible aggregation property and a toxicity of copper compounds.

But these nanoparticles can be used in multicomponent sorption materials to improve arsenic removal properties. For example, rice-husk biochar-stabilized iron and copper oxide nanoparticles has maximum capacity of 20.32 mg As/g, but it is significantly higher than biochar without additives (about 1 mg As/g) [35].

Copper-based nanostructured adsorbents are completely unusable for remediation of arsenic-contaminated soils and sediments due to a toxicity of copper compounds, which can pollute ecosystems in this case.

2.4 Applications and Perspectives of Other Different Nanostructured Adsorbents for Arsenic Compounds' Removal

There are a lot of other adsorbents for arsenic compounds' removal, including different oxides, zeolites, carbon materials, etc., but they are less usable than iron-based.

According to work [21], γ-aluminum oxide nanoparticles are completely ineffective in arsenic removal (about 0.8 mg As(III)/g and 1.0 mg As(V)/g). Magnesium oxide nanoparticles have high arsenate adsorption capacity (98 mg/g) but do not participate in redox reactions, which improve As(III) removal [36].

Nanoscale hierarchically porous zeolitic imidazolate framework-8 produced in situ on ZnO nanoparticles is twice as effective in As(III) removal as the sample without imidazolate [37]. This material has an adsorption capacity of 104.9 mg/g, but is significantly more expensive than iron-based adsorbents and is unsuitable for remediation of arsenic-contaminated soils and sediments due to zinc pollution of ecosystems.

3 Conclusion

Therefore, there are extremely many various adsorbents for arsenic compounds' immobilization and removal, but some of these adsorbents are very expensive (titanium-based), several materials are ineffective (γ-aluminium oxide and non-modified biochars), and some adsorbents are unsuitable for wide environmental application (copper-based and zinc-based).

Iron-based sorption materials are low-cost, high-effective in arsenic compounds' immobilization or removal and environmental friendly. Also, zero-valent iron nanoparticles, magnetite, and multicomponent adsorbents based on them can be easy separated from water due to magnetic properties.

Consequently, iron-based multicomponent adsorbents are interesting for many researchers, who are working to improve arsenic compounds' immobilization and removal.

Acknowledgements The authors thank colleagues and students Chemical Technological Faculty of National Technical University of Ukraine «Igor Sikorsky Kyiv Polytechnic Institute» for actively participating in the discussion on the study topic.

References

1. X. Wan, M. Lei, T. Chen, Review on remediation technologies for arsenic-contaminated soil. Front. Environ. Sci. Eng. **14**(2), 1–14 (2020)
2. E. Shaji, M. Santosh, K. Sarath et al., Arsenic contamination of groundwater: a global synopsis with focus on the Indian Peninsula. Geosci. Front. **12**(3), 101079 (2021)
3. M. Litynska, T. Dontsova, O. Yanushevska et al., Development of iron-containing sorption materials for water treatment from arsenic compounds. East.-Eur. J. Enterp. Technol. **10**(110), 35–42 (2021)
4. S. Koley, Future perspectives and mitigation strategies towards groundwater arsenic contamination in West Bengal, India. Environ. Qual. Manage. **4**(31), 75–97 (2021)
5. D. Moulick, S. Samanta, S. Sarkar et al., Arsenic contamination, impact and mitigation strategies in rice agro-environment: an inclusive insight. Sci. Total Environ. **800**, 149477 (2021)
6. G. Genchi, G. Lauria, A. Catalano et al., Arsenic: a review on a great health issue worldwide. Appl. Sci. **12**(12), 6184 (2022)
7. V.S.T. Ciminelli, D.C. Antônio, C.L. Caldeira et al., Low arsenic bioaccessibility by fixation in nanostructured iron (Hydr)oxides: quantitative identification of As-bearing phases. J. Hazard. Mater. **353**, 261–270 (2018)
8. A. Abejón, A. Garea, A. Irabien, Arsenic removal from drinking water by reverse osmosis: minimization of costs and energy consumption. Sep. Purif. Technol. **144**, 46–53 (2015)
9. M. Litynska, N. Tolstopalova, I. Astrelin et al., Influence of foreign ions on the adsorption of arsenate on iron(III) oxides and hydroxides. Voprosy Khimii i Khimicheskoi Tekhnologii **3**, 22–29 (2019)
10. E.A. Hull, M. Barajas, K.A. Burkart et al., Human health risk from consumption of aquatic species in arsenic-contaminated shallow urban lakes. Sci. Total Environ. **770**, 145318 (2021)
11. Y. Zhang, B. Xu, Z. Guo et al., Human health risk assessment of groundwater arsenic contamination in Jinghui irrigation district, China. J. Environ. Manage. **237**, 163–169 (2019)
12. J. Fan, X. Chen, Z. Xu et al., One-pot synthesis of nZVI-embedded biochar for remediation of two mining arsenic-contaminated soils: arsenic immobilization associated with iron transformation. J. Hazard. Mater. **398**, 122901 (2020)
13. J. Nikić, A. Tubić, M. Watson et al., Arsenic removal from water by green synthesized magnetic nanoparticles. Water **11**(12), 2520 (2019)
14. I. Bonadies, (2019) Nanoscale materials in water purification, in *Nanoscale Materials in Water Purification,* pp. 231–246
15. R. Soni, A.K. Pal, P. Tripathi et al., An overview of nanoscale materials on the removal of wastewater contaminants. Appl Water Sci **10**(8), 189 (2020)
16. T.A. Dontsova, S.V. Nahirniak, I.M. Astrelin, Metaloxide nanomaterials and nanocomposites of ecological purpose. J. Nanomater. **2019**, 5942194 (2019)
17. T. Pasinszki, M. Krebsz, Synthesis and application of zero-valent iron nanoparticles in water treatment, environmental remediation, catalysis, and their biological effects. Nanomaterials **10**(5), 917 (2020)
18. U.S. Rashid, B. Saini-Eidukat, A.N. Bezbaruah, Modeling arsenic removal by nanoscale zero-valent iron. Environ. Monit. Assess. **192**(2), 110 (2020)
19. M. Litynska, T. Dontsova, Suspension sorbents for removal of arsenic compounds and humates from water. Water Water Purif. Technol. Scien. Tech. News **3**(28), 14–25 (2020)

20. R. Tamayo, R. Espinoza-González, F. Gracia et al., As(III) removal from aqueous solution by calcium titanate nanoparticles prepared by the sol gel method. Nanomaterials **9**(5), 733 (2019)
21. S. Ghosh, R. Prabhakar, S.R. Samadder, Performance of γ-aluminium oxide nanoparticles for arsenic removal from groundwater. Clean Technol. Environ. Policy **21**(1), 121–138 (2018)
22. G. Sappa, M. Barbieri, P. Viotti et al., Assessment of zerovalent iron nanoparticle (nZVI) efficiency for remediation of arsenic-contaminated groundwater: two laboratory experiments. Water **14**(20), 3261 (2022)
23. M.A.V. Ramos, W. Yan, X.Q. Li et al., Simultaneous oxidation and reduction of arsenic by zero-valent iron nanoparticles: understanding the significance of the core−shell structure. J. Phys. Chem. C **113**(33), 14591–14594 (2009)
24. P. Singh, P. Pal, P. Mondal et al., Kinetics and mechanism of arsenic removal using sulfide-modified nanoscale zerovalent iron. Chem. Eng. J. **412**, 128667 (2021)
25. J. Raez, A. Arencibia, Y. Segura et al., Combination of immobilized TiO_2 and zero valent iron for efficient arsenic removal in aqueous solutions. Sep. Purif. Technol. **258**, 118016 (2021)
26. J. Suazo-Hernández, P. Sepúlveda, K. Manquián-Cerda et al., Synthesis and characterization of zeolite-based composites functionalized with nanoscale zero-valent iron for removing arsenic in the presence of selenium from water. J. Hazard. Mater. **373**, 810–819 (2019)
27. M. Ainiwaer, X. Zeng, X. Yin et al., Thermodynamics, kinetics, and mechanisms of the co-removal of arsenate and arsenite by sepiolite-supported nanoscale zero-valent iron in aqueous solution. Int. J. Environ. Res. Public Health **19**(18), 11401 (2022)
28. C. Zhou, C. Han, X. Min, T. Yang, Enhancing arsenic removal from acidic wastewater using zeolite-supported sulfide nanoscale zero-valent iron: the role of sulfur and copper. J. Chem. Technol. Biotechnol. **96**(7), 2042–2052 (2021)
29. L. Xu, K. Yan, Y. Mao et al., Enhancing the dioxygen activation for arsenic removal by Cu_0 nano-shell-decorated nZVI: synergistic effects and mechanisms. Chem. Eng. J. **384**, 123295 (2020)
30. T.K. Das, A.N. Bezbaruah, Comparative study of arsenic removal by iron-based nanomaterials: potential candidates for field applications. Sci. Total Environ. **764**, 142914 (2021)
31. J. López-Luna, L.E. Ramírez-Montes, S. Martinez-Vargas et al., Linear and nonlinear kinetic and isotherm adsorption models for arsenic removal by manganese ferrite nanoparticles. SN Appl. Sci. **1**(8), 950 (2019)
32. S. Ashraf, A. Siddiqa, S. Shahida et al., Titanium-based nanocomposite materials for arsenic removal from water: a review. Heliyon **5**(5), e01577 (2019)
33. M. Deng, X. Wu, A. Zhu et al., Well-dispersed TiO_2 nanoparticles anchored on Fe_3O_4 magnetic nanosheets for efficient arsenic removal. J. Environ. Manage. **237**, 63–74 (2019)
34. K. Reddy, K. McDonald, H. King, A novel arsenic removal process for water using cupric oxide nanoparticles. J. Colloid Interface Sci. **397**, 96–102 (2013)
35. N. Priyadarshni, P. Nath, N. Chanda, Sustainable removal of arsenate, arsenite and bacterial contamination from water using biochar stabilized iron and copper oxide nanoparticles and associated mechanism of the remediation process. J. Water Process Eng. **37**, 101495 (2020)
36. L. Guo, R. Lei, T.C. Zhang et al., Insight into the role and mechanism of polysaccharide in polymorphous magnesium oxide nanoparticle synthesis for arsenate removal. Chemosphere **296**, 133878 (2022)
37. L. Shi, Z. Shu, K. Wang, et al., Nanoporous zeolitic imidazolate framework-8 nanoparticles for arsenic removal. ACS Appl. Nano Mater. (2023)

Nanoelectronics

CO_2 Hydrogenation Over Bulk and Loaded NiFe Catalysts: The Effect of Carrier

A. G. Dyachenko, O. V. Ischenko, V. E. Diyuk, S. V. Gaidai, A. V. Yatsymyrskyi, O. V. Pryhunova, O. V. Goncharuk, M. V. Borysenko, O. V. Mischanchuk, Olga Niemiec, and V. V. Lisnyak

Abstract The structure and surface properties of bulk and loaded bimetallic nickel–iron (NiFe) catalysts were studied in detail by various characterization technologies, such as X-ray diffraction, scanning electron microscopy, nitrogen porosimetry, temperature-programmed reduction, and temperature-programmed desorption mass-spectrometry. We demonstrate the dependence of the catalytic activity of bulk NiFe catalysts against the Ni/Fe ratio. Based on the experimental observations, the possible mechanism of carbon dioxide (CO_2) hydrogenation to methane (CH_4) on the surface of the active bulk catalyst and that loaded on carbon nanotubes was proposed. The CO_2 conversion and CH_4 selectivity mainly depend on the nature of the carrier. Based on the example of the catalysts loaded on carbon carriers, the effect of surface morphology on the CO_2 conversion and CH_4 selectivity is shown. We showed the role of the initial carriers, namely, crystal structure, texture, and surface morphology, on the formation of active sites of nanocomposite NiFe catalysts based on the alumina with different porosities.

A. G. Dyachenko (✉) · M. V. Borysenko · O. V. Mischanchuk
Chuiko Institute of Surface Chemistry, National Academy of Sciences of Ukraine, Kyiv 03164, Ukraine
e-mail: dyachenko.alla@yahoo.com

O. V. Ischenko · V. E. Diyuk · S. V. Gaidai · A. V. Yatsymyrskyi · O. V. Pryhunova · V. V. Lisnyak
Taras Shevchenko National University of Kyiv, Kyiv 01601, Ukraine

O. V. Goncharuk
National Technical University of Ukraine, Igor Sikorsky Kyiv Polytechnic Institute, Kyiv 03056, Ukraine

A. G. Dyachenko · O. Niemiec
Institute of Physical Chemistry, Polish Academy of Sciences, 01-224 Warsaw, Poland

O. Fesenko and L. Yatsenko (eds.), *Nanoelectronics, Nanooptics, Nanochemistry and Nanobiotechnology, and Their Applications*, Springer Proceedings in Physics 297,
https://doi.org/10.1007/978-3-031-42708-4_14

1 Introduction

Methanation of carbon dioxide (CO_2) with electrolytically generated hydrogen (H_2) from renewable energies enables chemical energy storage in a cycle [1] and contributes to the decrease of atmospheric CO_2 pollution [1–3]. Production of synthetic natural gas is of increased interest since it can easily be stored and transported in the existing gas infrastructure while being reused for energy generation [4]. Using bimetallic bulk catalysts in the methanation reaction is much more efficient than monometallic ones [5–9]. Adding the iron component to the traditional monometallic nickel catalyst significantly improves the conversion of CO_2 and increases the yield of the target product–methane (CH_4). At the same time, the iron amount should be regulated to prevent the formation of undesirable co-products, such as carbon monoxide (CO) [5, 6, 9, 10]. Finding the optimal ratio between the active components in the composition of the bulk NiFe catalysts is a crucial step in the study of their effectiveness in the CO_2 methanation reaction and the determination of the mechanism of CH_4 formation [5]. In the future, this directed us to use these compositions as part of the loaded catalysts. It is possible to increase the contact surface with reagent molecules by increasing the dispersion of the active mass of the catalyst by applying a certain amount of the active component to the surface of the carrier [10–12]. In addition, the catalyst carrier participates in heterogeneous catalytic processes by creating additional sites for the adsorption of molecules from the gas phase [13]. The most popular oxide carriers for the methanation reactions are silica (SiO_2) and alumina (Al_2O_3) [10, 11, 13, 14]. An important characteristic of oxide carriers is their porosity, which affects the distribution and localization of the deposited metal phase. For example, the microporous structure of titanium oxide blocks the ability of active metals in the micropores to react with molecules from the gas phase. Although TiO_2 is an active catalyst for many environmental processes [15, 16], including the photocatalytic reduction of CO_2 [17]. Also, in the process of synthesis of catalysts loaded on oxide carriers, it is possible for the carrier to interact with metals and the formation of spinels. Such interaction is not always beneficial for the reaction catalyst because it can provoke the formation of by-products. Carbon-based supports are an excellent alternative to oxides. Carbon nanotubes [18–21], graphite materials [22], and activated carbon [23] have a good surface area; their pore structures can be adjusted, thus favoring a lower interaction with the active metallic catalyst due to its inert characteristic. The carbon-based support can promote the formation of Met_xC_y, which is not an active phase for the methanation process and typically deactivates the catalytic metal sites [24].

We found some factors influencing catalyst efficiency, including the effects of (i) the ratio of components in the active NiFe phase; (ii) the amount of the active NiFe phase in the composition of the loaded catalyst; and (iii) the nature of the carrier.

Nevertheless, we found that in addition to these factors, the carrier structure plays a significant role [25, 26]. We have determined that the mechanism of methane formation on the surface of bulk and deposited catalysts is different [5, 6, 27, 28]. The nature of the carrier surface influences the formation of intermediate products of the reaction

and the catalytic performance of the catalysts [11, 13, 28]. The pore size distribution in oxide carriers determines the catalytic performance and the reaction product distribution. It can profoundly affect the dispersion and reducibility of catalytic metals and regulate the mass transport performance. In this line, the increasing catalyst pore sizes lead to higher ratios of C_2^+ formation due to the enhancement of product diffusion. A narrow distribution of pore sizes limits the particle size of catalytic metals that prevents the C–C bond growth [29, 30]. All these factors affect the CO_2 conversion efficiency and selectivity toward CH_4, regulating the CH_4 formation mechanism.

In this study, we have compared the catalytic performance in the CO_2 methanation of the bulk and loaded NiFe catalysts and have conducted a comparative analysis of the effect of different carriers on the CH_4 formation process.

2 Experimental

2.1 Synthesis of Bulk NiFe Catalysts

To study the catalytic activity of the bulk NiFe catalysts in the CO_2 hydrogenation reaction, samples with a specified weight ratio of Ni and Fe metals were synthesized by the method of decomposition of metal salts. The synthesis of these catalysts can be conventionally divided into three stages. At the first stage, the calculated amounts of individual metals in a given ratio are subjected to co-dissolution in excess of nitric acid during heating. In the process of gradual evaporation of the solution, hydroxides of the corresponding metals are formed, and their subsequent thermal degradation leads to the formation of metal oxides, which are precursors of catalysts. The second stage is the reduction of the obtained oxides in the H_2/He gas flow at the temperature determined by the thermoprogrammed reduction (TPR) method [5]. The final stage is the formation of active sites of the catalyst in the reaction medium. This stage is carried out directly in the reactor before the study of catalytic activity.

2.2 Synthesis of Loaded NiFe Catalysts

Loading the active mass on the carriers was carried out by wet impregnation. The principle of the wet impregnation method consists of the delivery of cations forming the active metal catalyst to the carrier surface by ion sorption from water-soluble metal salts with subsequent removal of the solvent and thermal decomposition of adsorbed anions. As a result, we get a composite in which particles of transition metal oxides are localized on the surface of the carrier. These oxide particles are the precursors of the final product, namely, mono- or bimetallic catalyst loaded on the carrier surface. To form a catalytically active compound, the active transition metals were dissolved in concentrated nitric acid, similar to the procedure used to prepare

massive metal catalysts. For loading onto the surface of the carrier, a nitrate solution with 80 wt% of Ni and 20 wt% of Fe was prepared. The mass of the carrier was impregnated with the nitrate solution in order to obtain the amount of loaded active mass of 5–20 wt%. The obtained wet substance was dried in a sand bath at 150 °C and then calcined at 250–300 °C for a day.

Further formation of the catalyst was carried out by reducing with hydrogen gas in helium gas flow at the selected reduction temperature determined by the temperature-programmed reduction method with a reducing hydrogen gas (H_2) made to flow across the catalyst under gradually increasing thermal conditions (H_2-TPR).

2.3 Temperature-Programmed Reduction (H_2-TPR)

The reducibility of the NiFe catalysts (bulk and supported on different carriers) was studied with H_2-TPR using thermal analysis. The thermograms were recorded using a Derivatograph Q-1500D (MOM, Hungary) operated in the temperature range of 50–600 °C at a heating rate of 5 °C/min. Experiments were conducted with 30–50 mg of sample loaded in an alumina crucible with a bottom perforated with small holes and covered with a perforated lid.

2.4 Textural Characterization

Nitrogen adsorption–desorption isotherms were measured on an ASAP 2405N adsorption analyzer at 77.4 K. Before adsorption measurements, the samples were outgassed at 110 °C for 2 h in a vacuum chamber. The standard Brunauer–Emmett–Teller (BET) method [31, 32] was used to calculate the specific surface area (S_{BET}). The total pore volume V_p was evaluated by converting the volume of adsorbed N_2 at the relative equilibrium adsorption pressure of 0.98–0.99, to the volume of liquid nitrogen per gram of adsorbent. Textural parameters: microporous, macroporous, and mesoporous surface areas (S_{micro}, S_{macro}, and S_{meso}), microporous, mesoporous, and macroporous volumes (V_{micro}, V_{meso}, V_{macro}, and V_p), and the average pore radius $R_{p,V}$ were found as in [13].

2.5 X-Ray Powder Diffraction (XRD)

X-ray diffraction (XRD) patterns of metal oxide (as-synthesized) and metal NCs (after testing in the catalytic process) were recorded on a DRON-3M powder diffractometer with monochromatic CuKα radiation ($\lambda = 0.15418$ nm) and CoKα radiation ($\lambda = 0.17903$ nm) over an angular range from 10° to 80°. X-ray tube operation parameters: voltage of 40 kV, current of 15 mA, scanning speed 2° min^{-1}. Interpretation of

the phase composition was performed using the integrated X-ray powder diffraction software suite PDXL from https://www.rigaku.com/support/software/pdxl. The crystalline structure of samples was analyzed using the JCPDS Database (International Center for Diffraction Data, PA, 2001). The average sizes of nanosized crystallites (d, nm) were estimated according to the Scherrer equation [33].

2.6 Scanning Electron Microscopy (SEM)

The images of uncoated samples of bulk or supported catalysts were captured on a Tescan Mira 3 GMU LV-FE-scanning electron microscope equipped with an energy dispersion X-ray (EDX) spectrometer from Oxford Instruments. The microscope was used in the back-scattered electron (BSE) mode to capture high-quality BSE SEM images with the INCA software.

The chemical analysis was carried out by collecting the EDX spectra from the selected areas with an Oxford INCA system. A ZAF procedure was used to calculate the concentration of analyzed elements from an X-ray spectrum emitted by a solid sample bombarded with a focused beam of electrons to obtain a localized chemical analysis with the EDX detector.

2.7 Catalytic Evaluation

The catalytic performances were studied in a flow reactor at atmospheric pressure [5, 13]. The reaction gas mixture consisted of 2 vol% CO_2, 55 vol% H_2, and 43 vol% He (helium was used as a carrier gas). The total gas flow rate was 0.1 l/min, and the catalyst weight was 1 g. The reaction components and products were monitored using a Shimadzu GC-2014 gas chromatograph equipped with a thermal conductivity detector. A column filled with 5A molecular sieves was used to separate the gas mixture components.

As a rule, the catalytic experiment was carried out in two heating modes. During the first heating, the catalyst was worked in the reaction mixture with the formation of active sites of the catalyst surface. This stage is considered by us to be the final stage of catalyst synthesis. During the second heating, the catalytic performance of the sample under study was directly determined. Equations (1–3) [13] were used to calculate the CO_2 conversion and the CH_4 and CO yields:

$$X_{CO_2} = \left(1 - \frac{[CO_2]_{out}}{[CO_2]_{out} + [CH_4]_{out} + [CO]_{out}}\right) \times 100\%, \quad (1)$$

$$Y_{CH_4} = \frac{[CH_4]_{out}}{[CO_2]_{out} + [CH_4]_{out} + [CO]_{out}} \times 100\%, \quad (2)$$

$$Y_{CO} = \frac{[CO]_{out}}{[CO_2]_{out} + [CH_4]_{out} + [CO]_{out}} \times 100\%, \quad (3)$$

where $[CO_2]_{out}$, $[CO]_{out}$, and $[CH_4]_{out}$ are the volume percentages (vol%) of CO_2, CO, and CH_4 gases, correspondingly, in gas mixtures sampled at the reactor outlet.

2.8 TPD MS Investigation

After the catalytic experiment completion, when reaching maximum CO_2 conversion, the reactor with the catalyst was cooled to room temperature [13, 34]. Under such conditions, the catalyst surface contains adsorbed particles formed during the reaction at the stage of maximum CO_2 conversion and the highest methane yield.

During the course of TPD MS studies, a small catalyst amount was transferred to a quartz cell in a flow of reaction gases, then, it was connected to a thermal desorption system with mass spectrometric analysis. After that, the cell was evacuated and heated at a rate of 14 °C per min. The temperature range of the TPD MS study was 30–800 °C. Thermal desorption of particles from the surface occurs with different activation energy, the value of which allows to estimate the state of the catalyst surface.

3 Result and Discussion

3.1 Characterization of Bulk NiFe Catalysts

The reducibility of the synthesized monometallic and bimetallic bulk catalysts was investigated by H_2-TPR. Figure 1 shows the weight-normalized reduction profiles in the temperature range of 50–550 °C.

The TPR profiles can be divided into four temperature regions that correspond to different thermal transformations of the tested samples (Fig. 1). The first region (Part 1 in Fig. 1, 30–120 °C) corresponds to weight loss due to water desorption; the second region (Part 2 in Fig. 1, 120–220 °C) is because of thermal decomposition of Ni and Fe hydroxides with the formation of the corresponding oxides or spinels; the third and fourth regions (Parts 3 and 4 in Fig. 1, above 330 °C) are assigned to the reduction of oxide precursors to the metallic state. The peak positions and intensity of H_2-TPR profiles (in Parts 1 and 2 in Fig. 1) are similar for monometallic Ni100 and bimetallic NiFe powders. The TPR profiles in Part 3 reflect the weight loss due to the reduction of the metal oxides to respective metals. One peak is characteristic for the Ni100 and Ni75Fe25 powders, while for the Ni90Fe10 and Ni80Fe20 powders, the TPR profile is more complex, which is a sign of a more complex structure of these samples. The TPR profile of the Fe100 powder is different from other ones registered

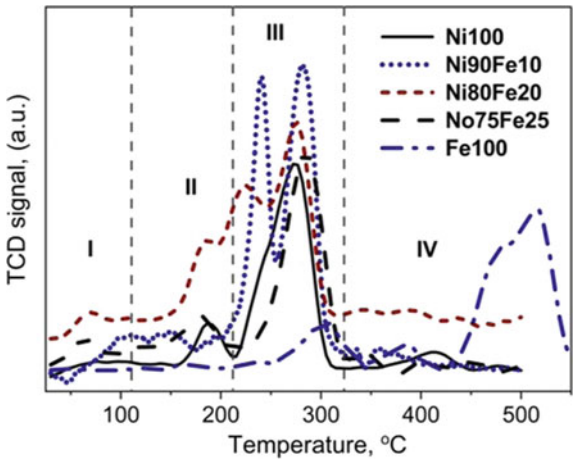

Fig. 1 H_2-TPR profiles of the monometallic Ni and Fe catalysts, and the bimetallic NiFe bulk catalysts of different compositions

for mono- and bimetallic powders. It is due to the high-temperature resistance of Fe-containing compounds. In the case of the Fe100 powder, on the temperature scale, the weight loss is shifted to a higher temperature (> 500 °C). On the basis of the H_2-TPR results, it can be summarized that 320 °C is the appropriate temperature for reducing prepared oxide precursors up to their metallic state in the process of the bulk NiFe catalyst formation.

The catalytic behavior of the NiFe bimetallic powders with various ratios of metals was evaluated in the temperature range of 150–450 °C. The phase diagram presented in Fig. 2 demonstrates the data of CO_2 conversion and CH_4/CO yield at 350 °C for a number of catalysts. The reasons for good catalytic performance can be analyzed based on the experimental results obtained during the CO_2 methanation over the NiFe bulk catalysts with the different Ni/Fe ratios and the binary phase diagram of Ni–Fe system [35]. We assume that the composition of the most effective catalysts is in the heterogeneous region of the coexistence of γ-Ni(Fe) solid solutions (with 60–70 and 80–100 wt% Ni) and an individual compound $FeNi_3$. The powder with 75 wt% of Ni and 25 wt% of Fe demonstrates a low methane yield. According to the Ni–Fe phase diagram, the individual compound $FeNi_3$ exists in the Ni region of 72–77 wt% [36].

The structure and morphology of the surface of Ni80Fe20 and Ni75Fe25 catalysts with high and low catalytic activities, respectively, were investigated by XRD and SEM. After the first stage of synthesis, the examination of the structure of Ni–Fe-containing samples by XRD demonstrates the formation of oxide phases of Ni and Fe (Fig. 3). After successive stages of the reduction of oxide phases by hydrogen and the prepared catalysts used in the CO_2 methanation reaction, the XRD patterns show a subset of reflections corresponding to the cubic face-centered crystalline phase with lattice parameters of 3.54–3.56 Å (Table 1). These values are averaged between those for the monometallic cubic phases of Ni (3.520 Å) and Fe (3.568 Å). This observation may indicate the existence of various cubic face-centered phases, including the $FeNi_3$ intermetallic compound and the binary Ni–Fe solid solutions [36]. The presence of a

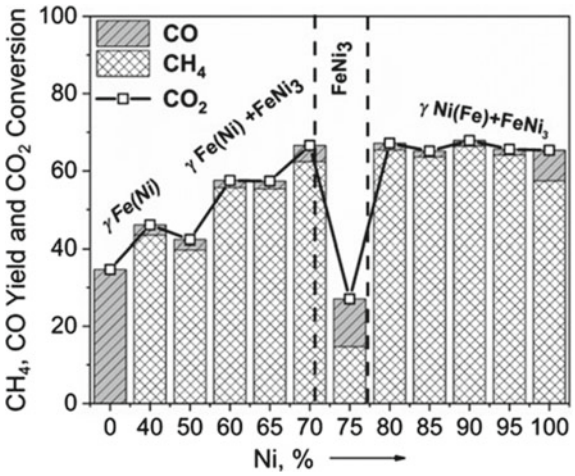

Fig. 2 CH_4/CO production and CO_2 conversion as a function of the Ni content in the composition of the NiFe bulk catalysts and the corresponding phases of the Ni–Fe phase diagram

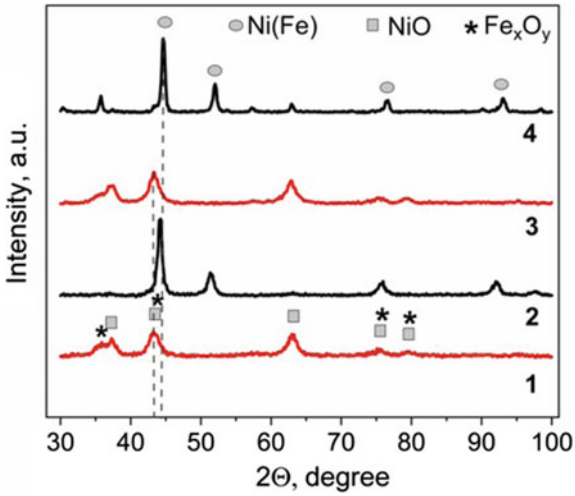

Fig. 3 XRD patterns of Ni75Fe25 (1) and Ni80Fe20 (3) powders in the form of co-precipitated Ni and Fe oxides and after reduction with hydrogen and exposure in the catalytic CO_2 methanation process (2) and (4), respectively

small amount of NiO in the XRD patterns can be explained by passivation. Typically, after the completion of the catalytic reaction, the catalyst samples were subjected to the process of passivation in air, as a result of this procedure metallic catalyst surface was covered with a thin oxide film.

Bulk NiFe catalysts of different compositions have different surface morphology, as demonstrated by the SEM method. Figure 4 proves the significant difference in the microphotographs of individual nickel and iron metals. The nickel surface consists of round-shaped grains with a size of 100–200 nm, which agglomerate into particles of 0.1–0.5 μm, forming a macroporous surface (Fig. 4a, b).

Table 1 XRD data for the NiFe samples in the oxide and metallic forms taken before and after reduction with hydrogen and subsequent exposure in the catalytic CO_2 methanation process, respectively

Sample	Phase	Lattice parameter, Å	Crystallite size, nm
Ni80Fe20 (oxide form)	NiO	4.182	5–7
	Fe_3O_4	8.367	12–19
Ni80Fe20 (metal form)	Ni/Fe	3.537	9–13
Ni75Fe25 (oxide form)	NiO	4.186	5–8
	Fe_2O_3	8.338	5–8
Ni75Fe25 (metal form)	Ni/Fe	3.561	18–23

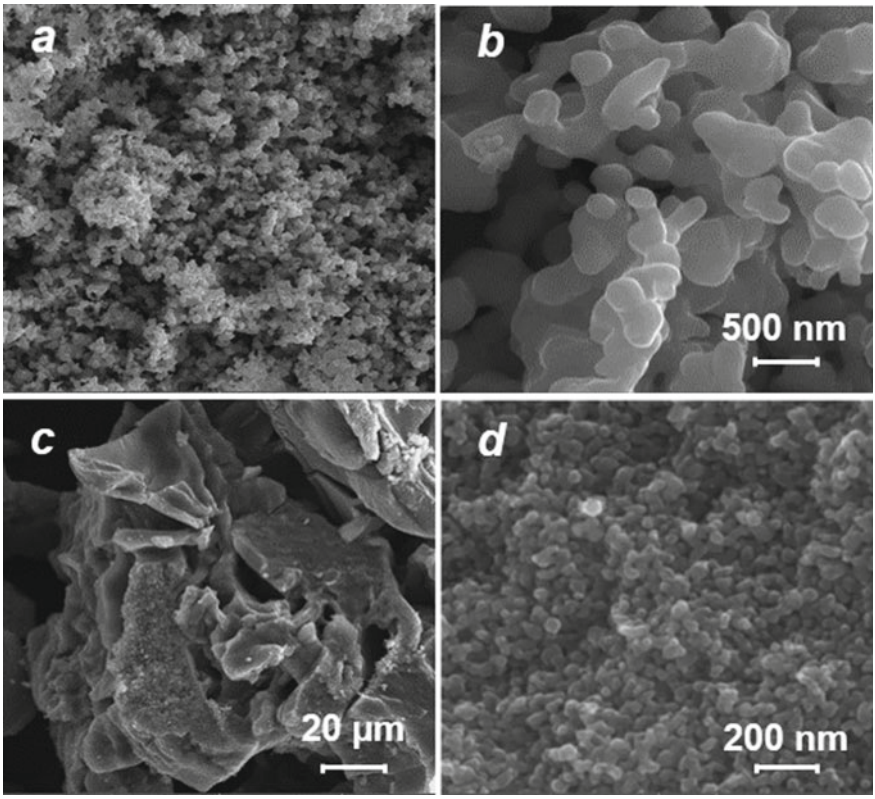

Fig. 4 SEM images of bulk monometallic **a**, **b** Ni100 and **c**, **d** Fe100 catalysts

Figure 4c, d demonstrate that the surface of the monometallic Fe100 catalyst is completely different from that of the monometallic Ni100 one. This catalyst has a smooth flat surface composed of "scales" layered on top of each other. The particles have an irregular shape, with an average size of about 100 μm. During the formation of bimetallic structures, the morphological features of the surface of both nickel and iron are compiled. Figure 5 presents microphotographs of the most effective catalyst (Ni80Fe20) and the sample with the lowest catalytic activity (Ni75Fe25). In fact, that the active Ni80Fe20 catalyst has a highly defective surface compared to inactive one (cf. Fig. 5a, b and 5c, d in pairs).

The Ni80Fe20 catalyst exists as large agglomerates, several tens of microns in size, formed due to the sintering of small spherical particles with a diameter of 80–100 nm. Also, macropores (diameter 100–200 nm) and mesopores (diameter 50 nm) are observed on the microphotograph of the Ni80Fe20 catalyst (Fig. 5b). Contrasting to the Ni80Fe20 catalyst, the SEM images of the Ni75Fe25 catalyst also show large agglomerates with a smooth, non-porous surface (Fig. 5c, d). Agglomerates with such a surface are formed as a result of the sintering of smaller (20–40 nm) metal

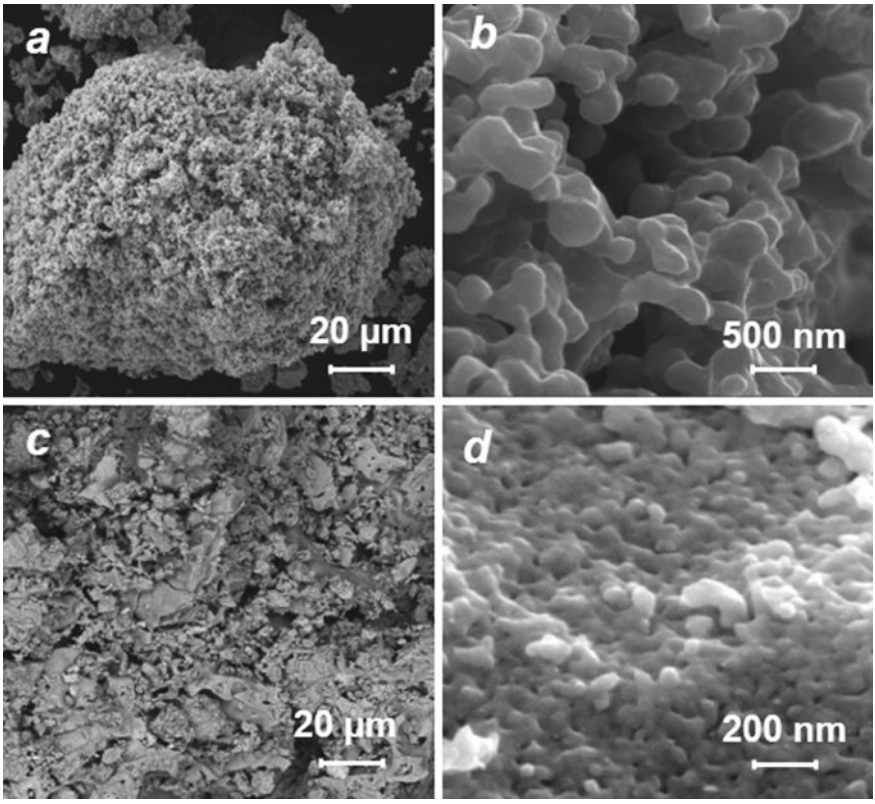

Fig. 5 SEM images of bulk bimetallic **a**, **b** Ni80Fe20 and **c**, **d** Ni75Fe25 catalysts

nanoparticles, compared to the active Ni80Fe20 catalyst, with the formation of a denser structure, which negatively affects the catalytic activity of the Ni75Fe25 catalyst.

Figure 6 shows the changes in the relative concentrations of the gas mixture components (CH_4, CO, and CO_2) at the reactor outlet chromatographically recorded during the second temperature rise. For the individual nickel sample, the CO_2 conversion starts at above 200 °C increasing intensively, reaching a maximum of 60% at 400 °C (Fig. 6a). In this case, the main reaction product is methane with a small amount (8%) of CO, the reaction by-products. Adding a small amount of iron (10 wt%) to the Ni-monometallic catalyst significantly affects the CO_2 methanation process, and the conversion of carbon dioxide becomes more rapid. The yield of synthesized methane increases to 63–66%, while the CO yield decreases to 3% (Fig. 6b). A further increase in the concentration of iron content in the catalyst composition to 20 wt% promotes the process of CO_2 hydrogenation to CH_4 (Fig. 6c). However, the formation of CO cannot be excluded completely. The amount of CO (2 vol%) in the gas mixture remains approximately the same in the entire temperature range of the study.

Further studies have shown that the catalytic performance of the Ni75Fe25 catalyst differs considerably from the previously reported catalysts. Figure 6d shows that the CO_2 conversion over the Ni75Fe25 catalyst is significantly lower than found for other NiFe catalysts. As one can see, it reaches a maximum of 25% at 370 °C. At the same time, CH_4 and CO are equally formed in amounts of 12–15 vol%. The reason for this behavior of the NiFe catalyst, consisting of 75 wt% Ni and 25 wt% Fe, should be sought in its structural features. Possibly, the main reason is the formation of the $FeNi_3$ intermetallic compound that occurs at this ratio of Ni to Fe. In many bimetallic systems, heterogeneous contacts at the interface have an increased catalytic activity compared to homogeneous compositions close to them in chemical composition [37]. Therefore, forming an individual compound with a stoichiometric composition reduces the catalytic activity by default. When the NiFe catalyst contains 50 wt% of iron and above, the CO_2 conversion drops to 40% (Fig. 6e). The CH_4 yield is also significantly reduced. So, the studies of the NiFe catalysts with higher Fe contents in the CO_2 methanation reaction are beyond interest. The Fe100 catalyst shows low catalytic performance in this reaction [5, 36]. In its presence, the process selectivity shifts toward the formation of CO, see Fig. 6f.

TPD MS is used to study catalytic processes occurring at the solid–gas interface [38]. This method allows recording the particles desorbed from the solid surface at different temperatures. The resulting TD profiles allow us to assess the state of the catalyst surface during the catalytic reaction, determine the type and state of adsorbed particles on its surface, and propose a model of the reaction mechanism.

The study of the methanation process on bulk NiFe catalysts by TPD MS was carried out on samples with high (Ni80Fe20) and low (Ni75Fe25 and Ni50Fe50) catalytic activities. The thermodesorption temperature maxima (T_m) for all studied samples can be divided into three temperature ranges. The first range is from 50 to 180 °C for species that weakly bound to the catalyst surface; the second is from 200 to 350 °C for species whose desorption occurs at a temperature close to the

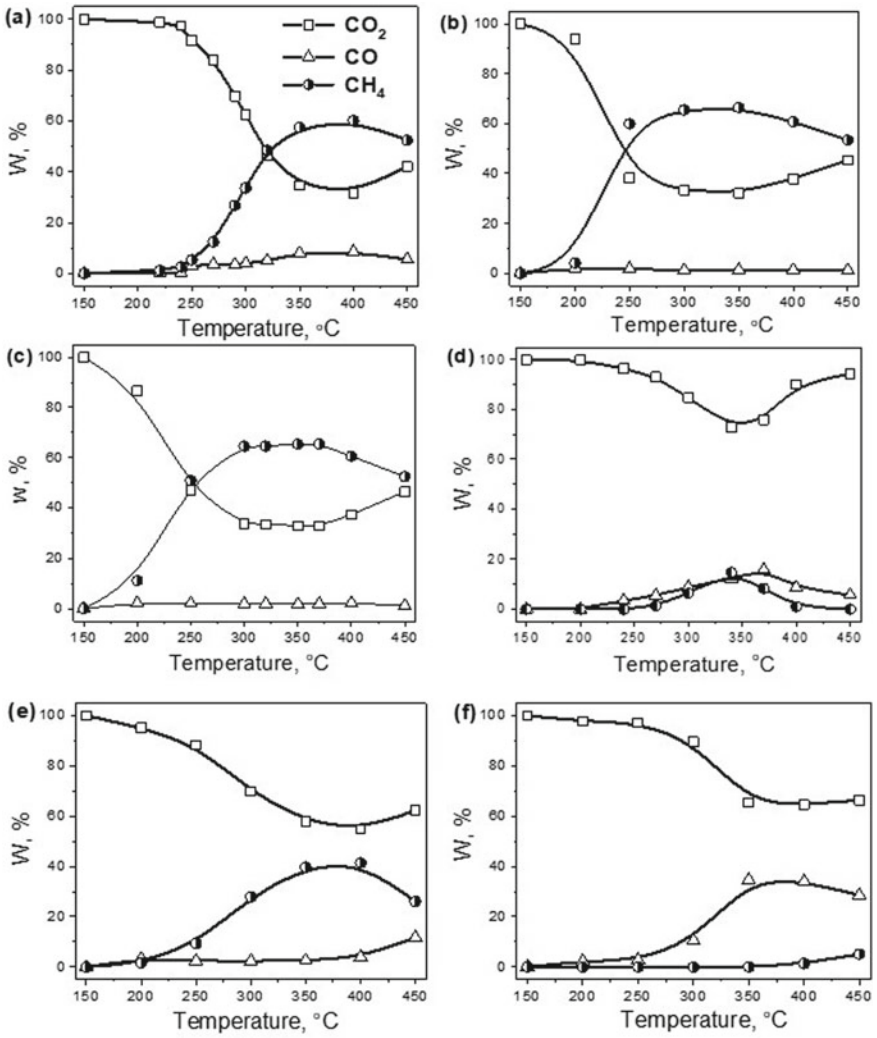

Fig. 6 Volume percentage (W, %) of CH_4, CO, and CO_2 gases at different temperatures in the outlet gas mixture after catalytic CO_2 methanation using **a** Ni100, **b** Ni90Fe10, **c** Ni80Fe20, **d** Ni75Fe25, **e** Ni50Fe50, and **f** Fe100 catalysts

temperature window of the CO_2 methanation reaction; the third is from 400 to 500 °C for species strongly bound to the catalyst surface.

Figure 7 shows the profiles of CO* (m/z 28), CO_2* (m/z 44), and H_2O* (m/z 18) species desorbed from the Ni80Fe20, Ni75Fe25, and Ni50Fe50 catalysts. It can be seen that for the active Ni80Fe20 catalyst, the TD maxima of CO and CO_2 are registered at $T_m = 100$, 150, 300 °C (Fig. 7a), while the TD spectra of CO* and CO_2* from the surface of the Ni75Fe25 and Ni50Fe50 catalysts (Fig. 7b, c) show

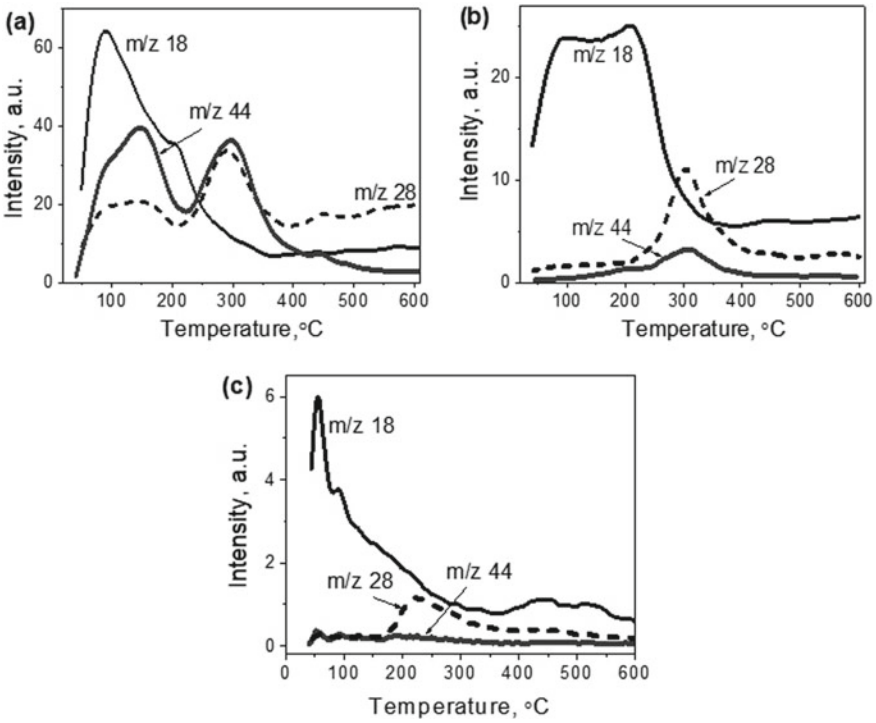

Fig. 7 TD profiles of desorbed species CO_2^* (m/z 44), CO^* (m/z 28), and H_2O^* (m/z 18) from the surface of catalysts **a** Ni80Fe20, **b** Ni75Fe25, and **c** Ni50Fe50 catalysts

only one maximum at 300 °C, and the intensity of the CO peak is much higher than that of CO_2.

According to the data obtained, we assumed that the CO_2 molecule adsorbed on the surface of the Ni75Fe25 sample could decompose into CO* and O*, while CO molecules are strongly chemisorbed on the catalyst surface, preventing future passage of hydrogenation. These results are consistent with the literature data [39, 40], indicating that the process of CO_2 methanation on the surface of catalysts should adsorb CO_2 molecules. Since this process can occur on different active sites of the catalyst with different activation energies, it further affects the reaction mechanism and the composition of the resulting gas mixture.

In Ref. [41], the authors demonstrate that the inactive catalysts are characterized by a single TD peak with T_m in the middle-temperature range, while the CO_2 TD profiles recorded for the active catalysts have several temperature maxima over the entire temperature range. Consequently, different sites for the adsorption of CO_2 are present on the surface of the active catalyst. They are further participating in the pathways of CH_4 formation. Accordingly, the CO_2 conversion and CH_4 yield are high in the presence of such catalysts. This observation is consistent with the results of the study of catalytic activity (Fig. 2). They showed that in the series of the studied

NiFe catalysts, the lowest values of CO_2 conversion and CH_4 yield at a temperature of 300 °C (Fig. 6d) were observed for the Ni75Fe25 catalyst.

For the active Ni80Fe20 catalyst, the intensity of TD CO_2 and CO profiles is almost the same at 300 °C. The TD profiles of H_2O (m/z 18), which are depicted in Fig. 7, confirm actually that oxygen in the catalytic reaction is produced by dissociated CO_2, not water, over the NiFe catalysts.

These profiles have not peaked in the temperature range of the passage of the catalytic CO_2 methanation reaction. An important observation is the absence of profiles of intermediate oxygen-containing compounds like HCO*, H_2CO*, and others in the TD spectra of the studied samples [36].

Notably, the TD profiles of all desorbed particles from the surface of Ni80Fe20 and Ni75Fe25 have a symmetrical shape. Their desorption from the surface of the catalysts occurs by the dissociative mechanism, when CO, CO_2, and H_2O particles are formed on the catalyst surface layer by recombination from the corresponding atoms [6, 36, 38]. The methanation process on catalysts of this type should include the complete dissociation of the carbon dioxide molecule into separate carbon and oxygen atoms, followed by their interaction with hydrogen and the formation of methane and water, respectively.

Based on the data obtained, one can conclude that the process of CO_2 methanation on the bulk Ni–Fe catalysts can occur by the direct hydrogenation of CO_2 to CH_4. The following scheme depicts the pathways:

$$CO_2 + [\,] \rightarrow [O \ldots C \ldots O], \tag{4}$$

$$[O \ldots C \ldots O] \rightarrow [C] + 2[O], \tag{5}$$

$$H_2 + 2[\,] \rightarrow 2[H], \tag{6}$$

$$[C] + [H] \rightarrow [CH] + [\,], \tag{7}$$

$$[CH] + [H] \rightarrow [CH_2] + [\,], \tag{8}$$

$$[CH_2] + [H] \rightarrow [CH_3] + [\,], \tag{9}$$

$$[CH_3] + [H] \rightarrow CH_4 + 2[\,], \tag{10}$$

$$[O] + [H] \rightarrow [OH] + [\,], \tag{11}$$

$$[OH] + [H] \rightarrow H_2O + 2[\,], \tag{12}$$

where [] is the free site on the catalyst surface.

In accordance with the above pathways, CO_2 chemisorbed on the active site of the catalyst, which is located at the interface, undergoes complete dissociation to C_{ads}^* and O_{ads}^* due to the formation of an active complex (Eqs. 4, 5). The adsorbed carbon then reacts rapidly with available hydrogen (from the gas phase or adsorbed on the catalyst surface), resulting in the formation of methane (Eqs. 7–10). Taking into account the fact that nickel is able to adsorb a significant amount of hydrogen with a low activation energy of adsorption [38, 42], the interaction of adsorbed carbon and hydrogen atoms should occur very quickly, which does not allow for registering intermediate CH^*, CH_2^*, and CH_3^* particles in the TD spectra. Water formation occurs by a similar mechanism from adsorbed oxygen and available hydrogen atoms (Eqs. 11, 12). The rate-determining step in this process is most likely the formation of water.

3.2 NiFe Catalysts Loaded on the Carbon Carriers

The most effective method of increasing the activity of the catalyst is its loading on an inert carrier [43, 44]. In this way, it is possible to improve the selectivity of the process for a target product and achieve a higher yield of products or to lower the temperature at their maximum yields. The choice of catalyst carrier to achieve the desired result is an important point in synthesis and further research. Below, the results of the study of the catalytic properties of NiFe catalysts loaded on different carriers are presented. The used carriers can be divided into two groups, namely, carbon and oxide carriers. The carbon carriers include synthetic nanodiamonds (SND), graphite nanoplatelets (GNP), thermally expanded graphite (TEG), and carbon nanotubes (CNTs). All these carriers are characterized by high specific surface area and significant thermal stability.

Loading of the active component on the surface of carbon carriers was carried out by impregnation from nitrate solutions. Studies of catalyst activity in a flow reactor showed a tendency to increase the CH_4 yield with increasing temperature. For catalysts loaded on SND or CNTs, nearly complete conversion of CO_2 occurs at 300 °C, and the catalyst work remains stable up to 400–450 °C. The catalysts based on the GNP and TEG carriers are less active, and in their presence, the minimum temperature of the total CO_2 conversion is registered at 350–375 °C. The behavior of these catalysts is different in the temperature range of 350–450 °C while CO_2 conversion is a maxima. A slight increase of the methane amount over 60%NiFe/GNP catalyst is observed, and methane yield is decreased over 60%NiFe/TEG (Table 2).

This behavior of catalysts is obviously due to the impact of the carbon carrier (GNP or TEG) on the distribution of the active mass on its surface and on the availability of catalytically active sites for the reacting molecules. The GNP has a more ordered

Table 2 Catalytic properties of the NiFe catalysts loaded on carbon carriers

Sample	*$T_1 \rightarrow T_2$, °C	CH_4 Yield, %	S_{BET}, m^2/g
20% NiFe/SND	300 → 400	78.7 → 90.4	190
20%NiFe/MWCNTs	300 → 400	83.7 → 85.8	140
60%NiFe/MWCNTs	300 → 450	70.2 → 85.4	120
60%NiFe/GNP	375 → 450	70.9 → 71.4	23
60%NiFe/TEG	350 → 450	71.8 → 67.2	50

*The temperature at 100% conversion of CO_2, where T_1 is the temperature at the first analysis point probed at 100% conversion of CO_2, T_2 is the highest temperature over the catalyst exposed in the reaction mixture used for the CO_2 methanation

structure than the TEG, which positively affects the magnetic and conductive properties [45–47]. The SEM photos prove a significant structural difference between TEG and GNP. The TEG has a sponge-like structure [22], while the GNP looks chaotically layered on other plates. These structure features prevent the reactants' access to the active sites on the catalyst. It is because the loaded bimetallic phase is tightly confined inside the TEG honeycombs or between the plates of the GNP. The lack of promising results in the catalytic efficiency of the NiFe/TEG catalyst demonstrates the ineffectiveness of further studies.

More promising are the results of the CO_2 methanation studies over the catalysts loaded on SND and CNTs. The research results presented in [48, 49] show that the NiFe/CNTs and NiFe/SND catalysts provoke of high level of CO_2 conversion and CH_4 yield. For comparison, the activity of the CoFe [5] and the bulk CoNi catalysts [27] is significantly reduced when loaded on the surface of the carbon carrier.

The phase composition of the NiFe/CNTs and the pristine CNTs was studied by the XRD method (Fig. 8). The XRD pattern shows graphite reflections positioned at $2\theta = 30.2°$ (002), 50.5° (100), 52.03° (101), and 63.17° (004) and relative to the pristine CNTs. Also, the XRD pattern shows a weak reflection at $2\theta = 60.9°$ (200) from crystalline Ni contained in the pristine CNTs.

Figure 8b shows a micrograph of the NiFe/CNT samples after their exposure in the CO_2 methanation. The particles of the supported catalytically active phase are located along the entire length of CNTs and in their tangles (see insert in Fig. 8b). Both separate small metal particles and their aggregates can be distinguished. The EDX analysis data of the Ni80Fe20/CNTs catalyst and the calculated ratios show that the amount of the loaded phase at most points of the EDX analysis exceeds the value which is specified at the preparation. Besides, the ratio between the components in the loaded phase becomes variable [49].

The study of the mechanism of the catalytic process on the surface of a nanocomposite catalyst is a difficult task. This statement is especially true when the active mass is localized on the surface of the carrier. The surface of pristine carrier is inert and has no active sites for the activation and interaction of reacted molecules but we can not completely exclude the involvement of the carrier in the catalytic process [13, 23]. Catalyst carriers do not only allow the dispersion of active sites, increasing

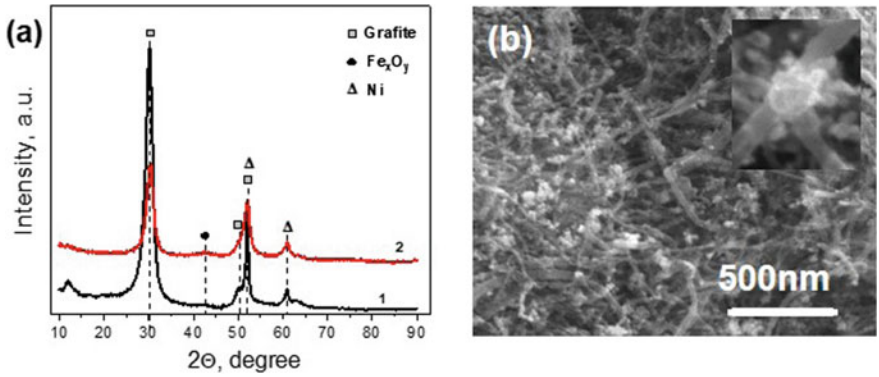

Fig. 8 **a** XRD patterns: (*1*)—pristine CNTs and (*2*)—NiFe/CNTs catalyst, **b** SEM micrograph of NiFe/CNTs

the contact area with reagent molecules, but also create an additional opportunity for their adsorption. Of great importance are those areas of the catalyst where the active sites is near the adsorption sites of the carrier surface. In such areas of the catalyst surface, the mechanism of formation of reaction products may differ from the processes occurring on a separate active sites. These conclusions are provided with results of SEM observation of loaded catalysts. Usually, TD profiles of desorbed particles from the surface of such catalysts are multi-peaked, and the separation of individual peaks as the determination of their T_m becomes problematic. We used a specific technique for the TPD MS studies that allows "freezing" the reaction, namely to fix the time when the catalyst surface contains a variety of active sites and adsorbed species with different desorption energies. These sites reflect a certain stage of the catalytic process, i.e., each active site has a specific intermediate "species" adsorbed on it, which is detected by the mass spectrometer during desorption at a certain T_m temperature. Therefore, different intermediate particles corresponding to each stage of the catalytic reaction of the CO_2 methanation are detected in the MS spectra. For the catalysts of 60 wt% NiFe/CNTs and 20 wt% NiFe/CNTs, the desorption of particles with m/z: 44, 30, 29, 28, 16, and 15, corresponding to the (CO_2), (H_2CO*), (HCO*), (CO*), (O*), and (CH_3*) species, takes place in the temperature range of the maximum conversion of CO_2 to CH_4, see Fig. 9a, b. Similar profiles were obtained for the NiFe/SND nanocomposite catalysts [48]. It can explain similar catalytic behavior of CNTs- and SND-based nanomaterials in the CO_2 methanation process.

A nanocomposite catalyst (NC) has a much larger surface for the adsorption of reactant molecules. The elementary acts of the catalytic reaction occur on the surface of the active NiFe bimetallic site. However, the carrier sites with physisorbed CO_2 or H_2 molecules bordering the active catalyst center provide additional adsorption sites that have significantly impacted the formation of intermediate compounds. Under the conditions of the catalytic experiment with excess hydrogen on the catalyst surface, the formation of skeletal hydrocarbons C_2^+ is unlikely. We can propose the

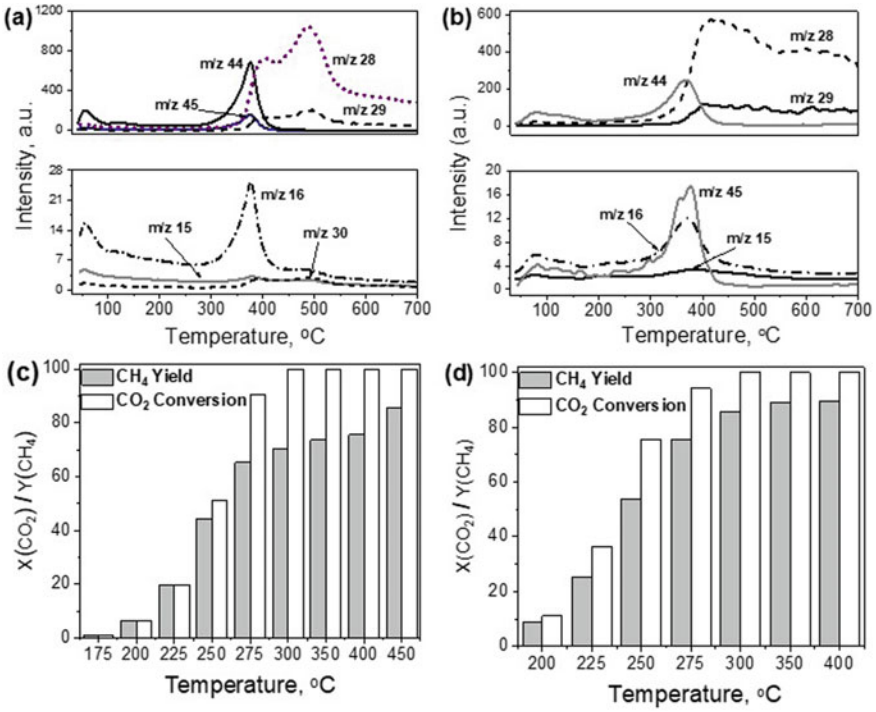

Fig. 9 **a**, **b** TPD profiles of desorbed particles from the catalysts and **c**, **d** $X(CO_2)/Y(CH_4)$ versus temperature

mechanism of CO_2 conversion to CH_4 via intermediate compounds, see Eqs. (13–20). According to the mechanism, CO_2 (m/z 44) and H_2 molecules can be adsorbed on the catalyst active sites (Eqs. 13 and 14). According to Eq. (15), the intermediate compound HCO_2* (m/z 45) can be formed by adding a hydrogen atom to the adsorbed CO_2. Further hydrogen adding and oxygen removing lead to the formation of CH_4 (m/z 16), as can be seen from Eqs. (17 and 18).

According to Eqs. (19 and 20), the intermediate compounds: HCO* (m/z 29) and CO* (m/z 28) can be formed simultaneously with the main process. The resulting CO* is not an independent reaction product because we did not register CO molecules by GC. Therefore, the CO* is desorbed from the surface by a recombination mechanism. These CO* species can participate in the further process of the CH_4 formation by the reverse reaction, see Eq. (20), or can be strongly adsorbed on the catalyst surface, blocking the active surface sites.

Considering the highly intensive TD profile of m/z 28, the CO* species can be formed by Eq. (20) and by the decomposition of CO_2 molecules adsorbed on the surface Eq. (21). Further, the reaction proceeds with the addition of a hydrogen atom, see Eqs. (23), (17), and (18). For the sample of 60 wt% NiFe/CNTs, intense CO* peaks (m/z 28) were recorded at 400 and 500 °C. The intensity of the peak at

500 °C is 30% higher than the peak at 400 °C. For the sample of 20 wt% NiFe/CNTs, the intensity of the CO* peak (m/z 28) becomes maximum in the range of 400–500 °C and then remains at a high level. Thus, CO* desorption occurs from different active sites on the surface. It can be assumed that the presence of a large amount of adsorbed CO* inhibits the catalytic conversion of CO_2 to CH_4.

The GC results show that for the 20 wt% NiFe/CNTs catalyst, the CH_4 yield increases with temperature and reaches the maximum value (89%) at 350 °C. Increasing the amount of Ni80Fe20 active mass on the surface of the carrier to 60 wt% does not lead to an increase in the CH_4 yield in the same temperature range, but on the contrary, decreases it to 76% (Fig. 9c, d). Thus, we have a case when a larger number of active sites can increase the number of intermediate compounds that are strongly chemisorbed on the surface and do not participate in the formation of the targeted product.

$$CO_2 + [\,] \rightarrow [CO_2], \tag{13}$$

$$H_2 + 2[\,] \rightarrow 2[H], \tag{14}$$

$$[CO_2] + [H] \rightarrow [HCO_2] + [\,], \tag{15}$$

$$[HCO_2] + [H] \rightarrow [H_2CO] + [O], \tag{16}$$

$$[H_2CO] + [H] \rightarrow [H_3C] + [O], \tag{17}$$

$$[H_3C] + [H] \rightarrow CH_4 + 2[\,], \tag{18}$$

$$[H_2CO] + [\,] \rightarrow [HCO] + [H], \tag{19}$$

$$[HCO] + [\,] \rightarrow [CO] + [H], \tag{20}$$

$$[CO_2] + [\,] \rightarrow [CO] + [O], \tag{21}$$

$$[CO] + [H] \rightarrow [HCO] + [\,], \tag{22}$$

$$[HCO] + [H] \rightarrow [H_2CO] + [\,]. \tag{23}$$

3.3 NiFe Catalysts Loaded on Aluminum Oxide Carriers

Bulk Ni80Fe20 catalyst with high conversion rates of CO_2 to CH_4 was loaded on the surface of Al_2O_3 by impregnation. Several types of aluminum oxide with different crystal structures and textural characteristics were used in order to prepare the NiFe nanocomposite (NC) catalysts (Table 3). Before the loading, the carrier was calcined at a temperature of 300–400 °C to remove impurities from the alumina surface. The reduction temperature was estimated by H_2-TPR measurements (Fig. 10). TPR curves have different temperature intervals of weight loss. The reduction of the oxide phase to the metallic state for the NiFe/A3 NC takes place passed at 330 °C. This temperature is similar to that for the bulk catalyst of the same composition. For the NiFe/A2 NC, the reduction process occurs at 250 °C. Obviously, the type of carrier affects the formation of the transition metal oxide phases and their further transformations in the reducing atmosphere.

It was shown in [11, 13] that the reduction of nanooxide precursors to metallic catalysts does not significantly affect the size distribution of pores in the resulting product. Therefore, the formation of a porous structure of the NiFe NCs catalyst based on highly dispersed alumina oxides (with loaded bimetallic active mass) occurs at the stage of localization of metal oxide precursors on the surface of the carrier.

Table 3 Textural characteristics of carriers and catalysts

Sample	[a]Specific surface area, $m^2\ g^{-1}$			
	S_{BET}	S_{micro}	S_{meso}	S_{macro}
Al_2O_3 (A1)	106.4	6.7	99.3	0.4
NiFe/A1	83.4	4.0	78.9	0.5
Al_2O_3 (A2)	46.8	2.5	43.1	1.2
NiFe/A2	37.9	1.2	35.7	1.1
Al_2O_3 (A3)	210.5	32.8	176.7	1.0
NiFe/A3	145.4	33.4	111.7	0.2

Sample	$R_{p,V}$	Specific volume, $cm^3\ g^{-1}$			
		V_p	V_{micro}	V_{meso}	V_{macro}
Al_2O_3 (A1)	6.5	0.219	0.004	0.206	0.009
NiFe/A1	8.1	0.166	0.002	0.153	0.011
Al_2O_3 (A2)	14.6	0.203	0.002	0.170	0.031
NiFe/A2	14.5	0.159	0.001	0.132	0.026
Al_2O_3 (A3)	11.3	0.579	0.014	0.542	0.023
NiFe/A3	4.8	0.203	0.013	0.186	0.004

[a]Specific surface area in total (S_{BET}), of nanopores (S_{nano}), mesopores (S_{meso}), macropores (S_{macro}), and pore volumes (V_p, V_{nano}, V_{meso}, V_{macro}) at pore radius $R < 1$nm, 1nm $< R <$ 25nm, and $R >$ 25 nm, respectively. $R_{p,V}$ represents the average pore radius [50]

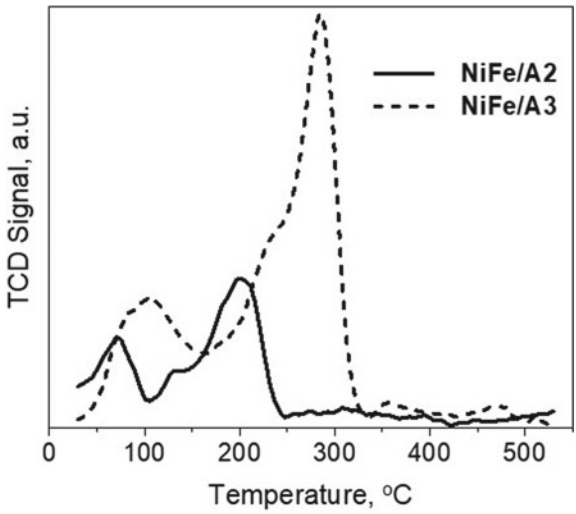

Fig. 10 H_2-TPR profiles for Ni80Fe20/A2 and Ni80Fe20/A3 NCs

Clearly, the structural characteristics of the alumina carrier play a crucial role in the formation of the active centers of the NiFe catalyst and their surface distribution. Three types of aluminum oxide were used to load the active NiFe composition. All of them are characterized by different specific surface areas and by different porosities. The porous structures of types A1 and A2 carriers have preferable mesoporosity with a minor contribution of macropores. The alumina carrier of type A3 is a mesoporous–microporous sorbent. The prepared NCs catalysts, where NiFe bimetallic active mass is loaded on the alumina surface, have the different resulting textures.

The nitrogen adsorption-desorption isotherms for the NiFe/A1 and NiFe/A2 NCs and the corresponding pore size distribution data are similar to the initial alumina (A1 and A2) carriers (Fig. 11a, c). According to the IUPAC classification, they belong to the L2 type, and the corresponding hysteresis loops belong to the H3 type. The NCs based on the A1 and A2 carriers show a decrease in adsorption capacity. This decrease is due to a shortage in the total volume of pores. At the same time, the ratio of micropores, mesopores, and macropores does not change significantly. The nitrogen adsorption isotherm measured for the NiFe/A3 NC differs significantly from that of the respective A3 carrier (Fig. 11e). The hysteresis loops observed for the A3 carrier and for the NiFe/A3 NC can be classified as type H3 and H4 hysteresis loops, respectively [51].

Figure 11b, d, f show the incremental distribution of pores by size calculated from the nitrogen adsorption isotherm. All carriers and related NCs have a predominantly mesoporous structure. For the NCs based on A1 and A2 carriers, micro- and macropores do not contribute much to the total porosity; factually, their contribution is either insignificant or absent. In contrast, a contribution of micropores in the total porosity of the NCs based on the A3 carrier is recognizable. Notably, the A3 carrier has a more developed specific surface area of 210 $m^2\ g^{-1}$ in contrast to the A2 and A1 carriers.

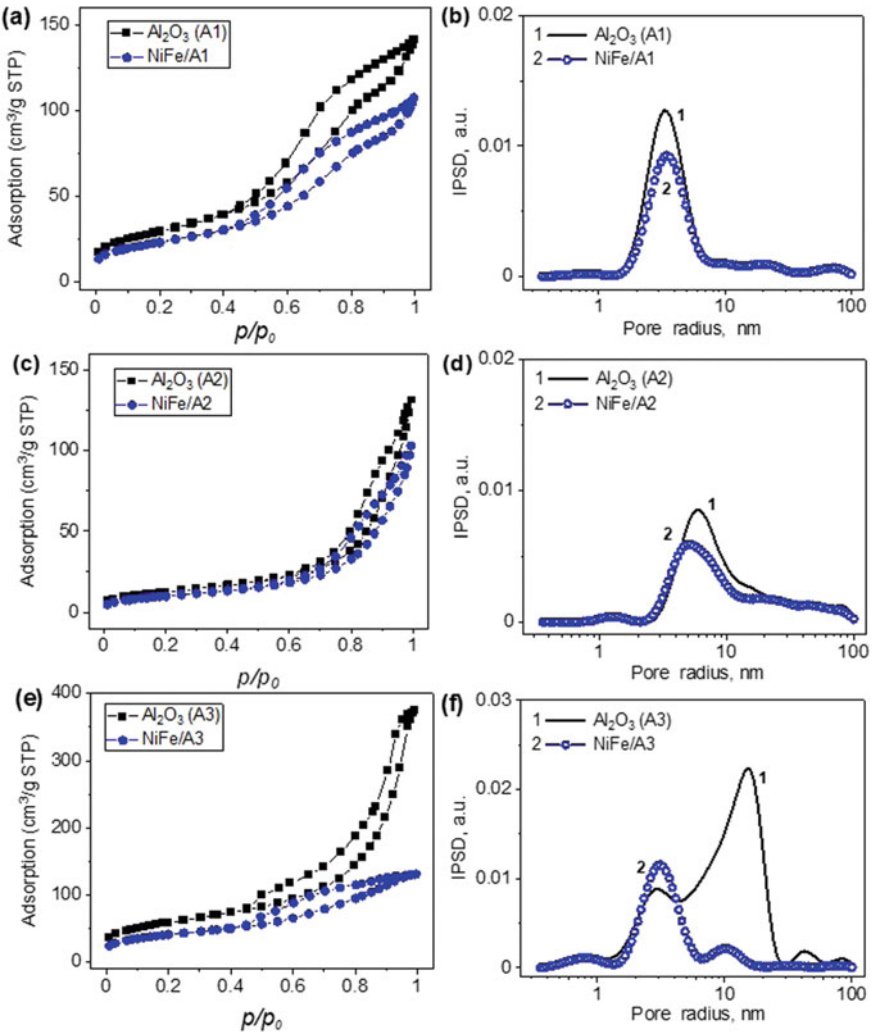

Fig. 11 **a**–**f** Textural parameters of alumina (A1–A3) carriers (*1*) and NiFe/(A1–A3) NCs (*2*): **a**, **c**, **e** nitrogen adsorption/desorption isotherms and **b**, **d**, **f** incremental pore size distributions

However, after a load of bimetallic NiFe particles, the specific surface area of the resulting NC based on the A3 carrier decreases more than that of the NCs based on the A1 or A2 carriers after the same operation. The specific surface area of the NiFe/A3 NC is lesser by 30% than that of the A3 carrier (cf. 145 and 211 $m^2\ g^{-1}$ in Table 3). Moreover, the distribution of pores by size also changes after loading the NiFe particles. The specific porosity decreases entirely and precisely at the expanse of mesopores available in the A3 carrier. If one compares the contribution of mesopores to the total porosity of the A3 carrier and the NiFe/A3 NC based on it, it will be clear

that it is less by 38% for the latter. From another hand, in comparison with the A3 carrier, the fraction of micropores for the NiFe/A3 NC is slightly higher.

As one can see from Table 3, after loading of nanoscale bimetallic NiFe particles on the A2 or A1 carrier, the specific surface area of the resulting NCs is 22% lesser than that of the respective carrier (cf. 106 to 83 m^2 g^{-1} and 47 to 38 m^2 g^{-1} in Table 3). In contrast, the specific surface area of NiFe/A3 NC is 30% lesser than that of the A3 carrier.

Furthermore, the respective NiFe/A3 and NiFe/A2 NCs maintain a preferable mesoporosity. In fact, the contribution of micropores and macropores to the total porosity is equally insignificant for both A1 and A2 carriers and composites based on them.

The calculated incremental pore size distributions for the A3 and NiFe/A3 NC demonstrate a part of microporosity in the structure of the A3 carrier. A ratio for this type of pore increases for the NiFe/A3 nanocomposite if referenced with that for the A3 carrier.

Obviously, the related pore size distribution changed significantly. The ratio of mesopores with sizes of 2–8 nm increased. However, the contribution of mesopores with a radius up to 40 nm, as in the A3 carrier, is practically absent (Fig. 11f).

The crystal structure of the initial carriers, as well as their textural characteristics, has differences and affects the formation of the loaded catalyst active mass. XRD patterns of the studied carriers and the related NCs (Fig. 12) demonstrate the differences between the crystalline structure of the A2 and A3 carriers and the registered reflections of loaded metals. The XRD patterns of the alumina carriers were recorded using the CuKα radiation, and the CoKα radiation was used to record the XRD patterns for the nanocomposite catalysts with the loaded NiFe active phase.

The crystal lattice of the A2 carrier contains the reflections of α- and γ-modifications of alumina (Fig. 12 a). One can see the broadening of the reflexes peaked at $2\theta = 52.85°$ and 59.9° and assigned to α-Al_2O_3 and γ-Al_2O_3 phases. This situation is possible due to the superposition of the reflection of the metallic nickel.

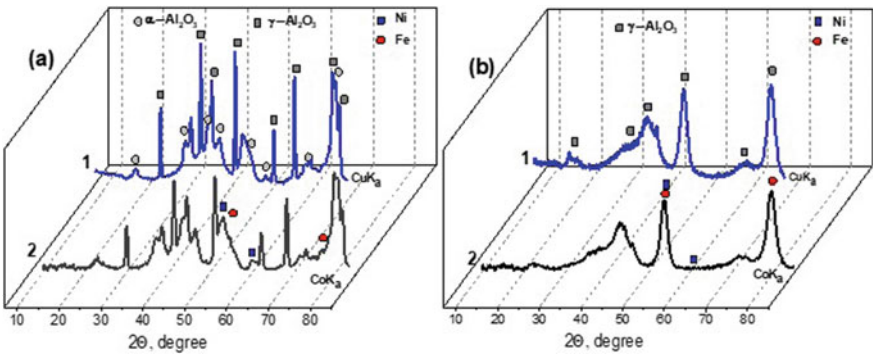

Fig. 12 XRD patterns of **a** Ni80Fe20/A2 and **b** Ni80Fe20/A3 NCs (curve 1) and the respective carriers (curve 2)

The presence of metallic iron is proved by the appearance of shoulders for two reflections centered at $2\theta = 54.75°$ and 79.5° (Fig. 12a). The structure of the carrier A3 has features typical for the γ-Al_2O_3 crystal lattice exclusively. The reflection assigned to the metallic nickel phase is registered only at $2\theta = 52.85°$. The reflections of the metallic iron phase are identified at $2\theta = 54.75°$ and 79.5°.

The surface morphology of the used carriers is different. The A2 carrier is composed of large agglomerates of particles 10–50 μm in size. Additionally, on the SEM micrographs (Fig. 13a), small non-aggregated particles of 3–7 μm in size are visible. They have the shape of irregular tetragonal or pentagonal prisms, the surface of which has defects in the form of cracks located on the side faces. Inclusions of small particles, the size of which does not exceed 3 μm, are also visible in the cracks. This structure is typical for the surface of high-temperature α-Al_2O_3 [44]. The A3 carrier (γ-Al_2O_3) has no distinct individual particles. Its surface has a loose structure due to an aggregation of nanoscale particles (Fig. 13b). Such surface morphology explains the significant difference in the values of the specific surface area of the studied carriers, namely, 46 and 210 m^2/g for α- and γ-Al_2O_3, respectively.

The surface morphology of α-Al_2O_3 (A2) does not change significantly because of the active phase loading. The SEM micrograph shows that the active phase in the

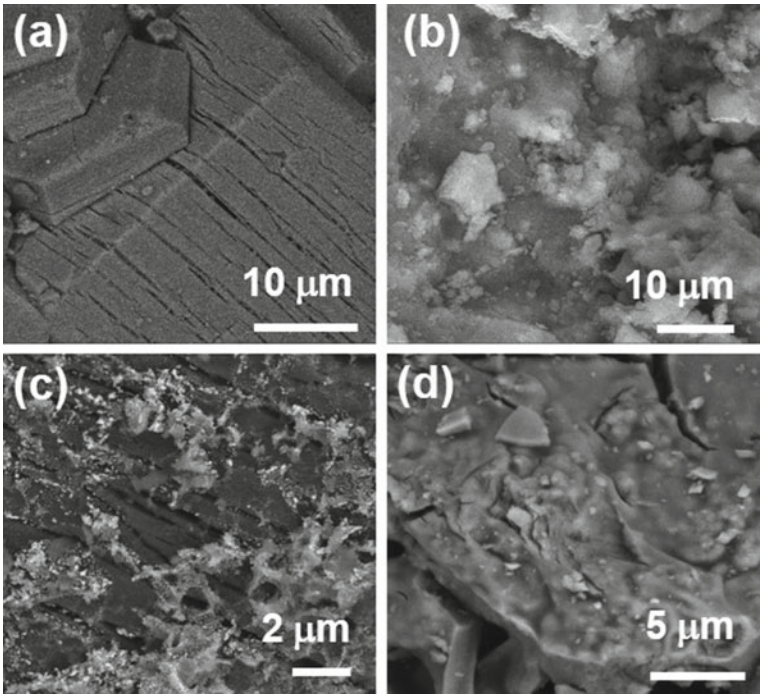

Fig. 13 SEM micrographs of **a** A2 and **b** A3 carriers and NCs based on them **c** NiFe/A2 and **d** NiFe/A3

Ni80Fe20/A2 NC catalyst is like a "net". This net covers some agglomerates of the carrier (Fig. 13c).

Typically, the loaded Ni80Fe20 particles do not penetrate the surface cracks characteristic of α-Al_2O_3. But, they are localized on the geometric surface of the carrier and are available for further catalytic CO_2 methanation. Comparing the SEM micrographs of the surface of γ-Al_2O_3 before and after the loading of the active phase, we consider that in the preparation of the Ni80Fe20/γ-Al_2O_3 NC catalyst, the structure of the carrier surface undergoes significant changes. Thus, in (Fig. 13d), we observed the absence of graininess and, consequently, high dispersion, which is observed for the initial γ-Al_2O_3. The NC catalyst surface is smooth and comprises with small fragments ranging in size from 200 nm to several microns. They are chaotically placed on the carrier surface and maybe the fragments of the loaded active phase. The EDX analysis (Table 4) shows that the ratio between the components in the bimetallic active phase for the Ni80Fe20/A2 NC catalyst remains within limits specified at the preparation: Ni (80 wt%)–Fe (20 wt%). For the Ni80Fe20/γ-Al_2O_3 NC catalyst, the related metal content in the Ni80Fe20 active mass is 26–42 at.% of Fe to 74–58 at.% of Ni. So, the iron-enriched areas can be recorded with the EDX analysis. In our opinion, increasing the amount of Fe on the surface decreases catalytic activity and promotes the formation of CO molecules.

An important question is how the difference in the textural characteristics of the carrier and its crystal structure affects the catalytic properties of the studied NC catalysts. The catalytic activity of alumina-based NCs catalysts was evaluated with the same procedure as for the bulk catalysts. GC results of the evaluation of CO_2 conversion over NiFe/Al_2O_3 nanocomposites (including A1, A2, and A3 carriers) are presented in Fig. 14.

The GC analysis results indicate the intensive CO_2 conversion into CH_4 at 200 °C in the presence of the Ni80Fe20/A1 and Ni80Fe20/A2 NC catalysts. The total CO_2 conversion occurs at 275 and 250 °C in the presence of Ni80Fe20/A1 and Ni80Fe20/A2 catalysts respectively. But, the Ni80Fe20/A3 catalyst does not show similar catalytic activity. The presented dependences demonstrate an obvious difference in the impact of the type of carrier on the catalytic activity of the loaded active NiFe mass. When the active phase is loaded on α-Al_2O_3, this has a significant positive effect. And the total conversion of CO_2 and 100% selectivity toward CH_4 are

Table 4 EDX analysis results

Ni80Fe20/A2				Ni80Fe20/A3			
EDX, at.%				EDX, at.%			
O	Al	Fe	Ni	O	Al	Fe	Ni
47.3	31.6	3.9	17.2	66.2	28.7	1.4	3.8
42.9	29.9	9.1	18.0	66.2	27.8	2.5	3.5
61.8	34.4	0.9	2.9	66.2	31.0	1.1	1.7
61.4	35.9	0.6	2.1	66.7	29.2	1.3	2.9

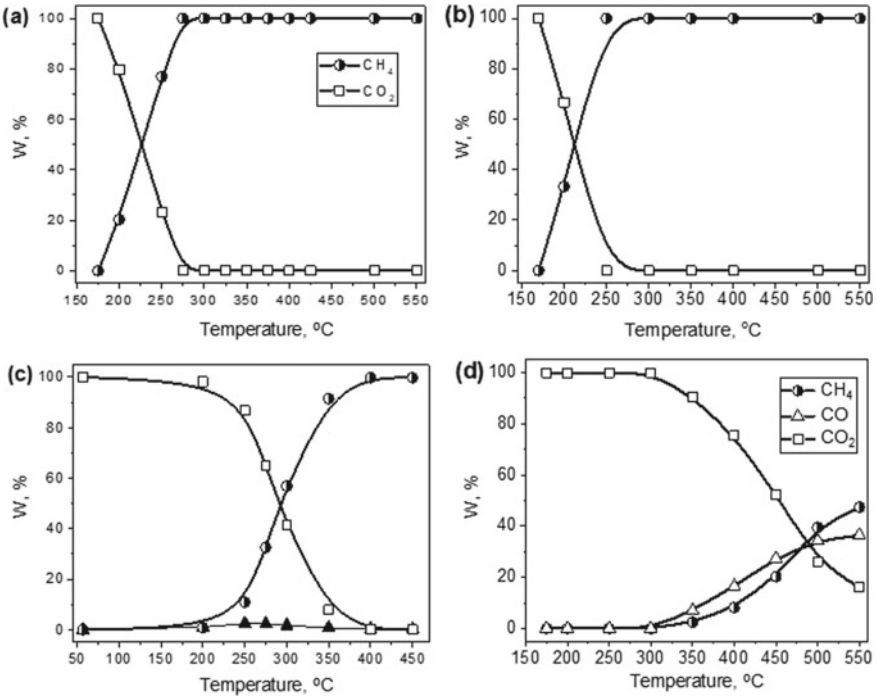

Fig. 14 Temperature dependence of the volume percentage of CH_4, CO, and CO_2 (W, %) for the CO_2 methanation over **a** Ni80Fe20/A1, **b** Ni80Fe20/A2, **c** Ni50Fe50/A2, and **d** Ni80Fe20/A3 NC catalysts

observed at 250 °C (Fig. 14a–c). For the γ-Al_2O_3 carrier, the CO_2 conversion is 80–90%, while CO is GC detected as the reaction co-product (Fig. 14d).

For the Ni80Fe20/A3 NC catalyst, the CO_2 methanation reaction begins at above 300 °C. That is why the maximum conversion (88%) of the initial CO_2 is observed at 550 °C (Fig. 14c). The amount of CO obtained between 350 and 450 °C exceeds the amount of CH_4, the maximum yield of which reaches 50 vol % at high temperature.

As can be seen from the above data, the highest activity is shown by the catalysts loaded on α-Al_2O_3 (A1 and A2 carriers). Fig. 14 demonstrates the course of the temperature profiles where the catalytic activity depends not only on the type of carrier but also on the ratio of components in the active NiFe phase. As seen from Fig. 14c and b, for the Ni50Fe50/A2 NC catalysts, the total conversion of CO_2 to CH_4 is observed at 400 °C. But, for the Ni80Fe20/A2 NC catalyst, this temperature is much lower at about 250 °C.

It is clear that the structural, textural, and morphological features of the studied carriers determine the properties of the resulting alumina-based bimetallic nanocomposites. The porosity of the carrier determines the localization of the loaded active mass. The use of aluminum oxide (A3) as a catalyst carrier causes the adsorption of catalytic active metal phases in micropores, as a result the active phase becomes

partially inaccessible to reactant molecules from the gas phase. The TPR profiles and catalytic performance approved this observation.

The porous structure of NCs based on the A1 and A2 carriers is characterized by preferable mesoporosity. These carriers have a small number of macropores. Both types of pores contribute to the efficient course of the CO_2 methanation reaction. The mesopores are the principal working pores of the prepared catalysts for the molecules interaction. Macropores are the way to deliver reactant molecules that can fill the inner volume of the NCs catalyst. As a result, the catalytic processes can occur not only on the outer surface of the catalyst grains but also inside the inner porous volume. In the NiFe/A3 NC catalyst, the micropores prevent the catalytic processes since the metal particles trapped in the micropores become inaccessible to the reactant molecules and cannot be involved in catalysis.

4 Conclusion

The bulk NiFe catalysts with a nickel content in the range of 60–70 wt% and 80–95 wt% showed the high catalytic activity in the reaction of CO_2 methanation. The addition of iron (5–20 wt%) to the catalyst composition significantly increases its catalytic efficiency compared to the monometallic nickel catalyst. The highest CO_2 conversion and CH_4 yields were registered for the catalyst with the composition of Ni (80 wt%)–Fe (20 wt%). The formation of intermetallic $FeNi_3$ compound in the Ni75Fe25 catalyst, which surface is enriched with iron, leads to a rapid decrease of catalytic activity. The analysis of TD profiles of desorbed species from the surface of bulk NiFe catalysts indicates the CO_2 methanation reaction occurs due to the complete breakdown of CO_2 molecules (splitting into carbon and oxygen atoms) and the formation of CH_4 by the recombination mechanism with the gradual addition of hydrogen atoms to the carbon atoms.

Loading the active mass of NiFe catalyst with the ratio of Ni (80 wt%)–Fe (20 wt%) on the surface of carbon and alumina carriers causes 100% CO_2 conversion.

The selectivity of CH_4 formation and the temperature of complete CO_2 conversion on loaded catalysts depend on the nature of the carrier on which loaded the active NiFe mass. Among carbon carriers, nanocomposite NiFe/CNTs catalysts showed high activity of CO_2 conversion into CH_4. The distribution of the active mass of NiFe catalyst along the carbon nanotube bundles and their localization in the nodes contributes to the efficient formation of CH_4 at atmospheric pressure and 350 °C on the catalyst containing 20 wt% of Ni80Fe20. Increasing the amount of active mass to 60 wt% does not increase the CH_4 yield. The formation of CH_4 occurs by a mechanism via formation of oxygen-containing HCO_2*, H_2CO*, and HCO* species.

The study of the activity of alumina-based NiFe NCs catalysts demonstrated that the catalytic efficiency of the CO_2 methanation depends on the textural characteristics of the carrier.

The microporosity of the Al_2O_3 carrier (A3) has a negative impact on the conversion of CO_2 to CH_4 due to the loss of a part of active catalyst sites unavailable for the CO_2 methanation reaction passage due to their possible localization in the micropores. The ordered crystal structure of a-Al_2O_3 promotes the formation of the NiFe catalytically active sites.

References

1. M. Götz, J. Lefebvre, F. Mörs, A. McDaniel Koch, F. Graf et al., Renewable power-to-gas: a technological and economic review. Renew. Energy **85**, 1371–1390 (2016). https://doi.org/10.1016/j.renene.2015.07.066
2. K. Hashimoto, M. Yamasaki, K. Fujimura, T. Matsui et al., Global CO_2 recycling—novel materials and prospect for prevention of global warming and abundant energy supply. Mater. Sci. Eng. A **267**, 200–206 (1999). https://doi.org/10.1016/S0921-5093(99)00092-1
3. J. Lefebvre, M. Götz, S. Bajohr, R. Reimert, T. Kolb, Power-to-Gas through thermal integration of high-temperature steam electrolysis and carbon dioxide methanation—experimental results. Fuel Process. Technol. **132**, 83–90 (2015). https://doi.org/10.1016/j.fuproc.2014.10.040
4. P. Strucks, L. Failing, S. Kaluza, A short review on Ni-catalyzed methanation of CO_2: reaction mechanism, catalyst deactivation, dynamic operation. Chem. Ing. Tech. **93**, 1526–1536 (2021). https://doi.org/10.1002/cite.202100049
5. O.V. Ischenko, A.G. Dyachenko, I. Saldan, V.V. Lisnyak, V.E. Diyuk, A.V. Vakaliuk, A.V. Yatsymyrskyi, S.V. Gaidai, T.M. Zakharova, O. Makota, T. Ericsson, L. Häggström, Methanation of CO_2 on bulk Co-Fe catalysts. Int. J. Hydrog. Energy **46**, 37860–37871 (2021). https://doi.org/10.1016/j.ijhydene.2021.09.034
6. R. Meshkini Far, O.V. Ishchenko, A.G. Dyachenko, O. Bieda, S. Gaidai, V. Lisnyak, CO_2 hydrogenation into CH_4 over Ni–Fe catalysts. Funct. Mater. Lett. **11**, 1850057 (2018). https://doi.org/10.1142/S1793604718500571
7. Y.R. Dias, O.W. Perez-Lopez, CO_2 conversion to methane using Ni/SiO_2 catalysts promoted by Fe, Co and Zn. J. Environ. Chem. Eng. **9**(1), 104629 (2021). https://doi.org/10.1016/j.jece.2020.104629
8. A.V. Yatsymyrskyi, A.G. Dyachenko, E.V. Ischenko, T.M. Zakharova, S.V. Gaidai, V.E. Diyuk, V.V. Lisnyak, Carbon dioxide molecular interactions with hydrogenated Ni(111) surface: a DFT study. Molec. Cryst. Liq. Cryst., in press (2022). https://doi.org/10.1080/15421406.2022.2073032
9. M. Zhludenko, A. Dyachenko, O. Bieda, S. Gaidai, M. Filonenko, O. Ischenko, Structure and catalytic properties of Co–Fe systems in the reaction of CO_2 methanation. Acta Physica Polonica A **133**, 1084 (2017). https://doi.org/10.12693/APhysPolA.133.1084
10. G. De Piano, J.J.A. Gambo, A.M. Condó, S. Bengió, F.C. Gennari, Bimetallic Ni-Fe catalysts for methanation of CO_2: effect of the support nature and reducibility. Appl. Catal. A: Gen. **634**, 118540 (2022). https://doi.org/10.1016/j.apcata.2022.118540
11. A. Dyachenko, O. Ischenko, V. Diyuk, O. Goncharuk, M. Borysenko, O. Mischanchuk, T. Zakharova, O. Pryhunova, D. Sternik, V. Lisnyak, The catalytic efficiency of Fe-containing nanocomposites based on highly dispersed silica in the reaction of CO_2 hydrogenation. Res. Chem. Intermediat. **48**, 2607–2625 (2022). https://doi.org/10.1007/s11164-022-04720-x
12. S.V. Gaidai, V.S. Gryn'ko, M.G. Zhludenko, A.G. Dyachenko, V.M. Tkach, O.V. Ishchenko, Activity of carbon-fiber-supported Fe–Co catalysts in the CO_2 methanation reaction. J. Superhard. Mater. **39**, 122–128 (2017). https://doi.org/10.3103/S1063457617020071
13. A. Dyachenko, O. Ischenko, O. Goncharuk, M. Borysenko, O. Mischanchuk, V. Gun'ko, D. Sternik, V. Lisnyak, Preparation and characterization of Ni–Co/SiO_2 nanocomposite catalysts for CO_2 methanation. Appl. Nanosci. **12**, 349–358 (2022). https://doi.org/10.1007/s13204-020-01650-1

14. O. Goncharuk, O. Shipul, A. Dyachenko, O. Ischenk, L. Andriyko, A. Marynin, E. Pakhlov, O. Oranska, M. Borysenko, Silica-supported Ni and Co nanooxides: Colloidal properties and interactions with polar and nonpolar liquids. J. Molec. Liq. **285**, 397–402 (2019). https://doi.org/10.1016/j.molliq.2019.04.127
15. O. Linnik, E. Manuilov, S. Snegir, N. Smirnova, A. Eremenko, Photocatalytic degradation of tetracycline hydrochloride in aqueous solution at ambient conditions stimulated by gold containing zinc-titanium oxide films. J. Adv. Oxid. Technol. **12**, 265–270 (2009). https://doi.org/10.1515/jaots-2009-0218
16. O. Linnik, I. Petrik, N. Smirnova, V. Kandyba, O. Korduban, A. Eremenko, G. Socol, N. Stefan, C. Ristoscu, I.N. Mihailescu, C. Sutan, V. Malinovsch, TiO_2/ZrO_2 thin films synthesized by PLD in low pressure N-, C- and/or O-containing gases: structural, optical and photocatalytic properties. Digest J. Nanomater. Biostruct. **7**, 1343–1352 (2012)
17. P.R. Yaashikaa, P.S. Kumar, S.J. Varjani, A. Saravanan, A review on photochemical, biochemical and electrochemical transformation of CO_2 into value-added products. J. CO_2 Util. **33**, 131–147 (2019). https://doi.org/10.1016/j.jcou.2019.05.017
18. V.Y. Zabuga, O.O. Bochechka, G.G. Tsapyuk, V.E. Diyuk, A.M. Panova, V.V. Lisnyak, On multiwalled carbon nanotubes oxidation: Thermogravimetric, spectral and macrokinetic studies. Molec. Cryst. Liq. Cryst. **661**(1), 81–90 (2018). https://doi.org/10.1080/15421406.2018.1460257
19. I. Sulym, O. Goncharuk, D. Sternik, K. Terpilowski, A. Derylo-Marczewska, M.V. Borysenko, V.M. Gun'ko, Nanooxide/polymer composites with Silica@PDMS and Ceria–Zirconia–Silica@PDMS: textural, morphological, and hydrophilic/hydrophobic features. Nanoscale Res. Lett. **12**, 152 (2017). https://doi.org/10.1186/s11671-017-1935-x
20. D. Sternik, M.V. Galaburda, V.M. Bogatyrov, O. Oranska, B. Charmas, V.M. Gun'ko, Novel porous carbon/clay nanocomposites derived from kaolinite/resorcinol-formaldehyde polymer blends: synthesis, structure and sorption properties. Appl. Surf. Sci. **52530**, 146361 (2020). https://doi.org/10.1016/j.apsusc.2020.146361
21. E.V. Ischenko, V.K. Yatsimirsky, A.G. Dyachenko, M.V. Borysenko, E.V. Prilutskiy, I.V. Kongurova, Cu-Co-Fe oxide catalysts supported on carbon nanotubes in the reaction of CO oxidation. Polish J. Chem. **82**, 291–297 (2008)
22. E.V. Ischenko, L.Y. Matzui, S.V. Gayday, L.L. Vovchenko, T.V. Kartashova, V.V. Lisnyak, Thermo-exfoliated graphite containing $CuO/Cu_2(OH)_3NO_3$:(Co^{2+}/Fe^{3+}) composites: preparation, characterization and catalytic performance in CO conversion. Materials **3**, 572 (2010). https://doi.org/10.3390/ma3010572
23. G.G. Tsapyuk, V.E. Diyuk, R. Mariychuk et al., Effect of ultrasonic treatment on the thermal oxidation of detonation nanodiamonds. Appl. Nanosci. **10**, 4991–5001 (2020). https://doi.org/10.1007/s13204-020-01277-2
24. S.M. Hwang, C. Zhang, S.J. Han, H.G. Park, Y.T. Kim, S. Yang et al., Mesoporous carbon as an effective support for Fe catalyst for CO_2 hydrogenation to liquid hydrocarbons. J. CO_2 Util. **37**, 65–73 (2020). https://doi.org/10.1016/j.jcou.2019.11.025
25. A.G. Dyachenko, O.V. Ischenko, M.V. Borysenko, S.V. Gaidai, A.V. Yatsymyrskyi, G.G. Tsapyuk, O.V. Pryhunova, O.O. Kostyrko, $Co\text{-}Fe/Al_2O_3$ Nanocomposite catalysts of the process of CO_2 hydrogenation. Theor. Experim. Chem. **58**, 134–142 (2022). https://doi.org/10.1007/s11237-022-09731-8
26. O. Goncharuk, A. Dyachenko, E. Skwarek, O. Ischenko, L. Andriyko, M. Borysenko, I. Sulym, D. Sternik, K. Kowalska, M. Marynin, Structure of aluminosilicate-supported nickel and iron oxides nanocomposites in gaseous and aqueous media. Physicochem. Probl. Miner Process. **58**(2), 144375 (2022). https://doi.org/10.37190/ppmp/144375
27. O.V. Ishchenko, A.G. Dyachenko, A.V. Yatsymyrskiy, T.M. Zakharova, S.V. Gaidai, V.V. Lisnyak, R. Mariychuk, CO_2 methanation over Co-Ni catalysts. E_3S Web Conf. **154**, 02001 (2020). https://doi.org/10.1051/e3sconf/202015402001
28. A.G. Dyachenko, O.V. Ischenko, M.G. Zhludenko, S.V. Gaidai, T.M. Zakharova, A.V. Yatsymyrskyi, V.V. Lisnyak, CO_2 methanation over $Co\text{–}Ni/Al_2O_3$ and Co–Ni/SiC catalysts. Bulg. Chem. Comun. **52**, 342–347 (2020). https://doi.org/10.34049/bcc.52.3.5134

29. T. Xie, J. Wang, F. Ding, A. Zhang, W. Li, X. Guo et al., CO_2 hydrogenation to hydrocarbons over alumina-supported iron catalyst: effect of support pore size. J. CO_2 Util. **19**, 202–208 (2017). https://doi.org/10.1016/j.jcou.2017.03.022
30. T. Numpilai, N. Chanlek, Y. Poo-Arporn, S. Wannapaiboon, C.K. Cheng, N. Siri-Nguan et al., Pore size effects on physicochemical properties of Fe-Co/K-Al_2O_3 catalysts and their catalytic activity in CO_2 hydrogenation to light olefins. Appl. Surf. Sci. **483**, 581–592 (2019). https://doi.org/10.1016/j.apsusc.2019.03.331)
31. J. Rouquerol, F. Rouquerol, K.S.W. Sing, P. Llewellyn, G. Maurin, *Adsorption by Powders and Porous Solids: Principles, Methodology and Applications*, 2nd edn. (Academic Press, Amsterdam, 2013), p.646
32. S.J. Gregg, K.S.W. Sing, *Adsorption, Surface Area and Porosity* (Academic Press, London, 1982), 303 p
33. A. Monshi, M. Foroughi, R. Monshi, Modified Sherrer equation to estimate more accurately nano-crystallite size using XRD. World J. Nano Sci. Eng. **2**, 154–160 (2012). https://doi.org/10.4236/wjnse.2012.23020
34. V.L. Veselovskyi, E.V. Ischenko, S.V. Gayday, V.V. Lisnyak, A high efficient two phase CuO/$Cu_2(OH)_3NO_3$(Co^{2+}/Fe^{3+}) composite catalyst for CO-PROX reaction. Catal. Commun. **18**, 137–141 (2012). https://doi.org/10.1016/j.catcom.2011.11.024
35. M.L. Cubeiroa, H. Morales, Hydrogenation of carbon oxides over Fe/Al_2O_3 catalysts. Appl. Catal. A.: Gen. **189**, 87–97 (1999). https://doi.org/10.1016/S0926-860X(99)00262-8
36. R. Meshkini Far, A. Dyachenko, S. Gaidai, O. Bieda, M. Filonenko, O. Ishchenko, Catalytic properties of Ni-Fe systems in the reaction of CO_2 methanation at atmospheric pressure. Acta Physica Polonica A. **133**, 1088–1090 (2018). https://doi.org/10.12693/APhysPolA.133.1088
37. V.L. Budarin, V. Diyuk, L. Matzui, L. Vovchenko, T. Tsvetkova, M. Zakharenko, New prospective Ni-catalytic materials. J. Thermal Anal. Calorim. **62**, 345–348 (2000). https://doi.org/10.1023/A:1010140803562
38. R.J. Cvetanović, Y. Amenomiya, Application of a temperature programmed desorption technique to catalyst studies. Adv. Catal. **17**, 103–149 (1967). https://doi.org/10.1016/S0360-0564(08)60686-0
39. N. Nishimura, S. Kitaura, A. Mimura, Y. Takahara, Cultivation of thermophilic methanogen KN-15 on H_2–CO_2 under pressurized conditions. Ferment Bioeng. **73**, 477–480 (1992). https://doi.org/10.1016/0922-338X(92)90141-G
40. S. Fujita, H. Terunuma, M. Nakamura, N. Takezawa, Mechanisms of methanation of carbon monoxide and carbon dioxide over nickel. Ind. Eng. Chem. Res. **30**, 1146–1151 (2002). https://doi.org/10.1021/ie00054a012
41. X. Guo, D. Gao, H. He, A. Traitangwong, M. Gong, V. Meeyoo, Z. Peng, C. Li, Promotion of CO_2 methanation at low temperature over hydrotalcite-derived catalysts-effect of the unable metal species and basicity. J. Hydrog. Energy **46**, 518–530 (2021). https://doi.org/10.1016/j.ijhydene.2020.09.193
42. K.S.W. Sing, D.H. Everett, H. Raw, L. Moscou, R.A. Pieroti, J. Rouquerol, T. Siemieniewska, Reporting physisorption data for gas/solid systems with special reference to the determination of surface area and porosity. Pure Appl. Chem. **54**(11), 2201–2218 (1982). https://doi.org/10.1351/pac198254112201
43. M.A.A. Aziz, A.A. Jalil, S. Triwahyono, S.M. Sidik, Methanation of carbon dioxide on metal-promoted mesostructured silica nanoparticles. Appl. Catal. A Gen. **486**, 115–122 (2014). https://doi.org/10.1016/j.apcata.2014.08.022
44. M. Trueba, S. Trasatti, γ-alumina as a support for catalysts: a review of fundamental aspects. Eur. J. Inorg. Chem. **17**, 3393–3403 (2005). https://doi.org/10.1002/ejic.200500348
45. L.Y. Matzui, L.L. Vovchenko, O.A. Syvolozhskyi, O.S. Yakovenko, M.O. Borovoy, O.O. Gomon, A.G. Dyachenko, O.V. Ischenko, A.V. Vakaliuk, A.V. Bodnaruk, V.M. Kalita, Structure and magnetic properties of MWCNTs decorated by NiFe, CoFe, NiCo nanoparticles. Molec. Cryst. Liq. Cryst. **752**, 74–94 (2023). https://doi.org/10.1080/15421406.2022.2091275
46. O.S. Yakovenko, L.Y. Matzui, O.A. Syvolozhskyi, L.L. Vovchenko, O.A. Lazarenko, O.V. Ischenko, A.G. Dyachenko, A.V. Vakaliuk, V.V. Oliynyk, V.V. Zagorodnii, A.V. Bodnaruk,

V.M. Kalita, M.O. Borovoy, Epoxy composites filled with graphite nanoplatelets modified by FeNi nanoparticles: structure and microwave properties. Mater. Sci. Eng. B **283**, 115776 (2022). https://doi.org/10.1016/j.mseb.2022.115776

47. L.Y. Matzui, O.A. Syvolozhskyi, Y.O.S. Vovchenko, O.A. Lazarenko, T.A. Len, O.V. Ischenko, A.G. Dyachenko, A.V. Vakaliuk, V.V. Oliynyk, V.V. Zagorodnii, Electrical and electromagnetic interference shielding properties of GNP-NiFe hybrid composite with segregate structure of conductive networks. J. Appl. Phys. **131**, 055110 (2022). https://doi.org/10.1063/5.0071157
48. A.G. Dyachenko, O.V. Ischenko, G.G. Tsapyuk, S.V. Gaidai, O.V. Ischenko, T.M. Zakharova, G.D. Il'nitskaya, O.B. Loginova, Synthetic nanodiamonds (SNDs) containing bimetallic Ni(Co)–Fe composites: preparation, characterization and catalytic performance in the reaction of CO_2 methanation. Molec. Cryst. Liq. Cryst. **701**, 91–97 (2020). https://doi.org/10.1080/15421406.2020.1732566
49. A.G. Dyachenko, O.V. Ischenko, O.V. Prygunova, V.E. Diyuk, G.G. Tsapyuk, S.V. Gaidai, A.V. Yatsymyrskyi, T.M. Zakharova, E.O. Kostyrko, Ni–Fe, Co–Fe, and Co–Ni nanocomposites based on carbon nanotubes in the reaction of CO_2 methanation. Molec. Cryst. Liq. Cryst. **702**, 38–46 (2021). https://doi.org/10.1080/15421406.2021.1905281
50. V.M. Gun'ko, Composite materials: textural characteristics. Appl. Surf. Sci. **307**, 444–454 (2014). https://doi.org/10.1016/j.apsusc.2014.04.055
51. M. Thommes, K. Kaneko, A.V. Neimark, J.P. Olivier, F. Rodriguez-Reinoso, J. Rouquerol, K.S.W. Sing, Physisorption of gases, with special reference to the evaluation of surface area and pore size distribution (IUPAC Technical Report). Pure Appl. Chem. **87**, 1051–1069 (2015). https://doi.org/10.1515/pac-2014-1117

Formation of a Conducting Phase in Porous Glasses

I. Doycho, Ya. Lepikh, L. Filevska, E. Rysiakiewicz-Pasek, and V. Grinevych

Abstract A method of embedding a conductive phase into porous glass is proposed for increasing the conductivity of high-resistance samples. The method is based on the processing of samples with carbon-containing substances in special thermodynamic conditions. It is demonstrated that using the method, it is possible to create a reliable ohmic contact to porous substances. This makes it possible to use systems based on porous glass as active elements of resistive sensors. The possibilities of the method are illustrated by the example of the creation of a resistive to humidity sensor, capable of operating in a wide range of temperatures not destroyable for the system.

1 Introduction

Materials often used as active elements of most environmental monitoring sensors are sensitive primarily at their near-surface layers. Therefore, in order to achieve the best sensitivity of the material, it is to be strived the maximum possible unfolding of its surface. This deployment can be achieved by dispersing particles of matter down to nanometer sizes. However, it is difficult to operate successfully with individual particles of the indicated sizes; therefore, they are placed in a certain matrix containing small cavities in the form of through slits. In this case, an ensemble of nanoparticles is formed, consisting of the mentioned small particles of the substance and the matrix itself, in which they are placed. Since the matrix is a part of the ensemble, it must comply with certain restrictions of not affecting the properties of the substance under study. One of the main of such limitations is chemical inertness, that is, the matrix should not enter into chemical interaction with the substance under study and change its (or its own) chemical composition. Secondly, it must

I. Doycho · Ya. Lepikh · L. Filevska (✉)
Odesa I.I. Mechnikov National University, Dvoryanska Str., 2, Odesa 65082, Ukraine
e-mail: lfilevska@gmail.com; liudmyla.filevska@pwr.edu.pl

L. Filevska · E. Rysiakiewicz-Pasek · V. Grinevych
Department of Experimental Physics, Wrocław University of Science and Technology, Wrocław, Poland

O. Fesenko and L. Yatsenko (eds.), *Nanoelectronics, Nanooptics, Nanochemistry and Nanobiotechnology, and Their Applications*, Springer Proceedings in Physics 297,
https://doi.org/10.1007/978-3-031-42708-4_15

have a sufficiently strong skeleton, which will prevent both the aggregation of the nanoparticles of the ensemble and the mechanical destruction of the created system. And finally, if we are interested in the luminescent properties of the particles that make up the ensemble, the matrix should not be luminescent in spectral regions of the substance. These requirements are perfectly met by sparse silicate glass with through cavities of nanometer dimensions. The sizes of interpenetrating slots can vary from a few nanometers to several hundreds of nanometers. In addition, the quartz skeleton of the compound is strong enough, therefore, which limits the size of the formed particles, since they cannot exaggerate the size of the gaps. The columnar structure of the glass makes it possible to influence both the inner surface of the slits and the nanoparticles created inside them. In the most cases, it is convenient to create these nanoparticles by saturating the matrix with solutions of suitable substances. It is possible to extract sparse silicate glass from two-phase soda-borosilicate glass using a not very complicated technology [1].

2 Types of Porous Silicate Glass and the Technology of Their Creation

Two-phase sodium borosilicate glass has a complex chemical formula $SiO_2 \times [Na_2O \times B_2O_3]$. Its components have different furnace temperatures; besides, the sodium-borate component is chemically less stable. Therefore, by choosing the right temperature regime for charge maintenance during phase separation, it is possible to achieve the desired degree of their interweaving. Subsequently, by etching the sodium-borate phase by appropriate chemical treatment, it is possible to obtain a silicate skeleton with a larger or smaller preferred gap size. In this case, the most dispersed quartz particles will precipitate inside the slots in the form of silica gel. Silica gel prevents the aggregation of the elements of the created nanoparticles' ensemble [2]; however, if necessary, it can be eliminated by additional chemical treatment [3, 4]. Types of porous silicate glasses with column structure depending on the thermodynamic conditions of their production and subsequent chemical processing are shown in Table 1.

The water absorption–desorption method [5] for each of the indicated types of borehole silicate glass revealed the size distribution of slots. The corresponding

Table 1 Types of porous silicate glasses with column structure

	The low-phase separation temperature in the original glass is 490 °C	The high-phase separation temperature in the original glass is 650 °C
Type of glass after etching of the unstable phase	A	C
Type of glass after tinning	B	D

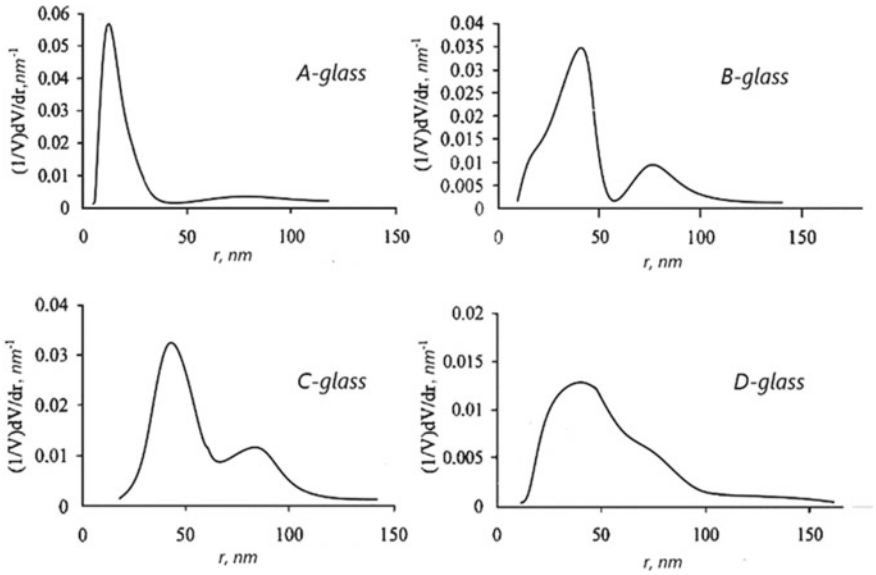

Fig. 1 Size distribution of pores for different types of porous glasses, obtained by the water adsorption/desorption method

graphs are shown in Fig. 1, from which it can be seen that glasses of all types have two preferred phases of the slot sizes. At the same time, glasses of types C and B are most similar in this parameter. In glasses of type D, these phases are almost not traced, and glasses of type A are the most finely spun. The similarity of pores' size distribution for glasses C and B is not of the same nature. In the first case, the spectra have the indicated form due to the silica gel in the slits, and in the second case, due to the etching of the slits in the finely scalded glass of type A. It should be noted that insignificant residues of stack gel remain in the slits of type B glass [1, 4].

3 Carbon Processing

Ensembles of nanoparticles formed in the matrix based on the specified glasses due to rather considerable intrinsic electrical resistance of such systems cause their usage mainly for luminescent-type sensors. At the present work, it is suggested to form inside the pores the nanoparticles' ensemble of a conducting substance for significant reduction of the sample resistance. This method will make it applicable as an active element in resistive-type sensors. Such substance is a carbon, which in the form of graphite exhibits excellent conductive properties, and because of this, the corresponding procedure is called carbon processing [6, 7].

Carbon treatment is able to reduce the electrical resistance of slotted glass samples by several orders of magnitude due to the inclusion of a conductive phase made of

graphite nanoparticles. This increase in conductivity can be beneficial for certain applications of certain types of glasses. In order to subject any type of glass to carbon treatment, it is saturated with a solution of a substance containing carbon. The best in this case is glucose: it is well soluble in water, and when heated to 180 °C, it is easily regenerated simply in the cavities of the matrix to carbon in the form of highly dispersed graphite with the release of water. The process is described by a well-known equation

$$C_6H_{12}O_6 \xrightarrow{(t)} 6C + 6H_2O,$$

which lasts about a day, and its completion can be judged visually by the blackening of the sample.

4 Creation of an Ohmic Contact to Porous Glass

One of the applications of carbon processing is the creation of an ohmic contact to a slotted glass sample [8]. This would make it possible to investigate a possible correlation between the luminescent and electrical properties of nanoscale systems in porous matrices. To achieve the specified goal, the carbon treatment of the system must be partial and is carried out as follows.

A standard sample of size 10 is immersed with the ends in a glucose solution to a depth of 0.5–1 mm using a clamp-like holder. This creates conditions that almost correspond to the typical problem of diffusion from a steady source. According to Fick's second law, at the stage of driving impurities into the system during time t at a distance x from the interface between the glucose solution and the plate, the glucose concentration C_x will occur

$$C_x = C_0 \mathrm{erfc}\left(\frac{x}{2\sqrt{Dt}}\right).$$

Here, C_0 is the initial concentration of the impregnative solution. The coefficient D is a certain analogue of the diffusion coefficient and is called the impregnation coefficient. It is significantly different from the diffusion coefficient, because, unlike it, it describes the penetration of not individual impurity atoms into the interatomic space of the sample, but the percolation of rather large glucose molecules into the nanoslits of the slotted glass, which are also quite large compared to the interatomic distances (see Fig. 1). The impregnation coefficient depends on the type of glass, more precisely its parameters such as porosity, pore size distribution, the presence of residual silica gel in the pores and its amount, as well as on the temperature at which the impregnation takes place.

The glucose distribution inside the slotted glass plate after it saturates the sample from both ends is schematically shown in Fig. 2. The depth of immersion of the plate

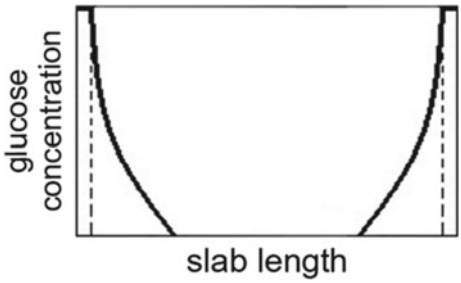

Fig. 2 Glucose distribution inside a slotted glass plate

into the solution is indicated by a dotted line. It is important that both curves do not show the configuration of the permeated glucose profile, but only reflect a decrease in its concentration when moving away from the source of impregnation.

It is noted that error function compliment converges rather slowly when expanded in a series. Therefore, for the analytical estimation of the concentration of permeated glucose at a small distance x from the source, expansion in the McLauren series is usually used, while at large distances, it is better to prefer the asymptotic representation of this function. For almost any specific case, it is enough to save only a few first terms in the corresponding expansions. Up to the first three terms in the first case, we have:

$$C_x \approx C_0\left[1 - \frac{2}{\sqrt{\pi}}\left(\frac{x}{2\sqrt{Dt}} - \frac{x^3}{6\sqrt{(Dt)^3}}\right)\right],$$

and in the second, respectively,

$$C_x \approx C_0\frac{\exp\left(-\left(\frac{x}{2\sqrt{Dt}}\right)^2\right)}{\left(\frac{x}{2\sqrt{Dt}}\right)\sqrt{\pi}}\left[1 - \frac{2Dt}{x^2} + \frac{12(Dt)^2}{x^4}\right].$$

Further, the slotted glass plate, which is saturated with glucose from both opposite ends, is subjected to annealing for the thermal decomposition of the penetrated glucose directly in the slots, during which the resulting graphite is simultaneously dispersed. This process is somewhat analogous to the diffusion from a confined source. If we assume that the concentration of glucose at the ends of the plate at the time of the start of the thermal decomposition procedure corresponds to C_0, and at an arbitrary point x was determined by the above equations and was equal to C_x, then the new concentration of C_{x1} at the moment of time t will be determined by the expression:

$$C_{x1} = C_x \exp\left(\frac{-x^2}{4Dt}\right).$$

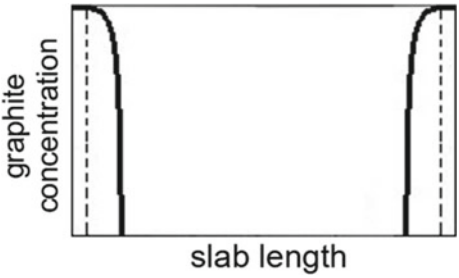

Fig. 3 Distribution of graphite nanoparticles in the formed ensemble

The distribution of graphite nanoparticles in the ensemble formed by the aforementioned heat treatment is shown in Fig. 3. Here, the depicted curves again do not correspond to the configuration of graphite in slotted glass, but only to a decrease in its amount when moving away from the end of the plate.

A comparison of the images in Figs. 2 and 3 shows that the graphite nanoparticles in the formed ensemble, unlike the glucose particles, are concentrated mainly near the ends, and when they are far from them, the specified concentration drops to zero quite quickly. In this way, areas with increased conductivity are formed at the ends of the plate, the presence of which does not affect the properties of the rest of the sample in any way. The indicated conductive sections smoothly transition into the slotted glass itself. Later, after processing the ends of the sample with any conductive paste, an ohmic contact with the slotted glass plate occurs.

5 Resistive Humidity Sensor Formed on Porous Glass

The simplest example of the practical use of an ohmic contact obtained in this way is the creation of a resistive humidity sensor on slotted glass [9].

Since the environment always contains a certain amount of moisture, then the slotted glass, like any other porous system, is capable of being saturated with water vapor by itself. The condition of hydrophilicity of the system in a wide range of humidity [10] corresponds to the presence of a wide range of crack sizes in any type of glass. Even in small quantities, their size can vary from about 10 to more than 100 nm (see Fig. 1). Due to the significant reduction of the electrical resistance of the system by water vapor, the use of slotted glass as an active element of a resistive humidity sensor would seem obvious [11, 12], but this is hindered by the very high electrical resistance of these compounds. For samples of standard size, it reaches many teraOhms, and its decrease with increasing environmental humidity even by tens of gigaOhms will remain almost imperceptible against this background. However, the use of carbon treatment not for the ends, but for the entire sample as a whole, can reduce the initial resistance of the obtained system by several orders of magnitude due to the conductive properties of graphite.

It should be noted that not every type of glass is suitable for use as a matrix for the active element of the humidity sensor. For example, type A glass is not suitable, because being saturated with an insufficient amount of glucose, its resistance after annealing will remain high, and excess glucose, turning into graphite nanoparticles after annealing, together with a large amount of residual silica gel, will fill the cracks and make the system insensitive to moisture. When processing type C glass, in addition to the mentioned drawback, it will be difficult to ensure reliable contact with it due to the increased roughness of the surface [13]. And in the case of type D glass, the conductive phase is generally able to shunt the sample. Therefore, type B glass should be considered suitable for use as a humidity sensor matrix. And in fact, it mostly contains quite small cracks with a small amount of silica gel, and it has a typical moderate surface roughness.

As a result of the carbon treatment of type B glass, in addition to the formation of an ensemble of graphite nanoparticles inside the glass, a graphite layer will be formed on its surface, which will provide a fairly reliable ohmic contact. The change in the resistance of the obtained system will be completely correlated with the humidity of the environment.

Figure 4 shows a typical dependence of the resistance of an ensemble of graphite nanoparticles in type B glass on humidity. The ensemble was formed by keeping the glass in a 40% aqueous glucose solution for a day, followed by annealing for two hours at 180 °C. Contacts to such a system were created using silicone paste. Measurements were made at room temperature. It can be seen that the decrease in system resistance when the relative humidity of the environment increases from 10 to 99% reaches three orders of magnitude.

It is notable that similar isotherms can be obtained at any temperature and they will hardly change. This statement applies even to negative temperatures, because at negative temperatures, air humidity is determined by the sublimation of ice. And

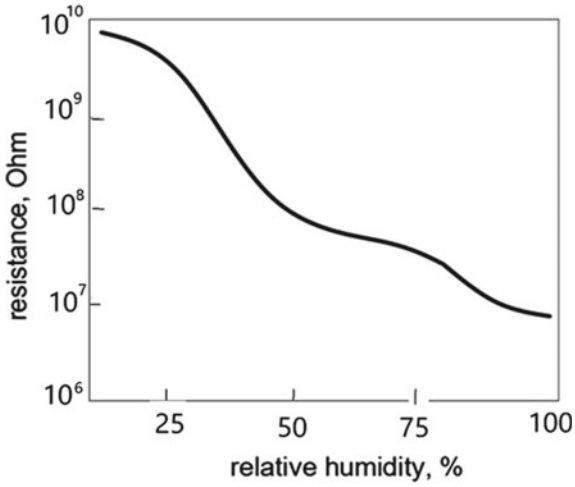

Fig. 4 Resistance–humidity dependence of graphite nanoparticles ensemble in type B glass at room temperature

individual water nanoparticles sorbed by the system are separated from each other by silica gel and graphite nanoparticles, so they are unchanged regardless of the surrounding temperature, and there is no aggregate state for them [13].

6 Conclusion

Carbon treatment leads to the formation of a conductive layer inside slotted glass of any type. This allows significantly reduce the initial electrical resistance of porous standard size glass.

Partial carbon treatment of standard samples of slotted glass allows to create at the ends of the sample an ohmic contact to an ensemble of nanoparticles in said glass for further applications.

A certain type of porous glass, after proper processing, may be used as an active element of a resistive-type humidity sensor, capable of operating at any temperature that does not destroy the system.

References

1. I.K. Doycho, Study of the photoluminescent properties of nanoparticles ensembles of dyes, ed. by V.A. Smyntyna, in *Non Equilibrious Processes in the Sensor Structures* (ONU (Odesa Mechnikov National University), Odesa, 2015), pp. 120–170
2. O.V. Tyurin, Y.M. Bercov, S.O. Zhukov, T.F. Levitskaya, S.A. Gevelyuk, I.K. Doycho, E. Rysiakiewicz-Pasek, Dye aggregation in porous glass. Opt. Appl. **40**(2), 311–321 (2010)
3. O.V. Mazurin, G.P. Roskova, V.I. Averianov, V. AntropovaT, *Biphasic glasses: structure, properties, applications* (NAUKA, Leningrad, 1991)
4. I.K. Doycho, V.S. Grinevych, L.M. Filevska, Porous silica glasses as a model medium for the formation of nanoparticles ensembles: review, in *Advanced Nanomaterials for Detection of CBRN, NATO Science for Peace and Security Series A: Chemistry and Biology*, pp. 283–294 (2020). https://doi.org/10.1007/978-94-024-2030-2_21
5. M.M. Dubinin, Kapilyarnye yavleniya i informatsiya o poristoy strukture adsorbentov, Izvestiya AN SSSR, ser. Khimicheskaya **1**, 101–125 (1978) (M.M. Dubinin, Capillary phenomena and information about the porous structure of adsorbents, Ed. of the USSR: Izvestiya of the Sov. Union Acad. of Sc. Chemical series Chemical **1**, 101–125 (1978))
6. S.A. Gevelyuk, I.K. Doycho, L.P. Prokopovich, E. Rysiakiewicz-Pasek, K. Marczuk, The influence of anneal of incorporated carbon on the photoluminescence properties of porous glass and porous silicon, ed. by L. Stoch, in *Polish Ceramic Bulletin 19, Ceramics 57, Porous and Special Glasses (Proceedings of the 4-th International Seminar PGL'98)* (Polish Ceramic Society, Krakow, 1998), pp. 59–64
7. S.A. Gevelyuk, I.K. Doycho, L.P. Prokopovich, E. Rysiakiewicz-Pasek, E.D. Safronsky, Influence of carbon multiple treatments on the photoelectrical properties of porous glasses. Radiat. Eff. Defects Solids **158**, 427–432 (2003). https://doi.org/10.1080/1042015022000037292
8. I.K. Doycho, Ya.I. Lepikh, Sposib vygotovlennya omichnogo kontaktu do shparystogo skla: MPK H01L21/28; B82B3/HO1L21/02 Zayavnyk ta patentovolodar Odesky Natsionalny universytet imeni I.I. Mechnukova.-N A2022 02802, zayavl. 25.07.2022 (Method for making ohmic contact to porous glass MPK H01L21/28 B82B3/00 HO1L21/02; Applicant and the Patent owner Odesa I.I. Mechnykov National university, Ukraine)

9. Ya.I. Lepikh, I.K. Doycho, Sensor vologosti na shparystomu skli: MPK G01N27/00/zayavnyk ta patentovolodar Odeski natsionalny universytet imeni I.I,Mechnykova. №: A2022 02804, zayavl. 25.07.2022 (Ya.I. Lepikh, I.K. Doycho, The humidity sensor on the porous glass: MPKG01N27/00 Applicant and The Patent Owner: Odesa I.I. Mechnykov National University, Ukraine, №: A2022 02804, app l. 25.07.2022)
10. H. Grange, J.-S. Danel, B. Desloges, V. Jousseaume, US patent 8739622 B2, Jun 3, 2014, G01N27/00
11. S.A. Gevelyuk, I.K. Doycho, E. Rysiakiewicz-Pasek, K. Marczuk, Relative changes of porous glass dimensions in humid ambiance. J. Porous Mater. **7**, 465–467 (2000)
12. S.A. Gevelyuk, I.K. Doycho, D.V. Lishchuk, L.P. Prokopovich, E.D. Safronsky, E. Rysiakiewicz-Pasek, Ya.O. Roizin, Linear extension of porous glasses with modified internal surface in humid environment, Optica Applicata **30**(4), 605–611 (2000)
13. E.D. Safronsky, Y.O. Roizin, E. Rysiakiewicz-Pasek, Application of porous glasses in oftalmic prostetic repair. J. Porous Mater. **11**, 21–29 (2004)

Electrical Properties of *p*-$CuCoO_2$/*n*-Si Heterojunction

D. P. Koziarskyi, I. P. Koziarskyi, and E. V. Maistruk

Abstract *p*-$CuCoO_2$/*n*-Si heterostructures were produced by radio frequency magnetron sputtering of $CuCoO_2$ thin films on *n*-Si crystalline substrates. The optical properties of $CuCoO_2$ thin films deposited on glass substrates are studied. The mechanisms of current transfer are analyzed based on temperature dependences of *I–V* characteristics. The influence of light on the electrical properties of the *p*-$CuCoO_2$/*n*-Si heterostructure is determined.

1 Introduction

$CuCoO_2$ belongs to the group of delafossites, which are known for a wide range of electrical properties. The conductivity of these compounds can vary from insulating to metallic materials. $CuCoO_2$ has found applications such as catalyst for oxygen evolution reaction [1], as thermoelectric materials [2] and as absorber materials [3].

Since these compounds simultaneously have a fairly good transparency to visible light and high electrical conductivity, they can be attributed to the group of transparent conductive oxides (TCO). TCO thin films are widely used as transparent electrodes in photoelectronic and lighting devices [4]. p-type TCOs give us the opportunity to manufacture transparent p–n heterojunctions, diodes and transistors, so their further research is quite promising [5, 6]. Since delafossite oxides have p-type semiconductor properties and fairly high optical transparency for visible light, they can be used for this purpose.

$CuCoO_2$ thin films are fabricated by using different deposition techniques such as sol–gel method [1, 3], ion exchange [2], RF magnetron sputtering [7], conventional solid-state reaction method [8] and low-temperature hydrothermal synthesis [9]. However, it is known that vacuum sputtering processes are more suitable for obtaining films of higher quality.

D. P. Koziarskyi (✉) · I. P. Koziarskyi · E. V. Maistruk
Department of Electronics and Power Engineering, Yuriy Fedkovych Chernivtsi National University, Chernivtsi 58002, Ukraine
e-mail: i.koziarskyi@chnu.edu.ua

O. Fesenko and L. Yatsenko (eds.), *Nanoelectronics, Nanooptics, Nanochemistry and Nanobiotechnology, and Their Applications*, Springer Proceedings in Physics 297,
https://doi.org/10.1007/978-3-031-42708-4_16

Therefore, the fabrication of the p-$CuCoO_2$/n-Si heterostructure by radio frequency magnetron sputtering of $CuCoO_2$ thin films on n-Si crystalline substrates is of certain scientific interest.

2 Experiment Details

Thin films of $CuCoO_2$ (thickness ~200 nm) were deposited on glass substrates (for optical studies) and on plane-parallel n-Si plates (for obtaining heterostructures) by radio frequency magnetron sputtering. The target for sputtering $CuCoO_2$ films was made from a stoichiometric mixture of CuO and CoO_2, which was pressed into a special aluminum cup. The aluminum cup has such a shape that the plasma does not interact with its material. The radio frequency magnetron sputtering system is installed in the UVN-70 universal vacuum unit. Deposition was carried out in an atmosphere of inert gas (argon) and at a magnetron frequency of 13.56 MHz. To obtain a high vacuum, a TMN-500 turbomolecular pump was used [10]. Substrate temperature $T_S = 653$ K, spraying was carried out in two stages $t_1 = 15$ min, $P_1 = 180$ W, $t_2 = 15$ min, $P_2 = 200$ W (t—spraying time, P—magnetron power).

The thickness of the films was determined by applying them to a sital substrate and then scribing and studying the interference pattern obtained with the Linnik MII-4 microinterferometer.

To carry out optical studies, thin films of $CuCoO_2$ were applied to the cover glass and the optical transmission spectrum was recorded using a spectrophotometer SF-2000 in the wavelength range of incident radiation $\lambda = 0.2$–1.1 μm [11].

The four-probe method was used to determine the surface resistance of films ($\rho_{\square} = 1$ MΩ/□) [12]. Considering the thickness of the film (200 nm), the specific resistance was $\rho = 20$ Ω·cm. Silver-based conductive paste was used as ohmic contacts to $CuCoO_2$ films and n-Si substrates.

A hardware and software complex based on Arduino, an Agilent 34410A digital multimeter and a Siglent SPD3303X programmable power source were used to measure the I–V characteristics of p-$CuCoO_2$/n-Si heterostructures. This complex was controlled by a personal computer using the software created by the authors in the LabVIEW environment.

An integrated light source with an illumination power density of 80 mW/cm^2 and close to AM1.5 was used to measure light I–V characteristics.

3 Results and Discussion

looseness-1The absorption coefficient of $CuCoO_2$ thin films was determined using the method of independent measurement of transmission and reflection coefficients. For Cu–CoO_2 films in the studied spectrum region, the light reflection coefficient is

$R \approx 20\%$. To calculate the coefficient of optical absorption of light α, we used the formula [10, 11]:

$$\alpha = \frac{1}{d} \ln \left[\frac{(1-R)^2}{2T} + \sqrt{\frac{(1-R)^4}{4T^2} + R^2} \right]. \quad (1)$$

The energy and type of optical transition of an electron from the valence band to the conduction band was determined from the analysis of the absorption coefficient using the expression for semiconductors:

$$\alpha = \frac{a_0 \left(h\nu - E_g\right)^n}{h\nu}, \quad (2)$$

where a_0 is a constant and n is determined by the type of optical transition of an electron from the valence band to the conduction band. To determine the type of optical transitions in thin $CuCoO_2$ films, the dependences $(\alpha h\nu)^x = f(h\nu)$ were constructed, where the values of x depend on different values of n.

The presence of a rectilinear region near the region of the own absorption edge on the spectral dependence $(\alpha h\nu)^2 = f(h\nu)$ for the $CuCoO_2$ film (Fig. 1) confirms the fact that the process of absorption of light photons occurs with the help of direct optical transitions ($n = ½$).

By extrapolating a straight section to the energy axis (Fig. 1), the optical band gap for the investigated films was determined, which was $E_g = 3.5$ eV. This value of energy for direct allowed optical transitions is in good agreement with literature data [8].

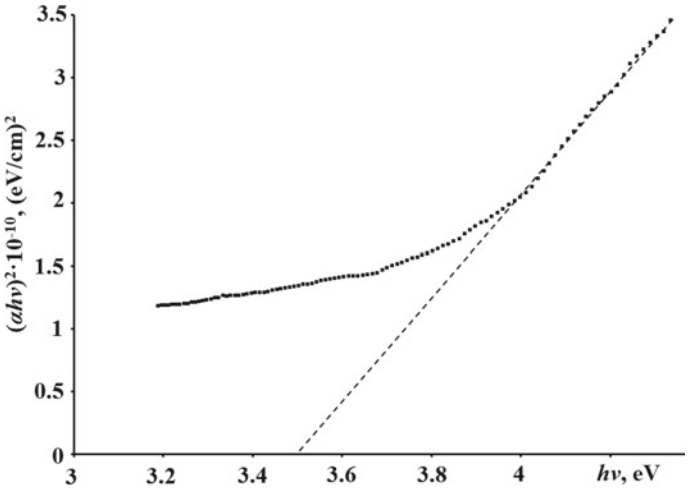

Fig. 1 Spectral dependence of the absorption coefficient $(\alpha h\nu)^2 = f(h\nu)$ of $CuCoO_2$ films

From the *I–V*-characteristics of the *p*-$CuCoO_2$/*n*-Si heterostructures presented in Fig. 2, it is seen that in the temperature range $T = 299$–343 K, these heterostructures have rectifying properties. The current rectification ratio is determined at $T = 294$ K and voltages $|V| = 0.7$. V is equal to RR ~ 10^3.

To estimate the height of the potential barrier $q\varphi_k$, we extrapolated the linear sections of the *I–V* characteristics in the region of forward biases to the voltage axis. The height of the *p*-$CuCoO_2$/*n*-Si heterojunction potential barrier determined in this way at room temperature is equal to $q\varphi_k \approx 0.53$ eV. Figure 3 shows the value of the height of the potential barrier at different temperatures.

Figure 3 shows that the height of the potential barrier decreases linearly from 0.53 to 0.46 eV with increasing temperature from $T = 299$ to 343 K. Such a change in the height of the potential barrier with temperature is described by the equation:

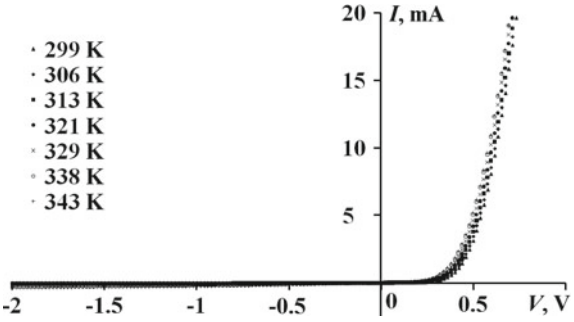

Fig. 2 *I–V* characteristics of the heterostructure of *p*-$CuCoO_2$/*n*-Si in the temperature range from 299 to 343 K

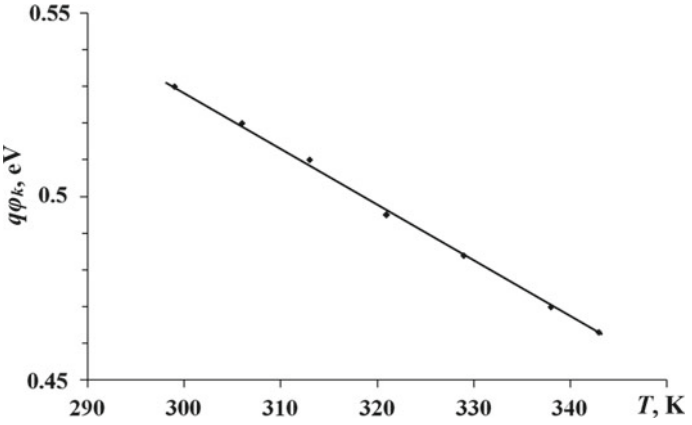

Fig. 3 Temperature dependence of the height of the potential barrier of the *p*-$CuCoO_2$/*n*-Si heterostructure

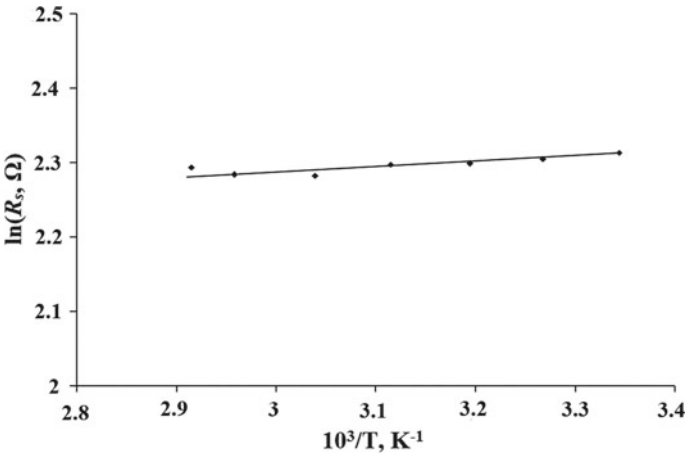

Fig. 4 Temperature dependence of the series resistance of the p-$CuCoO_2$/n-Si heterostructure

$$q\phi_k(T) = q\phi_k(0) - \beta_\phi T. \tag{3}$$

Using expression (3) and Fig. 3, the temperature coefficients of change of the height of the potential barrier and its height at 0 K were determined, which are equal to $d(q\varphi_k)/dT = -1.54 \cdot 10^{-3}$ eV/K and $q\varphi_k(0\ \text{K}) = 0.99$ eV, respectively.

The temperature dependence of the series resistance is shown in Fig. 4. From the slope of the temperature dependence, $\ln(R_s) = f(10^3/T)$ determined the depth of the donor level which is $E_d = 0{,}07$ eV, near the bottom of the conduction zone of the base material.

The mechanisms of current transfer through the p-$CuCoO_2$/n-Si heterojunction at forward biases were determined from the analysis of I–V characteristics in the coordinates $\ln I = f(V)$ (Fig. 5).

From the straight-line sections on the dependence $\ln I = f(V)$ (Fig. 5) by the tangents of their angles of inclination to the voltage axis, the non-ideality factors of heterojunctions n at different temperatures were determined (Fig. 6).

From Fig. 6, it can be seen that at small forward biases of $0.05\ \text{V} < V < 0.4$ V, the non-ideality factor, determined from the slope of the linear dependences $\ln I = f(V)$ to the voltage axis, was $n \approx 2.1$–2.3, which indicates predominance of the generation-recombination mechanism of current transfer. At higher forward bias voltages of $0.4\ \text{V} < V < 0.6$ V, the value of the non-ideality factor $n \approx 3.5$–4.5 (Fig. 6) indicates the predominance of the tunnel mechanism of current transfer.

As can be seen from Fig. 6, the coefficient of non-ideality depends weakly on temperature, which is typical for tunneling mechanisms of forward current generation involving surface states at the interface and defects in the space charge region, and is described by the expression [13]:

$$I(V) = B \cdot \exp(\beta T) \cdot \exp(\alpha V), \tag{4}$$

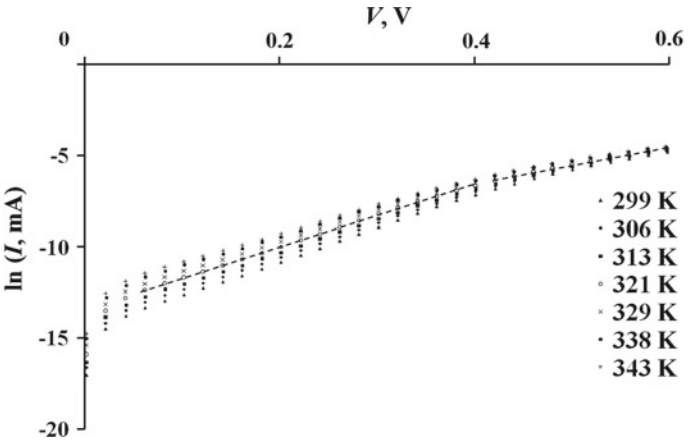

Fig. 5 Dependences $\ln I = f(V)$ at forward biases applied to the p-$CuCoO_2$/n-Si heterostructure at different temperatures

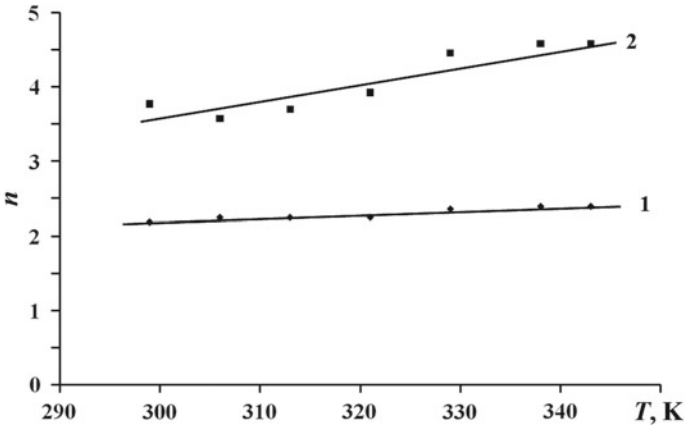

Fig. 6 Temperature dependence of the non-ideality factor at forward biases applied to the p-$CuCoO_2$/n-Si heterostructure: 1—(0.05 V < V < 0.4 V); 2—(0.4 V < V < 0.6 V)

where B, β and α are constants.

To analyze the mechanisms of current transfer at reverse biases for the p-$CuCoO_2$/n-Si heterostructure, an expression was used that describes the process of tunneling of charge carriers with the participation of surface states: The reverse branches of the I–V characteristics of the p-$CuCoO_2$/n-Si heterostructure at temperatures T = 299–343 K in the voltage range from $-$ 2 V < V < $-$ $3kT/q$ are described by the expression for tunneling current involving surface states:

$$I_{\text{rev}}^{t} \approx a_0 \exp\left(\frac{b_0}{\sqrt{\phi_k(T) - qV}}\right), \tag{5}$$

where a_0 and b_0 are parameters that are voltage independent.

From Fig. 7, it can be seen that at the reverse biases $-2\ \text{V} < V < -3kT/q$, the I–V characteristics in the coordinates $\ln(I_{\text{rev}}) = f(\varphi_k - qV)^{-1/2}$ have a linear character. This indicates the dominance of the tunneling mechanism of current transfer with the involvement of surface states through the p-$CuCoO_2$/n-Si heterojunction.

The I–V characteristics of the studied p-$CuCoO_2$/n-Si structures, which were measured at room temperature $T = 294$ K and under integral illumination under standard lighting conditions close to AM1.5 with an illumination power density of 80 mW/cm^2, are presented in Fig. 8.

From Fig. 8, it can be seen that p-$CuCoO_2$/n-Si heterostructures have a low photosensitivity at reverse bias.

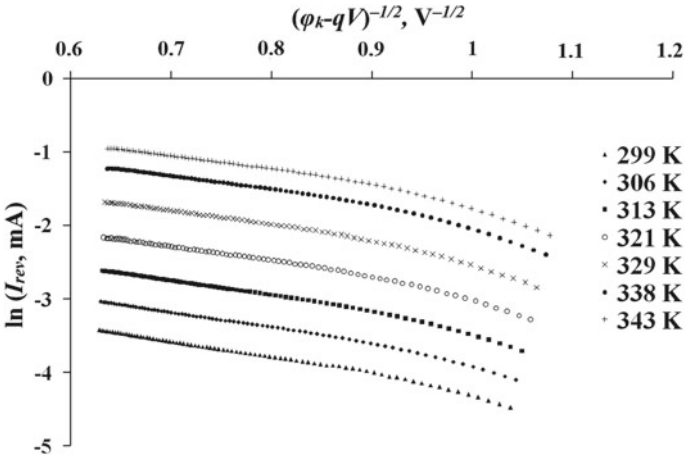

Fig. 7 Temperature dependences of reverse I–V characteristics for p-$CuCoO_2$/n-Si heterostructure

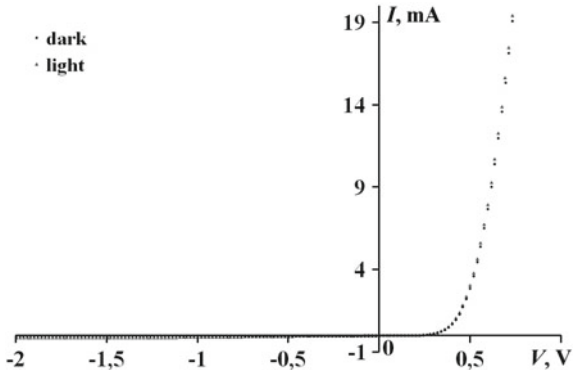

Fig. 8 Light I–V-characteristics of the heterojunction p-$CuCoO_2$/n-Si

4 Conclusion

Thin $CuCoO_2$ films (~200 nm thick) were applied to glass substrates and plane-parallel *n*-Si plates by RF magnetron sputtering. The resistivity of the $CuCoO_2$ films was $\rho = 20$ Ω·cm at $T = 300$ K. From the analysis of the absorption spectra of $CuCoO_2$ films, it was established that these films are direct band with the optical band gap $E_g = 3.5$ eV.

The *p*-$CuCoO_2$/*n*-Si heterostructure has rectifying properties. The current rectification ratio is equal to RR ~ 10^3. The presence of an energy barrier $q\varphi_k \approx 0.5$ eV on the *n*-Si side explains the diode characteristics of the heterostructure. In the *p*-$CuCoO_2$/*n*-Si structure, at forward biases of $0.05\ V < V < 0.4$ V, the generation-recombination mechanism of current transfer is dominant. When the forward bias voltage increases $V > 0.4$ V, the tunneling mechanisms of current transfer with the participation of surface states dominate. At reverse biases of $-2\ V < V < -3kT/q$ V, the tunneling mechanisms of current transfer with the participation of surface states also dominate.

The *p*-$CuCoO_2$/*n*-Si heterostructure has a low photosensitivity at reverse bias under AM1.5 radiation conditions.

References

1. M. De Koninck, S.C. Poirier, B. Marsan, $CuxCo_{3-x}O_4$ used as bifunctional electrocatalyst. J. Electrochem. Soc. **153**, A2103 (2006). https://doi.org/10.1149/1.2338631
2. M. Beekman, J. Salvador, X. Shi, G.S. Nolas, J. Yang, Characterization of delafossite-type $CuCoO_2$ prepared by ion exchange. J. Alloys Compd. **489**, 336 (2010). https://doi.org/10.1016/j.jallcom.2009.09.124
3. A. Amri, Z.T. Jiang, T. Pryor, C.-Y. Yin, S. Djordjevic, Developments in the synthesis of flat plate solar selective absorber materials via sol–gel methods: a review. Renew. Sust. Energ. Rev. **36**, 316 (2014). https://doi.org/10.1016/j.rser.2014.04.062
4. D.S. Ginley, C. Bright, Transparent conducting oxides. MRS Bull. **25**, 15 (2000). https://doi.org/10.1557/mrs2000.256
5. H. Kawazoe, H. Yanagi, K. Ueda, H. Hosono, Transparent p-type conducting oxides: design and fabrication of p-n heterojunctions. MRS Bull. **25**, 28 (2000). https://doi.org/10.1557/mrs2000.148
6. H. Kawazoe, M. Yasukawa, H. Hyodo, M. Kurita, H. Yanagi, H. Hosono, P-type electrical conduction in transparent thin films of $CuAlO_2$. Nature **389**, 939 (1997). https://doi.org/10.1038/40087
7. S. Suzuki, T. Miyata, T. Minami, p-type semiconducting Cu_2O–CoO thin films prepared by magnetron sputtering. J. Vac. Sci. Technol. A **21**, 1336 (2003). https://doi.org/10.1116/1.1580491
8. C. Ruttanapun, M. Sa-nguan-cheep, S. Kahatta, P. Buranasiri, P. Jindajitawat, Optical and electronic transport properties of p-type $CuCoO_2$ transparent conductive oxide. Proc. SPIE **8883**, 88831O (2013). https://doi.org/10.1117/12.2021992
9. Z. Du, D. Xiong, S.K. Verma, B. Liu, X. Zhao, L. Liu, H. Li, A low temperature hydrothermal synthesis of delafossite $CuCoO_2$ as an efficient electrocatalyst for the oxygen evolution reaction in alkaline solutions. Inorg. Chem. Front. **5**, 183 (2018). https://doi.org/10.1039/C7QI00621G
10. E.V. Maistruk, I.P. Koziarskyi, D.P. Koziarskyi, P.D. Marianchuk, V.V. Brus, Structure and optical properties of thin films CZTS obtained by the RF magnetron sputtering. Proc. SPIE **10612**, 1061215 (2018). https://doi.org/10.1117/12.2304801

11. E.V. Maistruk, I.P. Koziarskyi, D.P. Koziarskyi, G.O. Andrushchak, Optical properties of thin films CZTSe produced by RF magnetron sputtering and thermal evaporation, in *Proceedings IEEE CFP17F65-ART, 01PCSI28* (2017). https://doi.org/10.1109/NAP.2017.8190163
12. I.P. Koziarskyi, E.V. Maistruk, D.P. Koziarskyi, P.D. Maryanchuk, Electric properties of thin films $Cu_2ZnSnSe_4$ and $Cu_2ZnSnSe_2Te_2$ (S_2) obtained by thermal vacuum deposition. J. Nano-Electron. Phys. **10**, 01028 (2018). https://doi.org/10.21272/jnep.10(1).01028
13. A.L. Fahrenbruch, R.H. Bube, *Fundamentals of Solar Cells* (Academic Press, 1983) [ISBN: 9780323145381]

The Effect of Rare-Earth Metal Oxide Additives on Crack Growth Resistance of Fine-Grained Partially Stabilized Zirconia

V. V. Kulyk, Z. A. Duriagina, B. D. Vasyliv, V. I. Vavrukh, T. M. Kovbasiuk, P. Ya. Lyutyy, and V. V. Vira

Abstract Recently, the additives of rare-earth metal oxides are being used for obtaining partially stabilized zirconia ceramics aimed at applications in various high-temperature structural components. Corresponding sintering modes providing fine-grained microstructure formation are being developed. Due to the obtained correlations between the morphology parameters and resulting mechanical characteristics of ceramics, it is possible to reach a unique combination of their functional properties. In this work, zirconia ceramics stabilized with small percentages of rare-earth metal oxides have been studied in terms of sintering ability, elimination of the phase changes in zirconia, as well as employment of the transformation toughening mechanism during crack propagation. The metal oxides including rare-earth metal oxides (Y_2O_3, CoO, CeO_2, Fe_2O_3) were used as additives to reach a stabilizing effect on zirconia and manufacture ceramics with fine-grained microstructure. Series of ceramic specimens were prepared using conventional sintering in a temperature range of 1550–1620 °C. Fracture toughness test by indentation method and single-edge notch beam test under three-point bending were performed. Based on X-ray diffraction analysis and SEM studies of fracture surfaces of specimens, it was

V. V. Kulyk (✉) · Z. A. Duriagina · V. I. Vavrukh · T. M. Kovbasiuk · P. Ya. Lyutyy
Department of Materials Science and Engineering, Lviv Polytechnic National University, 12 S. Bandera Str., Lviv 79013, Ukraine
e-mail: kulykvolodymyrvolodymyrovych@gmail.com

Z. A. Duriagina
Department of Materials Engineering, The John Paul II Catholic University of Lublin, 14 Racławickie Al., 20-950 Lublin, Poland

B. D. Vasyliv
Department of Hydrogen Technologies and Alternative Energy Materials, Karpenko Physico-Mechanical Institute of the NAS of Ukraine, 5 Naukova Str., Lviv 79060, Ukraine

V. V. Vira
Department of Strength of Materials and Structural Mechanics, Lviv Polytechnic National University, 12 S. Bandera Str., Lviv 79013, Ukraine

O. Fesenko and L. Yatsenko (eds.), *Nanoelectronics, Nanooptics, Nanochemistry and Nanobiotechnology, and Their Applications*, Springer Proceedings in Physics 297,
https://doi.org/10.1007/978-3-031-42708-4_17

concluded that the maximum transformation toughening effect revealed for ZrO_2–Y_2O_3–CoO–CeO_2–Fe_2O_3 ceramics was related to a distinct change in the fracture surface pattern.

1 Introduction

Nowadays, zirconia ceramics doped with the stabilizing oxides Y_2O_3 [1–4], CeO_2 [5–7], MgO [8], or CaO [9] are being widely developed. The metastable tetragonal phase of zirconia ceramics is stabilized in such a way at room temperature. It is well known that transformation toughening of zirconia occurs due to the transformation of the tetragonal (t) phase into the monoclinic (m) one [10–14]. This process takes place in the crack tip vicinity under significant stresses, which can effectively improve crack growth resistance of ceramics. Therefore, increased strength and crack growth resistance of the ceramics can be ensured due to the tetragonal phase.

Additionally, other oxides can be added while producing these ceramics to improve their mechanical strength and physical properties [10, 15–25]. Partially stabilized zirconia ceramics having improved mechanical properties can be utilized in various high-temperature structural components [26–30]. These ceramics are also widely used in energy generation, chemical industry, and biomedical applications [31–42].

The authors of a number of works [43–45] showed that the sintering temperature may affect to a great extent the grain size, porosity, and mechanical behavior of zirconia. It was reported in the work [44] that a single-phase microstructure (m-ZrO_2) had been formed already after pressing the zirconia specimens without Y_2O_3 additive. In contrast, ceramics containing 1.5 mol% Y_2O_3 exhibited a single-phase microstructure (t-ZrO_2) after sintering at 1100 °C. As compared to the two last variants, for zirconia containing 8 mol% Y_2O_3, a single-phase microstructure (c-ZrO_2) was formed during pressing. The maximum pore diameter in all the compacts reached 12.5 nm after pressing. An increase in the pore diameter was found in specimens without Y_2O_3 additive when the temperature increased to 600 °C. Intense grain growth and lowering of porosity occurred with a further increase in sintering temperature to 1100 °C. In a similar way, specimens containing 1.5 and 8 mol% of Y_2O_3 additives exhibited significant pore growth with increasing the sintering temperature to 600 °C. Significant densification of the specimens, along with the slight growth of grains, was revealed with increasing temperature up to 1100 °C.

Several authors investigated the effect of conditions of zirconia ceramics preparation on the resulting grain size and mechanical behavior of prepared specimens [46–50]. The authors of the work [47] studied the evolution of grain growth in doped zirconia annealed at 1500 °C for several hours. The maximum grain size for 12Ti–ZrO_2 ceramic was found to reach while sintering at 1400 °C with for 70 h. Other authors [48] reported grain size of about 1 μm while sintering at 1500 °C for a few hours. In the work [49], a study on the grain growth of zirconia ceramics was performed. A maximum grain size of 20 μm was found for 8 mol% Y_2O_3–ZrO_2

ceramic after sintering at 1700 °C for 20 h. For Y_2O_3–ZrO_2 ceramic containing 4 mol% Y_2O_3, a maximum grain size of more than 11 μm was found after sintering at 1800 °C for 100 h. The authors of the work [50] investigated specimens of zirconia ceramics sintered at maximum temperature 1600 °C for 2 h. It was found that the maximum mean grain size is 0.35 μm.

Several scientists applied spark plasma sintering as one of the recently developed techniques for preparing bulk zirconia-based ceramics, namely ceria stabilized zirconia [51–53], yttria-stabilized zirconia [54, 55], and other ceramics [56–59].

In the work [60], the influence of the zirconia percentage on the crack growth resistance and strength of Al_2O_3–ZrO_2 ceramics was studied. The ceramics consisted of the monoclinic and tetragonal ZrO_2 phases and the α-Al_2O_3 phase. The percentage of the t-ZrO_2 phase decreased with increasing the total amount of ZrO_2. The formation of fine-grained Al_2O_3–ZrO_2 microstructure was reached due to adding 10–20% ZrO_2 that allows obtaining ceramics with improved mechanical properties. It was proven in the work [61] that mechanical properties of alumina doped with zirconia and yttria-stabilized zirconia can be effectively optimized due to both the flexural strength and fracture toughness determination.

The authors of the works [62, 63] studied YSZ ceramics stabilized with 3–5 mol% Y_2O_3. The chemical and phase compositions of the ceramics were found to relate to their mechanical properties [64]. 5YSZ ceramics sintered at 1450 °C for 2 h exhibited the highest fracture toughness. This is consistent with a comparatively high percentage of the tetragonal ZrO_2 phase [62]. Effects of the sintering mode and phase composition on mechanical behavior of YSZ ceramics doped with 6–8 mol% Y_2O_3 were studied in the work [63]. After sintering at 1600 °C for 2 h, 7YSZ ceramics showed the highest fracture toughness, similarly to the results published in [65].

In the work [66], correlations between the yttria percentage, phase balance, grain size distribution, morphology of the fracture surface, and strength for zirconia with addition of 3 to 8 mol% Y_2O_3 (YSZ ceramics) sintered at 1550 °C for 2 h in argon were analyzed. It was shown that 7YSZ ceramic containing the monoclinic and tetragonal ZrO_2 phases exhibited the fine-grained microstructure and, as a result, the highest strength.

This work is aimed at studying the effects of oxide additives and sintering temperature on the microstructure, microhardness, strength, and fracture toughness of fine-grained ZrO_2–Y_2O_3–CoO–CeO_2–Fe_2O_3 ceramics for various applications.

2 Materials and Methods

In this work, zirconia ceramics stabilized with oxides Y_2O_3, CoO, CeO_2, and Fe_2O_3 have been studied.

Three series of beam specimens of partially stabilized zirconia (PSZ) approximately 2.9 × 2.9 × 45 mm^3 in size were sintered in an argon atmosphere for 2 h at temperatures of 1550 °C, 1580 °C, and 1620 °C, respectively. An electric resistance furnace was used for sintering. For marking each series, corresponding sintering

temperatures were indicated, i.e., PSZ–1550, PSZ–1580, and PSZ–1620 (Table 1). To avoid phase transformations, the side surfaces of specimens after sintering were processed using a grinding and polishing machine for metallographic preparation. Such processing allowed reaching the required surface quality.

To measure microhardness of the studied ceramics, a NOVOTEST TC-MKB1 microhardness tester was used. At least ten indentations under each of the indentation load of 0.25 N, 0.49 N, 0.98 N, 1.96 N, 2.94 N, 4.91 N, and 9.81 N were made to determine the microhardness of the ceramics under study. The test was performed according to the relevant standards [67–69].

Various teams of scientists around the world have developed a large number of formulas for calculating the microhardness of brittle materials [70–79].

Vickers microhardness (in GPa) was calculated using the formula [68]:

$$H = 0.0018544\left(\frac{P}{d^2}\right), \tag{1}$$

where P is the indentation load (N) and d is the average length of the diagonals of the indentation imprint (mm).

The geometries of imprint and crack were estimated using an optical microscope Neophot-21.

To estimate fracture toughness of the ceramics, the critical stress intensity factor (SIF), K_{Ic}, was calculated as an indicator of the propensity of ceramics to brittle fracture [62, 80]. It is known about a number of methods for evaluating the fracture toughness of ceramics and cermets using Vickers indentation [81–83]. The developed formulas used for the K_{Ic} value calculation include both mechanical and physical characteristics, as well as experimentally determined coefficients. Recently, it was proven in the works [63, 84] that for the characterization of the ZrO_2–Y_2O_3 ceramics, the formula developed in [81] provides the best convergence of results with those obtained by traditional methods of fracture mechanics. This formula used in our work is as follows:

$$K_{Ic} = 0.016\left(\frac{E}{H}\right)^{1/2}\left(\frac{P}{c^{3/2}}\right), \tag{2}$$

where E is Young's modulus (GPa), H is microhardness (GPa), P is the indentation load (N), and c is the radial crack length (m).

Table 1 Marking of the investigated ceramics, their chemical compositions, and sintering modes

Series marking	System and chemical composition, mol%	Sintering mode	
		temperature, °C	Time, h
PSZ–1550	$90ZrO_2$–$1Y_2O_3$–1CoO–$7CeO_2$–$1Fe_2O_3$	1550	2
PSZ–1580	$90ZrO_2$–$1Y_2O_3$–1CoO–$7CeO_2$–$1Fe_2O_3$	1580	2
PSZ–1620	$90ZrO_2$–$1Y_2O_3$–1CoO–$7CeO_2$–$1Fe_2O_3$	1620	2

To study mechanical behavior of the ceramics, the three-point flexure test of ceramic specimens was performed in air at 20 °C with calculating fracture stresses [85, 86].

For comparison with the Vickers indentation method, a single-edge notch beam (SENB) test [87–89] was carried out as a conventional method of estimating the fracture toughness of the ceramics. The notch width was 0.1 mm. The SENB specimens were tested under three-point bend at 20 °C in air [90–99]. Corresponding formulas given elsewhere [87–89] were used for calculating the critical SIF K_{Ic} of the ceramics.

In both the cases (SENB and Vickers indentation tests), the average K_{Ic} value of five specimens for each series was calculated.

The microstructure and fracture surface analyses of material specimens were carried out using a Carl Zeiss EVO-40XVP scanning electron microscope (SEM). For an energy-dispersive X-ray (EDX) microanalysis, an INCA Energy 350 system was used. X-ray diffraction (XRD) analysis of specimens was performed on a DRON-4.07M diffractometer. The WinCSD program package was used to perform the procedures of indexing, refinement, and calculation of the zirconia phase weight percentages.

3 Results and Discussion

The phase compositions of the studied ceramics were determined based on the XRD analysis.

The XRD patterns for the studied ceramics exhibited two-phase structure with clear peaks of the t-ZrO_2 and m-ZrO_2 phases (Fig. 1). It was found that the peak heights of the t-ZrO_2 phase slightly increased for the material sintered at a temperature of 1580 °C, compared to that sintered at 1550 °C, whereas the peak heights of the m-ZrO_2 phase slightly decreased. Even more increase of peaks of the t-ZrO_2 phase and lowering of peaks of the m-ZrO_2 phase were observed for the material sintered at 1620 °C.

Such differences in the peak heights for obtained XRD patterns are consistent with the phase balance in the studied ceramics (Fig. 2). For ceramics sintered at 1550 °C, tetragonal phase fraction was about 82.6%, whereas for ceramics sintered at 1580 °C and 1620 °C, the fractions were 84.6% and 85.9%, respectively. For these ceramic series, monoclinic phase fractions were about 17.4%, 15.4%, and 14.1%, respectively. Therefore, correlations between the sintering temperature for the studied materials and percentages of the t-ZrO_2 and m-ZrO_2 phases were observed.

There are lots of works on microstructure-related microhardness and strength of zirconia-based ceramics [84, 92, 99–106]. For ZrO_2–8 mol% Y_2O_3 ceramics [63, 84], a gradual decrease in microhardness with an increase in the indentation load from 0.49 to 9.81 N was found. Such material behavior evidences the indentation size effect peculiar to ceramics [107]. However, the microhardness values for ZrO_2–8 mol% Y_2O_3 ceramics were found to yield on the plateau at the loads in a range of

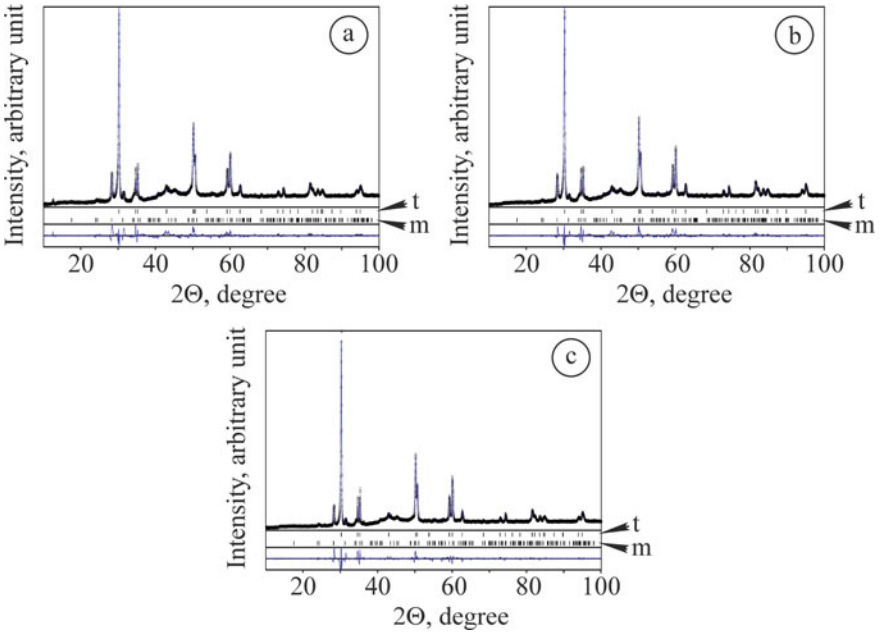

Fig. 1 XRD patterns of the studied ceramics (Table 1). Notation: t is tetragonal and m is monoclinic ZrO_2

Fig. 2 Phase balance in the studied ceramics (Table 1). Notation: t is tetragonal and m is monoclinic ZrO_2

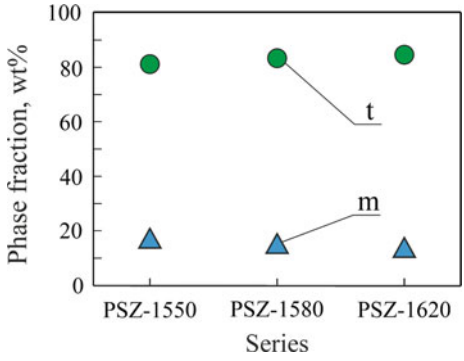

4.91–9.81 N. Such a phenomenon allows concluding that the values of microhardness and fracture toughness in this loading range are invariant.

In our work, the indentation loads of 0.25 N, 0.49 N, 0.98 N, 1.96 N, 2.94 N, 4.91 N, and 9.81 N were set and corresponding microhardness values were determined for the studied materials 1–3 (Fig. 3a).

The obtained microhardness vs load correlations are similar and can be divided into two parts. The first part of each dependence corresponds to low indentation loads (up to 0.98 N), whereas the second one corresponds to the range of 1.96–9.81 N.

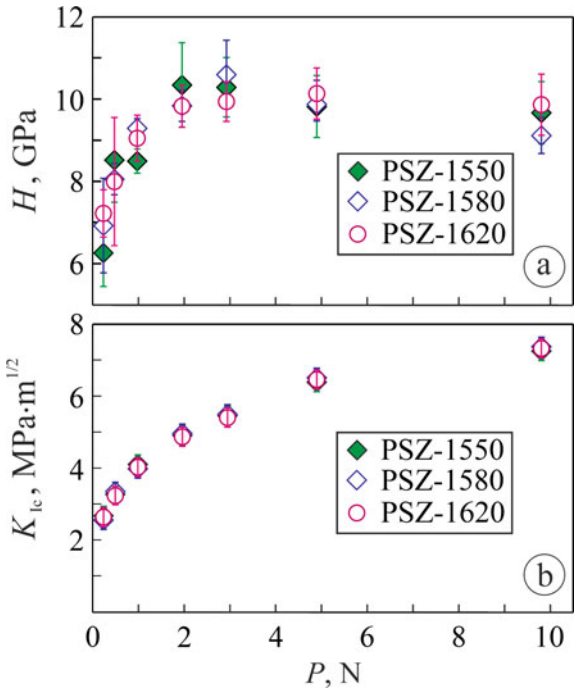

Fig. 3 Changes in mechanical characteristics of the studied ceramics depending on the indentation load: **a** Vickers microhardness; **b** fracture toughness measured by the Vickers method. The symbol marking corresponds to the series marking given in Table 1

In this range, the above-mentioned indentation size effect is observed. In contrast, the first part of each dependence exhibits the lowered microhardness values due to the indentation imprints commensurable with the average diameter of pores on the specimen surface. The average microhardness values for all the studied materials were revealed to yield on the plateau under the loads of 4.91–9.81 N (Fig. 3a). For this load range, a trend to increase invariant values of microhardness with an increase in the sintering temperature was found.

It is known that an increase in sintering temperature leads to intensive grain growth in yttria-stabilized zirconia. When the average grain size of the t-ZrO_2 phase becomes larger than the admissible one (about 1 μm for ceramics of this type), the retention of the metastable tetragonal zirconia is suppressed [108]. As the microhardness of t-ZrO_2 is higher than m-ZrO_2 [108], the lowering of microhardness occurs during indentation, due to the t–m transition. In our case, the t-ZrO_2 phase is stabilized mainly with CeO_2, in which content in the ceramics is 7 mol%. Such a CeO_2 amount allows the strong stabilization of the tetragonal crystal structure to be achieved. A slight decrease in the m-ZrO_2 phase fraction with an increase in sintering temperature of the ceramics (Fig. 2) is consistent with a slight increase in the microhardness of the ceramics (Fig. 3a).

To construct a graph for studying the changes in fracture toughness of the ceramics with a change in the sintering temperature from 1550 °C through 1580 °C to 1620 °C, the values of the material microhardness obtained under the indentation load in the

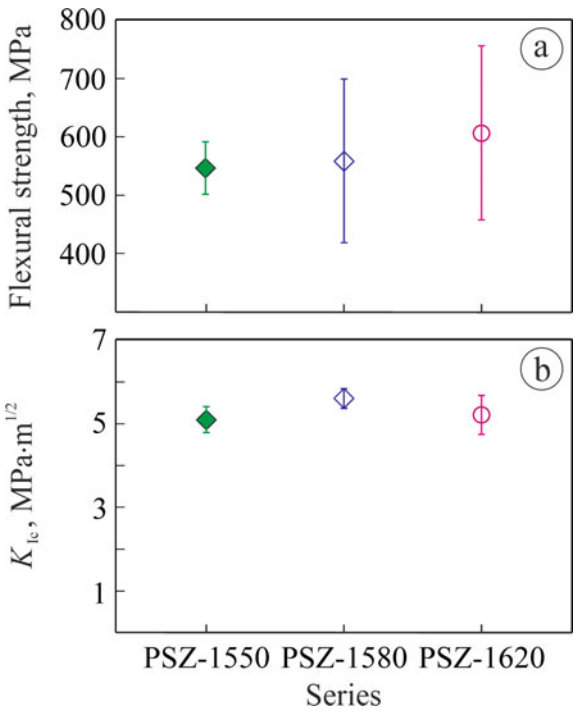

Fig. 4 Changes in mechanical characteristics of the studied ceramics (Table 1): **a** flexural strength; **b** fracture toughness measured by the SENB method under three-point bending

range of 0.25–9.81 N were taken (Fig. 3b). Surprisingly, a slight difference between obtained levels of fracture toughness for the studied materials was found.

In contrast to such a little difference in values of fracture toughness measured by the Vickers method for the studied materials, distinct changes in both the flexural strength and fracture toughness measured by the SENB method under three-point bending while increasing the sintering temperature were found (Fig. 4).

It should be noted that the ceramic sintered at 1550 °C has both the lowest flexural strength and fracture toughness measured by the SENB method (Fig. 4). No significant difference in fracture toughness was found for all the studied ceramics. However, the best result was obtained for the ceramic sintered at 1580 °C (Fig. 4b). It is assumed that in such conditions, the highest bond strength between recrystallized t-ZrO_2 grains is achieved. Although no distinct difference was revealed at low magnifications in the microstructure images (Fig. 5a, c, e) and corresponding images of fracture surfaces (Fig. 5b, d, f), the above assumption is confirmed by the images of microstructure (Fig. 6a, c, e) and fracture surfaces (Fig. 6b, d, f) taken at high magnifications. In particular, slightly increased t-ZrO_2 grains are observed in the ceramic sintered at 1580 °C compared to those in the ceramic sintered at 1550 °C.

Besides, no signs of transgranular fracture of the m-ZrO_2 phase particles were found in the ceramic sintered at 1580 °C (Fig. 6d), whereas in that sintered at 1620 °C a comparatively large number of cleavage facets were revealed (Fig. 6f). This obviously is a reason for the lower fracture toughness of the last material series.

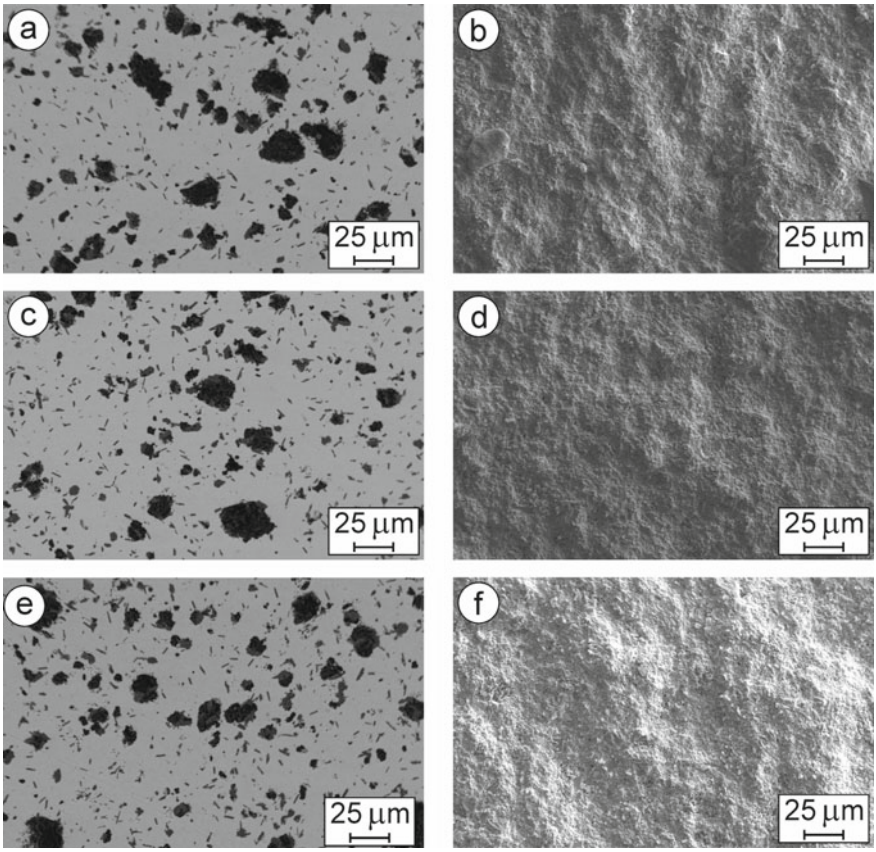

Fig. 5 SEM **a**, **c**, **e** microstructures (BSD images at low magnifications) and **b**, **d**, **f** fractography (SE images at low magnifications) of specimen series **a**, **b** PSZ–1550, **c**, **d** PSZ–1580, and **e**, **f** PSZ–1620 (Table 1)

The weaker areas consisting of freely transformed m-ZrO_2 grains adjoin the coarse particles of the m-ZrO_2 phase in the ceramic sintered at 1620 °C. Such local weakening affects the fracture toughness of the material by lowering it. In contrast, no effect of the local weakening on flexural strength of this ceramic was found. Therefore, coarse particles of the m-ZrO_2 phase contribute dominantly to increasing the strength of a bulk material.

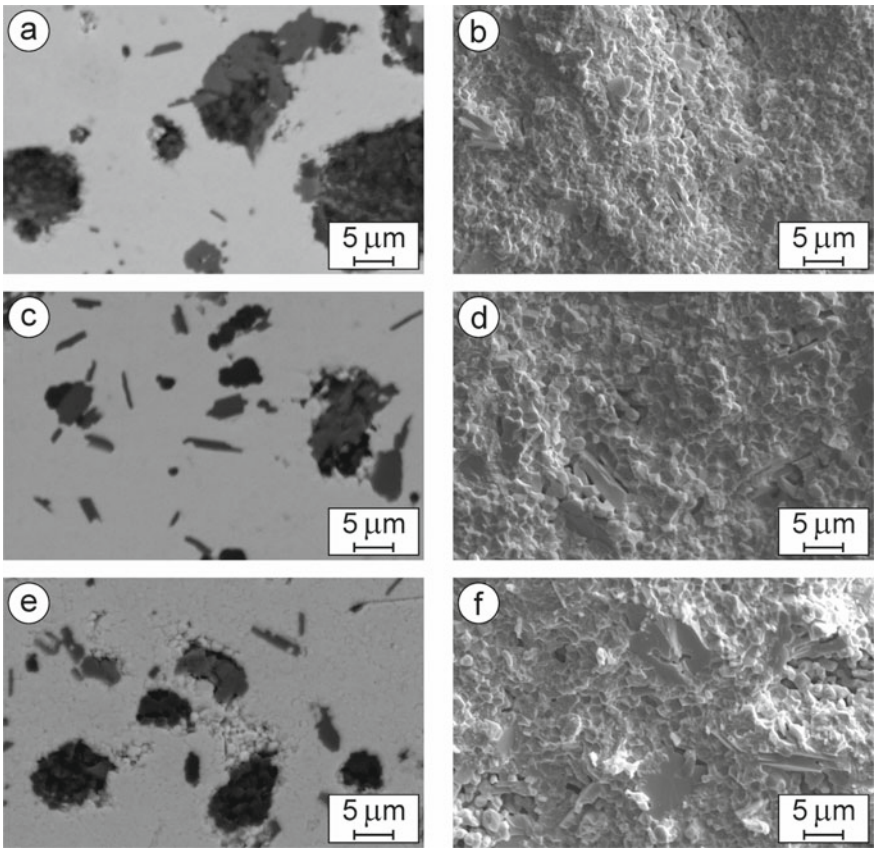

Fig. 6 SEM **a**, **c**, **e** microstructures (BSD images at high magnifications) and **b**, **d**, **f** fractography (SE images at high magnifications) of specimen series **a**, **b** PSZ–1550, **c**, **d** PSZ–1580, and **e**, **f** PSZ–1620 (Table 1)

4 Conclusion

In this work, a stabilizing effect of small percentages of oxides Y_2O_3, CoO, CeO_2, and Fe_2O_3 on zirconia ceramics has been studied.

1. It was shown that the metal oxide additives made it possible to reach the stabilization of the tetragonal ZrO_2 phase and manufacture ceramics with fine-grained microstructure.
2. The maximum transformation toughening effect in ZrO_2–Y_2O_3–CoO–CeO_2–Fe_2O_3 ceramics was found to correlate with features of fracture surface morphology. Compared to the ceramic sintered at 1550 °C, slightly increased grains of the tetragonal ZrO_2 phase were revealed in the ceramic sintered at 1580 °C. The formed microstructure allowed implementing high-energy

consuming fracture micromechanism involving tetragonal to monoclinic ZrO_2 phase transformation toughening without transgranular cleavage fracture of monoclinic ZrO_2 phase particles.

Acknowledgements The authors are thankful to the staff of the Scientific Equipment Collective Use Center "Laboratory of Advanced Technologies, Creation and Physicochemical Analysis of a New Substances and Functional Materials" at Lviv Polytechnic National University (https://lpnu.ua/ckkno) for their kind help in performing X-ray diffraction studies.

References

1. J. Chevalier, S. Deville, E. Munch et al., Critical effect of cubic phase on aging in 3 mol% yttria-stabilized zirconia ceramics for hip replacement prosthesis. Biomaterials **25**, 5539–5545 (2004). https://doi.org/10.1016/j.biomaterials.2004.01.002
2. S. Deville, L. Gremillard, J. Chevalier et al., A critical comparison of methods for the determination of the aging sensitivity in biomedical grade yttria-stabilized zirconia. J. Biomed. Mater. Res. B Appl. Biomater. **72B**, 239–245 (2005). https://doi.org/10.1002/jbm.b.30123
3. Y. Kharchenko, Z. Blikharskyy, V. Vira et al., Nanostructural changes in a Ni/NiO cermet during high-temperature reduction and reoxidation, in *Nanomaterials and Nanocomposites, Nanostructure Surfaces, and Their Applications. Springer Proceedings in Physics*, vol. **246** (2021), pp. 219–229. https://doi.org/10.1007/978-3-030-51905-6_17
4. A.R. Studart, F. Filser, P. Kocher et al., Fatigue of zirconia under cycling loading in water and its implications for the design of dental bridges. Dent. Mater. **23**, 106–114 (2007). https://doi.org/10.1016/j.dental.2005.12.008
5. M. Alfano, G.D. Girolamo, L. Pagnotta et al., Processing, microstructure and mechanical properties of air plasma-sprayed ceria–yttria co-stabilized zirconia coatings. Strain **46**, 409–418 (2010). https://doi.org/10.1111/j.1475-1305.2009.00659.x
6. G.D. Girolamo, C. Blasi, M. Schioppa et al., Structure and thermal properties of heat treated plasma sprayed ceria–yttria co-stabilized zirconia coatings. Ceram. Int. **36**, 961–968 (2010). https://doi.org/10.1016/j.ceramint.2009.10.020
7. B.D. Vasyliv, V.Y. Podhurs'ka, O.P. Ostash et al., Influence of reducing and oxidizing media on the physicomechanical properties of ScCeSZ–NiO and YSZ–NiO ceramics. Mater. Sci. **49**(2), 135–144 (2013). https://doi.org/10.1007/s11003-013-9593-3
8. G. Chen, Q. Li, Y. Ling, H. Zheng, J. Chen, Q. Jiang, K. Li, J. Peng, M. Omran, L. Gao, Phase stability and microstructure morphology of microwave-sintered magnesia-partially stabilised zirconia. Ceram. Int. **47**, 4076–4082 (2021). https://doi.org/10.1016/j.ceramint.2020.09.281
9. G. Chen, Y. Ling, Q. Li et al., Crystal structure and thermomechanical properties of CaO-PSZ ceramics synthesised from fused ZrO_2. Ceram. Int. **46**, 15357–15363 (2020). https://doi.org/10.1016/j.ceramint.2020.03.079
10. J. Chevalier, L. Gremillard, A.V. Virkar et al., The tetragonal-monoclinic transformation in zirconia: lessons learned and future trends. J. Am. Ceram. Soc. **92**, 1901–1920 (2009). https://doi.org/10.1111/j.1551-2916.2009.03278.x
11. A. Kumar, P. Kumar, A.S. Dhaliwal, Structural studies of zirconia and yttria doped zirconia for analysing it phase stabilization criteria. IOP Conf. Ser.: Mater. Sci. Eng. **1033**, 012052 (2021). https://doi.org/10.1088/1757-899X/1033/1/012052
12. A.D. Ivasyshyn, B.D. Vasyliv, Effect of the size and form of specimens on the diagram of growth rates of fatigue cracks. Mater. Sci. **37**(6), 1002–1004 (2001). https://doi.org/10.1023/A:1015669913601

13. T.K. Gupta, J.H. Bechtold, R.C. Kuznicki et al., Stabilization of tetragonal phase in polycrystalline zirconia. J. Mater. Sci. **12**, 2421–2426 (1977). https://doi.org/10.1007/bf00553928
14. H.G. Scott, Phase relationships in the zirconia–yttria system. J. Mater. Sci. **10**, 1527–1535 (1975). https://doi.org/10.1007/BF01031853
15. C. Piconi, S. Sprio, Zirconia implants: is there a future? Curr. Oral Health Rep. **5**, 186–193 (2018). https://doi.org/10.1007/s40496-018-0187-x
16. Y. Kharchenko, Z. Blikharskyy, V. Vira et al., Study of nanostructural changes in a Ni-containing cermet material during reduction and oxidation at 600 °C. Appl. Nanosci. **10**, 4535–4543 (2020). https://doi.org/10.1007/s13204-020-01391-1
17. M.F.R.P. Alves, S. Ribeiro, P.A. Suzuki et al., Effect of Fe_2O_3 addition and sintering temperature on mechanical properties and translucence of zirconia dental ceramics with different Y_2O_3 content. Mater. Res. **24**(2), e20200402 (2021). https://doi.org/10.1590/1980-5373-MR-2020-0402
18. V. Podhurska, B. Vasyliv, O. Ostash et al., Influence of treatment temperature on microstructure and properties of YSZ–NiO anode materials. Nanoscale Res. Lett. **11**, 93 (2016). https://doi.org/10.1186/s11671-016-1306-z
19. H.A. Shabri, M.H.D. Othman, M.A. Mohamed et al., Recent progress in metal-ceramic anode of solid oxide fuel cell for direct hydrocarbon fuel utilization: a review. Fuel Process. Technol. **212**, 106626 (2021). https://doi.org/10.1016/j.fuproc.2020.106626
20. B. Vasyliv, V. Podhurska, O. Ostash, Preconditioning of the YSZ–NiO fuel cell anode in hydrogenous atmospheres containing water vapor. Nanoscale Res. Lett. **12**, 265 (2017). https://doi.org/10.1186/s11671-017-2038-4
21. P. Khajavi, P.V. Hendriksen, J. Chevalier et al., Improving the fracture toughness of stabilized zirconia-based solid oxide cells fuel electrode supports: effects of type and concentration of stabilizer(s). J. Eur. Ceram. Soc. **40**, 5670–5682 (2020). https://doi.org/10.1016/j.jeurceramsoc.2020.05.042
22. T.A. Prikhna, O.P. Ostash, A.S. Kuprin et al., A new MAX phases-based electroconductive coating for high-temperature oxidizing environment. Compos. Struct. **277**, 114649 (2021). https://doi.org/10.1016/j.compstruct.2021.114649
23. S. Jiang, X. Huang, Z. He et al., Phase transformation and lattice parameter changes of non-trivalent rare earth-doped YSZ as a function of temperature. J. Mater. Eng. Perform. **27**, 2263–2270 (2018). https://doi.org/10.1007/s11665-018-3159-3
24. M.Y. Smyrnova-Zamkova, V.P. Red'ko, O.K. Ruban et al., The properties of nanocrystalline powder of 90% Al_2O_3–10% ZrO_2 (wt.%) obtained via the hydrothermal synthesis/mechanical mixing. Nanosistemi. Nanomater. Nanotehnol. **15**(2), 309–317 (2017). https://doi.org/10.15407/nnn.15.02.0309
25. S.S. Savka, D.I. Popovych, A.S. Serednytski, Molecular dynamics simulations of the formation processes of zinc oxide nanoclusters in oxygen environment, in *Nanophysics, Nanomaterials, Interface Studies, and Applications. Springer Proceedings in Physics*, vol 195 (2017), pp. 145–156. https://doi.org/10.1007/978-3-319-56422-7_11
26. T.A. Schaedler, R.M. Leckie, S. Kramer et al., Toughening of nontransformable t'-YSZ by addition of titania. J. Am. Ceram. Soc. **90**, 3896–3901 (2007). https://doi.org/10.1111/j.1551-2916.2007.01990.x
27. M. Zhao, W. Pan, C. Wan et al., Defect engineering in development of low thermal conductivity materials: a review. J. Eur. Ceram. Soc. **37**, 1–13 (2016). https://doi.org/10.1016/j.jeurceramsoc.2016.07.036
28. A.J. Santos, S. Garcia-Segura, S. Dosta et al., A ceramic electrode of ZrO_2–Y_2O_3 for the generation of oxidant species in anodic oxidation. Assessment of the treatment of Acid Blue 29 dye in sulfate and chloride media. Sep. Purif. Technol. **228**, 115747 (2019). https://doi.org/10.1016/j.seppur.2019.115747
29. Y. Yan, Z. Ma, J. Sun et al., Surface microstructure-controlled ZrO_2 for highly sensitive room-temperature NO_2 sensors. Nano. Mater. Sci. **3**, 268–275 (2021). https://doi.org/10.1016/j.nanoms.2021.02.001

30. B. Vasyliv, J. Milewski, V. Podhurska et al., Study of the degradation of a fine-grained YSZ–NiO anode material during reduction in hydrogen and reoxidation in air. Appl. Nanosci. **12**, 965–975 (2022). https://doi.org/10.1007/s13204-021-01768-w
31. A.D. Bona, O.E. Pecho, R. Alessandretti, Zirconia as a dental biomaterial. Materials **8**, 4978–4991 (2015). https://doi.org/10.3390/ma8084978
32. J. Gui, Z. Xie, Phase transformation and slow crack growth study of Y-TZP dental ceramic. Mater. Sci. Eng. A **676**, 531–535 (2016). https://doi.org/10.1016/j.msea.2016.09.026
33. D. Li, Y. Liu, Y. Zhong et al., Dense and strong ZrO_2 ceramics fully densified in <15 min. Adv. Appl. Ceram. **118**, 23–29 (2019). https://doi.org/10.1080/17436753.2018.1449580
34. N. Juntavee, S. Attashu, Effect of different sintering process on flexural strength of translucency monolithic zirconia. J. Clin. Exp. Dent. **10**, e821–e830 (2018). https://doi.org/10.4317/jced.54749
35. J. Zou, Y. Zhong, M. Eriksson et al., Tougher zirconia nanoceramics with less yttria. Adv. Appl. Ceram. **118**, 9–15 (2018). https://doi.org/10.1080/17436753.2018.1445464
36. R. Chintapalli, A. Mestra, F.G. Marro et al., Stability of nanocrystalline spark plasma sintered 3Y-TZP. Materials **3**, 800–814 (2010). https://doi.org/10.3390/ma3020800
37. B. Stawarczyk, M. Özcan, L. Hallmann et al., The effect of zirconia sintering temperature on flexural strength, grain size, and contrast ratio. Clin. Oral Invest. **17**, 269–274 (2013). https://doi.org/10.1007/s00784-012-0692-6
38. M. Amaral, P.F. Cesar, M.A. Bottino et al., Fatigue behavior of Y-TZP ceramic after surface treatments. J. Mech. Behav. Biomed. Mater. **57**, 149–156 (2016). https://doi.org/10.1016/j.jmbbm.2015.11.042
39. M.J. Kim, J.S. Ahn, J.H. Kim et al., Effects of the sintering conditions of dental zirconia ceramics on the grain size and translucency. J. Adv. Prosthodont. **5**, 161–166 (2013). https://doi.org/10.4047/jap.2013.5.2.161
40. M. Guazzato, M. Albakry, S.P. Ringer et al., Strength, fracture toughness and microstructure of a selection of all-ceramic materials. Part II Zirconia-based dental ceramics. Dent. Mater. **20**, 449–456 (2004). https://doi.org/10.1016/j.dental.2003.05.003
41. C. Gautam, J. Joyner, A. Gautam et al., Zirconia based dental ceramics: structure, mechanical properties, biocompatibility and applications. Dalton Trans. **45**, 19194–19215 (2016). https://doi.org/10.1039/c6dt03484e
42. J. Chevalier, What future for zirconia as a biomaterial? Biomaterials **27**, 535–543 (2006). https://doi.org/10.1016/j.biomaterials.2005.07.034
43. C.G. Soubelet, M.P. Albano, Differences in microstructure and mechanical properties between Y-TZP and Al_2O_3-doped Y-TZP/bioglass ceramics. Int. J. Appl. Ceram. Technol. **18**, 2237–2249 (2021). https://doi.org/10.1111/ijac.13864
44. M. Trunec, K. Castkova, P. Roupcova, Effect of phase structure on sintering behavior of zirconia nanopowders. J. Am. Ceram. Soc. **96**, 3720–3727 (2013). https://doi.org/10.1111/jace.12624
45. P. Duràn, M. Villegas, J.F. Fernàndez et al., Theoretically dense and nanostructured ceramics by pressureless sintering of nanosized Y-TZP powders. Mater. Sci. Eng **A232**, 168–176 (1997). https://doi.org/10.1016/S0921-5093(97)00099-3
46. L. Li, O. Van Der Biest, P.L. Wang et al., Estimation of the phase diagram for the ZrO_2–Y_2O_3–CeO_2 system. J. Eur. Ceram. Soc. **21**(16), 2903–2910 (2001). https://doi.org/10.1016/S0955-2219(01)00218-7
47. J.A. Allemann, B. Michel, H.B. Märki et al., Grain growth of differently doped zirconia. J. Eur. Ceram. Soc. **15**(10), 951–958 (1995). https://doi.org/10.1016/0955-2219(95)00073-4
48. N.M. Ersoy, H.M. Aydoğdu, B.U. Değirmenci et al., The effects of sintering temperature and duration on the flexural strength and grain size of zirconia. Acta Biomater. Odontol. Scand. **1**(2–4), 43–50 (2015). https://doi.org/10.3109/23337931.2015.1068126
49. T. Sakuma, Y. Yoshizawa, The grain growth of zirconia during annealing in the cubic/tetragonal two-phase region. Mater. Sci. Forum **94–96**, 865–870 (1992). https://doi.org/10.4028/www.scientific.net/MSF.94-96.865

50. B. Stawarczyk, A. Emslander, M. Roos et al., Zirconia ceramics, their contrast ratio and grain size depending on sintering parameters. Dent. Mater. J. **33**(5), 591–598 (2014). https://doi.org/10.4012/dmj.2014-056
51. M. Vojtko, V. Puchy, E. Múdra et al., Coarse-grain CeO_2 doped ZrO_2 ceramic prepared by spark plasma sintering. J. Eur. Ceram. Soc. **40**, 4844–4852 (2020). https://doi.org/10.1016/j.jeurceramsoc.2020.05.014
52. J. Grabis, D. Jankoviča, I. Šteins et al., Characteristics and sinterability of ceria stabilized zirconia nanoparticles prepared by chemical methods. Mater. Sci. **24**(3), 243–246 (2018). https://doi.org/10.5755/j01.ms.24.3.18288
53. A. Gupta, S. Sharma, N. Mahato et al., Mechanical properties of spark plasma sintered ceria reinforced 8 mol% yttria-stabilized zirconia electrolyte. Nanomater. Energy **1**(NME5), 306–315 (2012). https://doi.org/10.1680/nme.12.00018
54. M. Ahsanzadeh-Vadeqani, R.S. Razavi, Spark plasma sintering of zirconia-doped yttria ceramic and evaluation of the microstructure and optical properties. Ceram. Int. **42**(16), 18931–18936 (2016). https://doi.org/10.1016/j.ceramint.2016.09.043
55. L. An, A. Ito, T. Goto, Transparent yttria produced by spark plasma sintering at moderate temperature and pressure profiles. J. Eur. Ceram. Soc. **32**(5), 1035–1040 (2012). https://doi.org/10.1016/j.jeurceramsoc.2011.11.023
56. S. Kikuchi, K. Katahira, J. Komotori, Formation of titanium/zirconia based biomaterial fabricated by spark plasma sintering. J. Japan Inst. Met. Mater. **82**(9), 341–348 (2018). https://doi.org/10.2320/jinstmet.J2018017
57. Á.G. López, C.L. Pernía, C.M. Ferreiro et al., Spark plasma sintered zirconia ceramic composites with graphene-based nanostructures. Ceramics **1**(1), 153–164 (2018). https://doi.org/10.3390/ceramics1010014
58. E.F. Garcia, C.F.G. Gonzalez, A. Fernandez et al., Processing and spark plasma sintering of zirconia/titanium cermets. Ceram. Int. **39**(6), 6931–6936 (2013). https://doi.org/10.1016/j.ceramint.2013.02.029
59. Y.G. Chabak, V.I. Fedun, K. Shimizu et al., Phase-structural composition of coating obtained by pulsed plasma treatment using eroded cathode of T1 high speed steel. Probl. At Sci. Technol. **104**(4), 100–106 (2016)
60. O.M. Romaniv, I.V. Zalite, V.M. Simin'kovych et al., Effect of the concentration of zirconium dioxide on the fracture resistance of Al_2O_3–ZrO_2 ceramics. Mater. Sci. **31**(5), 588–594 (1996). https://doi.org/10.1007/BF00558793
61. O.M. Romaniv, B.D. Vasyliv, Some features of formation of the structural strength of ceramic materials. Mater. Sci. **34**(2), 149–161 (1998). https://doi.org/10.1007/BF02355530
62. V.V. Kulyk, Z.A. Duriagina, B.D. Vasyliv et al., Effects of yttria content and sintering temperature on the microstructure and tendency to brittle fracture of yttria-stabilized zirconia. Arch. Mater. Sci. Eng. **109**(2), 65–79 (2021). https://doi.org/10.5604/01.3001.0015.2625
63. V. Kulyk, Z. Duriagina, B. Vasyliv et al., The effect of sintering temperature on the phase composition, microstructure, and mechanical properties of yttria-stabilized zirconia. Materials **15**, 2707 (2022). https://doi.org/10.3390/ma15082707
64. Y. Zhang, K. Shimizu, X. Yaer et al., Erosive wear performance of heat treated multi-component cast iron containing Cr, V, Mn and Ni eroded by alumina spheres at elevated temperatures. Wear **390–391**, 135–145 (2017). https://doi.org/10.1016/j.wear.2017.07.017
65. Q.L. Li, Y.Y. Jiang, Y.R. Wei et al., The influence of yttria content on the microstructure, phase stability and mechanical properties of dental zirconia. Ceram. Int. **48**, 5361–5368 (2022). https://doi.org/10.1016/j.ceramint.2021.11.079
66. V. Kulyk, Z. Duriagina, A. Kostryzhev et al., The effect of yttria content on microstructure, strength, and fracture behavior of yttria-stabilized zirconia. Materials **15**, 5212 (2022). https://doi.org/10.3390/ma15155212
67. ASTM E 384-11, Standard test method for Knoop and Vickers hardness of materials (ASTM International, 2011). https://doi.org/10.1520/E0384-11
68. ASTM C 1327-03, Standard test method for Vickers indentation hardness of advanced ceramics (ASTM International, 2003). https://doi.org/10.1520/C1327-03

69. V.I. Zurnadzhy, V.G. Efremenko, I. Petryshynets et al., Mechanical properties of carbide-free lower bainite in complex-alloyed constructional steel: effect of bainitizing treatment parameters. Kov Mater. **58**(2), 129–140 (2020). https://doi.org/10.4149/km_2020_2_129
70. B.R. Lawn, M.V. Swain, Microfracture beneath point indentations in brittle solids. J. Mater. Sci. **10**(1), 113–122 (1975). https://doi.org/10.1007/BF00541038
71. B.R. Lawn, E.R. Fuller, Equilibrium penny-like cracks in indentation fracture. J. Mater. Sci. **10**(12), 2016–2024 (1975). https://doi.org/10.1007/BF00557479
72. A.G. Evans, E.A. Charles, Fracture toughness determinations by indentation. J. Am. Ceram. Soc. **59**(7–8), 371–372 (1976). https://doi.org/10.1111/j.1151-2916.1976.tb10991.x
73. R.F. Cook, G.M. Pharr, Direct observation and analysis of indentation cracking in glasses and ceramics. J. Am. Ceram. Soc. **73**(4), 787–817 (1990). https://doi.org/10.1111/j.1151-2916.1990.tb05119.x
74. B.R. Lawn, in *Fracture of Brittle Solids*, 2nd edn (Cambridge, 1993). https://doi.org/10.1017/CBO9780511623127
75. K. Tanaka, Elastic/plastic indentation hardness and indentation fracture toughness: the inclusion core model. J. Mater. Sci. **22**(4), 1501–1508 (1987). https://doi.org/10.1007/BF01233154
76. K. Niihara, R. Morena, D.P.H. Hasselman, Evaluation of K_{Ic} of brittle solids by the indentation method with low crack-to-indent ratios. J. Mater. Sci. Lett. **1**(1), 13–16 (1982). https://doi.org/10.1007/BF00724706
77. K. Niihara, A fracture mechanics analysis of indentation-induced Palmqvist crack in ceramics. J. Mater. Sci. Lett. **2**(5), 221–223 (1983). https://doi.org/10.1007/BF00725625
78. J.E. Blendell, The origins of internal stresses in polycrystalline alumina and their effects on mechanical properties (Cambridge, 1979). http://hdl.handle.net/1721.1/44234
79. B.R. Lawn, A.G. Evans, D.B. Marshall, Elastic/plastic indentation damage in ceramics: the median/radial crack system. J. Am. Ceram. Soc. **63**(9–10), 574–581 (1980). https://doi.org/10.1111/j.1151-2916.1980.tb10768.x
80. A. Nastic, A. Merati, M. Bielawski et al., Instrumented and Vickers indentation for the characterization of stiffness, hardness and toughness of zirconia toughened Al_2O_3 and SiC armor. J. Mater. Sci. Technol. **31**(8), 773–783 (2015). https://doi.org/10.1016/j.jmst.2015.06.005
81. G.R. Anstis, P. Chantikul, B.R. Lawn et al., A critical evaluation of indentation techniques for measuring fracture toughness: I, Direct crack measurement. J. Am. Ceram. Soc. **64**(9), 533–538 (1981). https://doi.org/10.1111/j.1151-2916.1981.tb10320.x
82. M.Y. Smyrnova-Zamkova, O.K. Ruban, O.I. Bykov et al., The influence of the ZrO_2 solid solution amount on the physicochemical properties of Al_2O_3–ZrO_2–Y_2O_3–CeO_2 powders. Powder Metall. Met. Ceram. **60**(3–4), 129–141 (2021). https://doi.org/10.1007/s11106-021-00222-4
83. J. Lankford, Indentation microfracture in the Palmqvist crack regime: implications for fracture toughness evaluation by the indentation method. J. Mater. Sci. Lett. **1**(11), 493–495 (1982). https://doi.org/10.1007/BF00721938
84. B. Vasyliv, V. Kulyk, Z. Duriagina et al., Estimation of the effect of redox treatment on microstructure and tendency to brittle fracture of anode materials of YSZ-NiO(Ni) system. East Eur. J. Enterp. Technol. **108/6**(12), 67–77 (2020). https://doi.org/10.15587/1729-4061.2020.218291
85. B.D. Vasyliv, V.Y. Podhurska, O.P. Ostash et al., Effect of a hydrogen sulfide-containing atmosphere on the physical and mechanical properties of solid oxide fuel cell materials, in *Nanochemistry, Biotechnology, Nanomaterials, and Their Applications. Springer Proceedings in Physics*, vol. 214 (2018), pp. 475–485. https://doi.org/10.1007/978-3-319-92567-7_30
86. J.M. Gere, S.P. Timoshenko, *Mechanics of Materials*, 4th edn. (PWS Publishing Company, Boston, MA, USA, 1997), p.912
87. ASTM E 399-20a, Standard test method for linear-elastic plane-strain fracture toughness of metallic materials (ASTM International, 2020). https://doi.org/10.1520/E0399-20A
88. ASTM C 1421-18, Standard test methods for determination of fracture toughness of advanced ceramics at ambient temperature (ASTM International, 2018). https://doi.org/10.1520/C1421-18

89. J. Kübier, Fracture toughness of ceramics using the SEVNB method: from a preliminary study to a standard test method, ed. by J. Salem et al., in *Fracture Resistance Testing of Monolithic and Composite Brittle Materials* (ASTM International, 2002), pp. 93–106. https://doi.org/10.1520/STP10473S
90. M. Ettler, G. Blaβ, N.H. Menzler, Characterization of Ni–YSZ-cermets with respect to redox stability. Fuel Cells **7**(5), 349–355 (2007). https://doi.org/10.1002/fuce.200700007
91. B.D. Vasyliv, Initiation of a crack from the edge of a notch with oblique front in specimens of brittle materials. Mater. Sci. **38**(5), 724–728 (2002). https://doi.org/10.1023/A:1024222709514
92. M. Radovic, E. Lara-Curzio, Mechanical properties of tape cast nickel-based anode materials for solid oxide fuel cells before and after reduction in hydrogen. Acta Mater. **52**(20), 5747–5756 (2004). https://doi.org/10.1016/j.actamat.2004.08.023
93. V.V. Kulyk, B.D. Vasyliv, Z.A. Duriagina et al., The effect of water vapor containing hydrogenous atmospheres on the microstructure and tendency to brittle fracture of anode materials of YSZ–NiO(Ni) system. Arch. Mater. Sci. Eng. **108**(2), 49–67 (2021). https://doi.org/10.5604/01.3001.0015.0254
94. T.B. Serbenyuk, T.O. Prikhna, V.B. Sverdun et al., Effect of the additive of Y_2O_3 on the structure formation and properties of composite materials based on AlN–SiC. J. Superhard. Mater. **40**(1), 8–15 (2018). https://doi.org/10.3103/S1063457618010021
95. M.Y. Smyrnova-Zamkova, O.K. Ruban, O.I. Bykov, et al., Physico-chemical properties of fine-grained powder in Al_2O_3–ZrO_2–Y_2O_3–CeO_2 system produced by combined method. Comp. Theory Pract. **18**(4), 234–240 (2018). https://kompozyty.ptmk.net/pliczki/pliki/1290_2018t04_maria-y-smyrnova-zamkova-.pdf
96. M. Andrzejczuk, O. Vasylyev, I. Brodnikovskyi et al., Microstructural changes in NiO–ScSZ composite following reduction processes in pure and diluted hydrogen. Mater. Charact. **87**, 159–165 (2014). https://doi.org/10.1016/j.matchar.2013.11.011
97. Y. Wang, M.E. Walter, K. Sabolsky et al., Effects of powder sizes and reduction parameters on the strength of Ni–YSZ anodes. Solid State Ionics **177**, 1517–1527 (2006). https://doi.org/10.1016/j.ssi.2006.07.010
98. J.W. Adams, R. Ruh, K.S. Mazdiyasni, Young's modulus, flexural strength, and fracture of yttria-stabilized zirconia versus temperature. J. Am. Ceram. Soc. **80**(4), 903–908 (1997). https://doi.org/10.1111/j.1151-2916.1997.tb02920.x
99. O.P. Ostash, B.D. Vasyliv, V.Y. Podhurs'ka, et al., Optimization of the properties of 10Sc1CeSZ-NiO composite by the redox treatment. Mater. Sci. **46**(5):653–658 (2011).https://doi.org/10.1007/s11003-011-9337-1
100. B.D. Vasyliv, Improvement of the electric conductivity of the material of anode in a fuel cell by the cyclic redox thermal treatment. Mater. Sci. **46**(2), 260–264 (2010). https://doi.org/10.1007/s11003-010-9282-4
101. I. Danilenko, G. Lasko, I. Brykhanova et al., The peculiarities of structure formation and properties of zirconia-based nanocomposites with addition of Al_2O_3 and NiO. Nanoscale Res. Lett. **12**, 125 (2017). https://doi.org/10.1186/s11671-017-1901-7
102. V.Y. Podhurs'ka, B.D. Vasyliv, O.P. Ostash et al., Structural transformations in the NiO-containing anode of ceramic fuel cells in the course of its reduction and oxidation. Mater. Sci. **49**(6), 805–811 (2014). https://doi.org/10.1007/s11003-014-9677-8
103. I. Danilenko, F. Glazunov, T. Konstantinova et al., Effect of Ni/NiO particles on structure and crack propagation in zirconia based composites. Adv. Mater. Lett. **5**(8), 465–471 (2014). https://doi.org/10.5185/amlett.2014.amwc1040II
104. G.A. Gogotsi, S.N. Dub, E.E. Lomonova et al., Vickers and Knoop indentation behaviour of cubic and partially stabilized zirconia crystals. J. Eur. Ceram. Soc. **15**(5), 405–413 (1995). https://doi.org/10.1016/0955-2219(95)91431-M
105. B.D. Vasyliv, A procedure for the investigation of mechanical and physical properties of ceramics under the conditions of biaxial bending of a disk specimen according to the ring–ring scheme. Mater. Sci. **45**(4), 571–575 (2009). https://doi.org/10.1007/s11003-010-9215-2

106. O.N. Grigoriev, V.B. Vinokurov, T.V. Mosina et al., Kinetics of shrinkage, structurization, and the mechanical characteristics of zirconium boride sintered in the presence of activating additives. Powder Metall. Met. Ceram. **55**(11–12), 676–688 (2017). https://doi.org/10.1007/s11106-017-9855-y
107. Z. Peng, J. Gong, H. Miao, On the description of indentation size effect in hardness testing for ceramics: analysis of the nanoindentation data. J. Eur. Ceram. Soc. **24**, 2193–2201 (2004). https://doi.org/10.1016/s0955-2219(03)00641-1
108. V.V. Rodaev, A.O. Zhigachev, A.I. Tyurin et al., An engineering zirconia ceramic made of baddeleyite. Materials **14**, 4676 (2021). https://doi.org/10.3390/ma14164676

Electrical Conductivity Features of Metal–Carbon Nanocomposites

H. Yu. Mykhailova, M. M. Yakymchuk, E. G. Len, I. Ye. Galstian, M. Ya. Shevchenko, and E. A. Tsapko

Abstract Carbon nanostructures have a unique anisotropic structure that determines their electronic properties. The electrical conductivity of individual particles of carbon nanostructures and the conductivity of a composite or material containing such structures differ. For mass application of the thermoemission type of direct energy conversion in alternative sources, it is necessary, with maintaining the parameters of electron emission from the cathodes of the thermoemission converter, to significantly reduce its operating temperature, which can be achieved by reducing the output. The formation of metal- and carbon-containing composites opens the prospect of combining the advantages of both these types of materials, as well as the emergence of new characteristics in the created composites, which are not inherent in the original systems. Such features open up prospects for the creation of "cold" cathodes for thermophoto-emission energy converters based on composites of metal–carbon nanostructures. The electromechanical properties of metal–carbon nanostructures were studied. There is an increase in the maximum value of electrical conductivity up to 2 times compared to the original components, due to increasing contact area between the constituent particles of the composite, which increases the electrical conductivity due to increased free electrons in the carbon component during their transition from metal particles and deformation reduction.

H. Yu. Mykhailova (✉) · M. M. Yakymchuk · E. G. Len · I. Ye. Galstian · M. Ya. Shevchenko · E. A. Tsapko
G. V. Kurdyumov Institute for Metal Physics of the N.A.S. of Ukraine, 36 Academician Vernadsky Boulevard, Kyiv UA-03142, Ukraine
e-mail: mihajlova.halina@gmail.com

E. G. Len
Kyiv Academic University, N.A.S. and M.E.S. of Ukraine, Kyiv, Ukraine

I. Ye. Galstian
Institute for Solid State Research, Leibniz IFW Dresde, Dresden, Germany

O. Fesenko and L. Yatsenko (eds.), *Nanoelectronics, Nanooptics, Nanochemistry and Nanobiotechnology, and Their Applications*, Springer Proceedings in Physics 297,
https://doi.org/10.1007/978-3-031-42708-4_18

1 Introduction

The search for new materials and the study of their properties have always been and will be a priority direction in the development of science. Often, only new material makes it possible to solve questions that are considered unsolvable before its discovery. Targeted acquisition of new materials is a difficult task, new materials are often discovered by accident, and in this case, the first place is the study of their properties and the determination of possible areas of their application [1, 2]. An example of such materials is carbon nanotubes (CNTs), which were described in detail by Ijima in 1991 [3]. For more than 30 years, interest in studying their properties has not abated, which is due to their unusual electromechanical properties.

Materials with higher strength, modulus of elasticity, and electrical conductivity are needed by the aviation and space industries, energy, transport, medicine, machine and instrument construction, and other fields of science and technology. Nanostructured composite materials satisfy all these needs.

Composite materials are characterized by adjustable anisotropy and a gradient structure of properties, which is possible due to the directional orientation of fibers in the matrix, which is possible only when using powder technologies. Most of the published works [4–17] are devoted to composites with a polymer matrix, and there are significantly fewer works with a metal matrix. The main factors affecting the properties of metal-matrix composites reinforced with CNTs are: disparity in the properties of CNTs; difficulty of splitting agglomerates and uniform distribution of CNTs in the metal; the problem of compacting a mixture of metal powder and CNT; a wide variation in the ratio of the length to the diameter of the CNT (form factor); the possibility of chemical reactions between carbon and metal leading to the formation of carbides [18]. Sintering, high-temperature (one-sided) or isostatic (all-round) pressing, extrusion, and high-temperature rolling are used to compact metal–CNT composites. [19]. However, all these processes take place at high temperatures, so low-temperature methods of compacting nanocomposites, for example, intensive plastic deformation, are preferred [19]. Copper composites with CNTs obtained in this way [20, 21] have significant differences in microstructure and microhardness from pure copper without CNTs.

The influence of the size of metal particles on the electrical conductivity of the metal–CNT nanosystem

Nanosystems consisting of $LaNi_5$ metal particles were used to study the conductive properties; Cu with different concentrations of CNTs.

$LaNi_5$ microparticles were obtained by electric discharge in toluene. The metal–CNT nanosystem was obtained by mechanical mixing of the initial components in a certain proportion in an agate stage for 2 h. $LaNi_5$ microparticles with a diameter of 40 ± 10 μm and CNTs were used. The work function of microparticles of $LaNi_5$ is $\varphi = 3.6$ eV, CNT $- \varphi = 4.7$ eV.

Electron microscopic images of multilayer carbon nanotubes are presented in Fig. 1. Al_2O_3–Fe_2O_3–MoO_3 catalyst particles are observed at the ends of CNTs.

Statistical processing of images showed that the average diameter of CNTs is 10 ± 2 nm.

Figure 2 shows the dependence of the electrical conductivity (σ) $LaNi_5$ on their density during the forward and reverse strokes of the piston. When the volume in the cylinder under the piston changes, the minimum initial value of electrical conductivity was recorded at densities $\rho_0 = 2.72$ g/cm^3.

When the piston is slightly lowered (Fig. 2), $\sigma(\rho)$ jumps by six orders of magnitude due to rearrangement, compaction, and an increase in the total contact area between adjacent particles of the sample under study. Upon further compression of the powder samples, $\sigma(\rho)$ continues to increase smoothly for $LaNi_5$ and $LaNi_5$ nanocomposites with CNTs, while it remains practically unchanged for pure CNTs.

The process of unloading occurs during the return stroke of the piston. The growth of the volume of the sample and elastic relaxation is observed, which is minimal for $LaNi_5$ microparticles and maximal for the array of CNTs. A sharp drop in electrical

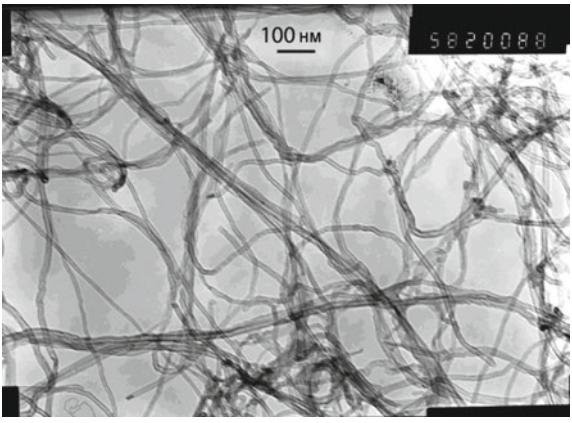

Fig. 1 Electron microscopic pictures of BVNT

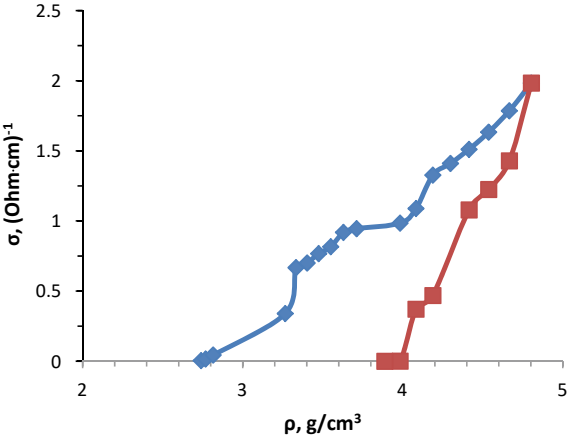

Fig. 2 Dependence of electrical conductivity σ on density ρ for $LaNi_5$ microparticles, average size $d = 40$ μm. ■—loading, ○—unloading

conductivity is caused by the completion of the elastic relaxation process, a decrease in the total contact area between nanotubes, $LaNi_5$ particles with CNTs and electrodes, and a finish with the opening of the electrical circuit. This process occurs at $\rho = 4.60$ g/cm^3.

Table 1 presents the values of electrical conductivity for all tested samples. It can be seen from the table that the electrical conductivity of the initial components of the compacted $LaNi_5$ particles is $\sigma = 1.98\ (\Omega{\cdot}\text{cm})^{-1}$ and that of the compacted CNT array is $\sigma = 0.78\ (\Omega{\cdot}\text{cm})^{-1}$. With an increase in the concentration of CNTs, the electrical conductivity increases, and at 20 wt% is $\sigma = 13.18\ (\Omega{\cdot}\text{cm})^{-1}$, which is an order of magnitude greater than the value of σ of the original components, respectively. The subsequent increase in CNT concentration contributes to a decrease in electrical conductivity. The increase in electrical conductivity upon contact between metal particles and CNTs is due to the transfer of electrons from the metal component to the carbon component.

During the contact of $LaNi_5$ metal with CNTs ($\varphi_{LaNi5} < \varphi_{CNTs}$), electrons will pass from the metal to CNTs and increase their concentration in the latter. According to Novoselov et al. [22], mobility decreases by $\mu \sim 1/n^{1/2}$ as the concentration of charge carriers increases. Therefore, the current density (electrical conductivity) will increase $\sim n^{1/2}$. An increase in the concentration of current carriers in CNTs due to charge transfer from the metal should lead to an increase in electrical conductivity. An increase in electrical conductivity by an order of magnitude during the establishment of electrical contacts between CNTs and metal is observed only at a certain concentration of CNTs.

Charge transfer means that CNTs have an excess charge, while metal particles lack them. As a result, CNTs and metallic $LaNi_5$ particles should have Coulombic attraction. Indeed, during compression, the most effective compounding of the $LaNi_5$ mechanical mixture with CNTs occurred at a concentration of CNTs of 20 wt%. It is obvious that at these concentrations, the mechanism of electron transfer from the metal to the CNT works most effectively.

A further increase in the concentration of CNTs changes the situation: The electrical conductivity of the mechanical mixture drops by 2–3 times, which is associated with a decrease in the average concentration of electrons in CNTs due to the presence of a denser layer of CNTs around the $LaNi_5$ metal particles, which contributes to

Table 1 Electrical conductivity of nanocomposites $LaNi_5 \pm c$ wt% CNT

	$LaNi_5 + c$ wt% CNT								
	0	1.6	4.3	8.3	15.7	20	24	30	100
σ_{max}, $(\Omega\ \text{cm})^{-1}$	1.98	1.76	2.34	3.8	10.4	13.18	8.7	1.77	0.78
$\sigma_{\rho max}$, $(\Omega\ \text{cm})^{-1}$	1.51	1.8	2.34	3.3	10.4	13.18	8.7	1.71	0.55
ρ_0, g/cm^3	2.73	1	0.78	0.75	0.76	0.8	0.75	0.51	0.12

σ_{max}—the maximum value of electrical conductivity;
$\sigma_{\rho max}$—the value of electrical conductivity at the maximum possible compression;
ρ_0—the density at which electrical conductivity is fixed (transition to the conductive state).

a decrease in electrical conductivity. The density of the transition to the conductive state when adding 2 wt% CNT to powdered $LaNi_5$ decreases by 2–3 times (Table 1). Strongly anisotropic nanotubes, along the axis of which the current mainly flows, connect the particles and thus reduce the density of the transition to the conducting state, while σ does not change significantly. At higher concentrations of CNTs, the transition to the conductive state decreases, due to some destruction of order, an increase in elasticity, and a significant decrease in electrical conductivity.

The thermo-EMF coefficient for the tested samples is 1.8 μV/K for the $LaNi_5$ array, adding 1.6 wt% CNT which leads to an increase in the coefficient to 27 μV/K. Anisotropic nanotubes connect $LaNi_5$ particles, provide electrical contact, and reduce the transition to the conductive state by 2.7 times. The concentration of nanotubes up to 5 wt% does not significantly affect the electrical conductivity but determines the thermoelectric characteristics of the nanocomposite.

For all samples of the $LaNi_5$-CNT system, at all values of ρ, the α sign is positive (the heated end of the samples is negatively charged, and the cold end is positively charged), which indicates hole conductivity [23]. A rapid decrease in the value of α during deformation is associated with an increase in the proportion of CNTs that have entered into electrical contact with $LaNi_5$ metal particles, which leads to an increase in the concentration of electrons in the nanotubes. They cause a decrease in the α coefficient at low concentrations (< 5 wt%) of nanotubes. The increase in the concentration of conduction electrons is also confirmed by the fact that the values of the coefficient α (27–31 μV/K) at the minimum density for all samples of the nanocomposite remain below the values of α (37–39 μV/K) for the array of nanotubes.

With an increase in the concentration of CNTs in the nanocomposite, the decreases in the coefficient α decrease due to an increase in the proportion of CNTs that are not in contact with $LaNi_5$ particles.

2 Conclusion

1. When metal particles with lower work output than nanotubes are added to CNTs, the radial electrical conductivity increases by more than an order of magnitude as a result of the transition of electrons from the metal to CNTs, the mobility of which is greater than in metals, which leads to the Coulomb interaction between different components and arrangement of the system.
2. At the concentration of 20 wt% of CNT, electrical conductivity is increased by an order of magnitude compared to the original components. It is due to the ordering of the nanosystem when the Coulomb attraction between metal particles and CNTs is established, which leads to their sticking and compaction and is explained by the maximum increase in the concentration of conduction electrons in nanotubes when they are transferred from the metal, which occurs at certain concentrations of CNTs.

References

1. V.V. Pogosov, Elementi fiziki poverhni, nanostruktur i tehnologij (Zaporizh.: ZNTU, 2010), 365 s. (in Ukrainian)
2. V.S.V. Nanohimiya, Nanosistemi. Nanomateriali (K.: Nauk. Dumka, 2008), 423 s. (in Ukrainian)
3. S. Iijima, Helical microtubules of graphitic carbon. Nature **354**, 56–58 (1991)
4. S.A. Curran, J. Talla, S. Dias, D. Zhang, D. Carroll, J. Appl. Phys. **105**, 073711–073718 (2009)
5. J.K.W. Sandler, J.E. Kirk, I.A. Kinloch, M.S.P. Shaffer, A.H. Windle, Polymer **44**, 5893–5899 (2003)
6. M.B. Bryning, M.F. Islam, J.M. Kikkawa, A.G. Yodh, Adv. Mater. **17**, 1186–1191 (2005)
7. E. Kymakis, I. Alexandou, G.A. Amaratunga, Synth. Met. **127**, 59–62 (2002)
8. M.B. Bryning, D.E. Milkie, M.F. Islam, J.M. Kikkawa, A.G. Yodh, Appl. Phys. Lett. **87**, 161909–161909-3 (2005)
9. V. Khanna, V. Kumar, S.A. Bansal, Mater. Res. Bull. **138**, 111224 (2021)
10. M. Foygel, R.D. Morris, D. Anez, S. French, V.L. Sobolev, Phys. Rev. B. V. **71**, 104201-8 (2005)
11. I. Balberg, Phys. Rev. Lett. **59**(12), 1305–1308 (1987)
12. C. Li, E.T. Thostenson, T.-W. Chou, Appl. Phys. Lett. **91**, 22314–22323 (2007)
13. J.G. Simmons, J. Appl. Phys. **34**(6), 1793–1803 (1963)
14. Q. Li, C.A. Rottmair, R.F. Singer, Compos. Sci. Technol. **70**, 2242–2247 (2010)
15. X. Zhang, W. Li, J. Ma, Y. Li, Y. Deng, M. Yang, Y. Zhou, X. Zhang, P. Dong, Compos. Struct. **244**, 112246 (2020)
16. A.V. Eleckij, B.M. Smirnov, Uspehi Fizicheskih Nauk. **163**(2), 33–60 (1993)
17. J. Keith Nelson (Springer Science & Business Media, 2009), 368 p
18. Polipropilen/Pod red. V. Pilipskogo, I. Yarceva (M.: Himiya, 1967), 16 s. (in Russian)
19. S.R. Bakshi, D. Lahiri, A. Agarwal, Carbon nanotubes reinforced metal matrix composites (CRC Press, Boca Raton, 2011), 295 p
20. A. Bachmaier, R. Pippan, Int. Mater. Rev. **53**(1), 41–62 (2013)
21. R.H. Hisamov, K.S. Nazarov, L.R. Zubairov, A.A. Nazarov, R.R. Mulyukov i dr, Fizika tverdogo tela. T. **57**(1), 37–42 (2015)
22. K.S. Novoselov, A.K. Geim, S.V. Morozov, D. Jiang, M.I. Katsnelson, I.V. Grigorieva, S.V. Dubonos, A.A. Firsov, Nat. Lett. **438**(10), 197–200 (2005)
23. I.V. Savelev, Kurs obshej fiziki, tom 3. (M.: Nauka, 1979), 213 p. (in Russian)

The Model of Giant Magnetoresistance, Built Taking into Account the Bulk Scattering of Spins in CPP Geometry

Ruslan Politanskyi, Maria Vistak, and Yurii Rudyak

Abstract The properties of the spin-valve structure, based on two ferromagnetic layers divided by a layer of non-magnetic metal, in the geometry of the current perpendicular to the plane are modeled. In addition to well-known classical two-channel conductivity model proposed by Nevill Mott, the developed model takes into account spin scattering on the surface between structures. The developed model uses equivalent electrical circuits to simulate a spin valve with parallel and antiparallel alignment. On the basis of this model, the dependences of the giant magnetic resistance on two geometric parameters of the structure—the ratio between the thickness of the free and the thickness of the fixed layers, and their ratio to the length of spin diffusion—are derived. Based on the developed model, numerical data are obtained for the spin valve, where the ferromagnetic layers are made of cobalt, permalloy, iron, and nickel. The portion of surface scattering in the giant magnetic resistance is also investigated. A general conclusion is made about the slight increase of the giant magnetic resistance due to the influence of surface scattering for structures based on cobalt, permalloy, and iron, but not for nickel. This outlines the scope of applicability of the developed model.

R. Politanskyi (✉)
Yuriy Fedkovych Chernivtsi National University, Chernivtsi Kotsyubynsky 2, Chernivtsi 58012, Ukraine
e-mail: r.politansky@chnu.edu.ua

M. Vistak
Danylo Halytsky Lviv National Medical University, Pekarska Street 69, Lviv 79010, Ukraine
e-mail: vistak_maria@ukr.net

Y. Rudyak
I. Horbachevsky Ternopil National Medical University, Voli Maidan 1, Ternopil 46001, Ukraine

O. Fesenko and L. Yatsenko (eds.), *Nanoelectronics, Nanooptics, Nanochemistry and Nanobiotechnology, and Their Applications*, Springer Proceedings in Physics 297,
https://doi.org/10.1007/978-3-031-42708-4_19

1 Methods of Modeling Giant Magnetic Resistance

Everspin Technologies has announced a new series of MRAM devices that have the world's highest performance in the non-regenerative memory market. According to the information given in [1], the bandwidth used by the reading and writing processes is about 400 Megabytes per second. At the same time, the recording density is from 8 to 64 Mbit. Such devices are potentially suitable for their use in IoT and embedded systems technologies.

According to IBM [2], MRAM devices are capable of displacing devices that are manufactured using SRAM technology at the last level of CPU cache memory. Another adventure of MRAM memory is high speed at the level achieving of a few nanoseconds for switching time, while switching current is about 0.5 mA and the task of finding the optimal switching speed value is another important aspect for the use of MRAM devices in the last level of cache memory. In 2016, IBM researchers together with Samsung [3] demonstrated MRAM switches for devices with a diameter of 11 nm, with a switching time of 10 ns, and a current of only 7.5 microamps. Such devices use perpendicular magnetic anisotropy, the bit error value is 10^{-10}, and the pulse duration is 10 ns.

To date, spintronic devices manufactured for magnetic memory and information processing mainly have a principle of operation based on the bistability of ordered spin states in ferromagnetic. Nevertheless, the use of ferromagnetic has limitations on the creation of high-density memory and the ability to retain recorded values, which is due to the field of random disturbances generated by the magnetic field of neighboring cells. These problems can be solved by using antiferromagnetic materials instead of ferromagnetic. In addition, it is very important that the switching speed of devices designed on antiferromagnetic materials is much higher than the speed of using ferromagnetic materials [4]. The use of antiferromagnetic materials requires the provision of manipulated and stable antiferromagnetic bistable states at ambient temperature, which is a rather rare phenomenon and is rarely covered in the literature.

Among the many technologies that have replaced CMOS technology, spintronic devices have attracted attention due to their potential advantages: overcoming the limitations associated with the power consumption and performance of microcircuits [5]. From the point of view of improving the computing process, spintronic devices have such potentially important advantages as much less value of power consumption than in semiconductors, short time of switching to the working state. Other important features of the devices are that they could surpass the capabilities of existing Boolean algebra techniques while enabling an entirely new class of computing architectures: processor memory, memory-coupled logic, and analog-neuromorphic computing [6, 7].

The process of reading information in modern spintronic devices is based on the phenomenon of giant magnetic resistance. The phenomenon of giant magnetic resistance arises is due to the significant dependence of the specific resistance on the mutual orientation of the directions of the electron spins that form the electric current and the magnetization of the sample. An electron, as is known, can have two

antiparallel directions of spin, oriented along and opposite to the direction of the external magnetic field. This dependence caused the asymmetry of the scattering of electrons with two different states in the volume and on the surfaces, which separate non-magnetic and a ferromagnetic material, and which the electron crosses.

These phenomena are also manifested differently in two typical experiments that allow detecting the phenomenon of giant magnetic resistance: perpendicular and parallel current flow relative to the plane of the studied samples.

Historically, equivalent electrical circuits modeled the phenomenon of giant magnetoresistance. However, such interpretation of this phenomenon is effective only when the current flows perpendicular to the plane of the sample. The two-current models of giant magnetic resistance and equivalent electrical circuits turned out to be contradictory, when the current flows parallel to the planes of a layers, according to modern investigations, and require consideration of a non-local conduction model [8].

Another common approach is to use equations to determine the electrochemical potential of electrons and the distribution of currents in the volume, as in the common model by Valet and Fert [8]. Methods for modeling electron point scattering are also being developed, like a model of free electrons with random point scatterers (FERPS) [9], which obviously require significant computing power. Especially for the problem of electron scattering on surfaces, that may have a significant number of defects, layers with mixing materials, and these features are significantly dependent on their manufacturing technologies is being solved. Therefore, the constants given in literary sources, which depend on scattering on the surface (asymmetry coefficient and specific characteristic resistance of the surface), are quite inconsistent.

Hence, the task of determining the influence of the surface on the effect of giant magnetoresistance is still relevant, and the construction of simple semi-empirical models can provide answers to important questions related to question.

It is obvious that for analysis, the method based on equivalent electrical circuits helps to understand many regularities that are important for practical applications, such as the ratio between sample thicknesses and the selection of materials for ferromagnetic and non-magnetic layers [10].

2 Methods of Researches (Equivalent Electrical Circuits of the Spin-Valve Structure)

The phenomenon of giant magnetic resistance is actively researched and used in information storage devices to implement reading and writing processes. The basic element of these devices is a spin valve, schematically shown in Fig. 1.

The main elements of the device shown in Fig. 1 are ferromagnetic layers with different thicknesses, separated by layer made of non-magnetic material. One of them has a greater coercive force, and its magnetization remains constant during the operation of the device; it is called the fixed layer. The other layer, which has

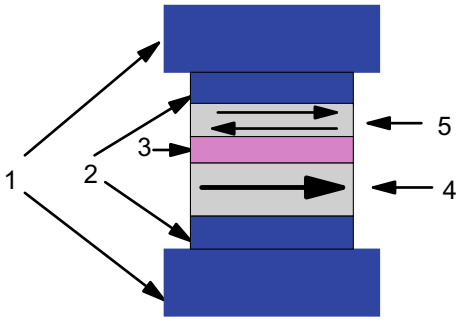

Fig. 1 Spin-valve structure. 1, 2—contacts with non-magnetic material of current conductors to the structure; 3—a layer of non-magnetic material separating the ferromagnetic layers; 5—a free layer; and 4—a fixed layer

a smaller coercive force, can easily change its magnetization; and it is called as the free layer.

Mott suggested using equivalent electrical circuits for the structure depicted in Fig. 1, which correctly reflect the asymmetry of the volume scattering of electrons in the "spin-up" and "spin-down" states. Two schemes represent the two states of the structure: with parallel and antiparallel directions of magnetization of the free and fixed layers, and which are shown in Fig. 2a, b respectively.

According to this model, the value of giant magnetic resistance without taking into account scattering on the surface GMR_{b0} can be determined [11] by the following formula:

$$\mathrm{GMR}_{b0} = \frac{d/D}{(1+d/D)^2} \cdot \frac{\left(1-\rho_{\downarrow}/\rho_{\uparrow}\right)^2}{\rho_{\downarrow}/\rho_{\uparrow}} \tag{1}$$

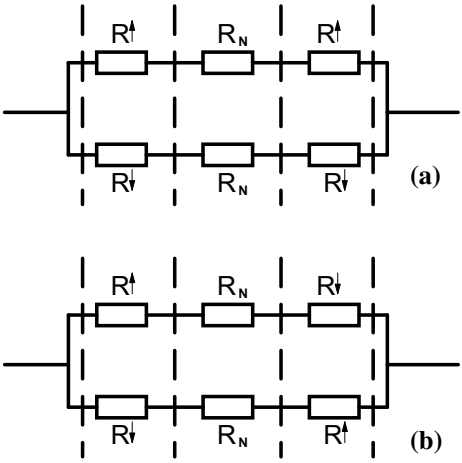

Fig. 2 Equivalent electric circuits of the spin valve in the classic model by Nevill Mott for parallel **a** and antiparallel **b** alignment of ferromagnetic layers

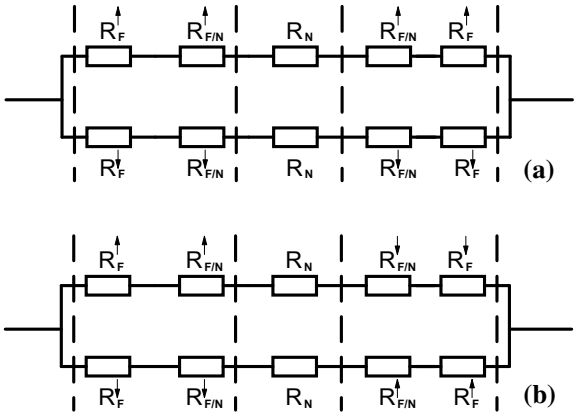

Fig. 3 Equivalent electric circuits of the spin valve, taking into account the asymmetry of scattering on the surfaces separating of ferromagnetic and non-magnetic metal for parallel **a** and antiparallel **b** direction of magnetization of ferromagnetic layers

where d/D is the ratio of the thickness of free and fixed layers; $\rho_{\downarrow}/\rho_{\uparrow}$ is the ratio of specific resistances of "spin-up" and "spin-down" conduction channels in ferromagnetic layers.

Formula (1) does not take into account the resistance of non-magnetic metal, which usually does not have a significant effect on the results obtained within the framework of this model. For example, the resistivity of copper is about 50 times greater than of cobalt for up-spin electrons and 200 for down-spin electrons.

Consider a model of a spin-valve structure, which, unlike the known one, takes into account the asymmetry of scattering on the surfaces separating the ferromagnetic material and the non-magnetic material. The electrical circuits for it are shown in Fig. 3a, b.

These circuits has two parallel branches. Each branch simulates the path of electrons with the same spin value: The upper branch models the path of electrons with spin-up, and the lower branch with the spin-down. For antiparallel alignment, the direction of the spin channels relative to the magnetization of the ferromagnetic changes to the opposite, and this can be seen from the electrical circuit in Fig. 3.

The value of the resistances, which contribute to scattering effects on the surfaces separating the ferromagnetic and non-magnetic metal, is defined as some resistivity acting in a thin near-surface layer. Consequently, two more constants appear, which determine the scattering processes on surfaces that have the dimension $Om \cdot m^2$ and are denoted as $\mathrm{AR}^{\uparrow}$ and $\mathrm{AR}^{\downarrow}$ for the scattering of electrons in the "spin-up" and "spin-down" states.

Then the resistances shown in Fig. 3 for the structure with the area of ferromagnetic layers and the non-magnetic layer separated by S can be determined as follows:

$$\begin{cases} R_F^{\uparrow} = \frac{d}{S} \cdot \rho^{\uparrow},\ R_{F/N,\gamma}^{\uparrow} = R_{N/F,\gamma}^{\uparrow} = \mathrm{AR}^{\uparrow}/S,\ R_N = \rho_0 \cdot d_0 \\ R_F^{\downarrow} = \frac{d}{S} \cdot \rho^{\downarrow},\ R_{F/N,\gamma}^{\downarrow} = R_{N/F,\gamma}^{\downarrow} = \mathrm{AR}^{\downarrow}/S \end{cases} \tag{2}$$

If, as in the previous model, the resistance of the non-magnetic layer is neglected, then the expressions for the resistances of the structure in states with parallel and antiparallel directions of magnetization R^{P} and R^{AP} and for the value of the giant magnetic resistance GMR have the following form:

$$R^{\mathrm{P}} = \frac{\left[(d+D)\cdot\rho^{\uparrow} + 2\cdot AR^{\uparrow}\right]\cdot\left[(d+D)\cdot\rho^{\downarrow} + 2\cdot AR^{\downarrow}\right]}{(d+D)\cdot\left(\rho^{\uparrow}+\rho^{\downarrow}\right) + 2\cdot\left(AR^{\uparrow}+AR^{\downarrow}\right)} \tag{3}$$

$$R^{\mathrm{AP}} = \frac{\left[d\cdot\rho^{\uparrow} + \left(AR^{\uparrow}+AR^{\downarrow}\right) + D\cdot\rho^{\downarrow}\right]\cdot\left[d\cdot\rho^{\downarrow} + \left(AR^{\uparrow}+AR^{\downarrow}\right) + D\cdot\rho^{\uparrow}\right]}{(d+D)\cdot\left(\rho^{\uparrow}+\rho^{\downarrow}\right) + 2\cdot\left(AR^{\uparrow}+AR^{\downarrow}\right)} \tag{4}$$

$$\begin{aligned}\mathrm{GMR} &= R^{\mathrm{AP}}/R^{\mathrm{P}} - 1 \\ &= \frac{\left[d\cdot\rho^{\uparrow} + \left(AR^{\uparrow}+AR^{\downarrow}\right) + D\cdot\rho^{\downarrow}\right]\cdot\left[d\cdot\rho^{\downarrow} + \left(AR^{\uparrow}+AR^{\downarrow}\right) + D\cdot\rho^{\uparrow}\right]}{\left[(d+D)\cdot\rho^{\uparrow} + 2\cdot AR^{\uparrow}\right]\cdot\left[(d+D)\cdot\rho^{\downarrow} + 2\cdot AR^{\downarrow}\right]} - 1.\end{aligned} \tag{5}$$

In order to describe the asymmetry of processes in electron channels with different directions of spins, other parameters could be used: coefficients of asymmetry of scattering in the volume and on the surface β and γ and averaged specific resistances of scattering in the volume and on the surface ρ_* and AR_*. Then the specific resistances of the up and down channels can be written in the following form:

$$\begin{cases} \rho^{\uparrow} = 2\cdot\varrho_*\cdot(1+\beta) \\ \rho^{\downarrow} = 2\cdot\varrho_*\cdot(1-\beta) \\ AR^{\uparrow} = 2\cdot AR_*\cdot(1+\gamma) \\ AR^{\downarrow} = 2\cdot AR_*\cdot(1-\gamma) \end{cases}. \tag{6}$$

Then the formula for GMR can be written in the following form:

$$\mathrm{GMR} = \mathrm{GMR}_{b0}\cdot\frac{1 + \frac{d+D}{dD}\cdot\frac{AR_*\cdot\gamma}{\varrho_*\cdot\beta} + \frac{1}{dD}\cdot\left(\frac{AR_*\cdot\gamma}{\varrho_*\cdot\beta}\right)^2}{1 + \frac{2}{d+D}\cdot\frac{AR_*}{\varrho_*}\cdot\left\{\frac{1+\gamma}{1+\beta} + \frac{1-\gamma}{1-\beta}\right\} + \frac{4}{(d+D)^2}\cdot\left(\frac{AR_*}{\varrho_*}\right)^2\cdot\frac{1-\gamma^2}{1-\beta^2}} \tag{7}$$

We see that this formula includes the geometric dimensions of the layers. In order to compare them with physical parameters, we will consider them relative to such a characteristic of the ferromagnetic as the spin diffusion length l_{sf}. Another parameter that determines the geometry of the device is the ratio between the thicknesses of the free and fixed layers d/D. Therefore, we enter two parameters that determine the geometry of the device:

$$k_1 = d/D; \quad k_2 = l_{\mathrm{sf}}/d. \tag{8}$$

We also introduce the notation that defines the material constant of the ferromagnetic:

$$\Delta = \frac{AR_*}{l_{sf}\varrho_*}. \tag{9}$$

Then Eq. (7) can be rewritten in the following form:

$$\mathrm{GMR} = \frac{4\beta^2}{1-\beta^2} \cdot \frac{k_1}{(1+k_1)^2} \cdot \frac{1 + \frac{1+k_1}{k_1 \cdot k_2} \cdot \left(\Delta \frac{\gamma}{\beta}\right) + \frac{1}{k_1 \cdot k_2^2} \cdot \left(\Delta \cdot \frac{\gamma}{\beta}\right)^2}{1 + \frac{2}{(1+k_1)\cdot k_2} \cdot \Delta \cdot \left\{\frac{1+\gamma}{1+\beta} + \frac{1-\gamma}{1-\beta}\right\} + \left(\frac{2}{(1+k_1)\cdot k_2}\right)^2 \cdot \Delta^2 \cdot \frac{1-\gamma^2}{1-\beta^2}} \tag{10}$$

It is obvious that if scattering on the surface ($\Delta = 0$) is not taken into account, then we proceed to Formula (1). If the asymmetry of the scattering on the surface is significant, and the thicknesses of the free and fixed layers are small, that is, if the scattering in the volume of the ferromagnetic layer can be neglected, we get a different approximation. To do this, in Formula (5), we subtract the multiplier determined by the following expression:

$$\mathrm{GMR}_{0s} = \frac{\left(AR^{\uparrow} - AR^{\downarrow}\right)^2}{4 \cdot AR^{\uparrow} \cdot AR^{\downarrow}} = \frac{4\gamma^2}{1-\gamma^2}. \tag{11}$$

Then the expression for GMR will have the following form:

$$\mathrm{GMR} = \mathrm{GMR}_{0s} \cdot \frac{1 + \frac{k_2 \cdot (1+k_1)}{k_1 \cdot k_2} \cdot \left(\Delta \cdot \frac{\gamma}{\beta}\right)^{-1} + k_1 \cdot k_2^2 \cdot \left(\Delta \cdot \frac{\gamma}{\beta}\right)^{-2}}{1 + \frac{(1+k_1)\cdot k_2}{2} \cdot \Delta^{-1} \cdot \left\{\frac{1+\beta}{1+\gamma} + \frac{1-\beta}{1-\gamma}\right\} + \left(\frac{(1+k_1)\cdot k_2}{2}\right)^2 \cdot \Delta^{-2} \cdot \frac{1-\beta^2}{1-\gamma^2}}. \tag{12}$$

3 Main Research Results

The developed model is applied to study the dependence of the giant magnetic resistance on the physical parameters of the ferromagnetic and the geometrical parameters of the structure for such ferromagnetic materials: cobalt, permalloy, nickel, iron, and cuprum as non-magnetic layer.

Table 1 shows the physical quantities used in the model for these two ferromagnetic materials.

Table 1 Physical quantities used to calculate the spin-valve structure under 80 K [12]

Ferromagnetic layer	Cobalt (Co)	Permalloy ($Ni_{80}Fe_{20}$)	Nickel	Iron
Coefficient of asymmetry of volume scattering, β	0.41	0.75	0.60	0.14
Specific averaged bulk resistivity, ϱ_*, $n\Omega m$	155	277	84.25	28.5
Coefficient of asymmetry of surface scattering, $\gamma_{F/Cu}$	0.68	0.75	0.30	0.55
Specific averaged resistivity of the surface, $2AR_{*F/Cu}$, $f\Omega m^2$	1.05	1.00	0.36	1.50
Spin diffusion length, l_{sf}, nm	50	5.1	5.5	5.5

The results of modeling spin-valve structures based on ferromagnetic layers made of cobalt and iron are shown in Fig. 4a, b, respectively.

These figures show two-parameter dependences of the giant magnetic resistance taking into account the asymmetry of electron scattering on the surfaces of separation of ferromagnetic and non-magnetic layers.

Based on the obtained results, it can be concluded that the ratio of the thickness of the fixed and free ferromagnetic layers has the greatest influence on the value of the giant magnetic resistance, and for all materials, GMR becomes greater while this ratio increases.

Both for cobalt and permalloy, the ratio of the thickness of the free layer and the spin diffusion length has no effect on the value of GMR, but not for iron and nickel. It is interesting that for iron GMR becomes greater, while the thickness of free layer decreases and is opposite for nickel. Graphs of the dependence of the GMR value on the thickness of the free layer for iron and nickel are shown in Fig. 5.

Next, it is investigated how in the developed model the asymmetry of scattering on the surfaces of layers affects the values of GMR. In general, GMR should become greater in this case. It is occurs that this is true for cobalt, permalloy, and iron. As can be seen from Fig. 6, the GMR value for nickel even decreases.

It is quite easy to understand the reason for this if pay attention to the value of the asymmetry parameter $\gamma_{Ni/Cu}$ for the surface scattering is given in Table 1. It has the smallest value among all those given and is only 0.3, which is more than half as much as for other materials. Obviously, for surfaces with low values of surface scattering asymmetry, models that are more accurate should be used.

For all other materials, the GMR value increases by an average of 10% due to surface scattering. At the same time, there is a slight average statistical deviation from this mean value on the set of all investigated geometric parameters of the structure, which is only 2%.

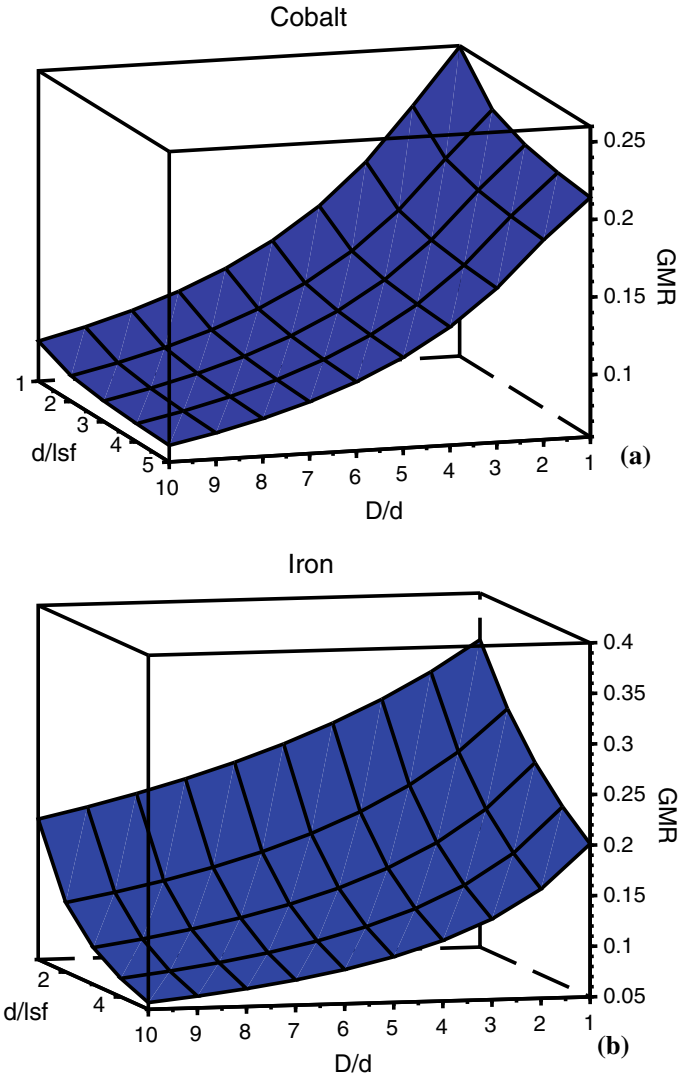

Fig. 4 Dependence of GMR on the geometrical parameters of the structure (d/l_{sf} is a ratio of free layer thickness and spin diffusion length; D/d is a ratio of fixed and free layer thicknesses) for cobalt (**a**) and iron (**b**)

4 Discussion of Results and Conclusions

Based on the assumption of independence of the spin conduction channels, an equivalent electric circuit of the spin valve for the CPP geometry is developed. The basis of the circuit is resistances that model each spin channel in two ferromagnetic layers and a non-magnetic material. In contrast to the existing classical scheme, resistances are

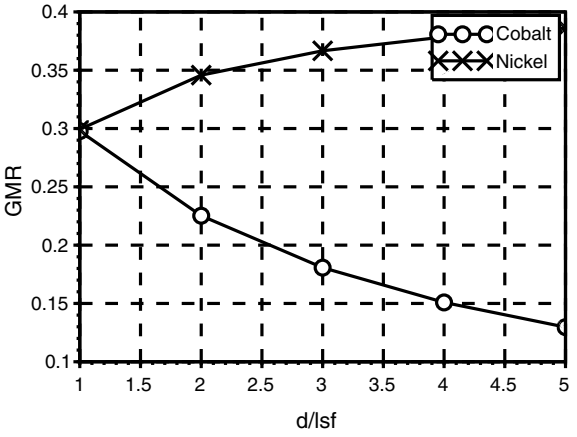

Fig. 5 Influence of the ration thickness of the free layer and spin diffusion length on the value of GMR for iron (star) and nickel (cross) both obtained at $\frac{D}{d} = 5$

added for simulating electron scattering processes on the surface. The values of the resistances are determined based on tabular data, where the asymmetry coefficients for scattering in the volume and on the surface, as well as the specific resistances in the volume and on the surface for ferromagnetic materials, are given. Structures based on cobalt, permalloy, iron, and nickel are investigated.

Based on the developed model, the dependences of the giant magnetic resistance on the geometric parameters of the structure are calculated. This makes it possible to determine the optimal thickness of ferromagnetic layers in the process of designing the device.

The effect of surface scattering on the value of the giant magnetic resistance is studied. As expected, this value increases for all investigated materials, except for nickel, for which the calculated value turned out to be smaller than without taking into account scattering on the surface. This limits the use of this model for materials with a small surface scattering asymmetry, such as nickel. For such materials, it is necessary to use models based on the electrochemical potential with probability of reflection or transmission of electrons with different spins on the surfaces that separate the layers.

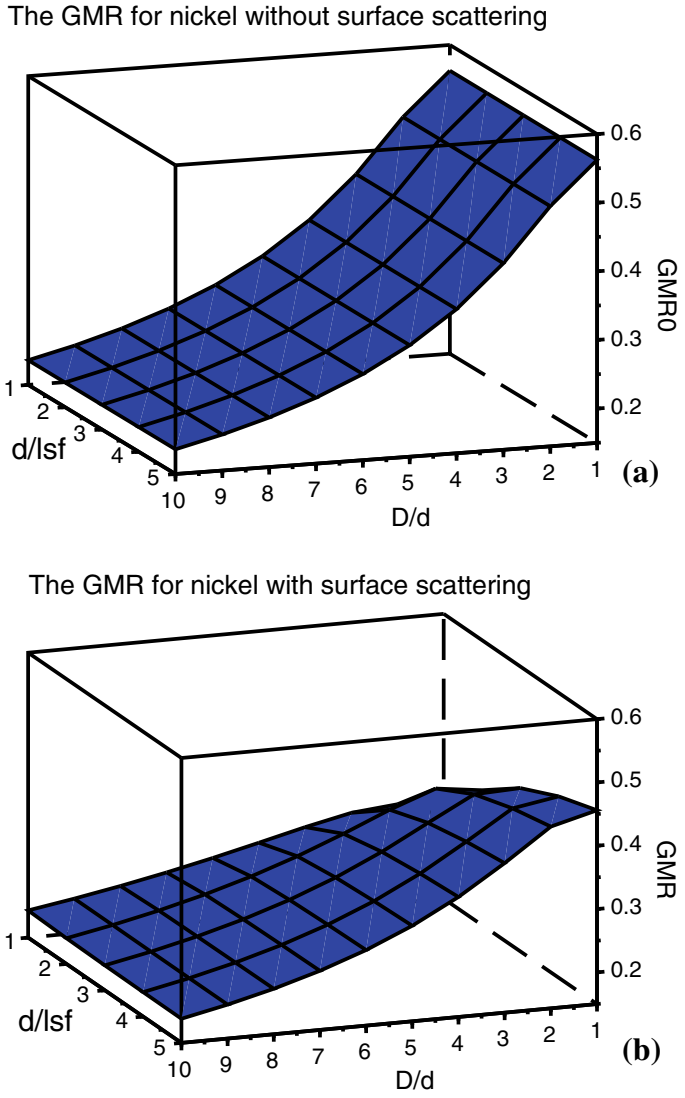

Fig. 6 GMR for nickel without surface scattering (**a**) and with surface scattering (**b**)

References

1. R. Mertens, *Everspin Launches a New Family of SPI Interface MRAM Products* (2022). https://www.mram-info.com/everspin-launches-new-family-spi-interface-mram-products
2. R. Mertens, *IBM to Reveal the World's First 14 nm STT-MRAM Node* (2020). https://www.mram-info.com/ibm-reveal-worlds-first-14nm-stt-mram-node
3. R. Mertens, *IBM Demonstrated 11 nm STT-MRAM Junction, Says Time for STT-MRAM is Now*. https://www.mram-info.com/ibm-reveal-worlds-first-14nm-stt-mram-node

4. R. Mertens, *Control of Bistable Antiferromagnetic States for Spintronics* (2022). https://www.spintronics-info.com/control-bistable-antiferromagnetic-states-spintronics
5. J. Kim, A. Paul, P.A. Crowell, S.J. Koester, S.S. Sapatnekar, J.P. Wang, C.H. Kim, Spin-based computing: device concepts, current status, and a case study on a high-performance. Proc. IEEE **103**(1), 106–130 (2015)
6. Y. Zhang, Q. Zheng, X. Zhu, Z. Yuan, K. Xia, Spintronic devices for neuromorphic computing. Sci. China Phys. Mech. Astron. **63**, 277531 (2020)
7. J. Grollier, D. Querlioz, K.Y. Camsari, K. Everschor-Sitte, S. Fukami, M.D. Stiles, Neuromorphic spintronics. Nat. Electron **3**, 360–370 (2020)
8. X. Zhang, W. Butler, in *Handbook of Spintronics* (Y. Xu (ed.), Springer, Berlin/Heidelberg), pp. 15–16 (2016)
9. X.G. Zhang, W.H. Butler, Conductivity of metallic films and multilayers. Phys. Rev. B **51**(15), 10085–10103 (1995)
10. R.L. Politansky, L.F. Politanskyi, I.I. Grygorchak, A.D. Veriga, Modeling of spin valves of magnetoresistive fast-acting memory. J. Nano Electron Phys. **10**(6), 06027 (2018)
11. R. Politanskyi, M. Vistak, A. Veryga, R. Tetyana, Modelling of spintronic devices for application in random access memory. IAPGOŚ **1**, 62–65 (2020)
12. X. Zhang, W. Butler, in *Handbook of Spintronics* (Y. Xu (ed.), Springer, Berlin/Heidelberg), p. 147 (2016)

The Threshold of Laser-Induced Damage of Image Sensors in Open Atmosphere

I. V. Matsniev, V. L. Andriichuk, O. O. Chumak, A. G. Derzhypolsky, L. A. Derzhypolska, V. M. Khodakovskiy, O. O. Perederiy, and A. M. Negriyko

Abstract The study results of nano- and microstructural elements of CMOS video systems matrices destruction by pulsed laser radiation, laser beams propagation in the open atmosphere over kilometer distances and the impact of the atmosphere turbulence on the focusing of laser beams over long distances are presented. A short review of the literature is provided for a better understanding of the problem and ways to solve it. The laser-induced damage threshold (LIDT) defined as laser pulse radiation energy required to disable a video surveillance camera is about 1 mJ in the camera aperture. At energies in the camera aperture up to 0.14 mJ, the camera is "blinded" at the moment of the pulse, but quickly recovers and starts working again in its usual mode. At energy levels from 0.14 to 1.7 mJ, irreversible changes in the functioning of the camera are observed, starting with the appearance of dark lines in the image to the complete irreversible darkening of the screen. A theoretical simulation of the propagation of a laser beam on a real atmospheric path was carried out. It is shown that the fluctuation of the refractive index leads to a change in the spatial–temporal properties of laser radiation, in particular, to a shift of the beam centroid, which in turn can significantly affect the size of the laser beam when it is focused at long distances.

1 Introduction

Unmanned aerial vehicles (UAVs) are increasingly used in both civilian and military fields, where UAVs are used for reconnaissance, fire control and electronic warfare, as well as strike systems, for the delivery and use of ammunition of various calibers from small, such as grenades, to barrage ammunition with a warhead mass of up to 50 kg, as in the Shahid-136 UAV. While military UAVs are often relatively large and complex, civilian market offers small and relatively inexpensive systems capable of

I. V. Matsniev · V. L. Andriichuk · O. O. Chumak · A. G. Derzhypolsky · L. A. Derzhypolska (✉) · V. M. Khodakovskiy · O. O. Perederiy · A. M. Negriyko
Institute of Physics, NAS of Ukraine, 46, Prospect Nauki, Kyiv 03028, Ukraine
e-mail: fizyka@iop.kiev.ua; d.liudmyl.flla@gmail.com

O. Fesenko and L. Yatsenko (eds.), *Nanoelectronics, Nanooptics, Nanochemistry and Nanobiotechnology, and Their Applications*, Springer Proceedings in Physics 297,
https://doi.org/10.1007/978-3-031-42708-4_20

streaming high-definition video, carrying a variety of other sensors, and transporting cargo. Today, such UAVs are widely used in military affairs, as shown particularly by the experience of Ukrainian-Russian war.

Among the modern methods of countering UAVs, lasers are primarily considered as means of blinding and destruction of optical video surveillance systems, as well as means of detection, recognition, and tracking of UAVs. A laser can also be used to detect atmospheric attenuation and turbulence on inclined trajectories, which is critical to operation of high-power laser weapons aimed at destroying UAVs. Various laser functions and their role for detection, recognition, tracking, and combating UAVs are discussed and summarized in numerous publications, particularly in [1, 2].

When using a laser to damage optoelectronic surveillance systems equipped with UAVs, it is important to consider the following factors:

- Sensitive elements of optoelectronic surveillance systems (photoreceptors, CCD, and CMOS matrices) are integrated circuits consisting of photoreceivers, optical filters, electronic components—conductors, electrodes, transistors, and amplifiers. Structurally, the elements are made in the form of thin films of nano- and micrometer thickness and cross-sectional dimensions of the micrometer range of materials with different optical, electrical, thermal, and mechanical properties, mainly silicon with different doping, as well as some metals, for example, aluminum, and their oxides.

These matrices have limitations on the permissible level of light flux, and exceeding these threshold levels of light energy leads to their failure.

- Surveillance systems are designed in such a way that an image is projected onto a sensitive element located close to the focal plane of optical system. This leads to high concentration on the sensitive element of light energy from the laser beam directed at the input aperture of the surveillance system. Protection of optical-electronic video surveillance systems of UAVs against damage by laser radiation is complicated by the fact that the design of video system provides for the propagation of optical radiation to the sensitive matrix with minimal losses, and artificial reduction of energy flow of the laser beam to a safe level, for example, using optical filters, interferes with the operation of the video system.
- In contrast to the mechanical destruction of the UAV body, the threshold levels of laser energy density on the surface of the UAV, necessary to damage the light-sensitive matrix of the surveillance system, are several orders of magnitude lower. The concentration of laser energy by an optical lens contributes to the destruction of the matrix both as a result of thermal action of laser radiation and the resulting changes in the electrical properties of the components of the matrix, and as a result of other processes caused by the action of powerful short light pulses on the electronic components of the sensitive element, in particular, avalanche ionization.
- In real atmosphere conditions, the propagation of a laser beam is accompanied by radical changes in the spatial distribution of its energy as a result of dynamic changes in the optical characteristics of the atmosphere of different spatial and temporal scales along the optical path of the laser beam. These changes must be

taken into account when determining laser source energy that is safe for UAV video surveillance systems.

Thus, the determination of threshold energy levels of laser sources at which remote irreversible destruction of the optical matrices of UAV video systems occurs is required as well as the determination of the local threshold of destruction by laser radiation of complex optically and structurally heterogeneous systems, which are the matrices of video surveillance systems. And also an assessment of influence of atmospheric turbulence on the propagation of laser beams and changes in the distribution of their energy density at typical UAV operating distances.

This work presents the results of the research into the destruction of nano- and microstructural elements of CMOS matrices of video systems by pulsed laser radiation and research into the spread of laser beams in the open atmosphere over kilometer distances, the effect of the optical heterogeneity of the atmosphere on the focusing of laser beams over long distances. A review of the literature on the subject is provided for a better understanding of the problem and ways of solving it.

2 Analysis and Research of the Mechanisms of Pulse Laser Radiation on CMOS, CCD Cameras

2.1 The main reason for the failure of video surveillance systems due to the action of laser radiation is the destructive effect of focused laser radiation on the light-sensitive matrix of the receiving element (see Fig. 1).

Arrays are particularly vulnerable to pulsed lasers because of the optical gain, which can be described as the ratio of the energy density at the array to the energy density at the lens entrance aperture and can be 106 or greater (e.g., a gain of 106 for a 25.4 mm lens, the wavelength of light 532 nm [3, 4]). Simply put, the lens system forms an image of a distant point source, which is a laser, on a light-sensitive matrix in the form of a spot with a size from units to hundreds of micrometers. This focused light energy can damage the electronic array, turning into thermal energy

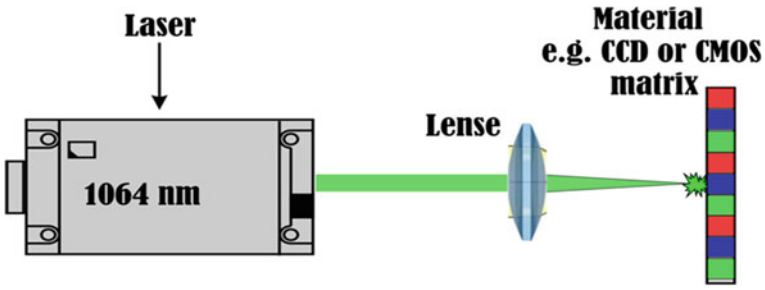

Fig. 1 Concentration of laser energy on the photosensitive matrix

that is enough to break electrical connections or connect conductors that should be insulated, change the phase state (melt or vaporize) of individual chip elements, etc.

It should be noted that powerful laser radiation with a wavelength that lies within the spectral sensitivity range of the image sensor passes unhindered through the optical system and can cause damage, since the photosensitive material of the electronics in the sensor, as a rule, absorbs radiation at these wavelengths well, and energy losses laser radiation when propagating through the optical system is minimal.

2.2 Laser-induced damage thresholds (LIDTs) of photosensitive matrices of video surveillance systems have been studied for several decades by various groups. We will give a brief review of the reference on this problem.

One of the earliest works [4] by Chenzhi Zhang et al., in which studies of LIDT on a CCD matrix using nanosecond pulses of 1064 nm, was published.

The work examined CCDs EG&G Model RA2048J, 2048 × 64 elements (fully functional, packaged CCDs with removable covers), and Itek Optical Systems Model VLA577 E57D, 2048 × 96 elements, which were cut but not mounted chips.

The laser radiation source used in these experiments was an active Q-modulated Nd:YAG laser operating at a fundamental wavelength of 1064 nm with a repetition rate of 10 Hz and a pulse duration of 10 ns (FWHM). A 76 cm focusing lens was used to achieve a spot size on samples in the range of 270–480 μm.

Damage probability curves for chips showed that the onset of morphological damage was 1.3 J/cm^2 for CCD matrices.

The physical mechanism of laser-induced CCD degradation is as follows:

1. Doped polysilicon clock lines have strong linear and nonlinear absorption of 1.06 μm laser light.
2. The narrow insulating oxide between the two polysilicon lines was damaged by heat conduction from the adjacent molten polysilicon lines.
3. The shielding effect created by the polysilicon clock lines provided dynamic substrate protection as little dark leakage was observed.

The work of Schwarz et al. found that the nanosecond thresholds of 532 nm for color and monochrome CMOS and CCD sensors range from 0.03 to 0.1 J cm−2 [5, 6].

The tested sensors were irradiated with a pulsed laser with pulse duration of 10 ns and a continuous laser with a wavelength of 532 nm. In the case of monochrome CMOS cameras exposed to pulsed laser radiation, the first damage to the sensor was observed at fluxes of 0.1 J/cm^2. No damage was observed below the level of 0.043 J/cm^2. This may mean that the pulsed laser radiation causes a change in the band gap of the semiconductor or a change in the insulation area, leading to an increase in the leakage current. The shape of the damage is mostly round and somewhat elongated in the horizontal direction. As the current flow was further increased, the point damage began to develop star-shaped edges around the circular center, starting at a value of 14.9 J/cm^2. The camera sensor was completely destroyed in the sense that the output image no longer responded to incident light at 2.9 kJ/cm^2.

Burgess et al. published data on LIDT remote damage of visible and short-wave infrared cameras using a continuous 1070 nm source and laser exposure times from

microseconds to continuous waves [7]. Lens plane irradiance causing damage at 0.5 ms exposure was 0.4 W cm^2 for silicon cameras.

The Porton Down Range was chosen for this study because it has a variety of experimental track ranges of up to several kilometers. A single-mode fiber laser with a power of 0.5 kW and a propagation path of 500 m was chosen to provide adequate exposure to the target for CW laser damage.

Using the setup described above, the camera was exposed to flashes of laser light with durations of 0.5, 5, 50, 150, and 250 ms and different fluencies. For each flash, the laser emission as a function of time was recorded by a photodiode, and the camera was checked for damage by blocking the objective lens and visually inspecting the output image. In contrast to the laboratory results, there was no discernible trend in the probability of damage with time of exposure. This can be understood because the laser radiation changes rapidly (on ms time scales) due to scintillation in the atmosphere. Thus, the time dependence of the damage threshold is actually "washed out" by the atmosphere, and is rather a cumulative change in temperature.

Guo et al. [8] performed LIDT measurements on CMOS sensors using a 1064 nm pulsed laser and found the damage threshold to be 0.38 Jcm^2, with varying degrees of line damage ranging from 0.64 to 1.0 J/cm^2.

Using a single-pulse laser with duration of 60 ns and 1064 nm to irradiate the CMOS detector, typical experimental phenomena were observed and the corresponding energy density threshold values were measured. The camera FMVU-03MTM/C (B/W) was used as the investigated CMOS object. Its image sensor is a Micron MT9V022 CMOS that contains 752 × 480 pixels with a size ($d \times d$) of 6 μm × 6 μm. The image area is approximately 4.55 mm (horizontal) × 2.97 mm (vertical).

The cross-sectional structure of a CMOS pixel on a low-doped P-type silicon substrate forms two high-doped N-type regions called the source electrode and the drain electrode. A silicon insulating layer is then created on the surface of the silicon by high-temperature oxidation, outside the silicon insulating layer between the source and drain electrodes, an aluminum layer called the gate electrode is created. The photosensitive element is located outside the aluminum layer. CMOS pixels are mutually isolated.

With the growth of the laser energy density, the point-like defects first appeared in the output image, followed by black half lines and crossed black lines defects. Thus, according to the results of the experiment, the process of hard damage of the CMOS matrix can be divided into three stages. Based on the structure and working principle of CMOS, studying the three-stage damage mechanism through theoretical analysis, it was found that the point damage was caused by the increase of leakage current due to structural defects as a result of thermal effects, the damage in the form of black line and in the form of cross black lines was caused by signal interruption due to the fact that the conductors in the circuit of the device were interrupted. As the laser energy density increased, the damaged zone expanded. If the laser energy density has reached 1.95 J/cm^2, the black lines have covered most of the detector pixels, but the detector is still not completely desensitized, the undamaged area can transmit the image because the CMOS pixels are separated from each other.

2.3 Experimental studies of the destructive effect of pulsed laser radiation on CMOS matrices.

As can be seen from the review of the literature, the failure of the optical sensor of the video camera can be due to several reasons.

First, it is the direct destruction of light-sensitive elements (pixels) of the matrix and its electronic components (conductors, contacts, p–n junctions, elements of integrated circuits) as a result of the thermal action of the laser pulse. Given the significant heterogeneity of the elemental composition and spatial structure inherent in the photosensitive matrix, which changes on micron and submicron scales, caused by the technology of manufacturing sensor integrated circuits, the mechanisms of thermal action of short intense laser pulses and the consequences of such action for the operation of electronic circuits can be very diverse from phase transitions in circuit components to mechanical re-commutation of electrical circuit elements.

Second, with a significant increase in light flux, a large concentration of electric charge carriers is formed, which leads to a number of nonlinear processes in the flow of currents, the action of which additionally strengthens this effect.

These two reasons, which lead to damage to the video camera, can differently shape the requirements for the parameters of the focused beams.

A number of experiments were conducted to identify and analyze the mechanisms of failure of optoelectronic surveillance systems (cameras) by laser radiation, as well as to form the necessary threshold parameters of radiation.

At the first stage of work, bench laboratory tests were performed with the direct impact of laser pulses of different energies on the camera sensor. At the same time, the threshold value of the energy of the pulses, necessary to disable the camera, was determined. The operating modes of the camera under experimental conditions were also investigated to find out the mechanism of its failure. Figure 2 shows the diagram of the stand of the first stage of testing. During the experiments, L laser pulses with a wavelength of $\lambda = 1064$ nm, a pulse duration of $\tau \sim 15$ ns, and a pulse energy of $E = 32$ mJ were used.

Calibrated filters F were used to weaken the beam. After passing through the filters, the laser radiation entered the camera lens C.

In order to control the influence on the functioning of the camera, we chose the method of recording signals generated by the camera sensor which determines the degree of damage to the camera by laser pulses and its loss of functional properties.

The camera was connected to a PC and, in parallel, to an oscilloscope. This made it possible to control the operating modes of the camera. At the first stage of experiments, webcams with a CMOS matrix with a resolution of 640 × 480 pixels (standard CMOS matrix) were used. Logitech cameras (Gembird CAM-100U-B model, hereinafter Camera 1) and Genius (FaceCam 1000X model, hereinafter Camera 2) were used. As is known from the general ideas about the operation of the CMOS-matrix video processor, it reads from each pixel a signal corresponding to the pixel's illumination, forms color information using a Bayer filter and encodes color information in the format set by the camera's interface processor. Next, the video frame is transferred to the interface processor using an 8-bit parallel (in our case) interface, where it can be mixed with sound data and transferred to a computer

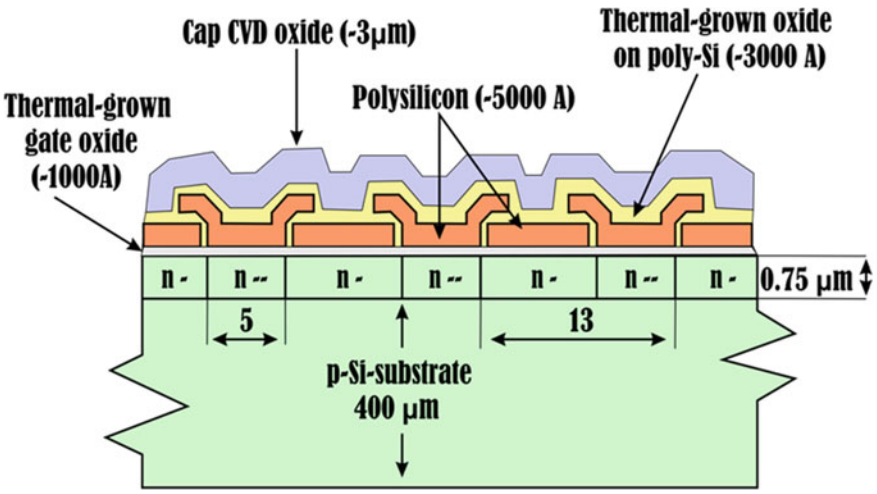

Fig. 2 Longitudinal section of the active area of the CCD matrix [2]

via USB. To monitor the described process, outputs were soldered to the inside of the video camera, which allow connecting it to an oscilloscope for monitoring the camera's operating modes in accordance with Fig. 3.

Figure 4 shows the internal part of the camera prepared for connection to the oscilloscope and its placement in the working diagram.

The key point of the video camera is that the data from the matrix is transferred to the interface processor in the form of rectangular pulses on a parallel 8-bit bus at the pixel clock frequency PXCLK. In our research, we read the value of the most significant bit (DATA7, D7). Data is structured into groups by line (HD, HSYNC) and frame (VD, VSYNC) synchronization signals. Figure 5 shows oscillograms of data pulses for different modes of operation of the camera in normal mode at different levels of camera illumination, the intensity of laser irradiation increases for images

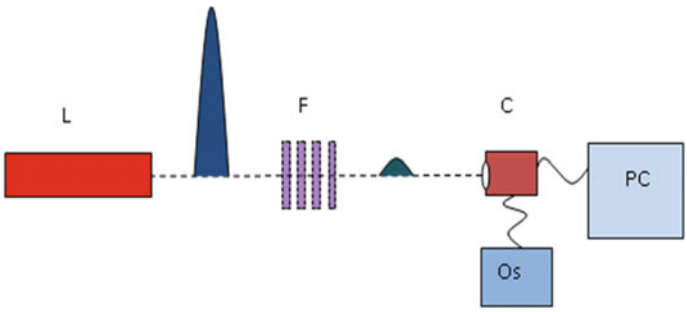

Fig. 3 Experimental setup

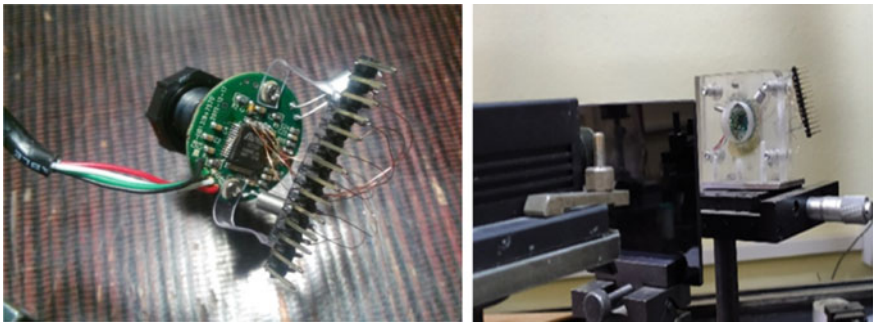

Fig. 4 Installation of the circuit for reading signals from the video camera and placing the camera on the stand (Camera 1)

from top to bottom. On the right, video images from the camera are shown for illustration (Figs. 5, 7, 8 and 9).

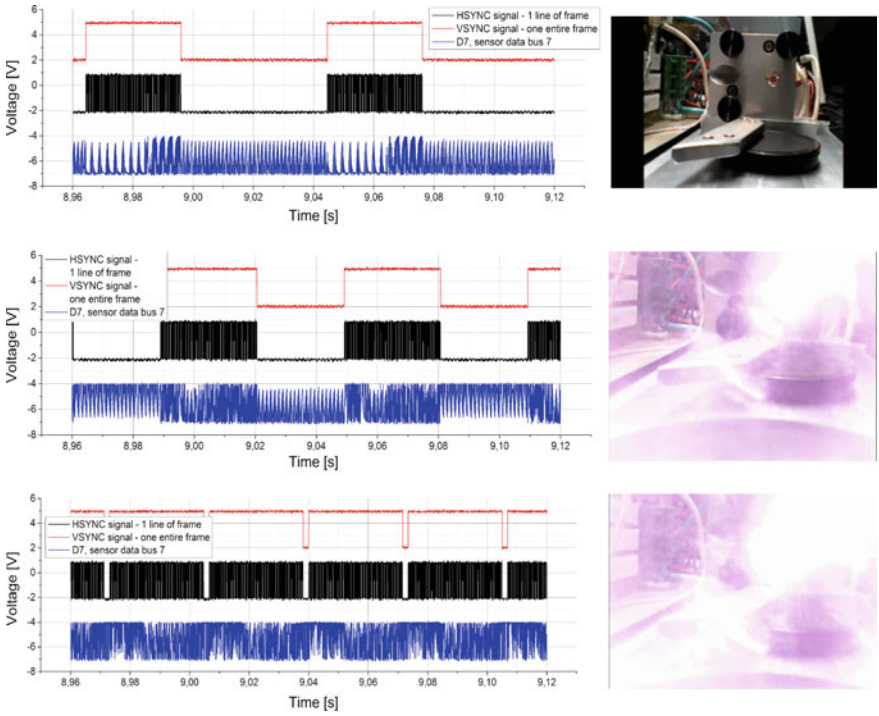

Fig. 5 Oscillograms of signals from the video camera and corresponding images from the camera. The energy of the laser pulse is less than 0.14 mJ in the camera aperture, increasing from top to bottom

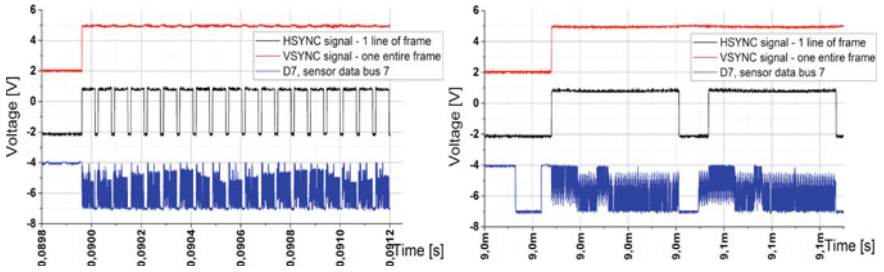

Fig. 6 Detailing of the oscillogram elements for the camera's standard mode of operation when the energy in the camera aperture is less than 0.14 mJ

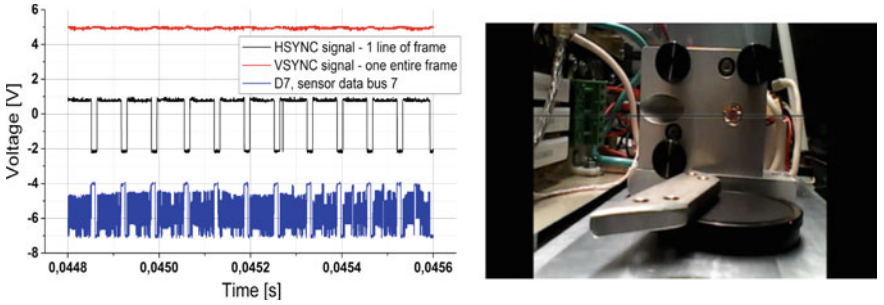

Fig. 7 Signal oscillogram and video image of the camera at the energy level in the camera aperture of 0.14 mJ. The image shows a transverse band of irreversible damage to the matrix sensor

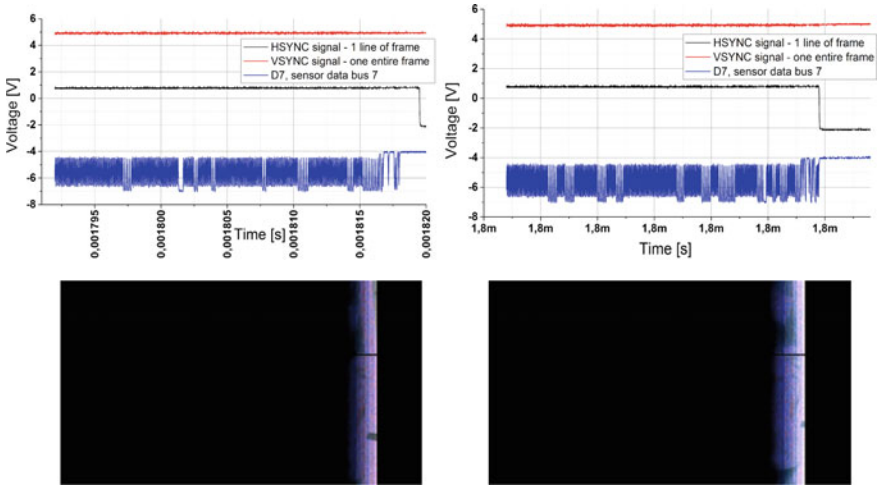

Fig. 8 Signal oscillogram and video image of the camera at the energy level in the camera aperture of 1.7 mJ. Irreversible damage to the matrix sensor, the camera is not functional

Fig. 9 Irreversible damage to the matrix sensor, the camera is not functional. The energy in the camera aperture is more than 1.7 mJ

When laser radiation with an energy of more than 1.7 mJ is applied to the matrix of the CMOS camera, data ceases to flow to the interface processor. At the same time, two cases are observed: In the first, the data signal from the output of camera 1 D7 was not in the form of rectangular pulses, as it should be in normal operation, but in a form close to sinusoidal at the pixel clock frequency PXCLK with a chaotic change in amplitude. In the second case, the D7 camera 2 data signal was a normal rectangular shape, but a black screen was transmitted, and the VSYNC frame rate was independent of illumination, unlike normal operation as it shown at Figs. 6, 7 and 8. Note that no visible damage is observed on the matrix after exposure to this laser radiation (Fig. 10).

Previous laboratory experiments established that the threshold value of the pulse energy for the camera to fail is about 1 mJ. At lower energies, the camera is "blinded" at the moment of the pulse, but quickly recovers and starts working again in its usual mode. However, if laser radiation of the appropriate level continues to be sent to the camera at a sufficient frequency, the camera will be permanently blinded. It was also noted that at energies close to the threshold values, the camera can withstand several pulses before failing.

3 Conditions of Remote Focusing of Laser Radiation in the Atmosphere: Theory, Simulation, Experiment

The remote damage implementation of UAV video surveillance systems is still a relevant problem for analyzing and estimating the laser beam limit parameters focusing on a real atmospheric track at a distance of hundreds of meters. It is known that dynamic atmosphere inhomogeneities radically change the transverse energy distribution in the laser beam (see Fig. 11).

Here we present the model, theoretical calculations, and experiments considering the laser beam propagation and focusing conditions on an atmospheric path from 500 m.

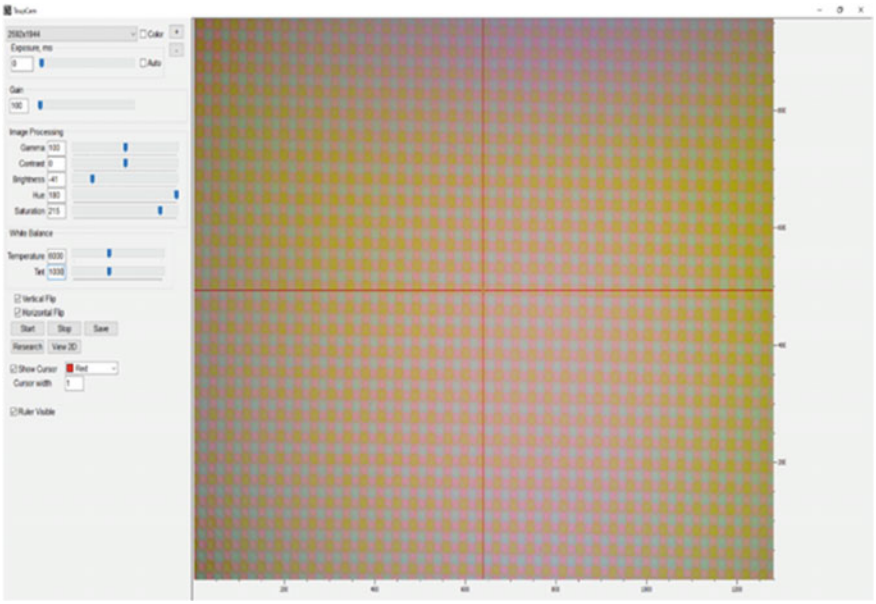

Fig. 10 Image of the pixel structure of the CMOS matrix sensor after exposure to a laser pulse with an energy of more than 1.7 mJ in the camera aperture (the camera is not functional). No visible violations of the structure were recorded (Confotec MR SOL confocal microscope)

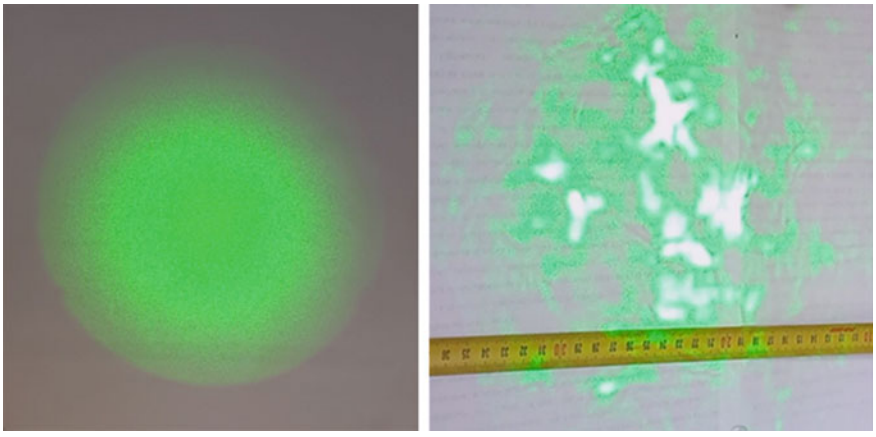

Fig. 11 Influence of open atmospheric path conditions on the transverse-spatial energy distribution in a laser beam. Laser beam at the collimator output (left) and after 2 km travel in open air (right)

While a laser beam propagates through the atmosphere, its spatiotemporal characteristics are changed due to optical inhomogeneities constantly existing in the real atmosphere [9–11]. However, when the beam propagates mainly vertically or at a significant angle to the horizontal, which corresponds to the real schemes of tracking and damaging UAVs, the influence of atmospheric turbulence on the propagation of laser beam radiation is reduced. Consequently, it is essential to theoretically model the atmosphere properties and the light beam parameters propagating through a heterogeneous medium in order to develop optimal communication protocols, remote sensing, and beam-focusing systems.

Random fluctuations of an atmosphere refractive index have a considerable effect on the laser beam properties leading to its broadening, random beam centroid displacement, and intensity fluctuations. As known, refractive index fluctuations are described statistically [12]. Even having a small amplitude, the influence of refractive index fluctuations on the beam propagation is not unnoticed. Instead, this influence only increases when the beam radiation propagates over long distances. The reason is the integral effect of many collisions of the laser beam with atmospheric inhomogeneities. Considering the turbulence forces and the wide range of inhomogeneity sizes in the atmosphere, it becomes more difficult to describe the beam propagation on real atmosphere paths.

As a matter of fact, theoretical analysis of the spatial properties of the beam and the fluctuations of its transmission coefficient in the atmosphere are complicated by the change in the statistical properties of radiation. It should be noted that laser beam, propagating through a turbulent atmosphere (especially over long distances), undergoes constant and considerable collisions with eddies. Thus, initially coherent laser radiation acquires some properties of Gaussian statistics [13, 14].

It is widely held that the usefulness and usage of proposed fourth-moment equations in early studies [15, 16] are limited by their complexity. Later on, an alternative approach based on a photon distribution function (PDF) in a phase (coordinate-momentum) space and its kinetic equation [17–21] was proposed. Moreover, in the most general case, the evolution of the PDF can be described by the Boltzmann–Langevin kinetic equation [22]. In the strong turbulence case, the effect of atmospheric inhomogeneities on the laser radiation scattering can be explained by the action of random forces. Such forces are expressed through a refractive index gradient. At the same time, the movement of particles along classical trajectories describes a laser beam nature [17]. For all the above mentioned, a more general method, typical for describing multiparticle systems where collisions occur, is to use the collision integral [22]. In addition, the Langevin approach is excellent for modeling the random nature of photon-eddy collisions [23]. Moreover, the Boltzmann–Langevin equation simultaneously includes both a collision integral and a Langevin source of fluctuations.

The constructed PDF theory makes it possible to estimate intensity fluctuations, transmission coefficient, and beam centroid position, as well as to study the dynamics of changes in a beam size depending on a wide range of atmospheric channel parameters. In turn, estimating these parameters allows for determining the limitations and optimal parameters of beam-focusing problems. Considering the above, the photon

density function method in the phase space is more than appropriate for the theoretical study of laser radiation in a turbulent atmosphere.

The photon density distribution function for coordinates r and pulses q is defined by analogy with the density distribution functions in plasma physics and solid-state physics [23]:

$$\hat{f}(r,q,t) = \frac{1}{V}\Sigma_k e^{(-ik\cdot r)} b^{\dagger}_{(q+\frac{k}{2})} b_{(q-\frac{k}{2})}, \tag{1}$$

where $b^{\dagger}(b)$ is the bosonic quantum operator of photon creation (annihilation) with the wave vector q; $V \equiv L_x L_y L_z \equiv SL_z$ is the normalizing volume. It should be noted that all operators are in the Heisenberg representation. The laser beam propagates in the z-axis direction, and at the same time, a paraxial approximation is performed, which means only a small divergence of the beam components takes place. It is necessary to choose system boundary conditions large enough, to avoid its effect on the light beam propagation. The sum over k on the right-hand side of Eq. (1) consists only of wave vectors that satisfy the inequality $k \ll \frac{\omega}{c}$, where ω is the characteristic radiation frequency, and c is the speed of light in a vacuum. This limitation does not significantly affect the precision of the beam description since its characteristic dimensions considerably exceed the radiation wavelengths.

Kinetic equation describing the evolution of photon density function in the phase space is represented by the Boltzmann–Langevin equation [22]

$$\partial_t f^{\wedge}(r,q,t) + c_q \cdot \partial_r f^{\wedge}(r,q,t) = K^{\wedge}(r,q,t) - \nu_q^{\wedge}\{f^{\wedge}(r,q,t)\}, \tag{2}$$

where $c_q = \frac{\partial \omega_q}{\partial q} = \frac{cq}{q_0}$ is the speed of photons. As emphasized above, the Langevin source of fluctuations (the first term on the right-hand side of Eq. (2)) describes the random nature of the fluctuations of individual photon-eddy collisions. The Langevin approach is widely used in solid-state physics [23, 24] and quantum optics [25]. This approach uses a stochastic differential equation to model the dynamics of physical systems (see [26]). The second term on the right-hand side of Eq. (2) is the collision integral corresponding to the dissipation of the distribution function associated with the randomization of the photon wave vectors $q_{\perp}$:

$$\nu_q\{f^{\wedge}(r,q,t)\} = \frac{2\pi\omega_0^2}{c}\int \mathrm{d}k'\psi(k'_{\perp}) \times \big(f(r,q,t) - f\big(r,q+k'_{\perp},t\big)\big),$$

where $\psi(k'_{\perp})$ is a function describing the light scattering process on local atmosphere heterogeneities. It follows from the latter that only a wave vector component normal to the propagation direction changes when collisions occur. Therefore, both equations, $K^{\wedge}(r,q,t)$ and $\nu_q^{\wedge}$, consist of parameters that describe radiative and atmospheric characteristics.

When a beam propagates over long distances, the Boltzmann–Langevin equation (2) reduces to the collisionless Boltzmann equation [17, 27]:

$$\partial_t f^{\wedge}(r,q,t) + c_q \cdot \partial_r f^{\wedge}(r,q,t) + F(r) \cdot \partial_q f^{\wedge}(r,q,t) = 0 \tag{3}$$

The PDF operator $f^{\wedge}(r,q,t)$ describing the photon density in (r,q)-space, after summation over the q values, gives the photon density (or intensity) only in r-space:

$$I^{\wedge}(r,t) = \sum_q f^{\wedge}(r,q,t) = \frac{1}{V} \sum_{q,k} \mathrm{e}^{-ik\cdot r} b^{\dagger}_{qq+\frac{k}{2}} b_{q-\frac{k}{2}}. \tag{4}$$

However, it should be mentioned that the characteristic sizes of spatial inhomogeneities, which are described by the functions $f^{\wedge}(r,q,t)$ and $I^{\wedge}(r,t)$, are much smaller than the optical wavelength $\lambda = (2\pi/q_0)$, where $q_0 = \omega_0/c$; then, in Eqs. (1) and (4), the sum over k is limited by its small values, $k \ll k_0$, but at the same time large enough to satisfy the spatial precision of a beam description. In this case, the characteristic size δr and the characteristic wave vector δq of the radiative inhomogeneity must satisfy an inequality $\delta r \delta q \ll \frac{1}{2}$. It explains which optical properties a PDF can describe [27].

Intensity fluctuations (the fourth moment in terms of field operators) are defined by

$$\Gamma_4(r_1,r_2) \equiv \left\langle I^{\wedge}(r_1,t) I^{\wedge}(r_2,t) \right\rangle = \frac{1}{V^2} \sum_{q,k,q',k'} \mathrm{e}^{-i\left(k\cdot r_1 + k'\cdot r_2\right)} \left\langle b^{\dagger}_{q+\frac{k}{2}} b_{q-\frac{k}{2}} b^{\dagger}_{q'+\frac{k'}{2}} b_{q'-\frac{k'}{2}} \right\rangle \tag{5}$$

Averaging $\langle \ldots \rangle$ simultaneously includes both quantum–mechanical averaging of operators $I^{\wedge}$ and averaging over a large number of the beam "runs" through different realizations of the turbulent profile (additionally includes averaging over diffuser configurations if a phase diffuser is used to obtain partially coherent beams). Because these averages are different in nature, they can be performed independently.

Usually, the fluctuations of the refractive index δn are Gaussian random variables and are described by the covariance $\langle \delta n(r) \delta n(r^{\wedge\prime})$. The covariance is determined by the Fourier form, $\psi(k)$, which in a statistically homogeneous environment is defined by

$$\left\langle \delta n\left(r - r'\right) \delta n(0) \right\rangle = \int \mathrm{d}k e^{-ik\cdot\left(r-r'\right)} \psi(k). \tag{6}$$

The spectrum of refractive index fluctuations is often described by the von Kármán formula

$$\psi(k) = 0.033 C_n^2 \frac{\exp[(-kl_0/2\pi)]^2}{\left(k^2 + L_0^{-2}\right)^{11/6}}, \tag{7}$$

where l_0 and L_0 are the inner and outer turbulence radii that determine the minimum (in the order of millimeters) and maximum (in the order of tens of meters) sizes of

turbulent eddies, C_n^2 is the structural constant for refractive index fluctuations that describe their amplitude.

The photon distribution function in the phase space makes it possible to estimate the beam radius:

$$R_b^2 \equiv \left\langle r_\perp^2 \right\rangle = \frac{\int \mathrm{d}r_\perp \int \mathrm{d}q r_\perp^2 f(r_\perp, q, t)}{\int \mathrm{d}r_\perp \int \mathrm{d}q f(r_\perp, q, t)}, \tag{8}$$

where $f \equiv \left\langle f^\wedge \right\rangle$. At long distances (8) reduces to

$$R_b^2 = \frac{r_0^2}{2}\left(1 - \frac{z}{F}\right)^2 + \frac{2z^2}{r_1^2 q_0^2} + \frac{4z^3 c\alpha}{3\omega_0^2}, \tag{9}$$

where $\alpha = \frac{\pi\omega_0^2}{2c} \int \mathrm{d}k' k'^2 \psi\left(k'\right)$, ω_0 and q_0 are the central radiation frequency and its corresponding wave vector, $\frac{r_0}{\sqrt{2}}$ is the initial beam radius, $r_1^2 = \frac{r_0^2}{\left(1+2r_0^2\lambda_c^{-2}\right)}$, parameter λ_c considers the phase-mixing effect when using partially coherent radiation ($r_1 = r_0$ corresponds to coherent radiation), z is the propagation distance, F is the radius of the curvature of the wavefront. It is noticeable that the turbulent term at large enough propagation distances or under strong turbulence (for C_n^2 large values) can dominate the diffraction term (the second one) and the term that considers the focusing and initial beam size.

In early works describing beam propagation over short distances, the asymptotic approximation was often used for the average value of the beam width [9]:

$$R_b^2 = \frac{r_0^2}{2}\left(1 - \frac{z}{F}\right)^2 + \frac{2z^2}{r_1^2 q_0^2} + \frac{4z^2}{\rho_0^2 q_0^2}, \tag{10}$$

The initial beam sizes significantly change under strong turbulence or at long distances of laser beam propagation [28], even considering beam focusing (see Fig. 12).

In addition, a transmission coefficient should be considered separately:

$$\eta^2 \geq \int\limits_A d^2 r_1 \int\limits_A d^2 r_2 \Gamma_4(r_1, r_2), \tag{11}$$

where A is the detector area, and the correlations of the beam center displacement are represented by

$$\sigma_{\mathrm{BW}}^2 = \int\limits_R d^2 r_1 d^2 r_2 (r_1 \cdot r_2) \Gamma_4(r_1, r_2) \tag{12}$$

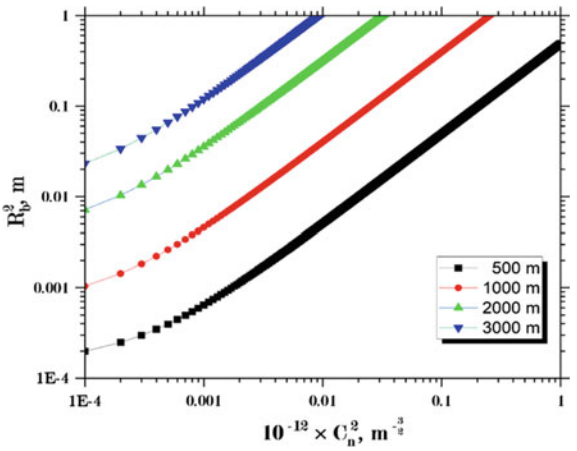

Fig. 12 Laser beam radius versus turbulence strength C_n^2. Solid curves denote an approach to high turbulence, and solid curves with symbols—an approach to low turbulence. Coherent beam and atmosphere channel parameters: $r_0 = 0.01$ m, $l_0/2\pi = 10^{-3}$ m, $L_0 = 50$ m, $q_0 = 10^7$ m^{-1}

Such values are essential if the beam radius during detection exceeds the typical detector size. Transmission coefficient fluctuations make it possible to estimate the spatial and energy characteristics of radiation that hits the detector. Estimating the average displacement of the beam centroid allows us to consider the beam deviation as a whole from the initial position of the beam center (such an effect is known as the so-called beam wander).

The processing of these measurements, obtained in real experiments and during the measurement of beam sizes, was carried out according to the ISO standard recommendations [29]. ISO standards define the rules of correct experiment conduct to determine the diameter of focused laser radiation, using the values of the second-order moments and the beam axis.

In order to find them, it is necessary to carry out an iterative calculation procedure correcting an integration area according to the beam sizes. Currently, according to ISO [29], the generally accepted diameter (recorded as D4σ) is considered to be 86% of its power for a Gaussian beam.

According to ISO [29], to accurately calculate the diameter of the focused image; first, it is necessary to find the centroid coordinates of the cross-sectional beam power density $I(x, y, z)$. Its coordinates are determined by the expressions:

$$\overline{x}(z) = \frac{\iint_{-\infty}^{+\infty} I(x, y, z) x \mathrm{d}x\mathrm{d}y}{\iint_{-\infty}^{+\infty} I(x, y, z) \mathrm{d}x\mathrm{d}y},$$

$$\overline{y}(z) = \frac{\iint_{-\infty}^{+\infty} I(x, y, z) y dx dy}{\iint_{-\infty}^{+\infty} I(x, y, z) dx dy}, \tag{13}$$

Note that special attention is paid to the procedure for choosing the real limits of integration since the final result of determining the diameter depends significantly on this. The next step in the calculation was finding the second-order moments:

$$\sigma_x^2(z) = \langle x^2 \rangle = \frac{\iint_{-\infty}^{+\infty} I(x, y, z)(x - \overline{x})^2 \mathrm{d}x\mathrm{d}y}{\iint_{-\infty}^{+\infty} I(x, y, z)\mathrm{d}x\mathrm{d}y},$$

$$\sigma_y^2(z) = \langle y^2 \rangle = \frac{\iint_{-\infty}^{+\infty} I(x, y, z)(y - \overline{y})^2 \mathrm{d}x\mathrm{d}y}{\iint_{-\infty}^{+\infty} I(x, y, z)\mathrm{d}x\mathrm{d}y} \tag{14}$$

$$\sigma_{xy}^2(z) = \langle xy \rangle = \frac{\iint_{-\infty}^{+\infty} I(x, y, z)(x - \overline{x})^2 (y - \overline{y})^2 \mathrm{d}x\mathrm{d}y}{\iint_{-\infty}^{+\infty} I(x, y, z)\mathrm{d}x\mathrm{d}y}$$

Figure 13 shows a schematic representation of an astigmatic beam propagation in the general case. The axes and angles of divergence are displayed.

The beam diameter in its own coordinate system is defined by the expressions:

$$d_{\sigma x}(z) = 2\sqrt{2}\left\{\left(\sigma_x^2 + \sigma_y^2\right) + \gamma\left[\left(\sigma_x^2 + \sigma_y^2\right)^2 + 4(\sigma_{xy}^2)^2\right]^{\frac{1}{2}}\right\}^{\frac{1}{2}}$$

$$d_{\sigma y}(z) = 2\sqrt{2}\left\{\left(\sigma_x^2 + \sigma_y^2\right) - \gamma\left[\left(\sigma_x^2 + \sigma_y^2\right)^2 + 4(\sigma_{xy}^2)^2\right]^{\frac{1}{2}}\right\}^{\frac{1}{2}}, \tag{15}$$

where the coefficient γ is determined by the expression:

$$\gamma = \mathrm{sgn}\left(\sigma_x^2 - \sigma_y^2\right) = \frac{\sigma_x^2 - \sigma_y^2}{\left|\sigma_x^2 - \sigma_y^2\right|}.$$

The beam diameter average value is determined by the expression:

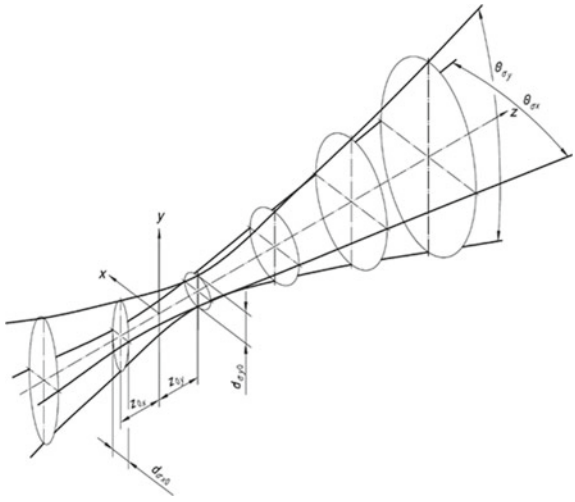

Fig. 13 Parameters of a focused astigmatic beam

$$d_\sigma(z) = 2\sqrt{2}\left(\sigma_x^2 + \sigma_y^2\right)^{\frac{1}{2}} \tag{16}$$

Statistical processing of the obtained results should be carried out for each focusing distance. Namely, the determination of the average value and root-mean-square deviation for the parameters dσ on the entire received data set (different frames for each exposure plus data obtained at different exposures plus the calculation results with various integration areas) (Fig. 14).

As mentioned above, the selection of the region of integration is a separate important process in this method, which can significantly affect the calculation results. The first- and second-order moments are calculated from the measured distributions, and the corresponding integration is performed on a subset of the measured data, the so-called integration zone (see Fig. 14). By choosing this zone incorrectly, we can get a case where the noise will give a significant useless contribution to the final result, which in turn will give an incorrect final result. That is why, in many cases, the correct choice of the integration zone is crucial for obtaining reliable results.

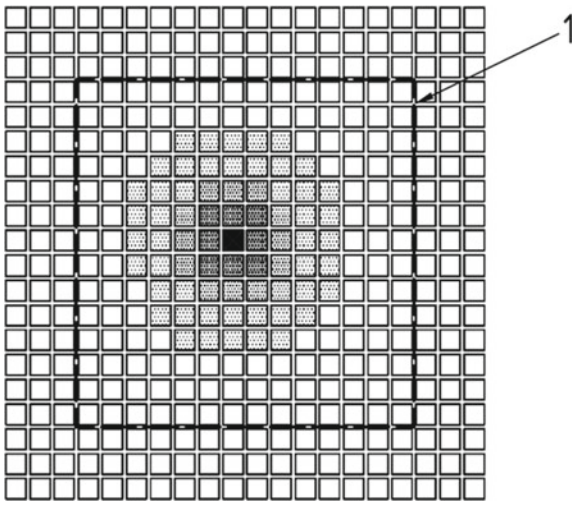

Fig. 14 Selection of the integration zone to determine the dimensions of the focused beam

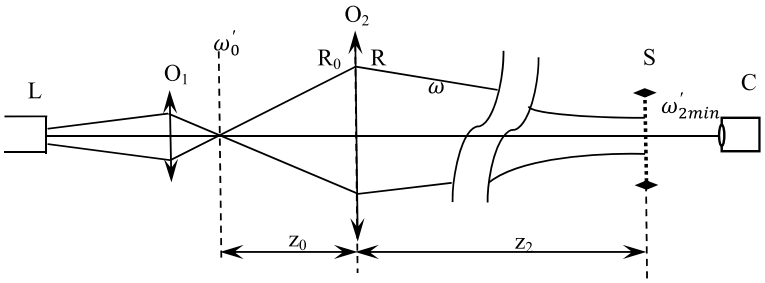

Fig. 15 Optical scheme of a telescopic system for focusing a laser beam on a distant target

To correctly select the integration zone, a procedure must be followed that relates the size and position of the region of integration to the size and position of the measured power density distribution. Since, in the beginning, we do not know the exact data to relate these parameters. Therefore, the method for determining the beam diameter according to ISO [29] uses an iterative procedure. First, all integrations in Eqs. (13) and (14) are performed over the area centered at the beam centroid, while it is limited to three times the beam width in the *x*- and *y*-directions. This region of integration should roughly correspond to the beam length and position. Using it, we will obtain the initial beam position and size values. These values are used to calculate the other regions of integration. Here the iterative method begins as the new beam position and size values are calculated from the new integration domain. This procedure should be repeated until convergence of the result is obtained. Since this technique is developed on an ISO basis, it allows fast and high-accuracy analysis of experimental data even in field conditions. It is worth noting that the additional connection of this program to the video camera, which captures the beam in real experiments, provides the final result in real time. The latter is very convenient for correctly estimating all important parameters during laser beam-focusing experiments.

4 Experiments on Focusing of Laser Radiation on a Real Atmospheric Track

A laboratory stand for metrological support of experimental studies of the laser beam propagation in the atmosphere under the conditions of an open path has been created at the training ground of the National Research Center of Ukraine "INSTITUTE OF METROLOGY"; based on this stand, a 1000 m atmospheric path has been prepared with the possibility of conducting experimental studies of the laser radiation effect on the functional properties of optical-electronic systems under the conditions of an open certified path.

A model setup was assembled to conduct experiments on focusing a laser beam at a given distance (the principle optical scheme, considering the calculations above, is in Fig. 15).

Changing the distance z_0 changes the wave front curvature radius R at the system output after the second lens O_2. Microlens are used for the short-focus lens O_1 (the microlens choice depends on the initial size of the laser beam). For the long-focus lens O_2 with a large aperture, the telephoto lens of the Maksutov MTO1000A system with a focal length of 1084 mm and an output aperture with a diameter of 108 mm are used. The laser beam is focused on the diffuse-scattering screen S set at a given distance z_2 (1000 m). The image from the screen surface is registered by camera C, which is connected to a computer for recording and further image processing or real-time processing. A ZWO ASI120MM-S camera for astronomical observations with a 1/3″ CMOS matrix with a resolution of 1280 × 960 pixels and a 12-bit ADC

is used for image registration. Trial-focusing experiments were performed with a 532 nm, 50 mW laser (a frequency-doubling diode-pumped solid-state laser).

By adjusting the focus of the lens O_2, we achieve the minimum spot size on the screen in the scheme recording part. After that, for the existing state of beam focusing, a range of exposures is selected based on the histogram of intensity values in the camera field of view. For several exposure values, a dark frame with blanked laser beam and five beam spot frames are taken from the selected range for further processing and determination of the focused beam size. Figure 16 shows a fixed image of a focused laser beam at a 1000 m distance with shutter speed of 1 ms. The beam axes and the region of integration are also marked.

The algorithm of the developed program is as follows. First, a preparatory stage is performed, which includes setting the exposure of the camera and obtaining a dark frame. Next, the program in a continuous cycle receives a single frame from the camera and displays it on the screen, subtracts the dark frame, determines the position of the spot in the frame (x_0, y_0) according to the first order moments (13) and, in the zero approach, the diameter of the spot d_σ according to the second-order moments (14). The obtained instantaneous value of the diameter of the spot d_σ is used to calculate the average value of $d_{\sigma 10}$ over ten measurements, which allows to smooth out instantaneous rapid changes in the diameter of the spot. The previously stored minimum value $d_{\sigma \min}$ is compared to the current value $d_{\sigma 10}$ and, if necessary, updated. Also, for clarity and assessment of the correctness of the program, a circle corresponding to the position and diameter of the spot is drawn. After that, the cycle returns to receive the next frame from the camera. The averaging range of ten frames is selected so that the dynamics of the average value of the diameter is commensurate with the dynamics of manual refocusing of the system.

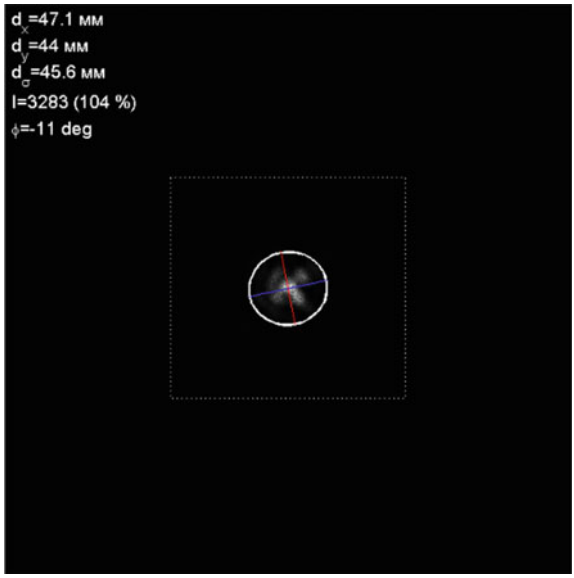

Fig. 16 Measurement of the dimensions of a focused laser beam at a distance of 1000 m

It is worth noting that the image is dynamic, constantly changing, moving, and flickering due to the movement of air flows along the path of the beam. That is why, in order to correctly determine the size of the beam, five frames were recorded for each exposure and several different exposures. Also, due to the lack of relevant data in the technical characteristics of the camera, before starting the experiments, a check of linearity of the matrix response was carried out using calibrated light filters for a possible correction of the signal. According to the results of the measurements, the response of the matrix is linear in the entire range of values. Thus, matrix linearity calibration turned out to be unnecessary.

When processing the measurement data at a distance of 1000 m, the dependence obtained from the previous series of measurements at distances from 50 to 225 m was extrapolated to assess the convergence of the results. This is particularly important given that the 1000 m measurements were conducted under significantly different conditions than the previous series. So, measurements at a distance of 1000 m were carried out during the day in the presence of sunlight. This, firstly, means different atmospheric conditions for the propagation of the beam, and, secondly, significant background illumination of the screen (much higher than in the previous series of experiments). This greatly complicates the compensation of the background when calculating the diameter of the beam.

Also, due to the significantly larger size of the beam, the optical system for recording the beam image was rebuilt and recalibrated to adapt to the new image scale. Therefore, the convergence of new data with the extrapolation of previous results is an indicator of the correct consideration of new circumstances and measurement conditions, as well as evidence of the high robustness of the developed measurement technique and software for determining the beam size in real time. The new approximation of the dependence of beam diameter on the distance, taking into account the full set of data, can be accepted as a refined result.

Figure 17 shows the experimental data of beam diameter measurements at distances from 50 to 1000 m with displayed confidence intervals of 3σ together with the extrapolated dependence obtained from the previous series of measurements and a new approximation obtained taking into account the point 1000 m.

As can be seen from the above graphs, the extrapolation of the previous results describes the experimental data very well, taking into account the point 1000 m (the difference between the extrapolation and the experimental data is significantly less than 3σ), and the inclusion of new data reduces the intercept of the approximation (from 0.8 to 0.49), which indicates a decrease in systematic error.

5 Conclusions

1. On the basis of the conducted research, it was established that the threshold value of the pulse energy of laser radiation, sufficient to disable a video surveillance camera, is equal to about 1 mJ in the camera aperture. At energies in the camera aperture up to 0.14 mJ, the camera is “blinded” at the moment of the pulse,

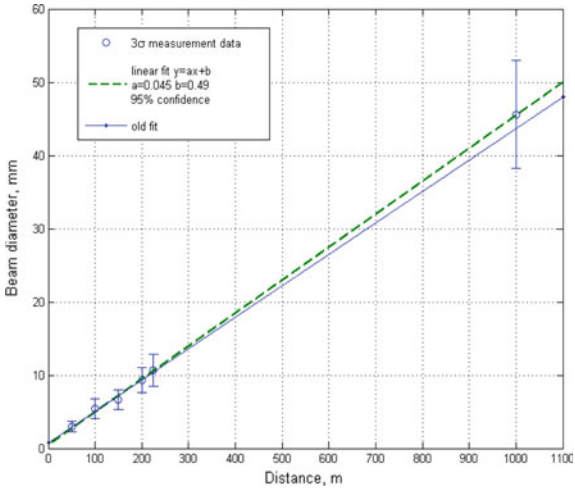

Fig. 17 Experimental data of beam diameter measurements at distances from 50 to 1000 m

but quickly recovers and starts working normally again. At an energy in the camera aperture from 0.14 to 1.7 mJ, irreversible changes in the functioning of the camera are observed, starting with the appearance of dark bands in the image to the complete cessation of image transmission by the camera.

2. Theoretical modeling of the propagation of a laser beam on a real atmospheric path shows that the fluctuation of the refractive index leads to a change in the spatiotemporal properties of laser radiation, so that the turbulent term in the expression for the radius of the focused beam can be dominant compared to the diffraction term. Real experiments on focusing a laser beam at distances of more than 1000 m were conducted, a technique was developed, and software was written to determine the size of the beam in real time. This software is made in the MATLAB mathematical package and uses in its calculations the international standard for laser beam focusing ISO 11146-1:2005. The work of the technique was tested on a real atmospheric track at the National Scientific Center "INSTITUTE OF METROLOGY."

The work was supported by project No. IF-2022/1-2 of the National Academy of Sciences of Ukraine.

References

1. O. Steinvall, The potential role of lasers in combating UAVs, part 1: detection, tracking, and recognition of UAVs, in *Proceedings of the SPIE 11866, Electro-Optical and Infrared Systems: Technology and Applications XVIII and Electro-Optical Remote Sensing XV*, vol. 118660S (12 September 2021). https://doi.org/10.1117/12.2597554
2. O. Steinvall, The potential role of laser in combating UAVs: part 2; laser as a countermeasure and weapon, in *Proceedings of the SPIE 11867, Technologies for Optical Count-measures*

XVIII and High-Power Lasers: Technology and Systems, Platforms, Effects V, vol. 1186707 (12 September 2021). https://doi.org/10.1117/12.2601755
3. C. Westgate, D. James, Visible-band nanosecond pulsed laser damage thresholds of silicon 2D imaging arrays. Sensors **22**, 2526 (2022). https://doi.org/10.3390/s22072526
4. C. Zhang, L. Blarre, R.M. Walser, M.F. Becker, Mechanisms for laser-induced functional damage to silicon charge-coupled imaging sensors. Appl. Opt. **32**, 5201–5210 (1993)
5. B. Schwarz, G. Ritt, B. Eberle, Impact of threshold assessment methods in laser-induced damage measurements using the examples of CCD, CMOS, and DMD. Appl. Opt. **60**, F39–F49 (2021)
6. B. Schwarz, G. Ritt, M. Körber, B. Eberle, Laser-induced damage threshold of camera sensors and micro-opto-electro-mechanical systems, in *Proceedings of the SPIE 9987, Electro-Optical and Infrared Systems: Technology and Applications XIII* (Edinburgh, UK, 28–29 September 2016)
7. C. Burgess, L. Hill, L. Lewins, C. Westgate, Modelled and experimental laser-induced sensor damage thresholds to continuous wave infrared sources, in *Proceedings of the SPIE 10797, Technologies for Optical Countermeasures XV*, vol. 107970T (9 October 2018). https://doi.org/10.1117/12.2326401
8. F. Guo, R. Zhu, A. Wang, X. Cheng, Damage effect on CMOS detector irradiated by single-pulse laser, in *Proceedings of the SPIE 8905, International Symposium on Photoelectronic Detection and Imaging 2013: Laser Sensing and Imaging and Applications*, vol. 890521 (19 September 2013). https://doi.org/10.1117/12.2034724
9. R. Fante, Electromagnetic beam propagation in turbulent media. Proc. IEEE **63**, 1669–1692 (1975)
10. R. Fante, Electromagnetic beam propagation in turbulent media: an update. Proc. IEEE **68**, 1424–144 (1980)
11. Y. Kravtsov, Propagation of electromagnetic waves through a turbulent atmosphere. Rep. Prog. Phys. **55**, 39–113 (1992,1)
12. V.I. Tatarskii, *The Effect of the Turbulent Atmosphere on Wave Propagation* (National Technical Information Service, U.S. Department of Commerce, Springfield, VA, 1971)
13. R. Dashen, Path integrals for waves in random media. J. Math. Phys. **20**, 894–920 (1979)
14. M. Gracheva, A. Gurvich, Strong fluctuations in the intensity of light propagated through the atmosphere close to the earth. Sov. Radiophys. **8**, 511–515
15. GOST 2.701–2008. http://docs.cntd.ru/document/1200069439
16. G.P. Berman, A.A. Chumak, Phys. Rev. A **74**, 013805 (2006)
17. G. Berman, A. Chumak, Influence of phase-diffuser dynamics on scintillations of laser radiation in Earth's atmosphere: long-distance propagation. Phys. Rev. A **79**, 063848 (2009,6). https://doi.org/10.1103/PhysRevA.79.063848
18. O. Chumak, R. Baskov, Strong enhancing effect of correlations of photon trajectories on laser beam scintillations. Phys. Rev. A **93**, 033821 (2016,3)
19. O. Chumak, E. Stolyarov, Phase-space distribution functions for photon propagation in waveguides coupled to a qubit. Phys. Rev. A **88**, 013855 (2013,7). https://doi.org/10.1103/PhysRevA.88.013855
20. O. Chumak, E. Stolyarov, Photon distribution function for propagation of two-photon pulses in waveguide-qubit systems. Phys. Rev. A **90**, 063832 (2014,12). https://doi.org/10.1103/PhysRevA.90.063832
21. R. Baskov, O. Chumak, Laser-beam scintillations for weak and moderate turbulence. Phys. Rev. A **97**, 043817 (2018,4). https://doi.org/10.1103/PhysRevA.97.043817
22. A. Rarenko, A. Tarasenko, A. Chumak, Electron-photon fluctuations and their role in the photomagnetic effect. Ukr. J. Phys. **37**, 1577 (1992)
23. M. Scully, M. Zubairy, *Quantum Optics* (Cambridge University Press, 1997)
24. S. Kogan, S. Kogan, *Electronic Noise and Fluctuations in Solids* (Cambridge University Press, 1996)
25. A. Bharucha-Reid, S. Chatterji, *Probabilistic Analysis and Related Topics* (Academic Press, 1978)

26. R. Baskov, O. Chumak, Fourth-order moment of the light field in atmosphere. J. Opt. **22**, 105603 (2020,9). https://doi.org/10.1088/2040-8986/abb2f1
27. V.L. Andriichuk, O.O. Chumak, L.A. Derzhypolska, I.V. Matsniev, *Laser Beam Fluctuations for Long Distance Propagation in the Turbulent Atmosphere* (2022). https://arxiv.org/abs/2206.02487
28. R. Dashen, Path integtals for waves in random media. J. Math. Phys. **20**, 894920 (1979)
29. ISO 11146–1:2005, Lasers and Laser-Related Equipment Test Methods for Laser Beam Widths, Divergence Angles and Beam Propagation Ratios Part 1: Stigmatic and Simple Astigmatic Beams. https://www.iso.org/standard/33625.html

Korteveg-de-Vries Soliton Equation in Pulse Wave Modelling

S. V. Vasylyuk, D. V. Zaitsev, and A. V. Brytan

Abstract In the early stages of blood flow research, the widely used Bernoulli equation was applied to describe blood behavior in large vessels, while the Poiseuille formula was used to estimate capillary flow behavior within a single vessel, accounting for the significant resistance of blood. These expressions were derived assuming a steady laminar incompressible flow, with fluid particles moving along constant streamlines and the velocity profile in the radial direction u(r) remaining constant in time and not changing in the axial flow direction at a given point [1]. However, such models fail to capture the emergence and movement of arterial pulse waves, which are a critical and versatile physiological phenomenon that have garnered significant interest for investigation and modeling. In this section, we will explore the use of soliton theory for modeling pulse waves. The underlying concept is that the behavior of a real pulse wave shares many similarities with solitons. In the realm of mathematics, solitons are defined as localized stationary solutions to nonlinear partial differential equations or their generalizations, such as differential-difference or integro-differential equations. Notably, various physical situations and phenomena can be described by the same equations, including the Korteweg-de Vries equation, the Sine-Gordon equation, and the Schrödinger nonlinear equation. Specifically, the elastic interaction between solitons and local perturbations plays a crucial role in this context. The method of pulse waves modeling based on soliton solution of Korteweg-de Vries equation is considered in this work, and test calculations in Maple 8 environment are made. The results obtained allow us to speak about the

S. V. Vasylyuk (✉) · A. V. Brytan
Physics Faculty, Taras Shevchenko National University of Kyiv, 0322 Hluskova Ave. 4-b, Kyiv, Ukraine
e-mail: s.vasyliuk@nubip.edu.ua

D. V. Zaitsev
Shupyk National Healthcare University of Ukraine, Saksaganskogo Street, 75, Kyiv 01033, Ukraine
e-mail: dmytro_zaitsev@nuozu.edu.ua

S. V. Vasylyuk
IT Department, National University of Life and Environmental Sciences of Ukraine, Heroyiv Oborony St., 15, Kyiv 03041, Ukraine

O. Fesenko and L. Yatsenko (eds.), *Nanoelectronics, Nanooptics, Nanochemistry and Nanobiotechnology, and Their Applications*, Springer Proceedings in Physics 297,
https://doi.org/10.1007/978-3-031-42708-4_21

applicability of soliton theory for pulse wave modeling. It is planned to analyze the possibility of further application of N-soliton solution for medical purposes.

1 Introduction

Historically the beginning of the investigation of blood flow takes off the implementation famous Bernoulli equation for describing blood behavior in large vessels. Also for initial estimating of capillary flow behavior with significant blood resistance inside single vessel Poiseuille formula is used. Both expressions are obtained for a case of the velocity profile calculating for a steady laminar incompressible flow, by solving the force balance applied to the fluid. In this assumption, the fluid particles move along constant streamlines while the velocity profile in the radial direction $u(r)$ does not change in the axial flow direction and for a certain point it is constant in time [1]. However, such types of models cannot allow to describe the emergence and subsequent movement of arterial pulse waves. By the way, the importance and versatility of this physiological phenomenon cause the significant interest in its investigation and modeling [2].

From the physical point of view, blood flow is a rather complex process; many researchers even call it the third mode of flow. Difficulties in modeling this process are caused by many factors: both purely "physical" (e.g., the fact that blood itself is non-Newtonian fluid, despite it flows through blood vessels) and the need to take into account various regulatory functions. For this reason, most models based on the theory of mathematical hemodynamics are quite complicated and difficult to apply.

There is a huge amount of mathematical models for behavior modeling of arterial pulse wave. Actually, this set can be divided into two branches. First is applied to the initiation and propagation of pulse wave in aorta and cardiovascular system in general. One of the simplest models in this area is the Windkessel model [3] which gives the expression for pressure in aorta during cardiac cycle as a function of cardiac stroke time dependence form. This is also known as two element's model or analog model. According to the form of mathematical apparatus used in this model, it is possible to draw analogy between blood and electric circuit. This idea became a basis of consideration of cardiovascular system as analog of electric circuit. One of the classic models is the model proposed by Westerhof [4]. Westerhof has interpreted the pressure and flow pulses as complex waves consisting of a forward traveling and a backward traveling component. The forward wave is associated with the ejection of blood from the heart and the backward wave is associated with physical reflections caused by the mechanical discontinuities in the arterial tree. In the diastolic phase, both waves are considered to have destructive superposition, whereas in the systolic phase, both waves are considered to have constructive superposition. The constructive superposition can also explain the increase of peak pressure of the waveform during its propagation in some arteries which is referred to as steepening. Such representation of cardiovascular system further also was developed into approach of lamped [5, 6] and distributed [7] parameter system One of the main goals of such

modeling is obtaining a realistic and detailed pulse wave profile during cardiac cycle in aorta and explain its further propagation. The use of this approach makes it possible to simplify the consideration of such an effect as the expansion of the vessel lumen during the movement of a pulse wave.

But, if we consider the blood flow and wave propagation in a separate vessel, the application of the hydrodynamic equation becomes a more convenient and rigorous approach [8]. Simultaneously for completing this system of equations, it is necessary to add the elasticity equation for tube wall motion under varying internal pressure. The vessel walls are often assumed to be Hookean material, namely linear relation between stress and strain. However, taking into account the interaction of blood flow with a deformable vessel wall significantly complicates the distribution of this problem, which forces us to use various model representations [9].

This part considers the approach of modeling pulse waves using soliton theory. The basic idea is that the nature of a real pulse wave is very similar to the properties of solitons. The central role is played by the properties of the elastic interaction between solitons and solitons with local perturbations [10–12].

2 Properties of Solitons. The Possibility of Using KdV Equation to Describe the Pulse Wave

Soliton is a localized stationary or stationary on average perturbation of a homogeneous or spatially periodic nonlinear medium [10]. Up to the beginning of the 1960s, soliton was called a soliton wave—a wave packet of a constant shape, propagating with a steady speed over the surface of a heavy liquid of a finite depth and in plasma. Nowadays, many different physical objects fall underneath the definition of soliton. The first classification of soliton can be made according to the number of spatial dimensions, along which the stationary perturbation of a nonlinear medium is localized. The one-dimensional soliton includes classical soliton waves in liquids, domain walls in ferro- and antiferromagnetics, 2p-pulses and envelope solitons in nonlinear optics [13–15].

In mathematical terms, solitons are localized stationary solutions of nonlinear partial differential equations or their generalizations (differential-difference, integro-differential, etc., equations). In many cases different physical situations and phenomena are described by the same equations, e.g., the Korteweg-de Vries equation, the Sine–Gordon equation, the Schrödinger nonlinear equation, the Kadomtsev–Petviashvili equation [10–14]. Linear equations (except the one-dimensional wave equation) have no localized stationary solutions. Solitons are essentially nonlinear objects whose behavior and properties are fundamentally different from the behavior of wave packets of small amplitude. The difference is especially strong if the soliton has a topological charge; i.e., if the configuration of the wave field in the presence of the soliton is topologically different from the configuration of the unperturbed state. So, a number of equations having soliton solutions belong to the class of equations

where the inverse scattering problem is applicable and most of them are integrable Hamiltonian systems [15–18].

In [10], the process of fluid flow through an elastic thin-walled tube is considered. The nonlinear differential equations of these processes are derived; the modeling of a solitary (pulse wave) is performed on the basis of the Korteweg-de Vries models and the modified nonlinear Schrödinger equation. The main advantage of these models is that the pulse wave propagation process is considered quite deeply when they are derived. These models describe only some of the phenomena observed in the cardiovascular system due to the complexity of the blood flow process.

Here we consider the pulse wave without taking into account the processes of blood flow regulation; we consider the pulse wave as the propagation of a solitary (pulse) wave in an elastic thin-walled tube. Based on this, we chose the Korteweg-de Vries equation as a model:

$$u_t + 6uu_x + u_{xxx} = 0. \tag{1}$$

The dimensional equation KdF for the velocity $u(t, x)$ for perturbation in a channel with a rectangular cross section has the form.

Equation (1), as one of the partial solutions, has the so-called soliton solution of the form:

$$u(t, x) = \frac{A}{ch^2[b(x - vt)]}, \tag{2}$$

in which A, b and v are parameters determined by the direct substitution (2) in (1). In this case, A and v have the dimension of velocity (v is the speed of the soliton wave), and b has the dimension of length.

In Eq. (1), h is the dimensional depth of the channel. As for the speed u_0, which is included in (1), there are two versions of its physical content.

This is the speed of its own flow in the channel, which is considered a given value. In the case of the cardiovascular system of its own speed, independent of the system itself, no, so this content is not suitable for speed u_0.

This is the speed that is a consequence of the desired speed $u(t, x)$ and can be interpreted as the speed of capture (speed of entrainment). It must be defined together with the solution $u(t, x)$ and in this sense is a certain analog of eigenvalue. This case will be considered as one that forms the blood flow.

We will simulate the pulse wave with a soliton solution of the KdF equation. Since no one has deduced the KdF equation for a channel with a round cross section, we will use a simple analogy, as a result of which we can postulate the equation:

$$u_t + uu_x + u_0 Su_{xxx} = 0, \tag{3}$$

in which S is the cross-sectional area of the aorta in the immediate vicinity of the heart (hereinafter we can take into account that SS can be a function of u due to

vascular elasticity, and velocity u_0 can be a function of x in the transition from aorta to arteries, capillaries, etc.).

For solution (2), we consistently find:

$$u_t = 2Abv\frac{sh[b(x-vt)]}{ch^3[b(x-vt)]};$$

$$uu_x = -2A^2b\frac{sh[b(x-vt)]}{ch^5[b(x-vt)]};$$

$$u_{xxx} = -8Ab^3\frac{sh[b(x-vt)]}{ch^3[b(x-vt)]} + 24Ab^3\frac{sh[b(x-vt)]}{ch^5[b(x-vt)]}.$$

Substituting the right-hand sides of these three relations in (3), we find the equation:

$$\left\{2Abv - 8Ab^3u_0S\right\}\frac{sh[b(x-vt)]}{ch^3[b(x-vt)]} + \left\{24Ab^3u_0S - 2A^2b\right\}\frac{sh[b(x-vt)]}{ch^5[b(x-vt)]} = 0,$$

which can be satisfied by equating to zero both curly braces. As a result, we obtain two ratios:

$$v - 4b^2u_0S = 0; \tag{4}$$

$$12b^2u_0S - A = 0, \tag{5}$$

which includes four unknown quantities: A, b, v, and u_0. Equation (4) makes it possible to immediately find the blood flow velocity u_0, which is stimulated by the soliton velocity v:

$$u_0 = \frac{v}{4Sb^2}. \tag{6}$$

Substituting this in Eq. (5), we can find the amplitude factor A:

$$A = 3v. \tag{7}$$

Now only two values remain undefined: the pulse rate of the soliton v and the parameter b, which determines the width of the soliton.

As for the parameter b, it is quite obvious from Eq. (6) that in the general case it can be sought in the form:

$$b = \frac{\beta}{\sqrt{S}}, \tag{8}$$

where β is a dimensionless indefinite parameter that can be interpreted as a dimensionless representation of factor b. Taking into account (8), the relation (6) takes the form:

$$u_0 = \frac{v}{4\beta^2}. \tag{9}$$

Equation (9) shows that the parameter β satisfies the condition $\beta > \frac{1}{2}$, since the blood flow velocity u_0 is always less than the pulse velocity of the soliton v.

Solution (2), taking into account (7) and (8) takes the form:

$$u(t, x) = \frac{3v}{ch^2\left(\beta \frac{x-vt}{\sqrt{S}}\right)}. \tag{10}$$

We will determine the two remaining parameters (β and v) based on known physiological facts.

In particular, it is known that the pulse velocity of the soliton v in the aorta (at the exit of the heart) is 5-8 m/s [1-4] (while the blood flow velocity u_0 in it is 0.5-1 m/s [1-4] (I found the figure in [1-4]). That is, the pulse rate v at the exit of the heart is 10/6 times greater than the current velocity u_0. For certainty, we will use the value $(v/u_0) = 16$, which corresponds to the pulse rate of the soliton $v = 8$ m/s.

$$\beta = \frac{1}{2}\sqrt{\frac{v}{u_0}},$$

Therefore, using the formula, obtained from (9), we can find: $\beta = 2$.

The last thing left to do is check the results, knowing the normal heart rate—1 beat per second. This means that between two consecutive pulse waves in the form of a soliton (between two heartbeats) the period should be: $T = 1$ s. The test comes down to the fact that with such a pulse, the solitons should not intersect with great accuracy (then the condition of separation (solitude) of the soliton wave is met). To perform this test, use the solution (10).

Before we put this in (10) $x = 0$, on the grounds that the point of exit of the aorta from the heart will be considered the origin. Then from (10) we obtain a special (not arbitrary) soliton-like boundary condition:

$$u(t, 0) = \frac{3v}{ch^2\left(\frac{\beta vt}{\sqrt{S}}\right)}, \tag{11}$$

which in this consideration is considered to form a physiologically healthy heart rhythm, and any deviations from this limit condition will lead to arrhythmias (more on this later). If we put $t = T$ in the argument of this boundary condition, then this argument takes the form:

$$\frac{\beta v T}{\sqrt{S}}. \tag{12}$$

The only value in this argument that has not yet been discussed is the cross section S of the artery directly at the exit of the heart (at the point $x = 0$). For it, we use the value $S \sim 4 \times 10^{-4}$ m^2. Then the value of argument (12) can be estimated by substituting the numerical values of all quantities: $\beta = 2$, $v = 8$ m/s, $T = 1$ s, $S = 4$. As a result, we will have

$$\frac{\beta v T}{\sqrt{S}} = 800.$$

If we use the analytical or graphical representation of the hyperbolic cosine, it is obvious that as the value of argument (12) increases, the function $ch\ (x)$ increases in proportion to e^x. That is, for the value of $ch\ (800) \to \infty$, or $1/(ch^2(800) \to 0)$ obtained here. This means that the solution (10) in the form of a sequence of one-soliton pulse waves at the obtained parameters is physically correct, because with a good margin provides separation of each soliton, as well as blood flow velocity $u_0 = 0.5$ m/s at the beginning of the aorta.

If the boundary condition (11) is violated, i.e., it ceases to be soliton-like, then other solutions of Eq. (3) are realized: multi-soliton solutions with different pulse velocities v, or solutions in the form of cnoidal waves. The latter, however, also require a special boundary condition.

3 Soliton Solution of the Korteweg-de Vries Equation by Perturbation Method

The Korteweg-de Vries equation is considered:

$$u_t + 6uu_x + u_{xxx} = 0 \tag{13}$$

In [10, 11], the method of forming the N-soliton solution of this equation is presented. The general solution of the Korteweg-de Vries equation consists of a soliton and a non-soliton part. In our case, we consider a solution in which the local perturbations (non-soliton part) are negligibly small. That is, we are building a somewhat idealized model that does not take into account small local perturbations. Hirota [11] showed that in general the N-soliton solution has the form:

$$u = 2\frac{\mathrm{d}^2}{\mathrm{d}x^2} \ln F, \tag{14}$$

where F is the determinant of some matrix [11].

Substituting (14) into (13), once integrating and assuming the integration constant equal to zero, we obtain:

$$F_{xt}F - F_xF_t + F_{xxxx}F - 4F_{xxx}F_x + 3F_{xx}^2 = 0. \tag{15}$$

For further analysis, it is convenient to enter the operator:

$$D_x^m D_t^n ab = (\partial_x - \partial_{x'})^m (\partial_x - \partial_{x'})^n a(x,t)b\big(x',t'\big)\Big|_{\substack{x'=x\\ t'=t}}. \tag{16}$$

So, Eq. (15) can be rewritten as:

$$\big(D_xD_t + D_x^4\big)F \cdot F = 0. \tag{17}$$

Next, suppose that the function F could be represented as a formal series:

$$F = 1 + \varepsilon f^{(1)} + \varepsilon^2 f^{(2)} + \cdots, \tag{18}$$

where

$$f^{(1)} = \sum_{i=1}^{N} e^{\eta_i}, \quad \eta_i = k_i x - \omega_i t + \eta_i^0, \tag{19}$$

where $k_i, \omega_i, \eta_i^{(0)}$—are constants.

In the case of the Korteweg-de Vries equation, this formal series ends. Indeed, substituted (18) into (17), we found

$$\big(D_xD_t + D_x^4\big)\big(1 + \varepsilon f^{(1)} + \varepsilon^2 f^2 + \cdots\big)\big(1 + \varepsilon f^{(1)} + \varepsilon^2 f^2 + \cdots\big) = 0$$

And equated to zero, the coefficients for each degree of ε, we obtained

$$O(1)\colon 0 = 0 \tag{20a}$$

$$O(\varepsilon)\colon 2\big(\partial_x\partial_t + \partial_x^4\big)f^{(1)} = 0 \tag{20b}$$

$$O\big(\varepsilon^2\big)\colon 2\big(\partial_x\partial_t + \partial_x^4\big)f^{(2)} = -\big(D_xD_t + D_x^4\big)f^{(1)}f^{(1)} \tag{20c}$$

$$O\big(\varepsilon^3\big)\colon 2\big(\partial_x\partial_t + \partial_x^4\big)f^{(3)} = -2\big(D_xD_t + D_x^4\big)f^{(1)}f^{(2)}. \tag{20d}$$

Equation (20b) is a homogeneous equation. As a solution of this equation, we took Eq. (19). If we try to continue the calculations of the next parts of the series, starting with solution Eq. (7) for an arbitrary random N, we could encounter the

analytical difficulties. More often, we can obtain equations solutions for $N = 1, 2$, and then hypothesize the structure of the solution for an arbitrary random N and prove it by induction method. For $N = 1 f^{(1)} = e^{\eta_1}$. Then it follows from Eq. (8b) that $\omega_1 = -k_1^3$. We could obtain $f^{(2)}$ from the relation (8c), which reduces to $\left(\partial_x \partial_t + \partial_x^4\right) f^{(2)} = 0$.

So $f^2 = 0$. and the series sequence breaks off. Therefore, for $N = 1$ we have:

$$F_1 = 1 + e^{\eta_1}, \quad \omega_1 = -k_1^3, \quad u = \frac{k_1^2}{2} \operatorname{sech}^2 \frac{1}{2}\left(k_1 x - k_1^3 t + \eta_1^{(0)}\right)$$

For $N = 2$, we take Eq. (20b) as a solution

$$f^{(1)} = e^{\eta_1} + e^{\eta_2}, \quad \eta_i = k_i x - k_i^3 t + \eta_i^{(0)}$$

Then (20c) reduces to the equation:

$$2\left(\partial_x \partial_t + \partial_x^4\right) f^{(2)} = -2\left((k_1 - k_2)(-\omega_1 + \omega_2) + (k_1 - k_2)^4\right) e^{\eta_1 + \eta_2}$$

That is have a solution [3]

$$f^{(2)} = e^{\eta_1 + \eta_2 + A_{12}} e^{A_{ij}} = \left(\frac{k_i - k_j}{k_i + k_j}\right)^2 \tag{21}$$

(note that $k_1 \neq k_2$). Substituting $f^{(1)}$, $f^{(2)}$ in (20d), we make sure that the right-hand side of (8d) is zero, so let's take it $f^{(3)} = 0$. Thus, for $N = 2$

$$F_2 = 1 + e^{\eta_1} + e^{\eta_2} + e^{\eta_1 + \eta_2 + A_{12}}$$

The function $u = 2d^2(\ln F_2)/\mathrm{d}x^2$ corresponds to the two-soliton solution of the Korteweg-de Vries equation. Performing similar calculations for $N = 3$, we obtain:

$$F_3 = 1 + e^{\eta_1} + e^{\eta_2} + e^{\eta_1 + \eta_2 + A_{12}} + e^{\eta_1 + \eta_2 + A_{13}} + e^{\eta_2 + \eta_3 + A_{23}} + e^{\eta_1 + \eta_2 + \eta_3 + A_{12} + A_{13} + A_{23}} \tag{22}$$

where the coefficients A_{ij} are determined by Formula (21) (Function u dependence of the coordinate is obtained on the basis of Eqs. (14) and (22) is shown on Fig. 1).

Based on the above, it is hypothesized that the structure of the general N-soliton solution has the form [3]:

$$F_N = \sum_{\underline{\mu}=0,1} \exp\left(\sum_{i=1}^{N} \mu_i \eta_i + \sum_{1 \leq i < j}^{N} \mu_i \mu_j A_{ij}\right),$$

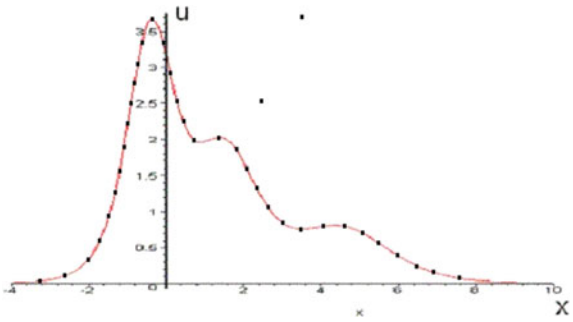

Fig. 1 Function u dependence of the coordinate is obtained on the basis of Eqs. (14) and (22)

where the sum of $\underline{\mu}$ runs on all sets μ_i, $i = \overline{1, \ldots, N}$. Note that μ_i, $i = \overline{1, \ldots, N}$—they are associated with the phase shift of solitons during scattering.

4 Application of the Theory of Solitons to Detailed Modeling of a Pulse Wave

It is assumed that the pulse wave is a set of pulses interacting with each other in time. Since a soliton is a solitary wave that elastically interacts with arbitrary local perturbations, it makes sense to consider the system of interacting solitons as a model. That is, we put the correspondence between: 1 pulse—for soliton. So, the N-soliton solutions of the Korteweg-de Vries equation are used as the analytical form of soliton waves [10].

$$u = 2\frac{\mathrm{d}^2}{\mathrm{d}x^2} \ln F_N$$

The potential u is a complex function represented as a combination of exponential functions with base e. The obtained solution u includes $3N$ parameters, through which variables $\eta_i = k_i x + \omega_i t - h_i^{(0)}$ are determined, where k_i, ω_i, $\eta_i^{(0)}$ are the parameters of this system.

The following properties of solitons were used:

(1) The amplitude of the ith soliton, which does not closely interact with other solitons, is directly proportional to the corresponding parameter k_i, namely

$$u_{\max i} = \frac{1}{2}k_i^2.$$

(2) The argument of the point of maximum of the ith soliton is determined by the following expression:

$$x_{\max i} = \frac{-\omega_i t + h_i^{(0)}}{k_i}.$$

(3) The velocity in phase c is defined as the ratio of the coefficients at $\boldsymbol{x}$ and $\boldsymbol{t}$. For the ith soliton, it is equal.

$$c_i = {}^{\omega_i}\!/_{k_i}$$

For this system, all phase velocities are considered to be the same, since we assume that the real pulse wave does not change in time or, at least, for some period of time. That is $c_1 = c_2 = \cdots = c_N$

Using these properties, we obtain a system of equations as in [3]:

$$\begin{cases} \frac{1}{2}k_i^2 = u_i, \quad i = \overline{1, N}; \\ -\frac{-\omega_i t + h_i^{(0)}}{k_i} = x_i, \quad i = \overline{1, N} \\ \frac{\omega_i}{k_i} = \frac{\omega_{i+1}}{k_{i+1}}; \quad i = \overline{1, N-1} \end{cases}$$

As the values of the local maxima, we take the values of the coordinates of the vertices of each "hump" of the real pulse wave obtained experimentally.

5 The Soliton Theory Application to Intermittent Pneumatic Compression; Influence on Thrombus Release

The resulting system consists of $3N - 1$ equations, and we have $3N$ unknowns; therefore, one of the parameters we choose arbitrarily. Take $\omega_1 = 1$, then this system is solved definitely. Solving this system, we could obtain the solution of Eq. (1) that is agreed with the theory in [10] ideas of applying the apparatus of mathematical modeling in medicine of pulse waves and in pneumatic device.

A recent survey of healthcare practitioners in North China revealed that the main concern with intermittent pneumatic compression (IPC)—supply is the fear of a thrombus release due to the soliton waves appearing in veins. This was expected by 35% of respondents [18]. And this is actually one of the first objections to discuss when getting acquainted with IPC in Ukraine. To assess the incidence of symptomatic pulmonary embolism (PE) in patients undergoing IPC therapy we performed a literature review searching the MEDLINE database with no language restrictions from January 1, 2017, until December 31, 2020. We consider two scenarios: when IPC starts after the onset of thrombosis, and when thrombosis occurs after IPC starts.

The first option is more often in unfavorable conditions, when an adequate diagnosis of thrombosis meets difficulties. These can be cases with mute blood clots, with low scores on the thrombotic risk scale, when it is not possible to perform routine ultrasound diagnostics, or when some vessels are less visible on the sensor.

Table 1 Incidence of symptomatic PE in patients undergoing IPC therapy

	Patients with IPC		Patients without IPC	
	Total	Symptomatic PE cases	Total	Symptomatic PE cases
Neurosurgery, neurology [20, 21]	3870	10 (0.26%)	3218	37 (1.15%)
Orthopedic, traumatology [22–24]	607	2 (0.33%)	1238	15 (1.21%)
Oncology [25–27]	688	5 (0.73%)	370	7 (1.9%)
Other [27, 28]	20,324	6 (0.03%)	10,819	6 (0.06%)
Total	25,489	23 (0.09%)	15,645	65 (0.42%)

In 2015, the CLOTS-3 study report appeared. In stroke, thromboprophylaxis by IPC begins post-factum, when the thrombotic risk is already increasing. Although the authors excluded patients with symptoms of pre-existing thrombosis, the risk of having a thrombus was not entirely low. Initial ultrasound was not performed, and the control one was unable to fully visualize the veins in almost half of the patients. Commenting on this, the authors noted: "There was a concern that the application of IPC to patients who may already have a deep vein thrombosis might displace the thrombus and increase the risk of PE. However, this potential risk has not been documented in the randomized controlled trials so far. We have not identified any case reports that provide convincing evidence that this has occurred" [19].

The second scenario is more typical when the IPC is used for thromboprophylaxis. We identified nine trials with 40,667 participants, and the main results are presented in Table 1.

Although thrombosis is more common with IPC than with heparin, dangerous complications such as clinical or fatal PE occur in less than 1% of cases. Moreover, some sources [20, 21, 24, 28], show that the risk of PE with heparin may be higher than with IPC. This is probably because the IPC mimics physical activity. A thrombus that grows during IPC therapy is adapted to motor load, while the anatomical structure of a "heparin" thrombus may not be strong enough for soliton fluctuations. Another reason may be that during IPC, the thrombus progresses mainly in those veins unreachable to the external mechanical pressure. Therefore, IPC therapy just does not interfere with such a blood clot, in particular, does not break it.

6 Conclusion

At the moment, there are many systems analyzing pulse waves (in most cases, mathematical statistics methods are used for the analysis). The idea of applying the apparatus of mathematical modeling in this topic seems to us auspicious, but most of mathematical models are quite complicated and difficult to apply in practice.

The method of pulse waves modeling based on soliton solution of Korteweg-de Vries equation is considered in this work, test calculations in Maple 8 environment are made. The results obtained allow us to speak about the applicability of soliton theory for pulse wave modeling. It is planned to analyze the possibility of further application of *N*-soliton solution for medical purposes.

A significant causal relationship between PE and IPC procedures has not yet been established. The incidence of symptomatic PE developing during IPC therapy is 0.03–0.73% and varies depending on the patient profile. However, caution should be when prescribing IPC therapy for ones with suspected venous thrombosis. More thorough further research is desirable in soliton wave's usage in medicine.

References

1. A. Chalyi, (ed.), *Medical and Biological Physics (Textbook for Students of Higher Medical Institutions)* (Nova Knyha, 2017)
2. M. Koen, A. Jordi, P. Joaquim, K. Ashraf, S. Patrick, V. Pascal, P. Kim, S. Spencer, Pulse wave propagation in a model human arterial network: assessment of 1-D numerical simulations against itro measurements. J. Biomech. **40**(15), 3476–3486 (2007)
3. R. Burattini, Identification and physiological interpretation of aortic impedance modeling, in *Modelling Methodology for Physiology and Medicine*, eds. by E. Carson, C. Cobelli (Academic, San Diego, 2001), Chap. 8, pp. 213–252
4. N. Westerhof, P. Sipkema, G.V.D. Bos, G. Elzinga, Forward and backward waves in the arterial system. Cardiovasc. Res. **6**(6), 648–656 (1972)
5. K. Naik, P. Bhathawala, Mathematical modeling of human cardiovascular system: a lumped parameter approach and simulation. World Academy of Science, Engineering and Technology, Open Science Index 122. Int. J. Math. Comput. Sci. **11**(2), 73–84 (2017)
6. J.E. Traver, C. Nuevo-Gallardo, I. Tejado, J. Fernández-Portales, J.F. Ortega-Morán, J.B. Pagador, B.M. Vinagre, Cardiovascular circulatory system and left carotid model: a fractional approach to disease modeling. Fractal Fractional **6**(2), 64 (2022)
7. X. Hanguang, A. Alberto, Z. Mingfu, Modeling and hemodynamic simulation of human arterial stenosis via transmission line model. J. Mech. Med. Biol. **16**(5), 1650067 (2015)
8. A.K. Khalid, Z.S. Othman, C.T.M.N.M. Shafee, A review of mathematical modelling of blood flow in human circulatory system. J. Phys. Conf. Ser. **L1988**, l012010 (2022)
9. D. Bessems, M. Rutten, F. Van de Vosse, A wave propagation model of blood flow in large vessels using an approximate velocity profile function. J. Fluid Mech. **580**, 145–168 (2007)
10. A.N. Volobuev, Fluid flow in tubes with elastic walls. Phys. Usp. **38**(2), 169 (1995)
11. M. Ablovitz, H. Sigur, *Solitons and the Method of the Inverse Problem* (Mir, Moscow, USSR, 1987)
12. T.G. Darmaev, A.S. Tsybikov, B.V. Khabituev, Mathematical simulation of pulse waves based on the theory of solitons and Korteweg-de Vries equation. Matematicheskoe modelirovanie pulsovyih voln na osnove teorii solitonov i uravneniya Kortevega de Friza//Vestnik BGU **9**(1), 35–39 (2014)
13. A. Newell, *Solitons in Mathematics and Physics* (Mir, Moscow, USSR, 1989)
14. J.L. Lam, *Vvedenie v teoriu solitonov [Introduction to the Theory of Solitons]* (Mir, Moscow, USSR, 1983)
15. B.E. Zakharov (ed.), *Teoriya solitonov: metod obratnoy zadachi [Theory of Solitons: Method of the Inverse Problem]* (Nauka, Moscow, USSR, 1980)
16. S.E. Trullinger, V.E. Zakharov, V.L. Pokrovsky (eds.), *Solitons* (Elsevier, Amsterdam, 1986)

17. Y.S. Kivshar, B.A. Ma1omed, Dynamics of solitons in nearly integrale systems. Rev. Mod. Phys. **61**, 763 (1989)
18. B. Sun et al., A survey of knowledge and application of mechanical thromboprophylaxis among the medical staff of intensive care units in North China. Clin. Respir. J. **12**(4), 1591–1597 (2018)
19. M. Dennis et al., The clots in legs or stockings after stroke (CLOTS) 3 trial: a randomised controlled trial to determine whether or not intermittent pneumatic compression reduces the risk of post-stroke deep vein thrombosis and to estimate its cost-effectiveness. Health Technol. Assess. **19**, 1–90 (2015)
20. I.D. Stulin et al., Profilaktika trombozov ven nizhnikh konechnosteĭ i tromboémbolii legochnoĭ arterii u nevrologicheskikh bol'nykh v usloviiakh reanimatsionnogo otdeleniia s ispol'zovaniem preryvistoĭ pnevmokompressii" [Prevention of venous thrombosis of the lower extremities and pulmonary embolism in neurological patients in the intensive care unit using intermittent pneumatic compression]. Zhurnal nevrologii i psikhiatrii imeni S.S. Korsakova. **118**,10, 25–29 (2018)
21. S. Chibbaro et al., Evolution of prophylaxis protocols for venous thromboembolism in neurosurgery: results from a prospective comparative study on low-molecular-weight heparin, elastic stockings, and intermittent pneumatic compression devices. World Neurosurg. **109**, e510–e516 (2018)
22. K.I. Kim et al., Pneumatic compression device does not show effective thromboprophylaxis following total knee arthroplasty in a low incidence population. Orthop. Traumatol. Surg. Res. **105**(1), 71–75 (2019)
23. V. Tyagi et al., The role of intraoperative intermittent pneumatic compression devices in venous thromboembolism prophylaxis in total hip and total knee arthroplasty. Orthopedics **41**(1), e98–e103 (2018)
24. J.H. Nam et al., Does preoperative mechanical prophylaxis have additional effectiveness in preventing postoperative venous thromboembolism in elderly patients with hip fracture?—Retrospective case-control study. PLoS One **12**(11), e0187337 (2017)
25. T. Hata et al., Efficacy and safety of anticoagulant prophylaxis for prevention of postoperative venous thromboembolism in Japanese patients undergoing laparoscopic colorectal cancer surgery. Ann. Gastroenterol. Surg. **3**(5), 568–575 (2019)
26. Y.J. Jung et al., Venous thromboembolism incidence and prophylaxis use after gastrectomy among korean patients with gastric adenocarcinoma: the PROTECTOR randomized clinical trial. JAMA Surg. **153**(10), 939–946 (2018)
27. J. Dong et al., Effect of low molecular weight heparin on venous thromboembolism disease in thoracotomy patients with cancer. J. Thorac. Dis. **10**(3), 1850–1856 (2018)
28. P. Dhakal et al., Effectiveness of sequential compression devices in prevention of venous thromboembolism in medically ill hospitalized patients: a retrospective cohort study. Turk. J. Haematol. **36**(3), 193–198 (2019)

Nanooptics

Spectral Properties of Thin Films of Squaraine Dyes, Deposited on Silver and Gold Nanoparticles

A. M. Gaponov, O. L. Pavlenko, O. P. Dmytrenko, M. P. Kulish, T. M. Pinchuk-Rugal, T. O. Busko, T. Yu. Nikolaienko, V. B. Neimash, and O. D. Kachkovsky

Abstract Optical absorption spectra of films of squaraine dye $C_{28}H_{27}O_2N_2$ deposited at different rates on quartz substrates, silver and gold nanoparticles, and silver nanoparticles coated with radiation-modified polyethylene glycol were studied. It was shown that depending on the rate of deposition of molecules, J- and H-type aggregates are formed. The J-aggregation changed when dyes were deposited on silver and gold nanoparticles, this could be confirmed by the significant restructuring of the spectrum and bathochromic shift of the absorption band. The quantum chemical calculations for the complex of the dye with silver nanoparticle, which consists of 128 Ag atoms, were carried out. It was shown that the alternation of charges appears on the atoms of the dye molecule. This was noticeably different from the charges observed for the atoms of the free molecule, which points to the interaction in the dye-AgNP complex that can lead to a shift of the absorption spectra. Calculations of the electronic structure of the complex containing the dye $C_{28}H_{27}O_2N_2$ with polyethylene glycol (PEG) indicate that changes in the optical absorption spectrum are caused by rearrangement and formation of new molecular orbitals, delocalized on both components of the complex.

A. M. Gaponov · O. L. Pavlenko (✉) · O. P. Dmytrenko · M. P. Kulish · T. M. Pinchuk-Rugal · T. O. Busko · T. Yu. Nikolaienko
Taras Shevchenko National University of Kyiv, 64/13 Volodymyrska Street, Kyiv, Ukraine
e-mail: olpavl57@gmail.com

V. B. Neimash
Institute of Physics, National Academy of Sciences, 46 Nauky Ave., Kyiv, Ukraine

O. D. Kachkovsky
Institute of Bioorganic Chemistry and Petrochemistry, National Academy of Sciences, 1 Murmanska Street, Kyiv, Ukraine

O. Fesenko and L. Yatsenko (eds.), *Nanoelectronics, Nanooptics, Nanochemistry and Nanobiotechnology, and Their Applications*, Springer Proceedings in Physics 297,
https://doi.org/10.1007/978-3-031-42708-4_22

1 Introduction

Organic dyes with a π-conjugated system of electrons are widely used in high-technological industries, for example as functional materials for the solar cells, sensors, as well as in biology and medicine [1–6]. Their chromophores provide high-intensity spectral properties that are very sensitive to environmental conditions [7, 8]. Therefore, it is very important to study the mechanisms of the interaction of dyes with other molecular structures, including drugs and nanoparticles [9]. At the same time, it is important to take into account not only their own π-conjugated structure, but the molecular interaction between them considering their properties to form different types of aggregation [10–15]. Since the interaction mechanisms of π-conjugated compounds have taken into account not only the molecular structure and topology, but also the spatial organization and the number of injected charges, it is advisable to model the complexes of such systems around other compounds and nanoparticles.

Among the various types of π-conjugated dyes, squaraines are characterized by highly intensive optical properties, having a central square fragment in the polymethine chromophore, in which oxygen (O) or sulfur (S) atoms are located. Location of the atoms in the four-membered ring, modification by functional groups these factors all determine the shift of the optical absorption spectrum to the long-wavelength region, due to changes in the location of the n-type electronic levels and delocalized π-molecular orbitals. All of which are important for solving many photophysical and medical-biological problems [10, 16–18]. Therefore, it is important to study the spectral properties of squaraine dye molecules, when they interact with gold and silver nanoparticles, including those covered with special coatings [9, 19].

The purpose of this work was to study the optical properties for films of squaraine dyes $C_{28}H_{27}O_2N_2$ on different substrates, including those made of Au, Ag, Ag-PEG nanoparticles, and to establish the mechanisms of functionalization of these dyes using quantum chemical calculations and modeling.

2 Experimental and Theoretical Part

The squaraine dye $C_{28}H_{27}O_2N_2$ with intensive absorption at 631 nm in dichloromethane (DCM) was described earlier [14].

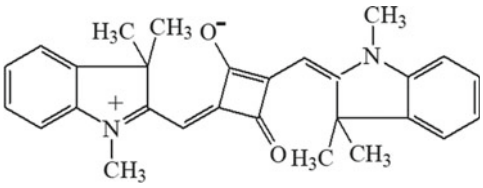

In order to study the mechanisms of interaction between squaraine dyes and NPs of gold Au [20], silver Ag, and Ag-PEG [21], the thin films were prepared by vacuum thermal deposition of dye molecules onto cleaned and annealed quartz substrates, at a pressure of 5×10^{-6} torr with a deposition rate of $\leq$ 0.04–0.08 nm/s. The thickness of the dye films didn't exceed 100 nm, which was controlled by a quartz sensor.

Absorption spectra of films deposited on quartz substrates, gold and silver nanoparticles, including those coated with PEG, as well as a dye solution in dichloromethane, were obtained using a Shimadzu UV-1800 spectrophotometer.

Quantum chemical calculations of the geometry, charge distribution, electronic structure and molecules and their complexes were carried out by the density functional method (DFT, B3LYP, 6-31G, d, p) and the semiempirical method AM1 in the software package Gaussian 09 [22].

To study the interaction of a dye molecule with the surface of silver nanoparticles, the nanoparticle-containing 128 Ag atoms [23], located in the nodes of a face-centered cubic lattice with a lattice constant of 4.0853 Å, was chosen. The determination of the spatial structure of the constructed silver nanoparticle-dye model system was carried out by the quantum–mechanical method GFN1-xTB [24], which belongs to the semiempirical methods of the DFTB family, based on the tight-binding approximation [25] in the density functional theory (DFT). Optimization of the system geometry was carried out in the xTB package (version 6.1.4) [26, 27] CREST package (version 2.7.1) which was used to search for possible conformations of molecular structures [26, 28].

At the first stage of studying the interaction of the dye molecule, with the surface of silver nanoparticles, the coordinates of the Ag atoms were set as fixed. The initial structures of the complexes were obtained as a result of the optimization of the geometry of the system built from the component parts of the complex, located at a distance greater than the sum of the van der Waals radii of the atoms that were currently present. After that, leaving the coordinates of the Ag atoms fixed, the search for conformers for the dye molecule in the complex was carried out. From among the obtained structures, the structure of the complex with the lowest energy of the electronic subsystem was chosen.

3 Results and Discussion

3.1 Study of Optical Absorption Spectra of Films of Squaraine Dyes Deposited on Gold and Silver Nanoparticles

Vacuum thermal deposition of squaraine dye $C_{28}H_{27}O_2N_2$ with different rates on quartz substrates was accompanied by shift of the optical absorption band compared to the position of the band in dichloromethane solution. The peak of the optical absorption spectrum was at 640 nm for the solution, but the sputtering led to the shift

of the band from this position to both the blue and red regions, which depended on the rate of deposition of the dye. It was established that the specified displacement was caused by the formation of aggregates of H- and J-type dyes in the films. The first of them led to a shift of the absorption band to the short-wavelength region, and the second one to a shift towards the region of longer wavelengths [8, 14]. The repeating dimmer of dyes was the main structural element of these aggregates. As a result of the formation of dimmers, there was a splitting of the energetic levels, typical for the monomer phase of the dye, and, as a result, two spectral transitions were made possible. For this dye, when H-aggregates were formed in the films, the absorption peak shifted to 526 nm, and when J-aggregates appeared, the maximum of the band reached a position near 680 nm. The obtained shift of the optical absorption to the red region is important for the use of dyes as a photosensitizing element that extends the absorption region to the near-IR range. The specified shift of the absorption into the IR region is effective for expanding the phototherapeutic window in photodynamic therapy and also can be used in the production of photovoltaic devices, sensors, and solar energy elements [1–7].

It is obvious that the formation of J-aggregates was influenced not only by rates of vacuum deposition, but also by the type and surface of substrate. The use of metal substrates formed in the form of nanoparticles was especially important. Figure 1 shows AFM images for dye films with different rates of deposition on a quartz substrate, pre-coated with a silver layer.

It could be seen that the surface of the dye films significantly depended not only on the deposition rate, but also on the choice of the substrate. Thus, in the case of a slower rate of deposition of the dye on quartz substrates, the size of the islands was 0.7–2.8 nm, while at higher speeds these sizes increased significantly to 19.8 * 73.6 nm. In the case of slower deposition of the dye on a thin silver film applied to a quartz substrate, the size of the islands corresponded to 3×38 nm. It could be assumed that the differences in the morphology of the films were due to the presence of different types of aggregate stacking. It could be assumed that the differences in the morphology of the films were due to the presence of different kinds of aggregates.

The optical absorption spectra for the squaraine dye in the solution, in films on quartz and silver substrates deposited at different rates, were presented in Fig. 2.

The spectra of optical absorption of squaraine dye, depending on the aggregation state, the type of substrate, and the deposition rate all underwent significant changes. In the case of the dye solution, a rather narrow absorption band appeared, the maximum of which was located near 631 nm. For films, the spectra were radically rearranged. The spectrum for a film deposited at a higher rate of ≥ 1 nm/s was quite complex. The main component of this band was concentrated near the maximum of the band at the position of 525 nm, that was, it underwent a significant shift toward shorter wavelengths in the absorption for the peak of the squaraine solution. Such a hypsochromic shift of the absorption band indicated that the H-aggregates formed in this film. Their presence was of less interest from the point of view of extending the absorption range into the IR region. However, this absorption band was complex because it included several inflections near 560, 630, 680 nm and occupied a very

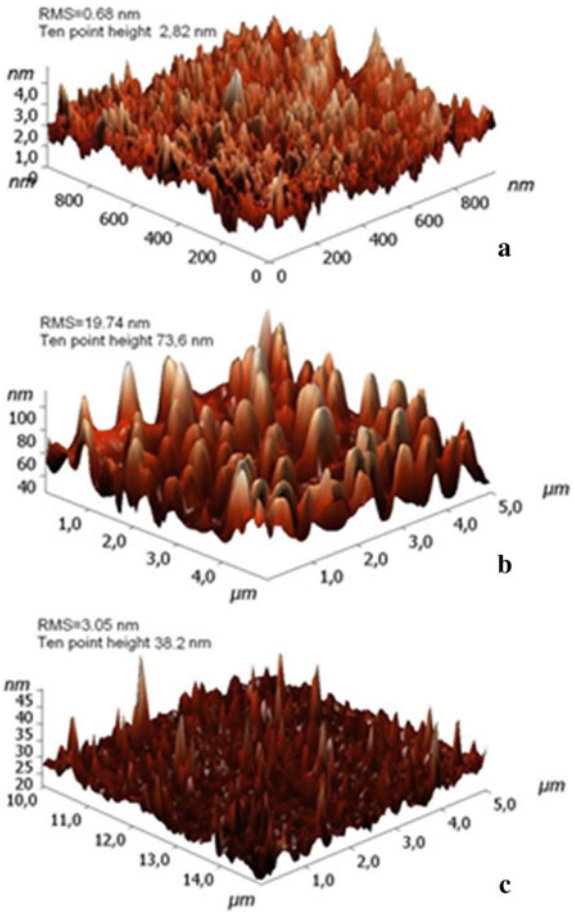

Fig. 1 AFM images for squaraine dye films, deposited on quartz substrates with deposition rates: ≤ 0.04–0.08 nm/s (the first mode) (**a**) ≥ 1 nm/s (the second mode) (**b**), on a silver substrate (the first mode) (**c**)

wide range from 450 to 750 nm. This behavior of the curve indicated some intermediate state of formation of not only H-type aggregates, but also J-type aggregates. At the same time, there were dye molecules that were not part of the aggregates that remained in the film.

Spectrum 3 for film, deposited at the second mode, was characterized by broad peak with maximum near 680 nm. Thus, this band underwent a bathochromic shift compared to the position of the peak for the squaraine dye in the solution. However, it retained a significant extension into the short-wave region and covered the range from 470 to 730 nm. The curve 3 had a short-wavelength shoulder in the area of curve 1. Therefore, it could be assumed, that at a lower deposition rate (0.004–0.08 nm/s) of the dye on the quartz substrate, as well as for the curve 2, H-aggregates appeared to some extent during deposition of molecules, that didn't form the great aggregates, but most of the dyes formed the J-type aggregates.

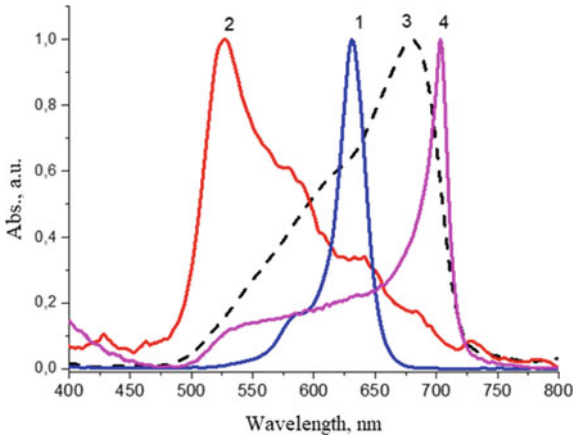

Fig. 2 Normalized optical absorption spectra of squaraine dye in solution ($3.14 \pm 0.06 \times 10^5$ M L^{-1}), and on quartz substrates, and at different deposition modes: curve 1—absorption of dye in solution: 2—absorption of a film prepared with a deposition rate of $\geq$ 1 nm/s (the first mode); 3—absorption of a film prepared with a deposition rate $\leq$ 0.04–0.08 nm/s (the second mode). The thickness of the films was 100 nm, the substrate was made of quartz

Deposition of the dye on a thin silver substrate led to a noticeable restructuring of the spectrum, the curve 4. Despite the fact that the absorption range remained similar to the previous case, curve 3, the shape of the spectrum and its position changed significantly. An important feature is the subsequent shift of the absorption band to the red region with the appearance of a slope near 703 nm. Compared to the band position for the solution, the shift in the latter case was 72 nm. The half-width of this band was sharply reduced compared to the bands represented by curves 2 and 3. However, the absorption in the shorter-wavelength region remained almost in the form of a shelf that captured the regions of all other curves.

The specified behavior of the spectrum for the slow deposition of the dye film on the silver substrate indicated on the formation of J-aggregates with a more perfect structure compared to the case, depicted by curve 3. That was confirmed not only by a more selective absorption in the form of a peak near 703 nm, but also by a decrease in the absorption, which corresponded to the presence of dye molecules and their H-aggregates. It is possible that by selecting the size of the nanoparticles of the substrate and the rate of deposition of the dye, it was possible to achieve the necessary characteristics of the absorption spectra, including for enhancing the absorption in the phototherapeutic window.

The absorption spectrum of a dye, slowly deposited on a quartz substrate, covered with gold nanoparticles, was significantly different from its appearance for a film deposited on a substrate made of gold nanoparticles, Fig. 3.

It is easy to see, that a band with a maximum near 520 nm appeared in the optical spectrum for the Au film, which is characteristic of gold nanoparticles with a size of 20 nm. The spectrum of the optical absorption for the dye film deposited on gold

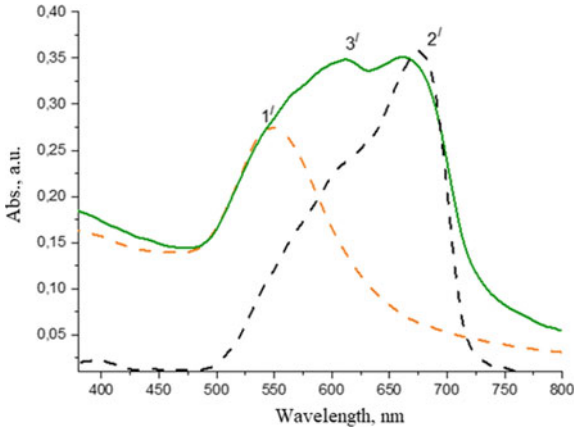

Fig. 3 Normalized spectra of the optical absorption of a squaraine dye film deposited on a quartz substrate ($1^{/}$), spectrum of Au gold nanoparticles ($2^{/}$), and dye, deposited at a speed of 0.04–0.08 nm/s on a substrate of Au gold nanoparticles ($3^{/}$). The thickness of the dye films was 100 nm

nanoparticles differed from the similar spectrum for the film deposited on silver nanoparticles, Fig. 2.

In the optical absorption spectrum for a dye film deposited on gold nanoparticles, a broadband with two maxima near 630 and 650 nm was observed. From the appearance of this spectrum, it could be assumed that H-type aggregates were absent at this deposition rate. At the same time, there was a coexistence of dye molecules both in the monomer phase and in J-type aggregates, but both phases are sufficiently disordered, which led to a significant broadening of the peaks. It could be stated that the mentioned conditions of obtaining of the films, deposition on the silver nanoparticles, from the point of view of obtaining more perfect J-aggregates and expanding the spectrum into the red region, were better. On the other hand, the optical density spectrum for dye films, deposited on Au particles had a broadband, which is a manifestation of the interaction of dye molecules with gold nanoparticles and, as a result, their photosensitization.

It is obvious that in the case of this interaction, a rearrangement of the electronic structure and optical transitions can be expected, which can be observed during quantum modeling of the behavior of the energy spectra of the dye positioned near the nanoparticles.

3.2 Quantum Chemical Modeling of the Properties of Complexes of Squaraine Dye a with a Silver Nanoparticle

Modeling of the interaction of squaraine dyes with noble metal nanoparticles, which are characterized by the presence of surface plasmon resonance, is important for establishing photosensitization mechanisms. For example, such an interaction was

considered with the selection of a silver nanowire consisting of 128 Ag atoms arranged in the FCC lattice.

The system, which included a molecule of squaraine dye and silver nanoparticles, is shown in Fig. 4.

This mutual arrangement of the molecule and Ag nanoparticle caused interaction that led to significant changes in the distribution of charges on the chromophore atoms of the dye molecule in the presence of a silver nanoparticle, Fig. 5.

It could be seen that the presence of a dye molecule on the surface of a silver nanoparticle led to change in the charge distribution on the carbon chromophore atoms compared to similar charge distribution for a free dye molecule that was not in the complex. Thus, in the free state of the molecule, there was a large negative charge on the nitrogen, oxygen, and carbon atoms which were closest to them. For

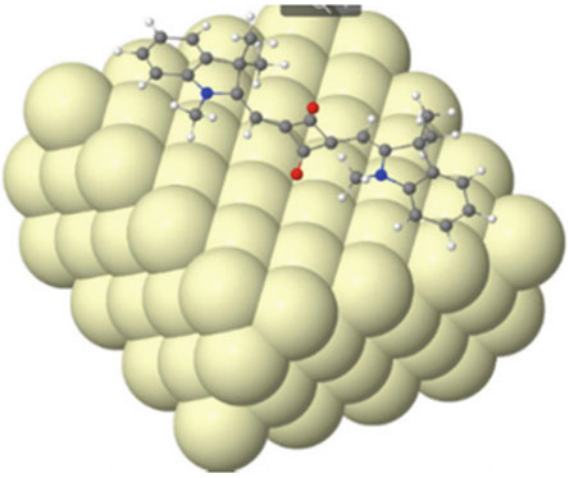

Fig. 4 Optimized geometry of the silver nanoparticle and squaraine dye complex

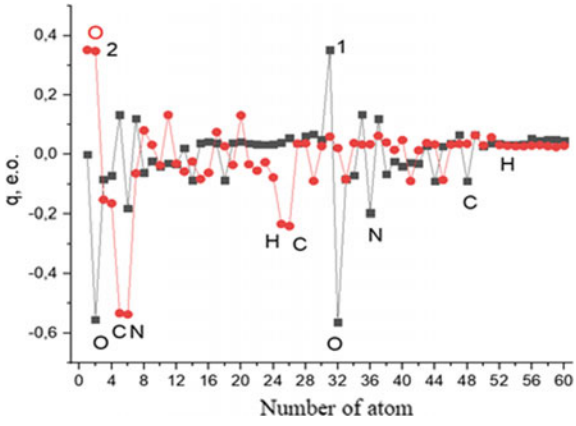

Fig. 5 Charge distribution on carbon atoms of free dye molecule (1,) and in a complex with silver nanoparticle Ag 128 ( )

hydrogen atoms, especially those in methyl groups, CH_3 has slightly positive values. At the same time, C–H bonds are significantly polarized.

In the case of interaction between the atoms of the molecule and the silver nanoparticle in the complexes, the large negative charges on the oxygen atoms disappear and become close to the charge on the carbon atoms. For hydrogen atoms during interaction, the positive charges changed little, as did the polarization of C–H bonds. An important feature for the distribution of charges during the interaction between the dye molecule and nanoparticle of light was the appearance of a significant alternation of charges on carbon atoms. It can be assumed that the described changes in the distribution of charge values were the main part that caused the shift in the position of the optical absorption band, obtained for silver nanoparticles and their complex with squaraine dye molecules.

3.3 Absorption Spectra of Films of Silver Nanoparticles Covered with Radiation-Modified Polyethylene Glycol

Figure 6 shows the absorption spectra of films of silver nanoparticles coated with polyethylene glycol. The intensive band of plasmon resonance of silver nanoparticles with a size of 56–62 nm was located at 415 nm and had a slight asymmetry in the form of a shoulder at 460 nm.

Absorption occurs in the ultraviolet region due to polyethylene glycol irradiated with high-energy electrons. The spectrum of polyethylene glycol had a sharp maximum at 200 nm with a low-intensity peak in the region of 240–300 nm, which indicated the predominant preservation of its electronic structure after irradiation.

The absorption spectrum of the silver nanoparticle film and the squaraine dye thermally deposited on it is shown in Fig. 7, curve 3.

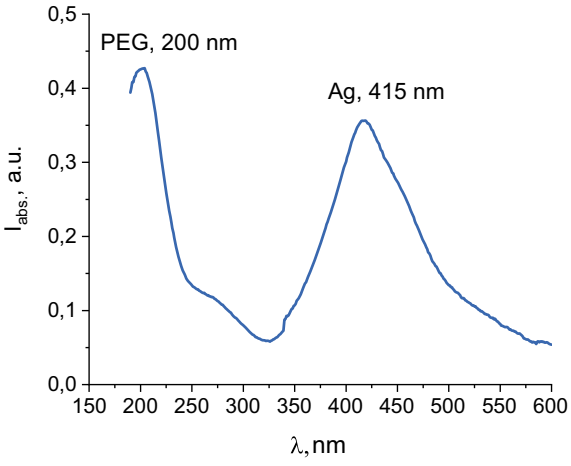

Fig. 6 Absorption spectra of a film of silver nanoparticles coated with polyethylene glycol

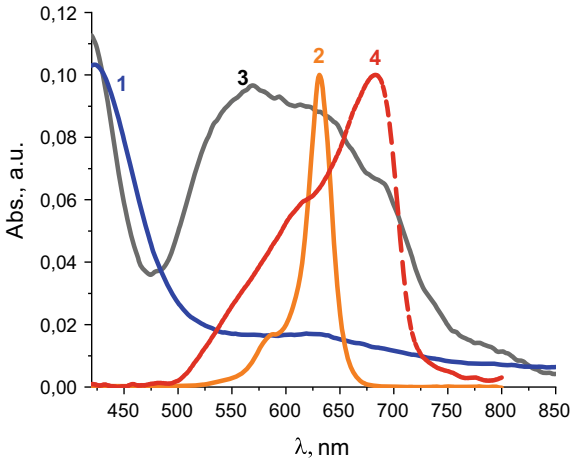

Fig. 7 Absorption spectra of a film of silver nanoparticles with a polyethylene glycol shell (1), absorption spectrum of a dye in a dichloromethane solution (2), absorption spectrum of a dye when sprayed on a quartz substrate (4), absorption spectrum of a composite layer-by-layer film of silver nanoparticles with a sprayed dye (3) (spectra 2 and 3 are normalized to the maximum absorption of the dye in the solution)

In comparison with the spectrum characteristic of a solution of this dye in dichloromethane, curve 2, and also compared to the spectrum of the dye thermally deposited on a silicon substrate, curve 4, there was a significant transformation of the absorption spectrum of the dye on silver nanoparticles coated with polyethylene glycol.

Thus, as can be seen from curve 4, during deposition on a quartz substrate, there was a shift of the absorption peak to the long-wavelength region from 631 nm for the solution to 681 nm in the film, which, as was shown in [8, 14], was explained by the formation of J-type aggregates between dye molecules.

Deposition of dyes under the same conditions as those used for the film with spectrum 4 on a film of silver nanoparticles with radiation-modified polyethylene glycol led to the appearance of not only a long-wave maximum at 690 nm, which could be a sign of the formation of J-type aggregates between the dyes, but also a wide short-wavelength band with the highest intensity at 566 nm, typical for the formation of H-type aggregates, which was also reported in works [8, 14] and others. The absorption maximum in the vicinity of the typical for the solution of this dye at 630 nm was also preserved, but it was more extended.

In general, the absorption region of the dye when it was deposited on radiation-modified polyethylene glycol with silver nanoparticles broadened in the region from 500 to 750 nm. It was obvious that the aforementioned aggregation occurred in the near-surface layers of the sprayed film, but there was a high probability of interaction with the polyethylene glycol on which the dye was applied. Let us consider the

influence of the interaction of dye molecules with polyethylene glycol, the contribution of which was important in the formation of absorption spectra. In the quantum chemical calculations, chain link of the polyethylene glycol polymer was chosen as a representative of radiation-modified PEG, covering silver nanoparticles. In the first stage, PEG-link was located at the dye molecule at a distance of 3,5 Å and then optimization of the geometry of the complex with further analysis and comparison with the characteristics of individual components were performed.

In Fig. 8, the optimized geometry of the dye molecule (a), the polyethylene glycol link (b), and their complex (c) is shown.

The dye is a π-conjugated and symmetrical molecule relative to the square acid fragment. The oxygen atoms of the central fragment have negative charge values of – 562 e.o. Nitrogen atoms of indolenine groups were also characterized by values of negative charges and amount to − 0.577 e.o.

The carbon framework of the dye molecule was characterized by the alternation of charge values on the atoms, with the exception of the four extreme atoms of the phenolic rings with negative numbers, Fig. 9a.

The polymer link of polyethylene glycol, Fig. 9b, in contrast to the π-conjugated framework of the dye molecule, was a saturated carbon structure, the carbon atoms of which have almost the same values of positive charges, which were close to zero: 0.014 and 0.07 e.o., the difference of which was due to the presence of a chain break. Oxygen atoms replacing every third carbon atom in the saturated carbon framework had sharply negative charge values, for those in the central framework − 0.51 and − 0.55 e.o. for oxygen atoms of hydroxy groups at the end of the chain.

As can be seen from Fig. 9a, the presence of a polyethylene chain next to a dye molecule led to a significant redistribution of charges on it. The largest changes were observed for nitrogen atoms 4, 12, which changed the amount of charge from −

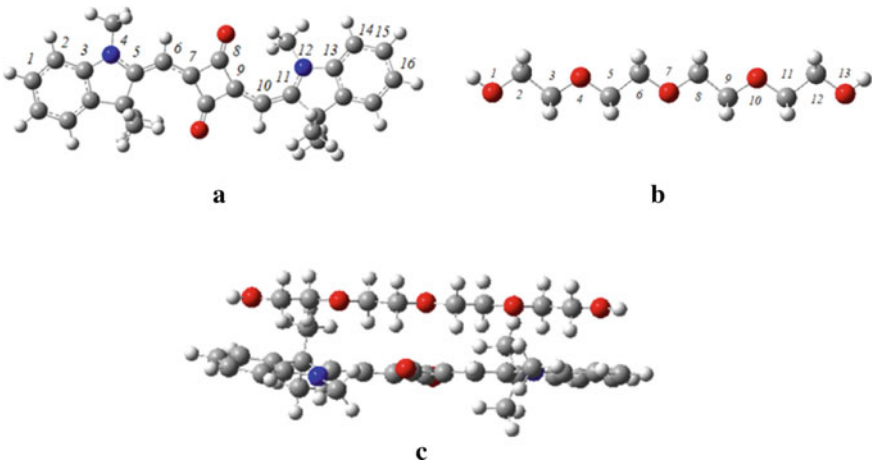

Fig. 8 Optimized geometry of the dye molecule (**a**) and polyethylene glycol chain (**b**) (with numeration of the atoms) and their complex (**c**)

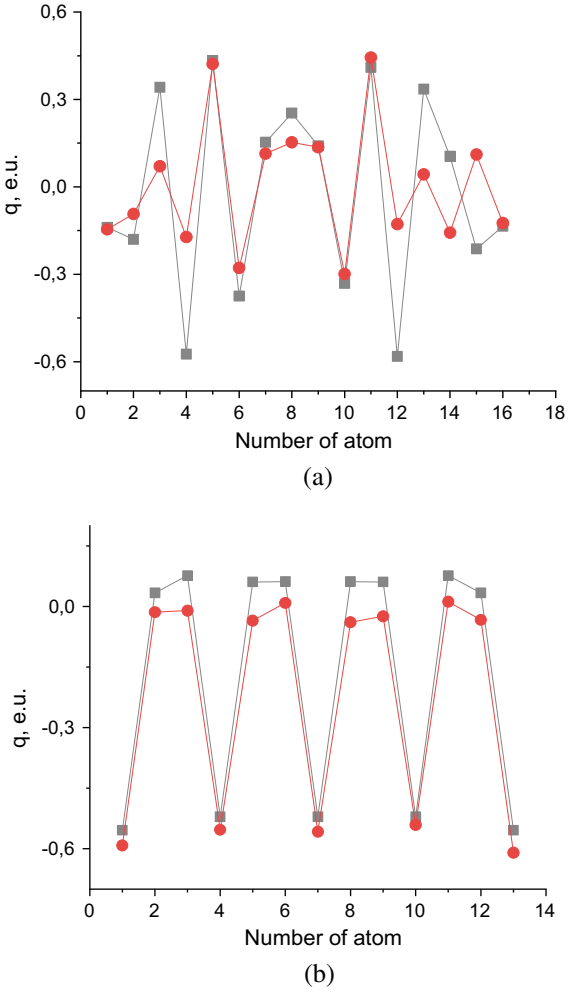

Fig. 9 Charge distribution on dye atoms and polyethylene glycol units (black squares) both independently and in the complex (red rings) (according to the numbering in Fig. 8a, b)

0.6 to − 0.2 e.o., as well as carbon atoms located near the oxygen atoms of the square fragment. Such changes were felt by the conjugated carbon framework, in particular atoms 3 and 13 of the phenolic rings.

At the same time, the polyethylene glycol chain, the charge distribution for which in the complex and independently is shown in Fig. 9b, was also characterized by changes in charges, carbon atoms lose their positive charge from 0.08 to 0.01, while oxygen atoms only slightly decreased the amount of negative charges: from − 0.55 to − 0.56 e.o. for four atoms in the chain according to the numbering in Fig. 8b.

Let‘s consider how such significant charge redistribution affected the electronic structure of the dye-PEG complex, Fig. 10.

The dye’s electronic levels HOMO and LUMO which were also the ground electronic transition orbitals, are at − 4.47 and − 2.24 eV, respectively, and determined

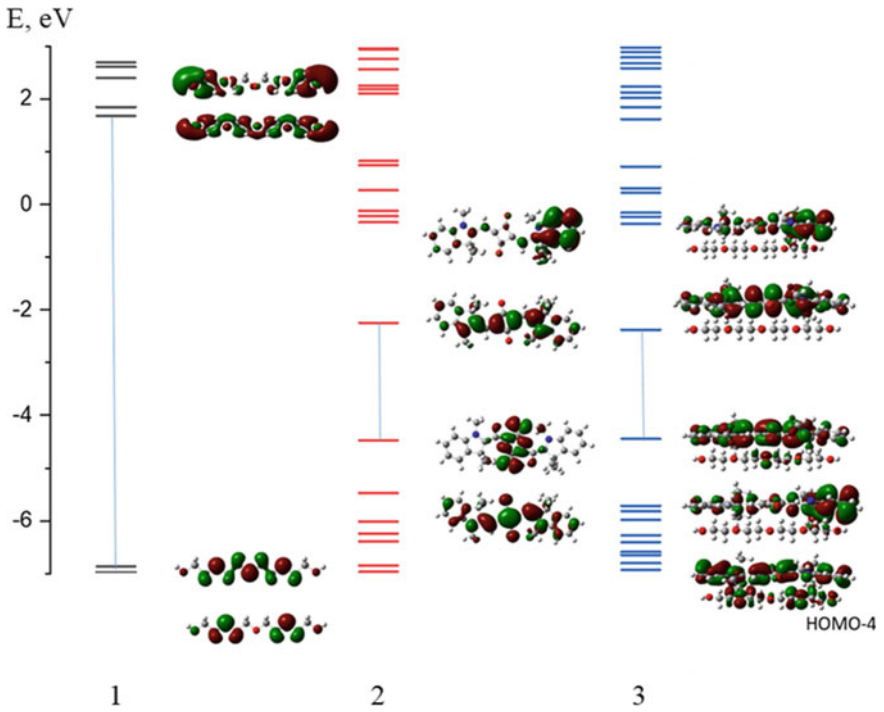

Fig. 10 Energy levels and shapes of molecular orbitals of polyethylene glycol (1), squaraine dye (2) and the complex of polyethylene glycol with dye (3) in the region of the energy gap

the dye's absorption at 543 nm, Fig. 11, which nearly by 100 nm differed from the experimental data of the absorption peak in the solution. Molecular orbitals were delocalized along the chromophore of the dye.

The energy levels of polyethylene glycol were in a different range, molecular orbitals are localized on C–H bonds and as could be seen from Fig. 10, curve 2; the experimental absorption spectrum of radiation-modified PEG has a maximum at 200 nm; while the calculated value of the absorption maximum was at 164 nm, Fig. 11, curve 1, the HOMO and LUMO levels were at − 6.85, 4.4 eV. The transition between these molecular orbitals made the main contribution to the intensity of the absorption spectra of PEG.

During the formation of the complex, there was a slight shift in the electronic levels of the dye for HOMO = 4.443 eV and for LUMO = 2.37 eV, the nature of the main electronic transition remained typical for the dye, but it shifted to 594 nm.

Calculations of higher excited electronic transitions for the complex indicated that there were transitions between orbitals that are simultaneously localized on both components of the complex, in particular from the HOMO-4 orbital to the LUMO.

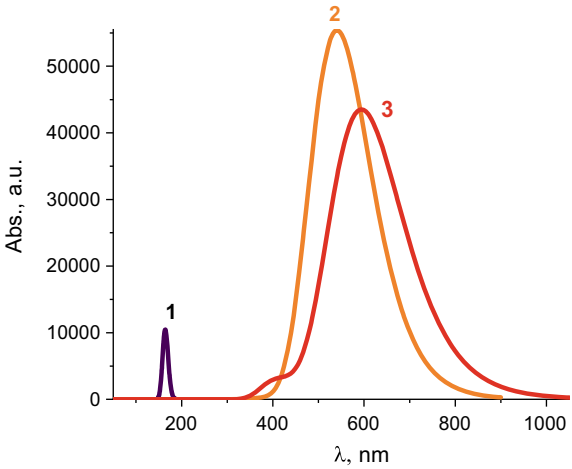

Fig. 11 Absorption spectra of the polyethylene glycol link (1), the squaraine dye (2) and the complex of polyethylene glycol with the dye (3) were calculated (spectrum 1 and 3 multiplied by 500 due to insufficient calculated intensity)

4 Conclusions

The optical absorption spectrum of squaraine dye films deposited on a quartz substrate is significantly different from similar spectra of solutions in dichloromethane. Depending on the deposition rate, there is a shift of the absorption bands in both the blue and red regions, which indicates the formation of H- and J-type aggregates. At the same time, these bands are complex and located in a wide spectral range, which indicates the coexistence of dye molecules with its aggregates of different types.

Deposition of films of squaraine dye molecules on silver cover of quartz substrate leads to the appearance of sharp red-shifted band in the absorption spectra due to more perfect morphology of the J-aggregates.

Deposition on gold nanoparticles leads to broadening of the absorption spectrum compared to the spectrum of the dye on the quartz substrate. The behavior of this spectrum also indicates the formation of J-type aggregates, but they are characterized by a more imperfect morphology and the presence of unarranged molecules.

Quantum chemical calculations of the optimized geometry of the complex of dye molecule and Ag nanoparticle show charge redistribution on the carbon atoms of the dye compared to the charges of free molecule. This change of the supramolecular structure of the dye influences on the aggregation and is responsible for the change in the spectral properties of the molecules.

Deposition of films of squaraine dye molecules on silver nanoparticles covered with radiation-modified polyethylene glycol leads to a significant broadening of the absorption spectra, signing the formation of both J- and H-type aggregates.

Quantum chemical calculations of squaraine dye complexes with a polyethylene glycol link indicate changes in the charges of nitrogen atoms of indolenine groups, oxygen atoms of the squaraine group, and nearby carbon atoms of the dye. The

highest occupied and lowest unoccupied molecular orbitals of the complex are localized on the chromophore of the dye and determine the main electronic transition of the complex. LUMO level of the complex shifts leading to shift of the absorption band of the complex. The electron transition HOMO-4–LUMO+1 occurs due to the participation of orbitals located simultaneously on both components of the complex and contributed to the short-wavelength region of the absorption spectrum.

References

1. K. Jiang, Q. Wei, J.Y.L. Lai et al., Alkyl chain tuning of small molecule acceptors for efficient organic solar cells. Joule **3**(12), 3020–3033 (2019). https://doi.org/10.1016/j.joule.2019.09.010
2. Y. Zhang, B. Kan, Y. Sun et al., Nonfullerene tandem organic solar cells with high performance of 14.11%. Adv. Mater. **30**(18), 1707508 (2018). https://doi.org/10.1002/adma.201707508
3. Y. Zhou, G. Long, A. Li et al., Towards predicting the power conversion efficiencies of organic solar cells from donor and acceptor molecule structures. J Mater. Chem. C. **6**(13), 3276–3287 (2018). https://doi.org/10.1039/c7tc05290a
4. A.J. Hodgson, K. Gilmore, C. Small et al., Reactive supramolecular assemblies of mucopolysaccharide, polypyrrole and protein as controllable biocomposites for a new generation of intelligent biomaterials. Supramol. Sci. **1**(2), 77–78 (1994). https://doi.org/10.1016/0968-5677(94)90013-2
5. B. Yang, F. Yao, T. Hao et al., Development of electrically conductive double-network hydrogels via one-step facile strategy for cardiac tissue engineering. Adv. Healthcare Mater. **5**(4), 474–488 (2016). https://doi.org/10.1002/adhm.201500520
6. A.M. Martins, G. Eng, S.G. Caridade et al., Electrically conductive chitosan/carbon scaffolds for cardiac tissue engineering. Biomacromolecules **15**(2), 635–643 (2014). https://doi.org/10.1021/bm401679q
7. H.A. Shindy, Characterization, mechanisms and applications in the chemistry of cyanine dyes: a review. Eur. J. Mol. Biotechnol. **14**(4), 158–170 (2016). https://doi.org/10.1016/j.dyepig.2017.06.029
8. J.L. Bricks, A.D. Kachkovsky, Y.L. Slominskii et al., Molecular design of near infrared polymethine dyes: a review. Dyes Pigm. **121**, 238–255 (2015). https://doi.org/10.1016/j.dyepig.2015.05.016
9. K. Kneipp, Chemical contribution to SERS enhancement: an experimental study on a series of polymethine dyes on silver nanoaggregates. J. Phys. Chem. C **120**(37), 21076–21081 (2016). https://doi.org/10.1021/acs.jpcc.6b03785
10. N. Narayanan, V. Karunakaran, W. Paul et al., Aggregation induced Raman scattering of squaraine dye: implementation in diagnosis of cervical cancer dysplasia by SERS imaging. Biosens. Bioelectron. **70**(15), 145–152 (2015). https://doi.org/10.1016/j.bios.2015.03.029
11. V.V. Egorov, Nature of the optical band shapes in polymethine dyes and H-aggregates: dozy chaos and excitons. Comparison with dimers, H*- and J-aggregates. R. Soc. Open Sci. **4**, 160550 (2017). https://doi.org/10.1098/rsos.160550
12. A. Kaczmarek-Kedziera, D. Kedziera, Molecular aspects of squaraine dyes aggregation and its influence on spectroscopic properties. Theor. Chem. Acc. **135**(9), 214 (2016). https://doi.org/10.1007/s00214-016-1971-0
13. Y. Meng, Y. Fang, C. Yuan et al., 2-aryloxybenzo[d]oxazoles As deep blue solid-state emitters: synthesis, aggregation-induced emission properties and crystal structure. Dyes Pigm. **187**, 109127 (2020). https://doi.org/10.1016/j.dyepig.2020.109127
14. V.A. Brusentsov, O.L. Pavlenko, A.M. Gaponov et al., Aggregation of squarain dyes in deposited films. Nanosistemi Nanomateriali Nanotehnologii **15**(4), 589–597 (2017)

15. O.L. Pavlenko, A.M. Gaponov, A.I. Lesiuk et al., Electronic structure of the cyanine dye bases within the solvents and films. Nanosistemi Nanomateriali Nanotehnologii **17**(1), 145–154 (2019)
16. V.V. Kurdiukov, O.I. Tolmachev, O.D. Kachkovsky et al., Electron structure and nature of electron transitions of squaraine and thiosquaraine as well as their 1,2-isomers. J. Mol. Struct. **1076**, 583–591 (2014). https://doi.org/10.1016/j.molstruc.2014.07.076
17. S. Yagi, H. Nakazumi et al., Squarylium dyes and related compounds. Top. Heterocycl. Chem. **14**, 133–181 (2008). https://doi.org/10.1007/7081_2008_117
18. D.E. Lynch, M.Z. Chowdhury, N.-L. Luu et al., Water soluble bis(indolenine)squaraine salts for use as fluorescent protein-sensitive probes. Dyes Pigments **96**, 116–124 (2013). https://doi.org/10.1016/j.dyepig.2012.07.015
19. L.A. Bulavin, N.A. Goncharenko, O.P. Dmytrenko et al., Heteroassociation of antitumor agent doxorubicin with bovine serum albumin in the presence of gold nanoparticles. J. Mol. Liq. **284**, 633–638 (2019)
20. O.A. Yeshchenko, V.B. Kozachenko, Naumenko et al., AP Gold nanoparticle plasmon resonance in near-field coupled Au NPs layer/Al film nanostructure: dependence on metal film thickness photonics and nanostructures. Fundament. Appl. **29**, 1–7 (2018). https://doi.org/10.1016/j.photonics.2017.12.005
21. V.B. Neimash, G.D. Kupiansky, I.V. Olhovik, et al., Formation of silver nanoparticles in pva-peg hydrogel under electron irradiation. Ukr. J. Phys. **64**, 1 (2019). https://doi.org/10.15407/ujpe64.1.41
22. Gaussian 09, Revision A.02, M.J. Frisch, G.W. Trucks, H.B. Schlegel, G.E. Scuseria, M.A. Robb, J.R. Cheeseman, G. Scalmani, V. Barone, G.A. Petersson, H. Nakatsuji, X. Li, M. Caricato, A. Marenich, J. Bloino, B.G. Janesko, R. Gomperts, B. Mennucci, H.P. Hratchian, J.V. Ortiz, A.F. Izmaylov, J.L. Sonnenberg, D. Williams-Young, F. Ding, F. Lipparini, F. Egidi, J. Goings, B. Peng, A. Petrone, T. Henderson, D. Ranasinghe, V.G. Zakrzewski, J. Gao, N. Rega, G. Zheng, W. Liang, M. Hada, M. Ehara, K. Toyota, R. Fukuda, J. Hasegawa, M. Ishida, T. Nakajima, Y. Honda, O. Kitao, H. Nakai, T. Vreven, K. Throssell, J.A. Montgomery, Jr., J.E. Peralta, F. Ogliaro, M. Bearpark, J.J. Heyd, E. Brothers, K.N. Kudin, V.N. Staroverov, T. Keith, R. Kobayashi, J. Normand, K. Raghavachari, A. Rendell, J.C. Burant, S.S. Iyengar, J. Tomasi, M. Cossi, J.M. Millam, M. Klene, C. Adamo, R. Cammi, J.W. Ochterski, R.L. Martin, K. Morokuma, O. Farkas, J.B. Foresman, D.J. Fox, Gaussian, Inc., Wallingford CT (2016). https://gaussian.com/citation/
23. M. Chen, J.E. Dyer, K. Li, D.A. Dixon, Prediction of structures and atomization energies of small silver clusters, (Ag) n, n < 100. J. Phys. Chem. A **117**(34), 8298–8313 (2013). https://doi.org/10.1021/jp404493w
24. P. Pracht, E. Caldeweyher, S. Ehlert, S. Grimme, A robust non-self-consistent tight-binding quantum chemistry method for large molecules (2019). Preprint. ChemRxiv: https://doi.org/10.26434/chemrxiv.8326202.v1
25. M. Elstner, D. Porezag, G. Jungnickel et al., Self-consistent-charge density-functional tight-binding method for simulations of complex material properties. Phys. Rev. B **58**(11), 7260 (1998). https://doi.org/10.1103/PhysRevB.58.7260
26. S. Grimme, C. Bannwarth, P. Shushkov, A robust and accurate tight-binding quantum chemical method for structures, vibrational frequencies, and noncovalent interactions of large molecular systems parameterized for all spd-block elements (Z = 1–86). J. Chem. Theory Comput. **13**(5), 1989–2009 (2017). https://doi.org/10.1021/acs.jctc.7b00118
27. C. Bannwarth, S. Ehlert, S. Grimme, GFN2-xTB—an accurate and broadly parameterized self-consistent tight-binding quantum chemical method with multipole electrostatics and density-dependent dispersion contributions. J. Chem. Theory Comput. **15**(3), 1652–1671 (2019). https://doi.org/10.1021/acs.jctc.8b01176
28. S. Grimme, Exploration of chemical compound, conformer, and reaction space with meta-dynamics simulations based on tight-binding quantum chemical calculations. J. Chem. Theory Comput. **15**(5), 2847–2862 (2019). https://doi.org/10.1021/acs.jctc.9b00143

Optical Transitions in Nanosystems with Germanium Quantum Dots

Serhii I. Pokutnii

Abstract It is shown that the radiation intensities, as well as the lifetimes associated with electron transitions between quasistationary and stationary states arising above a spherical surface of a single germanium quantum dot, take significant values compared to similar values in germanium/silicon nanosystems. This effect will make it possible to create a new generation of efficient light-emitting and photodetector devices based on germanium/silicon heterostructures with germanium quantum dots. In addition, long-lived quasistationary and stationary states will make it possible to realize high-temperature quantum Bose-gases states in the nanosystem under study.

1 Introduction

The germanium/silicon nanosystems with germanium quantum dots (QDs) belonged to the second type of heterostructures. In these nanosystems, the spatial separation of electrons and holes was experimentally discovered. In this case, electrons were localized above the QD surface, while holes moved into QD [1–6]. These excited states have been called spatially indirect excitons (SIE) [1–5]. In such nanosystems, space-indirect interband transitions between the electron and hole states were observed [1–4]. In nanosystems consisting of single germanium QDs placed in a silicon matrix, no significant intensity of interband optical transitions has been established so far [4, 5]. This was due to the small value of the overlap integral of the electron and hole wave functions (about a few hundredths) in such a nanosystem [4, 5, 7]. A solution to the problem of increasing the intensity of radiative recombination made it possible to create new devices for optoelectronics and modern microelectronics on a single silicon substrate [4–7].

S. I. Pokutnii (✉)
Chuiko Institute of Surface Chemistry of National Academy of Sciences of Ukraine, 17 General Naumov Street, Kyiv 03164, Ukraine
e-mail: pokutnyi.serg@gmail.com

Institute of Physics of National Academy of Sciences of Ukraine, 46 Nauky Ave., Kyiv 03028, Ukraine

O. Fesenko and L. Yatsenko (eds.), *Nanoelectronics, Nanooptics, Nanochemistry and Nanobiotechnology, and Their Applications*, Springer Proceedings in Physics 297,
https://doi.org/10.1007/978-3-031-42708-4_23

In experimental work [5], photoluminescence was studied in Ge/Si heterostructures with double layers of vertically aligned germanium QDs. A sevenfold increase in the intensity of photoluminescence was found in comparison with semiconductor structures. This increase in intensity was due to the penetration of electrons into the germanium QDs. In this case, the overlap integral of the wave functions of the electron and the hole substantially increased [4].

Using electron beam lithography in [6], linear germanium QD chains on silicon substrates were created. In the chains, the average QD radii of germanium did not exceed 30 nm. It was found that in these nanostructures a photoluminescence signal in the infrared spectral region (0.20–1.14) eV was observed up to room temperature [1–6].

The theory of SIE, consisting of a hole moving in a germanium QD, and the electron is localized over the spherical interface (QD—silicon matrix), was developed in [8, 9]. The theory predicted a significant increase in the SIE-binding energy $E_{\text{ex}}(a)$ (where a is the QD radius) (by almost two orders of magnitude) in this nanosystem, compared with the exciton binding energy in a silicon single crystal. In this SIE, the electron and the hole were separated by centrifugal potential, as well as polarization interaction with the spherical interface (QD—matrix) [9].

It was shown in [8, 9] that quasistationary SIE-states with energies $E_{1,l}(a) > 0$ ($n = 1, l = 0, 1, 2, \ldots$ were the main and orbital quantum numbers of an electron), as well as stationary SIE-states with energies $E_{1,l}(a) < 0$. These quasistationary SIE-states and stationary SIE-states arose above the spherical surface of a single germanium QD placed in a silicon matrix [8, 9].

It was shown in [7] that, in this nanosystem, the hole emerging from the germanium QD into the silicon matrix caused a direct electronic transition in real space between the electron level located in the conduction band of the silicon matrix and the hole level located in the bandgap of the silicon matrix. This led to a significant increase in the intensity of radiative recombination in the nanosystem.

At present, the optical properties of germanium/silicon heterostructures with germanium QDs have not been adequately studied. In this paper, in contrast to [7], the radiation intensities, as well as the lifetimes due to electronic transitions between the quasistationary and stationary SIE-states are being researched. It is shown that the radiation intensities as well as the lifetimes due to electron transitions between quasistationary and stationary SIE-states take significant values compared to similar values in nanosystems consisting of single germanium QDs placed in a silicon matrix.

2 Optical Transitions in Nanosystem

In [8, 9], a nanosystem model was used, which consisted of spherical germanium QD of radius a with dielectric permittivity $\varepsilon_2 = 16.3$, placed in the silicon matrix with a permittivity $\varepsilon_1 = 11.7$. It was assumed that the hole h with the effective mass $(m_h/m_0) = 0.39$ was located in the center of the germanium QD, and the electron e with the effective mass $(m_e/m_0) = 0.98$ was localized along the spherical surface

of the QD in the silicon matrix (m_0 is free electron mass). In the nanosystem, the ground electronic level was in the silicon matrix, and the main hole level was in the germanium QD.

The Hamiltonian SIE in [8, 9] contained the energy of electron–hole Coulomb interaction, the energy of the polarization interaction of an electron and a hole with a QD surface, as well as the centrifugal energy of the SIE. In [9], the energy spectrum $E_{n=1,l}(a)$ of SIE-states ($n = 1, l$) was obtained by the variational method as a function of the radius a QD. The variational the hydrogen-like radial wave functions were used [9]:

$$\begin{aligned} &R_{1,l}(r) = A_l(r-a)^l \exp(-j_l(r-a)/a), \\ &A_{1,l}^2 = (2j_l/a)^{3+2l}\left(4(2l)!\left(j_l^2 + 4(2l+1)!j_l + (2l+2)!\right)^{-1}\right) \end{aligned} \tag{1}$$

where r is distance of the electron e from the QD center, $j_l(a)$—was a variational parameter.

It was shown that the inclusion of the centrifugal energy of the exciton in the Hamiltonian caused a positive potential barrier. Such a potential barrier has led to the fact that, in the zone of surface SIE-states in the nanosystem, starting from QD radius a, is higher than some critical QD radius $a_c^*(n = 1, l)$ at first, quasistationary SIE-states with energies $E_{1,l}(a) > 0$ appeared. With increasing QD radius $a > a_c(1, l) > a_c^*(1, l)$, the quasistationary SIE-states were converted to stationary SIE-states with energies $E_{1,l}(a) < 0$ [9]. The critical QD radii for these states ($n = 1, l \leq 3$) had corresponding values [9]: $a_c^*(1, l) = 8.04$ nm; 11.1 nm; 15.5 nm; $a_c(1, l) = 6.54$ nm; 8.35 nm; 11.95 nm; 17.34 nm. In [9] it was shown that in the range of QD radii $a \geq a_0 = 20.8$ nm, the quasistationary and stationary ($n = 1, l$) SIE-states were transferred into the states of two-dimensional SIE-states localized over the flat germanium/silicon interface. The binding energies $E_{1,l}(a)$ SIE-states asymptotically approached the value E_{ex}^{2D}, which characterizes the binding energy of a two-dimensional SIE-states.

In this case, quasistationary and stationary states formed a zone of surface SIE-states. The band of stationary SIE-states $E_{1,l}(a)$ with a width $\Delta E = E_{ex}^{2D} = 82$ meV was located in the bandgap of the silicon matrix (where E_{ex}^{2D} is the binding energy of the two-dimensional SIE). The band of quasistationary SIE-states $E_{n=1,l}(a)$ with a width $\Delta E = E_{1,l=3}^{\max}\left(a = a_c^*(1, l = 3)\right) \cong 248.4$ meV was located in the conduction band of the silicon matrix. In this case, the zone of surface SIE-states contained a finite number of levels ($n = 1$, $l \leq 3$). It was found that the optical absorption in the nanosystem was caused by electron interband transitions between quasistationary and stationary SIE-states, as well as electron intraband transitions between stationary SIE-states [9].

It was shown in [8, 9] that in a Ge/Si nanosystem with germanium QDs with average radii a upon absorption of a quantum of light by energy

$$\hbar\omega_{ex(1,l)}(a) = E_{g(Ge)} - \Delta E_{c(Si)} + E_{1,l}(a), \tag{2}$$

in the bandgap of the silicon matrix, an stationary SIE-state with energy $E_{1,l}(a) < 0$ appeared. In this case, a quasistationary SIE-state with energy $E_{1,l}(a) > 0$ appeared in the conduction band of the silicon matrix. In Formula (2), $\left|E_{1,l}(a)\right|$ is the SIE binding energy, and the value $\left(E_{g(\mathrm{Ge})} - \Delta E_{c(\mathrm{Si})}\right) = 330$ meV (where $E_{g(\mathrm{Ge})}$ is the bandgap energy of the germanium QD, $\Delta E_{c(\mathrm{Si})}$ is the shift of the bottom of the conduction band of the silicon matrix relative to the bottom of the conduction band of germanium QD).

The intensity $I_{1,l}^{1,l+1}(a)$ of the dipole-allowed optical transitions between the SIE-states $(n = 1, l)$ and $(n = 1, l + 1)$ in QD radius a is determined by the square of the overlap integral of exciton wave functions $R_{1,l}(r)$ and $R_{1,l+1}(r)$ (1) [10]:

$$I_{1,l}^{1,l+1}(a) \approx \left| \int_a^{\infty} R_{1,l}(r) R_{1,l+1}(r) r^2 \mathrm{d}r \right|^2 \delta\left(\hbar\omega - \hbar\omega_{ex(1,l)}(a)\right) \tag{3}$$

In (3) the radiation energy $\hbar\omega_{ex(1,l)}(a)$ is determined by Formula (2). Integrating in (3), taking into account (1), we obtain an expression that describes the relative intensity $I_{1,l}^{1,l+1}(a)$ of optical transitions

$$\begin{aligned} I_{1,l}^{1,l+1}(a) \approx{}& (2j_l)^{(2l+3)}(2j_{l+1})^{(2l+5)}(j_l + j_{l+1})^{-(4l+8)} \\ & \left[(2l+1)!(j_l + j_{l+1})^2 + 2(2l+2)!(j_l + j_{l+1}) + (2l+3)!\right]^2 \\ & \left[4(2l)!j_l^2 + 4(2l+1)!j_l + (2l+2)!\right]^{-1} \\ & \left[4(2l+2)!j_{l+1}^2 + 4(2l+3)!j_{l+1} + (2l+4)!\right]^{-1} \end{aligned} \tag{4}$$

3 Lifetimes of SIE-States in a Nanosystem

The lifetimes $\tau_{1,l}^{1,l+1}(a)$ of SIE-states caused by transitions between SIE-states $(n = 1, l)$ and $(n = 1, l + 1)$ with energies $E_{1,l+1}(a) = \hbar\omega_{1,l+1}(a)$ and $E_{1,l}(a) = \hbar\omega_{1,l}(a)$, in the Ge/Si nanosystem with germanium QDs can be described by the expression:

$$\tau_{1,l}^{1,l+1}(a)/\tau_{ex} = \left(3/\tilde{\varepsilon} f_{1,l}^{1,l+1}(a)\right)\left(c\mu_{ex}a_{ex}^{2D}\hbar^{-1}\right)^3\left(E_{ex}^{2D}/\Delta E_{1,l}^{1,l+1}(a)\right)^2 \tag{5}$$

In Formula (5), the exciton lifetime $\tau_{ex} = \hbar/E_{ex}^{2D}$ in the nanosystem ($E_{ex}^{2D} = 2\hbar^2/\mu_{ex}\left(a_{ex}^{2D}\right)^2$ is the 2D-SIE binding energy), $\tilde{\varepsilon} = 2\varepsilon_1\varepsilon_2/(\varepsilon_1 + \varepsilon_2)$ is the permittivity of the nanosystem, $(\mu_{ex}/m_0) = m_e m_h/(m_e + m_h)$ is the reduced SIE mass, $a_{ex}^{2D} = \tilde{\varepsilon}(m_0/\mu_{ex})\left(\hbar^2/m_0 e^2\right)$ is the 2D-SIE Bohr radius, c is the speed of light, the value $\Delta E_{1,l}^{1,l+1}(a)$ is the distance between the SIE levels $(n = 1, l)$ and $(n = 1, l + 1)$, that is

$$\Delta E_{1,l}^{1,l+1}(a) = \left[E_{1,l+1}(a) - E_{1,l}(a)\right] \tag{6}$$

In this case, the oscillator strength $f_{1,l}^{1,l+1}(a)$ of the transition between the SIE-states $(n = 1, l)$ and $(n = 1, l + 1)$ was described by Formula [11]:

$$f_{1,l}^{1,l+1}(a) = 4\left(\Delta E_{1,l}^{1,l+1}(a)/E_{ex}^{2D}\right)\left(D_{1,l}^{1,l+1}(a)/ea_{ex}^{2D}\right)^2 \tag{7}$$

Dipole moments $D_{1,l}^{1,l+1}(a)$ and oscillator strengths $f_{1,l}^{1,l+1}(a)$ of the transitions between SIE-states $(n = 1, l)$ and $(n = 1, l + 1)$ were received in [11–17].

4 Numerical Results and Discussion

Let us estimate the intensity values $I_{1,l}^{1,l+1}(a)$ (4), as well as lifetimes $\tau_{1,l}^{1,l+1}(a)$ (5), depending on the radius a of germanium QDs caused by optical transitions between the SIE-states $(n = 1, l)$ and $(n = 1, l + 1)$. Intensity $I_{1,0}^{1,1}(a_1)$, as well as the lifetime $\tau_{1,0}^{1,1}(a_1)$, of the intraband transition in QDs with an average radius $a_1 = 10$ nm between stationary SIE-states $(n = 1, l = 0)$ with energy $E_{1,0} = -42$ meV and $(n = 1, l = 1)$ with energy $E_{1,1} = -26$ meV (with the nanosystem parameters $j_0 = 2.06$ and $j_1 = 2.22$ taken from [6]) took the value $I_{1,0}^{1,1}(a_1) = 0.10$ and $\tau_{1,0}^{1,1}(a_1) = 7.9 \times 10^{-4}$ s (see Table 1).

As a result of the interband transition in QDs with an average radius $a_2 = 11.5$ nm between the stationary SIE-state $(n = 1, l = 1)$ with energy $E_{1,1} = -45$ meV and the quasistationary SIE-state $(n = 1, l = 2)$ with energy $E_{1,2} = 28$ meV (with the nanosystem parameters $j_1 = 2.14$ and $j_2 = 2.26$ taken from [9]) the relative intensity $I_{1,1}^{1,2}(a_2)$ and lifetime $\tau_{1,1}^{1,2}(a_2)$ have taken the values $I_{1,1}^{1,2}(a_2) = 0.15$, and $\tau_{1,1}^{1,2}(a_2) = 3.7 \times 10^{-5}$ s (see Table 1). Intensity $I_{1,2}^{1,3}(a_3)$ and lifetime $\tau_{1,2}^{1,3}(a_3)$ of the interband transition in quantum dots with an average radius $a_3 = 16$ nm between the stationary SIE-state $(n = 1, l = 2)$ with energy $E_{1,2} = -78$ meV and the quasistationary SIE-state $(n = 1, l = 3)$ with energy $E_{1,3} = 126$ meV (with the nanosystem parameters $j_2 = 2.24$ and $j_3 = 2.36$ taken from [9]) had such the value $I_{1,2}^{1,3}(a_3) = 0.44$ and $\tau_{1,2}^{1,3}(a_3) = 4.4 \times 10^{-6}$ s (see Table 1). Intensity $I_{1,2}^{1,3}(a_3)$ and lifetime $\tau_{1,2}^{1,3}(a_3)$ of the interband transition in quantum dots with an average radius $a_3 = 16$ nm between the stationary state SIE $(n = 1, l = 2)$ with energy $E_{1,2} = -78$ meV and the quasistationary state $(n = 1, l = 3)$ with energy $E_{1,3} = 126$ meV had such the value $I_{1,2}^{1,3}(a_3) = 0.44$ and $\tau_{1,2}^{1,3}(a_3) = 4.4 \times 10^{-6}$ s (see Table 1). It should be noted that transitions between the SIE-states $(n = 1, l = 2)$ and $(n = 1, l = 3)$ can occur at room temperature.

Quasistationary and stationary SIE-states $(n = 1, l)$ with large values of the orbital quantum number l (with $l \leq 3$) were included in the process of optical absorption in the zone of surface SIE-states with increasing QD radius a. With increasing l, SIE binding energies $\left|E_{1,l}(a)\right|$ are growing (see Table 1). In this case, the average

Table 1 Calculated values of the normalized intensities $I_{1,l}^{1,l+1}(a)$ (4), as well as lifetimes $\tau_{1,l}^{1,l+1}$ (5) (expressed by seconds), caused by optical transitions between the SIE-states ($n = 1$, l) with the energy $E_{1,l}(a)$ (expressed by meV) and ($n = 1$, $l + 1$) (where $l = 0, 1, 2$) with energy $E_{1,l+1}(a)$ (expressed by meV) in a germanium quantum dot with an mean radius a (expressed by nm)

a (nm)	$(1, l) \to (1, l + 1)$	$E_{1,l}$ (meV)	$E_{1,l+1}$ (meV)	$E_{1,l}^{1,l+1}$ (meV)	$\hbar\omega_{ex(1,l)}$ (meV)	$\hbar\omega_{ex(1,l+1)}$ (meV)	$f_{1,l}^{1,l+1}$	$I_{1,l}^{1,l+1}$	$\tau_{1,l}^{1,l+1}$ (10^{-6}) s
10.0	$(1, 0) \to (1, 1)$	− 42	− 26	16	288	304	0.48	0.10	790
11.5	$(1, 1) \to (1, 2)$	− 45	28	73	285	358	0.49	0.15	37
16.0	$(1, 2) \to (1, 3)$	− 78	126	204	252	456	0.54	0.44	4.4

$E_{1,l}^{1,l+1}(a) = E_{1,l+1}(a) - E_{1,l}(a)$ (expressed by meV) is the distance between the SIE levels ($n = 1$, l) and ($n = 1, l + 1$), energy $\hbar\omega_{ex(1,l)}(a)$ (2) of an electron transition (expressed by meV), oscillator strengths $f_{1,l}^{1,l+1}(a)$ (7)

distance between the electron and the hole decreases with increasing l. This leads to the fact that the overlap integral of the exciton wave functions $R_{1,l}(r)$ (1) and $R_{1,l+1}(r)$ (1) also increases with increasing l.

Therefore, the value of the intensity $I_{1,2}^{1,3}(a_3) = 0.44$ (for $l = 2$) will be four times greater than the intensity $I_{1,0}^{1,1}(a_1) = 0.10$ (for $l = 0$) (see Table 1). Such a significant increase in the intensity $I_{1,2}^{1,3}(a_3)$ is due to the fact that the interband electron transition between the quasistationary SIE-state ($n = 1$, $l = 3$) and the stationary SIE-state ($n = 1$, $l = 2$) will be a direct transition in real space. In this case, the electron passes from the quasistationary SIE-state ($n = 1$, $l = 3$) located in the conduction band of the silicon matrix to the stationary SIE-state ($n = 1$, $l = 2$), which is located in the bandgap of the silicon matrix.

For the appearance in the nanosystem with germanium QDs with radii $a_1 = 10$ nm of SIE levels $\left(E_{1,0} = -42\ \text{meV}\right)$ and $(E_{1,1} = -26\ \text{meV})$, according to (2), light quanta with following energies $\hbar\omega_{ex(1,0)}(a_1) = 288$ meV and $\hbar\omega_{ex(1,1)}(a_1) = 304$ meV are required. As a result of the absorption of light quanta with energies $\hbar\omega_{ex(1,1)}(a_2) = 285$ meV and $\hbar\omega_{ex(1,2)}(a_2) = 358$ meV in the nanosystem with germanium QDs with radii $a_2 = 11.5$ nm, according to (2), the SIE levels $\left(E_{1,1} = -45\,\text{meV}\right)$ and $(E_{1,2} = 28\,\text{meV})$ arise, respectively. In such a nanosystem containing germanium QDs with average radii $a_3 = 16$ nm, of SIE levels $\left(E_{1,2} = -78\,\text{meV}\right)$ and $\left(E_{1,3} = 126\,\text{meV}\right)$, were formed upon absorption of a quantum of light, according to (2), with energies $\hbar\omega_{ex(1,2)}(a_3) = 252$ meV and $\hbar\omega_{ex(1,3)}(a_3) = 456$ meV, respectively. Such energies $\hbar\omega_{ex(1,l)}(a)$ (2) were contained in the infrared spectral region (0.20–1.14) eV, which was observed under experimental conditions up to room temperature [1–6].

It follows from Formula (5) that high lifetimes have SIE-states caused by optical transitions with the smallest distance $E_{1,l}^{1,l+1}(a)$ (6) between them. Therefore, the state that is due to optical transitions between the SIE-states ($n = 1$, l) and ($n = 1$, $l + 1$) has the longest lifetime $\tau_{1,0}^{1,1}(a_1) = 7.9 \times 10^{-4}$ s (see Table 1). The transition between the SIE-states ($n = 1$, $l = 2$) and ($n = 1$, $l = 3$), which occurs at room temperature, also determines the SIE-state with a high lifetime $\tau_{1,2}^{1,3}(a_3) = 4.4 \times 10^{-4}$ s (see Table 1). Such values of the lifetime $\tau_{1,2}^{1,3}$ exceed by four orders of magnitude the corresponding lifetimes of excitons in silicon [4, 5].

5 Conclusion

A mechanism is proposed for a significant increase (four times) in the intensities of optical interband and intraband transitions between quasistationary and stationary SIE-states arising above a spherical surface of a single germanium QD placed in a silicon matrix. These optical electronic transitions occur in the real space of the silicon matrix. Such a mechanism, apparently, will apparently solve the problem of a significant increase in the radiative intensity in germanium/silicon heterostructures with germanium QDs. This will provide an opportunity to develop fundamental and

applied foundations, allowing to create a new generation of effective light-emitting and photodetector devices based on germanium/silicon heterostructures with germanium quantum dots. The theoretically predicted long-lived SIE-states, apparently, will make it possible to realize high-temperature quantum Bose-gases SIE-states in the nanosystem under study.

References

1. S.A. Rudin, V. Zinovyev, J.V. Smagina et al., J. Appl. Phys. **131**, 035302 (2022)
2. S.A. Rudin, V. Zinovyev, J.V. Smagina et al., J. Cryst. Growth **593**, 126763 (2022)
3. J.V. Smagina, V. Zinovyev, A.F. Zinivieva et al., J. Lumines. **249**, 119033 (2022)
4. A.I. Yakimov, A.A. Bloshkin, A.V. Dvurechenskii, JETP Lett **90**, 569 (2009)
5. A.F. Zinovieva, V.A. Zinovyev, A.I. Nikiforov et al., JETP Lett **104**, 823 (2016)
6. Z.V. Smagina, A.V. Dvurechenskii, V.A. Seleznev, Semiconductors **49**, 749 (2015)
7. S.I. Pokutnyi, Physica B Phys. Condens. Matter **616**, 4130598 (2021)
8. S.I. Pokutnyi, Low Temp. Phys. **42**, 1151 (2016)
9. S.I. Pokutnyi, Low Temp. Phys. **44**, 819 (2018)
10. A.l.L. Efros, A.L. Efros, Sov. Phys. Semiconductors **16**, 772 (1982)
11. S.I. Pokutnyi, Eur. Phys. J. Plus. **135**, 74 (2020)
12. S.I. Pokutnyi, Phys. Solid Stat. **39**, 634 (1997)
13. S.I. Pokutnyi, Phys. Solid Stat. **39**, 528 (1997)
14. S.I. Pokutnyi, Y.N. Kulchin, V.P. Dzyuba, J. Nanophoton. **10**, 036008 (2016)
15. V.G. Klyuev, D.V. Volykhin, O.V. Ovchinnikov et al., J. Nanophoton. **10**, 033507 (2016)
16. S.I. Pokutnyi, Physica Status solidi (b) **173**, 607 (1992)
17. S.I. Pokutnyi, Semiconductors **30**, 1015 (1996)

Co-Doped CdS Quantum Dots and Their Bionanocomplex with Protein: Interaction and Bioimaging Properties

I. D. Stolyarchuk, R. Wojnarowska-Nowak, S. Nowak, M. Romerowicz-Misielak, O. V. Kuzyk, O. O. Dan'kiv, and A. I. Stolyarchuk

Abstract Semiconductor nanoparticles (SNPs) or quantum dots (QDs), due to their unique optical properties, constitute significant materials for many areas of nanotechnology and bionanotechnology. In the present work, we report on spectroscopy studies of interactions between CdS-based diluted magnetic semiconductor nanoparticles and model proteins type of human serum albumin (HSA). To probe this interaction, in addition to conventional UV–Vis absorption and photoluminescence spectroscopic methods, we have used micro-Raman spectroscopy and technique of magneto-optical Faraday rotation, which is important for case of nanoparticles with magnetic impurities. It was proved that, in all cases, the fluorescence quenching of HSA by the QDs depends on the size and temperature. In the steady-state fluorescence studies, the interaction parameters including binding constants, number of binding sites, and quenching constants were determined. The results on Faraday rotation spectra are more informative for diluted magnetic SNPs. In this case, the influence of the added proteins on spin exchange interactions can be extracted. Obtained data enable us to find optimal QDs concentration useful for carcinoma cells bioimaging. However, in the case of CdS:Co (CdS:Mn) QDs-HSA biocomplex used for labeling this molecule, the concentration of QDs should be higher. The low toxicity as well as high stability of the QDs-HSA bioconjugates in the case of their use as bioimaging probes for the 143b osteosarcoma cells has been demonstrated.

I. D. Stolyarchuk (✉) · O. V. Kuzyk · O. O. Dan'kiv · A. I. Stolyarchuk
Department of Physics and Information Systems, Drohobych Ivan Franko State Padagogical University, 24 I. Franko Street, Drohobych 82100, Ukraine
e-mail: i.stolyarchuk@dspu.edu.ua

R. Wojnarowska-Nowak
Center for Microelectronics and Nanotechnology, Institute of Materials Engineering, University of Rzeszow, 16 Rejtana Street, 35-959, Rzeszow, Poland

S. Nowak · M. Romerowicz-Misielak
Department of Biotechnology, Institute of Biology and Biotechnology, College of Natural Sciences, University of Rzeszow, Pigonia 1, 35-310, Rzeszow, Poland

O. Fesenko and L. Yatsenko (eds.), *Nanoelectronics, Nanooptics, Nanochemistry and Nanobiotechnology, and Their Applications*, Springer Proceedings in Physics 297,
https://doi.org/10.1007/978-3-031-42708-4_24

1 Introduction

In the past few decades, semiconductor nanoparticles (SNPs), nanocrystals (NC), or quantum dots (QD) have been attracted much attention because of their unique electrical, magnetic, optical, and catalytic properties resulting mainly from the confinement effect [1, 2]. From the point of view of biomedical applications, II–VI semiconductor-based nanoparticles are the most studied. Since their introduction as labels in cellular imaging in 1998 [3], numerous reports have shown the advantages of this kind of semiconductor nanoparticles before organic fluorophores [4–8]. These advantages include broad absorption spectra, narrow photoluminescence spectra, size-tunable spectra and superior resistance to photobleaching, photostability, signal multiplexing, and high sensitivity [9]. The main photophysical properties of quantum dots in comparison with chemical dyes are provided in Table 1.

Table 1 Photophysical properties of quantum dots and chemical dyes [13–15]

Properties	QDs	Organic fluorophores
Photostability	Superior	Low
Photoluminescence lifetime	Longer (>10 ns)	Shorter (< 10 ns)
Photoluminescence (PL) phenomenon	Present	Present
Photobleaching threshold	High resistance to photobleaching, as well as photo and chemical degradation	Poor resistance
Quantum yield	High (10–90%)	Lower
Excitation–emission range	Wide (UV–vis–IR)	VIS
Excitation band	Broadband	Narrowband
Emission band	Narrowband (FWHM ~25–40 nm)	Broadband
Molar extinction coefficients	High	Lower (~10–100 × lower than QDs)
Additional advantages	Size-dependent emission spectra	Fixed emission wavelength
	Excitation of multicolor light	Excitation of monochromatic light
	Large Stokes shifts	–
	Efficient fluorescence resonance energy transfer (FRET) donors	–

(continued)

Table 1 (continued)

Properties	QDs	Organic fluorophores
	Easy surface modification and change in optical and utility properties	–
	Easily observable by conventional microscopic and spectroscopic techniques	Easily observable by conventional microscopic and spectroscopic techniques

II–VI semiconductor compounds have another functionality as a basic matrix for diluted magnetic semiconductors (DMSs), where a fraction of semiconductor cations are replaced by transition metals (3*d* or 4*f* elements) [10]. Among DMSs 3*d*-doped (Mn, Co, etc.) II–VI semiconductor-based nanoparticles are the most promising because of their chemical stability and strong fluorescence in visible regions. The main feature of bulk DMSs is the strong *s*, *p–d* spin exchange interaction between the band carriers and the magnetic ions which results in a high sensitivity for the applied magnetic field [11]. II–VI-based DMSs quantum dots are useful as a novel probe in biosensors as well as for bioimaging due to unique size-dependent on their optical and electrical properties. These nanoparticles are brightly fluorescent, enabling their use as imaging probes both in vitro and in vivo studies [12].

Magnetic targeting, on the other hand, applies a magnetic field to appeal magnetic nanoparticles circulating in the blood to the tumor site where the magnet is placed, increases the accumulation of nanocrystals in tumor, and as a result, increases sensitivity on fluorescence and therapeutic efficiency. Co-existence of quantum confinement effect and *s*, *p–d* exchange interaction opens new way for the practical use of DMSs quantum dots in bionanotechnology and nanomedicine [16].

One of the main decisive parameters for the use of QDs in bionanotechnology is the functionalization of their surface with appropriate (bio)molecules to ensure the stability of colloidal solutions in combination with effective labeling of the corresponding biological objects. It is the combination of nanoparticles with selected biological or chemical ligands such as proteins, antibodies, or DNA sequences that leads to the creation of highly functional bionanomaterials (bionanocomplexes), which opens up the broadest prospects for their use in bio- and nanomedicine [17]. In the same time, for the potential use of II–VI-based DMSs QDs, the behaviors of them in bloodstream need to be understood. Human serum albumins are one of the most abundant proteins in blood plasma and are involved in the transport of a variety of endogenous and exogenous ligands. Distribution, transportation, physiological, and toxicological actions of the ligands are closely related to their binding with proteins. The binding ability of DMSs QDs with albumins in the bloodstream may have an important impact on the structure and function of serum albumins. So, it is very significant to investigate the interaction between the QDs and the major carrier protein like HSA [12, 16, 18–21].

The human serum albumin (HSA) is the most abundant and one of the most important proteins in blood plasma. It was first described by Denis in 1840, and it is one of the earliest known proteins in the human body. This protein occurs in the plasma, cerebrospinal fluid, and lymph. HSA is produced by liver, and it provides more than 50% of the total proteins of plasma. Albumin has many different and very important physiological functions: connecting and handling to the cells a variety of endogenous and exogenous ligands (including hormones, metabolites, ions, or fatty acids), drug transportation, toxins binding, and oncotic pressure maintaining (through the water-binding capacity) [22–26]. It can be also a diagnostic marker for determining some diseases like inflammatory states [23]. From the biochemical point of view, albumin is a protein composed of three α-helical domains (I–III), which are divided into two sub-domains: A and B. By the presence of the elastic loop, it is possible to move of relative domains to each other, which makes the structure of protein easily adapted to binding a large number of ligands [24]. As mentioned above, the protein plays an important role in the transportation of many ligands, and during this property, it is used to create new diagnostic methods, contrast agents, or drugs [25]. The covering of QDs by natural protein seems to be promising solution for reducing their toxicity. Therefore, forming the DMSs QDs + HSA complexes is important in order to remove toxicity of the CdS-based DMSs QDs. The toxic effect of QDs is mainly related to the processes occurring on the surface of nanoparticles. The HSA covering is neutral and slightly changes the properties of the QDs.

Recently, we reported spectroscopy studies of the interaction of II-VI-based semiconductor nanoparticles with HSA [21, 27–30]. Herein, we report on optical and magneto-optical studies of CdS, CdS:Co, and CdS:Mn nanoparticles and their interaction with model proteins type of HSA. Obtained data enable us to find optimal QDs concentration useful for carcinoma cells bioimaging. The low toxicity as well as high stability of the QDs-HSA bioconjugates in the case of their using as bioimaging probes for the 143b osteosarcoma cells has been demonstrated.

2 Experimental

Aqueous synthesis of QDs offers many benefits for biological studies. The basic principle of chemical synthesis of nanostructured materials (the so-called bottom-up method) is to initiate chemical reactions and control the nucleation and growth of the reaction products. This can be achieved by conducting the reactions within a confined environment or controlling the reaction process via dynamic binding of surface ligands. In colloidal solution synthesis, controlling the size or shape is done by adjusting the ratio of the chemical concentrations, selecting capping material, value of pH, and temperature. Nanocrystals of CdS, CdS:Co, and CdS:Mn were synthesized in aqueous medium by a chemical precipitation technique using cadmium chloride $CdCl_2$, cobalt chloride $CoCl_2$ or manganese chloride $MnCl_2$ and sodium sulfide Na_2S in the presence of polyvinylalcohol (PVA) as the capping agent. A

theoretical consideration of the probability of chemical reactions in the system Cd^{2+}–Co^{2+} (Mn^{2+})–S^{2-}–H_2O in the case of the synthesis of nanocrystals has shown that the optimal ranges of a change of the molar concentration of precursors and the pH value of the medium are within the limits of (10^{-4}–10^{-2}) mol/L and (3–5), respectively. For Mn doping, an aqueous solution of $MnCl_2$ was added directly to the solution of $CdCl_2$ in the ratio 97:3. Since all initial reaction conditions require cadmium to be in an excess of 2 to 1 sulfur, the latter is a limiting reagent and is completely consumed as particles mature. The addition of more sulfur allows the particles to grow to larger sizes [31].

Transmission electron microscopy (TEM) was used in order to confirm the structure of the grown nanoparticles: estimate shape and determine the average size of nanocrystals as well as their composition and crystal structure. A TEM instrument Tecnai Osiris X-FEG TEM microscopy that provides maximum resolution of 0.136 nm has been used.

The QD-HSA bionanocomplex can be easily prepared by mixing the set amount of albumin with colloidal solution of QDs to obtain a certain concentration of reagents. For QDs-HSA bionanocomplex preparation, a HSA solution was added to the colloidal QDs, stirred, and incubated for at least 15 min to several hours at room temperature. The QDs concentration was fixed to 30×10^{-6} M, and the HSA concentrations were in the range of 30×10^{-6} M to 6.5×10^{-6} M for the photoluminescence analysis. HSA was purchased from PJSC Biofarma (Ukraine) at the concentration of 1.5×10^{-6} mol L^{-1}. The size of bionanocomplexes was investigated by Innova (Bruker) atomic force microscopy (AFM).

The absorption spectra of HSA, CdS, CdS:Co and CdS:Mn QDs and HSA-QDs solutions were recorded at room temperature, with using a UV–Vis Evolution 300 (Thermo Scientific) spectrophotometer. Photoluminescence spectra of the SNPs, and CdS-based QDs under interaction with different concentrations of HSA were measured by means of F-2500 Hitachi spectrofluorometer. An excitation wavelength of 325 nm was chosen to record the emission intensity in the wavelength region from 350 to 750 nm, at room temperature. Similar study was performed with excitation wavelength of 543 nm, which was applied for cancer cell imaging.

The oscillation spectra were obtained using Fourier transform infrared (FTIR) spectrometer Vertex 70v (Bruker) equipped with the attenuated total reflectance (ATR) technique. The measurements were performed with 64 scans and 1 cm^{-1} spectral resolution. The Raman spectra were acquired with the Smart Raman DXR (Thermo Scientific) spectrometer in the narrow spectral range of 1000–1800 cm^{-1}. The 14 mW power and 780 nm wavelength semiconductor laser were used as a light source.

Faraday rotation measurements were carried out using a home-designed setup with a water-cooled electromagnet for producing magnetic field of 5T. As the rotation angle is proportional to the distance traveled by the light experimental measurements of this effect in low-dimensional semiconductor structures deposited on thick substrates is a problematic task [32–34]. After passing through a focusing lens and a polarizer (Rochon prism), monochromatic light becomes a linear polarized and

then propagates through the studied film sample placed in the water-cooled electromagnet with magnetic field up to maximum induction 5T. Behind the electromagnet, the analyzer (Wollaston prism) splits the beam on two ones, which then pass through chopper. In such a manner, these two beams were modulated by a phase shift of 180°. In the absence of magnetic field, a balance was achieved by equalizing the intensities of the two light beams, and when the electromagnet was switched on the resultant unbalanced signal can be recorded by using photodetector system, which includes photomultiplier tube, lock-in amplifier, and personal computer. The described setup allows to register the rotation angle of 10^{-4} rad. Measurements were performed separately for 1.0 cm quartz cell without nanoparticles and same quartz cell with nanoparticles and biocomplexes QDs-HSA for comparison in temperature range of 293–300 K.

The human osteosarcoma 143b cell line was used for the bioimaging properties of colloidal nanoparticles and CdS:Co (CdS:Mn) QDs-HSA complexes' examination. The cells were maintained in Dulbecco's Modified Eagle's medium (DMEM), supplemented with fetal bovine serum (FBS, 10%), and penicillin–streptomycin (1%) antibiotic, in 5% CO_2 at 37 °C. After centrifugation (7 min, 4 °C, 600 g), the cells were seeded in a 96-well plate at a density of 8.0×10^4 cells per mL, and incubated during 24 h. The QDs were mixed with DMEM medium in order to obtain 30×10^{-5} M, 20×10^{-5} M, and 8.0×10^{-5} M concentration of QDs. An aliquot (0.1 mL) of the prepared solution was added to each well and incubated during 24 h. In the next experiment, osteosarcoma cells were fixed by pre-cooled methanol and the cell membrane was permeated by 0.1% Triton X-100 reagent. 0.1 mL aliquot of CdS:Co (CdS:Mn) NPs suspended in phosphate-buffered saline was added to the cells and incubated for 10 min. The same procedure was used for the treatment of cells by CdS:Co (CdS:Mn) NPs-HSA bionanocomplexes, with 1.2×10^{-5} M of maximum concentration of protein. Cell nuclei were stained with Hoechst 33342 fluorescent dye as a standard method. The images were taken by IN Cell Analyzer 2000 automated microscope (GE Healthcare, UK). The images were taken with two different excitation/emission filters: 543/605 nm for the CdS:Co (CdS:Mn) NPs and the CdS:Co (CdS:Mn) QDs-HSA bionanocomplexes and 350/455 nm for Hoechst 33342. The osteosarcoma cells were treated with QDs and bionanocomplexes with the same concentrations as for photoluminescence measurements.

3 Results and Discussion

The TEM images of the colloidal QDs CdS and CdS:Co are shown in Fig. 1. As can be seen, the shape of the nanoparticles is close to spherical and the average diameter of the nanoparticles is found to be approximately from 4.8 to 5.2 nm (Fig. 2a, b). In the AFM image of the colloidal QDs and QDs-HSA bioconjugate, some larger structures can be also observed (Fig. 2). Averaged size of QDs-HSA bioconjugates (or bionanocomplexes) was confirmed by AFM measurement, and it was about 10–15 nm. This aggregate can be created by sample drying in air atmosphere.

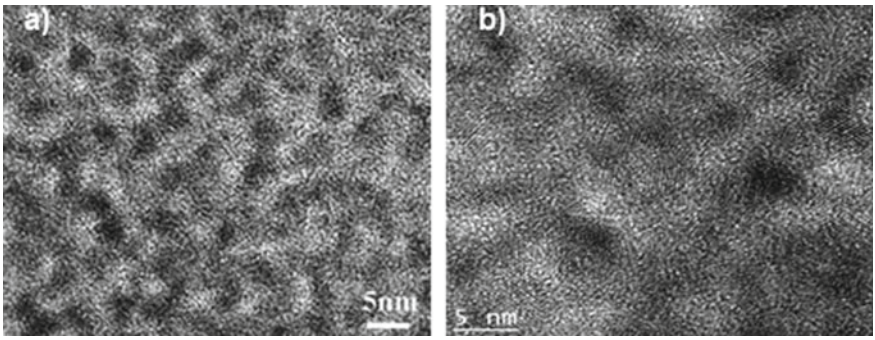

Fig. 1 TEM images of CdS (**a**) and CdS:Co (**b**) colloidal nanoparticles

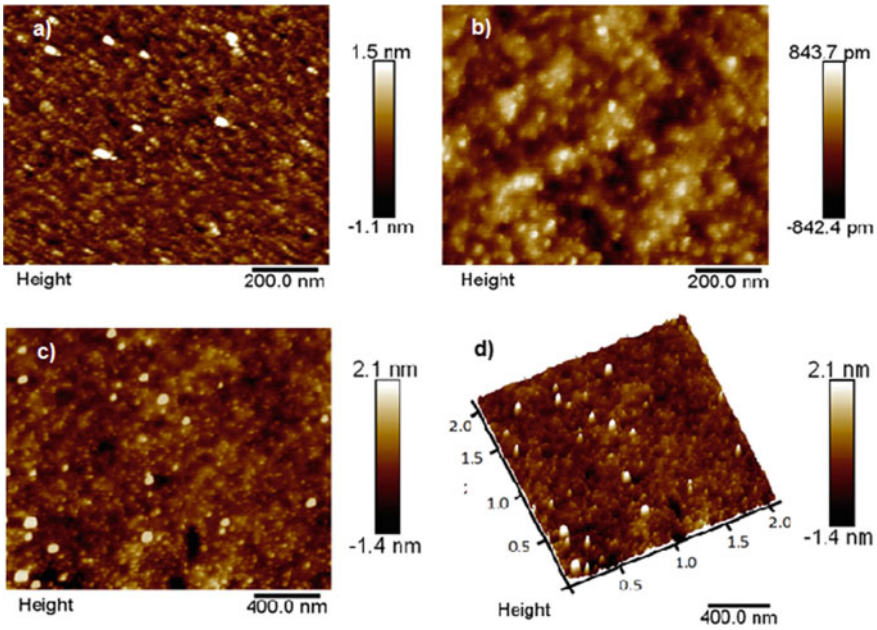

Fig. 2 AFM images of the quantum dots CdS:Co (**a**), human serum albumin (**b**) and their biocomplex-2D (**c**), -3D (**d**)

Figure 3 shows EDX results on the content of chemical elements for CdCoS QDs. All of the compounds are clearly visible in the structure of the material.

For the evaluation of optical properties of pure QDs, pure HSA and QDs-HSA biocomplex absorption spectra are recorded and analyzed. Figures 4, 5 and 6 show optical density as a function of photon energy for studied samples. An addition of HSA to colloidal CdS, CdS:Co, or CdS:Mn nanoparticles, as for the CdTe nanocrystals [27–29], leads to a gradual decrease of optical density and broadening of exciton

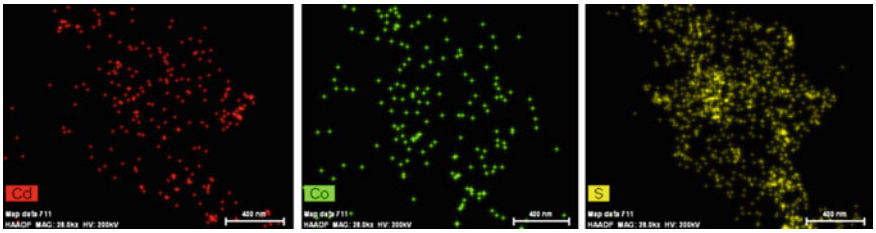

Fig. 3 EDX scheme of the presence of chemical elements: Cd, Co, and S in the CdCoS QDs structure

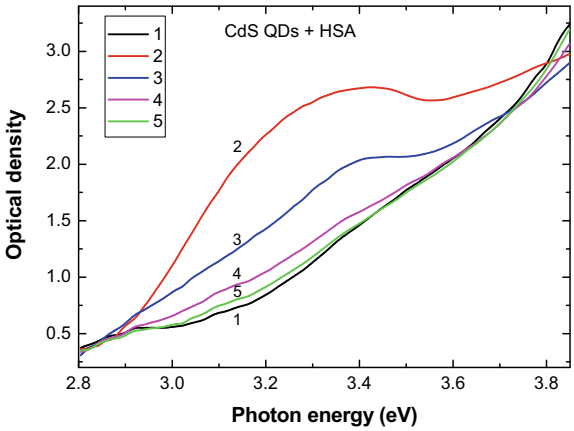

Fig. 4 Optical density as function of photon energy for solution of colloidal QDs CdS and HSA: 1—HSA, 2—CdS, 3—HSA—1.5 mmol L^{-1} CdS, 4—HSA—0.9 mmol L^{-1} CdS, 5—HAS—0.6 mmol L^{-1} CdS

structure. However, energy position of the exciton bands is not shifted. The obtained results indicate that the binding process between the QDs and the protein molecules does not change the electron states in the QD.

Photoluminescence spectra of HSA under interaction with QDs have been recorded on spectrofluorometer upon the excitation wavelength optimal for the investigated QDs. The measurements have been performed at temperature range 293–300 K. The changing of photoluminescence properties of HSA by the presence of QDs is described in several scientific reports [16, 35–38]. The fluorescence of HSA mainly comes from tryptophan, tyrosine, and phenylalanine amino acids. When small molecules are bound to HSA, the changes the protein luminescence are mainly due to the tryptophan side chains [39, 40]. The phenomenon of fluorescence quenching is commonly registered; however, sometimes the strengthening of the light emission is noticed. The modification of the QDs photoluminescence by the HSA presence is not so thoroughly described.

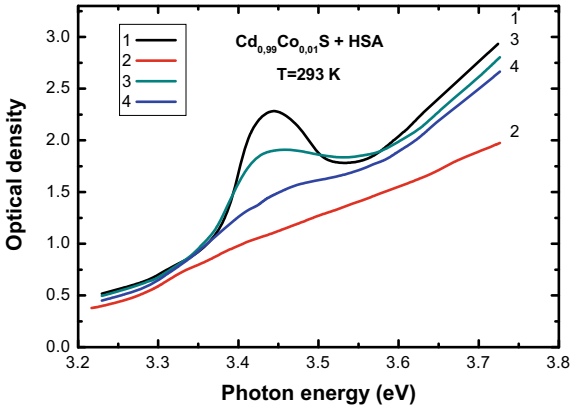

Fig. 5 Optical density as function of photon energy for solution of colloidal QDs $Cd_{0,99}Co_{0,01}S$ and HSA: 1—QDs $Cd_{0.99}Co_{0.01}S$, 2—HSA, 3—HSA + 0.5×10^{-3} mmol L^{-1} QDs, 4—HSA + 1.2×10^{-3} mmol L^{-1} QDs

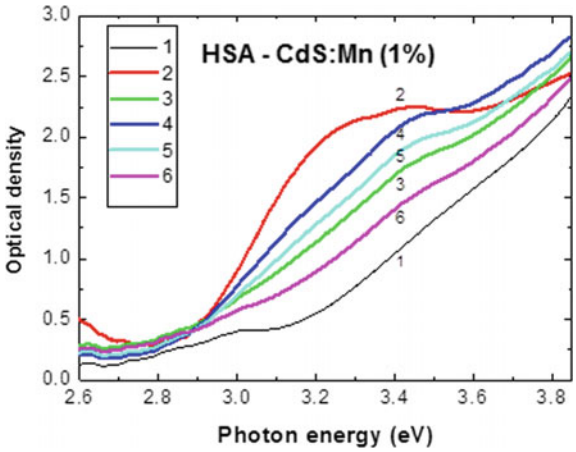

Fig. 6 Absorption spectra of colloidal QDs CdS:Mn (Mn–1%), HSA and their solutions: 1—HSA, 2—QDs $Cd_{0,9}Mn_{0,1}S$, 3—HSA + 0.6×10^{-3} mmol L^{-1} QDs, 4—HSA + 0.9×10^{-3} mmol L^{-1} QDs, 5—HSA + 1.2×10^{-3} mmol L^{-1} QDs, 6—HSA + 1.5×10^{-3} mmol L^{-1} QDs

Figures 7, 8 and 9 show photoluminescence spectra of colloidal nanoparticles of CdS, CdS:Co, and CdS:Mn, an HSA solution and their combinations, respectively. In all cases, the photoluminescence intensity with the addition of HSA is decreased and the quenching effect occurs. In similar behavior, we also observed in photoluminescence spectra HSA in the range between 270 and 470 nm when we added of colloidal solution of QDs. HSA has a strong fluorescence emission band at 336 nm, with the excitation wavelength at 250 nm. When different amounts of CdS, CdS:Co or CdS:Mn QDs are added to the HSA solution, the decrease in the fluorescence

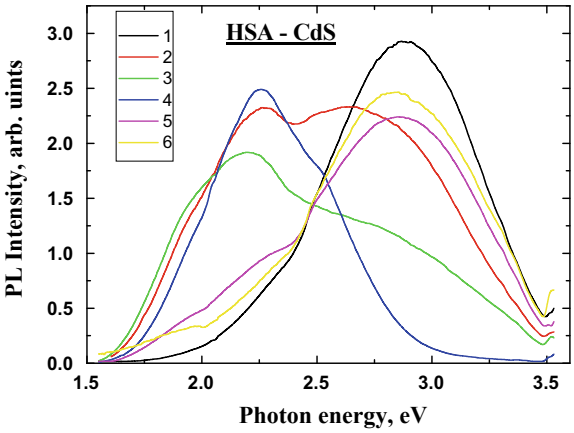

Fig. 7 PL spectra as function of photon energy for solution of colloidal QDs CdS and HSA: 1—HSA, 2—HSA + 1.2 × 10^{-3} mmol L^{-1} QDs, 3—HSA + 0.9 × 10^{-3} mmol L^{-1} QDs, 4—CdS, 5—HSA + 0.6 × 10^{-3} mmol L^{-1} QDs, 6—HSA + 0.3 × 10^{-3} mmol L^{-1} QDs

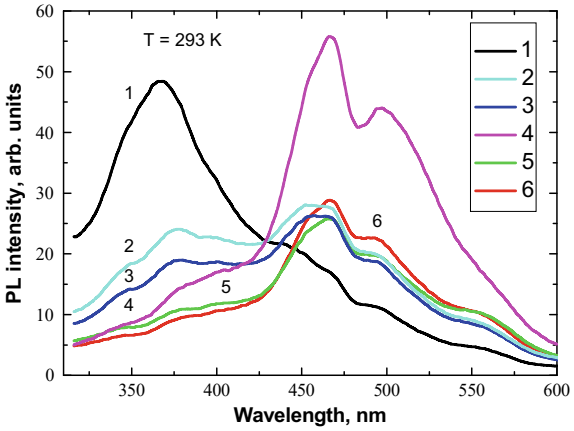

Fig. 8 PL spectra of biocomplex QDs CdS:Co (Co = 1%)—HSA for different concentrations of QDs in HSA: 1—HSA, 2—HAS—0.1 × 10^{-3} mmol/L CdS:Co, 3—HAS—0.3 × 10^{-3} mmol/L CdS:Co, 4—CdS:Co (Co = 0.5%), 5—HAS—0.9 × 10^{-3} mmol/L CdS:Co, 6—HAS—1.5 × 10^{-3} mmol/L CdS:Co

intensity of protein is observed (Fig. 10). These suggest that the quenching effect occurs in the CdS or CdS:Co QD-HSA complex and may lead to changes in the protein conformation [41].

Fluorescence quenching is a powerful tool for determining the type of interaction between protein and quenchers dispersed in a solution. The photoluminescence quenching mechanism can be calculated by the Stern–Volmer equation [42]:

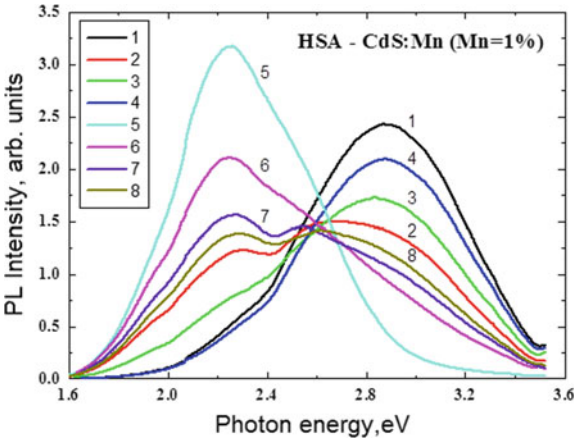

Fig. 9 PL spectra of biocomplex QDs CdS:Mn (1%)—HSA for different concentrations of QDs. 1—HSA, 2—HSA + 0.9 × 10^{-3} mmol/L QDs, 3—HSA + 0.6 × 10^{-3} mmol/L QDs, 4—HSA + 0.3 × 10^{-3} mmol/L QDs, 5—QDs CdS:Mn (Mn = 1%), 6—HSA + 1.8 × 10^{-3} mmol/L QDs, 7—HSA + 1.5 × 10^{-3} mmol/L QDs, 8—HSA + 1.2 × 10^{-3} mmol/L QDs

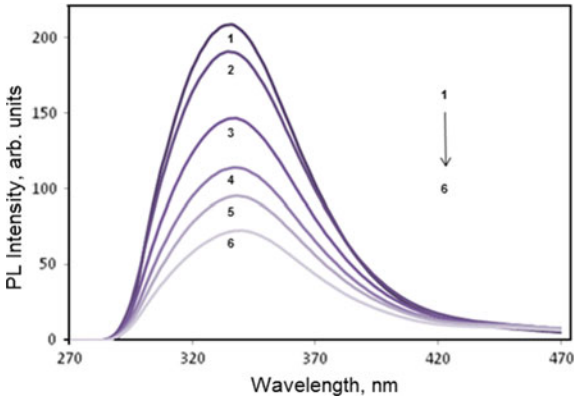

Fig. 10 Photoluminescence spectra of 10 mg/ml HSA with different concentrations of CdCoS (1%) QDs: 1—10 mg/ml HSA, 2—10 mg/ml HSA—0.1 mg/ml QDs, 3—10 mg/ml HSA—0.2 mg/ml QDs, 4—10 mg/ml HSA—0.3 mg/ml QDs, 5—10 mg/ml HSA—0.4 mg/ml QDs, 6—10 mg/ml HSA—0.5 mg/ml QDs

$$\frac{F_0}{F} = 1 + k_q \tau_0 [Q] = 1 + K_{sv}[Q], \tag{1}$$

where F_0 and F are the fluorescence intensities before and after the addition of the quencher, K_q is the quenching rate constant of the bimolecular, τ_0 is the average lifetime of the fluorophore without quencher, K_{SV} and $[Q]$ are the Stern–Volmer dynamic quenching constant and the concentration of the quencher, respectively.

In Fig. 11, the Stern–Volmer plots for CdS-based DMS nanoparticles solutions with HSA were shown. The results for CdS and CdS:Mn with small concentration of manganese (up 3%) are similar, especially in the range from 0 to 0.5 mM QDs in HSA solution, the F_0/F factor is the same. Quenching constants K_{SV}, bimolecular quenching constants K_q, binding constants K_b, and number of binding sites—n for interaction of HSA with QDs were calculated and presented in Table 2. Obtained results suggest of static mechanism of quenching with ground-state complex formations.

As a method for the chemical structure determination as well as the conformation changes of molecules and interaction between molecules [43, 44], the FTIR spectroscopy was applied in order to compare the oscillation spectra of the HSA and the QDs-HSA biocomplexes. The results of oscillation spectra can give important information about the processes occurring during a biocomplex formation. The obtained results are shown in Fig. 12 and presented in Table 3.

Infrared spectra of HSA contain typical lines corresponding to amide bands of proteins. Amide I band mainly occurs in the region of 1600–1700 cm^{-1} and amide II

Table 2 Quenching constants K_{sv}, bimolecular quenching constants K_q, binding constants K_b, and number of binding sites—n for interaction of HSA with QDs

System	CdS:Mn (1%)		CdS:Co (1%)		CdS:Co (0.5%)	
T, K	293	298	293	298	293	298
K_{sv}, L mol^{-1}	6.62×10^4	5.84×10^4	9.84×10^3	8.34×10^3	7.37×10^4	6.35×10^4
K_q, L $mol^{-1}c^{-1}$	6.62×10^{12}	5.84×10^{12}	9.84×10^{11}	8.34×10^{11}	7.37×10^{12}	6.35×10^{12}
K_b	1.11×10^6	1.52×10^6	2.17×10^6	2.68×10^6	1.78×10^6	1.98×10^6
n	1.04	1.08	0.93	0.98	1.03	1.06
R^2	0.989	0.991	0.997	0.991	0.992	0.988

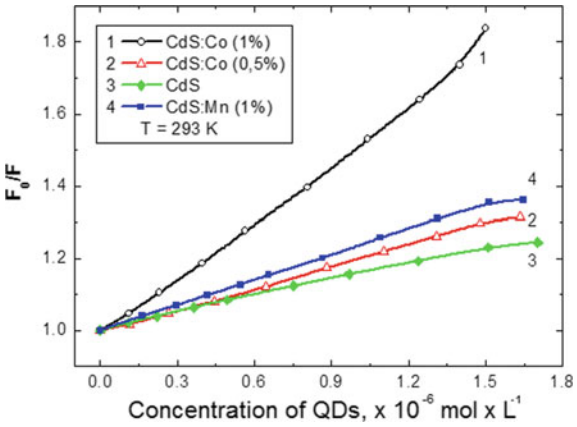

Fig. 11 Stern–Volmer plots for HSA photoluminescence quenching by different DMSs QDs at 293 K

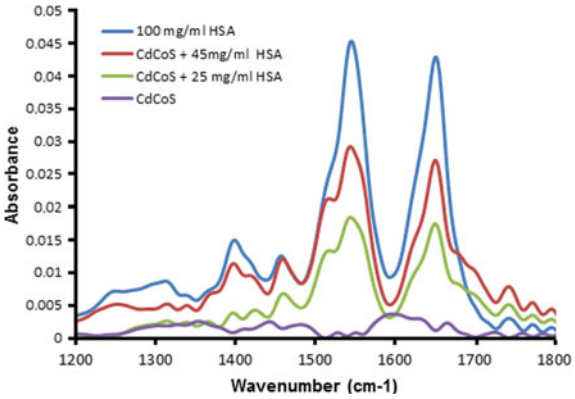

Fig. 12 FTIR spectra of quantum dots CdS:Co, human serum albumin, and their biocomplex

Table 3 Identification of the lines observed in the FTIR spectra (Fig. 12): s—strong, m—medium, w—weak

Position of line (cm^{-1}) HSA	Position of line (cm^{-1}) CdS:Co-HSA	Identification [45–48]
1651 (s)	1650 (s)	Amide I (C=O stretch, CN stretch, CCN deformation, NH bend)
1546 (s)	1541 (s)	Amide II (NH bend, CN stretch, CO in plane, CC, NC stretch)
1446 (w)	1452 (w)	C–H bend
1402 (m)	1390, 1410 (m)	COO-stretch and C–H bend
1236 (w)	1238 (w)	Amide III (CN stretch, NH bend, CO in plane, CC stretch)

band in the region of 1500–1550 cm^{-1}. Amide I corresponds mainly to the stretching vibration of peptide carbonyl group (C=O), but also to CN stretching, CCN deformation, NH bending vibrations. Amide II band is attributed to C–N stretching coupled with N–H bending vibrations and in less intense to CO, CC, NC stretching vibrations [45, 46]. Apart from these two main lines, other characteristic signals for the HSA protein were reported. The weak line observed at 1236 cm^{-1} corresponds to the amide III band, and it can be assigned mainly to CN stretching, and NH bending vibrations [45, 46]. Other bands are assigned to the chemical group of the amino acids in the HSA protein and to molecule's skeleton.

Both the amide I and amide II lines indicate the secondary structure of protein (especially amide I) [47, 48]. Shifting of position of the peak maximum is not large, from 1650 to 1651 cm^{-1} for amide I and from 1546 to 1547 cm^{-1} for amide II. However, the peak's shapes and peak's intensity slightly changed also and confirmed

only slightly modification in the secondary structure of the HSA protein after interaction with the CdS:Co QDs. Collected Raman spectra confirmed results based on the analysis of infrared spectra. The major line observed at 1657 cm^{-1} in Raman spectra and at 1650 cm^{-1} for FTIR spectra assigned to the amide I bonds is characteristic for the α-helical protein structure [44]. α-helix and β-sheets are the most common type of secondary structure of protein. The α-helix is coiled in a right-handed structure and is stabilized by hydrogen bonding occurring between successive turns of the helix. In β-sheets conformation (named zig-zag), an amino acids lie either parallel or antiparallel to one another, and the hydrogen bonds are localized between the strands [48]. The mentioned amide I line was shifted from 1651 to 1650 cm^{-1} in FTIR spectra and from 1657 to 1651 cm^{-1} in Raman spectra, and its intensity decreased, indicating a slight reduction of α-helical folding protein type. That means HSA conformation is not much changed, and the protein structure is similar to natural one.

The rotation of the polarization of light after passing a medium in a longitudinal magnetic field is a magneto-optical phenomenon known as Faraday effect. Different types of media in different aggregate states (solid states, liquids, gases) can exhibit Faraday rotation. In CdS-based DMS, the observed enhancement of the Faraday rotation is mainly associated with strong *s*, *p–d* exchange interaction between band carriers (*s*, *p*) and Mn (Co) local moments (*d*). Going from bulk crystals to nanocrystals opens new avenues for optoelectronic applications these materials, such as in current sensors, magnetic field sensors, optical modulators, and optical isolators [49–51].

Figure 13 shows the results of the spectral dependence of the Faraday rotation angle for bionanoconjugates CdS:Mn-HSA. This figure separately shows the Faraday rotation of albumin (without the semiconductor phase), semiconductor nanoparticles, and the general Faraday rotation of their solution. The increase in the absolute value of the angle of rotation in the latter case assumes the contribution of semiconductor particles. It was noted that the angle of rotation of the Faraday phase of a semiconductor quantum dot has a negative sign in the case of CdS:Mn quantum dots and the QDs-HSA bioconjugate. This indicates the paramagnetic nature of not only nanoparticles but also their biocomplexes with human serum albumin. The obtained results of high sensitivity of bioconjugates to the external magnetic field open the prospects of their practical application as effective magnetic field sensors (MRI) and computed tomography (CT) in the study of both in vitro and in vivo biological tissues.

The obtained results suggest that the bioconjugates of CdS-based DMS QDs-HSA could be utilized as diagnostic and drug delivery tools, which could help in the diagnosis and treatment of cancer and many other diseases. Because of their combination of magnetic and fluorescent properties, these bionanoconjugates open up the unique possibility of controlled target-directed applications. For example, the unique optical properties of QDs allow them to be widely used in medicine for diagnostic purposes, including detection of cancer cells, as well as their labeling and tracking, especially with using a fluoresce microscopy technique [52–55] and other bioimaging methods [56, 57]. Many researches focus on an early cancer diagnosis such as breast cancer, cervical carcinoma, prostate cancer, and hepatocellular carcinoma [13]. Functionalized quantum dots seem to be the most promising material, which can be combined

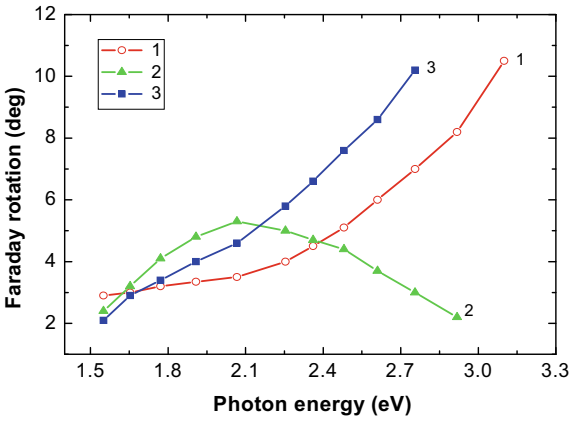

Fig. 13 Faraday rotation of biocomplex QDs-HSA at 293 K: 1—quartz cell, 2—QDs CdS:Mn (1%), 3—HSA, 4—biocomplex QDs CdS:Mn (1%)-HSA

with selected biological or chemical ligands like proteins or DNA sequences. They can detect the cancer cells or other molecules as magnificent fluorescent probes [53].

The main function of the immune system is to protect the host from foreign substances. However, improper recognition of nanoparticles as foreign agents by the immune cells may result in a multi-level immune response against the nanoparticles and eventually lead to toxicity in the host and/or lack of therapeutic efficacy [58]. Therefore, covering the QDs with specific molecules can complicate its interaction with the immune system while covering the surface of the nanoparticles with human protein may cause greater biocompatibility of the material. The QDs may become invisible to the immune system and in this way to deceive them if their surface possesses the specific HSA antigen.

A current imaging techniques like X-ray, computed tomography, or ultrasound are very important for the cancer diagnosis, but they have two major limitations. They do not have sufficient sensitivity (especially in the case of small numbers of malignant cells) and sufficient specificity. Quantum dots imaging probes provide the potential to fulfill the requirements for cancer cell imaging [59], and searching for nanoparticles with optimal properties for bioimaging and diagnostic applications is still widely pursued [60–63].

The human osteosarcoma cell line was selected to determine the interaction of the CdS, CdS:Co, and CdS:Mn QDs-HSA bionanocomplex with cancer cells. Osteosarcoma is a primary malignant bone tumor in adults, young people, and children. A 5-year survival rate among patients is between 50 and 63% [64]. The tumor is frequently localized in femur and tibia bones, but the cancer diagnosis is very difficult and often too ineffective. Researchers proved that osteosarcoma cells have numerous genetic mutations and other abnormalities, which additionally hinder effective diagnosis and treatment [65]. An early detection is particularly important because the tumor is prone to metastasize. It inhibits effective treatment in a later phase of the disease. Search for a new method in order to understand osteosarcoma cancer better and make more accurate diagnosis is still necessary.

Both types of pure CdS and CdS:Mn QDs do not penetrate into the living osteosarcoma cells. The fluorescence of QDs is not detected inside the cells. The emission of light is noticed only on the surface of cells which suggests that the QDs interact with cells and covered them. Only damaged or dead cells have a relatively higher uptake of the QDs, and fluorescence inside these cells is noticed. This suggests that pure CdS QDs can be used as a marker for the determination of vitality of the damaged cell.

To improve the diffusion through the cell membrane without cells modification, and increase the biocompatibility, the surface of nanoparticles should be modified by connecting some chemicals [66–68]. In the present study, the 134b osteosarcoma cells were fixed by methanol and permeabilized by Triton X-100, for improving QDs migration through the cell membrane. The fluorescence intensity of intracellular QDs was noticed after 10 min incubation and was stable during 24 h (the results obtained after 3, 6, 9, and 24 h incubation were not changed). However, cells under QDs traded could be imaged even after 30 days, the images are still clear and informative. The CdS and CdS:Mn QDs are recognized as strong cell fluorescent indicators, which can be used for the cells marking. The fluorescence of the QDs is strong and clearly visible as orange color in Fig. 14a. The Hoechst 33342 fluorescent dye was used as a standard for cell nucleus localization, and it is visible as blue color in Fig. 14b.

The QD-HSA bionanocomplex is recognized as a more biocompatible fluorescence material, which can be used for fluorescence analytical methods as a measuring probe. The QDs-HSA biocomplex fluorescence is recorded in the whole cell except the nucleus (Fig. 15), which is marked by a standard fluorescence dye–Hoechst 33342. However, the strongest signal was noticed around the nuclear membrane. It suggests that most of CdS:Co QDs-HSA bioconjugate are located on the surface of nuclear membrane and cannot penetrate it. Similar conclusions are also described by Kuo et al. [69]. The fluorescence intensity of intracellular QD-HSA bionanocomplex was noticed even after very short incubation (10 min) and stability during 24 h.

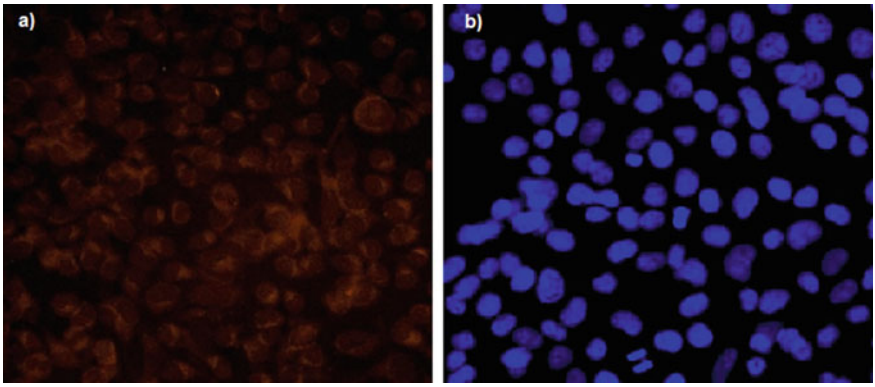

Fig. 14 Fluorescence imaging: **a** CdS:Mn QDs fluorescence inside the cells, **b** Hoechst 33342 fluorescent dye inside nucleus

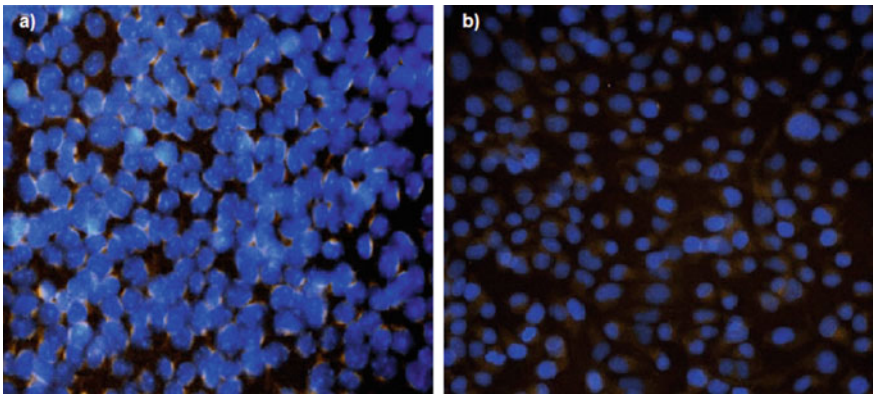

Fig. 15 143 b cells incubated with **a** CdS:Mn QDs-HSA (orange) and Hoechst 33342 (blue), **b** CdS:Co QDs-HAS (orange) and Hoechst 33342 (blue)

Additionally, cells treated with bioconjugate could be imaged even after 30 days. Under the same procedure, there was no detectable emission from the control cells without QDs and from the intercellular space in the case of samples under QDs-HSA biocomplexes treatment. Additionally, the morphology of the cells treated with defined concentrations of QDs and QDs-HSA biocomplexes under standard conditions was not changed, compared to the control. This indicates non-cytotoxic effect of the CdS:Co QDs-HSA bioconjugate in the case of presented bioimaging. More complicated system than the one described above is presented by Meng et al. [70] CdTe/ZnS quantum dots were conjugated with BSA and additionally, with folic acid (FA) for FA-BSA-QDs complex forming. According to the authors, this system can be used for monitoring cancer cells with overexpression of FA receptors such as human nasopharyngeal carcinoma cells.

The obtained results confirmed a good luminescence intensity and stability of the CdS:Co (CdS:Mn) QDs-HSA bioconjugates and could be used for marking and tracking other organelles or molecules, with additional biofunctionalization.

4 Conclusions

The addition of HSA to colloidal CdS-based DMSs QDs leads to a gradual decrease of optical density and broadening of exciton structure through biocomplex formation. The mechanism of photoluminescence quenching biocomplexes CdS, CdS:Co (CdS:Mn) QDs-HSA is static. Different parameters including binding constants (Kb), number of binding sites (n), quenching constants (K_{SV}), and bimolecular quenching rate constants (K_q) were calculated and the results revealed the formation of very stable complexes between HSA and CdS:Co (CdS:Mn) QDs in solution. The high biocompatibility and low toxicity as well as high stability of the CdS-based DMSs

QD-HSA biocomplex can be potentially employed for bioimaging osteosarcoma cells with minimal adverse effects.

The Faraday rotation study of biocomplexes CdS:Mn QDs-HSA indicates a high sensitivity and promising application of QDs CdS:Mn not only as fluorescent labels as well as effective magnetic field sensors (MRI) in the study in vitro and in vivo biological tissues.

References

1. G. Cao, *Nanostructures & Nanomaterials: Synthesis, Properties and Applications* (Imperial College Press, London, 2004). https://doi.org/10.1021/ja0409457
2. J.F. Donegan, Y.P. Rakovich, *Cadmium Telluride Quantum Dots. Advances and Applications.* (Taylor and Francis Group, New York, 2013). https://doi.org/10.1201/b16378
3. M.J. Bruchez, M. Morrone, P. Gin, S. Weiss, A.P. Alivisatos, Semiconductor nanocrystals as fluorescent biological labels. Science **281**(5385), 2013 (1998). https://doi.org/10.1126/science.281.5385.2013
4. W.C.W. Chan, S. Nie, Quantum dot bioconjugates for ultrasensitive nonisotopic detection. Science **281**(5385), 2016 (1998). https://doi.org/10.1126/science.281.5385.2016
5. J.B. Blanco-Canosa, M. Wu, K. Susumu, E. Petryayeva, T.L. Jennings, P.E. Dawson, W.R. Algar, I.L. Medintz, Recent progress in the bioconjugation of quantum dots. Coord. Chem. Rev. **263–264**, 101 (2014). https://doi.org/10.1016/j.ccr.2013.08.030
6. M. Diaz-Gonzalez, A. Escosura-Muniz, M. Fernandez-Arguelles, F. Alonso, J. Costa-Fernandez, Quantum dot bioconjugates for diagnostic applications. Top. Curr. Chem. **378**(2), 35 (2020). https://doi.org/10.1007/s41061-020-0296-6
7. H. Gil, Th.W. Price, K. Chelani, J. Bouillard, S. Calaminus, G. Stasiuk, NIR-quantum dots in biomedical imaging and their future. Science **24**, 102189 (2021). https://doi.org/10.1016/j.isci.2021.102189
8. S. Pandey, D. Bodas, High-quality quantum dots for multiplexed bioimaging: a critical review. Adv. Colloid Interface Sci. **278**, 102137 (2020). https://doi.org/10.1016/j.cis.2020.102137
9. A.L. Rogach, *Semiconductor Nanocrystal Quantum Dots: Synthesis, Assembly, Spectroscopy and Applications* (Springer-Verlag/Wien, 2008). https://doi.org/10.1007/978-3-211-75237-1
10. I.L. Medintz, H.T. Uyeda, E.R. Goldman, H. Mattoussi, Quantum dot bioconjugates for imaging, labelling and sensing. Nat. Mater. **4**(6), 435 (2005). https://doi.org/10.1038/nmat1390
11. T.M. Samir, M.M.H. Mansour, S.C. Kazmierczak, H.M.E. Azzazy, Quantum dots: heralding a brighter future for clinical diagnostics. Nanomedicine **7**(11), 1755 (2012). https://doi.org/10.2217/nnm.12.147
12. J. Peng, F. Hai, L. Tao, C. Lin, A. Shiyun, Probing the interaction of flower-like CdSe nanostructure particles targeted to bovine serum albumin using spectroscopic techniques. J. Lumin. **131**, 1724 (2011). https://doi.org/10.1016/j.jlumin.2011.03.070
13. D. Chen, J. Liu, X.-F. Yu, M. He, X.-F. Pei, Z.-Y. Tang, Q.-Q. Wang, D.-W. Pang, Y. Li, The biocompatibility of quantum dot probes used for the targeted imaging of hepatocellular carcinoma metastasis. Biomaterials **29**, 4170 (2008). https://doi.org/10.1016/j.biomaterials.2008.07.025
14. J.A. Gaj, J. Kossut, *Introduction to the Physics of Diluted Magnetic Semiconductors* (Springer Series in Materials Science, 2010). https://doi.org/10.1007/978-3-642-15856-8
15. D.D. Awschalom, D. Loss, N. Samarth, *Semiconductor Spintronics and Quantum Computation* (Springer-Verlag, Berlin, Heilderberg, 2002). https://doi.org/10.1007/978-3-662-05003-3
16. M. Ghali, Static quenching of bovine serum albumin conjugated with small size CdS nanocrystalline quantum dots. J. Lumin. **130**, 1254 (2010). https://doi.org/10.1016/j.jlumin.2010.02.034

17. A. Soldado, L. Cid Barrio, M. Diaz-Gonzalez, A. de la Escosura-Muniz, J.M. Costa-Fernandez, Advances in quantum dots as diagnostic tools. Adv. Clin. Chem. **107,** 1 (2022). https://doi.org/10.1016/bs.acc.2021.07.001
18. J. Wang, L. Liu, B. Liu, Y. Guo, Y. Zhang, R. Xu, S. Wang, X. Zhang, Spectroscopic analyses on sonocatalytic damage to bovine serum albumin (BSA) induced by ZnO/hydroxylapatite (ZnO/HA) composite under ultrasonic irradiation. Spectrochimica Acta Part A Mol. Biomol. Spectrosc. **75**(1), 366 (2010). https://doi.org/10.1016/j.saa.2012.03.076
19. S. Chinnathambi, A.N. Hanagata, Biocompatible CdSe/ZnS quantum dot micelles for long-term cell imaging without alteration to the native structure of the blood plasma protein human serum albumin. RSC Adv. **7**, 2392 (2017). https://doi.org/10.1039/C6RA26592H
20. H. Ehzari, M. Safari, M. Samimi, M. Shamsipur, M.B. Gholivand, A highly sensitive electrochemical biosensor for chlorpyrifos pesticide detection using the adsorbent nanomatrix contain the human serum albumin and the Pd:CdTe quantum dots. Microchem. J. **179**, 107424 (2022). https://doi.org/10.1016/j.microc.2022.107424
21. R. Wojnarowska-Nowak, J. Polit, A. Zieba, I.D. Stolyarchuk, S. Nowak, M. Romerowicz-Misielak, E.M. Sheregii, Colloidal quantum dots conjugated with human serum albumin—interactions and bioimaging properties. Opto Electron. Reviewer **25**, 137 (2017)
22. M. Otagiri, V. Tuan Giam Chuang Albumin, *Medicine: Pathological and Clinical Applications* (Springer, 2016). https://doi.org/10.1007/978-981-10-2116-9
23. S.J. Rosenthal, J.C. Chang, O. Kovtun, J.R. McBride, I.D. Tomlinson, Biocompatible quantum dots for biological applications. Chem. Biol. **18**, 10 (2011). https://doi.org/10.1016/j.chembiol.2010.11.013
24. J. Gburek, K. Gołab, K. Juszczynska, Renal catabolism of albumin—current views and controversies. Postępy Higieny i Medycyny Doświadczalnej **65**, 668 (2011). https://doi.org/10.5604/17322693.964329
25. A. Miller, W.W. Jedrzejczak, Albumina—funkcje biologiczne i znaczenie kliniczne, Postępy Higieny i Medycyny Doświadczalnej **55**, 17 (2001). https://pubmed.ncbi.nlm.nih.gov/11355530/
26. C.H. Park, T. Maack, Albumin absorption and catabolism by isolated perfused proximal convoluted tubules of the rabbit. J. Clin. Invest. **73**, 767 (1984). https://doi.org/10.1172/JCI111270
27. A.I. Savchuk, I.D. Stolyarchuk, P.M. Grygoryshyn, O.P. Antonyuk, T.A. Savchuk, Interaction of human serum albumin with CdTe quantum dots probed by optical spectroscopy methods. Proc. SPIE **9066**, 906618 (2013) (6 p). https://doi.org/10.1117/12.2048905
28. I.D. Stolyarchuk, R. Wojnarowska-Nowak, J. Polit, E.M. Sheregii, S. Nowak, M. Romerowicz-Misielak, CdTe quantum dots and their bioconjugate with human serum albumin for fluorescence imaging. Phys. Chem. Solid State **18**, 166 (2017). http://lib.pnu.edu.ua:8080/bitstream/123456789/929/1/2291-6510-1-PB.pdf
29. R. Wojnarowska-Nowak, J. Polit, A. Zieba, I.D. Stolyarchuk, S. Nowak, M. Romerowicz-Misielak, E.M. Sheregii, Synthesis and characterization of human serum albumin passivated CdTe Nanocrystallites as fluorescent probe. Micro Nano Lett. **13**(3), 326 (2018). https://doi.org/10.1049/mnl.2017.0054
30. O.V. Kuzyk, I.D. Stolyarchuk, O.O. Dan'kiv, R.M. Peleshchak, Baric properties of quantum dots of the type of core (CdSe)—multilayer shell (ZnS/CdS/ZnS) for biomedical applications. Appl. Nanosci. (2022). https://doi.org/10.1007/s13204-022-02604-5
31. A.I. Savchuk, I.D. Stolyarchuk, T.A. Savchuk, M.M. Smolinsky, O.A. Shporta, L.M. Shynkura, Monitoring of incorporation of magnetic ions into II–VI semiconductor nanocrystals by optical and magneto-optical spectroscopy. Thin Solid Films **541**, 79 (2013). https://doi.org/10.1016/j.tsf.2012.10.127
32. A. Arnaud, F. Silveira, E.M. Frins, A. Dubra, C.D. Perciante, J.A. Ferrari, Precision synchronous polarimeter with linear response for the measurement of small rotation angles. Appl. Opt. **39**, 2601 (2000). https://doi.org/10.1364/ao.39.002601
33. M.–H. Kim, V. Kurz, G. Achas, C.T. Ellis, J. Cerne, Measurements of the infrared complex Faraday angle in semiconductors and isolators. J. Opt. Soc. Am. B **28**, 199 (2011). https://opg.optica.org/josab/abstract.cfm?uri=josab-28-2-199

34. S.V. Melnichuk, A.I. Savchuk, D.N. Trifonenko, Contribution of intracentre transitions to the Faraday effect in cobalt-containing semimagnetic semiconductors. Phys. Solid St. **38**, 731 (1996). https://www.researchgate.net/publication/234180106_Contribution_of_intracenter_transitions_to_the_Faraday_effect_in_cobalt-containing_semimagnetic_semiconductors
35. B. Nithyaja, K. Vishnu, S. Mathew, P. Radhakrishnan, V.P.N. Nampoori, Studies on CdS nanoparticles prepared in DNA and bovine serum albumin based biotemplates. J. Appl. Phys. **112**, 064704 (2012). https://doi.org/10.1063/1.4752750
36. Q. Xiao, S. Huang, W. Su, P. Li, J. Ma, F. Luo, Y. Liu, Systematically investigations of conformation and thermodynamics of HSA adsorbed to different sizes of CdTe quantum dots. Colloids Surf. B Biointerfaces **102**, 76 (2013). https://doi.org/10.1016/j.colsurfb.2012.08.028
37. D. Wu, Z. Chen, X. Liu, Study of the interaction between bovine serum albumin and ZnS quantum dots with spectroscopic techniques. Spectrochim. Acta A Mol. Biomol. Spectrosc. **84**, 178 (2011). https://doi.org/10.1016/j.saa.2011.09.027
38. J. Hemmateenejad, S. Yousefinejad, Interaction study of human serum albumin and ZnS nanoparticles using fluorescence spectrometry. J. Mol. Struct. **1037**, 317 (2013). https://doi.org/10.1016/j.molstruc.2013.01.009
39. A. Sulkowska, Interaction of drugs with bovine and human serum albumin. J. Mol. Struct. **614**, 227 (2002). https://doi.org/10.1016/S0022-2860(02)00256-9
40. P.N. Naik, S.T. Nandibewoor, S.A. Chimatadar, Non-covalent binding analysis of sulfamethoxazole to human serum albumin: fluorescence spectroscopy, UV–vis, FT-IR, voltammetric and molecular modeling. J. Pharm. Anal. **5**(3), 143 (2015). https://doi.org/10.1016/j.jpha.2015.01.003
41. E.A. Bhogale, N. Patel, J. Mariam, P.M. Dongre, A. Miotello, D.C. Kothari, Systematic investigation on the interaction of bovine serum albumin with ZnO nanoparticles using fluorescence spectroscopy. Colloids Surf. B Biointerfaces **102**, 257 (2013). https://doi.org/10.1016/j.colsurfb.2012.08.023
42. J.R. Lakowicz, *Principles of Fluorescence Spectroscopy* (Springer Science & Business Media, New York, 2006). https://doi.org/10.1007/978-0-387-46312-4
43. J. Liang, Y. Cheng, H. Han, Study on the interaction between bovine serum albumin and CdTe quantum dots with spectroscopic technique. J. Mol. Struct. **892**, 116 (2008). https://doi.org/10.1016/j.molstruc.2008.05.005
44. J.N. Tian, J.Q. Liu, W.Y. He, Z.D. Hu, X.J. Yao, X.G. Chen, Probing the binding of scutellarin to human serum albumin by circular dichroism, fluorescence spectroscopy, FTIR, and molecular modeling method. Biomacromol **5**, 1956 (2004). https://doi.org/10.1021/bm049668m
45. A. Barth, P.I. Haris, *Biological and Biomedical Infrared Spectroscopy* (IOS Press, Amsterdam, 2009). https://worldcat.org/title/608670799
46. A.I. Ivanov, R.G. Zhbankov, E.A. Korolenko, E.V. Korolik, L.A. Meleshchenko, M. Marchewka, H. Ratajczak, Infrared and Raman spectroscopic studies of the structure of human serum albumin under various ligand loads. J. Appl. Spectrosc. **60**, 399 (1994). https://doi.org/10.1007/BF02606317
47. J. Kong, S. Yu, Fourier transform infrared spectroscopic analysis of protein secondary structures. Acta Biochim. Biophys. Sinica **39**(8), 549 (2007). https://doi.org/10.1111/j.1745-7270.2007.00320.x
48. C. Ota, S. Noguchi, K. Tsumoto, The molecular interaction of a protein in highly concentrated solution investigated by Raman spectroscopy. Biopolymers **103**(4), 237 (2015). https://doi.org/10.1002/bip.22593
49. A.I. Savchuk, V.I. Fediv, I.D. Stolyarchuk, T.A. Savchuk, A. Perrone, Magneto-optical faraday effect in II-VI based semimagnetic semiconductor nanocrystals. Physica Status Solidi (c) **3**(4), 1160. https://doi.org/10.1002/pssc.200564628
50. A.I. Savchuk, I.D. Stolyarchuk, V.V. Makoviy, O.A. Savchuk, Magneto-optical Faraday rotation of semiconductor nanoparticles embedded in dielectric matrices. Appl. Opt. **53**(10), B22 (2014). https://doi.org/10.1364/AO.53.000B22
51. A. Perrone, A.I. Savchuk, H. De Rosa, I.D. Stolyarchuk, V.V. Makoviy, M.M. Smolinsky, O.A. Savchuk, Magnetic field sensing properties of diluted magnetic semiconductor based nanocomposites. Sens. Lett. **10**, 1 (2013). https://doi.org/10.1166/sl.2013.2783

52. W.C. Chan, D.J. Maxwell, X. Gao, Luminescent quantum dots for multiplexed biological detection and imaging. Curr. Opin. Biotechnol. **13**(1), 40 (2002). https://doi.org/10.1016/s0958-1669(02)00282-3
53. E.B. Voura, J.K. Jaiswal, H. Mattoussi, S.M. Simon, Tracking metastatic tumor cell extravasation with quantum dot nanocrystals and fluorescence emission-scanning microscopy. Nat. Med. **10**(9), 993 (2004). https://doi.org/10.1038/nm1096
54. L.-W. Liu, S.-Y. Hu, Y. Pan, J.-Q. Zhang, Y.-S. Feng, X.-H. Zhang, Optimizing the synthesis of CdS/ZnS core/shell semiconductor nanocrystals for bioimaging applications. Beilstein J. Nanotechnol. **5**, 919 (2014). https://doi.org/10.3762/bjnano.5.105
55. S. Zheng, J.-Y. Chen, J.-Y. Wang, L.-W. Zhou, Q. Peng, Effects of cell cycle on theuptake of water soluble quantum dots by cells. J. Appl. Phys. **110**, 124701 (2011). https://doi.org/10.1063/1.3669364
56. H. Mansur, A. Mansur, J. Gonzales, Protein-semiconductor quantum dot hybrids for biomedical applications. Phys. Status Solidi **96**, 1435 (2012). https://doi.org/10.1002/pssc.201100251
57. V. Poderys, M. Matulionyte, A. Selskis, R. Rotomskis, Interaction ofwater-soluble CdTe quantum dots with bovine serum albumin. Nanoscale Res. Lett. **6**(9), 1 (2011). https://doi.org/10.1007/s11671-010-9740-9
58. Q. Jiao, L. Li, Q. Mu, Q. Zhang, Immunomodulation of nanoparticles in nanomedicine applications. BioMed Res. Int. **2014**, 1 (2014). https://doi.org/10.1155/2014/426028
59. H. Zhang, D. Yee, C. Wang, Quantum dots for cancer diagnosis and therapy: biological and clinical perspectives. Nanomedicine **3**(1), 83 (2008). https://doi.org/10.2217/17435889.3.1.83
60. O. Mashinchian, M. Johari-Ahar, B. Ghaemi, M. Rashidi, J. Barar, Y. Omidi, Impacts of quantum dots in molecular detection and bioimaging of cancer. Bioimpacts **4**(3), 149 (2014). https://doi.org/10.15171/bi.2014.008
61. M.R. Rodriguez-Torres, C. Velez, B. Zayas, O. Rivera, Z. Arslan, M.N. Gonzalez-Vega, D. Diaz-Diestra, J. Beltran-Huarac, G. Morell, O.M. Primera-Pedrozo, Cyto-compatibility of direct water synthesized cadmium selenide quantum dots in colo-205 cells. J. Nanopart. Res. **17**(266), 1 (2015). https://doi.org/10.1007/s11051-015-3064-8
62. M. Vibin, R. Vinayakan, A. John, V. Raji, N.S. Rejiya, A. Abraham, Cytotoxicity and fluorescence studies of silica-coated CdSe quantum dots for bioimaging applications. J. Nanopart. Res. **13**(6), 2587 (2011). https://doi.org/10.1007/s11051-010-0151-8
63. B.J. Jankiewicz, D. Jamiola, J. Choma, M. Jaroniec, Silica–metal core–shell nanostructures. Adv. Colloid Interface Sci. **170**, 28 (2012). https://doi.org/10.1007/s11051-010-0151-8
64. H.H. Luu, Q. Kang, J. Kyung Park, W. Si, Q. Luo, W. Jiang, H. Yin, A.G. Montag, M.A. Simon, T.D. Peabody, R.C. Haydon, C.W. Rinker-Schaeffer, T.C. He, An orthotopic model of human osteosarcoma growth and spontaneous pulmonary metastasis. ClinExp Metastasis **22**(4), 319 (2005). https://doi.org/10.1007/s10585-005-0365-9
65. C. Cappadone, C. Stefanelli, E. Malucelli, M. Zini, C. Onofrillo, A. Locatelli, M. Rambaldi, A. Sargenti, L. Merolle, G. Farruggia, A. Graziadio, L. Montanaro, S. Iotti, p53-dependent and p53-independent anticancer activity of a new indole derivative in human osteosarcoma cells. Biochem. Biophys. Res. Commun. **467**(2), 348 (2015). https://doi.org/10.1016/j.bbrc.2015.09.154
66. J. Liu, R. Hu, J. Liu, B. Zhang, Y. Wang, X. Liu, W.C. Law, L. Liu, L. Ye, K.T. Yong, Cytotoxicity assessment of functionalized CdSe, CdTe and InP quantum dots in two human cancer cell models. Mater. Sci. Eng. C Mater. Biol. Appl. **57**, 222 (2015). https://doi.org/10.1016/j.msec.2015.07.044
67. M. Johari-Ahar, J. Barar, A.M. Alizadeh, S. Davaran, Y. Omidi, M.R. Rashidi, Methotrexate-conjugated quantum dots: synthesis, characterisation and cytotoxicity in drug resistant cancer cells. J. Drug Target. **15**, 1 (2015). https://doi.org/10.3109/1061186X.2015.1058801
68. A.A. Mansur, S.M. de Carvalho, H.S. Mansur, Bioengineered quantum dot/chitosan-tripeptide nanoconjugates for targeting the receptors of cancer cells. Int. J. Biol. Macromol. **82**, 780 (2016). https://doi.org/10.1016/j.ijbiomac.2015.10.047
69. K.W. Kuo, T.H. Chen, W.T. Kuo, H.Y. Huang, H.Y. Lo, Y.Y. Huang, Cell uptake and intracellular visualization using quantum dots or nuclear localization signal-modified quantum dots with

gold nanoparticles as quenchers. J. Nanosci. Nanotechnol. **10**(7), 4173 (2010). https://doi.org/10.1166/jnn.2010.2193

70. H. Meng, J.Y. Chen, L. Mi, P.N. Wang, M.Y. Ge, Y. Yue, N. Dai, Conjugates of folic acids with BSA-coated quantum dots for cancer cell targeting and imaging by single-photon and two-photon excitation. J. Biol. Inorg. Chem. **16**(1), 117 (2011). https://doi.org/10.1007/s00775-010-0709-z
71. Y. Du, K. Rajamanickam, T.R. Stumpf, Y. Qin, H. McCulloch, X. Yang, J. Zhang, E. Tsai, X. Cao, Paramagnetic quantum dots as multimodal probes for potential applications in nervous system imaging. J. Inorg. Organomet. Polym. Mater. **28**, 1 (2018). https://doi.org/10.1007/s10904-017-0766-7
72. S.A. Wolf, D.D. Awschalom, S.A. Buhrman, J.M. Daughton, S. von Molnár, M.L. Roukes, A.Y. Chtchelkanova, D.M. Treger, Spintronics: a spin-based electronics vision for the future. Science **294**(5546), 1488 (2001). https://doi.org/10.1126/science.1065389